Electromagnetic Field Interaction between Overhead High Voltage Power Transmission Line and Buried Utility Pipeline

K. N. Ramli[1, 2], Raed A. Abd-Alhameed[1], H. I. Hraga[1], D. T. W. Liang[1], and P. S. Excell[3]

[1]Mobile and Satellite Communications Research Centre, University of Bradford, Bradford BD7 1DP, UK
[2]Faculty of Electrical and Electronic Engineering, Universiti Tun Hussein Onn Malaysia (UTHM)
Parit Raja 86400, Batu Pahat, Johor, Malaysia
[3]Centre for Applied Internet Research, Glyndwr University, Wrexham LL11 2AW, Wales, UK

Abstract— This work presents the development of a new approach of modelling the source excitation and the penetration of structures by continuous propagating electromagnetic (EM) plane waves. The technique incorporates the solution of time-dependent Maxwell's equations and the initial value problem as the structures are illuminated by the plane waves. The propagation of waves from source excitation is simulated by solving a finite-difference Maxwell's equation in the time domain. Subgridding method is used to condense the lattice at the point of interest locally for observing field distribution in high resolution. The computational burden due to huge number of time steps has been eased by employing quasi-static approach. An example of induced EM fields near an underground pipeline runs parallel to a 132 kV overhead power transmission line (OHTL) has been presented which paves the way in the development of new approach of EM fields interaction modelling.

1. INTRODUCTION

Finite-difference based on integral formulation [1, 2] has been used in the published literature to improve the accuracy of the finite-difference formulation near the surfaces that does not fit in the lattice or small objects such as thin wires which alter the electromagnetic field distribution significantly. In this case, analytical expressions have been established to express the field near a particular object for precise evaluation of the integrals. Many researchers in the past have been prompted to investigate the subgridding technique as an approach to circumventing the problem [3, 4]. The first advantage of using this method is simple to implement for complicated dielectric or metal structures due to arbitrary electrical parameters can be assigned to each cell on the grid. Second, the entire computational spaces need not to be discretised with a fine grid as it puts unreasonable burden on the computer processing time. The ultimate objective of research in this area is to access the appropriateness of the method in determining the amount of EM penetrating fields between OHTL and underground utility pipeline. The aim of the present work is to develop the general code for solving the electric and magnetic fields within arbitrary metal or dielectric structures, while maintaining a boundary of uncertainty low reflection level in two-dimensional approach.

FDTD technique has been well known over the years of its strength with robust simulation technique for transient electromagnetic interactions. In this research work, two-dimensional FDTD technique is used with subgridding to model the utility pipeline and the overhead high voltage power transmission line. FDTD technique has been applied to the high voltage power transmission line analysis in the published literature. Dedkova and Kriz [5] proposed a new effective approach to evaluate the distribution of voltage and current along the nonlinear transmission line by using FDTD method. An improved technique was proposed by Tang et al. [6] to calculate the transient inductive interference in underground metallic pipelines due to a fault in nearby power lines. The frequency-dependent problem in the analysis of transient interference was solved in phase domain based on FDTD method. Lu and Cui [7] used FDTD method to calculate the wave processes of voltage and current distributed along the three-phase 500 kV busbars and the power lines without load in the substation of multi-conductor transmission lines (MTL). The iterative formulas were presented to determine the boundary conditions at the node of the branches. The work was extended to transmission line network and non-uniform line [8].

2. METHOD

Figure 1 depicts the cross section and the dimension of a common corridor in which a buried utility pipeline runs parallel to a 132 kV overhead power transmission line. The height from the ground to the bottom conductors was 15 m. The overhead ground wire was located at the top of the tower. In this case, the height to the earth surface is 27 m. The phase conductors for the bottom, middle and

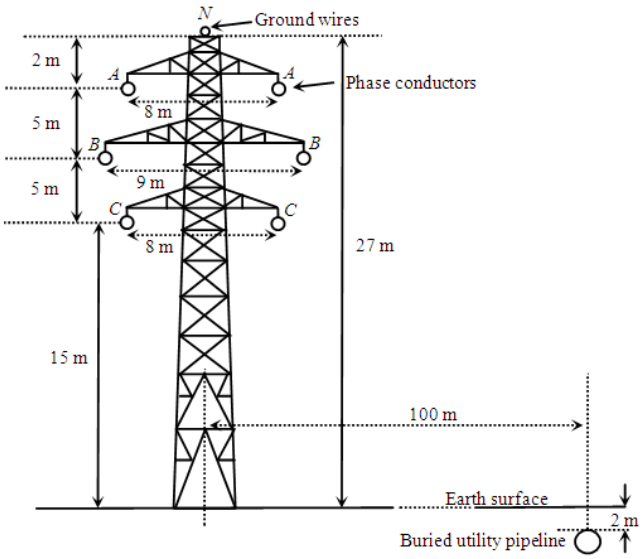

Figure 1: Outline of standard circuit 132 kV steel lattice transmission high voltage suspension towers (not to scale).

top were collocated horizontally with a separation of 4.0 m, 4.5 m and 4.0 m respectively between two adjacent conductors. The three phase steel lattice transmission high voltage suspension tower was designed with 6 cables. These cables were used as the source signal which propagates inside the problem space. Each of the 2 cables carries the same phase of the AC current. The simulation was carried out using the quasi-static FDTD at the transformed intermediate frequency of 460 kHz and the overall model was then transformed back to the proposed lower frequency of 50 Hz. Quasi-static approximation was obtained by using the expression [9–11]:

$$\vec{E}(f) = \left(\frac{\omega}{\omega'}\right)\left[\frac{\sigma'(f') + j\omega'\varepsilon(f')}{\sigma(f) + j\omega\varepsilon(f)}\right]\vec{E}'(f') \tag{1}$$

where $\vec{E}(f)$ is the resultant internal electric field (V/m), $\vec{E}'(f')$ is the scaling internal electric field (V/m), f is the frequency of interest (Hz), f' is the scaling frequency (Hz), ω is the angular frequency of interest (s^{-1}), ω' is the scaling angular frequency (s^{-1}), σ is the conductivity of the object (S/m), and σ' is the scaling conductivity of the object (S/m). By assuming $\omega\varepsilon(f) \ll \sigma(f)$ and $\omega'\varepsilon'(f' \ll \sigma'(f')$, then Equation (1) can be approximated as follows [9–11]:

$$\vec{E}(f) \cong \left[\frac{f\sigma'(f')}{f'\sigma(f)}\right]\vec{E}'(f') \tag{2}$$

Sinusoidal wave excitation of 460 kHz ($\lambda = 652.17$ m) was applied at each of the power transmission line cables. The pipeline was separated at a distance of 100 m from the steel lattice suspension towers and buried 2 m beneath the surface of the earth. The soil in the common corridor was designed to be inhomogeneous. The computational region at the coarse grids was discretised at a spatial resolution of 2,609 cells per wavelength ($\Delta y = \Delta z = 25$ cm). Subgridding involves local mesh refinement in the pipeline and some part of the ground in order to determine the propagation of the waves inside that area while observing the change in the fields. The computational space for the main region was 521 cells ×145 cells (130.25 m×36.25 m). The computational space for subgrid area was 10 cells ×10 cells. The ratio of the coarse to the fine grids was 4 : 1.

3. SIMULATION RESULTS

Subgrid technique was validated by illustrating example in Fig. 2. The problem space was excited by sinusoidal wave source at 1800 MHz. The fields at the same point without subgrid (Fig. 2(a)) and with subgrid (Fig. 2(b)) were observed and compared. In addition, they were found to be identical to each other as depicted in Fig. 3.

The computation efforts can be reduced using quasi-static method due to the largest computational size was less than 0.2λ. The simulation was carried out by assuming normal condition

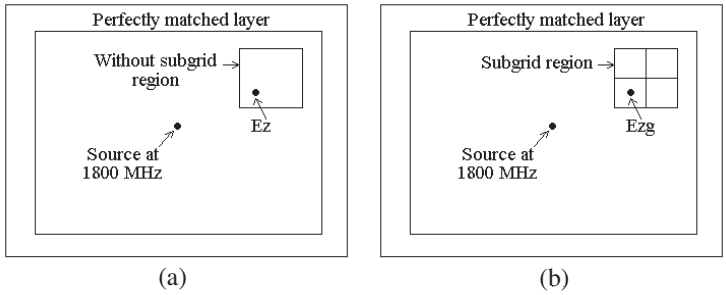

Figure 2: Problem space: (a) without subgrid, (b) with subgrid.

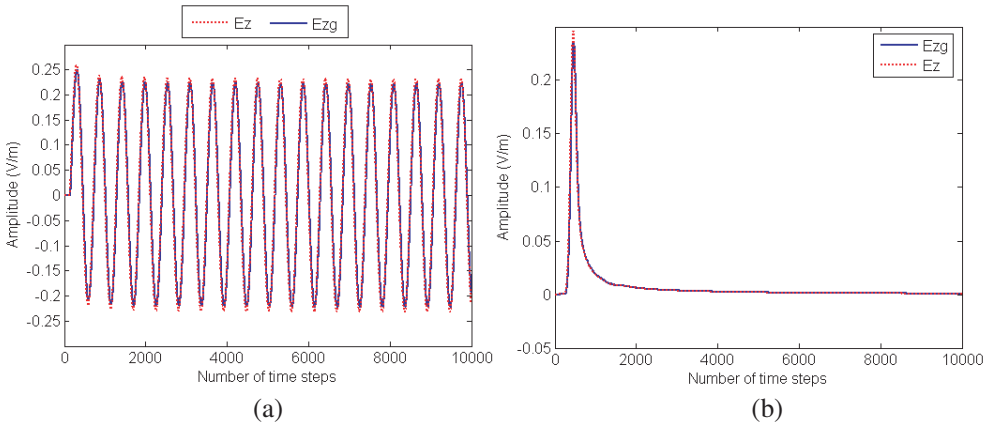

Figure 3: The electric field at one point without subgrid (E_z) and with subgrid (E_{zg}): (a) when sinusoidal wave was excited, (b) when gaussian pulse was excited.

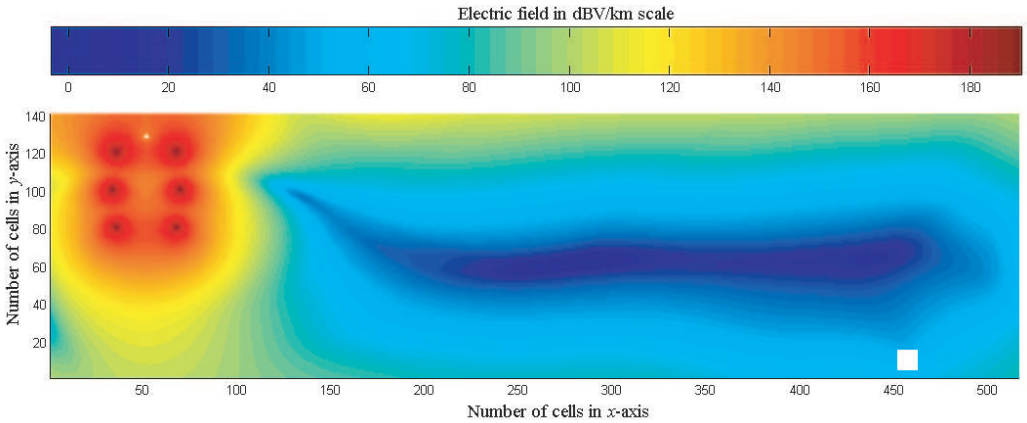

Figure 4: The electric field E_z distribution in the main FDTD grid.

of OHTL. Fig. 4 illustrates the electric field distribution in the main FDTD grid. The EM wave propagates from the 6 cables of the suspension tower to the surrounding area of air, ground and the pipeline. It varies from 1.0 V/km (0 dBV/km) to 1.78×10^9 V/km (185 dBV/km). The fields inside the metallic pipeline were found to be zero as depicted in Fig. 5(a) due to the excess electrons at the surface of the metal preventing any incoming propagating waves from penetrating the pipeline. The electric field distribution surrounding the pipeline alters from 3.16 V/km (10 dBV/km) to 1.0×10^3 V/km (60 dBV/km). Some of the waves were reflected back to the surface of the ground thus producing induced EM fields as shown in Fig. 5(b). The results were verified by comparing them with [12] which shows good agreements. Phase imbalance in the line may be produced due to the difference in the relative distance of each phase from the nearby pipeline. Under fault condition, the currents on the faulty phases of transmission lines were high. This in turn will induce AC voltage on the pipeline and create shock hazard rather than corrosion.

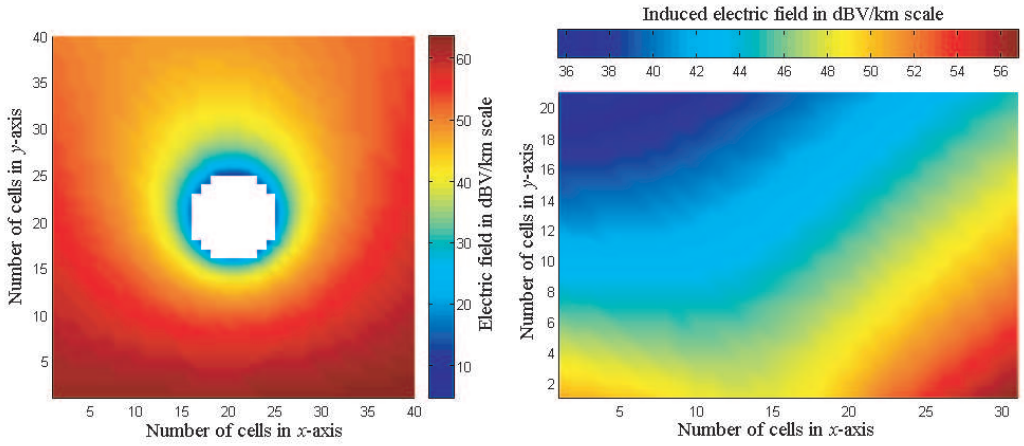

(a) (b)

Figure 5: (a) The electric field E_{zg} distribution in the subgrid section. (b) The induced electric field E_z at 1.75 m above pipeline.

4. CONCLUSIONS

An approach to model the interaction between overhead transmission lines and buried utility pipeline at power-line frequency has been presented. This uses the FDTD technique for the whole structure of the problem combined with subgridding method at the object of interest. The computational burden due to huge number of time steps in the order of tens of millions has been eased to tens of thousands by employing the method called quasi-static approach. The use of inhomogeneous soil in the common corridor permits a non-trivial proximity region of authentic ground properties to be simulated. Profound investigation of the interaction between electromagnetic fields and natural or utility arrangement with different electrical characteristics at different level of spatial resolution can be assisted by such tools. The combination of frequency scaling FDTD subgridding approach with arbitrary inhomogeneous soil element model paves the way in the development of new approach of EM fields interaction modelling.

ACKNOWLEDGMENT

The financial support from Ministry of Higher Education Malaysia and Universiti Tun Hussein Onn Malaysia (UTHM) is gratefully acknowledged.

REFERENCES

1. Taflove, A. and S. C. Hagness, *Computational Electrodynamics: The Finite-Difference Time-Domain Method*, 3rd Edition, Artech House, Boston, 2005.
2. Shreim, A. M. and M. F. Hadi, "Integral PML absorbing boundary conditions for the high-order M24 FDTD algorithm," *Progress In Electromagnetics Research*, Vol. 76, 141–152, 2007.
3. Ramli, K. N. and R. A. Abd-Alhameed, "Modelling of complex electromagnetic problems using FDTD subgridding methods," *9th Informatics Workshop for Research Students*, 200–201, University of Bradford, UK, 2008.
4. Wang, S. M., F. L. Teixeira, R. Lee, and J. F. Lee, "Optimization of subgridding schemes for FDTD," *IEEE Microwave and Wireless Components Letters*, Vol. 12, 223–225, 2002.
5. Dedkova, J. and T. Kritz, "FDTD analysis of a nonlinear transmission line," *Proceedings of Progress In Electromagnetics Research Symposium*, 282–285, Beijing, China, 2009.
6. Tang, J., X. Cui, L. Qi, T. Lu, L. Li, P. Zhu, G. Yang, and W. Zhang, "Analysis of transient inductive interference in underground pipelines due to faults on nearby power lines," *COMPEL: The International Journal for Computation and Mathematics in Electrical and Electronic Engineering*, Vol. 26, 1346–1363, 2007.
7. Lu, T. and X. Cui, "Transient analysis of wave processes for multi-conductor transmission lines with branches using FDTD," *IEEE International Symposium on Electromagnetic Compatibility*, Vol. 2, 699–703, 2000.
8. Lu, T., L. Qi, J. Li, and X. Cui, "Application of multi-conductor transmission lines on the transient analysis in power substation," *Asia-Pacific Conference on Environmental Electromagnetics*, 198–201, 2003.

9. Guy, A. W., S. Davidow, G. Y. Yang, and C. K. Chou, "Determination of electric current distributions in animals and humans exposed to a uniform 60-Hz high-intensity electric field," *Bioelectromagnetics*, Vol. 3, 47–71, 1982.
10. Golestani-Rad, L., B. Elahi, and J. Rashed-Mohassel, "Investigating the effects of external fields polarization on the coupling of pure magnetic waves in the human body in very low frequencies," *BioMagnetic Research and Technology*, Vol. 5, 1–5, 2007.
11. Gandhi, O. P. and J. Chen, "Numerical dosimetry at power-line frequencies using anatomically based model," *Bioelectromagnetics*, Vol. 13, 43–60, 1992.
12. Amer, G. M., "Novel technique to calculate the effect of electromagnetic field of H.V.T.L. on the metallic pipelines by using EMTP program," *18th International Conference and Exhibition on Electricity Distribution (CIRED)*, 1–5, Turin, Italy, 2005.

Multimode Asymmetrical Optical Power Splitter Utilizing Hollow Structured-waveguide

M. Kamil Abd-Rahman[1], **N. Syafiqah Mohamed-Kassim**[1], **A. Annuar Ehsan**[2], **and M. H. M. Yusoff**[1]

[1]Faculty of Applied Sciences, Universiti Teknologi MARA, Shah Alam 40450, Malaysia
[2]Institute of Microengineering and Nanoelectronics, Universiti Kebangsaan Malaysia Bangi, Selangor, Malaysia

Abstract— A novel design of multimode asymmetric hollow Y-junction optical power-splitter is proposed. This Y-junction simply utilizes the technique of shifting the axis of the arm of the output port so that the required power-splitting ratio can be obtained. The transmission characteristics were simulated using non-sequential ray-tracing technique. The hollow-waveguide structure has cross-section area of 1×1-mm^2 and was coated with 45-nm-thick reflective layer to enhance reflectivity in the waveguide channel. The waveguide splits the output power asymmetrically in the range of 93% to 7% with ±3% splitting-ratio accuracy. The insertion loss at the shift-port has a minimum value of 5.50 to a maximum of 16.38 dB for 0.00 to 0.90-mm shifting of the axis respectively. While the optical excess loss at the shift-port varies from 1.58 to 4.34 dB.

1. INTRODUCTION

Multimode fiber has useful applications in optical interconnects and local area network for short communication systems. It has the advantage over single mode fiber such as simplicity of fiber splicing and provides higher coupling efficiency to light sources. Deployment of multimode fiber system would not be possible without utilizing optical components such as optical power splitters, couplers and wavelength division multiplexer, which would realized the applications of planar waveguide technology at low cost. Symmetrical multimode Y-junction planar waveguide couplers have been comprehensively studied [1–5]. However, there was not much report on multimode asymmetrical planar waveguide power splitter of optimum design to satisfy the applications in multimode fiber system. R. Griffin et al. have reported that asymmetric coupling can be achieved by varying the size of the tap-off line or tap-line [6] and has presented a typical relationship between the tap-off ratio and waveguide tap width [7].

In this paper, we propose a novel design of multimode asymmetrical Y-junction coupler, which employs the technique of shift-axis at the arm of the output port to allow preferred portion of the optical power to propagate to the output port. Non-sequential ray tracing technique [8] was used to simulate and predict the transmission characteristics of the waveguide coupler.

2. WAVEGUIDE AND DESIGN

The basic configuration of the proposed asymmetrical Y-junction is shown in Figure 1. It consists of an input port P_1, a symmetry Y-junction in the middle section, shift-axis section at output port P_2 and a fix output port, P_3. The axis of the output arm is shifted in the range of 0.1 mm to 0.9 mm from the main axis of the output port P_2 to create various asymmetry output power ratios.

A 1×1-mm^2 square cross section of embedded core region of the 1×2 asymmetric coupler was designed on 20×20-mm^2 acrylic surface with refractive index of 1.49 using AutoCAD software as shown in Figure 2(a). The core region was coated with 45nm-thick layer of gold with refractive index of 0.47. Acrylic material is being used as the substrate because it has a robust characteristic which expected not to break down by thermal degradation, photodegradation or depolymerisation [8]. Gold coating was chosen to enhance the reflectivity of the waveguide. Infra-red reflects more than 95% of incident light in gold waveguide [9].

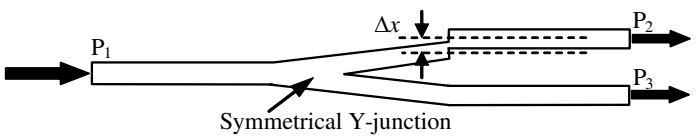

Figure 1: Basic configuration of proposed asymmetrical Y-junction splitter.

3. NON-SEQUENTIAL RAY TRACING

The modeling of the multimode waveguide coupler was performed using Zemax software, where the approach was based on non-sequential ray tracing technique. This technique was performed to predict the ray propagations along the waveguide and to determine the power outputs. Ray tracing has been referred to be the most suitable technique to analyze and simulate the highly multimode Y-junction waveguide [10]. The 2D layout performed on Zemax is shown in Figure 2(b).

Figures 3(a) and (b) show the surface image of the output light intensity at both output ports. Intensity at P_2 shows obviously lower light intensity compared to P_3 which has almost full output intensity. The cross-section through the center of output intensity gives almost Gaussian shape profile. The branching ratio and excess loss for the asymmetrical coupler was measured and is shown in Figure 4. At $\Delta x = 0\,\text{mm}$, there is 50 : 50 ($P_2 : P_3$) output coupling ratio and P_2 ratio gradually reduced to about 20% at $\Delta x = 0.9\,\text{mm}$. Concurrently, output power ratio at port P_3 increases to 90%.

The calculated branching ratio of the Y-junction coupler shows continuous output power variation and this would conveniently allow preferred branching ratio to be produced to within ±3% accuracy of the fabricated design. The excess loss of this system varies from about 0.04 to 2.58 dB as the port axis-shifting is increased. The increased in excess loss is generally due to deviated rays exiting at the juncture of the shift-axis port, which is dis-aligned from the route. Low excess loss of 0.04 dB is contributed by the high reflecting surface of the gold layer.

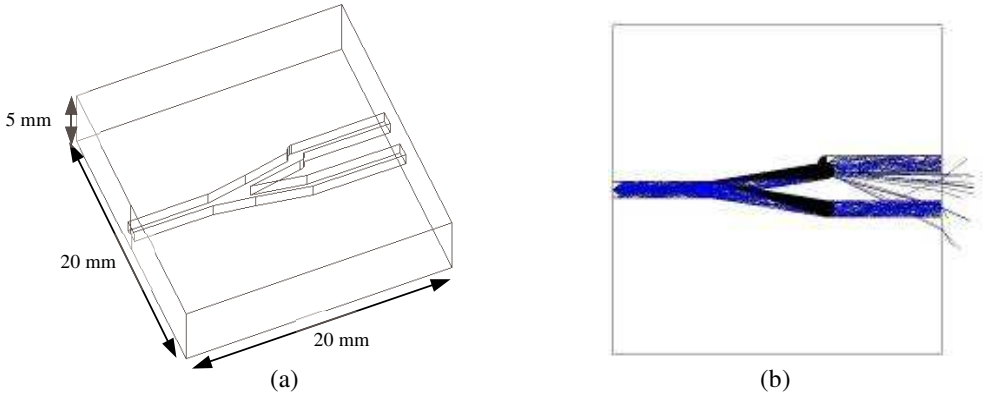

Figure 2: (a) 3D CAD design of asymmetrical Y-junction coupler, and (b) Ray propagation in the waveguide, where ray directed out of waveguide at P_2.

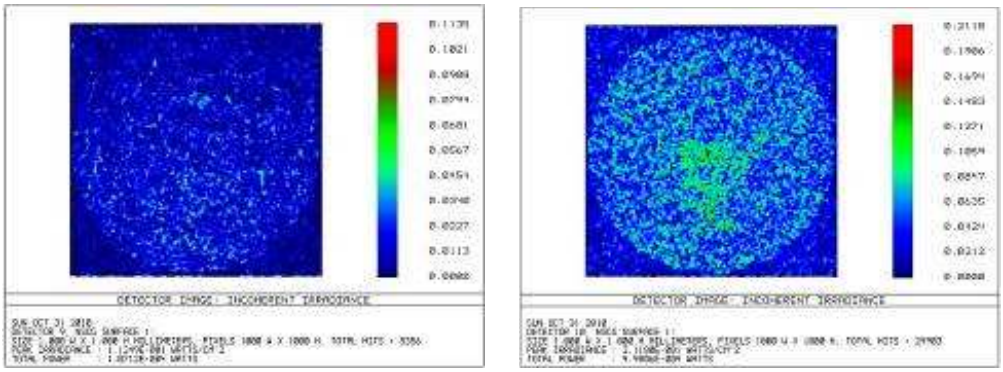

Figure 3: Image of the output intensity of the asymmetrical coupler at port (a) P_2 and (b) P_3.

4. EXPERIMENT AND MEASUREMENT

The $1 \times 1\text{-mm}^2$ cross-section waveguide designed using AutoCAD was engraved into $20 \times 20\text{-mm}^2$ acrylic substrate using Roland's EGX-400 desktop machine to allow 1 mm core diameter of plastic

optical fiber, POF to fit in firmly into it.

The parameters of the waveguide were configured in the CAD/CAM tool. The 5 mm-thick acrylic block was engraved using 1 mm diameter end mill with spindle rate of 30,000 rpm. A 45 nm-thick-layer of gold was coated into the waveguide using sputtering coating technique to enhance the reflectivity of the waveguide. Figure 5 shows one of the fabricated samples and experimental set up of power measurement. POFs of 1-mm diameter were inserted into the input and output ports for optical power measurements.

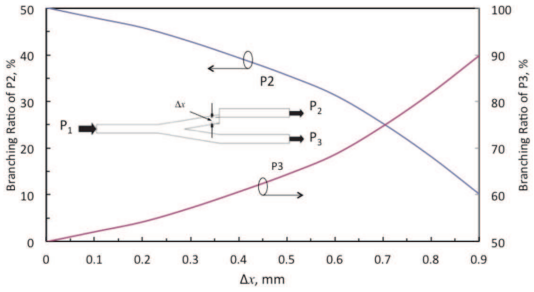

Figure 4: Simulation of asymmetric Y-junction coupler showing branching ratio against P_2 shift-axis Δx.

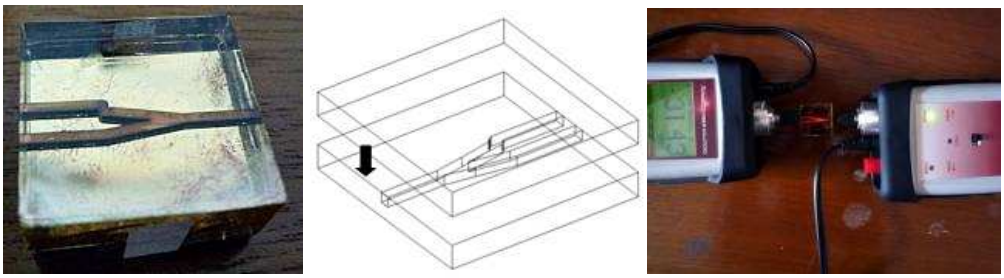

Figure 5: Coupler device (a) that has been fabricated and coated with gold (Picture was taken from the transparent bottom layer), (b) 3D diagram of engraved waveguide and topper, (c) test and measurement setup.

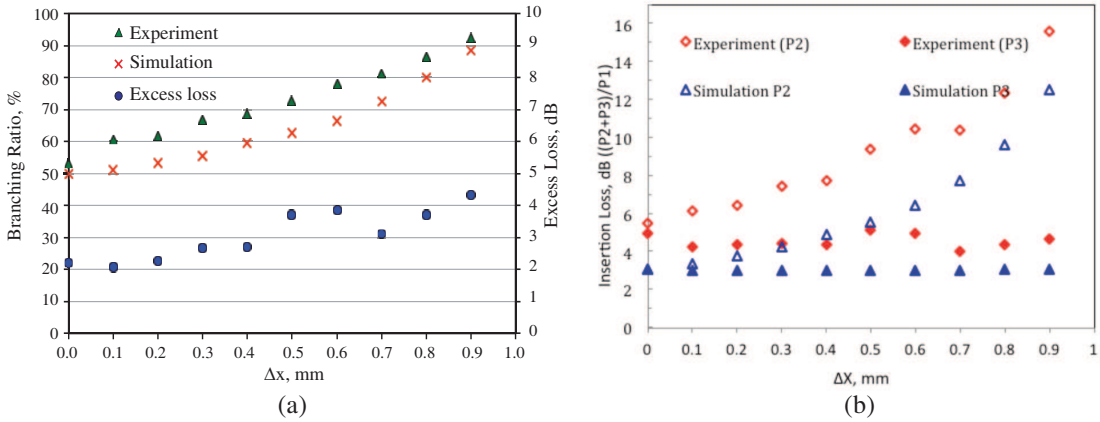

Figure 6: (a) Experimental results for fabricated asymmetric Y-branch coupler showing branching ratio and excess loss against Δx. (b) Insertion loss for experimental against insertion loss for calculated branching characteristics for proposed type of Y-junction coupler with shift-axis port.

Three sets of asymmetric coupler having ten different output splitting ratios were fabricated and measured. The output coupling ratios can be measured in the range of 3% to 97% with ±3% splitting ratio accuracy. The output power measurements of this device have been performed using

Advanced Fiber Solution FF-OS417 as a light source operating at a wavelength of 650 nm and optical power meter OM210. Experimental measurement set up is shown in Figure 5(c). The insertion loss at P_2 has a minimum value of 5.5 dB to a maximum of 16.38 dB at various shift-axis Δx.

Figure 6(a) shows experimental excess loss and measured branching characteristics of the fabricated and simulation of asymmetrical Y-junction coupler at 650 nm. As shown in the figure, the branching ratio has discrepancy of ±5% between the experimental and simulation result. The experimental data of the asymmetrical branching ratio matched close to the calculated values. The excess losses of the two ports vary corresponding to a branching ratio from 53% to 93%. The experimental data of the insertion loss (Figure 6(b)) is slightly higher than simulated data (≈1.74% to 2.21%). The discrepancies might be caused by waveguide imperfection and fabrication error.

5. CONCLUSIONS

The designing of multimode asymmetrical Y-junction coupler as optical component for optical power splitter utilizing hollow structured was demonstrated. These designs have been constructed using a combination structure of Y-junction and technique of shifting the port of the output arm, which these correspond to various port-shift of 0.9 mm to 0.1 mm with 0.1 mm interval. Experimental set up has been performed to measure the output performances of the model device which matched closely the results from non-sequential ray tracing simulation model. The experimental results have shown the output power split asymmetrically in the range of 93 to 7% with ±3% splitting ratio accuracy. The insertion loss obtained was from 5.50 to 16.38 dB. While the optical excess loss varies from 1.58 to 4.34 dB.

ACKNOWLEDGMENT

We acknowledge the Faculty of Applied Science, Universiti Teknologi MARA, Shah Alam for the facilities and to RMI (UiTM) and MOHE for the financial support through FRGS grant (FRGS/1/10/ST/UITM/02/02).

REFERENCES

1. Ehsan, A. A., S. Shaari, and M. K. A. Rahman, "Metal 1×2 plastic optical fiber (POF) spliter for video over POF system application," *Proceeding of Asia Communications and Photonics Conference (ACP 2009)*, Art. No. 5377587, Shanghai China, November 2–6, 2009.
2. Choon, G. C., P. H. Sang, C. K. Byeong, H. A. Seung, and Y. J. Myung, "Fabrication of large-core 1×16 optical power splitters in polymer using hot-embossing process," *Photonics Technology Letters*, Vol. 15, No. 6, June 2003.
3. Mizuno, H., O. Sugihara, S. Jordan, N. Okamoto, M. Ohama, and T. Kaino, "Replicated polymeric optical waveguide devices with large core connectable to plastic optical fiber using thermo-plastic and thermo-curable resins," *Journal of Lightwave Technology*, Vol. 24, No. 2, February 2006.
4. Kassim, N. S. M., A. A. Ehsan, M. H. M. Yusoff, and M. K. A. Rahman, "Fabrication and simulation of multimode symmetrical and asymmetrical Y-junction optical power splitters," *International Conference on Photonics 2010 (ICP 2010)*, Langkawi, Malaysia, July 2010.
5. Henry, W. M. and J. D. Love, "Asymmetric multimode Y-junction splitters," *Optical and Quantum Electronics*, Vol. 29, 379–392, 1997.
6. Ehsan, A. A., S. Shaari, M. K. Abd Rahman, and K. M. R. Kee Zainal Abidin, "Optical code generating device using $1 \times N$ asymmetric hollow waveguide couplers," *Acta Photonica Sinica*, 2008.
7. ZEMAX EE, Zemax Development Corporation, 2008.
8. Takagi, A., K. Jinguji, and M. Kawachi, "Design and fabrication of broad-band silica-based optical waveguide transition section," *IEEE Photonics Technology Letters*, Vol. 14, No. 8, 2002.
9. Loebich, O., "The optical properties of gold," *Gold Bull*, Vol. 5, No. 1, 2, 1972.
10. Bierhoff, T., W. Walbabenstein, A. Himmler, E. Griese, and G. Mrozynski, "Ray tracing technique and its verification for the analysis of highly multimode optical waveguides with rough surfaces," *IEEE Transactions on Magnetics*, Vol. 37, No. 5, 2001.

Localized Optical Modes and Enhancement of Some Optical Phenomena in Spiral Media

V. A. Belyakov
Landau Institute for Theoretical Physics, Russian Academy of Sciences
Chernogolovka, Moscow 142432, Russia

Abstract— Localized optical modes in spiral media are investigated. One of the most studied media of this kind are chiral liquid crystals (CLC). Because the CLCs demonstrate common for all spiral media optical properties the studying of the problem is performed for the certainty for CLCs. A brief survey of the recent experimental and theoretical results on the low threshold distributed feedback (DFB) lasing in chiral liquid crystals (CLC) and new original theoretical results on the localized optical modes in spiral media (edge (EM) and defect (DM) modes) are presented.

1. INTRODUCTION

Recently there was a very intense activity in the field of localized optical modes, in particular, edge (EM) and defect (DM) modes in chiral liquid crystals (CLC) mainly due to the possibilities to reach a low lasing threshold for the mirrorless distributed feedback (DFB) lasing [1–4] in chiral liquid crystals. The EM and DM existing as a localized electromagnetic eigen state with its frequency close to the forbidden band gap or in the forbidden band gap, respectively, were investigated initially in the periodic dielectric structures [5]. The corresponding EM and DM in chiral liquid crystals, and more general in spiral media, are very similar to the EM and DM in one-dimensional scalar periodic structures. They reveal abnormal reflection and transmission [1, 2] and allow DFB lasing at a low lasing threshold [3]. Almost all studies of the EM and DM in chiral and scalar periodic media were performed by means of a numerical analysis with the exceptions [6, 7], where the known exact analytical expression for the eigen modes propagating along the helix axes [8, 9] were used for a general studying of the DM. The used in [6, 7] approach looks as a very fruitful one because it allows to reach easy understanding of the DM and EM physics and it is why it deserves further implementation in the studying of the EM and DM. In the present paper analytical solutions of the EM and DM mode (associated with an insertion of an isotropic layer in the perfect cholesteric structure) are presented and some limiting cases simplifying the problem are considered.

2. BOUNDARY PROBLEM

To investigate EM in a CLC, we have to consider a boundary problem, i.e., transmission and reflection of light incident at a CLC layer along the spiral axis, which was solved in many papers (see [10–12]). We assume that the CLC is represented by a planar layer with a spiral axis perpendicular to the layer surfaces. We also assume that the average CLC dielectric constant ε_0 coincides with the dielectric constant of the ambient medium. This assumption practically prevents conversion of one circular polarization into another at layer surfaces [11, 12] and allows taking only two eigenwaves with diffracting circular polarization into account. Because the boundary problem was solved in many papers (see [10–12]), so we give here only final expressions for the amplitude transmission T and reflection R coefficients for light incident at a CLC layer of thickness L.

$$\begin{aligned} R &= i\delta \sin qL / \left\{ (q\tau/\kappa^2)\cos qL + i\left[(\tau/2\kappa)^2 + (q/\kappa)^2 - 1\right]\sin qL \right\}, \\ T &= \exp[i\kappa L]\left(q\tau/\kappa^2\right) / \left\{ \left(q\tau/\kappa^2\right)\cos qL + \mathrm{i}\left[(\tau/2\kappa)^2 + (q/\kappa)^2 - 1\right]\sin qL \right\}, \end{aligned} \tag{1}$$

where $q = \kappa\left\{1 + (\tau/2\kappa)^2 - [(\tau/\kappa)^2 + \delta^2]^{1/2}\right\}^{1/2}$, $\varepsilon_0 = (\varepsilon_\parallel + \varepsilon_\perp)/2$, $\delta = (\varepsilon_\parallel - \varepsilon_\perp)/(\varepsilon_\parallel + \varepsilon_\perp)$ is the dielectric anisotropy, and $\varepsilon_\parallel$, and $\varepsilon_\perp$ are the local principal values of the CLC dielectric tensor [7, 8], $\kappa = \omega\varepsilon_0^{1/2}/c$ and c is the speed of light, $\tau = 4\pi/p$, where p is the CLC pitch.

The values of the reflection coefficient and eigenwave amplitudes excited in the layer close to the stop-band edges are strongly oscillating functions of the frequency (see Fig. 1 and Fig. 2). At the points of maxima close to the stop-band edges the eigenwave amplitudes are much larger than the incident wave amplitude. It turns out that the amplitude maxima frequencies coincide with the frequencies of zero reflection for a nonabsorbing CLC (see Fig. 2).

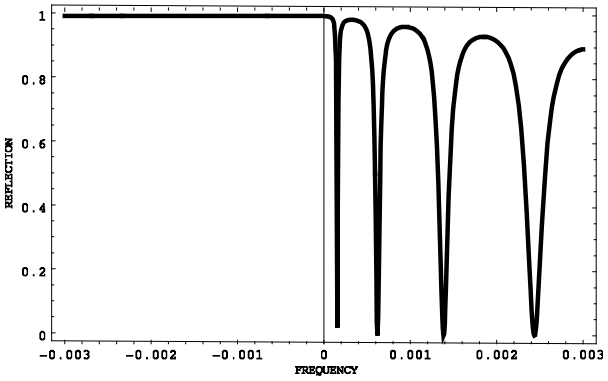

Figure 1: Intensity reflection coefficient R calculated versus the frequency for a nonabsorbing CLC layer ($\delta = 0.05,\ N = L/p = 250$). Here and in all figures below, $\delta(\nu - 1)$ is plotted at the frequency axis ($\nu = 2(\omega - \omega_B)/(\delta\omega_B) - 1)$).

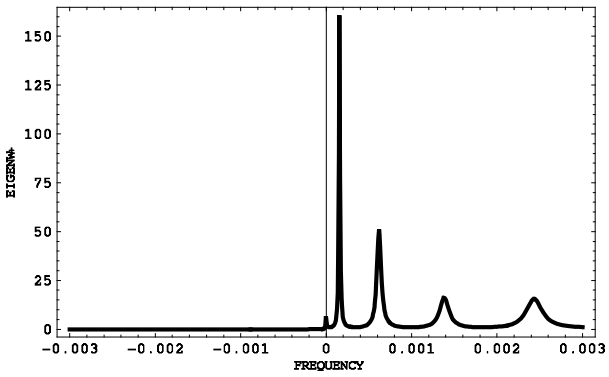

Figure 2: Squared eigenmode amplitude calculated versus the frequency for a nonabsorbing CLC layer ($\delta = 0.05,\ N = L/p = 250$).

3. EDGE MODE (NONABSORBING LC)

In a nonabsorbing CLC, $\gamma = 0$ in the general expression for the dielectric constant $\varepsilon = \varepsilon_0(1 + i\gamma)$). The calculations of the reflection R and transmission coefficients (Here and below R and T are the intensity reflection and transmission coefficients) as functions of the frequency in accordance with Eq. (1) (Fig. 1) give the well-known results [8–12], in particular, $T + R = 1$ for all frequencies. The mentioned relation between the amplitudes of eigenwaves excited in the layer and incident waves at the specific frequencies shows that the energy of radiation in the CLC at the layer thickness for these frequencies is much higher than the corresponding energy of the incident wave at the same thickness. Hence, in complete accordance with [13], we conclude that at the corresponding frequencies, the incident wave excites some localized mode in the CLC. To find this localized mode, we have to solve the homogeneous system (see [14]). The solvability condition for this homogeneous system determines the discrete frequencies of these localized modes:

$$\mathrm{tg}qL = i\left(q\tau/\kappa^2\right) / \left[(\tau/2\kappa)^2 + (q/\kappa)^2 - 1\right]. \tag{2}$$

In the general case, solutions of Eq. (2) for the EM frequencies ω_{EM} can to be found only numerically. The EM frequencies ω_{EM} turn out to be complex quantities, which can be presented as $\omega_{\mathrm{EM}} = \omega^0_{\mathrm{EM}}(1 + i\Delta)$, where Δ is a small parameter in real situations. Fortunately, an analytic solution can be found for a sufficiently small Δ ensuring the condition $LImq \ll 1$. In this case, the ω^0_{EM} are determined by the conditions

$$qL = n\pi \quad \text{and} \quad \Delta = -\frac{1}{2}\delta(n\pi)^2/(\delta L\tau/4)^3, \tag{3}$$

where n is the edge mode number ($n = 1$ corresponds EM frequency closest to the stop-band edge).

The field distributions for the EM numbers $n = 1, 2, 3$ are presented in Fig. 3. The Fig. 3 shows that the EM field is localized inside the CLC layer and its energy density experiences oscillations inside the layer with the number of the oscillations equal to the EM number n. However, the total field at each point of the CLC layer is represented by two plane waves propagating in the opposite directions [14], and hence the intensities of the waves propagating in the opposite directions can be calculated separately at any point in the layer. These distributions are of a special interest close to the layer surfaces. Fig. 4 shows the intensity coordinate distributions for the waves directed inside and outside the layer close to the layer surfaces. We can see that at the layer surface, the intensity of the wave directed inside the layer is strictly zero, but the intensity of the wave propagating outside the layer is non zero (although small). This means that the EM energy is leaking from the layer through its surfaces and EM life-time τ_m is finite. For sufficiently thick CLC layers as their thickness L increases the EM life-time τ_m, as analytical solution shows [14], increases as the third power of the thickness and is inversely proportional to the square of the EM number n:

$$\tau_m \approx 1/\mathrm{Im}(\omega_{\mathrm{EM}}) = (L/c)(\delta L/pn)^2. \tag{4}$$

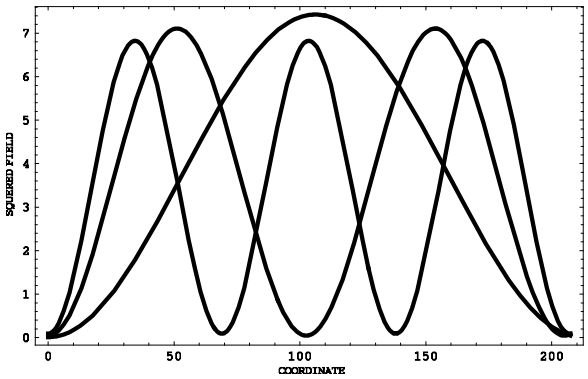

Figure 3: The calculated EM energy (arbitrary units) distributions inside the CLC layer versus the coordinate (in the dimensionless units $z\tau$) for the three first edge modes ($\delta = 0.05,\ N = 16.5,\ n = 1, 2, 3$).

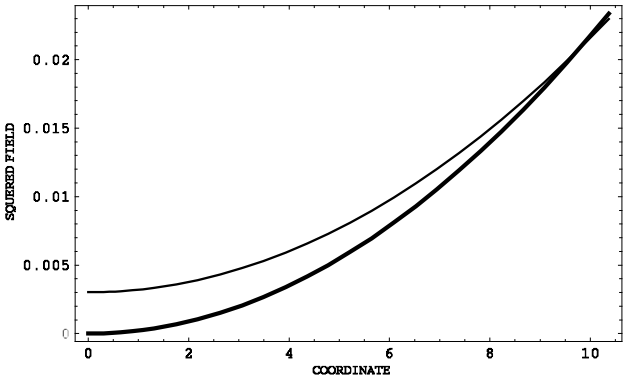

Figure 4: The calculated EM energy (arbitrary units) distributions close to the CLC layer surface versus the coordinate (in the dimensionless units $z\tau$) for the plane wave directed inside (bold line) and outside the layer for the first edge mode ($\delta = 0.05,\ N = 16.5,\ n = 1$).

4. ABSORBING LC

We assume for simplicity that the absorption in the LC is isotropic. We define the ratio of the imaginary part to the real part of the dielectric constant as γ, i.e., $\varepsilon = \varepsilon_0(1 + i\gamma)$. In Fig. 5, the $1 - R - T$ dependence on the frequency is presented for a positive γ. Now $R + T < 1$.

It happens that for each n the maximum absorption, i.e., maximal $1 - R - T$, occurs for

$$(n\pi)^2 = a^3\gamma, \tag{5}$$

where $a = \delta L\tau/4$ (In a typical situation, $a \gg 1$). From the Eq. (5), follows that the maximum absorption occurs for a special relation between δ, γ and L.

As was shown in [11, 15] just at the frequency values determined by (5), the effect of anomalously strong absorption reveals itself for an absorbing chiral LC (Fig. 5).

5. AMPLIFYING LC

We now assume that $\gamma < 0$, which means that the CLC is amplifying. If $|\gamma|$ is sufficiently small, the waves emerging from the layer exist only in the presence of at least one external wave incident on the layer, and their amplitudes are determined by the expression (1). In this case, $R + T > 1$ or $1 - R - T < 0$ which just corresponds to the definition of an amplifying medium.

However, if the imaginary part of the dielectric tensor, i.e., γ, reaches some critical negative value, the quantity $R+T$ diverges and the amplitudes of waves emerging from the layer are nonzero even for zero amplitudes of the incident waves. The corresponding γ is a minimum threshold gain at which the lasing occurs. The equation determining the threshold gain (γ) coincides with Eq. (2). However, it should be solved now not for the frequency but for the imaginary part of the dielectric constant (γ).

For a very small negative imaginary part of the dielectric tensor ($|\gamma|$ and $L|\mathrm{Imq}| \ll 1$) the threshold values of the gain for the EM can be represented by analytic expression:

$$\gamma = -\delta(n\pi)^2/(\delta L\tau/4)^3 \tag{6}$$

It also follows from Fig. 6 that the different threshold values of γ correspond to the different edge lasing modes (divergent R and T) in Fig. 6. This means that separate lasing modes can be excited by changing the gain (γ).

6. BOUNDARY PROBLEM FOR DM

The defect structure (DMS) which is under consideration here is shown at the Fig. 7. The solution of the boundary problem is carried out in the similar way as for a CLC layer above so we give below the final results (All simplifications accepted above for the CLC layer are accepted also for the DMS).

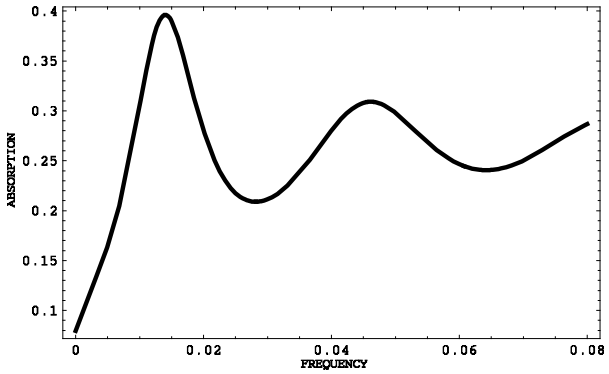

Figure 5: The absorption $1 - R - T$ calculated versus the frequency ($l = 300$, $l = L\tau = 4\pi N$, $\delta = 0.05$) (a) for $\gamma = 0.001$.

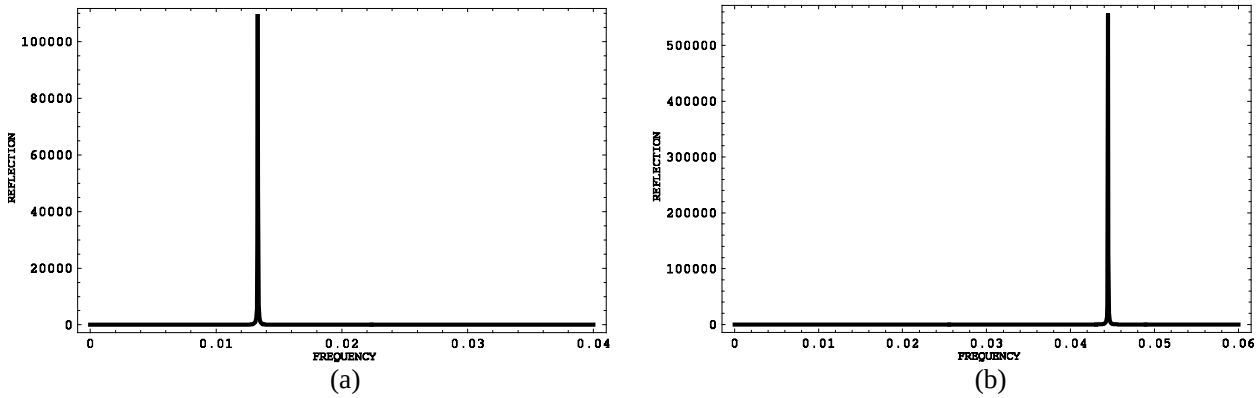

Figure 6: R calculated versus the frequency ($l = 300$, $l = L\tau$, $\delta = 0.05$) (a) close to the threshold gain for the first lasing edge mode ($\gamma = -0.00565$), (b) close to the threshold gain for the second lasing edge mode ($\gamma = -0.0129$).

There is an option to obtain formulas determining the optical properties of the structure depicted at Fig. 7 via the solutions found for a singl CLC layer [14]. If one use the expressions for the amplitude transmission $T(L)$ and reflection $R(L)$ coefficient (1) for a single cholesteric layer (see also [11, 12]) the transmission $|T(d, L)|^2$ and reflection $|R(d, L)|^2$ intensity coefficients for the whole structure may be presented in the following form:

$$|T(d, L)|^2 = |[T_e T_d \exp(ikd)]/[1 - \exp(2ikd) R_d R_u]|^2, \quad (7)$$

$$|R(d, L)|^2 = |\{R_e + R_u T_e T_u \exp(2ikd)/[1 - \exp(2ikd) R_d R_u]\}|^2, \quad (8)$$

where $R_e(T_e)$, $R_u(T_u)$ and $R_d(T_d)$ are the amplitude reflection (transmission) coefficients of the CLC layers (1) (see Fig. 7) for the light incidence at the outer (top) layer surface, for the light incidence at the inner top CLC layer surface from the inserted defect layer and for the light incidence at the inner bottom CLC layer surface from the inserted defect layer, respectively. It is assumed in the deriving of Eqs. (7), (8) that the external beam is incident at the structure (Fig. 7) from the above only.

The calculated reflection $|R(d, L)|^2$ spectra inside the stop band for the structure sketched at Fig. 7 for nonabsorbing CLC layers are presented at Fig. 8. The figures show minima in $|R(d, L)|^2$ at some frequencies inside the stop band at positions which depend on the defect layer thickness d. As it is known [1–3, 6, 7], the corresponding minima of $|R(d, L)|^2$ and maxima of $|T(d, L)|^2$ frequencies correspond to the defect mode frequencies.

For the layer thickness $d = p/4$, what is just one half of the dielectric tensor period in a cholesteric, these maxima and minima are situated just at the stop band center. In the d/p interval $0 < d/p < 0.5$ the defect mode frequency value moves from the high frequency stop band edge to the low frequency stop band edge. At Fig. 8, only $R(d, L)$ is presented because for a nonabsorbing structure $|R(d, L)|^2 + |T(d, L)|^2 = 1$.

The Fig. 8 shows that at some frequency the reflection coefficient $R(d, l) = 0$. One finds from (8)

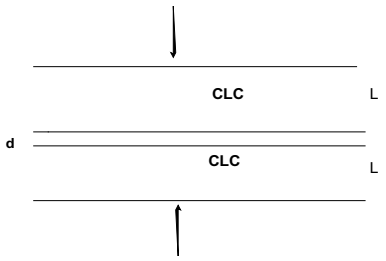

Figure 7: Schematic of the CLC DMS with an isotropic defect layer.

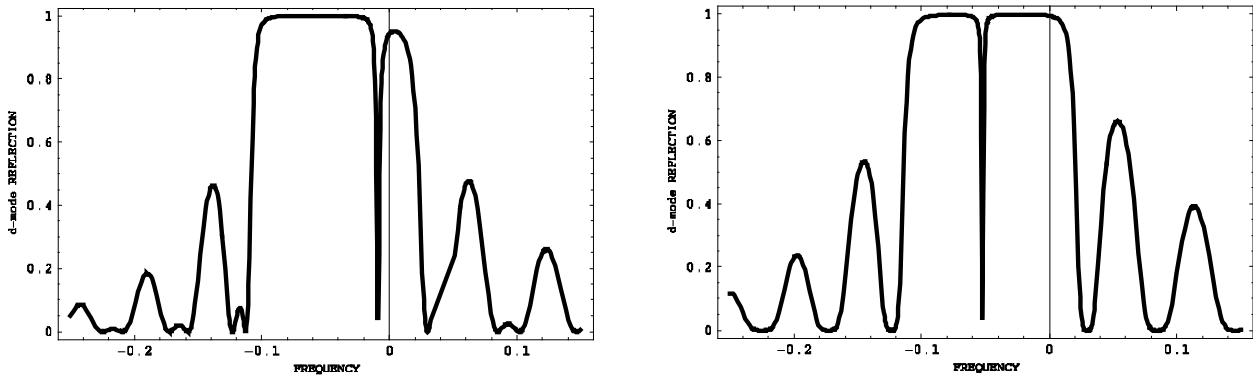

(a) (b)

Figure 8: $R(d, L)$ versus the frequency for a nonabsorbing CLC ($\gamma = 0$) at (a) $d/p = 0.1$ and (b) $d/p = 0.25$; $\delta = 0.05$, $l = 200$, $l = L\tau = 2\pi N$, where N is the director half-turn number at the CLC layer thickness L.

the equation determining the frequencies of the reflection coefficient zeros:

$$R_e[1 - \exp(2ikd)R_dR_u] + R_uT_eT_u\exp(2ikd) = 0. \tag{9}$$

7. DEFECT MODE

Similarly to the case of EM the DM frequency ω_D is determined by the zero value of the determinant $\mathrm{Det}(d, L)$ of the system corresponding to the boundary value solution for the structure depicted at Fig. 7 [16] :

$$\mathrm{Det}(d, L) = 4\Big\{\exp(2ikd)\sin^2 qL - \exp(-i\tau L)\left[\left(\tau q/\kappa^2\right)\cos q + i\left((\tau/2\kappa)^2 + (q/\kappa)^2 - 1\right)\sin qL\right]^2/\delta^2\Big\}. \tag{10}$$

Note, that the $\mathrm{Det}(d, L)$ at a finite length L does not reach zero value for a real value of ω for a nonabsorbing CLC however reaches zero value for a complex value of ω.

The dispersion equation following from (10) may be with the help of (8) reduced to the expression containing reflection coefficients R of the CLC layers:

$$1 - R_dR_u\exp(2ikd) = 0. \tag{11}$$

The field of DM in each CLC layer is a superposition of two CLC eigen modes [11, 12] and can be easily found. In particular, the coordinate dependence of the squared modulus of the whole field is presented at Fig. 9. The Fig. 9 shows that the larger dielectric anisotropy δ is the more sharp growth of the DM field toward the defect layer occurs. Similarly to the EM case at the external surfaces of the DMS only the amplitude of the wave directed toward the defect layer reduces strictly to zero. The amplitude of the wave directed outwards is small however does not reduce to zero. It is why there is a leakage of the DM energy outwards through the external surfaces of the DMS. The ratio of the corresponding energy flow to the whole DM energy accumulated in the DMS determines the inverse life-time.

For nonabsorbing CLC layers the only source of decay is the energy leakage through their surfaces. The analysis of the corresponding expressions [16] shows that the DM lifetime τ_m is dependent on the position of the DM frequency ω_D inside the stop band and reaches a maximum just at the middle of the stop band, i.e., at $k = \tau/2$.

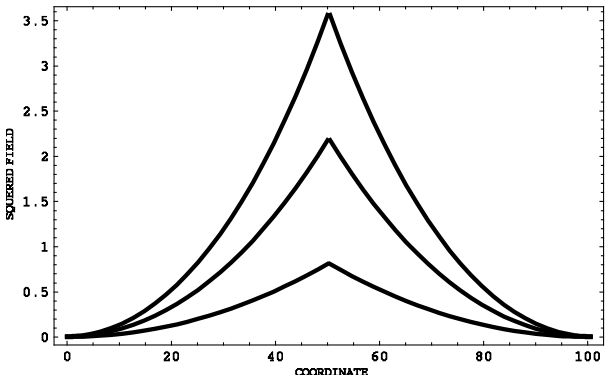

Figure 9: Coordinate dependence of the squared amplitude of the DM field (arbitrary units) at the DM frequency being at the stop band centre for various dielectric anisotropy values (from the top to the bottom $\delta = 0.05,\ 0.04,\ 0.025$) and the defect layer thickness $d = p/4$ for the cholesteric layer thickness $L = 50(p/2)$.

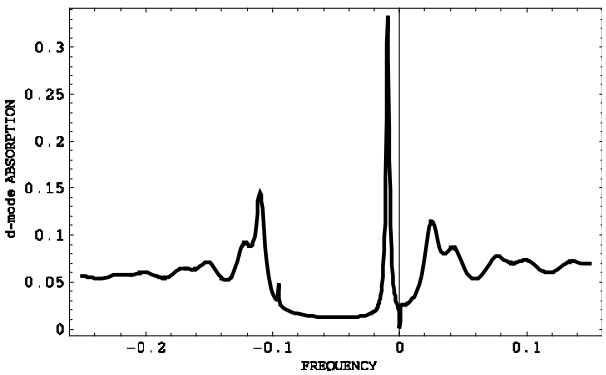

Figure 10: The total absorption for an absorbing CLC versus the frequency, $\gamma = 0.0003$; $d/p = 0.1$, $\delta = 0.05$, $N = 33$.

8. THICK CLC LAYERS

In the case of DMS with thick CLC layers ($|q|L \gg 1$) some analytic results related to DM can be also obtained by the same way as for EM. In particular, the defect mode life time τ reaches a maximum for the defect mode frequency at the stop band centre at fixed CLC layers thickness. For the DM frequency at the middle of the stoop band, i.e., at $k = \tau/2$, the DM life time τ_m is given by

$$\tau_m = 3\pi(L/p)\left(\varepsilon_0^{1/2}/\tau c\right)\exp\left[2\pi\delta L/p\right]. \tag{12}$$

The expression (12) reveals an exponential increase of τ_m with increase of the CLC thickness L.

9. ABSORBING LC

To take into account the absorption, we again accept $\varepsilon = \varepsilon_0(1 + i\gamma)$. There are some interesting peculiarities of the optical properties of the structure under consideration (Fig. 7). The total absorption $(1 - |T(d, L)|^2 - |R(d, L)|^2)$ at the DM frequency behaves itself unusually.

At a small γ for the DM frequencies the absorption occurs to be much more than the absorption out of the stop band (see Fig. 10). It is a manifestation of the so called "anomalously strong absorption effect" known for perfect CLC layers at the edge mode frequency [11, 15]. So, one sees that at the DM frequency ω_D the effect of anomalously strong absorption similar to the one for EM [11, 15] exists and more over the absorption enhancement for DM at small γ is higher than for EM. In the case of thick CLC layers ($|q|L \gg 1$) the dependence of γ, on L and other parameters ensuring maximal absorption, may be found analytically. For the position of ω_D just in the middle of the stop band the expression for γ ensuring maximal absorption takes the following form

$$\gamma = (4/3\pi)(p/\delta L)\exp[-2\pi\delta(L/p)] \tag{13}$$

10. AMPLIFYING LC

The calculation results for the transmission $|T(d, L)|^2$ and reflection $|R(d, L)|^2$ coefficients at $\gamma < 0$ show that for a small absolute value of γ the shape of the transmission $T(d, L)$ and reflection $|R(d, L)|^2$ coefficients is qualitatively the same as for zero amplification ($\gamma = 0$). For a growing absolute value of γ at some point a divergence of $|T(d, L)|^2$ and $|R(d, L)|^2$ happens (see Fig. 11) with no signs of noticeable maxima at other frequencies. The corresponding value of γ may be considered as close to the threshold value of the gain (γ) for the DFB lasing at the DM frequency. Continuing the increase of the absolute value of γ one finds that diverging maxima for $|R(d, L)|^2$ at the EM frequencies appear (without no traces of maximum at the defect mode frequency) for the gain being approximately four time more than the threshold gain for the DM (Fig. 11). The observed result show that the DM lasing threshold gain is lower than the corresponding threshold for the EM. Another conclusion following from this study is the revealed existence of some interconnection

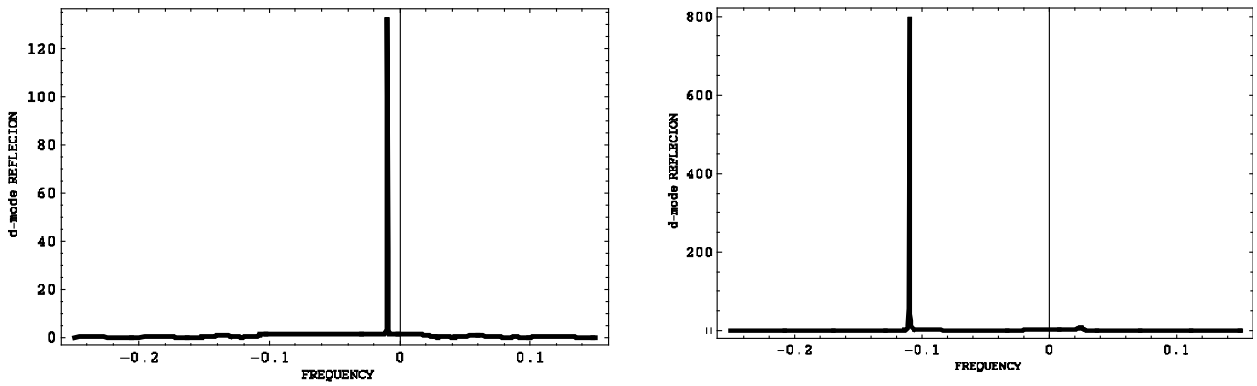

(a) (b)

Figure 11: $|R(d,L)|^2$ for an amplifying CLC versus the frequency, (a) $\gamma = -0.00117$; (b) $\gamma = -0.0045$, $d/p = 0.1$, $\delta = 0.05$, $N = 33$.

between the LC parameters at the lasing threshold which for thick CLC layers was found analytically for DM (see (13)) and for the EM (see (6)). Really, a continuous increase of the gain results in consequential appearance of a lasing at new EM with disappearance of lasing at the previous ones corresponding to more low thresholds (what was experimentally observed [3]).

The mention above interconnection between the LC parameters at the lasing threshold in the case of thick CLC layers ($|q|L \gg 1$) may be found analytically. If the DM frequency ω_D is located at the stop band centre the corresponding interconnection for the threshold gain (γ) is given by the formula:

$$\gamma = -(4/3\pi)(p/\delta L)\exp[-2\pi\delta(L/p)]. \tag{14}$$

The following from Eq. (13) exponentially small value of $|\gamma|$ for thick CLC layers confirms mentioned above statement about more low lasing threshold for DM compared to EM.

11. CONCLUSION

The performed analytical description of the EM and DM neglecting the polarization mixing allows one to reveal clear physical pictures of these modes which is applicable to the DM in general. For example, more low lasing threshold and more strong absorption at the DM frequency compared to the EM frequencies are the features of any periodic media. Note, that the experimental studies of the lasing threshold [3] agree with the corresponding theoretical result obtained above. Moreover, the experiment [3] confirms also the existence of some interconnection between the gain and other LC parameters at the threshold pumping energy for lasing at the DM and EM frequencies. For a special choice of the parameters in the experiment the obtained formulas may be directly applied to the experiment. However, in the general case, one has take into account a mutual transformation at the boundaries of the two circular polarizations of opposite sense. In the general case, the EM and DM field leakage from the structure is determined as well by the finite CLC layer thickness so by the leakage due to the polarization conversion. Only for sufficiently thin CLC layers or in the case of the DM frequency being very close to the stop band frequency edges the main contribution to the frequency width of the EM and DM is due to the thickness effect and the developed above model may be directly applied for the describing of the experimental data.

The defect type considered above is a homogenous layer. The developed approach is applicable also to a defect of "phase jump" type [2, 3, 6, 7] and so the corresponding results are practically the same as above. Namely, the equation related to the case of a "phase jump defect" one gets from the equations presented above by the substitution in the factor $\exp(2ikd)$ instead of $2kd$ the quantity $2\Delta\varphi$, where $\Delta\varphi$ is the spiral phase jump at the defect plane.

It should be mentioned also that the localized DM and EM reveal themselves in an enhancement of some inelastic and nonlinear optical processes in photonic LCs. As examples the corresponding experimentally observed effects for the enhancement of nonlinear optical second harmonic generation [17] and lowering of the lasing threshold [18] in photonic LCs have to be mentioned along with the theoretically predicted enhancement of Cerenkov radiation (Section 4 in [11] and Chapter 5 in [12]).

In the conclusion should be stated that the results obtained here for the EM and DM (see also [16] and [19]) clarify the physics of these modes and manifests a complete agreement with the

corresponding results of the previous investigations obtained by a numerical approach [13].

ACKNOWLEDGMENT

The work is supported by the RFBR grants 09-02-90417-Ukr_f_a and 10-02-92103-JP_a.

REFERENCES

1. Yang, Y.-C., C.-S. Kee, J.-E. Kim, et al., "Defect modes in chiral liquid crystals," *Phys. Rev. E*, Vol. 60, 6852, 1999.
2. Kopp, V. I. and A. Z. Genack, "Phase jump defect modes in chiral liquid crystals," *Phys. Rev. Lett.,* Vol. 89, 033901, 2003.
3. Schmidtke, J., W. Stille, and H. Finkelmann, "Observation of defect modes in chiral liquid crystals," *Phys. Rev. Lett.*, Vol. 90, 083902, 2003.
4. Shibaev, P. V., V. I. Kopp, and A. Z. Genack, "Studies of defect modes in chiral liquid crystals," *J. Phys. Chem. B*, Vol. 107, 6961, 2003.
5. Yablonovitch, E., T. J. Gmitter, R. D. Meade, et al., "Defect modes in solids," *Phys. Rev. Lett.*, Vol. 67, 3380, 1991.
6. Becchi, M., S. Ponti, J. A. Reyes, and C. Oldano, "Analytic approach to defect modes," *Phys. Rev. B*, Vol. 70, 033103, 2004.
7. Schmidtke, J. and W. Stille, "Theory of defect modes in liquid crystals," *Eur. Phys. J.,* Vol. 90, 353, 2003.
8. De Vries, H., "Optics of cholesteric liquid crystals," *Acta Crystallogr*, Vol. 4, 219, 1951.
9. Kats, E. I., "Theory of cholesteric liquid crystals optics," *Sov. Phys. JETP*, Vol. 32, 1004, 1971.
10. De Gennes, P. G. and J. Prost, *The Physics of Liquid Crystals*, Clarendon Press, Oxford, 1993.
11. Belyakov, V. A. and V. E. Dmitrienko, *Optics of Chiral Liquid Crystals*, p. 54 in *Soviet Scientific Reviews — Section A, Physics Reviews*, I. M. Khalatnikov, Vol. 13, 1–203, Harwood Academic Publisher, 1989.
12. Belyakov, V. A., *Diffraction Optics of Complex Structured Periodic Media*, Chapter 4, Springer Verlag, New York, 1992.
13. Kopp, V. I., Z.-Q. Zhang, and A. Z. Genack, "Localized optical modes," *Prog. Quant. Electron.*, Vol. 27, No. 6, 369, 2003.
14. Belyakov, V. A. and S. V. Semenov, "Edge modes in photonic liquid crystals," *JETP*, Vol. 109, 687, 2009.
15. Belyakov, V. A., A. A. Gevorgian, O. S. Eritsian, and N. V. Shipov, "Anomalous absorption," *Zhurn. Tekhn. Fiz.*, Vol. 57, 1418, 1987; *Sov. Phys. Technical Physics*, Vol. 32, No. 7, 843–845, 1987, English translation; *Sov. Phys. Crystalography*, Vol. 33, No. 3, 337, 1988.
16. Belyakov, V. A., "Analytic approach to defect modes theory," *MCLC*, Vol. 494, 127, 2008; *Ferroelectrics*, Vol. 364, 33, 2008.
17. Shin, K., H. Hoshi, D. Chang, K. Ishikawa, and H. Takezoe, "Nonlinear second harmonic generation in photonic LC," *Optics Lett.*, Vol. 27, 128, 2002.
18. Matsuhisa, Y., Y. Huang, Y. Zhou, et al., "Low threshold and high efficiency lasing," *Appl. Phys. Lett.*, Vol. 90, 091114, 2007.
19. Belyakov, V. A., "Analytic approach to the edge modes," *MCLC*, Vol. 453, 43, 2006; *Ferroelectrics*, Vol. 344, 163, 2006.

Photonic Crystal Based on CdSe Nanoparticles Embedded in a Glass Matrix

A. Labbani and A. Benghalia
Laboratoire Hyperfréquences et Semi-conducteurs, Faculté des Sciences de l'ingénieur
Université Mentouri Constantine, Route d'Ain El Bey Constantine 25000, Algérie

Abstract— We present the evolution of the dielectric permittivity of glass containing CdSe nanoparticles with various volume fractions f. The presence of the nano-objets in the host matrix permits to obtain a new composite material with tunable optical properties which can be described by Maxwell-Garnett theory. We study different aspects of photonic band gap (PBG) in one- and two-dimensional photonic crystals (PC's) using the finite difference time-domain (FDTD) method. We investigate the effect of the thickness of the shell layer on the PBG in 2D hexagonal (square) lattice consisting of air (CdSe) rods covered with CdSe (air) shell layer and embedded in a glass matrix. Changes in different structure parameters, such as the volume fraction, the lattice type and the thickness of the shell layer, can affect photonic band gap properties as location, number and width. Considered effects provide new possibilities for manufacturing photonic crystals with desired optical properties.

1. INTRODUCTION

Since the pioneering work of Yablonovitch [1] and John [2], it is now well acknowledged that photonic crystals (PC's) have the ability to control the propagation of electromagnetic waves. They scatter photons in manner similar to the scattering of electrons in semiconductor [3, 4]. A photonic crystal is composed of a periodic variation in space of dielectric permittivity which an external electromagnetic wave interacts. One of the most properties of PC's is that they can be designed to possess an absolute photonic band gap (PBG): a frequency region where light propagation in the crystal is totally prohibited, regardless of the polarization or propagation direction. This ability is the basis of a large number of possible applications of PCs, such as waveguides, microcavities and communication components.

In this letter, on the basis of numerical model we study the optical response of a glass matrix (SiO_2) doped with CdSe nanoparticles. To describe the optical properties of semiconductor grains in dielectric matrix, we use Maxwell-Garnett theory (MG) [5]. We have calculated the photonic band gaps in one-dimensional (1D) and two dimensional photonic crystals using FDTD method [6]. Our results show that the PBG sensitively depend on many factors, such as the filling factor, lattice type and the thickness of the shell layer.

2. STUDY OF PERMITTIVITY DIELECTRIC OF COMPOSITE MATERIAL

In this section, we have demonstrated that it is possible to modify the dielectric permittivity of a glass (SiO_2) containing CdSe nanoparticles. To calculate the dielectric permittivity $\tilde{\varepsilon}$, of such a new composite system, CdSe + glass, we use Maxwell-Garnett Theory [5] is expressed approximately by [7]:

$$\tilde{\varepsilon}(w) = \varepsilon_m \frac{\varepsilon_n(1+2f) + 2\varepsilon_m(1-f)}{\varepsilon_n(1-f) + \varepsilon_m(2+f)} \tag{1}$$

where ε_n is the dielectric permittivity of the CdSe nanoparticle, ε_m is the dielectric permittivity of the glass matrix and f is the volume fraction occupied by CdSe nano-objets. In order to describe the modification of the dielectric permittivity $\tilde{\varepsilon}$ of glass containing CdSe particles of various volume fractions f, MG theory has been applied [5]. In our simulation we used the experimentally determined values for CdSe from Palik [8]. As it was shown in Figures 1(a) and 1(b), it is evident that varying the filling factor strongly affects the real and imaginary parts of the dielectric permittivity of MG composite. The increasing of f has the effect of increasing $\tilde{\varepsilon}$. Figure 1(b) demonstrates that increasing f results in dramatic increase the absorption band spectra in the visible range. These absorption bands are the CdSe aggregates signature in the glass matrix.

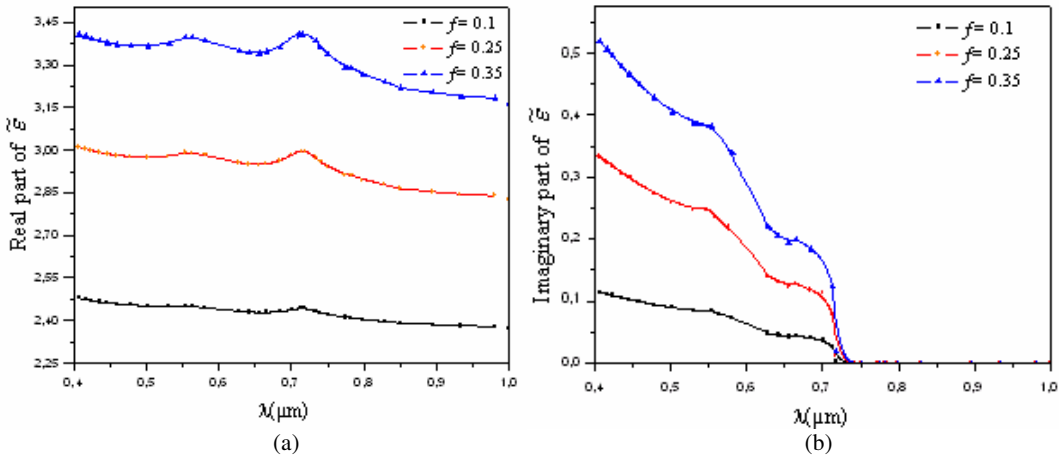

Figure 1: Modification of the (a) real part and (b) imaginary part of the dielectric permittivity $\tilde{\varepsilon}$ of SiO_2 containing CdSe nanoparticles.

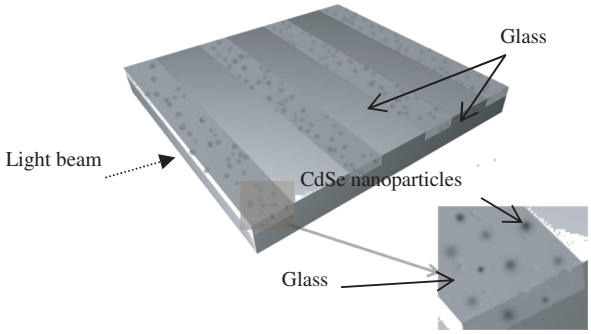

Figure 2: Schematic structure of the Bragg Mirror (CdSe + glass)/glass.

3. 1D PBG MODULATION EFFECTS DUE TO FILLING FACTOR

In order to investigate the influence of the filling factor f effect on the photonic band gap (PBG) we have calculated band structures of alternating layers of CdSe + glass and glass on a glass substrate, as shown in Figure 2 for $f = 35\%$ and 10%. We consider only normal incidence of electromagnetic wave on PC's. The thickness of the considered layers of the host matrix and the composite material are 0.126 μm and 0.1 μm respectively. The surrounding medium has a dielectric permittivity $\varepsilon_m = 2.11$ at $\lambda = 733.6$ nm.

Results are presented in terms of frequencies $wa/2\pi c$, where a is the lattice constant, c the speed of light in a vacuum and λ the vacuum wavelength.

The widths (Δw) for G1 and G2 gaps for $f = 35\%$ and 10% are given in Figures 3(a) and 3(b) respectively. We can see from Figure 3(a) that the value (Δw) for the G1gap is (0.0432) $wa/2\pi c$ and for G2 gap is (0.0437) $wa/2\pi c$. Similarly, the widths presented in Figure 3(b) for G1 and G2 gaps for $f = 10\%$ are (0.0147) $wa/2\pi c$ and (0.0129) $wa/2\pi c$, respectively. These results indicate that (Δw) increases with increasing f due to the increased refractive index contrast.

4. 2D PBG MODULATION EFFECTS DUE TO THE LAYER SHELL THICKNESS HEXAGONAL LATTICE

To illustrate the effect of the layer shell thickness on PBG, we have simulated this effect by choosing a hexagonal structure consisting of circular air (holes) rods covered with Cadmium Selenide (CdSe) shell layer and embedded in glass matrix as shown in Figure 4(a). Parameters $\varepsilon_{\text{CdSe}}$, ε_{air} and $\varepsilon_{\text{glass}}$ denote the dielectric permittivity of CdSe, air and background medium (glass), respectively. The values of the parameters are: $\varepsilon_{\text{CdSe}} = 7.879$, $\varepsilon_{\text{air}} = 1$ and $\varepsilon_{\text{glass}} = 2.116$ at wavelength $\lambda = 733.6$ nm. r_c and r_s are the radius of the inner rods and the outer radius of the shell layer, respectively. $\Delta r = r_s - r_c$ describe the shell layer thickness.

The PBGs for TE and TM polarization modes were calculated along the Γ-M-K-Γ edge for the Brillouin zone. The computational domain for the FDTD calculation consisted of one lattice

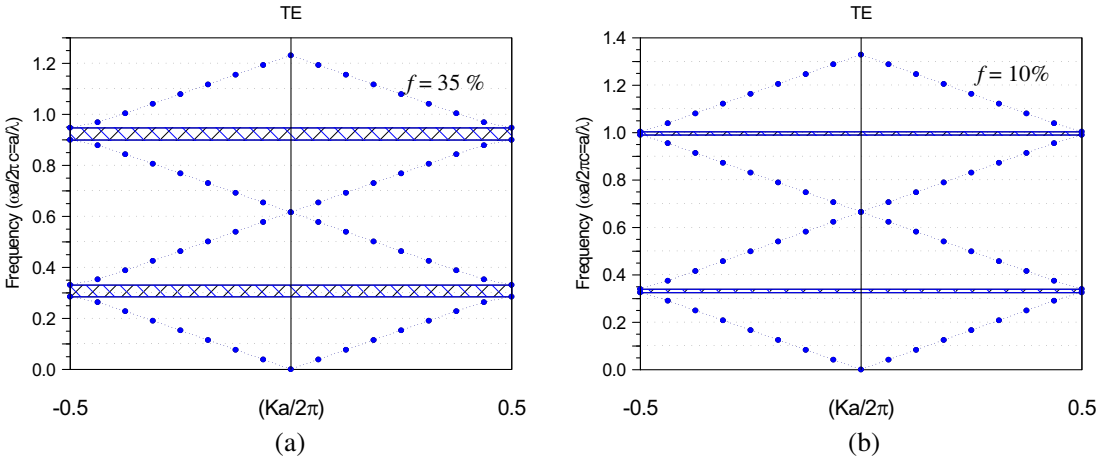

Figure 3: Photonic band structure of the Bragg mirror (a) $f = 35\%$ and (b) $f = 10\%$.

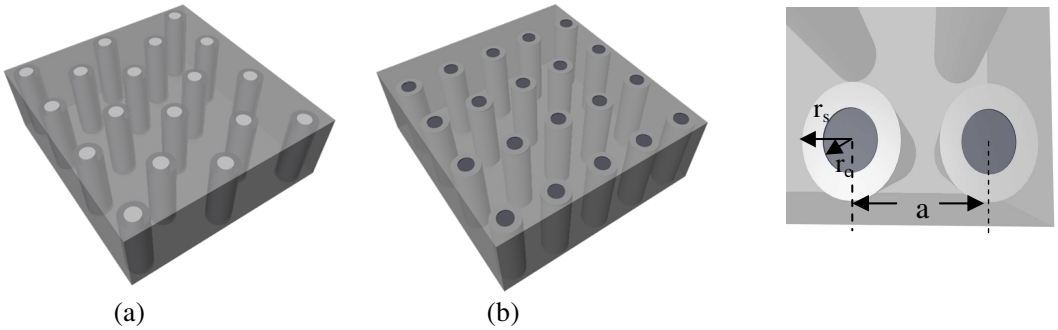

Figure 4: Schematic representation of the studied 2D, (a) hexagonal lattice, (b) square lattice photonic crystal.

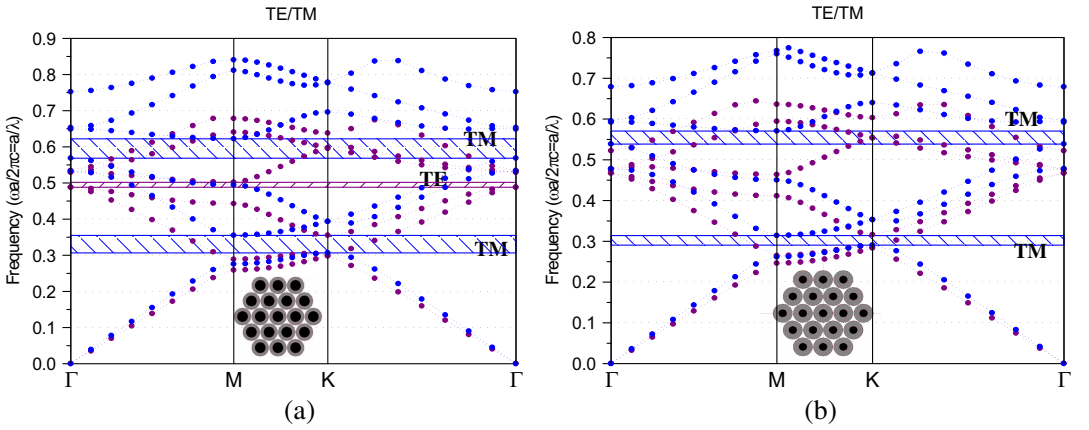

Figure 5: Band gap structure for TE and TM polarization modes in a 2D hexagonal lattice of air rods covered with CdSe shell layer for (a) $\Delta r = 0.16a$, (b) $\Delta r = 0.21a$.

unit cell, repeated infinitely by introducing periodic boundary conditions. The lattice unit cell was divided up into 64×64 discretization grid points. The dielectric permittivity at each grid point is defined by taking the average of the dielectric permittivity over 10×10 subgrid points. The convergence and numerical stability and precision of the calculation are tested by increasing the calculation resolution.

Figure 5(a) shows the photonic band structure for $r_c = 0.3a$, $r_s = 0.46a$ and $\Delta r = 0.16a$, where a is the lattice constant. There are two photonic band gaps for the TM polarization modes. Their respective widths (Δw) are (0.0483) $wa/2\pi c$ for the first gap (G1) and (0.0519) $wa/2\pi c$ for the second gap (G2). Similarly, one PBG is found for TE polarization mode in the frequency range (0.4893–0.5027) $wa/2\pi c$. Lets consider now the inner radius $r_c = 0.25a$, the outer radius remains $r_s = 0.46a$ and the thickness $\Delta r = 0.21a$. Figure 5(b) shows the dispersion curves for this case

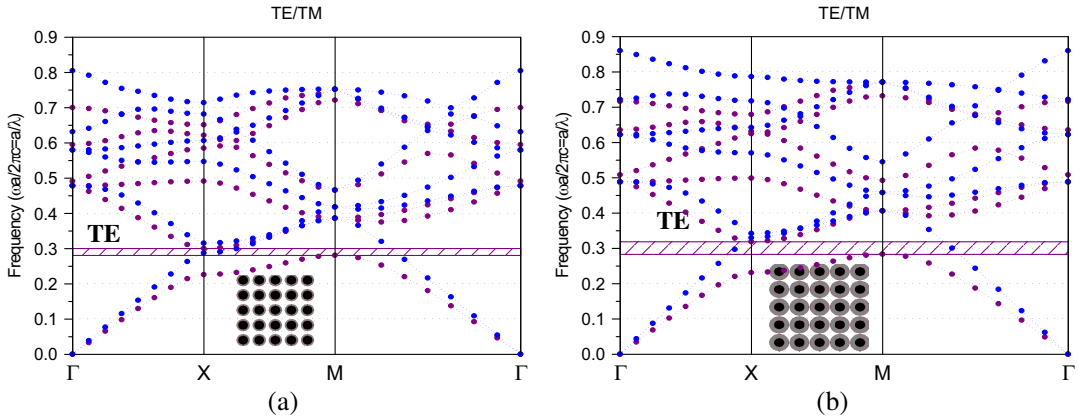

Figure 6: Band gap structure for TE and TM polarization modes in a 2D square lattice of CdSe rods covered with air shell layer for (a) $\Delta r = 0.05a$, (b) $\Delta r = 0.16a$.

and we can see that there are only two photonic band gaps for TM polarization modes; the value of (Δw) for the first gap (G1) is (0.0236) $wa/2\pi c$ and for the gap (G2) gap is (0.0295) $wa/2\pi c$. Comparing Figure 5(a) with Figure 5(b), we can find that, G1 and G2 gaps for TM polarization modes are affected by the thickness of the shell layer and the G1 gap completely disappears for TE polarization mode. Hence we have the conclusion that if Δr increases, the width and number of photonic band gaps are reduced and the position of PBGs is shifted.

4.1. Square Lattice

We think it would be interesting to see how the shell layer thickness affects the PBG with square lattice structure of air rods surrounded by a CdSe shell layer. The structural parameters are the same as in Section 4. Our results show that no PBG exist for such a polarization. We shall now study the inverse arrangement, CdSe core covered with air shell in a glass matrix.

Photonic band structure calculations demonstrated that for $r_c = 0.3a$, $r_s = 0.35a$ and $\Delta r = 0.05a$ there is only one photonic band gap, for TE polarization mode (Figure 6(a)). The value of (Δw) for the G1 gap is (0.02) $wa/2\pi c$. For $\Delta r = 0.16a$ the PBG width is (0.033) $wa/2\pi c$ at $r_s = 0.46a$. As has been shown in Figure 6(b) the width of TE gap increases as the shell layer gets thicker.

5. CONCLUSIONS

In this work we have demonstrated that it is possible to modify and tune the optical properties of a glass matrix in presence of CdSe nanoparticles. Changes in dielectric permittivity, allows us to obtain a nanocomposite material which can have tunable photonic band gaps. We have investigated photonic band structures for 1D and 2D photonic structure using FDTD method. Our results show that the filling factor, lattice type and the thickness of the shell layer have an important influence on the photonic band structure. This implies that if other parameters are fixed the thickness of the shell layer, or the volume fraction, for example, can be suitably chosen in order to obtain the largest PBG.

REFERENCES

1. Yablonovitch, E., "Inhibited spontaneous emission in solid-state physics and electronics," *Phys. Rev. Lett.*, Vol. 58, 2059–2061, 1987.
2. John, S., "Strong localization of photons in certain disordered dielectric superlattices," *Phys. Rev. Lett.*, Vol. 58, 2486–2488, 1987.
3. Joannopoulos, J. D., S. G. Johnson, J. N. Winn, and R. D. Meade, *Photonic Crystals: Molding the Flow of Light*, Princeton University Press, Princeton, 2008.
4. Sakoda, K., *Optical Properties of Photonic Crystals*, Springer, Germany, 2001.
5. Maxwell-Garnett, J. C., *Phil. Trans. R. Soc. A*, Vol. 203, 1904.
6. Taflov, A. and S. C. Hagness, *Computational Electrodynamics: The Finite-Difference Time-Domain Method*, Artech House Publishers, Boston, 2000.
7. Abdolvand, A., A. Podlipensky, G. Seifert, and H. Graener, "Electric field-assisted formation of Percolated silver nanolayers inside glass," *Opt. Express*, Vol. 13, 1266–1274, 2005.
8. Palik, E. D., *Handbook of Optical Constants of Solids*, Academic Press, New York, 1991.

Evaluating RF Signal Transmission over Radio-on FSO Links Using Aperture Averaging

Chedlia Ben Naila, **Abdelmoula Bekkali**, **Kazuhiko Wakamori**, **and Mitsuji Matsumoto**
Global Information and Telecommunication Studies (GITS/GITI), Waseda University, Tokyo, Japan

Abstract— Atmospheric turbulence-induced intensity fluctuations severely impair Free-Space Optical (FSO) communication systems, affecting the quality of the propagated laser beam and lead to significant performance degradation. By using aperture averaging technique, we investigate the performance of the FSO system using a Multiple Subcarrier Modulation (MSM) based on either Binary Phase Shift Keying (BPSK) or Quadrature Phase Shift Keying (QPSK) schemes under weak-to-strong atmospheric turbulence regimes. The performance is assessed in terms of the Bit-Error-Rate (BER) of the MSM-BPSK and MSM-QPSK systems by applying a modified model taking into consideration the aperture averaging.

1. INTRODUCTION

FSO systems have been recognized as a good wireless interconnecting technology for high-capacity communication networks, ensuring data rates similar to those offered by optical fiber systems but at the fraction of its deployment cost [1]. However, since the transmitted optical beam is propagating through the atmosphere, it may experience important distortions due to the refractive-index random variations, i.e., optical turbulence, caused by inhomogeneities of both air temperature and pressure [2, 3]. Therefore, it is of paramount importance to apply efficient techniques to mitigate the channel fading caused by the atmospheric turbulence. Considered as a simple form of spatial diversity, Aperture averaging consists in adopting a receiver lens whose aperture is larger than the correlation length of the intensity fluctuations [4]. The use of aperture averaging as a counter measure for the mitigation of the scintillation has been extensively considered in the literature [5, 7], leading to substantial scintillation fade reduction, especially in the strong turbulence regime.

Besides, we propose a model based on the multiple subcarrier modulation (MSM) over Intensity Modulation Direct Detection optical link. Being a sum of narrowband signals, the MSM provides greater immunity to intersymbol distortion and higher bandwidth efficiency than the single carrier modulation schemes. In our model, each subcarrier is modulated using either Binary Phase Shift Keying (BPSK) or Quadrature Phase Shift Keying (QPSK) schemes that effectively mitigate the signal scintillation and avoid the need for adaptive threshold normally required by optimum On-Off-keying (OOK) [8].

In this paper, we study the impact of aperture averaging on the MSM-FSO system using two different modulation schemes BPSK and QPSK, in the weak and the strong turbulence regimes. By using a modified model taking into consideration aperture averaging, we numerically analyze the system performance improvement in terms of the average bit error rate (BER). The remainder of the paper is organized as follows. Section 2 describes the optical propagation model and the aperture averaging technique. The mathematical modeling for the transmission of MSM signals over turbulent IM/DD optical link is discussed in Section 3. In Section 4, the performance improvement by aperture averaging is numerically assessed by considering the BER metric. Finally, Section 5 concludes the paper.

2. FSO CHANNEL CHARACTERISTICS

The most serious effects that affect severely the propagation of a laser beam propagating through the atmosphere are caused by the variations of the refractive index in the turbulent air. An important parameter that describes the strength of turbulence is the scintillation index $\sigma_I^2 = \langle I^2 \rangle / \langle I \rangle^2 - 1$, with I being the intensity of the optical wave [4]. In order to mitigate this turbulence-induced fading, we adopt in this paper the AA technique that exploits the dependence of the received power variance on the size of the receiver aperture in order to reduce this former significantly. Considering a collecting aperture size that is larger than the spatial scale size leads to a substantial decrease in the scintillation effect and subsquently an enhancement in the FSO system performance [4, 6]. In this way, the receiver can average these fluctuations over its aperture and, hence reduce the scintillation-induced fading compared to the case of a point receiver. The fading reduction by AA is usually characterized by the AA factor defined as $F = \sigma_I^2(D)/\sigma_I^2(0)$, where $\sigma_I^2(D) = \exp(\sigma_{\ln x}^2(D) +$

$\sigma^2_{\ln y}(D)) - 1$ and $\sigma_I^2(0)$ denote the scintillation indexes for a receiver lens of aperture diameter D and for a point receiver ($D = 0$), respectively [4]. For the case of the Gaussian-beam wave model considered in this paper, the detailed expressions of the log-variances $\sigma^2_{\ln x}(D)$ and $\sigma^2_{\ln y}(D)$ can be found in [4].

When the AA is used, it was pointed out that the lognormal distribution provides a good fit to the received irradiance fluctuations for many weak-to-strong scenarios [6]. Hence, the corresponding probability density function (PDF) adopted in this paper for computational purpose, reads [4]

$$p(I) = \frac{1}{I}\frac{1}{\sqrt{2\pi\sigma_I^2(D)}}\exp\left\{-\frac{\left(\ln\left(\frac{I}{\langle I\rangle}\right)+\frac{\sigma_I^2(D)}{2}\right)^2}{2\sigma_I^2(D)}\right\}, \quad I>0 \tag{1}$$

where $\sigma_I^2(D)$ is is the aperture-averaged scintillation index as defined earlier, and $\langle I\rangle$ denotes the mean intensity that is equal to the intensity without turbulence.

3. OPTICAL MSM SIGNAL TRANSMISSION OVER FSO LINK

In this work, we consider an optical intensity-modulated direct detection (IM/DD) system based on MSM technique in which high data rate streams are split into lower rate streams and then transmitted simultaneously over narrow-band subcarriers. In the MSM-FSO systems, N channels are multiplexed with subcarriers of different frequencies in the electrical domain. The subcarriers are themselves modulated using subcarrier either BPSK or QPSK modulation formats, which in turn modulate the intensity of a continuous wave laser acting as the optical carrier. At the receiver side, the incident optical field is focused onto a photo detector by a lens of diameter D, before being converted to an electrical signal, which is proportional to the instantaneous optical power. Afterwards, the recovered signal is fed into an RF demodulation block to retrieve the input multiplexed data.

The transmitted MSM signal for N subcarriers is given by [**?**]

$$\begin{aligned} s_{MSM}(t) &= \sum_{n=0}^{N-1} s_n(t) = \sum_{n=0}^{N-1} d_n(t)\cos(\omega_n t+\phi_n) \\ &= \sum_{n=0}^{N-1}\sum_{k=-\infty}^{\infty} d_k^{(n)} p_T(t-kT)\cos(\omega_n t+\phi_n),\ 0\le t<T_s \end{aligned} \tag{2}$$

where $d_n(t)$ is the nth binary data stream with $d_k^{(n)}$ being the binary values $\{-1,+1\}$ for $kT \le t \le (k+1)T$; $p_T(t)$ is a rectangular pulse, which equals unity for $0 \le t \le T$; $\{\omega_n = (2\pi n/T_s), n = 0,1,\ldots,N-1\}$ is the nth subcarrier frequency with T_s being the MSM symbol duration and ϕ_n, $\{\ 0 \le \phi_n \le 2\pi\}$ denotes the phase of the nth subcarrier.

The signal $s_{MSM}(t)$ is then used to modulate the optical intensity of the laser diode (LD) to be transmitted through fiber optics. However, the MSM-FSO system performance may be conspicuously degraded due to the LD nonlinearity that causes mixing of users signals, resulting in generation of harmonics and inter-modulation distortions (IMD). Given that the second-order IMD (IMD2) can be designed out of band when the transmission band is limited to a single octave, only the third-order IMD (IMD3) contributes to the interference [9].

In the abscence of atmospheric turbulence, by assuming that the FSO noise can be filtered in the photodetector, the current at the output of the photodetector is given as

$$I_r(t) = \rho P(t) + n(t) = \rho P_{r,0}\left(1+\sum_{n=0}^{N-1} m_n s_n(t) + a_3\left[\sum_{n=0}^{N-1} m_n s_n(t)\right]^3\right) + n(t), \tag{3}$$

$$P_{r,0}(t) = P(t)L_{FSO} + n_{FSO}(t) = L_{FSO}\left(P_0\left(1+\sum_{n=0}^{N-1} m_n s_n(t) + a_3\left[\sum_{n=0}^{N-1} m_n s_n(t)\right]^3\right)\right) + n_{FSO}(t) \tag{4}$$

where $P_{r,0}(t)$ characterizes the received optical power at the photo detector in the abscence of turbulence fluctuations with L_{FSO} including FSO channel losses; ρ is the photo detector responsivity,

P_0 represents the average transmitted optical power, a_3 is the third order nonlinearity coefficient, and m_n is the optical modulation index (OMI) for each subcarrier with $m_{Total} = \frac{1}{N}\sqrt{\sum_{n=0}^{N-1} m_n^2}$, and $n(t)$ is the additive white Gaussian noise with a double-sided power spectral density of $N_0/2$. The Gaussian noise models the noise processes in the optical link which include signal shot noise, thermal noise in the electronics following the photo detector, and relative intensity noise (RIN) inherent to the laser diode, and is given by [9]

$$N_0 = (RIN)\, I_{ph}^2 + 2e\rho I_{ph} + \frac{4K_B T_N}{R_L}, \quad I_{ph} = \rho P_{r,0} \tag{5}$$

where $P_{r,0}(t)$ is the received signal power in the absence of atmospheric effects given by Eq. (3), e is the electron charge, K_B is the Boltzmann's constant, T_N is the absolute temperature and R_L is the receiver circuit load resistance.

In the analysis to follow, we will present the relationship between the averaged carrier-to-noise and distortion ratio (CNDR) which takes into consideration IMD effect and the receiver aperture size in the presence of the atmospheric effects. For the sake of simplicity, we assume all the tones to be modulated with the same modulation index m_n then the OMI per subcarrier m_n is derived as $m_n = m_{Total}/\sqrt{N}, \quad n = 0, 1, \ldots, N-1$. The IMD3 term which falls into carrier ω_n among equally spaced N carriers can be described as [9]

$$\sigma_{IMD}^2 = \frac{1}{2}\left(\frac{3}{4}a_3 m_n^3 D_2(N,n) + \frac{3}{2}a_3 m_n^3 D_3(N,n)\right)^2 I_{ph}^2, \tag{6}$$

where $D_2(N,n) = \frac{1}{2}(N-2-\frac{1}{2}(1-(-1)^N)(-1)^n)$ and $D_3(N,n) = \frac{n}{2}(N-n+1) + \frac{1}{4}((N-3)^2-5) - \frac{1}{8}(1-(-1)^N)(-1)^{N+n}$ represent the number of intermodulation distortion products which influence the desired carrier.

Therefore, in the presence of atmospheric turbulence between the transmitter and the receiver, the received signal exhibits random irradiance fluctuations. Thus, $CNDR_n$ per subcarrier becomes a fluctuating term whose mean, referred to as $\langle CNDR_n \rangle$, assumes the form [4]

$$\langle CNDR_n \rangle = \frac{CNDR_{0,n}}{\left(1+1.63\sigma_R^{12/5}\Lambda\right)^2 + \sigma_I^2(D)\, CNDR_{0,n}}; \quad CNDR_{0,n} = \frac{\langle i_r \rangle^2}{\sigma_N^2 + \sigma_{IMD}^2} = \frac{\frac{1}{2}m_n^2 I_{ph}^2}{N_0 B_n + \sigma_{IMD}^2}, \tag{7}$$

where $CNDR_{0,n}$ represents the received CNDR in the absence of optical turbulence and B_n is the bandwidth per subcarrier required to pass the signal without distortion.

Finally, when the number of subcarriers is large, the total average $\langle CNDR \rangle$ over the entire MSM band can be derived based on law of large numbers (LLN)

$$\langle CNDR \rangle = \frac{1}{N}\sum_{n=0}^{N} \langle CNDR_n \rangle = \frac{1}{N}\sum_{n=0}^{N}\left[\frac{CNDR_{0,n}}{\left(1+1.63\sigma_R^{12/5}\Lambda\right)^2 + \sigma_I^2(D)\, CNDR_{0,n}}\right]. \tag{8}$$

Let us study the performance of MSM systems using subcarrier either BPSK or QPSK modulation techniques. The investigation of the BER helps in evaluating the degradation that incurs the FSO link carrying out the MSM signals due to the presence of the atmospheric turbulence. The BER depends on the average received power, the turbulence-induced fading over the aperture and the receiver noise which includes particularly the intermodulation distortion noise. We assume that the intermodulation distortion noise is Gaussian distributed so that the total noise defined in Eq. (5) is Gaussian.

For optical communication employing BPSK (with $M = 2$) and in the presence of the atmospheric effects, the total average bit error probability $< P_b >$ can be written as [4]

$$\langle P_b \rangle = \frac{1}{N}\sum_{n=0}^{N-1} \langle P_{b,n} \rangle = \frac{1}{N}\sum_{n=0}^{N-1}\left[\frac{1}{2}\int_0^\infty p_I(s)\mathrm{erfc}\left(\frac{\sqrt{\langle CNDR_n \rangle}\cdot s}{\langle i_r \rangle}\right) ds\right], \tag{9}$$

where $p_I(s)$ is the lognormal distribution as defined by Eq. (1).

When QPSK with $M = 4$ is employed and by assuming that the Gray-coded mapping is used at the transmitter, the average $\langle P_b \rangle$ reads

$$\langle P_b \rangle = \frac{1}{N} \sum_{n=0}^{N-1} \langle P_{b,n} \rangle = \frac{1}{N} \sum_{n=0}^{N-1} \left[\frac{1}{2} \int_0^{\infty} p_I(s) \text{erfc} \left(\frac{\sqrt{\sin^2\left(\frac{\pi}{4}\right) \langle CNDR_n \rangle} \cdot s}{\langle i_r \rangle} \right) ds \right]. \quad (10)$$

4. PERFORMANCE EVALUATION

In this section, we will compare the aperture averaging effect on the average BER when BPSK and QPSK modulation techniques are considered under different turbulence conditions. The main simulation parameters are shown in Table 1. Two cases of weak and strong turbulence will be considered for which we set $\sigma_R^2 = 0.4$ and $\sigma_R^2 = 20$, respectively.

We investigate the BER performance of the aperture averaging receiver while using BPSK and QPSK modulation in different turbulence regimes. Fig. 1 plots the variation of BER given by Eq. (9) and Eq. (10) as a function of the received optical power $P_{r,0}$ in the weak turbulence regime ($\sigma_R^2 = 0.4$). It can be seen that the performance improvement by fading reduction via aperture averaging is less significant when more complex modulation schemes are used. For example, in the weak turbulence regime ($\sigma_R^2 = 0.4$), with a 10 cm-aperture diameter, we obtain a BER of 10^{-6} for QPSK while BER decreases to about 10^{-9} when BPSK technique is used, all the values at a received power of -15 dBm. Besides, by increasing D from 5 cm to 20 cm, a gain of 40 dB in BER is achieved, for a received power of -15 dBm. In fact, the larger constellation sizes require higher received power to accurately discriminate among the transmitted symbols.

Table 1: MSM-FSO link parameters.

Symbol	Parameter	Value
λ	Operating wavelength	1550 nm
L	Link distance	1000 m
P_0	Transmitted optical power	20 dBm
ρ	Detector responsivity	0.8 A/W
RIN	Relative intensity noise	-150 dB/Hz
T_{abs}	Absolute temperature	300 K
R_L	PD load resistor	50 Ω
a_3	Third order IMD	0.17
B_n	Subcarrier Bandwidth	300 KHz
N	Number of carriers	64

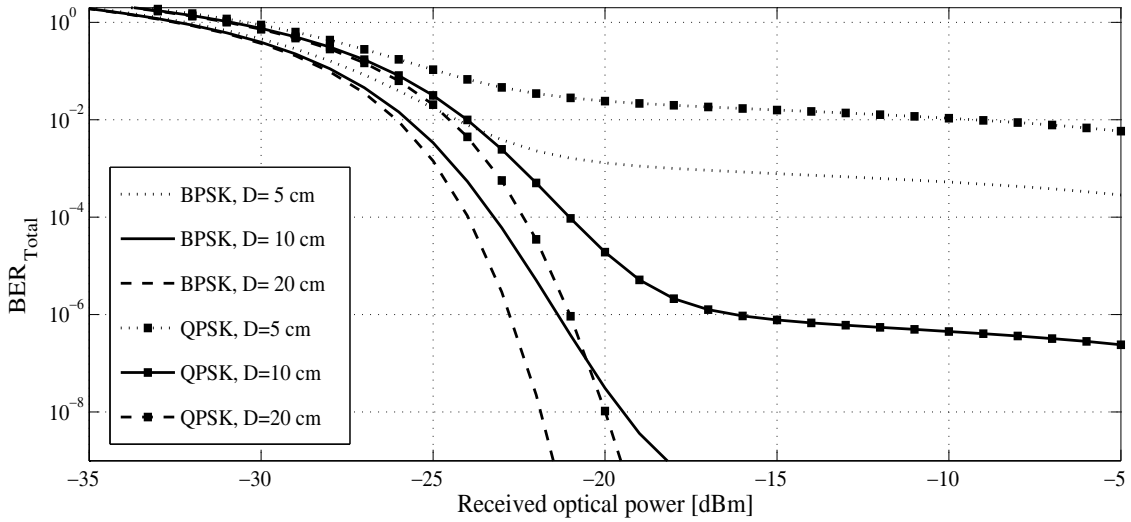

Figure 1: Average BER for BPSK and QPSK as a function of received optical power for various receiver aperture diameter D in the weak turbulence regime.

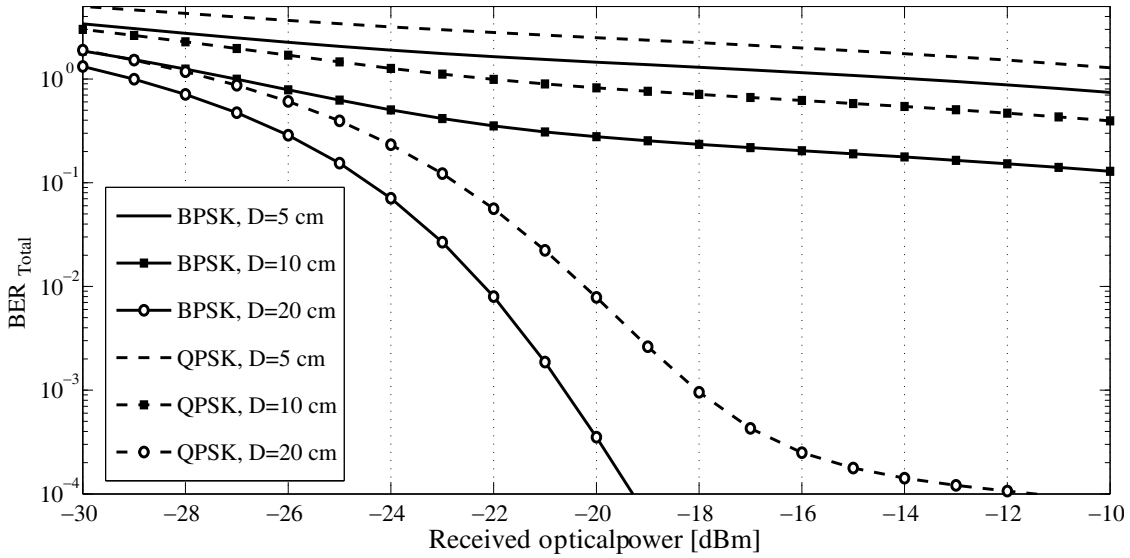

Figure 2: Average BER for BPSK and QPSK as a function of received optical power for various receiver aperture diameter D in the strong turbulence regime.

Now, let us consider the case of strong turbulence with $\sigma_R^2 = 20$. The use of aperture averaging leads to more significant performance improvement which is confirmed by the BER curves shown in Fig. 2: by increasing D from 10 cm to 20 cm, a gain of about 30 dB and 22 dB in BER can be obtained when using the BPSK and QPSK schemes, respectively, this for a received power of -20 dBm. However, if we compare the gain obtained by aperture averaging in the two modulation cases, we can clearly see that the MSM-FSO system using larger constellation size is more sensitive to the heavy turbulence. Besides, it is clear that for more complex modulation techniques no matter how large the receiver aperture size, the accepted BER level can not be attained only with the use of aperture averaging technique. More sophisticated mitigation techniques should be considered in order to reduce the turbulence-induced fading.

5. CONCLUSION

In this paper, we have studied the aperture averaging effect on the performance of MSM signals over a IM/DD optical link under weak and strong turbulence regimes when two different modulation techniques are considered: BPSK and QPSK. By using a modified model for the aperture averaging technique, we have provided a detailed theoretical analysis of the overall system performance in terms of the average CNDR as well as the average BER in the weak and the strong turbulence regimes taking into consideration the intermodulation distortion term due to the laser diode non-linearity. The evaluation of average BER behavior outlines that the use of aperture averaging technique can lead to significant performance improvement, especially as the scintillation-induced fading becomes more important. However, when higher order PSK modulation techniques are used, the fading reduction via aperture averaging is far less impressive than that for schemes employing smaller constellation sizes. Our results can serve as preliminary guidelines to the receiver design for terrestrial FSO systems based on MSM technique, where several technical issues, such as size and weight should be considered.

ACKNOWLEDGMENT

This research is supported by grant-in-aid of High-tech Research Center Project by the MEXT, Japan.

REFERENCES

1. Willebrand, H. and B. Ghuman, *Free Space Optics: Enabling Optical Connectivity in Today's Networks*, Sams Publishing, 2002.
2. Kazaura, K., et al., "Performance evaluation of next generation free-space optical communication system," *IEICE. Trans. Electron.*, Vol. 2, 381–388, 2007.
3. Wakamori, K., K. Kazaura, and I. Oka, "Expreriment on regional broad-band network using free-space-optical communication systems," *J. Light. Technol.*, 3265–3273, 2007.

4. Andrews, L. C. and R. L. Philips, *Laser Beam Propagation through Random Media*, SPIE, Bellingham, WA, 2005.
5. Yuksel, H., S. Milner, and C. C. Davis, "Aperture averaging for optimizing receiver design and system performance on free-space optical communication links," *J. Opt. Netw.*, Vol. 4, 462–475, 2005.
6. Vetelino, F. S., C. Young, L. C. Andrews, and J. Recolons, "Aperture averaging effects on the probability density of irradiance fluctuations in moderate-to-strong turbulence," *Appl. Opt.*, Vol. 46, 2099–2108, 2007.
7. Khaligi, M. A., N. Schwartz, N. Aitamer, and S. Bourennane, "Fading reduction by aperture averaging and spatial diversity in optical wireless systems," *J. Opt. Commun. Netw.*, Vol. 1, No. 6, 580–592, 2009.
8. Li, J., J. Q. Liu, and D. P. Taylor, "Optical communication using subcarrier PSK intensity modulation through atmospheric turbulence channels," *IEEE Trans. Commun.*, Vol. 55, No. 8, 1598–1606, 2007.
9. Al-Raweshidy, H. and S. Komaki, *Radio over Fiber Technologies for Mobile Communications Networks*, 1st Edition, Artech House Publishers, 2002.

Numerical Analysis of Novel Asymmetric SNOM Tips

Valeria Lotito[1, 2], **Urs Sennhauser**[1], **and Christian Hafner**[2]

[1]Electronics/Metrology Laboratory, EMPA, Swiss Federal Laboratories for Materials Testing and Research
Ueberlandstrasse 129, CH-8600 Dübendorf, Switzerland
[2]Department of Information Technology and Electrical Engineering, ETH Zurich
Gloriastrasse 35, Zurich 8092, Switzerland

Abstract— Our finite element analysis of novel scanning near field optical microscopy tips reveals that field localization and enhancement, fundamental for high resolution applications, can be achieved under linearly polarized excitation by introducing properly tailored asymmetries in a fully metal-coated tip. Therefore, superfocusing effects comparable to those observed under a complicated radially polarized excitation in an axisymmetric tip can be achieved with an easier injection procedure, with a significant simplification in experimental applications.

1. INTRODUCTION

Scanning near field optical microscopy (SNOM) is a valuable tool for the investigation of nanostructures today because it combines the potential of scanning probe technology with the power of optical microscopy [1]. The technique is based on the near field interactions between the sample and a probe, which plays a key role in the overall performance of the system.

In the search for optimized tip structures, fully metal-coated probes appear particularly attractive because of their high-volume manufacturability, the greater manufacturing reproducibility and the easier control over their shape. However, the behaviour of such probes is strongly dependent on the input polarization. If the structure is excited with a radially polarized mode, a localized ultrasmall hot spot with peak field amplitude much higher than the one of linearly polarized modes is generated, as opposed to a broad weak two-lobed distribution under a linearly polarized excitation. These properties can be explained in the light of the characteristics of the surface plasmon polaritons (SPPs) excited on the metal surface and converging towards the tip apex, which interfere constructively in case of radial polarization and cancel out due to the opposite charges on the opposite sides of the tip under linearly polarized excitation [2, 3].

Hence, for high resolution applications, a radially polarized excitation is required, which unfortunately imposes the need for a cumbersome procedure, extremely sensitive to misalignments [4]. In order to circumvent this problem, we propose the introduction of intentional asymmetries, properly tailored to get superfocusing effects similar to those observed under radial polarization by using a more easily excitable linearly polarized mode. More specifically, we have carried out a finite element analysis of two different configurations, one based on an oblique cut close to the tip apex stripping off both the metal coating and the inner core and the other consisting of asymmetric corrugations in the metal coating [5, 6]. A thorough analysis of the effects of geometric and material parameters has been undertaken, in order to optimize the probe structure in terms of full width at half maximum (FWHM) and peak value of the resulting distribution under linearly polarized excitation.

2. NUMERICAL MODEL

In order to assess the performance of our asymmetric probes, we developed a three-dimensional (3D) computational model using a finite element based software, Comsol Multiphysics. In fact, the presence of the asymmetry prevents us from adopting two-dimensional (2D) approximations or other numerical simplifications like the body of revolution finite difference time domain method possible for axisymmetric structures [7, 8]. We chose the finite element method for probe modelling because the use of unstructured grids allows the treatment of complicated geometries. The three structures we analyzed are sketched in Figure 1.

The axisymmetric probe (Figure 1(a)) was considered as a reference for comparison for our asymmetric configurations. The probe consists of a silica core ($n = 1.5$) coated with an aluminium layer ($n = 0.645 + 5.029i$ at the operating wavelength $\lambda = 532\,\text{nm}$): the inner silica cone has an initial radius of 225 nm and is rounded at the apex with a radius of curvature of 10 nm; the metal hollow cone exhibits an outer radius of 275 nm and a final rounding with 20 nm radius. Both the cones have a full apex angle of 30°. The modelling domain is a 1.6 µm high cylinder with radius of 1 µm.

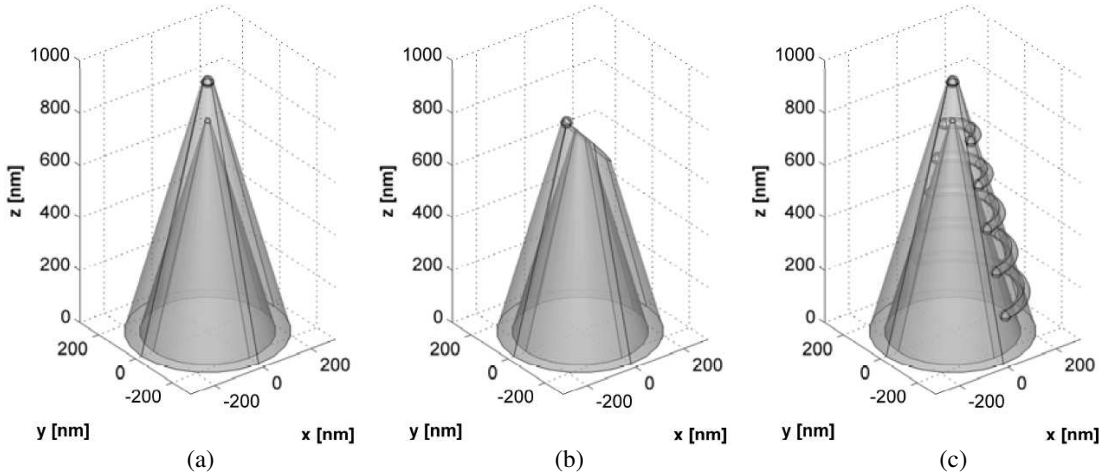

Figure 1: Sketch of the probe structures: (a) axisymmetric probe; (b) cut probe; (c) probe with asymmetric corrugations.

The tip with an oblique cut (Figure 1(b)) is based on a cut along a plane which is neither orthogonal nor parallel to the tip axis: the cut angle (defined as the angle between a plane orthogonal to the axis of the tip and the plane of the cut itself) and the cut height (meant as the height of the new tip apex after the cut measured from the bottom of the computational domain) can be varied.

The structure with asymmetric corrugations (Figure 1(c)) is based on the introduction of semicircular corrugations on the outer metal surface, which could consist in either bumps or grooves. Such surface corrugations are modelled by joining five truncated toroids of radius 20 nm with hemispherical terminations having the same radius: the toroidal sections are filled with air in case of a groove or with metal in case of a bump. Corrugations are limited to just one half of the tip, hence their angular extension, defined as opening angle, is less than 180°. The different configurations will be named after the initial of the filling material (a for air or m for metal) starting from the bottom corrugation.

Simulations have been carried out by propagating in a 3D analysis the eigenmodes calculated at the input port. Figure 2 reports the square of the norm of the electric field in a transverse plane located at 10 nm from the tip apex for the axisymmetric structure under radially polarized (R) and x- and y-linearly polarized excitation (called H and V respectively). In order to highlight the relative field strengths, fields are normalized to the R peak value of the axisymmetric probe. When the structure is excited with a radially polarized mode, a localized hot spot is created with FWHM of about 38 nm, while in case of linearly polarized excitation (independently of its polarization direction) broad two-lobed distributions extended over an area of approximately 400 nm and about 50 times weaker than the peak of the R distribution are obtained. The size of the R hot spot is mostly influenced by the diameter of the final metal rounding [9].

In the following section we will show how superfocusing effects comparable to the ones observed for the axisymmetric probe under radially polarized excitation can be achieved under linearly polarized excitation by introducing an asymmetry properly oriented with respect to the input linear polarization. The achieved field distributions can be optimized in terms of FWHM (which is related to the achievable resolution) and peak intensity by tuning some geometric and material parameters, namely (i) the cut height and angle for the probe based on an oblique cut and (ii) the alternation of bumps and grooves and the angular extension of the corrugations for the asymmetrically corrugated structure. The dependence of probe performance on the mutual orientation between the input linear polarization and the asymmetry will be examined as well.

3. ANALYSIS OF THE ASYMMETRIC PROBES

The near field distributions at 10 nm from the tip apex under linearly polarized excitation have been analyzed for both the asymmetric structures: Figure 3 reports an example of the near field distributions achieved for two probes, one based on an oblique cut (cut angle 50°; cut height 816 nm) and the other on corrugations (*amama*, opening angle 160°). Values are normalized to the radial peak of the axisymmetric structure. As visible, field localization and enhancement occur for the H linearly polarized mode which is oriented along the direction of the asymmetry (x in our case), while

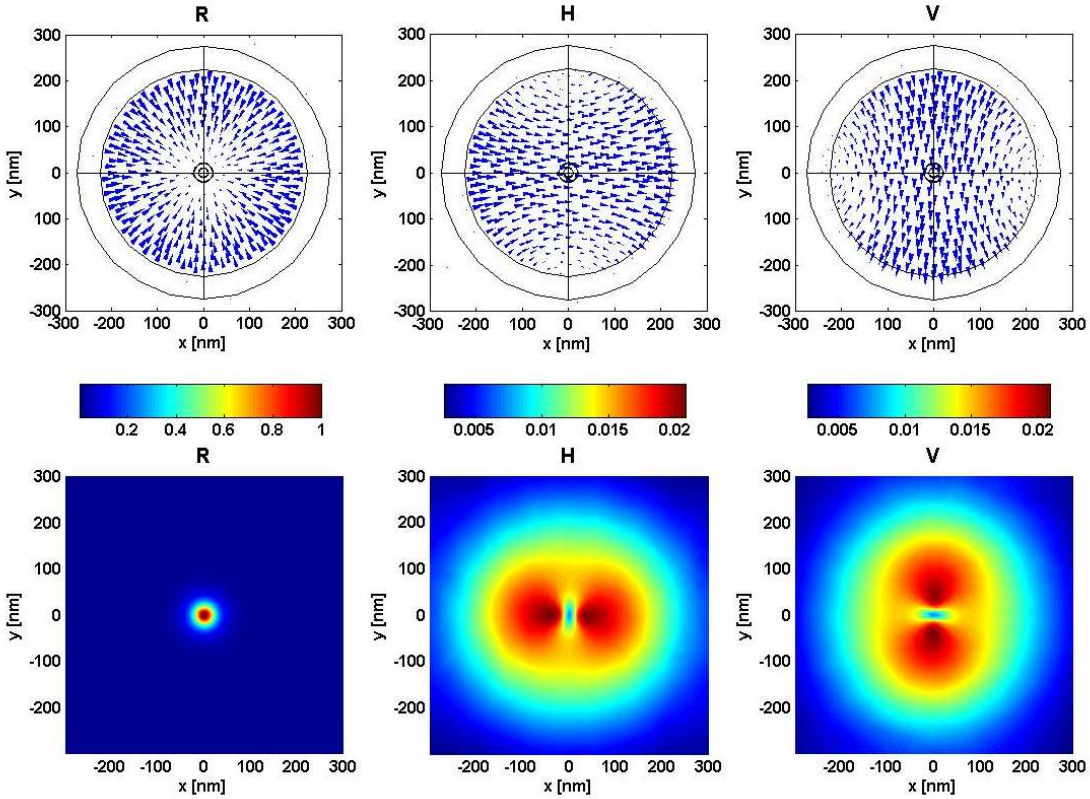

Figure 2: Radially (R) and x- and y-linearly polarized excitations (H and V) and corresponding near field intensity distributions at 10 nm from the tip apex for an axisymmetric probe.

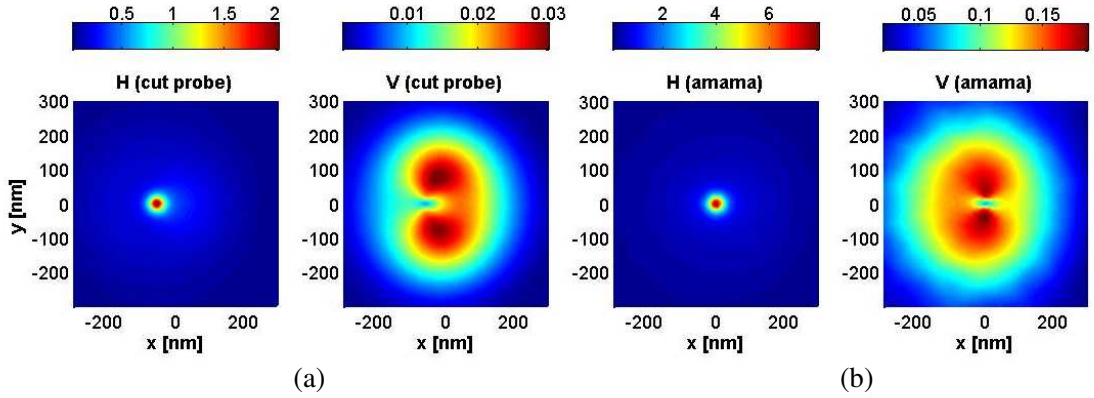

Figure 3: Near field intensity distributions at 10 nm from the tip apex under H and V polarized excitations for: (a) cut probe (cut angle 50°; cut height 816 nm); (b) probe with asymmetric corrugations (*amama*, opening angle 160°).

for the orthogonally polarized mode V, no substantial variation with respect to the axiysmmetric case is observed.

Probe optimization for the cut probe has been carried out by varying the cut angle from 20° to 60° with a step of 10° while keeping the cut height constant at 816 nm and by changing the cut height from 741 nm to 841 nm with a step of 25 nm at a cut angle of 30°. Figure 4 reports the peak value of the H distribution (normalized to the one of the standard axisymmetric probe under radially polarized excitation) and its FWHM. As apparent, stronger peak values are obtained for steeper cut angles and lower cut heights (Figures 4(b) and (d)). The FWHM of the H spot is not really sensitive to the cut angle (Figure 4(a)), while it deteriorates for bigger tip heights, which

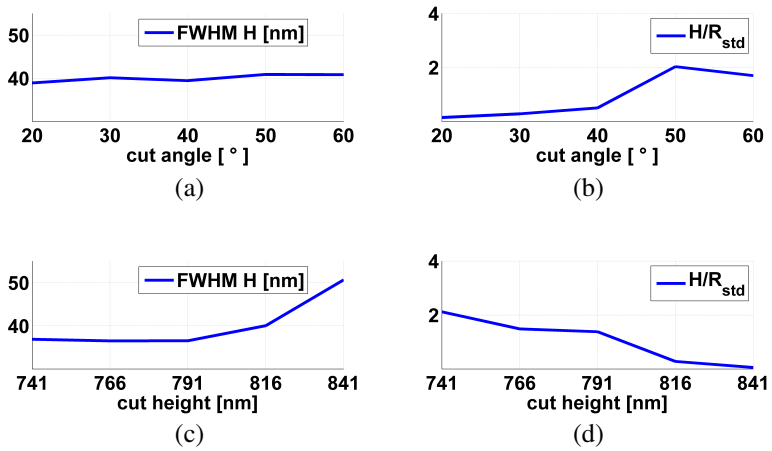

Figure 4: Behaviour of the cut probe under H polarized excitation: (a) FWHM of the H spot for variable cut angle; (b) comparison of the H peak value with respect to the one of the standard probe under radially polarized excitation (denoted by R_{std}) for variable cut angle; (c) FWHM of the H spot for variable cut height; (d) comparison of the H peak value with respect to the one of the standard probe under radially polarized excitation (denoted by R_{std}) for variable cut height.

means cuts closer to the original tip apex (Figure 4(c)). Therefore, an overall improvement occurs for steeper cut angles and lower cut heights, corresponding to stronger asymmetries.

As to the asymmetrically corrugated probe we analyzed all the possible permutations of air and metal, i.e., of grooves and bumps, in the five corrugations with an opening angle of 160°. We also examined the effects of the opening angle by changing this parameter from 110° to 160° with a step of 10° for the *amama* configuration. As can be observed in Figures 5(a) and (b), while field localization under H polarized excitation occurs for almost all the material permutations, with a value of FWHM in most of the cases comparable to the one of the radial spot for the axisymmetric structure, only few configurations give rise to peak values comparable or, in some cases, much superior to the radial peak of the axisymmetric probe, in particular those structures with an alternation of air, metal and air in the upper three corrugations. The FWHM is not much affected by the opening angle (Figure 5(c)), while the peak value goes up with an increase in the angular extension (Figure 5(d)).

The strong field localization achieved in case of a mode linearly polarized along the direction of the asymmetry results from the interplay of improved coupling mechanisms between the linearly polarized mode and the radially polarized one and between the inner SPP confined at the silica/metal interface and the outer SPP at the metal/air interface. The use of these promising asymmetric structures could entail an impressive simplification in mode injection procedures for high resolution SNOM applications.

As observed, field localization and enhancement take place only for an input linear polarization properly oriented with respect to the asymmetry. In fact, in all the cases the modification introduces a strong asymmetry along one specific spatial direction, with no asymmetry along the orthogonal direction. Previously we have examined only two possible mutual orientations of the asymmetry with respect to the input polarization direction, corresponding to the best and worst scenario respectively. In order to assess the sensitivity of the field localization to the relative alignment, we have studied the probe behaviour under different relative positions of the asymmetry and the input polarization direction. For the purpose of varying the mutual orientation, a rotation in the input polarization direction with the asymmetry kept along one specific direction is equivalent to a rotation in the direction of the asymmetry with a constant input polarization direction. We chose to follow the second route and rotated the asymmetry (either the cut or the corrugations) around the z axis from 0° to 45° with a step of 5°, with 0° corresponding to the asymmetry along the x direction as reported in Figures 1(b) and (c). For each of the rotated angles, we evaluated the field distributions under both H and V polarized excitation. Therefore, given α the angle by which the asymmetry is rotated, the relative orientation between the asymmetry and the H excitation is α, while the one with respect to the V excitation is $90°-\alpha$, which means that the whole range of mutual orientations goes from 0° to 90°. Note that such a range encompasses all the possible

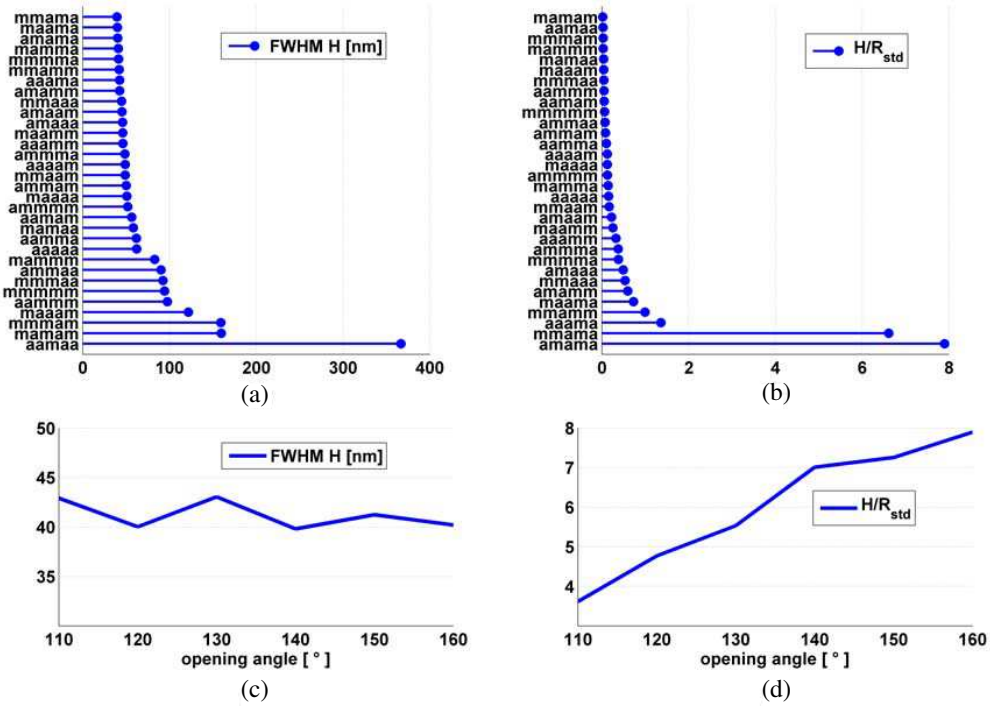

Figure 5: Behaviour of the corrugated probe under H polarized excitation: (a) FWHM of the H spot for different material permutations and 160° opening angle; (b) comparison of the H peak value with respect to the one of the standard probe under radially polarized excitation (denoted by R_{std}) for different material permutations and 160° opening angle; (c) FWHM of the H spot for the *amama* configuration with variable opening angle; (d) comparison of the H peak value with respect to the one of the standard probe under radially polarized excitation (denoted by R_{std}) for the *amama* configuration with variable opening angle.

mutual positions due to the fact that the asymmetries here considered possess an axis of symmetry. For each value of α, we evaluated the FWHM and the peak value of the near field distributions under H and V input polarization. As an example, in Figure 6, we report the graphs obtained for the *maama* structure with 160° opening angle.

For $\alpha = 0°$, no asymmetry is present along the y direction. Hence, no field localization occurs under V polarization. As α increases, the asymmetry along x is reduced, while an asymmetry along y appears and becomes gradually stronger. As a consequence, the asymmetry starts having less impact on the H distribution whose peak value begins to drop. On the contrary, the V distribution shrinks in size and climbs in peak value. At $\alpha = 45°$, the asymmetries perceived by both H and V are the same; hence the corresponding distributions are roughly identical. We calculated the average value of the FWHM and of the peak ratio over all the rotated positions (just one average for both H and V due to their equivalence) for different configurations with various geometric parameters (*amama* and *maama* with an opening angle of 160°; *amama 130°* with an opening angle of 130°; *cut 50°* and *cut 30°* with a cut height of 816 nm and a cut angle of 30° and 50° respectively; *cut 766* nm with a cut height of 766 nm and a cut angle of 30°) and estimated the maximum deviations from the corresponding average, as reported in Figure 7.

The analysis of polarization sensitivity reveals the importance to excite the structure with an input linear polarization suitably oriented with respect to the asymmetry, with maximum variation from the average value of the FWHM and peak value as high as nearly 500% and 100% respectively. However, as evident in Figure 6(a), the FWHM is almost constant and small over a wide range of misalignments from the best direction, and therefore high resolution could still be achievable provided that the peak value is sufficient for detection. This means that the tip behaviour does not deteriorate significantly within an acceptable tolerance range. In fibre based tips, the alignment could be complicated by both the polarization rotation within the probe and also by the lack of knowledge about the position of the asymmetry in the tip when mounted on the microscope. Nevertheless, such a problem can be overcome by the use of a cantilevered probe: in this case the position of the asymmetry relative to the cantilever is well known in the fabrication process, which

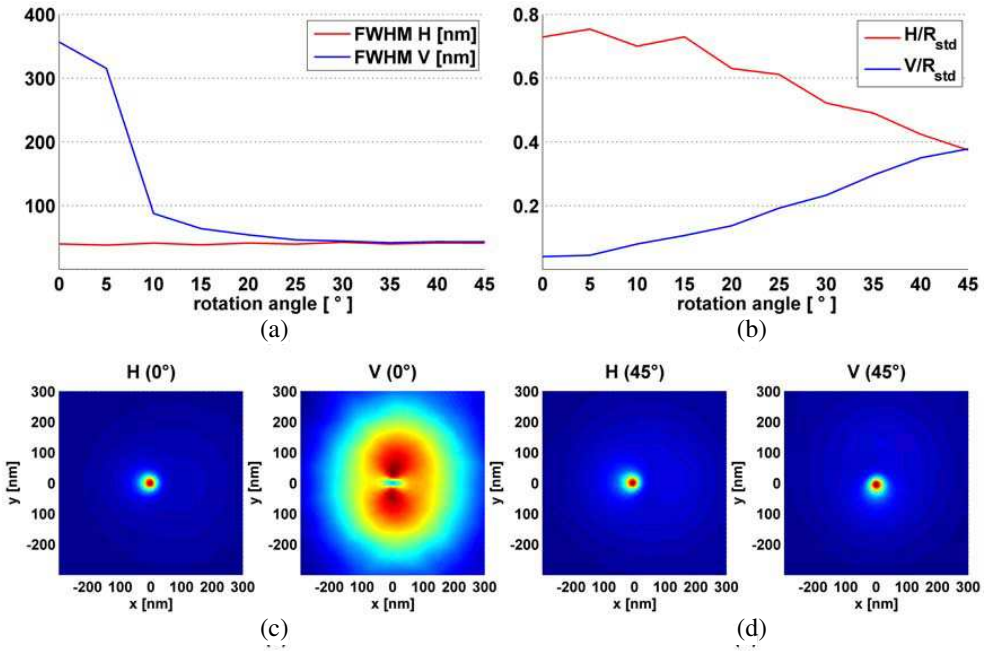

Figure 6: Behaviour of the corrugated probe *maama* with 160° opening angle under variable rotation angle α and H and V polarized excitation: (a) FWHM; (b) comparison of the peak value with respect to the one of the standard probe under radially polarized excitation (denoted by R_{std}); (c) near field distributions at 10 nm from the tip apex under H and V excitations for $\alpha = 0°$; (d) near field distributions at 10 nm from the tip apex under H and V excitations for $\alpha = 45°$.

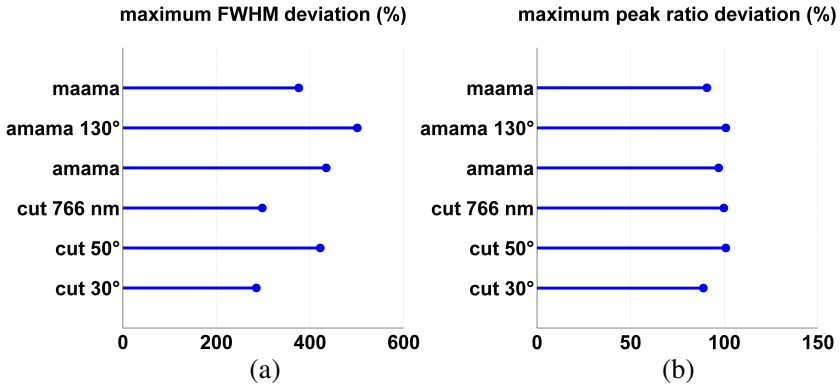

Figure 7: Maximum deviation of (a) FWHM (of both H and V) and (b) peak ratio (both H/R_{std} and V/R_{std}) from the corresponding average values for different asymmetric tips with various parameters.

makes it easier to align the input polarization properly with a broad tolerance range.

4. CONCLUSIONS

Our finite element based simulations have shown that carefully designed asymmetries introduced in an originally axisymmetric fully metal-coated tip can produce field localization under an excitation linearly polarized along a proper polarization direction. The presence of the asymmetry causes the electric fields associated with SPPs on the opposite sides of the tip not to have opposite phases any longer, a phenomenon that leads to destructive interference under linearly polarized injection in an axysimmetric structure. An overall analysis of both a cut probe and a tip with asymmetric corrugations has shown that this effect is enhanced when the asymmetry is extended over a broader region. In this way superfocusing can be achieved with a linearly polarized injection, which is much easier than a radially polarized one, with an enormous simplification in experimental applications.

An analysis under variable polarization direction has indicated a dramatic change in tip behaviour as the input polarization is rotated gradually from the direction of the asymmetry to the

orthogonal one, highlighting the need to excite the structure with a suitable input polarization direction. However, due to the stability of the FWHM over a sufficiently broad tolerance range of misalignment, good performance can be guaranteed as long as the position of the asymmetry is known with sufficient accuracy as is the case for cantilevered tips. For fibre based tips, performance could be less controllable, due to the difficulty in knowing the exact position of the asymmetry when the tip is mounted on the microscope and also because of the rotation of the polarization within the probe. However, in this case, our approach based on the effects of the introduction of an asymmetry could be extended to envisage asymmetries distributed along multiple spatial directions, which would reduce the performance sensitivity.

ACKNOWLEDGMENT

The authors gratefully acknowledge the support of the Swiss National Science Foundation (Project number 200021-115895).

REFERENCES

1. Novotny, L. and B. Hecht, *Principles of Nano-Optics*, Cambridge University Press, 2006.
2. Bouhelier, A., J. Renger, M. R. Beversluis, and L. Novotny, "Plasmon-coupled tip-enhanced near-field optical microscopy," *J. Microsc.*, Vol. 210, Pt. 3, 220–224, 2003.
3. Chen, W. and Q. Zhan, "Numerical study of an apertureless near field scanning optical microscope probe under radial polarization illumination," *Opt Express*, Vol. 15, No. 7, 4106–4111, 2007.
4. Tortora, P., E. Descrovi, L. Aeschimann, L. Vaccaro, H. P. Herzig, and R. Dändliker, "Selective coupling of HE_{11} and TM_{01} modes into microfabricated fully metal-coated quartz probes," *Ultramicroscopy*, Vol. 107, No. 2–3, 158–165, 2007.
5. Lotito, V., U. Sennhauser, and C. Hafner, "Finite element analysis of asymmetric scanning near field optical microscopy probes," *J. Comput. Theor. Nanosci.*, Vol. 7, No. 8, 1596–1609, 2010.
6. Lotito, V., U. Sennhauser, and C. Hafner, "Effects of asymmetric surface corrugations on fully metal-coated scanning near field optical microscopy tips," *Opt. Express*, Vol. 18, No. 8, 8722–8734, 2010.
7. Liu, L. and S. He, "Design of metal-cladded near-field fiber probes with a dispersive body-of-revolution finite difference time-domain method," *Appl. Opt.*, Vol. 44, No. 17, 3429–3437, 2005.
8. Antosiewicz, T. J. and T. Szoplik, "Corrugated metal-coated tapered tip for scanning near-field optical microscope," *Opt. Express*, Vol. 15, No. 17, 10920–10928, 2007.
9. Vaccaro, L., L. Aeschimann, U. Staufer, H. P. Herzig, and R. Dändliker, "Propagation of the electromagnetic field in fully coated near-field optical probes," *Appl. Phys. Lett.*, Vol. 83, No. 3, 584–586, 2003.

Electromagnetic Design of Solar Collectors

Anthony Centeno, Fang Xie, Jonathan D. Breeze, and Neil Alford
Department of Materials, Imperial College London, London SW7 2AZ, United Kingdom

Abstract— The solar energy harvesting efficiency of photovoltaic solar cells are limited by the fact that they function through the generation of free hole-electron pairs and only photons with energy equal to the band gap can be converted efficiently. If the incident photons were to be harvested by optical rectification then there is the possibility of higher conversion efficiency. Two key components in any solar rectifier would be plasmonic solar collectors and silver or gold nanowires. This paper reports on the analysis of these components using the Finite Difference Time Domain (FDTD) technique in rectangular and cylindrical coordinate systems.

1. INTRODUCTION

The energy harvesting efficiency of the solar spectrum using conventional semiconductor solar cells is limited by the fact that they function through the generation of free hole-electron pairs and only photons with energy equal to the band gap can be efficiently harvested. If the incident photons could be harvested by rectification rather than by free carrier generation then there is the possibility of much higher conversion efficiency.

Noble metals, such as gold and silver, have negative dielectric constants at these frequencies and plasmonic effects dominate. This means that the simple scaling of metal antenna from longer wavelengths is not possible. To design and analyze an optical collector computational electromagnetic modeling tools need to be employed. There has been much recent literature on localized surface plasmon resonance in metal nanoparticles and their applications (see for example [1–4]), with the Finite Difference Time Domain (FDTD) technique being employed by a number of workers [5–7].

If we consider the available solar power that can be harvested the maximum irradiance occurs in the visible part of the spectrum with a peak at around 500 nm. Hence, our solar collector needs to be effective in a band around this wavelength. A proposed design for a solar rectenna is shown in Figure 1. The solar collection is accomplished by a planar array consisting of plasmonic nonoparticles whose localized surface plasmon resonance (LSPR) is at the required wavelengths. The nanoparticles are closely coupled to produce a high electric field in the separation between the resonant elements. Current is induced into silver nanorods placed within the regions of high field. These nanorods could then act as the top electrode in a Metal-Insulator-Metal rectifier.

The main computational difficulty is obtaining an accurate material model for the metal at optical frequencies. This is accomplished by using a Drude model within the Finite Difference Time Domain algorithm. Further the electromagnetic propagation along both gold and silver nanowires is analyzed using an FDTD algorithm in the cylindrical coordinate system.

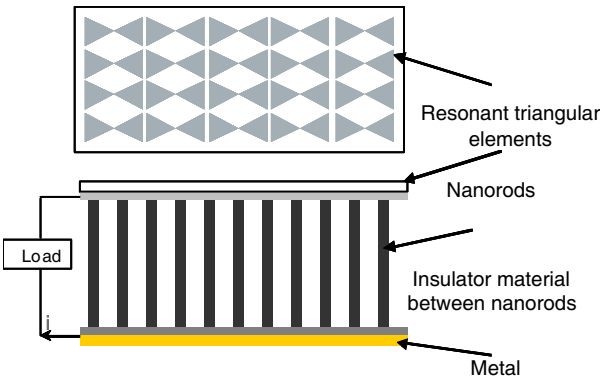

Figure 1: Proposed design for solar rectenna.

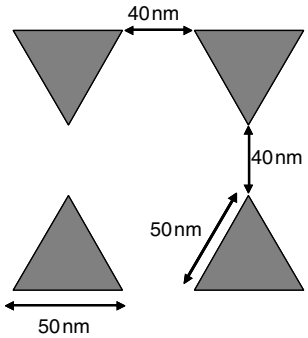

Figure 2: Size and separation of the metal nanoparticles in the array.

2. COMPUTATIONAL CONSIDERATIONS

In our FDTD calculations the dielectric function of silver and gold is represented using a Drude model [5]:

$$\varepsilon(\omega) = \varepsilon_\infty - \frac{\omega_p^2}{\omega^2 + i\gamma\omega} \tag{1}$$

where ω_p is the bulk plasmon frequency and γ is the characteristic collision frequency. The refractive index used for the metals is taken from Palik [8] and Equation (1) is fitted to these data. The values used for silver are $\varepsilon_\infty = 4.039$, $\omega_p = 1.39174 \times 10^{16}$ rad/s and $\gamma = 3.14223 \times 10^{13}$ rad/s, whilst for gold $\varepsilon_\infty = 10.7016$, $\omega_p = 1.39365 \times 10^{16}$ rad/s and $\gamma = 1.1747 \times 10^{13}$ rad/s.

The solar collectors considered are closely spaced triangular cross-section shaped nanoparticles, prisms, in infinite two-dimensional arrays, as depicted in Figure 2. By invoking periodic boundary conditions in the horizontal (x and y) directions an infinite periodic array is efficiently considered by calculating the scattering from a single pair of prism particles. We find the forward and backward scattering coefficients by considering the power flow through computational surfaces above and below the nanoparticle array, as previously described in reference [5]. The normalized absorption is then given by one minus the total scattering, where the total scattering is defined as the sum of the forward and backward scattering.

Although scattering will occur over all angles the fact that the array is periodic and the computational surfaces extend over the full computational domain means that the entire scattered field will pass through either the top or bottom computational surface. Perfectly matched layers (PML) are used to prevent any spurious reflections from the top or bottom of the computational domain.

3. ANALYSIS OF PLASMONIC COLLECTORS

The triangular prisms considered in our calculations have equilateral side dimensions and heights of 50 nm. The gap between the particles are considered to be the separation between the extremities, as depicted in Figure 2, which for the results shown here is 40 nm.

In this study, three cases are considered where the array is made up of gold or silver particles and also where, for each pair, one prism is Au and the other Ag. The results of absorption calculations are shown in Figure 3, for both x and y polarization when the particles are sitting in free-space.

The results show that silver has an absorption spectra with very distinct peaks compared to gold. This is considered to be due to the higher dielectric losses associated with gold, which effectively broaden out the absorption peaks due to the lower Q-factor. It was anticipated that the composite gold_silver array of nanoparticles might exhibit a broad absorption band, covering much of the visible spectrum but, as can be seen, this is not the case. The peaks at shorter wavelengths can clearly be attributed to silver whilst those at the longer wavelengths to gold. There are wavelengths in the "mid-band" where peaks that might have been expected are not observed. The peaks that are not seen in the composite case are considered to be due to the inter-particle coupling between particles in the same material cases. The composite material (Au_Ag) configuration alters this electromagnetic coupling. For the x-polarized incident field six absorption peaks can be identified. The three between 400 nm and 510 nm are due to silver whilst the three above 550 nm are due to gold.

4. INITIAL ANALYSIS OF SILVER AND GOLD NANOWIRES

Using an FDTD algorithm in cylindrical coordinates an initial study of the propagation of the electromagnetic wave along gold and silver nanowires has been carried out. An advantage of using cylindrical coordinates where the vectors are (r, φ, z), rather than (x, y, z), is that the fields can be calculated in a 2-dimensional form, which is a function of (r, z), and multiplied by $e^{jn\varphi}$, where n is an integer which specifies the azimuthal field variations. The radius of the wire considered is 20 nm and the azimuthal variation of the field is 1 ($n = 1$). The excitation field was an E-field normal to the wire at one angle. The results are shown in Figure 4. At the longer wavelengths the attenuation is due to radiation losses but as the field becomes confined to the surface there is a wavelength, clearly visible for the gold wire, where the attenuation is a minimum. We consider this to be due to the radiation losses having been significantly reduced whilst dielectric losses of the metal at this wavelength are still comparatively low. This point occurs for the silver nanowire well below the wavelength of visible light.

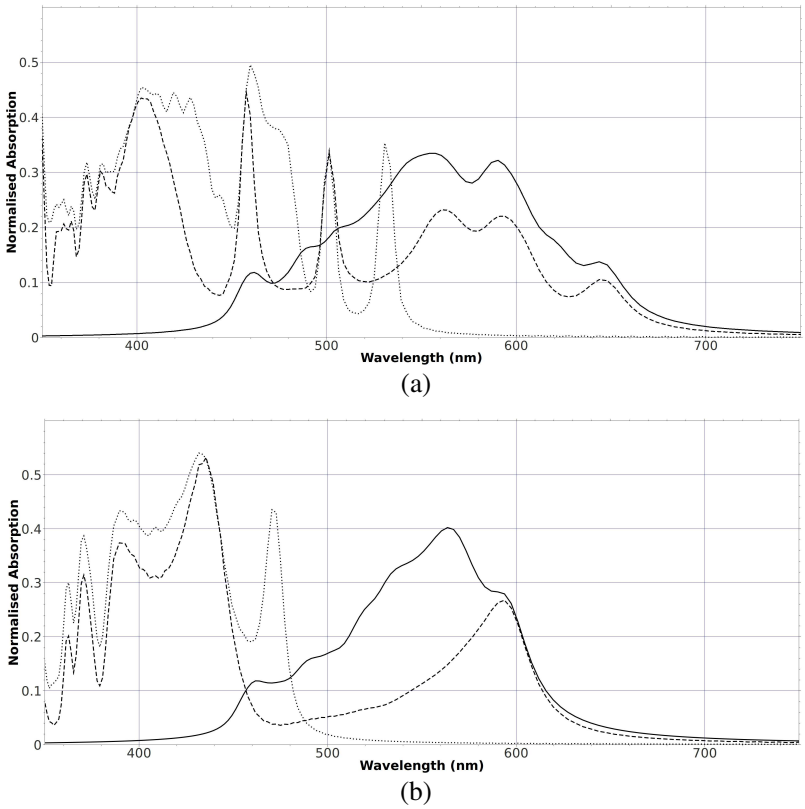

Figure 3: Absorption spectra for an array of prism nanoparticles. (a) x-polarized incident field (solid line — gold, light dotted line — silver, broken line-composite gold_silver pair). (b) y-polarized incident field(solid line — gold, light dotted line — silver, broken line-composite gold_silver pair).

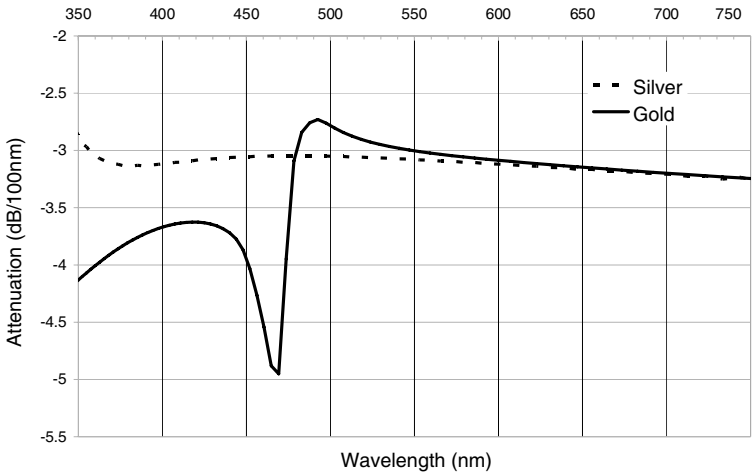

Figure 4: Attenuation per 100 nm of gold and silver nanowires of radius 20 nm.

5. DISCUSSION

The analysis of plasmonic solar collectors and nanowires has been carried out. The use of an array consisting of alternate gold and silver prisms shows that the spectral response is a complicated function of the electromagnetic coupling between the nanoparticles. The FDTD analysis of nanowires illustrated that there is clear cut off between radiation losses and dielectric losses and that there is a wavelength of minimum attenuation. Further analysis is required to see the effect of wire diameter on losses.

ACKNOWLEDGMENT

We acknowledge partial funding of this work from the Engineering and Physical Sciences Research Council and from the King Abdullah University of Science and Technology.

REFERENCES

1. Atwater, H. A. and A. Polman, "Plasmonics for improved photovoltaic devices," *Nature Materials*, Vol. 9, 205–213, 2010.
2. Xie, F., M. S. Baker, and E. M. Goldys, "Enhanced fluorescence detection on homogeneous gold colloid self-assembled monolayer substrates," *Chem. Mater.*, Vol. 20, 1788–1797, 2008.
3. Willets, K. A. and R. P. V. Duyne, "Localised surface plasmon resonance spectroscopy and sensing," *Annu. Rev. Phys. Chem.*, Vol. 58, 267–297, 2007.
4. Evanoff, D. D. and G. Chumanov, "Synthesis and optical properties of silver nanoparticles and arrays," *Chemphyschem*, Vol. 6, 1221–1231, 2005.
5. Centeno, A., B. Ahmed, J. D. Breeze, H. Reehal, and N. Alford, "Scattering of light into silicon by spherical and hemispherical silver nanoparticles," *Optics Letters*, Vol. 35, No. 1, 76–78, 2010.
6. Beck, F. J., A. Polman, and K. R. Catchpole, "Tunable light trapping for solar cells using localized surface plasmons," *J. of Appl. Phys.*, Vol. 105, 114310, 2009.
7. Sherry, L. J., S. H. Chang, G. C. Schatz, and R. P. V. Duyne, "Localised surface plasmon resonance spectroscopy of single silver nanocubes," *Nano Lett.*, Vol. 5, No. 10, 2034–2038, 2005.
8. Palik, E. D., *Handbook of Optical Constants of Solids*, Academic Press, 1985.

Channel Estimation in Through-The-Earth Communications with Electrodes

V. Bataller[1], **A. Muñoz**[1], **N. Ayuso**[2], **and J. L. Villarroel**[2]

[1]Advanced Research Laboratories of I3A, Walqa Technological Park, Cuarte, Huesca, Spain
[2]Aragón Institute for Engineering Research (I3A), University of Zaragoza, Zaragoza, Spain

Abstract— One of the main points in the design of a communication system is to know the channel behaviour for a given frequency band in terms of amplitude and phase. Free space communications channels have been characterized thoroughly for a large range of frequencies. But in the field of Through-The-Earth (TTE) communications, the work about channel characterization found in the literature is very scant and focused in magnetic propagation (induction loops). This paper presents a method of channel characterization for TTE communications with electrodes, and the tests and results done in real field measurements.

1. INTRODUCTION

TTE communication systems have been developed for establishing communication in confined areas as tunnel, mines or caves. Due to rock conductivity, electromagnetic waves suffer from skin effect attenuation. Because of that, TTE communication works in VLF-LF range. There are two possible medium access solutions: current injection by means of ground electrodes [1] and magnetic induction by inductive loops. In current injection a pair of electrodes is located underground and other pair in surface.

In TTE communication not only it is necessary to study the electrical noise present. A channel characterization is of paramount importance at time to model and simulate a communication system. A channel sounding allows obtaining the parameters of the channel impulse response expression $h(t)$, considering in this case a time invariant channel. The channel transfer function states that for a given input $x(t)$, the output $y(t)$ is the convolution of $x(t)$ and the impulse response $h(t)$. Knowing $h(t)$, it would be possible to predict the distortion that the receiver will suffer and to design equalizers or matched filters to compensate it.

On the other hand, if $h(t)$ is not known, a large number of parameters (channel attenuation, SNR, phase distortion) critical in system design are left to trial and error, which effectively multiplies time needed to design such systems and most important, designed systems are usually far from optimum.

The characterization of TTE communication channel with inductive loop has been studied theoretical and experimentally [1, 2]. In the electrodes case, several studies in the literature offer theoretical formulae that model the communication channel with electrodes. However, they are valid for big electrodes, with emitter and receiver in surface and with a large separation between them. This situation is not suitable for TTE communication system where the electrodes separation is relatively small, also its size. Moreover, the electromagnetic waves travel though the rock in this case.

For the channel object of study, electrodes effect is also considered, since it is not possible to isolate its impact in the measurements. Furthermore, in a real TTE communication application the electrodes contribution in the channel will be present. The electrode impedance generally presents a very high value that limits the current injected and so after the electric field generated [3]. In this paper a basic channel characterization method developed for TTE communication applications with electrodes is presented. This method has been applied in several locations, presenting here a couple of measurements done in surface.

2. CHANNEL SOUNDING METHODS

Many methods for communication channel estimation have been developed. They are based on setting $x(t) = \delta(t)$ (Dirac delta function). The output $y(t)$ is directly the impulse response $h(t)$. In practice, it is not possible to obtain a true delta (infinite amplitude and infinitesimal duration). Therefore, the measurement methods try to approximate an impulse function. They are grouped in two kinds of methods: Those that implement the estimation in time domain and those that work in frequency domain. A comparative of them does not show clear advantages of one method with regard to the other [4].

2.1. Time Domain Methods

The Periodic Pulse method excites the channel with a short-duration RF-pulse to approximate the delta function [6, 7]. This method was very used in the past. Another method, the Pulse Compression Technique states that a linear system impulse response can be estimated supplying it with white noise [8]. The impulse response can be obtained from the cross correlation between channel input and output. Deterministic signal with noise characteristics are employed as the pseudo-noise (PN) sequences. Their self-correlation offers a sharp peak in the zero-shift. This method has been employed in underground channel estimation with induction loop [1].

The Swept Time Delay Crosscorrelation method or Sliding Correlator Technique employs PN sequences but the signal in receptor is generated by a clock slightly slower than in emitter [10]. This method is employed in wireless channel sounding, since it allows measuring the amplitude and phase delay of different multipath signals. A comparative of different methods in time domain is done in [7], concluding that the method that employs the PN sequences is the most adequate for wideband radio channels.

2.2. Frequency Domain Methods

Some examples of the frequency domain method for underground communications in tunnels are shown in [11]. In this kind of methods, generally a Vector Network Analyser (VNA) is used to measure the parameter $S_{21}(f)$ at different frequencies, obtaining the channels frequency response. Main advantage of this method is that present a simple implementation. But it requires a wired reference signal common to emitter and receiver and sweep time is long. Solutions for the wired reference consider the use of synchronization between emitter and receiver by means of high precision clocks or with GPS receivers. Another solution employs a VNA without a direct connection, sending a triggering signal to the frequency analyzer. Another approximation is given by the digital down-conversion method, which is based on bandpass sampling the receiver signal with a sampling frequency twice the information bandwidth.

3. METHOD DEVELOPED

The channel sounding method developed is grouped in the frequency domain methods. In the emitter, a variable frequency tone is generated for a number of discrete frequencies in the band of interest. Receiver is in charge of estimating the amplitude and phase of the received tones, giving as a result an estimation of $S_{21}(f)$. But in order to do this a common reference is needed and a wired one is not appropriate in the case of TTE communications. Therefore, a solution to obtain a phase reference in receiver is required. In order to solve this, a fixed frequency sinusoidal tone is generated together with the sweep frequency signal, acting the first as a reference signal. Both tones (reference and sweep) are phase synchronized and have the same amplitude. This allows measuring the phase and amplitude variation at the different swept frequencies. As the emitter output power can be easily measured, the result is basic channel estimation in terms of amplitude and phase. Due to the low frequencies used (VLF-LF), neither multipath nor signal delays are considered.

The measurement equipment employed in transmission is formed by a PC which generates the transmission tones and does the control, an arbitrary signal generator and a pair of electrodes. In reception, signal is captured with a pair of electrodes connected to a low noise amplifier. After the amplification, signal is digitalized by a high rate A/D converter connected to the PC via USB port. The sampling frequency in generator and ADC is set to 2 MHz, the maximum allowed by ADC. All the instrument control as well as the data processing is implemented in Matlab scripts.

The frequency band to study is in the range of 3–150 kHz. These frequencies are a compromise between minimum bandwidth needed and signal generator output capability. Test signals are generated with the help of an IDFT (Inverse Discrete Fourier Transform) of 512 points in order to obtain orthogonal tones. The reference tone frequency is 3906.25 Hz which is the result of dividing the sampling frequency (2 Msps) by the IDFT size (512 points). Sweep tone frequency is calculated as integer multiples of the reference frequency ($n = 2.40$).

Sweep tone changes its frequency value every ten seconds. The emitter transmits the sweep continuously until the user stops the application, in a circular way. The receiver samples every second capturing a signal for 131 ms (2ˆ18 points) in order to limit the errors caused by the sampling operation. A Lagrange Interpolation is implemented as suggested in [12] to obtain a synchronized sampled signal. Although this solution would be applied, an error in data phase measurement will appear due to the linear interpolation applied and the A/D converter quantization [13]. This error

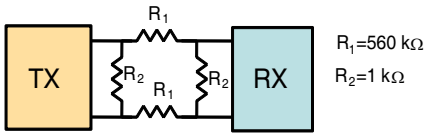

Figure 1: Calibration network.

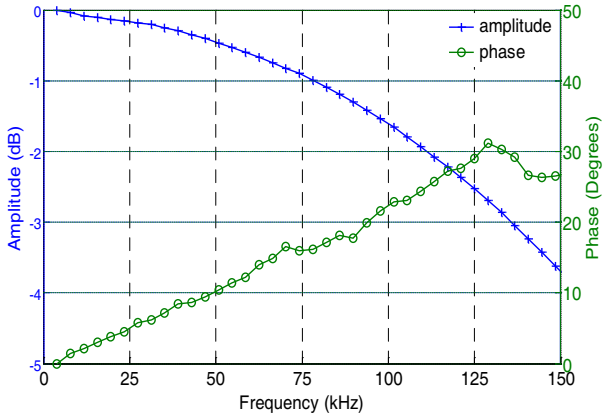

Figure 2: Calibration network frequency response.

increase with the frequency swept. Future studies will try to solve this inconvenient.

A DFT is latter calculated with the 262144 (2ˆ18) sample points, a power of two multiple of the emitter IDFT points (512×512). Thus, both the errors introduced by FFT computation and channel noise in receiver are minimized. As the frequential positions of the scanning are known in receiver, the relative amplitude and phase values for these samples are stored. For every frequency point only nine correct measurements are available (out of ten). This is due to the time needed in the emitter to store the signal in signal generator. The outliers that overcome 1 dB from the average of the nine samples are discarded, applying a new average that will be stored as correct value for each frequency.

The calculation of channel response is evaluated offline applying the LS (Least Squares) algorithm. According to this method, the frequency channel response follow the expression (1), with X a diagonal matrix with the value for each frequency sample $(x_1, \ldots, x_k)$ generated with the IDFT and Y the k frequency samples in the receiver. The measurement system has been calibrated with a resistance network shown in Fig. 1 in order to correct the measurement method systematic errors. It has been applied the Self-Calibration Measuring Technique (SCMT) [24].

$$\hat{H}_{LS} = X^{-1}Y \tag{1}$$

The frequency response of the network measured is drawn in Fig. 2. It can be seen that the generator does not present constant amplitude with frequency nor the phase response is zero, as it would be in an ideal system. This error is compensated in the measurements offline. As it has been commented before, the phase measurement presents some errors due to the desynchronization of generator and sampler frequencies. The phase trend has been represented in previous figure smoothing the response obtained.

The random errors are limited applying an average of the maximum values in the frequency sounding and the DFT method as proposed in [12].

4. EXPERIMENT CONDITIONS

Although the channel sounding has been developed to characterize the communication for underground applications, to prove that the method work and the results are consistent, it has been firstly tested in surface communication, presenting the results in this paper. The emitter and receiver present a four meters gap between the electrodes. The electrodes employed are steel bars, improving the contact with salty water and the wires used in emitter had no loops (minimum resistance and inductance).

As the electrodes impedance depends heavily on frequency [3], the soil injected current would not present a constant value for all the frequencies. However, it is of interest to know not only the isolated channel response but also with the load effect. So that it can be considered the effect of a total transmission channel that includes the electrodes. On the other hand, the impedance between the electrodes has been measured in previous studies [3] having obtained an impedance characterization and being able to isolate the channel response offline.

The measurements presented in this paper were taken in Walqa Technological Park (Huesca) in December 2009. The soil in this location is composed by four meters of gravels lying and sandstone

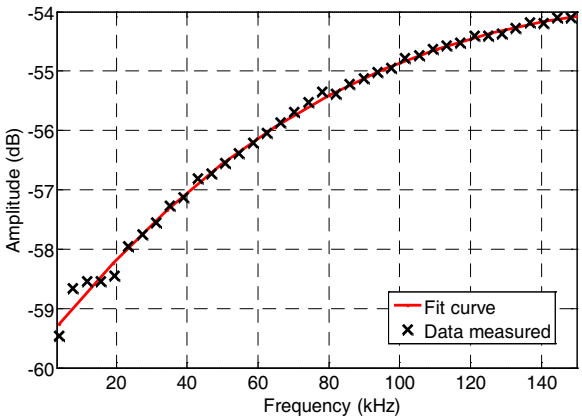

Figure 3: TTE channel frequential response amplitude.

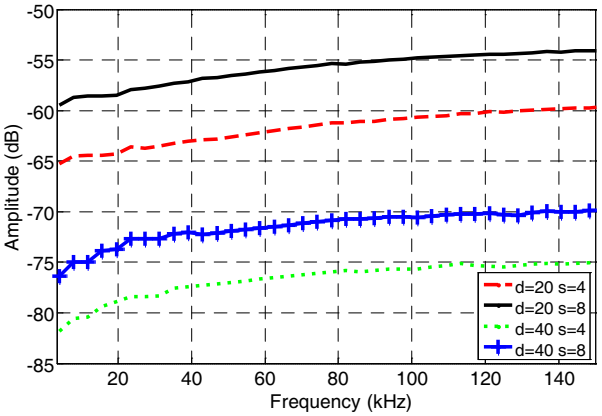

Figure 4: TTE channel frequential response with the distance (d) and the span (s).

and clay of Miocene with an aquifer in the contact surface.

For the experiments, the span between the electrodes in the emitter was fixed to four meters in order to avoid modifications in the emitter impedance, and in the receiver was set to 4, 8 and 12. For the separation between emitter and receiver were considered 20 meters at first and 40 m later.

5. RESULTS

The channels amplitude frequency response for TTE communications in surface is shown in Fig. 3. Due to the low accuracy in phase measurements, it has only been considered the amplitude channel response. These results are enough for TTE radio applications using amplitude modulations. For data transmission with phase modulations it will be necessary to characterize also the phase channel response in future tests.

It can be seen in previous figure that the amplitude response increases with frequency. This effect is a combination of the electrodes system impedance and the channel behaviour. The channel response has not been isolated from this value since this is the real situation that a TTE communication system with electrodes will find. In Fig. 4 it is shown the response for two different distances and electrode spans of receiver.

Analysing the results it can be appreciated that doubling the distance translates into a 16.5 dBV attenuation. Relative to variation in span, doubling its value to 8 m, increased received signal in 6 dBV. A further increase in span (12 m) resulted in a smaller 3.5 dBV increase. It should be noted that increasing the span also increases the perceived noise.

6. CONCLUSIONS

A variation of a frequency domain method has been used to estimate the impulse channel response. The test results reveal that channel attenuation rises very fast with distance and can be partially compensated with the span distance between electrodes. Unfortunately, the method used does not allow a precise phase measurement as is. Future work will be focused in a more accurate phase channel response measurement, correcting the errors due to the jitter of emitter and receiver clocks in order to have a complete channel description. Moreover, the channel sounder will be applied in underground locations in order to obtain a TTE channel characterization in different terrains.

ACKNOWLEDGMENT

This work has been funded by the projects TESSEO DPI 2009-08126 (MCYT, Spanish Government) and 2008/0486 (CyT, Aragón Government), and by the agreement between IAF, Aragón Government, the I3A (University of Zaragoza) 2008/0574 regarding the WALQA research laboratory.

REFERENCES

1. Gibson, D., "Channel characterisation and system design for sub-surface communications," Ph.D. Thesis, University of Leeds, 2003.

2. Ayuso, N., J. A. Cuchí, F. Lera, and J. L. Villarroel, "Through-the-earth magnetic field propagation: Modeling and experimental validation," *IEEE AP-S International Symposium on Antennas and Propagation and USNC/URSI National Radio Science Meeting*, Albuquerque, New Mexico, USA, 2006.
3. Bataller, V., "Método generalizado de diseño de transmisores para equipos de radiolocalización y comunicaciones subterráneas," Ph.D. Thesis, Universidad de Zaragoza, Spain, Nov. 2009 (in Spanish).
4. Mao, X. H., Y. H. Lee, and B. C. Ng, "Comparison of wideband channel sounding techniques," *PIERS Proceedings*, 400–404, Moscow, Russia, August 18–21, 2009.
5. Bryant, E. B., G. J. Brodin, and A. H. Kemp, "High resolution channel sounder with narrowband low interference characteristics," *IEEE Transactions on Aerospace and Electronic System*, Vol. 42, No. 2, Apr. 2006.
6. Rappaport, T. S., *Wireless Communications: Principles and Practice*, Prentice-Hall, New Jersey, 2002.
7. Parsons, J. D., D. A. Demery, and A. M. D. Turkmanil, "Sounding techniques for wideband mobile radio channels: A review," *IEEE Processing Communication, Speech and Vision*, Vol. 138, No. 5, 437–446, 1991.
8. Cooper, R. and C. McGillem, *Probabilistic Methods of Signal and Systems Analysis*, Rhinehart and Winston, Holt, 1971.
9. Albornoz, J. M., "A wide-band channel sounder," Master Thesis, The Ohio State University, 2001.
10. Haese, S., C. Moullec, P. Coston, and K. Sayegrih, "High resolution spread spectrum channel sounder for wireless communications systems," *IEEE International Conference on Personal Wireless Communications*, 170–173, 1999.
11. Nerguizian, C., C. L. Despins, S. Affes, and M. Djadel, "Radio-channel characterization of an underground mine at 2.4 GHz," *IEEE Transactions on Wireless Communications*, Vol. 4, No. 5, 2441–2453, 2005.
12. Liu, J. G., A. Schönecker, U. Frühauf, U. Keitel, and H. J. Gesemann, "Application of discrete Fourier transform to electronics measurements," *International Conference on Information, Communications and Signal Processing, ICIS*, Singapore, Sep. 9–12, 1997.
13. Fawzy, M. and M. S. P. Lucas, "Errors in sampled data phase measurement," *IEEE Transactions on Instrumentation and Measurement*, Vol. 34, No. 4, Dec. 1985.
14. Liu, J. G. and U. Frühauf, "Self-calibration measuring methods and applications to measurements of electrical quantities," *Measurement*, Vol. 26, 129–142, 1999.

Noise Characterization in Through-The-Earth Communications with Electrodes

A. Muñoz[1], **V. Bataller**[1], **N. Ayuso**[2], **P. Molina**[2], **A. Mediano**[2], **J. A. Cuchí**[2], **and J. L. Villarroel**[2]

[1]Advanced Research Laboratories of I3A, Walqa Technological Park, Cuarte, Huesca, Spain
[2]Aragón Institute for Engineering Research (I3A), University of Zaragoza, Zaragoza, Spain

Abstract— In the design of a Through-The-Earth (TTE) communication system a correct frequency band selection is of paramount importance. A key parameter for an optimum frequency selection is the Signal to Noise Ratio (SNR) available in the frequency band. Therefore, noise measurements with electrodes are needed in different situations in order to obtain a good characterization of human generated noise. This paper presents a method of noise measurement and analysis both in the frequency and time domains, applying it in two locations in order to find the optimal frequency bands.

1. INTRODUCTION

TTE communication systems have been developed in order to allow voice/data communication in confined areas as tunnels, mines or caves. Electromagnetic waves travel through the rock and, due to its conductivity, high frequency signals are attenuated by skin effect. Therefore, this kind of communication works in VLF-LF range. One solution to access the medium in TTE communications is current injection by means of ground electrodes [1]. In this technique a current is injected into the earth by a pair of transmitter electrodes (TX) allowing a receiver located at certain distance to detect some potential in the electrodes (RX).

The current injected into the earth depends on the electrode impedance. According to [2, 3], this impedance has a wide range and generally presents a high value that limits the current injected and thereafter the electric field generated. Some methods to improve the contact impedance are studied in [4, 5]. The impedance value decreases with frequency; however, the electrical field generated suffers from an exponential attenuation due to skin effect, increasing this value with frequency. Thus, a trade off is established in the frequency selection.

Although a larger current generates more electric field intensity, the range of communication is not very large due to the strong signal attenuation. Therefore the SNR is the main parameter to consider in receiver design. So electrical noise/interferences captured by the receiver electrodes have to be studied and measured.

In the literature, several TTE communication systems prototypes that work with electrodes [6–8] can be found as well as a commercial one designed by the GTE, the TEDRA® radio [9, 10]. For its development, it has been necessary to analyze and characterize the electrical ground noise. In this paper, a noise measurement method is developed and its validity demonstrated by using it in two locations, both in surface and inside a cave, in order to obtain a noise estimation for different situations where TTE communications usually are carried out. The noise data is analyzed in detail both in frequency and time domains. Many reduced interference bands suitable for TTE communications with electrodes were found, allowing an optimum design of a communication system.

2. SOURCES OF NOISE

In a TTE communication system several types of noise contribute to the receivers input: thermal noise, Earth-ionosphere noise and the human-generated noise. The latter comprises other communication signals in nearby frequencies (i.e., LORAN, time signals, RTTY, etc) and unintentionally generated interferences (i.e., power lines, motors, etc. . .). In the TTE communication with electrodes only the human-generated noise is studied because the other sources of noise are negligible in comparison with this contribution.

The noise profile depends strongly on the environment. In industrial areas there are a lot of unintentionally generated interferences: mains and its harmonics, machinery, inverters. . . These types of interferences are hard to classify because they are random in nature (except of mains supply). On the other hand, open field locations are much cleaner from electrical interferences but

some weak electrical noise can be appreciated caused by nearby electrical farm fences, inverters of broadcast towers, etc.

Besides these noise sources, many interferences coming from different radio stations that work in VLF-LF ranges can also be picked up by electrodes. Several powerful communication systems work in these frequency ranges such as beacons of navigation radio and time synchronization signals. So in this paper, only the human-generated signals in the VLF-LF band captured with electrodes will be measured.

3. NOISE MEASUREMENT METHOD

Electromagnetic noise measurements in earth have been carried out for geophysical and mining applications. In [12] a system developed to measure the earth noise with electrodes can be found but it works with a few discrete frequency data and in low frequency. Another application for geophysical studies is described in [13].

The United States Bureau of Mines carried out in the sixties a noise measurement campaign in several mines within a mines communications project [14–18]. In these locations, electromagnetic noise was captured with a calibrated loop antenna. Noise characterization measurements with electrodes in mines can also be found in [19], but for Medium Frequencies (MF). A similar study is presented in this paper but adapted for the frequency range of TTE communications (LF) and only characterizing intentionally human-generated noise.

The method developed to measure the noise with electrodes consists in a pair of electrodes grounded into the earth and separated 8 m, choosing the adequate ones for each contact surface [3]. A low noise amplifier (EG&G 5113) is used to reduce the overall noise figure in the measurement setup and to bandpass filter the signal. The lower and upper cut-off frequencies are set to 3 and 300 kHz respectively. Amplified/band limited signal is then acquired by means of a high rate A/D converter (DT9832A) which has a 16 bits resolution and communicates to the PC by USB interface. The sampling frequency is set to 2 Msps and temporal capture interval is 5 seconds, enough to evaluate slowly changing signals (bandwidth > 0.4 Hz). Once in the PC, the acquired signal is analyzed offline with a custom application developed in Matlab.

With data acquired, power spectral density (PSD) is calculated. As the periodogram method is not a consistent estimator of the PSD due to the high spectral leakage it presents, other calculation methods have been studied. The one finally selected is the short term FFT (STFT) applying the Welch method [21]. In this case, a modified periodogram is calculated for short segments of the time series. The number of samples chosen for the FFT are $2^{15}(65536)$ (~ 16 ms), while the window applied is a Hanning one with a 50% of overlap.

At first sight, frequency analysis showed that the majority of signals are of narrow bandwidth ($<$ 50 Hz) except for the exceptional case of Loran-C. In order to extract the data obtained from PSD, an automatic peak detection algorithm has been developed, identifying and classifying interferences. In this method, the derivative of the PSD is calculated, applying after that an average filter. High strong peaks in the PSD appear as a positive peak followed by a negative one in the derivate signal. The zero-crossing point corresponds to the peak position in frequency. By establishing positive and negative thresholds for the derivative signal these interferences can be detected. The threshold values have to be fixed according to the level of the interferences detection desired.

It can be possible that some temporal intermittent signals present high value in short time periods, not noticed with the PSD. Although with the presented algorithm it can be known the frequency bands with interferences, it is also interesting to know its temporal distribution. Therefore a time-frequency analysis with the STFT is applied to these frequency interferences. There is a time-frequency resolution trade-off when the STFT algorithm is applied. Other more complex methods could be employed for this analysis, like Continuous Wavelet Transform [22] or the Wigner-Ville method. These will be studied in a future work by the authors. Noise characterisation has been computed offline with a Matlab application that also allows an automatic noise analysis and that includes a dynamic data base for identifying the different interferences.

4. EXPERIMENT CONDITIONS

Many noise measurements have been captured in different locations of Spain. In this paper, as an example of them, the results for one surface measurement and one inside a cave are presented. The first measurement was captured in Belsué (Huesca). The second one was taken in Esteban Felipe cave (Huesca), also located in Belsué.

In the measurements, the electrodes employed were steel L-bar electrodes for surface measurements and copper braid for inside the caves [3]. Although the low noise amplifier presents high input impedance, techniques to improve the electrode contact have been applied [4]. The spam between the electrodes was fixed to 8 meters and the wires employed were multifillar copper wires 18 AWG.

5. RESULTS

Figure 1 depicts the average power spectral density of noise measured in Belsué (Huesca). Different interferences signals can be identified in this spectrum. The main ones are enclosed in Table 1 (in kHz) and marked in the figure. LORAN-C in the band 80–100 kHz presents a high value. The atomic clock DCF77 at 77.5 kHz can also be seen and the HBG time signal at 75 kHz. The interference with the highest value is located at 63.75 kHz. Regretfully, it has not been possible to identify its origin.

For the Esteban Felipe cave noise record, it has been applied the algorithm previously described to identify the interference signals and to find the optimal frequency band to communicate. As it has been explained before the derivative of the PSD and the average filter have been applied. The high value peaks in the PSD has been detected. For each of these points it has been recorded the PSD value, maximum and average of the noise amplitude spectrum.

It is worth to note the difference in the number of interferences showed in Figs. 1 & 2. This is because Fig. 1 noise was captured outside, so there was no room for soil to attenuate the interferences as in Fig. 2. In general, noise inside a natural cave will be significantly lower that it's outside counterpart.

As it has been commented before, not only is the frequency location of the interferences important but also its temporal distribution. Therefore in Fig. 3 represents the voltage excursions in dB between 1 and 99 percent of time, as well as the average value of the interferences detected applying the previous described method. Several noise-reduced bands can be detected around 30, 55 kHz, 70 and 80 kHz which could be used in a voice/data communication.

Interferences in the LORAN-C band are not detected because its pulses being very short in time and its energy spread between 90 and 110 kHz. However, as can be seen in Fig. 2, the maximum

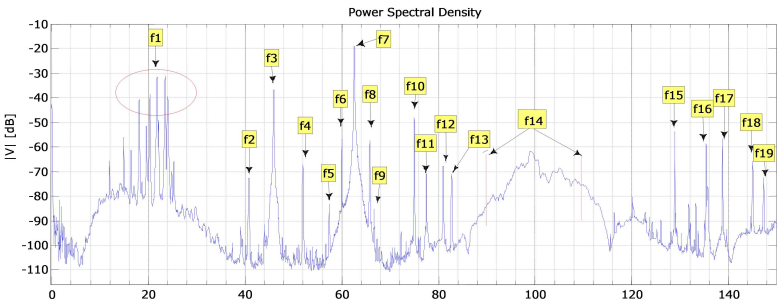

Code	Freq (kHz)	Origin	Country
f1	18-25	Navy	-
f3	45.9	US. Navy	I
f7	63.75	Unknown	-
f10	75	HBG TS	STZ
f14	90-110	LORAN-C	-

Figure 1: PSD of noise measurement in Belsué with most powerful interferences.

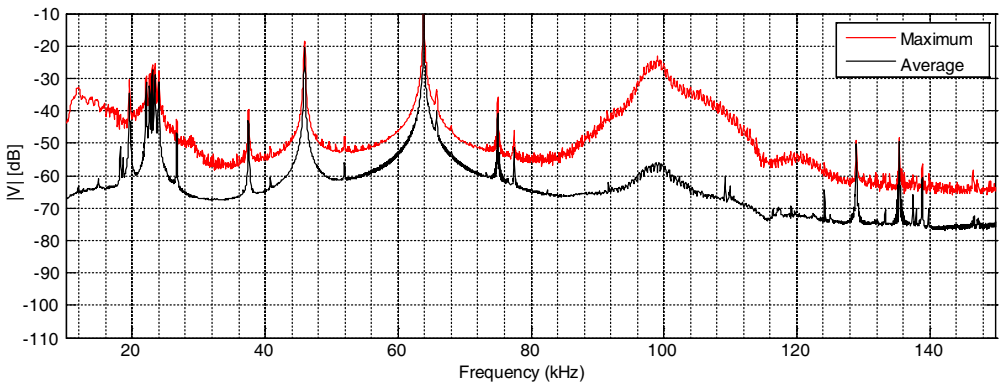

Figure 2: Noise amplitude spectrum measurement in Esteban Felipe cave (Huesca).

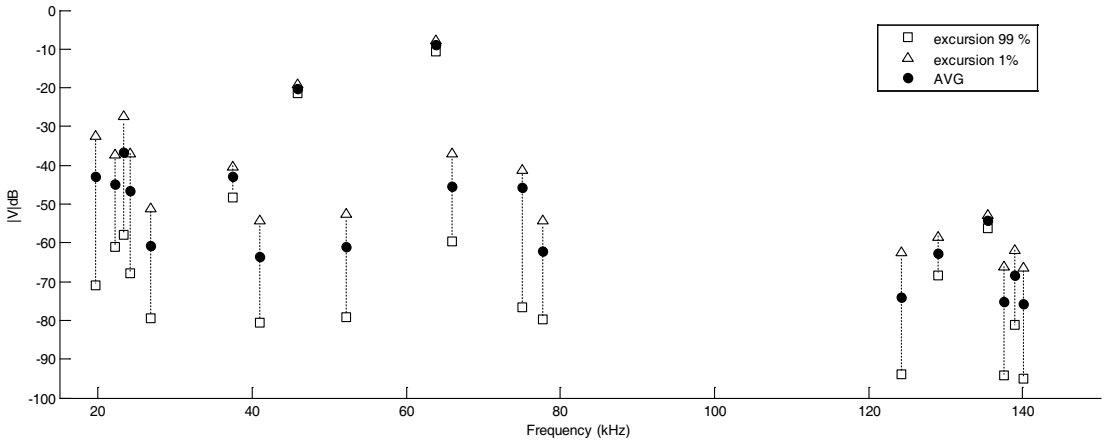

Figure 3: Voltage excursions of interferences in Esteban Felipe cave.

value can be very high. Therefore, besides interferences detection, average and maximum noise spectrum have to be studied.

6. CONCLUSIONS

In this paper two measurements of electrical noise with electrodes are presented, taken in surface and inside a cave, as well as the method developed to capture them. The data measured allow the study of noise in the band of TTE communication (VLF-LF).

A process for automatic detection of reduced noise bands has been presented. This application enables to find frequency niches suitable for TTE communications where no temporal spikes are present. To obtain this solution, a time-frequency analysis of these bands was applied.

As a result of the measurements analyzed, it can be concluded that it is very important to measure and characterize the noise with electrodes at the time to choose a communication frequency. An automatic interference detection process results very useful for these applications.

ACKNOWLEDGMENT

This work has been funded by the projects TESSEO DPI 2009-08126 (MCYT, Spanish Government) and 2008/0486 (CyT, Aragón Government), and by the agreement between IAF, Aragón Government, the I3A (Univ. of Zaragoza) 2008/0574 regarding the WALQA Research Laboratory.

REFERENCES

1. Gibson, D., "Channel characterisation and system design for sub-surface communications," Ph.D. Thesis, University of Leeds, 2003.
2. Bataller, V., "Método generalizado de diseño de transmisores para equipos de radiolocalización y comunicaciones subterráneas," Ph.D. Thesis, University of Zaragoza, 2009 (in Spanish).
3. Bataller, V., A. Muñoz, P. Molina, A. Mediano, J. A. Cuchí, and J. L. Villarroel, "Electrode contact impedance measurements in TTE communications," *DCIS'09*, Zaragoza, Spain, Nov. 2009.
4. Bataller, V., A. Muñoz, P. Molina, A. Mediano, J. A. Cuchí, and J. L. Villarroel, "Improving medium access in through-the-earth VLF-LF communications," *Journal of Communications*, Vol. 4, No. 4, May 2009.
5. http://www.zonge.com.au.
6. http://naylorgr.perso.cegetel.net.
7. Hunri, J. and C. Ebi, "Alpine cave radio earth-current at Hölloch," *CREG Journal*, No. 25, 4–5, 1996.
8. Hey, J., "An experimental Heyphone on 38.4 kHz," *CREG Journal*, No. 56, Dec. 2004.
9. Villarroel, J. L., J. A. Cuchí, A. Mediano, V. Viñals, V. Bataller, D. Salós, A. Muñoz, and F. Rosas, "TEDRA, the development of a software defined cave radio," *CREG Journal*, Vol. 67, Jun. 2007.
10. Muñoz, A., F. Lera, A. Mediano, V. Bataller, J. A. Cuchí, and J. L. Villarroel, "Design of a voice communication system for underground environments using current injection techniques," *ICWCUCA'08*, Val d'Or, Canada, Aug. 25–27, 2008.

11. U.S. Coast Guard, "Specification of the transmitted Loran-C signals," U.S. Dep. of Transportation, 1981.
12. Neuenschwander, E. F. and D. F. Metcalf, "A study of electrical earth noise," *Geophysics*, Vol. 7, No. 1, 69–77, 1942.
13. Frantti, G. F., "The nature of high frequency earth noise spectra," *Geophysics*, Vol. 28, No. 4, 547–562, 1963.
14. Bensema, W. D., M. Kanda, and J. W. Adams, "Electromagnetic noise in Robena No. 4 coal mine," U.S. B.O.M., Apr. 1974.
15. Adams, J. W., W. D. Bensema, and M. Kanda, "Electromagnetic noise in Grace Mine," U.S. B.O.M., 1974.
16. Kanda, M., J. W. Adams, and W. D. Bensema, "Electromagnetic noise in McElroy Mine," U.S. B.O.M., 1974.
17. Bensema, W. D., M. Kanda, and J. W. Adams, "Electromagnetic noise in Itmann Mine," U.S. B.O.M., 1974.
18. Scott, W. W., J. W. Adams, W. D. Bensema, and H. Dobroski, "Electromagnetic noise in Lucky Friday Mine," U.S. B.O.M., Oct. 1974.
19. Geyer, R. G., G. Keller, and T. Ohya, "Research on the transmission of electromagnetic signals between mine workings and the surface," U.S. B.O.M., Jan. 1972.
20. Oppenheim, A. V. and R. W. Schafer, *Discrete-Time Signal Processing*, 730–742, Prentice-Hall, 1989.
21. Welch, P., "The use of FFT for the estimation of power spectra: A method based on time averaging over short, modified periodograms," *IEEE Trans. on Audio Electroacoustics*, Vol. 15, No. 2, 70–73, Jun. 1967
22. Goswani, J., and A. Chan, *Fundamentals of Wavelets*, Ed. Wiley, Texas, 1999.

Detection of Movement and Impedance Changes behind Surfaces Using Ground Penetrating Radar

Şevket Demirci[1], **Enes Yiğit**[2], **and Caner Özdemir**[1]

[1]Department of Electrical-Electronics Engineering, Mersin University, Mersin, Turkey
[2]Vocational School of Technical Sciences, Mersin University, Mersin, Turkey

Abstract— In this paper, the utility of Ground Penetrating Radar (GPR) in electromagnetic empedance change detection is demonstrated through experimental results. For this purpose, two kinds of changes; namely human movement behind walls and water leakage from embedded pipes are considered for their electromagnetic detection. In the first case, the movement behind a wall is detected by real time monitoring of A-scan GPR data. The difference signals between two A-scan range profiles acquired at consecutive time instants are used as an indicator of the movement. In the second case, the leakage from a plastic pipe buried in an outdoor soil environment is identified through time series of B-scan images which are reconstructed by using a near-field back-projection algorithm.

1. INTRODUCTION

A common practice for the detection and localization of objects or interfaces beneath the surfaces is the Ground Penetrating Radar (GPR) imaging. While GPR is an issue long studied in radar community, there is still some implementation challenges associated with a certain specific application. These are; incorporation of optimal radar and antenna parameters for different complex mediums and targets, accurate modeling of the propagation of the electromagnetic (EM) waves through the subsurface, focused image formation, reliable interpretation of the data etc. Meanwhile, most of the GPR surveys generally concern with the imaging of stationary subsurfaces in which the ultimate goal is to obtain valuable information about the location and the size of the object from the resultant images. On the other hand, the potential of GPR to detect impedance changes between time intervals have been investigated in recent studies [1–3]. This can be accomplished by applying real-time imaging processes and taking different images of the subsurface environment at different time instants.

Thus, to illustrate and further evaluate these capabilities and implementation challenges of GPR, the aim of this paper is to assess whether GPR techniques can be efficiently used to detect the movement or life signs of human being behind walls and the water leaks in buried pipes. In the first attempt, it was aimed to find the movement of a person behind the wall with a continuous monitoring of A-scans. The "difference signals" between these consecutive range profiles were displayed in real time and exploited as an indication of the movement. In the second attempt, the problem of water leakage detection was considered. In our recent study [4], it was shown that this task can be accomplished for a plastic pipe buried in an ideal case of laboratory sand pool. The research effort described herein focuses on a more realistic situation of outdoor real soil environment. A series of B-scan measurements were carried out and the images reconstructed by a back-projection algorithm [5] were obtained to be able to get information about the location region of leakage.

The organization of the paper is as follows: In the following section, a brief overview of two-dimensional (2-D) GPR data collection and processing is provided. Section 3 presents the results of movement detection application. In the subsequent section, B-scan imaging results for water-leakage detection problem are demonstrated. Conclusions are given in the last section.

2. BASIC GPR PRINCIPLE

In this section, a brief formulation of GPR measurement techniques is given. Fig. 1(a) shows a schematic diagram of a 2-D monostatic measurement which uses stepped-frequency continuous-wave (SFCW) radar. At each synthetic aperture point, SFCW radar transmits a waveform of bandwidth B also called a burst which is divided into N single frequency subpulses equally spaced across the waveform bandwidth as shown in Fig. 1(b). Each subpulse has τ seconds duration and the time interval T between the pulses is set according to the desired unambiguous range.

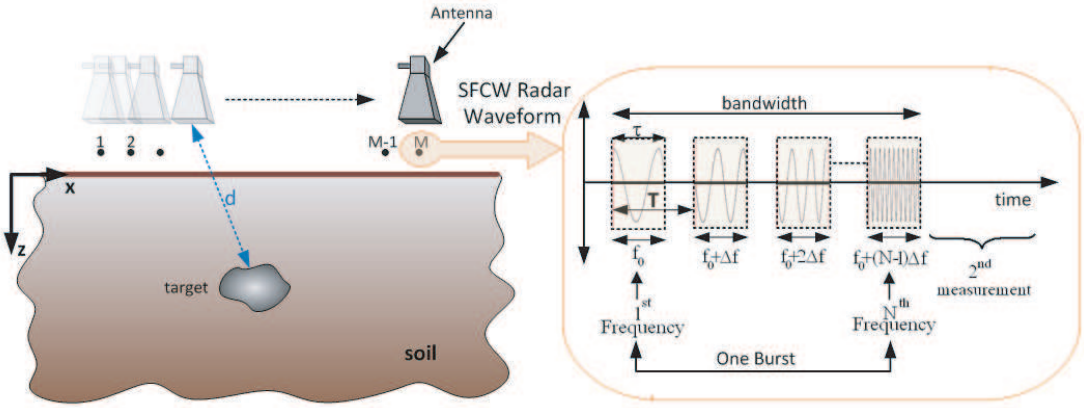

(a) (b)

Figure 1: 2-D monostatic GPR imaging problem. (a) Geometry. (b) Stepped-frequency waveform.

Assuming the starting carrier frequency is f_0 and the fixed frequency increment is Δf, the frequency of the nth pulse can be written as

$$f_n = f_0 + (n-1)\Delta f \quad n = 1, 2, \ldots, N \tag{1}$$

The processing can be initiated after receiving the magnitudes and phases of the back-scattered field for the whole transmitted frequencies. For this static measurement also called an A-scan, the frequency domain back-scattered field from a single point scatterer which is d distance away from the antenna can be written as

$$P(f_n) = \rho \cdot \exp\left(-j4\pi \frac{f_n}{v} d\right) \quad n = 1, 2, \ldots, N \tag{2}$$

where ρ represents the reflectivity of the target and v is the velocity of the wave propagation in the medium. For a homogeneous and lossless medium this velocity can be written as $v = c/\sqrt{\varepsilon_r}$ where c is the speed of the light in free-space and ε_r is the relative electric permittivity of the medium. The frequency variable is related with the wavenumber, which for the two-way propagation data is defined as $k = 4\pi f/v$. Hence, the back-scattered signal samples can also be represented in the spatial frequency domain as

$$P(k_n) = \rho \cdot \exp\left(-jk_n d\right) \quad n = 1, 2, \ldots, N \tag{3}$$

Noting that the linear relationship $z = v \cdot t/2$ between time t and depth z can be taken under the assumption of constant velocity v, the depth profile $p(z_n)$ of the medium can be estimated through the application of one-dimensional (1-D) Inverse Fourier Transform (IFT) to the spatial frequency data of Eq. (3). Furthermore, if 2-D images are desired, a B-scan has to be performed in which data are obtained by collecting a series of A-scan measurement along a synthetic aperture (see Fig. 1(a)). For each discrete point along the synthetic aperture, the back-scattered data is recorded and thus can be represented as $P(x_m, f_n)$. The focused images can then be obtained by applying the imaging algorithms which take the near-field effects into consideration. In this study, a back-projection imaging algorithm [5] with near-field corrections is used to obtain the B-scan images of the water leakage detection application.

3. RESULTS OF MOVEMENT DETECTION

In the first effort of our study, the goal was the experimental detection of the movement of a person behind a wall. The considered scenario was that a person was moving behind the wall and all other surroundings were static. For this purpose, a measurement set up for a 1-D scattering configuration was constructed as depicted in Fig. 2(a). We have assembled a SFCW radar using Agilent E5071B ENA vector network analyzer (VNA) and a rectangular horn antenna with a 30° beamwidth. The operating bandwidth was specifically selected as 3–5 GHz to satisfy the proper penetration of the EM wave through the wall which has a thickness of about 30 cm. In order to keep the reflection

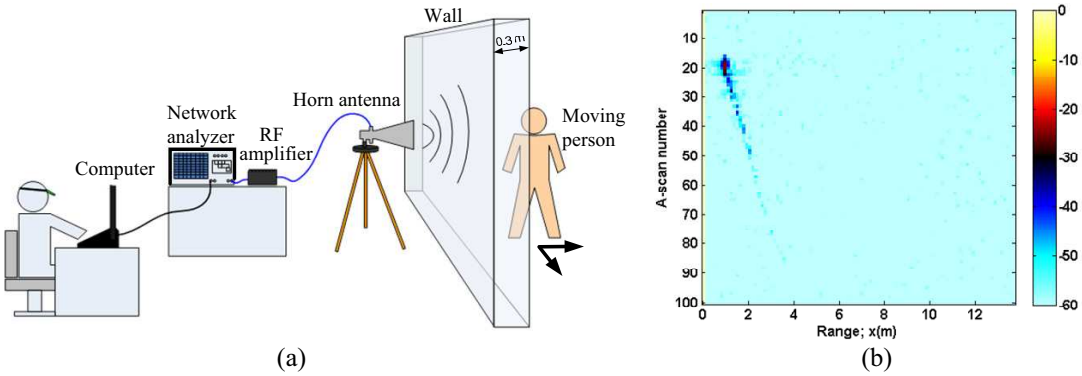

Figure 2: Thru-wall detection of movement: (a) Schematic diagram of the experiment. (b) Radar image.

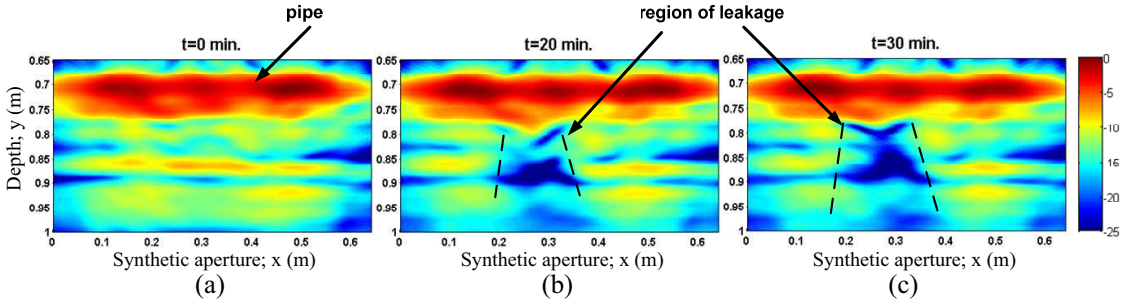

Figure 3: GPR images of water-leak experiments. (a) Image of the water-free pipe at $t = 0$. Image of the water-transporting pipe (b) at $t = 20$ min., (c) at $t = 30$ min. after starting of water leakage. (Depth axis is taken from the antenna phase center).

from the wall surface minimal, the monostatic antenna was put very close to the wall. Then, the transmission of continuum series of burst signals through the wall was started for desired time duration. Then, the measured back-scattered data for each burst was recorded to a computer via VNA's GPIB port and processed into A-scan range profiles by real-time processing. The "difference signals" between consecutive range profiles were then continuously monitored. The resultant radar image is depicted in Fig. 2(b) which clearly indicates the detection of human movement behind the wall.

4. RESULTS OF WATER LEAKAGE DETECTION

In the second effort, it was intended to test the effectiveness of GPR techniques in detecting and identifying the water leaks from plastic pipes. For this purpose, successive B-scan experiments were conducted in a partly homogeneous outdoor soil environment. A PVC pipe with a diameter of 5 cm was located at a depth of 20 cm from the ground surface. Before embedding the pipe in soil, a small hole is drilled for the leakage of water. First, a reference B-scan measurement of the water free pipe was performed. Then, after starting to injection of water into the pipe, three B-scan experiments at regular time intervals were performed. For each scan, a synthetic aperture of length 64 cm with 33 discrete spatial points and a frequency band from 0.8 to 5 GHz with 301 discrete frequency steps were used. Two double-ridged horn antennas with a length size of 0.5 m were utilized in a bistatic configuration during the measurements. After collecting data, the B-scan images were reconstructed by using a near-field back-projection algorithm. The obtained results for various time instants are shown in Fig. 3. From these figures it can be interpreted that, as the water content of the soil around the leak become larger for an evolved time, the size of the region that causes strong EM wave reflections become also larger. Hence, EM wave could not penetrate beneath this water-saturated region. This phenomenon manifests itself as voids in the GPR images providing valuable information about the location of the leak. As the time passed longer, the reflecting area become more and more larger and the leak position become more visible as evident in Fig. 3(c). Hence, it can be assessed that water leakages from plastic pipes can be successfully detected by GPR techniques.

5. CONCLUSIONS

This study demonstrated the ability of GPR to detect and localize the electromagnetic impedance changes through surfaces. It was validated that water leakage causes a void region in the time-series of GPR images. For the movement detection problem, a simple principle of differencing the consecutive A-scans was used to detect the movement change. Beside this simple solution, a number of additional works has to be done on this research area. Two of them are; real-time tracking of moving persons through walls by 2-D imaging and efficient detection of heartbeats and life signs of persons hidden by walls. These works will constitute the subject of our future research.

REFERENCES

1. Soldovieri, F., R. Solimene, and R. Pierri, "A simple strategy to detect changes in through the wall imaging," *Progress In Electromagnetics Research M*, Vol. 7, 1–13, 2009.
2. Sachs, J., M. Aftanas, S. Crabbe, M. Drutarovsky, R. Klukas, D. Kocur, T. T. Nguyen, P. Peyerl, J. Rovnakova, and E. Zaikov, "Detection and tracking of moving or trapped people hidden by obstacles using ultra-wideband pseudo-noise radar," *Proceedings of the 5th European Radar Conference — EuRAD 2008*, 408–411, Amsterdam, Netherlands, October 2008.
3. Eyuboglu, S., H. H. Mahdi, and H. J. Al-Shukri, "Detection of water leaks using ground penetrating radar," *3rd International Conference on Applied Geophysics — Geophysics 2003*, Orlando, USA, December 2003.
4. Yigit, E., S. Demirci, and C. Ozdemir, "On the imaging applications of ground penetrating radar," *Intern. Symp. on Electromagn. Theory — URSI-2010,* Berlin, Germany, August 2010.
5. Munson, D. C, J. D. O'Brien, and W. K. Jenkins, "A tomographic formulation of spotlight-mode synthetic aperture radar," *Proc. IEEE*, Vol. 71, No. 8, 917–925, 1983.

NLOS UWB Undermining Experimental Characterization & Performance Evaluation Using MB-OFDM

M. Ghaddar[1, 2] **and L. Talbi**[1, 2]

[1]University of Quebec in Outaouais, Gatineau, Canada
[2]Underground Communication Research Laboratory (LRCS), Val d'Or, Canada

Abstract— This paper reports on the statistical characterization and modeling of the Ultra-Wideband (UWB) propagation channel in an underground mine environment over the frequency range 3–10 GHz. Two kinds of transmission antennas, directional and omni-directional, were used to investigate the effect of the antenna directivity on the path loss propagation and on the time dispersion parameters in non line-of-sight (NLOS) underground galleries. The measurement and simulation results show that the directional-directional antenna combination yields better radiation efficiency for reducing the time dispersion parameters. Based on channel time domain parameters, and IEEE 802.15.3a working group specifications, Multi-band orthogonal frequency division multiplexing (MB-OFDM) physical (PHY) layer for short-range high data-rate is evaluated. Results indicate that the use of omnidirectional antennas in an underground mine is not realistic. In contrast, directional antennas offer a better performance in terms of capacity.

1. INTRODUCTION

Ultra-wideband (UWB) technology has shown to be attractive in high-speed data transmissions, short duration pulse, and low power communications compared to other wideband wireless systems. In 2002, the Federal communications commission (FCC) allocated a large spectral mask from 3.1 GHz to 10.6 GHz for unlicensed use of commercial UWB communication devices [1]. The UWB frequency mask depends on the application and the environment where the devices are used. For indoor and outdoor communications, the power spectral density of -41.3 dBm/MHz is allowed in the frequency range of 3.1–10.6 GHz.

Numerous narrowband and wideband channel measurements and models have been proposed in the literature for indoor and outdoor environments and for underground mine environments in the CANMET (the Canadian Center for Minerals and Energy Technology) experimental mine in Val d'Or, Canada.

The ultra-wideband propagation in underground environments is still a relatively new research challenge. To date, only a limited amount of work has been done in confined environments with rough surfaces. The modern exploitation of mineral resources, particularly in underground mines, requires remote control and high speed data transmission to be available. Therefore, for the design of build UWB systems, it is crucial to obtain data on the propagation channel characteristics by means of measurements in underground environments. The purpose of this paper is twofold: first, to report on the results of a UWB measurement campaign in an underground environment, in which different antenna directivities were used to extract NLOS UWB propagation characteristics and dispersive parameters, and second, to investigate the performance of the MBOFDM based PHY layer over IEEE UWB channel models in confined hostile environments with rough surfaces.

This paper is organized as follows. Section 2 provides a brief description of the underground mining environment and the measurement setup. Section 3 presents experimental data where the best fitting distribution along with the channel delay spreads have been evaluated in terms of the propagation distance and the antenna directivity. Section 4 investigates the MB-OFDM transmission in term of dispersive parameters, while Section 5 draws out the conclusion.

2. THE MEASUREMENT CAMPAIGN

2.1. Description of the Underground Mining Environment

The UWB measurements were performed in two typical galleries of a former gold mine at the 70 m underground level. The environment mainly consists of very rough walls. The ground was not flat and was sparse with puddles of water as shown in the photograph of Figure 1. The dimensions of the mine galleries vary between 2.5 m and 3 m in width and approximately 3 m in height. Fig. 1 illustrates NLOS underground gallery including transmit and receive antenna location arrangements.

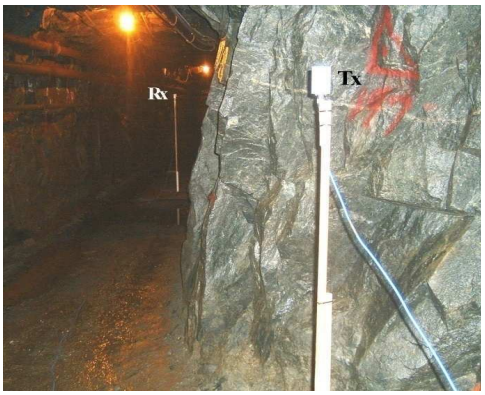

Figure 1: Pictures of the underground NLOS gallery and of the antenna locations.

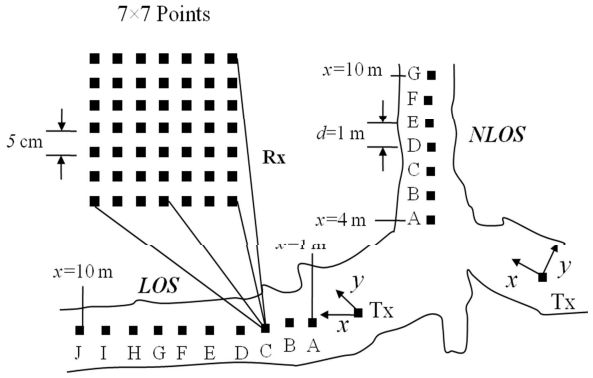

Figure 2: The underground gallery plan.

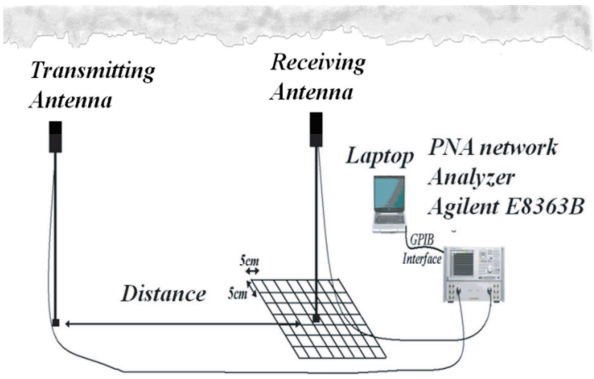

Figure 3: Overview of the measurement setup.

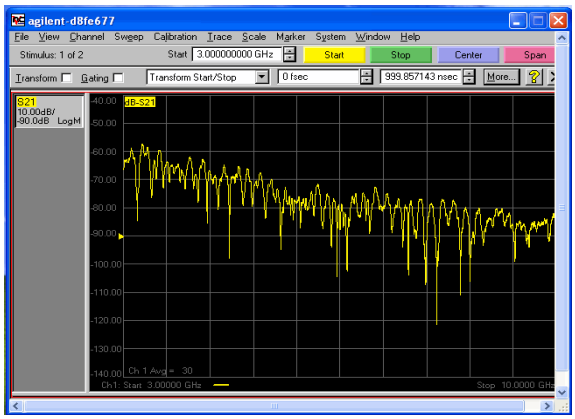

Figure 4: Channel transfer function measured with the Agilent E8363B network analyzer.

2.2. Experimental Procedure

During the measurements, the transmitter antenna was kept at fixed position, while the receiver antenna was moved throughout the gallery on a 49 point grid. As shown in Fig. 2, the grid was arranged as 7×7 points with spacing of 5 cm between each adjacent point. The distance of 5 cm corresponds to one half of the wavelength of the lowest frequency component for uncorrelated small scale fading. The receiver antenna displacement was in the range 4 m to 10 m. The transmitter and receiver antennas were maintained at the same height of approximately 1.7 m, and the channel was kept stationary by ensuring that there was no movement in the surrounding environment.

The UWB measurements were performed in the frequency domain using the frequency channel sounding technique based on S_{21} parameter. The measurement setup consisted of an E8363B network analyzer (PNA) and two different types of antennas, both are vertically polarized: a double bridged directional horn antenna DRG-118/A covering the frequency range from 1 to 18 GHz and an omni-directional antenna, EM-6116, covering the frequency range from 2 to 10 GHz. Fig. 3 shows the experimental setup for ultra wideband measurements. The transmitting port of the PNA swept 7000 discrete frequencies ranging from 3 GHz to 10 GHz uniformly distributed over the bandwidth and the receiving port measured the magnitude and the phase of each frequency component. Thus, at each distance between the transmitter and the receiver, the complex channel transfer function (CTF) was measured 30 times to reduce the effects of the random noise on the data measurements, and then stored on a computer hard drive via a GPIB interface. The sweeping time of the network analyzer was decreased to validate the quasi-static assumption of the channel. Fig. 4 shows a typical complex channel transfer function measured with the network analyzer. The theoretical delay resolution for the UWB signal is 143 ps , the inverse of the bandwidth, i.e., 1/BW and due to the use of windowing, the time resolution is estimated to be 2/BW. Consequently, the time axis was quantized into bins of 286 ps widths which correspond to a bin size slightly greater than the

Table 1: Measurement system parameters.

Parameters	**Values**
Bandwidth	7 GHz
Center Frequency	6.5 GHz
Frequency Sweeping Points	7000
Frequency Resolution	1 MHz
Time Resolution	286 ps
Maximum Delay Range	1 µs
Sweep Average	30
Tx-Rx Antennas Height	1.7 m

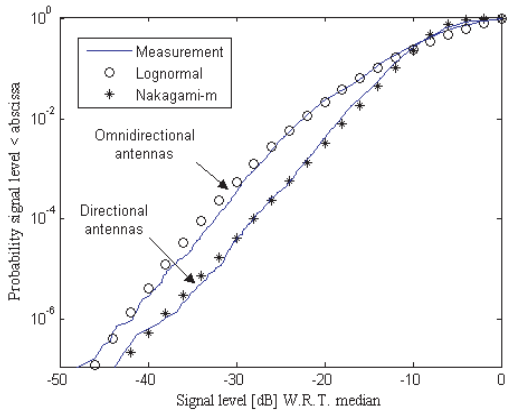

Figure 5: Statistical fading distribution of experimental data.

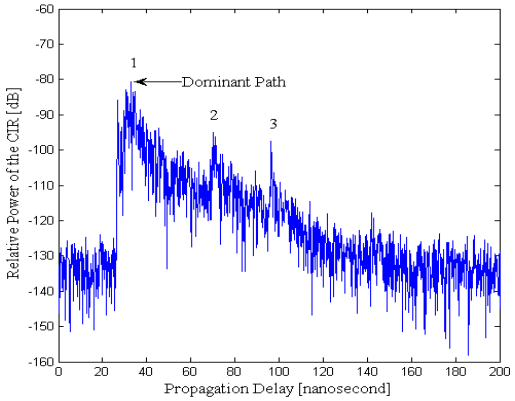

Figure 6: Relative power of the CIR for Tx omnidirectional — Rx omnidirectional.

pulse width and the frequency resolution of 1 MHz gave a maximum delay range of 1 µs, which was largely enough when compared to the highest maximum excess delay of all measurements.

Before the measurements, a calibration of the equipment was performed in order to reduce the influence of unwanted cables effects. Table 1 summarizes the parameters setup.

Since the measurements were performed in the frequency domain, the inverse Fourier transform (IFFT) was applied to the measured complex transfer function using a Kaiser window in order to obtain the channel impulse response (CIR). The Kaiser window with parameter $\beta = 6$ was designed as a finite impulse response (FIR) filter to reduce the side lobes of the CIR and to improve the dynamic range. The noise floor is then estimated to be -140 dBm.

3. MEASUREMENT RESULTS AND ANALYSIS

3.1. Experimental Data Distribution

To this end, it is essential to describe the probability distribution that the signal will exceed a specified reference level. A great number of statistical distributions exist such as Rayleigh, Nakagami-m and Lognormal.

In UWB channels empirical distribution of the fading markedly differs from Rayleigh fading. From the latest results generated by IEEE802.15sg3 [2], the lognormal distribution is recommended to best fit the measured amplitude fading in a UWB multipath channel. The cumulative distribution functions for both NLOS cases are depicted in Fig. 5. Best fits are obtained as follow: In the case of omni-directional antennas, the best fit is found to be Lognormal ($\sigma \approx 2$). However, when directional antennas are used, the distribution converges to Nakagami-m ($m \approx 1$) which is close to Rayleigh distribution.

3.2. Time Dispersion Characteristics

Figure 6 shows a typical power delay profile (PDP) of the channel measured using omni-directional antennas at both ends. To characterize the dispersive properties of the multipath channel and

Table 2: Mean, standard deviation and maximum of τ_m, τ_{rms} and $\tau_{\max}$ for different antenna arrangements.

	Omni - Omni		
	Mean	*std*	*Max*
τ_m [ns]	26.12	4.56	53.05
τ_{rms} [ns]	21.05	3.54	28.16
τ_{max} [ns]	238.70	158.15	431.71
	Direct - Direct		
	Mean	*std*	*Max*
τ_m [ns]	7.41	4.60	17.46
τ_{rms} [ns]	8.24	4.75	18.42
τ_{max} [ns]	64.08	25.27	102.00

Table 3: IEEE 802.15.3a specifications for UW-BOFDM based PHY layer.

Channel bandwidth (MHz)	528
Efficient bandwidth (MHz)	412.5
No. of data subcarriers	100
No. of guard carriers interval	10
No. of DC carriers	1
No. of pilot carriers	12
Cyclic prefix duration (ns)	70 ns
FFT size	128
P value	3.46
FFT duration (ns)	242.42
subcarrier spacing (MHz)	4.125
OFDM Symbol duration (ns)	312.42

Table 4: Uncoded channel bit rate using directional antennas for each 528 MHz sub-band.

Modulation	Data Rate (Mbps)	Data bits per OFDM symbol
QPSK	640	200
16-QAM	1280	400

hence, to evaluate its performance, the mean excess delay (τ_m), RMS delay spread (τ_{rms}) and maximum excess delay ($\tau_{\max}$) are computed [3] and given in Table 2 for each case.

4. MB-OFDM BASED PHY LAYER

Multi-band OFDM is one of the promising candidates for short-range high rate UWB communications. Multiband UWB, that is broadband OFDM, is normally designed to allow the transmission of high data rates over extremely hostile channels. The terms multiband communications and multicarrier communications are often used interchangeably [4]. Multiband transmission is defined as having non-overlapping bandwidths each of 528 MHz across the {3–10 GHz} spectrum mask, while OFDM transmission is the splitting of each 528 MHz band into many overlapping narrow-band sub-channels. In order to evaluate UWB-OFDM transmission, IEEE 802.15.3a standard has been approved for realistic UWB environments as shown in Table 3.

Generally, subcarrier spacing and cyclic prefixes (or guard interval) in OFDM systems are dedicated to strengthen the spectrum efficiency and hence reduce ISI to extend the system radio coverage. The channel cyclic prefix is adjusted to the duration that exceeds the excess delay of the channel's impulse response. This allows a higher number of data subcarriers to ensure efficient interleaving at the binary and subcarrier levels.

Based on the above discussion, it is clearly seen that a channel excess delay of about 238.70 ns using Omnidirectional antennas renders to be unpractical. However, the deployment of directional antennas has changed completely the propagation characteristics of the channel to become comparable to LOS transmission in term of time dispersive parameters. According to values given in Table 3, a channel excess delay of 64.08 ns might perform properly with a lower level of inter-symbol interference (ISI). Theoretically, channel bit rate transmission is calculated using [4]. With 100 subcarriers it is possible to squeeze $100 \times \log_2(M)$ bits into 312.42 ns pulse as given in Table 3. Practically, some bits in the sequence will be needed for synchronization, etc, plus low power requirement will result in losses at the receiver and the necessity to re-transmit data several times. Realistically, still GB/s rates are achievable in each of the sub-bands with the proper use of directional antenna in underground mines as shown in Table 4.

5. CONCLUSION

Wireless communication systems in underground mines are becoming an increasingly important part of the mining industry. In such hostile propagation environments, MB-OFDM based PHY layer becomes a potential candidate to UWB communications system. Thus, a characterization and modeling of the NLOS UWB propagation channel are presented in this paper. Although omni-directional antennas offer a better signal coverage in NLOS gallery, results show that, in short range high data rate UWB, omni-directional antennas render to be unpractical due to the very long excess delay they offer. However directional antennas have an efficiency effect to reduce the time dispersion parameters and lead to a better channel capacity.

REFERENCES

1. Federal Communications Commission, First order and report: Revision of part 15 of the Commission's rules regarding UWB transmission systems, April 22, 2002.
2. Zhang, J., R. A. Kennedy, and T. D. Abhayapala, "Performance of RAKE reception for ultra wideband signals in a lognormal fading channel," *Proceedings of International Workshop on Ultra Wideband Systems (IWUWBS 03)*, Oulu, Finland, June 2003.
3. Rappaport, T. S., *Wireless Communications: Principles and Practice*, 2nd edition, Prentice Hall PTR, Upper Saddle River, NJ, USA, 2002.
4. Kraemer, R., *Short-Range Wireless Communications; Emerging Technologies and Applications*, John Wiley and Sons Ltd., 2009.

The Effects of Defects on Magneto-inductive Waveguide

Ye Chen, Praveen Pasupathy, and Dean P. Neikirk
Department of Electrical and Computer Engineering, University of Texas, Austin, TX 78712, USA

Abstract— This paper investigates one-dimension magneto-inductive waveguide with defects. The magneto-inductive waveguide constructed by inductively coupled coils is analyzed based on its circuit model. The impedance discontinuities due to defect lead to MI wave reflection in the waveguide. The frequency and time domain characteristics of MI waveguide with defects are studied and the techniques to locate defects MI waveguide are provided.

1. INTRODUCTION

Magneto-inductive (MI) waves are excited and propagated along the waveguide due to magnetic coupling between the elements. MI waves can propagate within a passband near the resonant frequency of the elements [1]. The time varying current in an element will generate further current in its neighboring element through magnetic linked flux. This relationship contributes to supporting MI waves. The embodiment of the MI waveguide can be in the form of a finite array of uniformly spaced capacitively-loaded loops, split squared ring resonator and Swiss rolls [1–3]. MI waveguides have been developed in the applications of mirrors, interferometers, splitters, transducers, phase shifters and imaging lens [4–6] We have also examined how such an MI can be used as a distributed sensor in material such as concrete based on changes in the Q of the L-C resonator sub-elements that make up the MI waveguide [8].

In this paper, the ongoing work is summarized to understand the behavior of "point" defects in magneto-inductive waveguide. The characteristics of the 1-D waveguide with defects in frequency and time domain are explored. Based on the relationship between the relative positions of defects and time and frequency responses, techniques to determine the location of defects are developed.

2. ONE DIMENSION MI WAVEGUIDE

In this section, we will briefly present the theoretical background about 1-D inductive coupled MI waveguide. 1-D linear MI waveguide is constructed using a number of inductively coupled coils with center to center distance of d. With coaxial coupled coils, the mutual inductances between loops are positive that will result in a forward wave. The coil element is modeled by an inductance L, a capacitance C, resistance R and coupled to its neighbors by mutual inductance. The coil can be idealized as a simple resonant circuit, with self impedance of $Z = R+j\omega L+1/j\omega C$ and resonant frequency of f_0. Based on Ohm's Law, the circuits for coils satisfy:

$$Z_n I_n + \sum_{s=1}^{S} j\omega M_s \left(I_{n-s} + I_{n+s}\right) = V_n \tag{1}$$

where Z_n is self impedance of nth coil circuit, ω is the angular frequency, I_n and V_n are the alternating current and voltage, M_s is the mutual inductance between two elements spaced by sd. S indicates the number of considered neighboring interactions and V_n is zeros elsewhere except at the driver coil. We can substitute the traveling wave solutions $I_n = I_0 \exp(-nkd)$ to obtain the dispersion relationship,

$$\omega_0^2/\omega^2 - 1 + j/Q = \sum_{s=1}^{S} \kappa_m \cosh\left(skd\right) \tag{2}$$

where ω_0 is the angular resonant frequency, $Q = \omega L/R$ and $\kappa_i = 2M_i/L$ is the coupling factor between coils, k is propagation constant and complex, whose real and imaginary parts α and β indicate the attenuation coefficient and propagation coefficient respectively. The simulation is done with coaxial sensor array consisting of identical 5-turn coils uniformly spaced by 1 inch, as shown in Figure 1(a). Each coil has self-inductance of 2.89 μH and capacitance of 101 pF. The mutual inductance between the nearest neighbors is 0.31 μH. Bandwidth can be predicted roughly with only the nearest interaction by simplifying Equation (2). It shows that the MI waves can only propagate in the frequency range of $1/(1+\kappa_1) \leq (\omega/\omega_0)^2 \leq 1/(1-\kappa_1)$ [9].

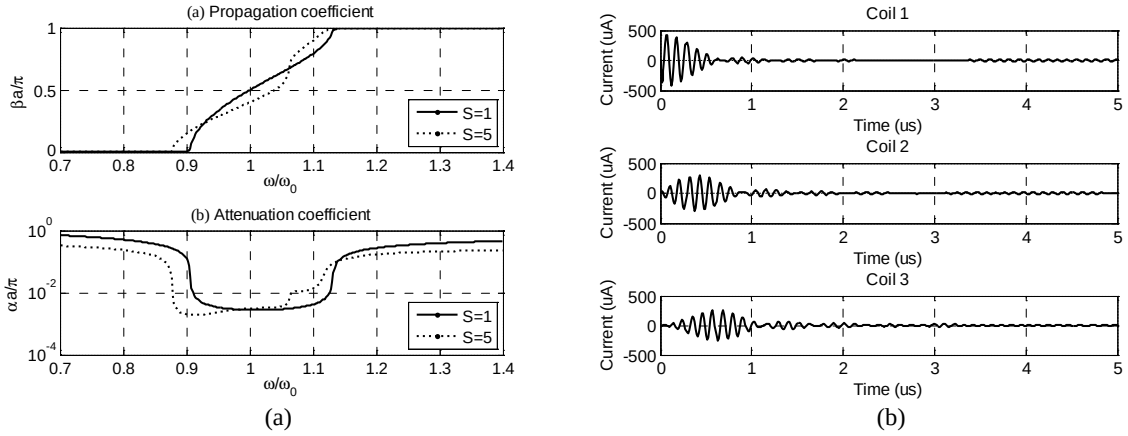

Figure 1: (a) Dispersion relationship of MI waveguide. (b) Current at the coil 1, 2 and 3 in time domain.

In time domain, MI waves propagate along the line of coils and the current in each coil is recorded as shown in Figure 1(b). Coil 1 is the first coil after the driver coil. The input driver voltage is a narrow unit pulse voltage that close to Delta functions. Since the MI waveguide is roughly a passband filter, the output is like sinc signal. The traveling speed is about 0.23 µs per coil.

3. ONE DIMENSION MI WAVEGUIDE WITH ONE DEFECT

The impedance discontinuity could be caused by the variances of resistance, self inductance, capacitance of coils and the mutual inductance that is raised by broken wire in nth coil in the array. The structure with mutual inductance discontinuity as the defect is investigated in the paper. According to the transmission line theory, the discontinuity in waveguide will cause wave reflections. If only the magnetic coupling from the nearest neighbor is considered, the reflective and transmission coefficient could be obtained as [4],

$$\begin{aligned} R &= \frac{\left(M_2^2 - M_1^2\right)\exp\left(kd\right)}{M_1^2\exp\left(kd\right) - M_2^2\exp\left(-kd\right)} \\ T &= \frac{M_1 M_2\left(\exp\left(kd\right) - \exp\left(-kd\right)\right)}{M_1^2\exp\left(kd\right) - M_2^2\exp\left(-kd\right)} \end{aligned} \tag{3}$$

where Z_1 and Z_2 are mutual impedance, $Z_1 = j\omega M_1$ and $Z_2 = j\omega M_2$. Since power is conserved, the two coefficients satisfy $|R|^2+|T|^2=1$. $|R|^2$ and $|T|^2$are power reflection and transmission coefficients. The strength of reflection depends on the ratio of Z_2 to Z_1 and value of kd. Figure 2(a) displays the power coefficient for the inductively coupled chain with one defect. The doubled gap decrease mutual inductance from 0.31 µH to 0.09 µH. The mutual impedance discontinuity introduces extra insertion loss in the passband.

The reflective waves are received due to the defect, as recorded in Figure 2(b). The time spent by the reflective waves travelling back to Coil 1 is the same as the time used by the incident wave reaching at the discontinuity junction. In the round trip, the time is doubled. Then we can determine the location of the defect based on the arriving time of the first reflective waves. For example, if the defect takes place at the forth coil, then reflective wave will propagate for distance of $6d$ to get back. The delay would be 1.38 µs, which coincide with the results in Figure 2(b).

4. ONE DIMENSION MI WAVEGUIDE WITH TWO DEFECTS

1-D sensor array with two defects are classified into two different structures. If the second defect takes place next to the first discontinuity, it means a defect with greater reflection will be introduced. This transmission line essentially only has one mutual inductance discontinuity with $Z_2 = j\omega M_3$. The discontinuity impedance ratio M_3/M_1 is much smaller than M_2/M_1, which would lead to a greater insertion loss in the frequency band.

If the second defect happens at another location, two mutual inductance discontinuities will be formed in the line of coils, as shown in Figure 3. It is like two "mirrors" are plugged into

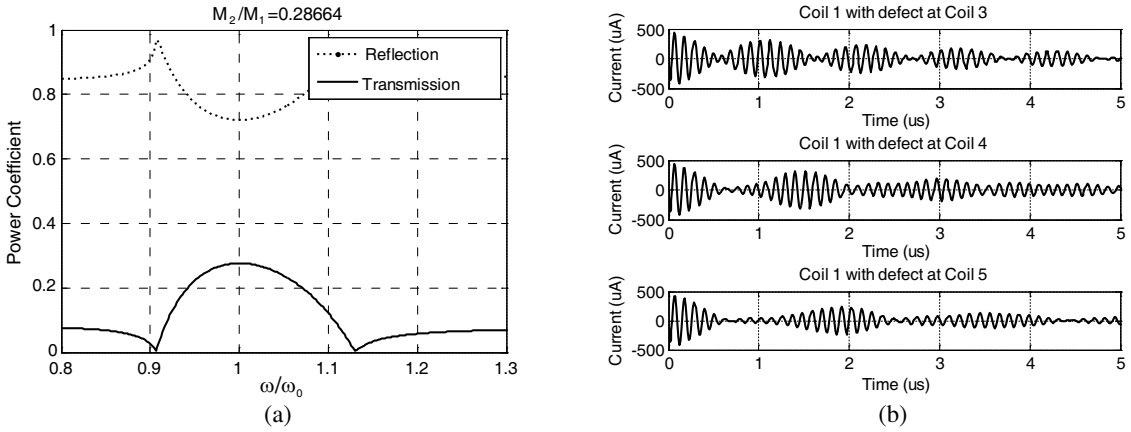

Figure 2: (a) Power coefficient vs. normalized frequency. (b) Current at coil 1 in time domain with three different locations of defects.

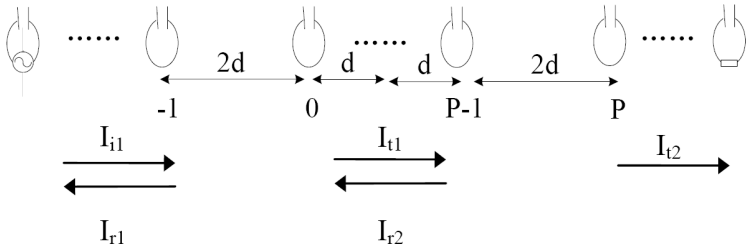

Figure 3: Schematic diagram of 1-D MI waveguide with two distributed defects.

the waveguide. The two reflectors act as a Fabry-Perot cavity [4]. The two reflectors divide the transmission line into three parts, and the current in each part can be described as in Equation (4).

$$I_n = \begin{cases} I_{i1} + I_{r1} = I\exp(-nkd) + R_1 I\exp(nkd) & (n \le -1) \\ I_{t1} + I_{r2} = T_1 I\exp(-nkd) + R_2 I\exp(nkd) & (0 \le n \le P-1) \\ I_{t2} = T_2 I\exp(-nkd) & (n \ge P) \end{cases} \tag{4}$$

where P equals to the number of coils working between the two discontinuities, R_1 and R_2 indicate the coefficients of backward waves for loop n ($n \le -1$ and $0 \le n \le P-1$), T_1 and T_2 are coefficients of forward waves for loop n ($0 \le n \le P-1$ and $n \ge P$). We assume the two discontinuities have the same mutual inductance Z_2. The circuits at the two junctions should satisfy,

$$\begin{aligned} &ZI_{-1} + Z_1 I_{-2} + Z_2 I_0 = 0 \\ &ZI_0 + Z_1 I_1 + Z_2 I_{-1} = 0 \\ &ZI_{P-1} + Z_1 I_{P-2} + Z_2 I_P = 0 \\ &ZI_P + Z_1 I_{P+1} + Z_2 I_{P-1} = 0 \end{aligned} \tag{5}$$

We substitute current expression into Equation (5) and eliminate Z, R_2 and T_1. Reflection coefficient R_1 and transmission coefficient T_2 caused by the cavity are solved as,

$$\begin{aligned} R_1 &= \frac{\left(M_2^2 - M_1^2\right)\left(M_2^2 - M_1^2\exp(2kd) - \exp(-2Pkd)\left(M_2^2\exp(2kd) - M_1^2\right)\right)}{\left(M_2^2\exp(-kd) - M_1^2\exp(kd)\right) - \left(M_1^2 - M_2^2\right)\exp(-2Pkd)} \\ T_2 &= \frac{M_1^2 M_2^2\left(2 - \exp(2kd) - \exp(-2kd)\right)}{\left(M_2^2\exp(-kd) - M_1^2\exp(kd)\right) - \left(M_1^2 - M_2^2\right)\exp(-2Pkd)} \end{aligned} \tag{6}$$

Both coefficients depend on the mutual inductance M_1 and M_2, the number of perfect loops inside the resonator P, and value of kd. We plot the reflection coefficient $|R|^2$ and transmission $|T|^2$ variations with normalized frequency for MI waveguide consisting of the same elements as used with different value of P in the coaxial array, as shown in Figure 4.

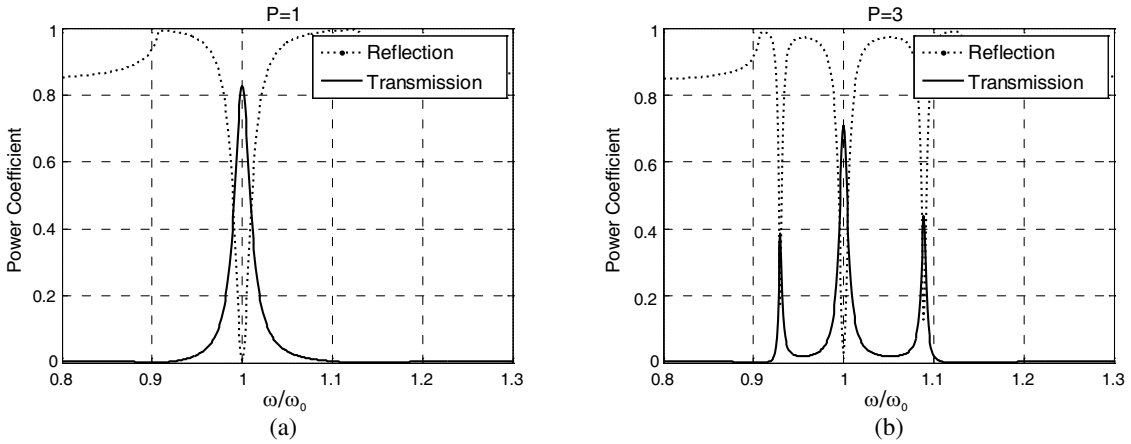

Figure 4: Power reflection and transmission coefficient vs. normalized frequency with $P = 1$ and $P = 3$.

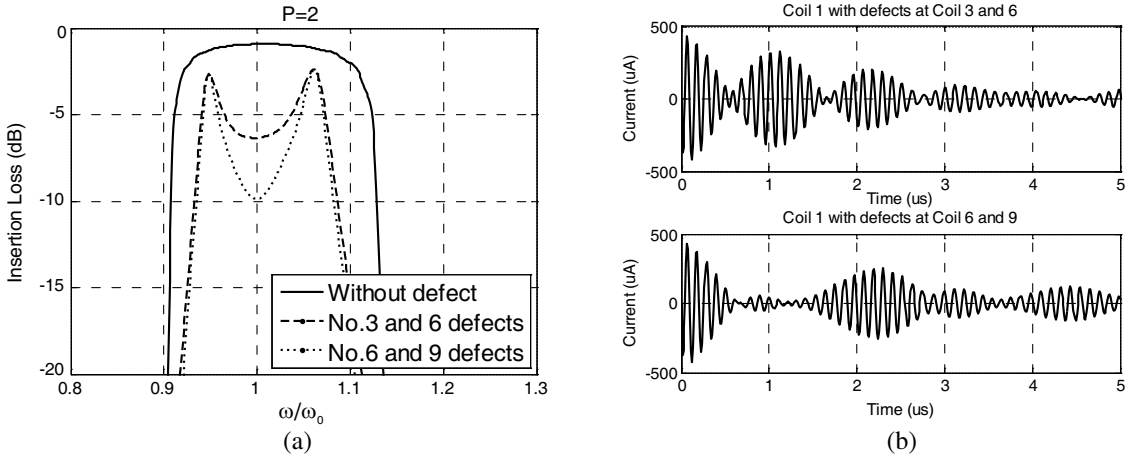

Figure 5: (a) Insertion loss vs. Normalized frequency. (b) Current at coil 1 in time domain with different locations of defects.

The peaks lie at frequency such that $\beta d = n\pi/(P+1)$, where $n = 1, 2, \ldots, P$. It satisfy the conventional cavity resonance principle that resonance occurs when the phase changes $2(N+1)\beta d$ accumulated in a cavity round trip is a integral multiple of 2π. The peaks in the transmitted power correspond to the low loss during the passband. If two different cavities have the same number of coils between them, the number and location of peaks would be identical. This would lead to multiple answers for the location of the defects. For example, it is hard to decide whether Coil 3 or Coil 9 is combined with Coil 6 only based on the frequency response, as shown in Figure 5(a). The time domain response is needed to get the information of the first defect in the line. From Figure 5(b), we can locate the first defect by examining the arriving time of first reflective waves. For Coil 3 and Coil 6, the time delay are 0.92 µs and 2.3 µs respectively. Then we can get the conclusion of the location of defects with the time domain response. From the study of the MI waveguide above, one or two defects in waveguide can be located. We can locate the corrosion exactly by monitoring the reflective waves and computing the number of peaks in the passband.

5. CONCLUSIONS

In this paper, we investigate the frequency and time domain characteristics of the MI waveguide with defects. When a defect is present the impedance discontinuity due to a single defect leads to MI wave reflection which introduces higher insertion loss in the pass band. The defect can be located in chain of coils by analyzing the current at the Coil 1 in time domain. If a second defect is introduced, we observe the two discontinuities act as a resonant cavity producing clear peaks and troughs in the pass band. The number of peaks in the passband provides the information about how far away the second defect is. The exact location of the second defect can be determined by examining the first received reflective waves. Thus based on the relationship between the relative

positions of two defects and frequency and time characteristics, the technique to determine the location of defects has been developed.

ACKNOWLEDGMENT

The research activities described in this paper were sponsored by the National Science Foundation through grant number CMMI-0825486 to the University of Texas at Austin. The cognizant program director is S. C. Liu.

REFERENCES

1. Shamonina, E., V. A. Kalinin, K. H. Ringhofer, and L. Solymar, "Magneto inductive waveguide," *Electron. Lett.*, Vol. 38, No. 8, 371–373, 2002.
2. Freire, M. J., R. Marques, F. Medina, M. A. G. Laso, and F. Martin, "Planar magneto-inductive wave transducers: Theory and applications," *Appl. Phys. Lett.*, Vol. 85, No. 19, 4439–4441, 2004.
3. Wiltshire, M. C. K., E. Shamonina, I. R. Young, and L. Solymar, "Experimental and theoretical study of magneto-inductive waves supported by one-dimensional arrays of 'Swiss Rolls'," *J. App. Phys.*, Vol. 95, No. 8, 4488–4493, 2004.
4. Syms, R. A., E. Shamonina, and L. Solymar, "Magneto-inductive waveguide devices," *IEE Proc. Micron. Antennas Propag.*, Vol. 153, No. 2, 111–121, 2006.
5. Nefedov, I. S. and S. A. Tretyakov, "On potential applications of metamaterials for the design of broadband phase shifters," *Micro. Opt. Technol. Lett.*, Vol. 45, No. 2, 98–102, 2005.
6. Freire, M. J. and R. Marques, "Planar magneto inductive lens for three-dimensional subwavelength imaging," *Appl. Phys. Lett.*, Vol. 86, No. 18, 182505, 2005.
7. Syms, R. A., E. Shamonina, and L. Solymar, "Magneto-inductive waveguide devices," *IEE Proc. Micron. Antennas Propag.*, Vol. 153, No. 2, 111–121, 2006.
8. Pasupathy, P., M. Zhuzhou, D. P. Neikirk, and S. L. Wood, "Unpowered resonant wireless sensor nets for structural health monitoring," *Proceedings of IEEE Sensors*, 697–700, Leece, Italy, Oct. 2008.
9. Syms, R. A., I. R. Young, and L. Solymar, "Low-loss magneto-inductive waveguide," *J. Phys. D: Appl. Phys.*, Vol. 36, No. 18, 3945–3951, 2006.

Peak to Average Power Ration Reduction in OFDM System Using Constant Envelope for Transmission via PLC Channel

El Ghzaoui Mohammed, **Belkadid Jamal**, **and Ali Benbassou**
Laboratory of Transmission and Data processing, University Sidi Mohammed Ben Abdellah, Fez, Morocco

Abstract— Power Line Communications have been the subject of an important research work. At the same time, the growing demand for multimedia communications provides a good prospect for PLC as a promising transmission technique for the "last mile" access network. Orthogonal Frequency Division Multiplexing (OFDM) is a spectrally efficient multicarrier modulation technique for high speed data transmission over multipath fading channels. High Peak-to-Average Power Ratio (PAPR) is a major drawback of OFDM. The high PAR of the OFDM signal has to be considered when setting the range of the digital-to-analog converter (DAC) and dimensioning the line-driver. This paper introduced an improved PAPR reduction scheme using constant envelope modulation. Furthermore, by utilizing continuous phase modulation (CPM) in a CE-OFDM system, the PAPR can be effectively reduced to 0 dB. The paper describes a CE-OFDM based modem for Power Line Communications (PLC) over the low voltage distribution network. Relying on a preliminary characterization of a PLC network, a complete description of the modem is given. The good performances of the BER have been checked by the simulation platform of PLC channel using Matlab.

1. INTRODUCTION

Considering last mile communications, PLC appears to be a promising alternative to conventional technologies such as digital subscriber line (DSL) particularly in rural or underdeveloped areas where the conventional telephone line is still not available to a large population at the global level. But the coverage of power line grid is far more superior to telephone networks. Furthermore, PLC is also a suitable candidate for local area networks (LAN) and home automation. The channel characteristics were investigated in detail by [1]. Investigations revealed that multi-carrier modulation schemes like orthogonal frequency division multiplexing (OFDM) can cope with the shortcomings of power lines as communication media [2–4].

OFDM is a bandwidth efficient multicarrier modulation where the available spectrum is divided into subcarriers, with each subcarrier containing a low rate data stream. OFDM has gained a tremendous interest in recent years because of its robustness in the presence of severe multipath channel conditions with simple equalization, robustness against Inter-symbol Interference (ISI), multipath fading, in addition to its high spectral efficiency. However, the Peak-to-Average Power Ratio (PAPR) is a major drawback of multicarrier transmission system such as OFDM [5]. Implementation of multicarrier system needs more precision Digital-to-Analog Converter (DAC) in Transmitter and more precision Analog-to-Digital Converter (ADC) in Receiver. The DAC clips all samples that exceed certain maximum amplitude, the clip level. Setting this level is a compromise between clipping probability and quantization noise level: decreasing the chip level will increase the average clip noise but decrease the quantization noise. It is usually set to that the total Signal-to-Noise Ratio (SNR) is minimized. A lower PAR will increase the SNR or allow for a DAC with lower resolution to be used. There are several techniques for PAR reduction in OFDM systems has been proposed in literature [6–9]. The most widely technique used in OFDM is the tone reservation scheme [10]. The tone reservation scheme shows very good PAR reduction performance when operation with optimized positions of the peak reduction tones (PRT). However, it is not easy to find the optimal PRT positions, and the performance of the tone reservation scheme degrades with no optimal PRT positions. To alleviate this problem, constant envelope OFDM (CE-OFDM) signal has been introduced in [11–13], which combines orthogonal frequency division multiplexing and phase modulation or frequency modulation. Furthermore, by utilizing continuous phase modulation (CPM) in a CE-OFDM system, the PAPR can be effectively reduced to 0 dB. Although the CPM has low spectral efficiency, it features low system complexity and favorable performance due to low PAR and robustness to amplitude variation and impulsive noise [14]. The CPM decreases the side lobe of the power spectrum by means of continuously connecting the phase that contains the information.

In the following sections, characteristics of the network are given in Section 2. In Section 3, the PAPR of OFDM signal is given. In Section 4, we give a brief insight on CPM modulation.

Then the CE-OFDM signal is introduced in Section 5. In Section 7, simulation results are shown for a real channel, the effect of numbers of branches and modulation order on the Bit Error Rate (BER) performance is investigated. OFDM-CPM is then compared with conventional OFDM under *HomePlug 1.0*.

2. POWER LINE CHANNEL MODEL

A mathematical multipath propagation model for the power line channels has been proposed in [15, 16]. The transfer function of the PLC channel in the frequency range of 1–30 MHz is given by

$$H(f) = \sum_{i=1}^{L} g_i e^{-(a_0+a_1 f^{\gamma})d_i} e^{-j2\pi f\tau_i}, \tag{1}$$

where L is the number of significant arrived paths at the receiver, a_0, a_1 the attenuation parameters, γ the exponent of the attenuation factor, typical values are between 0.5 and 1, g_i the weighting factor for ith path, τ_i the delay of ith path and d_i the length of ith path.

3. OFDM SIGNAL

The OFDM baseband waveform can be represented by

$$m(t) = \sum_{k=0}^{N-1} I_k e^{j2\pi \frac{k}{T_B} t} \quad 0 \le t \le T_B \tag{2}$$

N is the number of subcarriers, T_B is the signaling interval, and data symbol I_k modulates the kth subcarrier $\exp(jk\pi t/T_B)$. The data symbols are chosen from a complex set defined by an M-point signal constellation such as PSK or QAM. The average power of (2) is

$$P_s = \frac{1}{T_B} \int_0^{T_B} |m(t)|^2 dt = N. \tag{3}$$

The PAPR of the transmitted signal in (1) is defined as

$$PAPR_s = \frac{\max_{t\in[0,T_B)} |m(t)|^2}{P_s} \tag{4}$$

Notice that the absolute maximum signal power is N^2, so the PAPR can be as high as N. if N is large enough, based on the central limit theorem, the real and imaginary parts of $m(t)$ have Gaussian distribution and its envelope will follow a Rayleigh distribution. This implies a large PAPR. Equivalently, we can think of this as N sinusoids adding constructively to give a PAPR as large as N. It is impossible to send this high peak amplitude signals to the transmitter without reducing peaks. In the following section we introduce an improved PAPR reduction scheme using constant envelope modulation.

4. CE-OFDM-CPM SIGNAL DESCRIPTION

The baseband CE-OFDM signal is,

$$s(t) = Ae^{j\phi(t)} \tag{5}$$

where A is the signal amplitude.

The phase signal during the ith block is written as:

$$\phi(t) = \theta_i + 2\pi h c_N \sum_{k=1}^{N} I_{i,k} q_k(t - iT_B), \quad iT_B \le t < (i+1)T_B \tag{6}$$

where

$$\theta(t) = \phi(iT - \varepsilon) - \phi(iT + \varepsilon), \quad \varepsilon \to 0$$

The phase memory θ_i may be used in conjunction with a phase unwrapper at the receiver to ensure a continuous phase at the symbol boundaries and hence better spectral containment. Here h refers to modulation index; N is the number of sub-carriers $I_{n,k}$ represents M-PAM data

symbols; T_B is the ith block interval, and $q_k(t)$ represents the set of subcarrier waveforms. The normalizing constant, C_N, is set to $C_N = (2/N\sigma_I^2)$ where σ_I is the variance of the data symbols, and consequently the variance of the phase signal will be $\sigma_\Phi^2 = (2\pi h)^2$. Assuming that the data is independent and identically distributed, it follows that $\sigma_I^2 = (M^2-1)/3$.

To guarantee continuous phase, the memory terms set to

$$\theta_i = K \sum_{l=0}^{\infty} \sum_{k=1}^{N} [I_{i-l,k}\, A_b(k) - I_{i-1-l,k}\, A_e(k) \tag{7}$$

where

$$K = 2\pi h c_N, \quad A_b(k) = q_k(0), \quad A_e(k) = q_k(T_B - \varepsilon), \quad \varepsilon \to 0.$$

The benefit of continuous phase CE-OFDM is a more compact signal Spectrum [18].

5. APPLICATION IN PLC CHANNEL

In this section the performance of CE-OFDM-CPM in PLC channel is analyzed. Already discussed in [19], the principal problem in broadband PLC is the frequency selective fading, witch cause changes in the attenuation of power line channel.

CE-OFDM has the same block structure as conventional OFDM, with a block period, T_B, designed to be much longer than the maximum propagation delay $\tau_{\max}$. A guard interval of duration $T_g \geq \tau_{\max}$ is inserted between successive CE-OFDM blocs to avoid inter-block interference. At the receiver, $r(t)$ is sampled at the rate $f = 1/T_{sa}$ samp/s, the guard time samples are discarded and block time samples are processed. The received signal in discrete time model can be written as

$$r_p[i] = r[i] = \sum_{l=0}^{N_c-1} h[l]\, s[i-l] + n[i], \quad i = 0, \ldots, N_B - 1 \tag{8}$$

where $s[i]$ is the CE-OFDM signal, $h[l]$ is the impulse response for power line channel, $n[i]$ is the impulsive noise component in power line channel. Transmitting a cyclic prefix during the guard interval makes the linear convolution with the channel equivalent to circular convolution. Thus

$$r_p[i] = \frac{1}{N_{DFT}} \sum H[k] S[k] e^{j\frac{2\pi ik}{N_{DFT}}} \quad i = 0, \ldots, N_B - 1 \tag{9}$$

where $\{H[k]\}$ is the DFT of $\{h[i]\}$ and $\{S[k]\}$ is the DFT of $\{s[i]\}$. The effect of the channel simplifies to an IDFT, followed by a vector multiplication, followed by a DFT. Defined by $\{C[k]\}$, the FDE (frequency domain equalizer) attempts to correct the distortion caused by the channel, defined by $\{H[k]\}$. The FDE output is

$$\hat{s}[i] = \frac{1}{N_{DFT}} \sum_{k=0}^{N_{DFT}-1} R_p[k] C[k] e^{j\frac{2\pi ik}{N_{DFT}}}, \quad i = 0, \ldots, N_B - 1, \tag{10}$$

where $\{R_p[k]\}$ is the DFT of the processed samples $\{r_p[i]\}$ and $\{C[k]\}$ are the equalizer correction terms, which are computed as. For the minimum mean-squared error (MMSE) definition,

$$C[k] = \frac{H^*[k]}{|H[k]|^2 + (\frac{E_b}{N_0})^{-1}}, \tag{11}$$

6. EXPERIMENTAL AND SIMULATION RESULTS

The BER performance of CE-OFDM-CPM over PLC channel is evaluated using computer simulation. First let us see the influence of number of branches of the PLC channel. To determine the influence of branches, the power-line configuration with distributed branches was considered. The number of branches was increased as 2, 3 and 6. All line branches are open-ended, with no load connection. Figure 1 shows the transfer function for different number of branches. It is seen that the positions of deep notches are not changed. As the number of branches increase the attenuations tends to increase. Figure 2 shows the performance of the CE-OFDM-CPM system for various numbers of branches. It can be observed that to attain a bit error probability of 3.10^{-7} the SNR per bit of 20 dB, 35 dB, 44 dB, and more than 50 dB are needed for without branch, 2, 3, and more than 6 branches, respectively.

Figure 3 shows simulation results for $M = 4, 8, 16, 32, 64$ and 128. The bit error rate is plotted against the SNR. There are two main observations to be made. The first, for a fixed modulation

index, CE-OFDM has improved spectral efficiency with increase modulation order M at the cost of performance degradation. The second, from Figure 3, it can be seen that with M increasing the system requires augmenting the SNR in order to achieve a certain BER. For $2\pi h = 0.8$, if $M = 4$, to achieve BER of 10^{-7} the SNR need to be only about 24 dB. And if $M = 8, 16, 32, 64$ and 128 to achieve the same BER, the SNR need to be 28 dB, 33 dB, 37 dB, 43 dB and superior to 50 dB respectively. So M should not take too large value when SNR is limited. However, the larger M is, the higher the maximum data transmission rate of the system is. From Figure 3, it can be seen that, if let BER $\leq 10^{-7}$, the system can achieve about 32 Mbit/s and 112 Mbit/s data transmission rates when the SNR are about 23 dB and 50 dB respectively. In Figure 4, the performance of CE-OFDM-CPM is compared with the conventional OFDM (*HomePlug 1.0*) over PLC channel. In this case $2\pi h = 0.8$ and $M = 4$. Over the region 0 dB $\leq$ SNR $\leq$16 dB, the OFDM system performs better than the OFDM-CPM system. However, at high bit Signal-to-Noise Ratio (SNR)

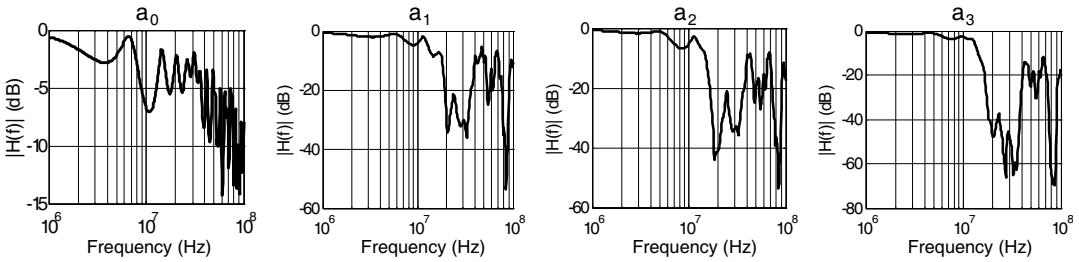

Figure 1: Experimental measurements of frequency response magnitude for PLC channel with distributed branch, (a_0) without branch, (a_1) 2 branches, (a_2) 3 branches and (a_3) 6 branches.

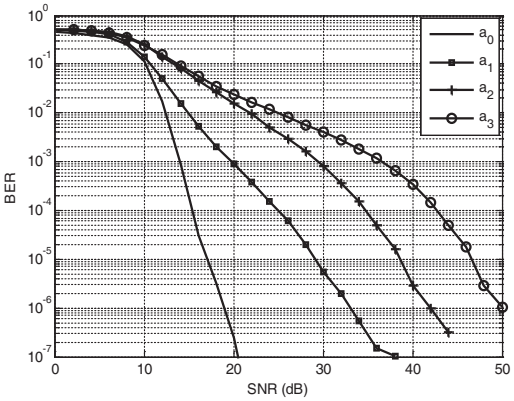

Figure 2: Simulation results for the CE-OFDM-CPM system for PLC channel for various numbers of branches. ($M = 4$, $N = 512$, $2\pi h = 1$, $J = 4$, MMSE).

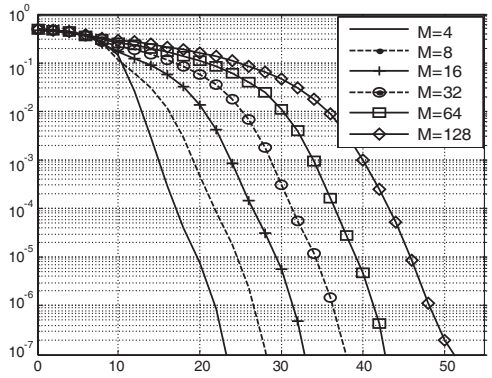

Figure 3: BER of CE-OFDM-CPM systems in channel (a_0). ($N = 512$, $2\pi h = 0.8$, $J = 4$, MMSE).

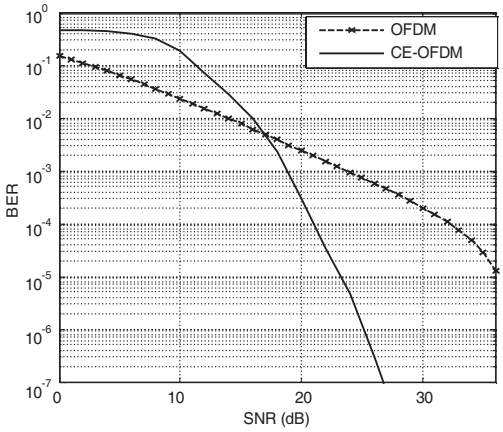

Figure 4: CE-OFDM-CPM versus OFDM under HomPlug 1.0.

the CE-OFDM is shown to outperform OFDM. At low SNR the OFDM-CPM phase demodulator receiver suffers from a threshold effect.

7. CONCLUSION

Together with the PLC transmission environment, a possible modulation technique is introduced in order to create a complete picture of the PLC transmission. Design parameters for a CE-OFDM-CPM communication system for high rate data transmission over power lines are specified. The high PAPR OFDM signal is transformed to a 0dB PAPR constant envelope waveform. The modulation parameters are adjusted to provide a desired BER performance without interrupting the data transmission when the channel condition is suddenly changed. Simulation results show that the adjustment of each tone power, symbol rate and modulation level can provide performance quite robust to time-varying power-line channel condition.

In this paper the performance of power line channel has been investigated. It has been observed that the data rate up to 112 Mbps can be attained by increasing the modulation level. Our simulation model is based on the measurements in the real PLC transmission environment. It is shown that the performance of typical medium voltage channel can be affected due to multipath phenomena. In addition, OFDM-CPM is compared with conventional OFDM under *HomePlug 1.0*. CE-OFDM-CPM is shown to outperform OFDM at high SNR. However, at low SNR the CE-OFDM-CPM phase demodulator receiver suffers from a threshold effect.

REFERENCES

1. Zimmermann, M. and K. Dostert, "The low voltage power distribution network as last mile access network-signal propagation and noise scenario in the HF-range," *AEÜ International Journal on Electronics and Communications*, Vol. 54, No. 1, 13–22, Jan. 2000.
2. Ma, Y. H., P. L. So, and E. Gunawan, "Performance analysis of OFDM systems for broadband power line communications under impulsive noise and multipath effects," *IEEE Transactions on Power Delivery*, Vol. 20, No. 2, 674–682, 2005.
3. Tellambura, C., "Computation of the continuous-time PAR of an OFDM signal with BPSK subcarriers," *IEEE Commun. Lett.*, Vol. 5, 185–187, May 2001.
4. Börjessona, P. O., H. G. Feichtingerb, N. Gripc, M. Isakssond, N. Kaiblingerb, P. Ödling, and L. Perssonc, "A low-complexity PAR-reduction method for DMT-VDSL," *5th International Symposium on Digital Signal Processing for Communication Systems (DSPCS'99)*, 164–169, Perth, Australia, Feb. 1999.
5. Lee, J. S., H. Oh, J. Kim, and J. Y. Kim, "Performance of scaled SLM for PAPR reduction of OFDM signal in PLC channels," *IEEE International Symposium on Power Line Communications and Its Applications*, ISPLC, 2009.
6. Yoo, S., S. Yoon, S. Y. Kim, and I. Song, "A novel PAPR reduction scheme for OFDM systems: Selective mapping of partial tones (SMOPT)," *IEEE Transactions on Consumer Electronics*, Vol. 52, No. 1, 40–43, Feb. 2006.
7. Tsai, Y. and G. Zhang, "Orthogonal frequency division multiplexingwith phase modulation and constant envelope design," *Proc. of IEEE Milcom 2005*, Atlantic City, NJ, Oct. 2005.
8. Thompson, S. C., A. U. Ahmed, J. G. Proakis, and J. R. Zeidler, "Constant envelope OFDM phase modulation: Spectral containment, signal space properties and performance," *Proc. of IEEE Milcom 2004*, Monterey, CA, Nov. 2004.
9. Thompson, S. C., J. G. Proakis, and J. R. Zeidler, "Binary OFDM phase modulation," *Proc. of IEEE Milcom 2003*, Boston, MA, Oct. 2003.
10. Dostert, K., *Powerline Communications*, Prentice-Hall, 2001.
11. Manfred, Z. and D. Klaus, "A multipath model for the power line channel," *IEEE Trans. Commun.*, Vol. 50, No. 4, 553–559, 2002.
12. Thompson, S. C., A. U. Ahmed, J. G. Proakis, and J. R. Zeidler, "Constant envelope OFDM — Part II: Spectral properties," *IEEE Trans. Commun.*, 2006.
13. Dai, H. and H. V. Poor, "Advanced signal processing for power line communications," *IEEE Commun. Mag.*, 100–107, May 2003.

Study of the Impact of Soft Faults on Multiconductor Transmission Lines

Maud Franchet[1], **Nicolas Ravot**[1], **and Odile Picon**[2]

[1]CEA, LIST, Embedded Systems Reliability Laboratory
Point courrier 94, Gif-sur-Yvette cedex 91191, France
[2]Université Paris-Est, ESYCOM, EA2552, 77454 Marne-La-Vallée, France

Abstract— As electronic devices are almost everywhere and more and more complex, the reliability of wiring networks becomes a crucial need. Although wiring diagnostic tools such as reflectometry work well for hard defects (short-open circuit), the interest is now on detecting soft faults. However in order to develop efficient diagnostic methods, a better understanding of their effects on multiconductor transmission lines (MTL) is needed. This is the purpose of this article.

1. INTRODUCTION

As electronic devices are more and more present and complex, attention has been raised on monitoring the health of their wiring networks. Consider this simple fact: there is a probability of 66% that a wiring defect appears in a plane of more than 20 years (cf. [1]). This makes more obvious the necessity of developing efficient methods of detection, all the more than their consequences can be costly and even tragic.

One method commonly used is called Reflectometry (cf. [1]). It is based on the injection of a probe signal into the wiring network and the analysis of the reflected ones measured at the injection point. This works well for severe faults (open or short circuits). However industrials are more and more interested in detecting degradations as soon as possible (soft faults) in order to limit costs and make some prognostic.Unfortunately, no method seems to be efficient enough for detecting faults at their early age in bundles (cf. [2]). Although the use of time frequency tools in the case of one single coaxial line (Wavelet transform in [3], Wigner Ville transform in [4]) show some improvement, a better understanding of the effects of soft faults (such a necessity has also been raised in [5]) on the electrical parameters (RLCG) of multiconductor transmission lines (MTL) and on Reflectometry signals is of crucial need in order to develop systematic and efficient methods. This is the purpose of our article.

An analytical study is feasible only in simple cases (e.g., under the weak coupling assumption, cf. [6]). In order to study more intricate and realistic structures (such as bundles), simulation tools and experimental data are needed. Here CST MWs and a Laplace code are used. Two kinds of soft faults are considered: fault A (only the dielectric coating is damaged), fault B (the dielectric and the conductor are degraded). Their consequences on RLCG parameters, in part two, and on all the voltages measured at the entrance of a bundle of coated wires are examined in part 4 (2 structures, defined in part one, are considered: MTL2 and MTL6, where 2 and 6 are the number of wires in the bundle which is over a ground plane). The third part is devoted to their impact on the characteristic impedances and the propagating velocities.

2. PRESENTATION OF THE STUDIED DEFECTS AND STRUCTURES

2.1. The Studied Structures

Two lossless structures are studied: MTL_2 (cf. Figs. 1, 2) and MTL_6 (cf. Figs. 3, 4). One objective is to see if the impact of a defect is the same for any number of conductors.

The per-unit-length (p.u.l.) capacitance and inductance matrices and the characteristic impedance matrix (size $n*n$) are denoted $C^{(n)}$, $L^{(n)}$ and $Z_c^{(n)}$. The diagonals elements of $C^{(n)}$ can be expressed in this way:

$$C_{i,i}^{(n)} = C_{ip}^{(n)} + \sum_{j=1, j\neq i}^{n} C_{i,j}^{(n)} \tag{1}$$

where, $r_c = 0.5\,\text{mm}$, $r_d = 1\,\text{mm}$, $h_R = h_G = 1\,\text{cm}$, $d = 2.5\,\text{mm}$, $x_1 = 70\,\text{cm}$, $L_f = 5\,\text{cm}$, $l = 2\,\text{m}$, $R_{NE} = R_{0G} = 204\ \Omega$, $R_{FE} = R_{lG} = 1000\ \Omega$. The line driven by $e(t)$ is called the generator circuit

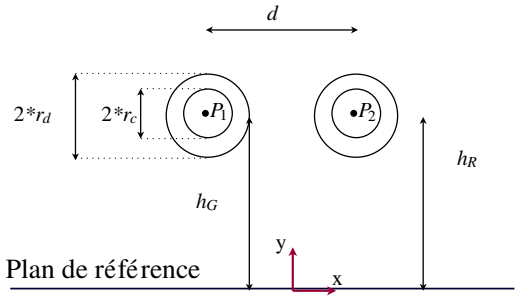

Figure 1: MTL_2's geometry.

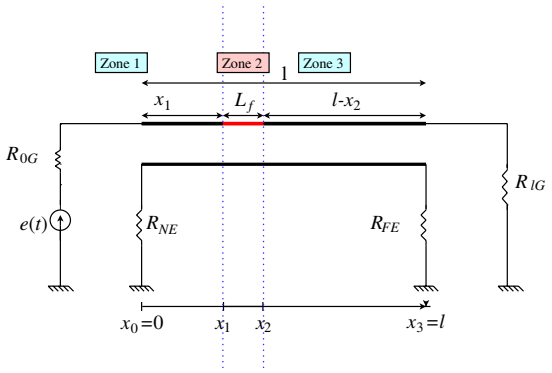

Figure 2: MTL_2's circuit.

and the other the receptor one. $v_G(0,t)$ is the generator circuit near-end voltage and $v_R(0,t)$ the receptor one.

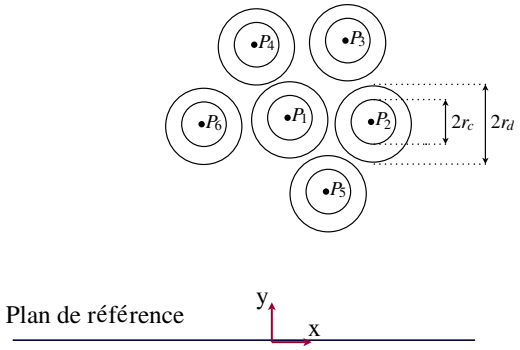

Figure 3: MTL_6's geometry.

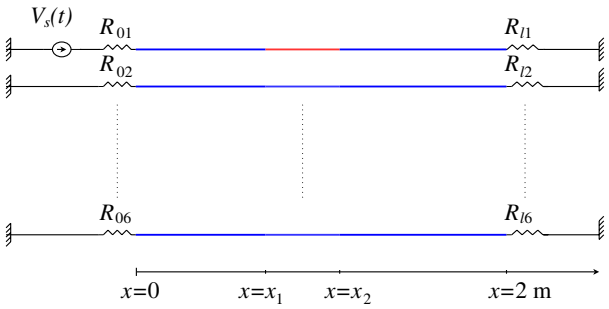

Figure 4: MTL_6's circuit.

where, $\forall i$, $R_{0i} = 50\ \Omega$ and $R_{li} = 1000\ \Omega$. The near-end voltage of line i is noted $v_i(0,\ t)$.

2.2. Definition of the Considered Faults

2 soft faults among the most frequent in wiring networks are considered.

The impact of these faults on L, C, Z_c and near end voltages will be studied for different levels of degradation:

$$\begin{cases} p_f \in \{p_{fi} = 0.1 \cdot i\,\text{mm}, \quad i = 0, \ldots, 5\} \quad \text{for} \quad Fault_A \\ p_f = 0\,\text{mm} \quad \text{and} \quad r_c \in \{r_{ci} = 0.2 + 0.1 \cdot i\,\text{mm}, \quad i = 0, \ldots, 3\} \quad \text{for} \quad Fault_B \end{cases} \tag{2}$$

For both MTL_2 and MTL_6, the defect will be located at 70 cm from the entrance of line 1.

3. STUDY OF THE IMPACT OF SOFT FAULTS ON THE P.U.L. PARAMETERS

3.1. Consequences of $Fault_A$

In this case, as only the dielectric coating of line 1 is damaged, $C^{(n)}$ is modified whereas $L^{(n)}$ remains unchainged (cf. [7] for more details on computation of L and C). Here are displayed the evolutions of $C_{ii}^{(6)}$ and $C_{ij}^{(2)}$ with p_f.

For both structures, the elements $C_{11}^{(n)}$ and $C_{1i}^{(n)}$ are the most affected by a change in p_{fi}. So $Fault_A$ mainly impacts the mutual capacitances between the degraded line and its neighbors. Then $\forall\ p_f$, $C_{16} > C_{15} > C_{14} > C_{13} > C_{12}$. We can assume that the closer is a line to the damaged one the more its characteristic parameters and propagating signals will be affected by $Fault_A$.

3.2. Consequences of $Fault_B$

Now the dielectric and the conductor are both damaged. As a consequence, both $L^{(n)}$ and $C^{(n)}$ vary. As MTL_2 and MTL_6 shows similar tendances for $Fault_A$, only MTL_2's results are considered here.

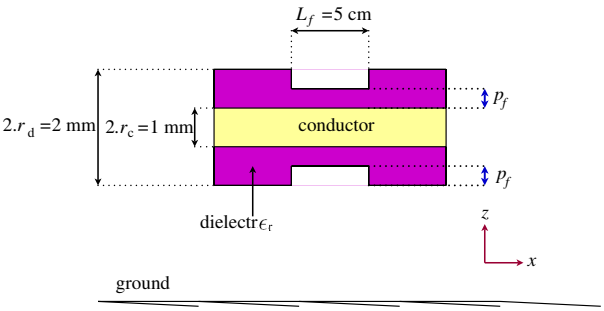

Figure 5: $FaultA$ (only the dielectric coating is damaged).

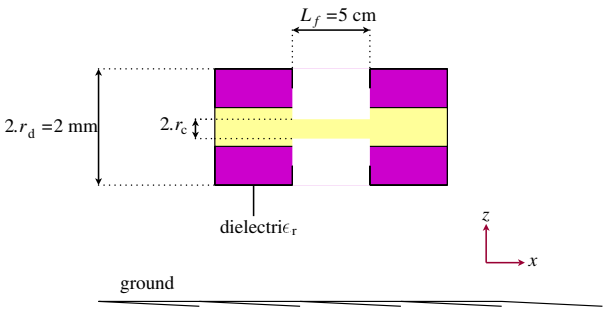

Figure 6: $FaultB$ (the dielectric and the conductor are damaged).

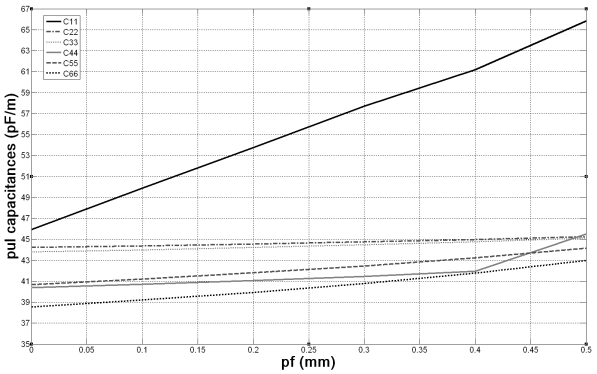

Figure 7: $C_{ii}^{(6)}$ versus p_f.

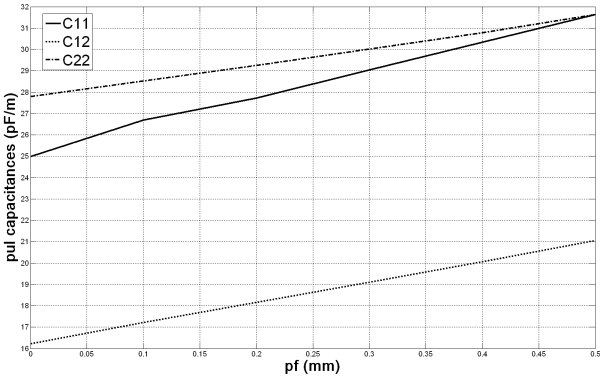

Figure 8: $C_{ij}^{(2)}$ versus p_f.

In this case, $C_{1j}^{(2)}$ and $C_{ii}^{(2)}$ are increasing functions of r_c, whereas $L_{11}^{(2)}$ rises by 25% as r_c decreases from 0.5 to 0.2 mm ($L_{12}^{(2)}$ and $L_{22}^{(2)}$ remain almost constant). Besides for this kind of fault too, the most affected elements are those linked to the damaged line (C_{11}, C_{12}, L_{11}).

As both defects modify the p.u.l. parameters, $Z_c^{(n)}$ and the n modal velocities of MTL_n will locally be changed too in the damaged portion. The way they are impacted is presented in the next section.

4. STUDY OF THE IMPACT OF SOFT FAULTS ON THE CARACTERISTIC IMPEDANCES AND ON THE PROPAGATING VELOCITIES

For both faults, the most impacted element of $Z_c^{(2)}$ is $Z_c^{(2)}(1,1)$, which is an increasing function of the level of degradation. However this rise remains quite small (6.8% in case of $Fault_A$). So the defects introduce 2 points of discontinuity (at x_1 and x_2) in the structure, where propagating waves will be reflected, with a low reflection coefficient. The observed tendances and conclusions are the same for MTL_6.

Concerning the velocities, we note a small increase, in case of $Fault_A$, as p_f decreases (with a maximum rise of 3.1% for $v_{m1}^{(2)}$ and 9.7% for $v_{m2}^{(2)}$). So the propagating waves will be locally speed up in the damaged zone. Furthermore modal velocities don't vary with the same amplitudes, which introduces a dispersion of the propagating waves. On the other hand, a modification of the conductor's radius ($Fault_B$) barely change the velocities. As a consequence, if a modification of propagating delays in a transmission line network is observed, one may deduce that a the dielectric coating of a line is somewhere damaged.

5. THE IMPACT OF SOFT FAULTS ON NEAR-END VOLTAGES

In both structure, a gaussian pulse ($\Delta f = 1$ GHz) is injected at line 1's near end. The simulations are run with CST MW's.

Considering first, the worst case of $Fault_A$ ($p_f = 0$ mm), let's see the impact on MTL_2 and MTL_6's near end voltages.

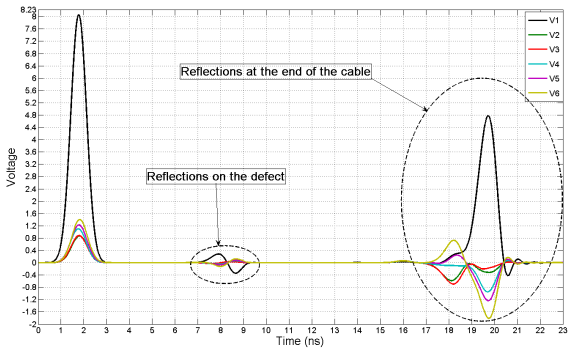

Figure 9: MTL_6's near-end voltages.

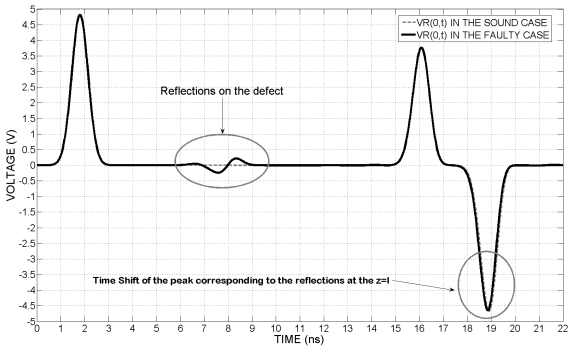

Figure 10: MTL_2's receptor near-end voltage in the sound and the faulty cases.

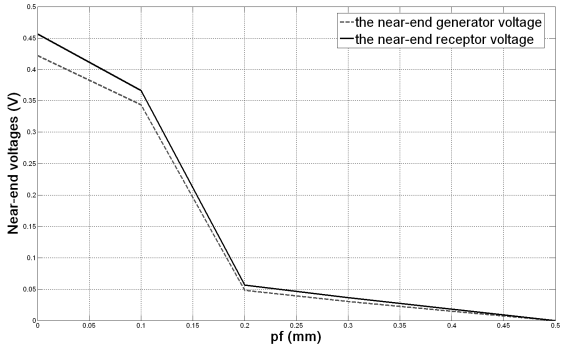

Figure 11: Evolution of MTL_2's peak-to-peak voltages.

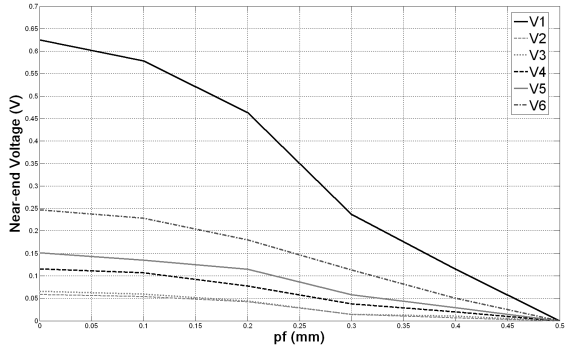

Figure 12: Evolution of MTL_6's peak-to-peak voltages.

One can observe 2 interesting areas. The first one corresponds to the reflections on the defect (at $x = x_1$ and $x = x_2$), which are of opposite signs for the generator voltage and the receptor ones. The second area corresponds to the reflections at the end of the bundle. As Fig. 10 points it out, the waves are sped up as they cross the damaged zone. Then the amplitude and the shape of voltages can vary a lot from a line to another (cf. Figs. 9, 12). This might be due to different level of coupling between lines and to the fact that some mode are more or less excited depending on the considered line.

Let's now consider the evolution of the peak-to-peak amplitude of the reflections with the level of degradation (for $Fault_A$).

One can now draw some conclusions. The most evident one is that the more the dielectric is degraded the more the amplitudes of the reflections on the defect are important. Then in MTL_2's case the near-end crosstalk voltage is more or at least as sensitive as the generator one to the defect. Considering MTL_6, this is not valid anymore. This might be due to the fact that more lines are considered here. As a consequence, losses caused by coupling effects are more important. However, one can notice that $V_1 > V_6 > V_5 > V_4 > V_3 \approx V_2$. So the reflections on the defect will be all the more high than the line is close to line 1. One can wonder if it is due to the fact that line 1 is the damaged line or the generator line. To sum up, would the defect be more visible close to the generator line or to the damaged one (which can be different from the line where the signal is injected)?

Changing the place of injection for MTL_6, it turns out that the amplitudes of the reflections on all lines are all the more important than the generator line is close to the damaged one. Here the best configuration (considering only one point of injection) for detecting the defect is obtained when line 1 is the generator line. This means that the best results are obtained when the generator line is the damaged one.

The shape of the voltages and the evolution of the peak-to-peak amplitudes with the level of degradation follow the same tendances for $Fault_B$. As a consequence, the conclusions about its impact on signals are the same.

6. CONCLUSIONS

We have presented here qualitative results about the impact of two kinds of soft faults on the characteristic parameters of MTL's structures. Some general conclusions can be drawn now. Considering first the p.u.l. parameters and the characteristic impedances, one can observe the similarity between results for 2 and 6 conductors. This enables us to extend the observed tendances to any kind of structure composed of n coated transmission lines.

Besides one can now define the signature of the studied fault:

- A local increase of the characteristic impedance of the damaged line and a global change in the whole matrix Z_c.
- A local increase of the propagating velocities (especially when the dielectric is damaged), which translates into a time-shift of the reflected waves observed in TDR.
- The presence of 2 reflected pulses of opposite signs, whose amplitudes are all the more high than the considered line is close to the damaged one.

These different observations can help to determine the best way to detect a defect, which is all the more important than, as seen here, soft fault translates into vary small modifications of the different studied parameters. They can indeed help to choose the best signal to inject (whose shape is adapted to the fault to be detected) and how it will be injected (e.g., on which line?).

Furthermore it could help to better understand and monitor the ageing of a cable.

REFERENCES

1. Basava, S. B. R., "Signal processing solutions to detection and location of cable faults in aging aircraft wiring using reflectometry methods," M.S. Thesis, Utah State University, 2003.
2. Griffiths, L. A., R. Parakh, C. Furse, and B. Baker, "The invisible fray: A critical analysis of the use of reflectometry for fray location," *IEEE Sensors Journal*, Vol. 6, No. 3, 697–706, June 2006.
3. Buccella, C., M. Feliziani, and G. Manzi, "Accurate detection of low entity cable faults by wavelet transform," *International Symposium on Electromagnetic Compatibility: EMC 2004*, Vol. 3, 936–941, Santa Clara, Cuba, August 9–13, 2004
4. Kwak, K. S., T. S. Yoon, and J. B. Park, "Load impedance measurement on a coaxial cable via time-frequency domain reflectometry," *SICE-ICASE, International Joint Conference,* 2006 .
5. Wheeler, K. R., D. A. Timucin, I. X. Twombly, K. F. Goebel, and P. F. Wysocki, "Aging aircraft wiring fault detection survey," NASA Ames Research Center, 2007.
6. Franchet, M., M. O. Carrion, N. Ravot, and L. Sommervogel, "Modelling the effect of a defect on crosstalk signals under the weak coupling assumption," *PIERS Proceedings*, 119–123, Xi'an, China, March 22–26, 2010.
7. Paul, C. R., *Analysis of Multiconductor Transmission Lines,* John Wiley & Sons, 1994.

Modeling and Diagnostic of Stator Faults in Induction Machines Using Permeance Network Method

Y. Amara and G. Barakat
GREAH, University of Le Havre, 25 rue Philippe Lebon, BP 540, 76058 LE HAVRE Cedex, France

Abstract— This paper presents an accurate and reasonably complicated model to simulate the faulty induction machines. The proposed model is based on a Permeance Network Method (PNM) coupled to the differential equation system governing the induction machine behavior in presence of stator faults. The proposed model allows taking into account the local magnetic saturation due to the relatively high fault current with moderate simulation time compared to the finite element method (FEM). Simulation results illustrating the impact of saturation in the case of some common stator faults such as stator inter-turn short circuits, shorted phase and open phase faults are presented and their comparison with those issued from coupled magnetic circuit based model proof the pertinence of the proposed approach. Experimental results validate the PNM approach in modeling saturated machines. The presented simulation results demonstrate the necessity to survey multiple quantities in order to distinguish between different fault signatures and in so doing to diagnose the type of a stator fault.

1. INTRODUTION

Three phase induction machines are the most widely used type of ac machines in industrial processes and they are frequently integrated in commercially equipment, featuring 80% of the motors in use. So, early faults detection and diagnosis reduces the machine shutdown time and repairing cost. Recent years, the research on the fault diagnosis and prognosis is in increasing. This research involves three domains, the fault modeling, fault extraction (detection) and classification (diagnosis) [1, 2].

Several recent studies have shown that stator winding faults are the second to bearing faults in incidences of occurrences in induction machines. Almost 30%–40% of all reported induction motor faults belong to this class of faults [3, 4]. They result from failure of turn-to turn insulation. So they start as undetected turn-to-turn faults that finally grow and culminate into major ones such as phase to phase or phase to ground faults that cause catastrophic failure of the machine [3–6]. Therefore, early detection of incipient fault detection has received much attention in recent years.

The efforts on electrical machines fault diagnosis including, chemical analysis, mechanical and magnetic measurement and motor current signature analysis (MCSA) techniques have been squared [1–10]. The success of the technique depends not only on its ability to distinguish between healthy and faulty states but also on its ability to discriminate between various faults. Many diagnostic techniques for induction machines can be extended easily to other types of electrical machines [8–11].

Machine modeling under fault conditions is a key to predicting its behavior. The analysis of stator faults can be made by different models. The availability of more powerful computers and the development of new machine models able to manage geometry together with electric and magnetic features, allow us to move on from the first models of faulty machines [4].

For the most faults, the harmonic contents of the stator current can be calculated satisfactory using linear models of the machine such as the Coupled Magnetic Circuit Method [CMCM] [12–14]. In the case of the stator faults, the fault current reaches several times the rated value of the phase current in the healthy case and generates by the way an important local saturation around the fault zone. This phenomenon impacts strongly the harmonic contents of the stator current and imposes the use of a nonlinear model for the calculation of this fault signature in the phase currents [9, 13, 14]. The FEM is more and more used for this purpose, but the computing time is too long.

Then the objective of this paper is to present an accurate and reasonably complicated model which is capable to predicting the performances of induction machines under stator faults. The proposed model is based on a permeance network approach for the magnetic circuit modeling coupled to the differential equation system governing the induction machine behavior for both the healthy case and the faulty case [14]. The proposed method allows the authors to take into account the local saturation in the magnetic circuit due to the strong short circuit currents as well as all the

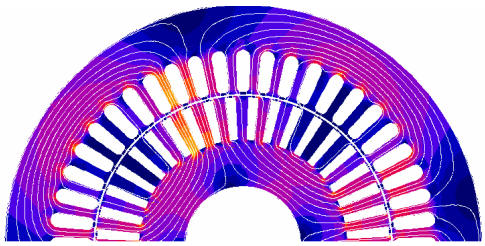

Figure 1: Flux tubes for a half part of an induction machine.

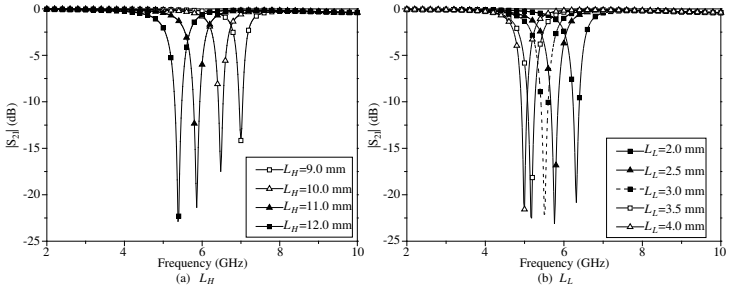

Figure 2: Permeance network of an induction machine.

space harmonics of the doubly slotted machine with a simulation time relatively weak compared to the finite element method.

2. PNM MODELING OF INDUCTION MACHINE UNDER STATOR FAULTS

2.1. Case of Healthy Machine

An electrical machine can be represented as a set of flux tubes (Fig. 1) characterized by their magnetic permeances.These permeances are expressed as functions of the machine geometry and the instantaneous fluxes flowing in each one of them [13–18].

Exploiting the flux tubes of Fig. 1, one can deduce the magnetic equivalent circuit of the induction machine as shown in Fig. 2 where one can distinguish the stator magnetic circuit region, the air-gap region as well as the rotor magnetic circuit region.

The stator slot currents are modeled by magneto-motive force (m.m.f.) sources in series with the tooth permeances.

To establish the relation between these m.m.f and the phase currents we consider a closed contour around a slot as shown in Fig. 3 and we associate a magneto-motive force (F_{si}) to the slot i. Using the magnetic and electric laws the following equation are deduced [15, 18]:

$$\begin{cases} \int \vec{H} \cdot d\vec{l} = n_{si} \cdot I_{si} = \sum\limits_{j} \frac{F_j}{P_j} \\ \sum\limits_{j} \frac{F_j}{P_j} - F_{si} + F_{si+1} = 0 \\ F_{si} - F_{si+1} = n_{si} \cdot I_{si} \end{cases} \tag{1}$$

By generalizing the above equations for all the teeth we can obtain the following compact matrix form:

$$[F_s] = [M_{is}] \cdot [I_s] \tag{2}$$

where $[F_s]$ is the vector of tooth m.m.f., $[I_s]$ is the vector of the phase currents $[M_{is}]$ is the matrix that relates the tooth m.m.f. to the phase currents and n_{si} is the number of the turns inside the slot carrying the current I_{si}.

In the same manner, the rotor bar currents are modeled by m.m.f. sources in series with the rotor tooth permeances.

The air-gap region is subdivided into a set of air-gap elements each one of them is modeled by a permeance in order to connect the stator tooth fluxes to the rotor tooth fluxes. The value of this permeance depends on the rotor position. By this manner, one can take into consideration the rotor motion.

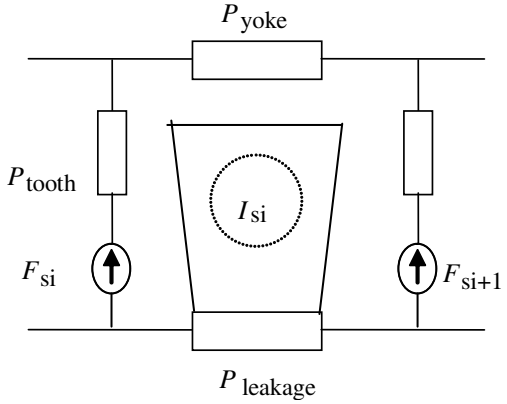

Figure 3: Closed contour around a slot.

Figure 4:

The different parameters in the air-gap permeances expression are expressed in terms of the stator and rotor slot dimensions and air-gap length and given in [15].

To take into account the magnetic circuit saturation, the B-H curve can be modeled by the Marrocco's formula [19] or also numerically by the use of Spline functions fitting the measured B-H curve.

The system of magnetic equations governing the machine is obtained by treating the permeance network of Fig. 2 in the same manner as an electric circuit. In this paper, node and branch equations are written considering stator phase and rotor loop currents as the entry of the system of equations. These equations are given by the following general form:

$$\begin{bmatrix} [\Re] & [N^t] \\ [N] & [P] \end{bmatrix} \cdot \begin{bmatrix} [\Phi_t] \\ [U] \end{bmatrix} = \begin{bmatrix} [M_i] \\ [0] \end{bmatrix} \cdot [I] \tag{3}$$

where $[\Re]$ is a diagonal reluctance matrix, $[P]$ is a permeance matrix, $[N]$ is a matrix where its general element equals to '1' if the flux is coming out from the node , to '-1' if the flux enters to the node and zero else, $[\Phi_t]$ is the vector of stator and rotor tooth fluxes, $[U]$ is the vector of stator and rotor node scalar magnetic potential, $[M_i$ is a matrix that relates the tooth m.m.f. to the stator phase and rotor mesh currents, and $[I]$ is the vector of stator phase and rotor mesh currents.

The developed magnetic network is related to the electrical differential equations of the stator phases by the calculation of the linkage fluxes issued from the tooth fluxes. In order to establish the relation between the linkage fluxes and tooth fluxes, one consider a coil 'k' of 'n'_c turns embraces 'y' teeth, as shown in Fig. 4, the linkage flux of this coil is equal to the fluxes of these 'y' teeth multiplied by the number of turns of this coil and given by the following equation:

$$\Psi_{ck} = \sum_{i=j+1}^{y+j+1} n_c \Phi_{Si} \tag{4}$$

where 'y' is the coil pitch, Φ_{Si} is the flux of the stator tooth 'i' and Ψ_{ck} is the linkage flux of the coil 'k'.

The linkage flux of the phase 'i' is equal to the sum of the linkage fluxes of the coils constituting this phase, i.e.,

$$\Psi_{pi} = \sum_{k} \Psi_{ck} \tag{5}$$

where Ψ_{pi} is the linkage flux of the phase 'i'.

By repeating the above equations for each one of the stator phases, one get the matrix form:

$$[\Psi_s] = [M_{\phi s}] \cdot [\Phi_s] \tag{6}$$

where $[M_\Phi]$ is the matrix that relates the stator phase linkage fluxes to the stator tooth fluxes.

As the studied machine is a squirrel cage induction machine and as the rotor meshes are defined by two consecutive bars, the flux linkage of a mesh is equal to the flux of the tooth embraced by these two bars.

To write the electrical equations, one consider, initially, a general m-phase delta connected induction machine with q rotor bars. The proposed model consists to replacing the q bars of the squirrel cage by an equivalent circuit containing $q+1$ coupled electric circuits [12, 14] as shown in Fig. 5 (with $L_{\sigma b}$ in the PNM case). The compact matrix form of the electrical equations is given by:

$$[V] = [R] \cdot [I] + [L_\sigma] \cdot \frac{d}{dt}[I] + \frac{d}{dt}[\Psi] \tag{7}$$

with

$$[R] = \begin{bmatrix} [R_{SS}] & [0] \\ [0] & [R_{RR}] \end{bmatrix}, \quad [L_\sigma] = \begin{bmatrix} [L_{\sigma S}] & [0] \\ [0] & [L_{\sigma R}] \end{bmatrix} \tag{8}$$

and

$$[\Psi] = \begin{bmatrix} [\Psi_S] \\ [\Psi_R] \end{bmatrix} = \begin{bmatrix} [M_{\phi S}] & [0] \\ [0] & [M_{\phi R}] \end{bmatrix} \cdot \begin{bmatrix} [\Phi_S] \\ [\Phi_R] \end{bmatrix} \tag{9}$$

where $[V]$ is the vector of stator and rotor voltages, $[I]$ is the vector of stator and rotor currents, $[R_{SS}]$ and $[L_{\sigma S}]$ are $m * m$ diagonal matrices of stator phase resistances and winding end leakage inductances respectively and $[\Psi]$ is the linkage flux vector. The $(q+1) * (q+1)$ resistance matrix $[R_{RR}]$ is derived from the equivalent circuit of Fig. 5 and is given in Equation (8), where R_b is the rotor bar resistance and R_e is the end ring portion resistance. The $(q+1) * (q+1)$ inductance $[L_{\sigma R}]$ matrix is determined with the same way as $[R_{RR}]$ by setting R_b to zero and replacing R_e by $L_{\sigma e}$ where $L_{\sigma e}$ is the end ring portion leakage inductance.

A new two matrices are also developed, to relate the mesh currents and electromotive forces (mesh linkage fluxes) to phase currents and electromotive forces. Then each one of $[M_{is}]$ and $[M_\Phi]$ is multiplied by the corresponding new matrix. The rotor resistance and inductance matrices remain unchanged.

To the set of magnetic and electric equations, one must add the mechanical equation of the shaft. The torque equation is established by deriving the magnetic co-energy with respect to the rotor angular position θ; thus the electromagnetic torque obtained is given by

$$T_{em} = \frac{1}{2} \sum_{i=1}^{Ns} \sum_{j=1}^{q} \frac{dP_{i,j}}{d\theta} U_{i,j}^2 \tag{10}$$

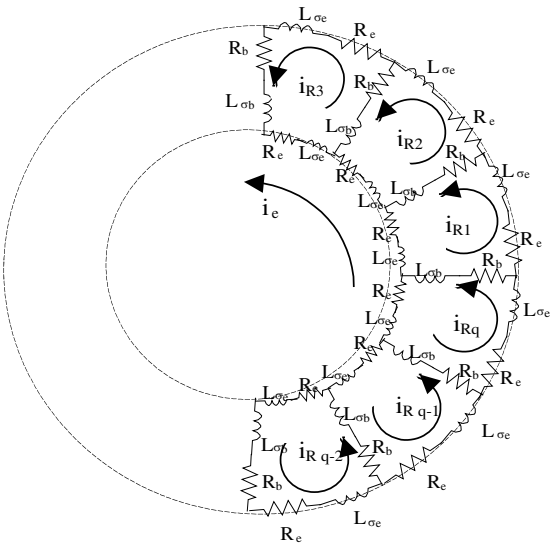

Figure 5: Equivalent circuit of the rotor cage showing meshes.

and the mechanical equation is given by

$$T_{em} = T_{res} + J\frac{d\Omega}{dt} + f\Omega \tag{11}$$

where Ω is the rotor angular speed, Ns is the number of stator teeth, T_{res} is the resistance torque; J is the motor+load inertia, f is the friction coefficient and $U_{i,j}$, is the scalar magnetic potential between the stator tooth 'i' and the rotor tooth 'j'.

2.2. Case of Stator Faults

The occurrence of inter-turnshort circuit in N_{CC} coils belonging to the stator phases results in adding N_{CC} dimensions to the stator related vectors of the electrical differential equations system [6]. In other words, one must rewrite the stator differential equations system with $m + N_{CC}$ where the N_{CC} represents the number of coils of short circuited turns. The additional elements of the matrix resistances and the matrix of the winding end inductances corresponding to the 'new' N_{CC} phases are determined as a multiple of the resistance and inductance values corresponding to the turn mean length. The additional elements of the matrices $[M_{is}]$ and $[M_{\varphi s}]$ are carried out with the same manner as the main phases by considering their respective turns. The rotor resistance and end ring leakage inductance matrices remain unchanged.

The shorted phase fault is represented by setting the voltage of this phase to zero. All the elements of resistances, inductances and connection matrices remain obviously unchanged.

Open circuit phase fault is represented by introducing a resistance of great value in series of the resistance of faulty phase. Therefore, only the resistance of faulty phase will be changed in the electrical equations. All the others elements remain unchanged. In all cases of faults, the star connection case of stator phases can be treated in the same manner as that for the healthy machine.

For both healthy and faulty cases the permeance network has the same topology. So, the magnetic equations remain unchanged.

3. SIMULATION RESULTS AND DISCUSSION

The proposed model was used to simulate a 4 kW, 230/400 V, 14.2/8.2 A, 2840 rpm, 2 poles, 24 stator slots, 30 rotor bars, Y connected, standard squirrel cage induction machine. Each stator phase contains 4 coils in series and each coil is constituted of 31 turns. The simulations were carried out for 100% of rated load in the healthy and faulty cases.

In order to validate the proposed model, an experimental test was carried out on the machine described above. Figures 6 and 7 show respectively the stator current Concordia's patterns and the spectrum of the Concordia's vector modulus for the experimental and simulation results. One can remark that the two results are closed to each other. The difference between the Concordia's patterns in the experimental and simulation results, is due to the inverter harmonics which are not taken into account in the simulation case.

The analytical studies show that the interaction of the resultant m.m.f and air-gap permeance of doubly slotted machine induces slot harmonics reflected in the time domain of the stator and rotor

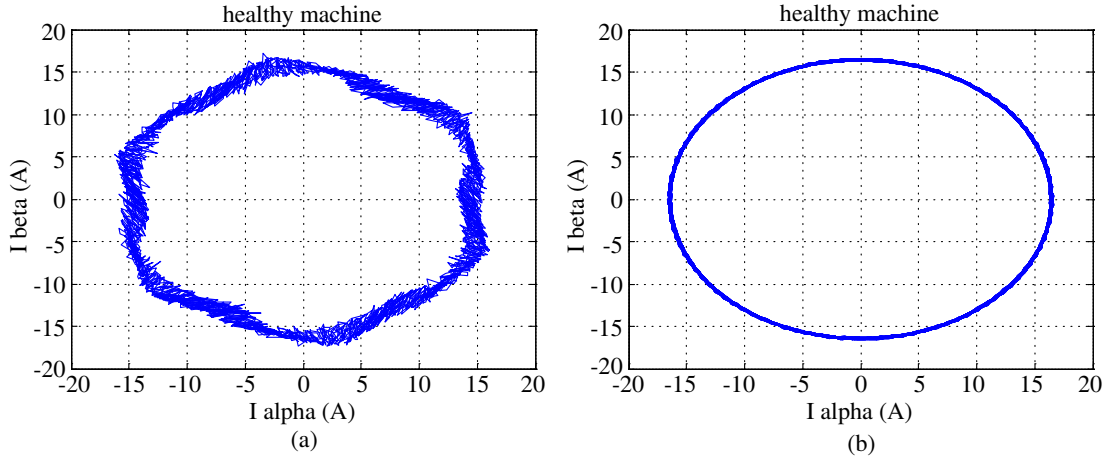

Figure 6: Concordia's current pattern of healthy machine: (a) Experimental results; (b) Simulation results.

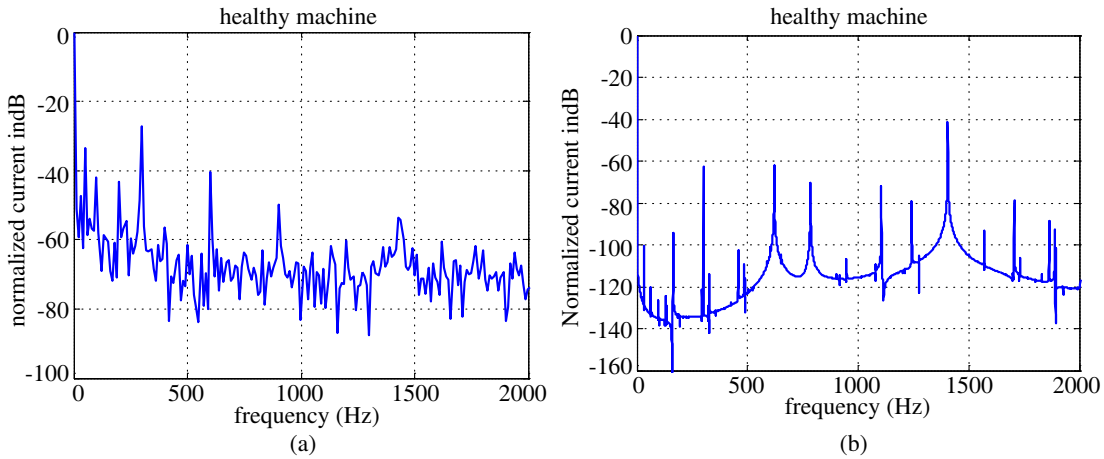

Figure 7: Spectrum of the Concordia's current vector modulus for healthy machine: (a) Experimental results; (b) Simulation results.

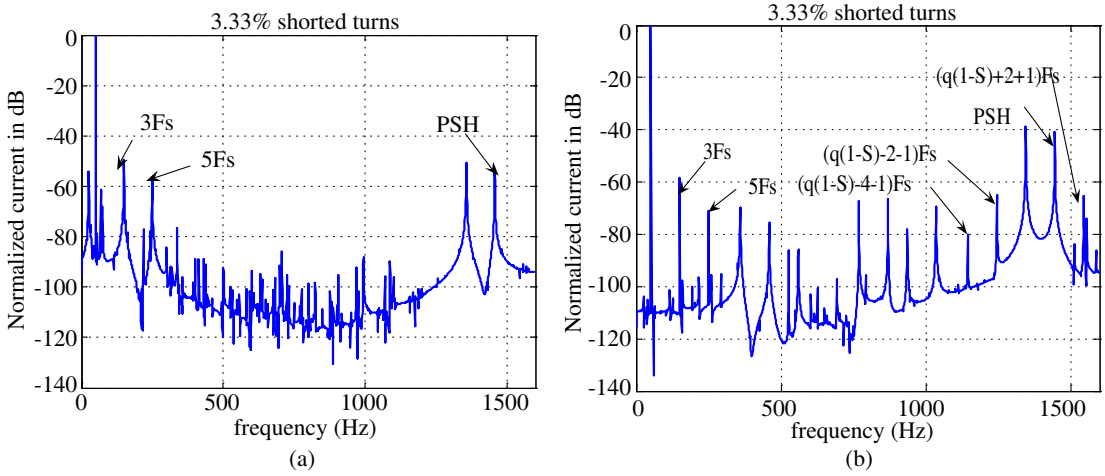

Figure 8: Faulty phase stator current spectrum for 3.3% shorted turns: (a) CMCM method; (b) PNM method.

currents and boosted by the machine asymmetries [12]. The harmonics appearing in the stator currents are given by:

$$f_{rh} = \left(kq\frac{(1-S)}{p} \pm v \right) f_s \tag{12}$$

where q is the number of rotor slots and p is the pole pair number, S is the slip and v is the supply harmonic index. In the case of stator faults, additional time harmonics resulting from the shorted turn currents or from the asymmetry of phase currents, will affect the harmonics already existing in the spectrum of stator and rotor currents and lead to affect the contribution of these slot harmonics in the stator currents.

The effect of saturation can be introduced to expression (12) simply as additional harmonics representing the fluctuation of the air-gap flux at twice the number of pole pairs and twice the frequency of the fundamental wave, then expression (12) becomes:

$$f_{rh} = \left(kq\frac{1-S}{p} \pm 2m_{sat} \pm v \right) f_s \tag{13}$$

where m_{sat} is an integer representing the indices of saturation harmonics.

The effect of saturation (nonlinearity) on the current signature was tested by comparing the simulation results (of the machine under inter turns short circuit fault) issued from linear model (CMCM) and nonlinear model (PNM) as shown in Fig. 8. Regarding Figs. 8(a) and (b) one can clearly remark that the harmonic content of phase currents spectrum differs from the linear model to nonlinear model. In fact, short circuit current saturates locally and strongly the magnetic circuit

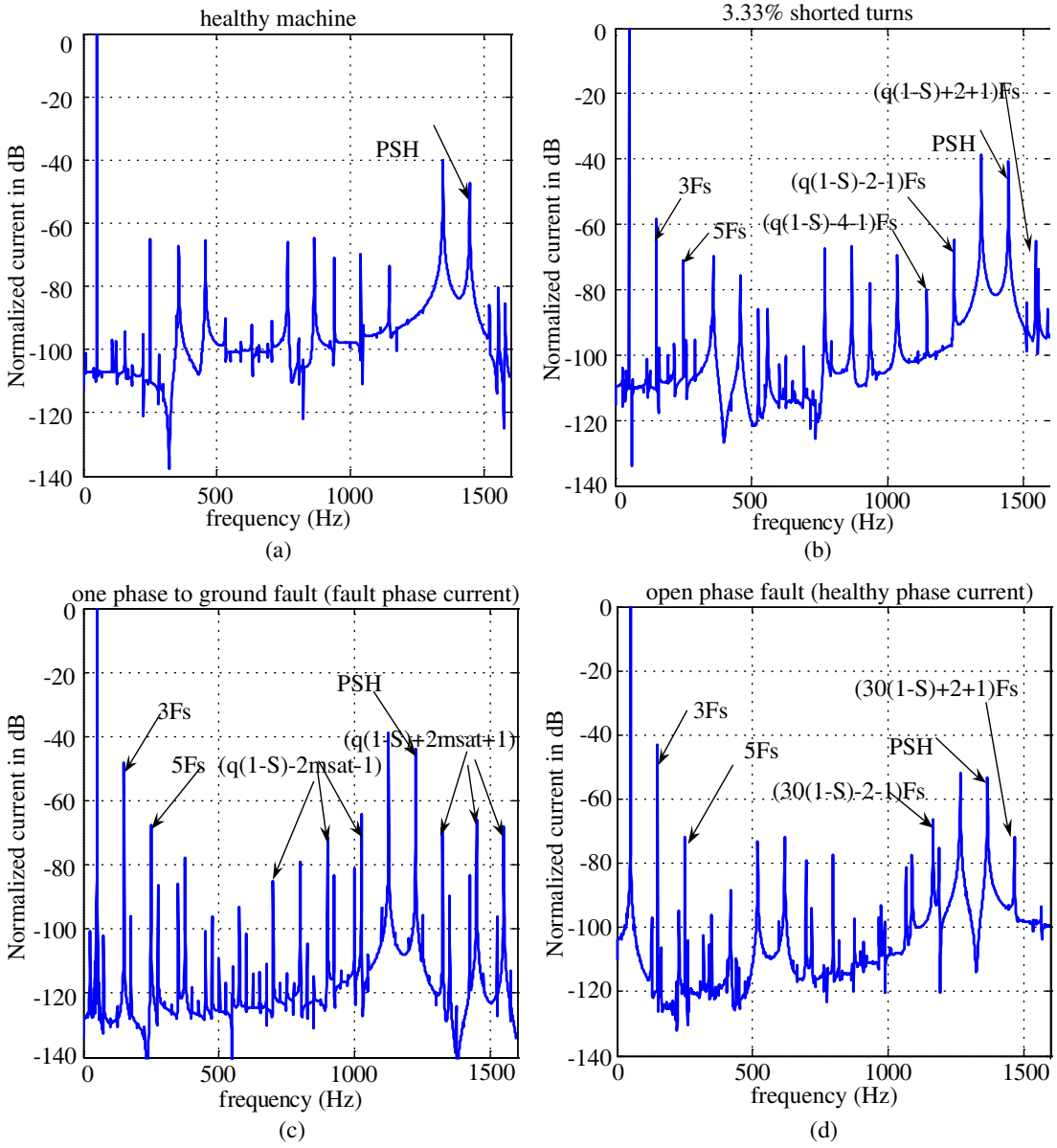

Figure 9: Stator current spectrums for: (a) Healthy case; (b) Inter-turns fault; (c) One phase to ground fault; (d) Open phase fault.

of the machine. In the case of PNM based model, this phenomenon causes the apparition in the stator current spectrum of new harmonics representing the saturation effect which the corresponding frequencies are given by relation (11).

Figure 9 shows the simulation results of stator currents for healthy and faulty cases. It can be seen that the principal slot harmonic (PSH) ($k = 1,\ v = 1$) appears according to (10), for all cases of operation but the contribution of this harmonic in the stator currents is different from one case to the other where it increases as the fault current increases and according to the type of fault. The third harmonic is also presented for the three types of faults. This third harmonic results from the interaction of the negative sequence current in the stator phases and the fundamental slip frequency current in the rotor bars. This interaction produces torque pulsating at twice the line frequency. The consequence speed ripple caused flux density component at three times the line fundamental frequency with respect to stator [20]. Finally, this flux produces the third harmonic in the stator current. The magnitude of the third harmonic increases as the fault severity increases. Some recent studies report the detection of third harmonic components in the line currents as a signature for stator faults. Unfortunately, this could be confused with the voltage unbalance present in the line voltage, machine constructional asymmetry and the saturation [20]. For all these reasons, the third

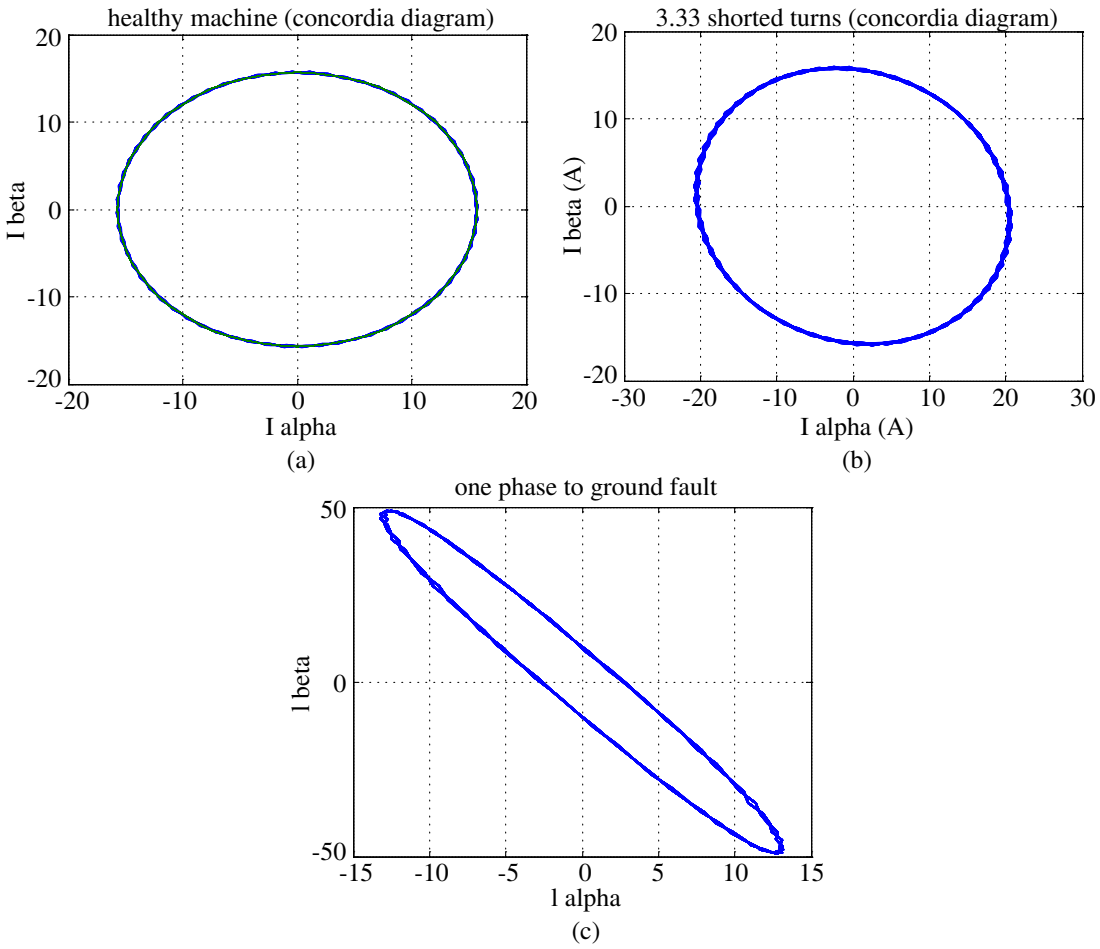

Figure 10: Concordia diagram of stator current for healthy and faulty cases: (a) Healthy machine; (b) Inter-turns fault; (c) One phase to ground fault.

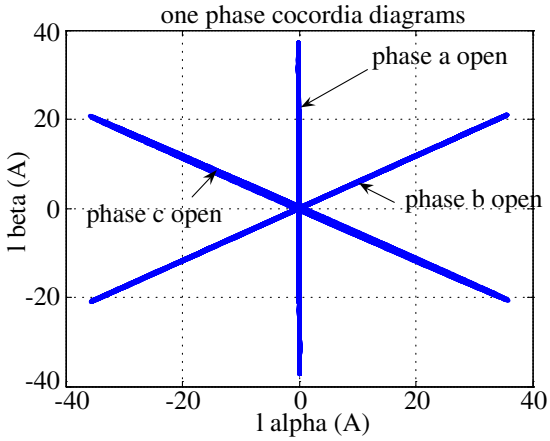

Figure 11: Concordia diagram of stator current under different open phase faults.

harmonic can not be used as stator fault signature. The saturation of the magnetic circuit due to the high fault currents causes the apparition of new harmonics in the current spectrum of faulty cases according to the relation (11) as shown in Fig. 9. The rank of these harmonics and their values depend on fault severity where one can remark that these harmonics appear more clearly in the case of the inter-turns short circuit and one phase to ground faults where the saturation is more strong than in the case of open phase fault.

Comparing the results of faulty cases, one can remark the difficulty to distinguish between the different fault signatures from the phase current spectrum and this imposes the necessity to

survey multiple quantities to distinguish between the different stator faults such as, for example, the Concordia's patterns of the stator current.

Figure 10 shows the Concordia's patterns of stator currents for the healthy and faulty cases. One can remark that in the healthy case the Concordia's pattern is a circle. When the fault occurs, the Concordia's pattern shape deviates according to the associated fault. The results show that for stator fault conditions, the shape of Concordia's vector pattern becomes elliptic. The ellipticity of Concordia's pattern is proportional to the fault severity and its major axis orientation depends on the fault type and faulty phase [22] as it is shown on Fig. 11 where, in the case of open phase fault, one can easily discriminate which phase is open.

4. CONCLUSION

In this paper, a robust and modular permeance network based model for the simulation of induction machine stator faults has been presented. The proposed model was used to study the most common stator faults such as stator inter-turn short circuits, shorted phase and open phase faults. The results have illustrated the advantage of the proposed model to take into account the impact of magnetic saturation on stator fault signatures. This feature was validated by experimental results in the healthy case. Finally, the presented work demonstrate the necessity to survey multiple quantities in order to distinguish between different fault signatures and in so doing to diagnose the type of a stator fault.

REFERENCES

1. Benbouzid, M. E. H., "Bibliography on induction motors faults detection and diagnosis," *IEEE Trans. Energy Conv.*, Vol. 14. No. 4, Dec. 1999.
2. Nandi, S., H. A. Toliyat, and X. Li, "Condition monitoring and faults diagnosis of electrical motors-A review," *IEEE Trans. Energy Conv.*, Vol. 20, No. 4, Dec. 2005.
3. Silva, A. M. D., R. J. Povinelli, and N. A. O. Demerdash, "Induction machine broken bar and stator short-circuit fault diagnostics based on three-phase stator current envelopes," *IEEE Trans. Ind. Elect.*, Vol. 55, No. 3, 1310–1318, March 2008.
4. Lee, S. B., K. Younsi, and G. Kliman, "An online technique for monitoring the insulation condition of ac machine stator winding," *IEEE Trans. Energy Conv.*, Vol. 2. No. 4, Dec. 2005.
5. Grubic, S., J. M. Aller, B. Lu, and T. G. Habetler, "A survey on testing and monitoring methods for stator insulation systems of low-voltage induction machines focusing on turn insulation problems," *IEEE Trans. Ind. Elect.*, Vol. 55, No. 12, 4127–4136, Dec. 2008,
6. Siddique, A., G. S. Yadava, and B. Sigh, "A review of stator fault monitoring techniques of induction motors," *IEEE Trans. Energy Conv.*, Vol. 20, No. 1, Mar. 2005.
7. Zidani, F., D. Diallo, M. E. H. Benbouzid, and R. Naït-Saïd, "A fuzzy-based approach for the diagnosis of fault modes in a voltage-fed PWM inverter induction motor drive," *IEEE Trans. Ind. Elect.*, Vol. 55, No. 2, 586–593, Feb. 2008.
8. Bellini, A., F. Filippetti, C. Tassoni, and G.-A. Capolino, "Advances in diagnostic techniques for induction machines," *IEEE Trans. Ind. Elect.*, Vol. 55, No. 12, 409–4126, Dec. 2008.
9. Mohammed, O. A., Z. Liu, S. Liu, and N. Y. Abed, "Internal short circuit fault diagnosis for PM machine using FE-based phase variable model and wavelet analysis," *IEEE Trans. Mag.*, Vol. 43, No. 4, Apr. 2007.
10. Thomson, W. T. and M. Fenger, "Current signature analysis to detect induction motor faults," *IEEE. Ind. App. Mag.*, Vol. 7, No. 4, 26–34, Jul./Aug. 2001.
11. Tu, X., L.-A. Dessaint, N. Fallati, and B. De Kelper, "Modeling and real-time simulation of internal faults in synchronous generators with parallel-connected windings," *IEEE Trans. Ind. Elect.*, Vol. 55, No. 6, 1400–1409, Jun. 2008.
12. Houdouin, G., G. Barakat, B. Dakyo, E. Destobbeleer, and C. Nichita, "A coupled magnetic circuit based global method for the simulation of squirrel cage induction machines under rotor and stator faults," *Proc. Electrimacs 2002*, CD-ROM, Montreal, Canada, Aug. 18–21, 2002.
13. Mahyob, A., M. Y. Ould Elmoctar, P. Reghem, and G. Barakat, "Coupled magnetic circuit method and permeance network method modeling of stator faults in induction machines," *International Power Electronics and Motion Control Conference EPE-PEMC 2008*, Poznan, Poland, Sep. 1–3, 2008.
14. Mahyob, A., P. Reghem, and G. Barakat, "Permeance network modelling of the stator winding faults in electrical machines," *IEEE Trans. Mag.*, Vol. 45, No. 3, 1820–1823, Mar. 2009.

15. Ostovic, V., *Dynamics of Saturated Electric Machines*, Spring-Verlag, New York, 1989.
16. Wan, S., A. Wang, Y. Li, and Y. Wang, "Reluctance network model of turbo-generator and its application in rotor winding inter-turn short circuit fault," *IEMDC2005*, San Antonio, Texas, USA, May 15–18, 2005.
17. Turowski, J., M. Turowski, and M. Kopec, "Method of three-dimensional network solution of leakage field of three-phase transformers," *IEEE Trans. Mag.*, Vol. 26, No. 5, 2911–2919, Sep. 1990.
18. Delforge, C. and B. Lemaire-Semail, "Induction machine modelling using finite elements and permeance network methods," *IEEE Trans. Mag.*, Vol. 31, No. 3, 2092–2095, May 1995.
19. Marrocco, A., "Analyse numérique de problèmes d'électrotechnique," *Ann. Sc. Math*, Québec, Vol. 1, 271–296, 1977.
20. Nandi, S., "Detection of stator faults in induction machines using residual saturation harmonics," *IEMDC2005*, San Antonio, Texas, USA, May 15–18, 2005.
21. Mohamed, A. A. and M. M. Medhat, "Application of AI tools in fault diagnosis of electrical machines and drives — an overview," *IEEE Trans. Energy Conv.*, Vol. 18, No. 2, Jun. 2003.

Interference from the Second Layer in Holographic Radar

M. Inagaki[1], **T. Bechtel**[2], **and V. Razevig**[3]

[1]Walnut Ltd., 1-19-13 Saiwaicho, Tachikawa, Tokyo, Japan
[2]Department of Earth and Environment, Franklin & Marshall College, Lancaster, PA, USA
[3]Remote Sensing Laboratory, Bauman Moscow State Technical University, Russia

Abstract— Holographic radar of Rascan type produce plan view subsurface images using five simultaneous frequencies. Since it is continuous wave radar with no time-of-flight data, the reflections coming from different depths are superimposed into a single plan view. The first reflection is usually dominant on the image. However, if the reflectivity is large at the second boundary both reflected waves are received and interference occurs. As a result the image looks different from ones produced by only a first reflection. This interference might affect the proper interpretation of radar images. However, there is a benefit in that by observing the pattern of interference over five frequencies, the distance between two boundaries could be determined.

1. INTRODUCTION

Holographic radars provide a plan view as opposed to the section view provided by conventional pulsed radar An advantage of plan view is the ability to reproduce the true shape of buried objects. However, holographic radar does not allow determination of vertical structures since all the reflections from different depths at the same horizontal location are compressed onto a single horizontal plane. Any reflection event that appears on the image is actually the result of summing all the reflections from different depths. Because of attenuation, the first reflection is usually dominant. However, if the dielectric contrast is larger at a second or deeper boundary one and the distance between the first and the second reflectors is sufficiently close relative to the material attenuation, the second reflection may become strong enough to influence to the first reflection and alter the radar image. In some circumstances, this could provide data related to the separation between the two boundaries. This paper describes numerical simulations to show the interference from a second layer in selected conditions, and reproduces the theoretical predictions experimentally.

2. HOLOGRAPHIC IMAGE

Holographic subsurface radars of the Rascan type produce images based on the phase difference between the subsurface or object beam, and a reference beam produced by the surface reflection, with the recorded phase differences at different points on the scanned surface plotted as a grey scale image. Two primary causes of the observed phase difference are target depth and signal frequency. An object appears black on the radar image if the depth and frequency produce constructive interference or positive maximum, and white for negative maximum. Destructive interference or cancellation between the subsurface (object) and surface (reference) beams can also occur, leading to zero net signal for certain targets at certain frequencies. If there are two reflectors in the path of the propagating wave, reflections will occur at their two depth positions. For instance, an underground void has two boundaries; the top and the bottom of the void. In this case, the two reflections may interfere with each other, and the net amplitude of the received wave can be either strengthened or weakened depending on the separation of the reflectors for a given frequency. If the reflectivity or the first boundary is large, the effect will be comparatively small. However, if the reflectivity of the second boundary is large, the interference from the second reflection cannot be ignored (See Figure 1).

3. SIMULATION

The interference effect has been theoretically simulated using a two boundary model. The model is shown in Figure 2. In Case 1, two plastic layers are separated with a void between them. In Case 2, the bottom plastic layer is replaced by rubber. Simulations have been carried out for both cases.

Actually, reflections occur at four boundaries (top, bottom and both sides) inside the void, and there are also multiples, creating complex reflection ray paths. However, to maintain simplicity, only the basic reflections, which are obviously expected to be dominant were considered. Only the top of the void (shown as u_1 in Figure 2) and the bottom of the void (shown as u_2 in Figure 2) were included in the model as sources of spherical electromagnetic waves. Following Huygen's principle,

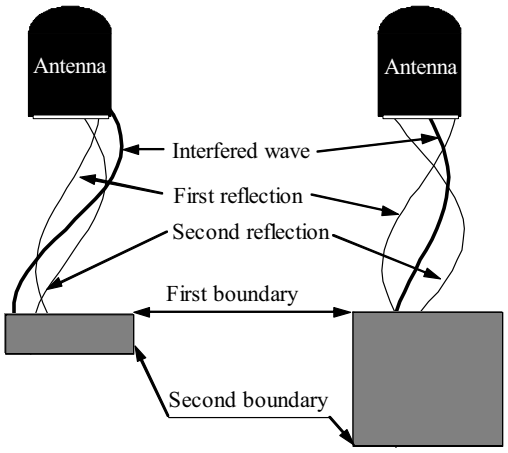

Figure 1: Interference between reflections from two boundaries.

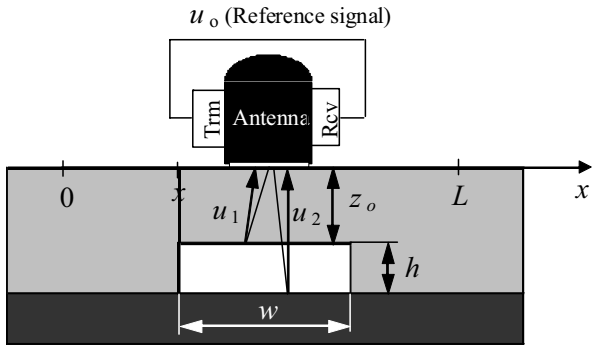

Figure 2: Model for simulation.

the response signal $u(x)$ will be the superposition of reflections from each point reflector multiplied by the roundtrip phase to that point [1]

$$u(x) = \int_0^L r(x') \left(K_1 \frac{RP^2(\theta_1)}{r_1^2} e^{i2r_1k_1} + K_2 \frac{RP^2(\theta_2)}{r_2^2} e^{i2r_2(k_1z_0+k_2h)/(z_0+h)} \right) dx', \tag{1}$$

where,

L — length of the scan line;

$r(x) = \begin{cases} 1, \ x \in [x_0, \ x_0 + w] \\ 0, \ x \notin [x_0, \ x_0 + w] \end{cases}$ — reflectivity function;

K_1, K_2 — amplitude coefficients;

RP — radiation pattern of antenna;

$r_1 = \sqrt{(x - x')^2 + z_0^2}$; $r_2 = \sqrt{(x - x')^2 + (z_0 + h)^2}$;

$k_1 = \sqrt{\varepsilon_1} 2\pi f/c$; $k_2 = \sqrt{\varepsilon_2} 2\pi f/c$ — wavenumbers;

$\theta_1 = \arccos \frac{z_0}{r_1}$; $\theta_2 = \arccos \frac{z_0+h}{r_2}$;

The term $(k_1z_o + k_2h)/(z_o + h)$ is included because the signal u_2 goes through the medium 1 (with wavenumber k_1) and also through the medium 2 (with wavenumber k_2).

It is necessary to know the amplitude coefficients K_1 and K_2 (note that these are different the wavenumbers denoted by the lower case letter k). When electromagnetic wave propagating in an isotropic medium with permittivity ε_1 is incident upon another isotropic medium with permittivity ε_2 (permeability μ=1 for both media), the reflection and transmission coefficients are [2]:

$$R = \left(1 - \sqrt{\varepsilon_2/\varepsilon_1}\right) / \left(1 + \sqrt{\varepsilon_2/\varepsilon_1}\right), \qquad T = 2 \Big/ \left(1 + \sqrt{\varepsilon_2/\varepsilon_1}\right) \tag{2}$$

In our case signal u_1 is reflected from the boundary between mediums 1 and 2. So

$$K_1 = \left(1 - \sqrt{\varepsilon_2/\varepsilon_1}\right) \Big/ \left(1 + \sqrt{\varepsilon_2/\varepsilon_1}\right) \tag{3}$$

Signal u_2 goes through the boundary between media 1 and 2, then reflects at the boundary between media 2 and 3, and at last goes through the boundary between media 2 and 1. So

$$K_2 = \left(2 \Big/ \left(1 + \sqrt{\varepsilon_2/\varepsilon_1}\right)\right) \cdot \left(\left(1 - \sqrt{\varepsilon_3/\varepsilon_2}\right) \Big/ \left(1 + \sqrt{\varepsilon_3/\varepsilon_2}\right)\right) \cdot \left(2 \Big/ \left(1 + \sqrt{\varepsilon_1/\varepsilon_2}\right)\right). \tag{4}$$

Using these formulae, a computer simulation has been carried out, with excerpts of the result shown in Figure 3. The reflections clearly appear at 18 mm void thickness. The reflection from the second boundary influences maximally at 33 mm void thickness for a 4.0 GHz signal frequency and at 39 mm thickness for a frequency of 3.6 GHz. The second reflector influence almost disappears at 54 mm. Two typical simulated images (non-influenced and influenced) are visually shown in Figure 4.

4. EXPERIMENT

In order to provide mutual validation, an experiment matching the simulation conditions has been carried out. The pictures of the actual model are shown in Figure 5. The upper picture is Case 1 (plastic void floor) and the bottom is Case 2 (Rubber floor). Plastic plates (thickness 3 mm each) were used for plastic layers. Rubber sheeting was for the void floor in Case 2. The nominal electrical properties of the model materials are shown in Table 1. The thickness of layer 1 is fixed at 12 mm. The void thickness is variable in 3 mm increments from 18 mm to 54 mm, and is controlled by the number of plastic plates. The experimental results are shown in Figure 6 (plastics floored void) and Figure 7 (rubber floored void).

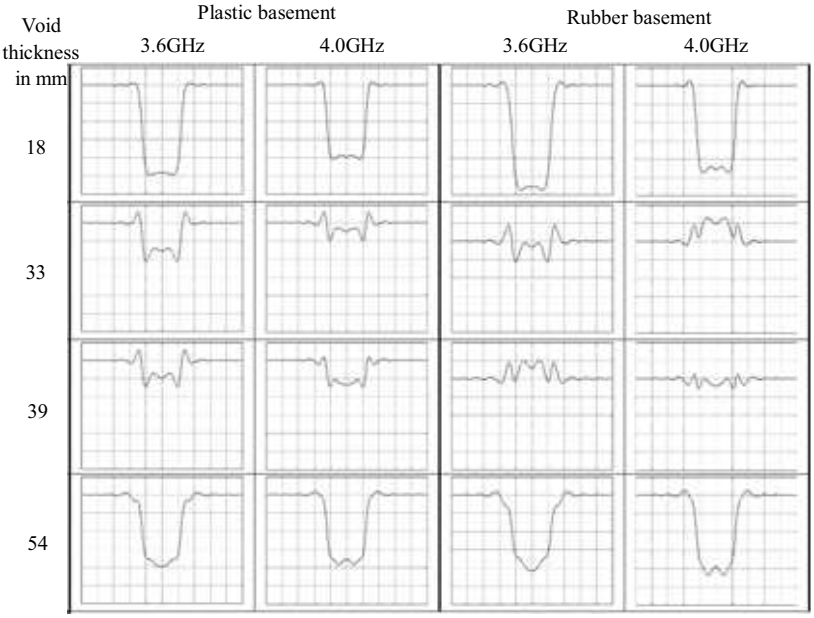

Figure 3: Simulated signal strength of superimposed reflections for two frequencies and four void thicknesses.

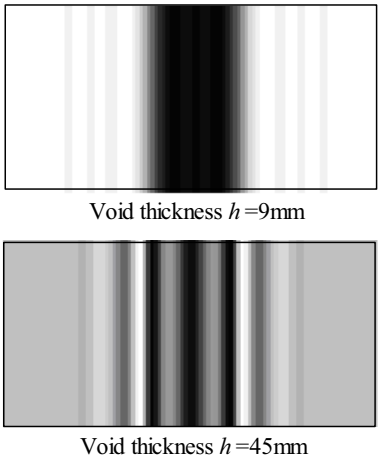

Figure 4: Simulated Rascan images for a rubber void floor with $f = 3.6$ GHz.

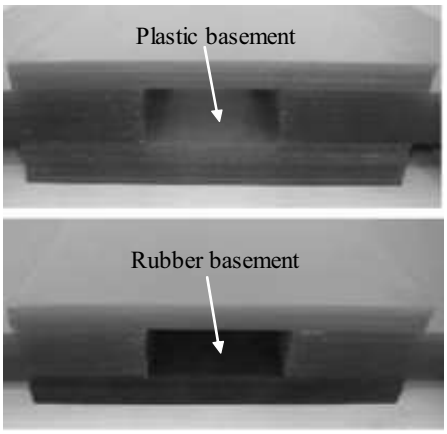

Figure 5: Specimens for experiment.

Table 1: Model electrical properties [4].

Property \ Material	Plastics	Rubber
Electric permittivity	2.7	8.3
Attenuation coefficient (1/m)	0	0.94

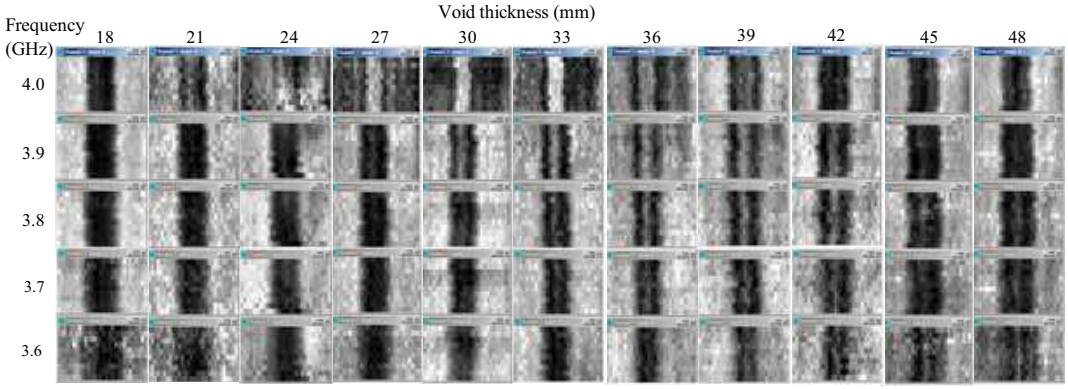

Figure 6: Actual GPR images (Plastic void floor).

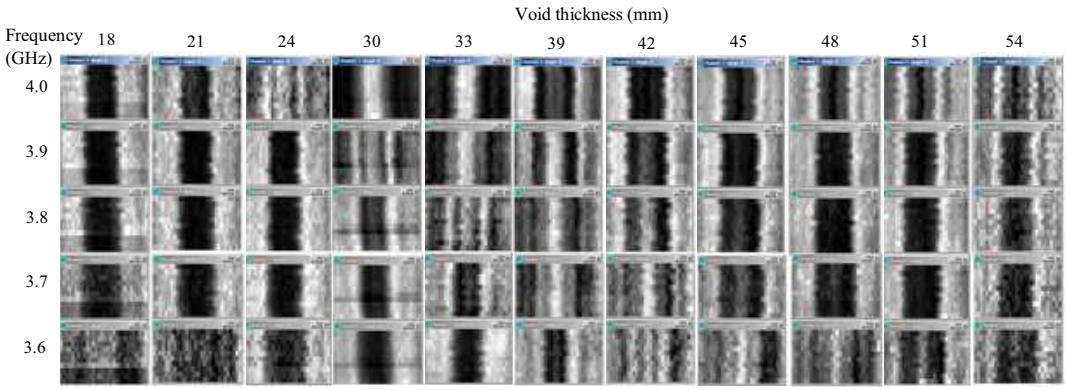

Figure 7: Actual GPR images (Rubber void floor).

The images at 18 mm void thickness appear as a black band between two grey bands. These are the typical reflected images from only the top of the void. They look very close to the simulated image (Figure 4 left). The image clearly changes with increasing void thickness. The influence becomes maximal at the 33 mm for $f = 4.0$ GHz. This is the position where the greatest interference occurs, and it is the same for the plastic and the rubber floors. The experimental phenomenon closely matches the simulation. The greatest interference shifts rightward in Figures 6 and 7 with frequency decrement, occurring at 42 mm to 45 mm for $f = 3.6$ GHz. This is particularly evident for the void with rubber floor, however, it is slightly ambiguous for the plastic floored void. The occurrence is a little shifted to thicker voids (by perhaps 3 to 5 mm) compared to the results of the simulation.

5. APPLICATION

The main advantage of holographic subsurface radar is the ability to accurately determine the plan view shape of buried objects. However the effect of target depth on the interference pattern provides depth/relief or volumetric information on the object as well. However, we have shown that the contrast pattern also depends upon the possible presence of multiple boundaries. Thus, if multiple boundaries are present, the separation and electrical property contrasts at these boundaries can affect the contrast pattern and possibly complicate the interpretation of the outline and relief or volumetric impression of the target.

There are some obvious cases where the phenomenon of interference from a second boundary

could be expected. For instance, impulse radar is widely applied to underground void detection. However impulse radar detects only the location of a void and destructive testing (e.g., a boring) is needed to confirm the thickness. In roadway inspections, there are many voids detected, many of which may be very thin and do not affect the road safety. Boring is a very time-consuming work. The holographic interference phenomenon described in this paper could be used for screening whether voids are relatively thick or thin, possibly reducing the time and cost of void detection work.

6. CONCLUSIONS

Interference can occur between the reflections from the first and the second boundaries presented by targets with finite thickness for certain combinations of target thickness, boundary electrical contrasts, and signal frequency. This has been theoretically and experimentally demonstrated. This phenomenon might affect proper interpretation of holographic radar images. However, since the degree of interference is partly dictated by the distance between two reflective boundaries this phenomenon could be useful. An example is the determination of underground void thickness based on imaging using separate discrete frequencies.

REFERENCES

1. Sheen, D. M., D. L. McMakin, and T. E. Hall, "Three-dimensional millimeter-wave imaging for concealed weapon detection," *IEEE Transactions on Microwave Theory and Techniques*, Vol. 49, No. 9, September 2001.
2. Kong, J. A., *Electromagnetic Wave Theory*, Wiley-Interscience, 1975, 1986, 1990; EMW Publishing since 1998, 2000, 2005, latest Edition: 1016 pages published, May 2008.
3. Windsor, C. G., A. Bulletti, L. Capineri, P. Falorni, S. Valenini, M. Inagaki, T. D. Bechtel, E. Bechtel, A. V. Zhuravlev, and S. I. Ivashov, "Depth information from holographic radar scans," *PIERS Proceedings*, 757–761, Moscow, Russia, August 18–21, 2009.
4. Inagaki, M. and Y. Okiyasu, "Attenuation coefficients of complex materials" *Proceedings of the Ninth International Conference on Ground Penetrating Radar, GPR2008*, Birmingham, UK, June 16–19, 2008
5. Inagaki, M., C. G. Windsor, T. Bechtel, E. Bechtel, S. Ivashov, and A. Zhuravlev, "Three-dimensional views of buried objects from holographic radar imaging," *PIERS Proceedings*, Moscow, Russia, August 18–21, 2009.

A Quasi Linear Sampling Method in Electromagnetic Inverse Scattering

G. H. Li, X. Zhao, and K. M. Huang
School of Electronics and Information Engineering, Sichuan University, Chengdu 610065, China

Abstract— We consider the electromagnetic inverse scattering problem of reconstructing the shape of perfect conducting scatterers, from knowledge of incident plane waves and the far-field patterns of scattered fields. Traditional Linear Sampling Method identifies the edge based on information from a large number of points, sampled from reconstruction region. In this case, not all the sampled points locate at the edge of scatterer. Avoiding sampling these unnecessary points, Quasi Linear Sampling Method is proposed. This new adaptive method determines an approximate initial point 'on' the edge of scatterer through a pre-defined empirical threshold value. From this initial point, other points on the edge are adaptively traced, under the assumption that the edge of scatterer is a continuous curve. Comparison of this newly proposed method with the old one shows that, improvement is achieved in decreasing computational effort while maintaining the similar reconstruction resolution.

1. INTRODUCTION

The inverse scattering problem is to determine the support of a scattering object (scatterer) from knowledge of scattered field from the scatterer. It, in the scientific community, has raised great interest for its promising applications [1, 2]. Nonlinear and ill-posed in the sense of Hadamard, this problem is difficult to be dealt with. Traditional methods, like linearizing approximation [3] and non-linear optimization scheme [4], solve the problem with low accuracy or long run time, respectively.

Colton and Kirsch, in 1996, proposed Linear Sampling Method (LSM) for the first time [5]. Unlike traditional approaches, LSM involves the solution of a linear Fredholm equation of the first kind and derives equivalence from the inverse problem [6]. Although LSM provides an accurate approximate reconstruction of details to some extent, it evaluates the norm on every sampling point in a grid [6, 7]. When the number of sampling points increases, reconstruction time becomes longer. To overcome this deficiency, we proposed an adaptive method (Quasi Linear Sampling Method, QLSM) when evaluating the norm. This method evaluates some sampling points, rather than every sampling point in the reconstruction region.

The plan of this paper is as follows. At the beginning, we will briefly introduce QLSM for solving the inverse scattering problem. We will then demonstrate the feasibility of QLSM over several test problems. Discussion about computational cost is followed. Finally, we note that, empirical threshold value has impact on reconstruction of the scatterer. An interpretation for this impact is presented.

2. PRINCIPLE AND IMPLEMENTATION

Far-field equation to be solved on a sampling point in two dimensional LSM is [6]

$$\int_{\Omega} u_{\infty}(\vec{x}, \vec{d}) g(\vec{d}, z) ds(\vec{d}) = \exp(j\pi/4 - jk\vec{x} \cdot z)/\mathrm{sqrt}(8\pi k), \tag{1}$$

where Ω, $\vec{d} \in \Omega = \{\vec{x} \in \mathbb{R}^2, \|\vec{x}\| = 1\}$, $u_{\infty}(\vec{x}, \vec{d})$, the electric far-field pattern received at observation angle $\vec{x}$ when plane wave is incident from angle $\vec{d}$, $g(\vec{d}, z)$, solution for a sampling point at z.

Euclidean norm $\|g(\vec{d}, z)\|$ becomes unbounded when z goes from the interior to the exterior of scatterer. Thus, this unbounded norm indicates the edge. By plotting the norm or its reciprocal, QLSM reconstructs the edge of the scatterer.

Assume that the edge of scatterer is a continuous curve in a simply connected area, and that $\|g(\vec{d}, z)\|$ on the edge satisfies empirical formula $|\|g(\vec{d}, z)\| - G_T| < \varepsilon$, where G_T is empirical threshold value, and ε is tolerance value. Let (i, j) denote the index of current point, where $1 \le i \le N_i$, $1 \le j \le N_j$. $N_i \times N_j$ is the total number of sampling points, as shown in Figure 1. QLSM proceeds as follows:

Step 1: Solve far-field Equation (1) for points $(N_i/2, 1)$ to $(N_i/2, N_j)$. Choose a point as current point (i, j), where $\|g(\vec{d})\|$ is nearest to G_T.

Step 2: Find solutions on eight points around (i, j), as shown in Table 1.

Step 3: Choose a point with the smallest norm, but larger than G_T, to be the next current point (i, j).

Step 4: Go back to Step 2, until iteration number reaches its maximum.

3. NUMERICAL RESULTS AND DISCUSSIONS

All the numerical reconstructions were performed with $N_i = N_j = 50$, uniformly distributed on a grid $[-2, 2]^2$. Frequency of plane wave is 600 MHz, incident from directions with $N = 45$. And these directions were also used to receive far-field pattern data. Empirical threshold value $G_T = 0.009$. Maximum iteration number is 100.

3.1. Reconstruction of a Pyramid

Figure 2 shows the exact geometry of pyramid scatterer. This pyramid is centered at $(0.0, 0.0, -0.5)$ at base. Its dimensions are: Bottom Width $(X) = 2.0$ m, Bottom Depth $(Y) = 1.0$ m, and Height $(Z) = 2.0$ m. The reconstructions of the pyramid are shown in Figure 3 and Figure 4, by QLSM and LSM, respectively. These two reconstructed objects have almost the same accuracy. That is, every point on the reconstructed projections is near the corresponding one on the exact geometry.

Table 1: Eight points to be evaluated around current point (i, j).

$i+1, j-1$	$i+1, j$	$i+1, j+1$
$i, j-1$	i, j	$i, j+1$
$i-1, j-1$	$i-1, j$	$i-1, j+1$

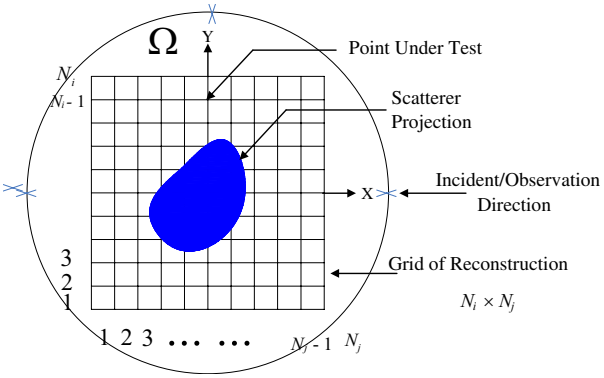

Figure 1: Reconstruction area in which far-field equation is solved.

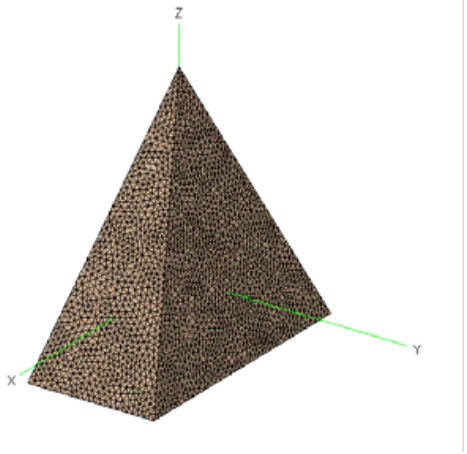

Figure 2: Exact geometry of pyramid scatter of PEC.

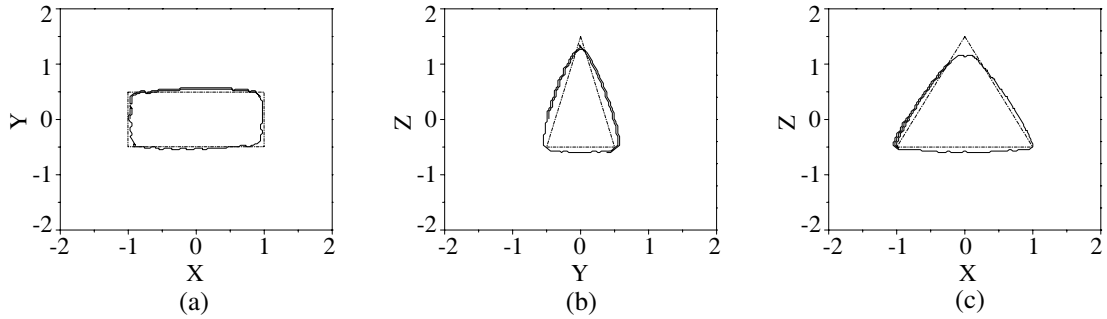

Figure 3: Reconstructions of pyramid by using QLSM with threshold value = 0.009: (a) Projection onto XY-plane, (b) projection onto YZ-plane, and (c) projection onto XZ-plane. The exact edge is shown with a black dash dot curve.

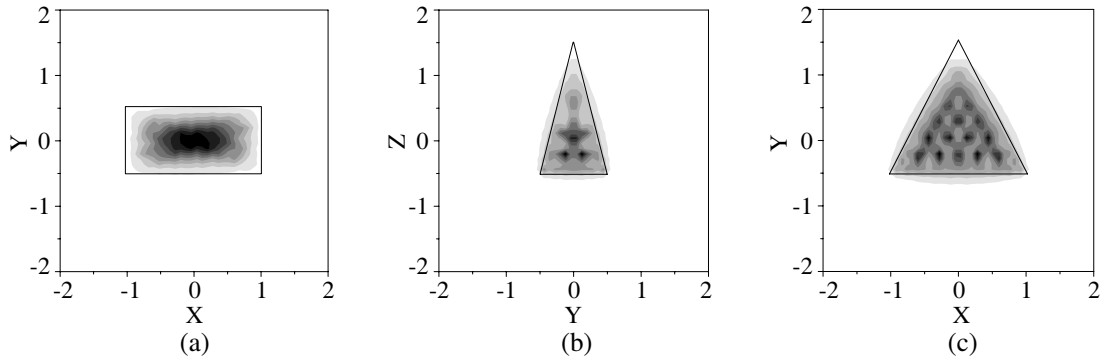

Figure 4: Reconstructions of pyramid by using LSM. (a) Projection onto XY-plane, (b) projection onto YZ-plane, and (c) projection onto XZ-plane.

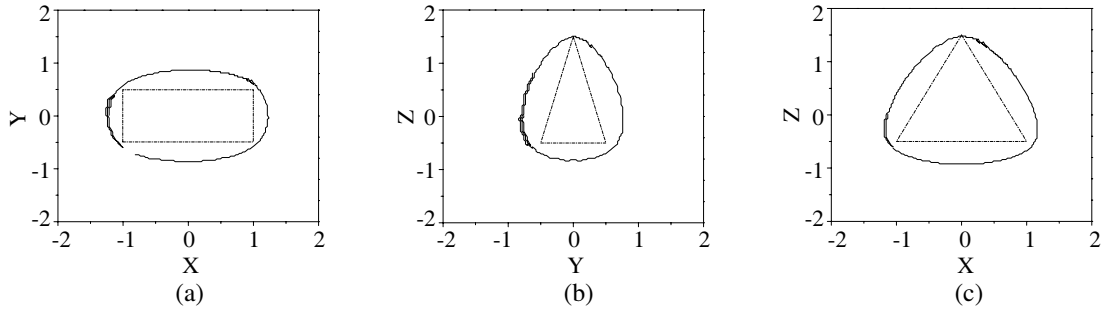

Figure 5: Reconstructions of pyramid by using QLSM with $G_T = 0.001$: (a) Projection onto XY-plane, (b) projection onto YZ-plane, and (c) projection onto XZ-plane.

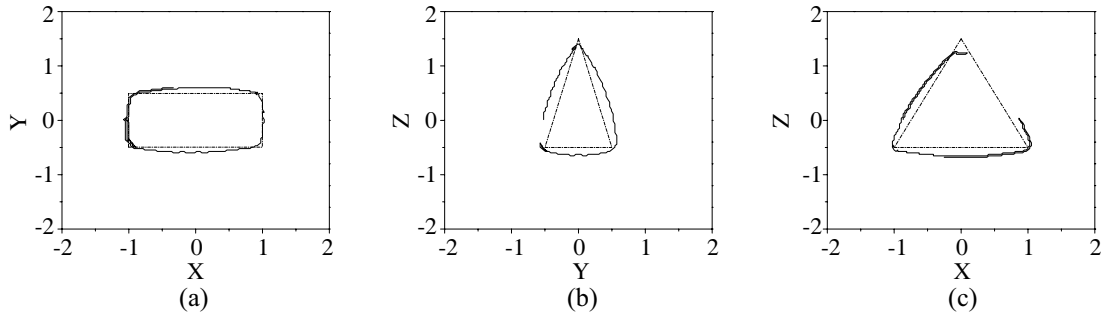

Figure 6: Reconstructions of pyramid by using QLSM with $G_T = 0.006$: (a) Projection onto XY-plane, (b) projection onto YZ-plane, and (c) projection onto $XZ-$plane.

3.2. Comparison of QLSM with LSM

The two methods, QLSM and LSM, reconstructed the scatterer with almost the same accuracy. QLSM, however, features low computational cost: shorter run time and fewer sampling points to solve the far-field Equation (1). LSM solves the far-field equation on every point in the grid of reconstruction region. Consequently, points far away from the scatterer increase run time but contribute nothing to the reconstruction. Unlike LSM, QLSM samples points near the edge of scatterer. These points are a small part of sampling points. As a result, QLSM evaluates fewer points and operates at a faster speed, due to an adaptive sampling scheme. A notable progress is made in computational effectiveness, as shown in Table 2.

3.3. Effect of Threshold Value on QLSM's Performance

We varied threshold value G_T to achieve the 'best visual' reconstruction. Reconstructions in Figure 5, Figure 6, and Figure 7 indicate that not all the threshold values are effective to reconstruct the scatterer. There exists a 'best' threshold value for a 'best visuality', just as the reconstruction in Figure 3. Any threshold value, lower or larger than the 'best' one, leads to inaccurate performance. Under the limit of a lower threshold value, the current point (i, j) in Step 1 of QLSM can only locate at a point where the norm of solution is large. This is because norms are larger outside the scatterer, while smaller inside. And in the following iterative process, only points similar to the

Table 2: A comparison between computation costs in reconstruction of projections.

	XY			YZ			ZX		
	QLSM	2DLSM	Ratio	QLSM	2DLSM	Ratio	QLSM	2DLSM	Ratio
Time/Second	10.58	39.57	26.74%	9.40	37.57	25.02%	9.49	39.24	24.18%
Point Sampled	642	50*50	25.68%	613	50*50	24.52%	654	50*50	24.16%

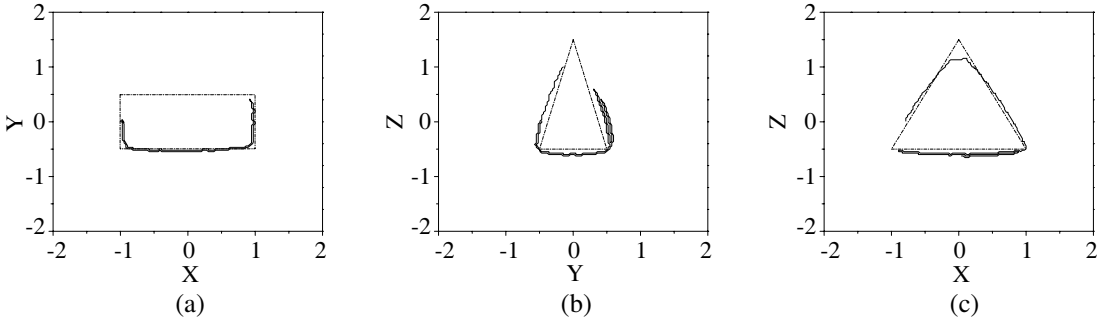

Figure 7: Reconstructions of pyramid by using QLSM with $G_T = 0.010$: (a) Projection onto XY-plane. (b) projection onto YZ-plane, and (c) projection onto XZ-plane.

current point can be recognized as points on the edge of scatterer. All the points selected would consequently form a shape with a larger area, rather than a projection of scatterer, as shown in Figure 5. On the other hand, neither can be a 'best visual' reconstruction performed, when threshold value is small. Points with smaller norms lie in the interior of scatterer. Once the norms of those points match threshold value, the following points obtained would also lie inside the scatterer. Hence, QLSM reconstructed the projections at a lower accuracy, as shown in Figure 7.

4. CONCLUSIONS

This paper presents a new adaptive scheme, QLSM, for solving inverse scattering problem. QLSM reconstructs scatterer with efficient computation: fewer sampling points and less run time, when compared with those of LSM. Meanwhile, reconstruction resolutions keep almost the same. QLSM's performance is partly dependent upon threshold value. A 'best' threshold value reconstructs a 'best' approximation to scatterer edges. Further study will adaptively determine threshold value by edge detection algorithm, such as canny algorithm. It is also worth proposing a new criterion for stopping the iteration.

ACKNOWLEDGMENT

This research was supported in part by grant 60801035 from the National Science Foundation China.

REFERENCES

1. Bolomey, J. C., "Recent European developments in active microwave imaging for industrial, scientific and medical applications," *IEEE Trans. Microwave Theory*, Vol. 37, No. 12, 2109–2117, 1989
2. Giakos, G. C., M. Pastorino, F. Russo, S. Chowdhury, N. Shah, and W. Davros, "Noninvasive imaging for the new century," *IEEE Instrumentation Meas. Mag.*, Vol. 2, No. 2, 32–35, 1999.
3. Pierri, R., A. Liseno, and F. Soldovieri, "Shape reconstruction from PO multifrequency scattered fields via the singular value decomposition approach," *IEEE Trans. Antennas Propagat.*, Vol. 49, No. 9, 1333–1343, 2001.
4. Cui, T. J., W. C. Chew, A. A. Aydiner, and S. Chen, "Inverse scattering of two dimensional dielectric objects buried in a lossy earth using the distorted born iterative method," *IEEE Trans. Geosci. Remote Sensing*, Vol. 39, No. 2, 339–346, 2001.
5. Colton, D. and A. Kirsch, "A simple method for solving inverse scattering problems in the resonance region," *Inverse Problems*, Vol. 12, No. 4, 383–393, 1996.
6. Colton, D., H. Haddar, and M. Piana, "The linear sampling method in inverse electromagnetic scattering theory," *Inverse Problems*, Vol. 19, No. 1, 105–137, 2003.
7. Cakoni and D. Colton, "The linear sampling method for cracks," *Inverse Problems*, Vol. 19, No. 2, 279–295, 2003.

Bistatic Radar Target Classification Using Time-frequency Analysis and Multilayered Perceptron Neural Network

Sung-Jun Lee and In-Sik Choi
Department of Electronic Engineering, Hannam University, Daejeon, Korea

Abstract— The performance of target classification using a bistatic radar cross section (RCS) of four different wire targets was analyzed. Short time Fourier transform (STFT) and continuous wavelet transform (CWT) were used for feature vector extraction from the bistatic RCS of each target, and a multilayered perceptron (MLP) neural network was used as a classifier. To compare the performance of the monostatic RCS and the bistatic RCS, we performed a simulation using the features extracted by STFT and CWT. The simulation results show that CWT yields better results than STFT. When CWT was used, the performance of the monostatic RCS was better than that of the bistatic RCS. However, when STFT was used, the performance of the bistatic RCS was better than that of the monostatic RCS. A comparison between the classification performances of monostatic RCS and bistatic RCS showed that bistatic RCS exhibits nearly same performance as monostatic RCS. Therefore, bistatic RCS is a good candidate for application to radar target classification in combination with a monostatic RCS.

1. INTRODUCTION

RCS is a function of various parameters, such as frequency, direction of incidence and scattering, and polarization. It is classified as monostatic and bistatic depending on the locations of the transmitter and the receiver [1]. When the locations of the transmitter and the receiver are the same, the directions of incidence and scattering are the same. In this case, the resulting RCS values are called monostatic RCS. Bistatic RCS is obtained by a bistatic radar that uses different locations of the transmitter and the receiver. Therefore, in the case of bistatic RCS, the directions of incidence and scattering are not same. Recently there has been a renewed interest in bistatic radars because of their ability to detect stealth targets [2]. Furthermore, applications of bistatic radars to the television broadcasting transmitters, synthetic aperture radar (SAR), air surveillance radars, and intrusion detection sensors have been introduced.

RCS contains useful information for target recognition, such as scattering centers and natural resonance frequencies. The scattering centers on the target are related to the early-time response and natural resonance frequencies of the target are related to the late-time response. The early-time response occurs while the field passes across the target, and the late-time response occurs after the field completely traversed the target. The natural resonance frequencies and the scattering centers are used as feature vectors for radar target recognition. We use the time-frequency transforms to extract these feature vectors simultaneously [3].

In this study, we extracted feature vectors for the monostatic RCS and the bistatic RCS of four different wire targets using STFT and CWT, which are time-frequency analysis methods. Then, the MLP neural network was used as a classifier. By the abovementioned process, we compared and analyzed the performance of radar target classification for monostatic RCS and bistatic RCS.

2. FEATURE VECTOR EXTRACTION OF TARGETS

2.1. RCS Calculation

We used four different wire targets to analyze the performance of radar target classification of the monostatic RCS and the bistatic RCS. Figure 1 shows the target geometry used in the simulations. Targets A and B have the same length, but different angles of wing. Targets C and D also have the same length, but different angles of wing. In this study, to obtain the RCS, we used the method of moments (MoM), although there are various methods to calculate RCS in the FEKO simulation tool. The frequency range was 7.8125 MHz–1 GHz with 128 point samplings and the HH polarization was considered. The monostatic RCS was calculated for each azimuth of counterclockwise rotated target from 0° to 150°, where the transmitter and the receiver were located at 0°. Like the monostatic RCS, the bistatic RCS was calculated for each azimuth. However, in the case of bistatic RCS, the transmitter was located at 0° and the receiver was located at 45°.

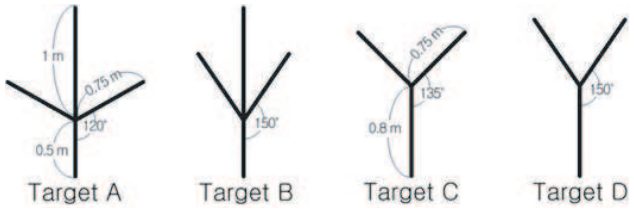

Figure 1: Targets used in the simulation.

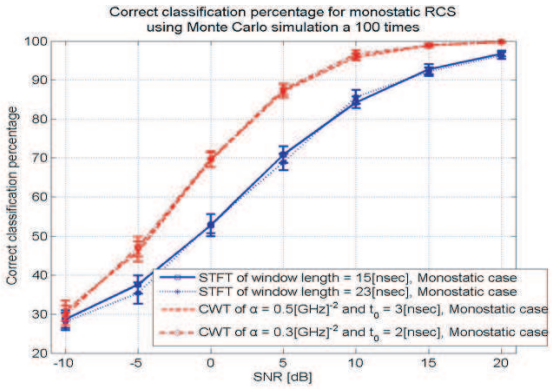

Figure 2: Classification percentage for SNR of monostatic RCS.

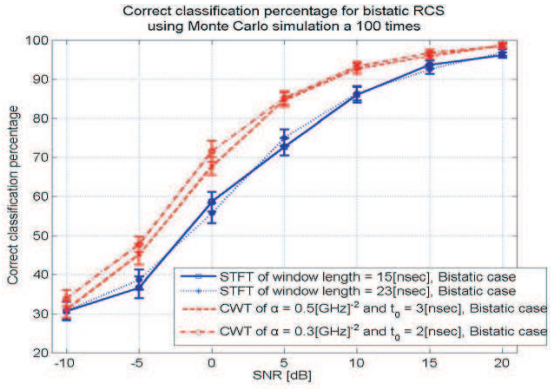

Figure 3: Classification percentage for SNR of bistatic RCS.

2.2. Extraction of Feature Vector

We extracted feature vectors for each target using STFT and CWT, which are time-frequency analysis methods. The feature vectors were extracted for each azimuth of the target. The feature vectors for the odd azimuth angle were used for training data of the neural network classifier and the feature vectors for the even azimuth angle were used for test data of the neural network classifier. We obtained the feature vectors of 128×128 dimensions, where the 15 nsec and 23 nsec window sizes were used in STFT, and we compressed the obtained feature vectors to 8×8 dimensions to be effectively used by the neural network classifier. Similarly, using CWT, we obtained feature vectors of 128×128 dimensions, where the center of wavelet (t_0) and the time-frequency resolution (α) of the wavelet basis function were $\alpha = 0.5\,\mathrm{GHz}^{-2}$ and $t_0 = 3\,\mathrm{nsec}$, respectively. Unlike the STFT, in the case of CWT, the entire time span was divided into early time ($0 < t < t_L$) and late time ($t > t_L$), where $t_L = 10\,\mathrm{nsec}$. The dimensions during earlytime were compressed to 8×10 and the dimensions during latetime were compressed to 32×6. Therefore, the final feature vector had $80 + 192 = 272$ dimensions in the CWT [3].

3. TARGET CLASSIFICATION EXPERIMENTS

In this study, a MLP neural network which has two hidden layers was used for classifying targets. The number of neurons of the first hidden layer was half of the feature vector dimensions, and the second hidden layer had one third the number of neurons of the first hidden layer. We obtained the feature vectors at azimuth angles of $0° \sim 150°$. The feature vectors corresponding to the odd azimuth angles were used for training data, and the feature vectors corresponding to the even azimuth angles were used for test. Figures 2 and 3 show the classification percentage as a function of the signal to noise ratio (SNR) for the monostatic RCS and the bistatic RCS, respectively. We performed 100 Monte Carlo simulations to enhance the reliability. The results of this simulation show that the classification performance using CWT is better than that using STFT regardless of the RCS being monostatic or bistatic. In addition, in the case of monostatic RCS, STFT with a window size of 15 nsec and CWT with $\alpha = 0.3\,\mathrm{GHz}^{-2}$ and $t_0 = 2\,\mathrm{nsec}$ yield slightly better results. In the case of bistatic RCS, STFT with a window size of 23 nsec and CWT with $\alpha = 0.3\,\mathrm{GHz}^{-2}$ and $t_0 = 2\,\mathrm{nsec}$ yield slightly better results. Figure 4 shows the comparison between the monostatic RCS and the bistatic RCS. This comparison indicates that STFT yields better results with bistatic RCS than monostatic RCS, and CWT yields better results with monostatic RCS than with bistatic RCS.

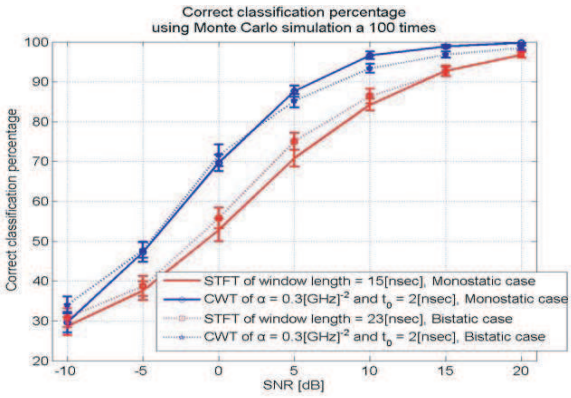

Figure 4: Classification percentage comparison between monostatic RCS and bistatic RCS.

4. CONCLUSIONS

In this study, we analyzed the performance of radar target classification using monostatic RCS and bistatic RCS for four different wire targets. Feature vectors of each target were extracted using STFT and CWT, which are time-frequency analysis methods. A MLP neural network was used as a classifier. According to the results of the simulation, the performance of the radar target classification using CWT is better than that using STFT, and performance is considerably influenced by the window size of STFT and α and t_0 of the wavelet basis function. Bistatic RCS exhibits good performance when STFT is used, whereas monostatic RCS exhibits slightly better performance when CWT is used. In this paper, by comparing the classification performance between monostatic RCS and bistatic RCS, we proved that bistatic RCS also has a considerably good target classification performance. Therefore, a bistatic RCS is a good candidate for application to radar target classification in combination with a monostatic RCS. Future investigations are necessary to optimize the system configuration of bistatic radars in order to achieve the best performance and simulations using real targets are also needed.

ACKNOWLEDGMENT

This work was supported by Basic Science Research Program through the National Research Foundation of Korea (NRF) funded by the Ministry of Education, Science & Technology (No. 2010-0016513).

REFERENCES

1. Glaser, J. I., "Some results in the bistatic radar cross section (RCS) of complex objects," *Proceedings of the IEEE*, Vol. 77, No. 5, 639–648, May 1989.
2. Gürel, L., H. Bagci, J. C. Castelli, A. Cheraly, and F. Tardivel, "Validation through comparison: Measurement and calculation of the bistatic radar cross section of a stealth target," *Radio Science*, Vol. 38, No. 3, 1046–1058, September 2003.
3. Choi, I.-S. and H.-T. Kim, "Efficient feature extraction from time-frequency analysis of transient response for target identification," *Microwave and Optical Technology Letters*, Vol. 26, 403–407, September 2000.

Low Frequency Radar Target Imaging Using Ramp Response Signatures in Arbitrary Directions

J. Chauveau, Y.-H. Wen, and N. de Beaucoudrey
IREENA, Fédération CNRS Atlanstic, Université de Nantes
La Chantrerie, Rue C. Pauc, BP 50609, 44306 Nantes Cedex 3, France

Abstract— Low frequency imaging in radar domain can have applications for stealthy or buried targets. The transient scattering response from a ramp waveform is related to the profile function of the target, namely its transverse cross-sectional area along the line-of-sight, and thus provides information about the target size, orientation and geometrical shape. Such ramp responses can be used to generate a 3-dimensional image of the global shape of the target. We have developed an algorithm able to reconstruct non-convex and/or separated objects using their ramp response signatures. For mutually orthogonal observing directions, this algorithm gives satisfactory target images, while its performance decreases in non-orthogonal cases. However, radar equipments often have a limited observing view range for remote and/or large-scale targets. Therefore, the goal of this study is to improve the performance of the algorithm for arbitrary observing directions.

1. INTRODUCTION

Low frequency imaging in radar domain is useful to characterize stealthy or buried targets. Indeed, lower frequency bands permit to counter the stealthiness obtained with composite materials absorbing electromagnetic waves in usual radar frequency bands. In the same way, Ground Penetrating Radar (GPR) systems operate in low frequency bands, since the wave attenuation in most soil increases with the frequency. These low frequency bands correspond to the Rayleigh and the resonance regions for object dimensions respectively small and of the same order compared to electromagnetic wavelengths. Unlike high frequency imaging, low frequency methods cannot bring high resolution, i.e., details on the target, but they provide information on the overall dimension and the approximate shape of the target. Three-dimensional (3D) microwave imaging by inverse scattering methods (diffraction tomography, ...) usually requires a considerable number of look angles for image reconstruction. On the contrary, a method proposed by Young [1], known as the "ramp response technique", needs no more than 3 viewing angles to generate an image. The ramp response of a radar target, first suggested by Kennaugh and Moffatt for radar identification [2], is defined by the far zone transient scattered wave resulting from illumination by a plane electromagnetic wave with a time domain ramp waveshape. In monostatic configuration, this ramp response is directly related to the "profile function" of the target, which is the transverse cross-sectional area of the target as a function of the distance along the line-of-sight [2]. Former 3D image generation from such ramp profile functions uses approximate limiting surfaces and is therefore limited to single convex objects [1]. That is why, we have developed a new algorithm able to reconstruct non-convex and/or separated objects using their ramp response signatures [3, 4]. For mutually orthogonal observing directions, this algorithm gives satisfactory target images, while its performance decreases in non-orthogonal cases.

We first introduce the ramp response and the corresponding profile function (Section 2). Then, we present the algorithm developed for reconstructing 3D target image from ramp profile functions (Section 3). Finally, results are given for mutually orthogonal directions (Section 4) and for arbitrary directions (Section 5).

2. RAMP RESPONSE AND PROFILE FUNCTION

The ramp response of a radar target is defined by the far zone transient scattered wave resulting from illumination by a plane electromagnetic wave with a time domain ramp waveshape. In time domain, the ramp response of a target, $h_r(t)$, is merely the second integral of its impulse response, $h_i(t)$. It can be expressed as the Inverse Fourier Transform (IFT) of the weighted transfer function, $H_r(j\omega)$ (with the angular frequency $\omega = 2\pi f$)

$$h_r(t) = \int_{-\infty}^{t}\int_{-\infty}^{t'} h_i(t'')dt''dt' = IFT\left[H_r(j\omega)\right] = IFT\left[H(j\omega)/(j\omega)^2\right] \quad (1)$$

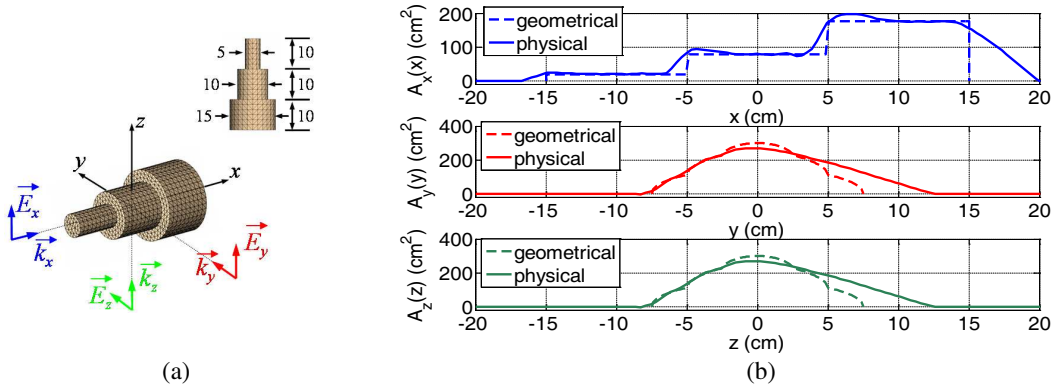

Figure 1: Example of a stepcylinder. (a) configuration with 3 orthogonal directions (dimensions in cm). (b) Physical and geometrical profile functions of the stepcylinder in 3 directions, x, y and z.

In monostatic configuration, $h_r(t)$ is directly related to the profile function of the target, $A(x)$, which is the transverse cross-sectional area of the target as a function of the distance along the line-of-sight [2]

$$h_r(t) \approx -\frac{1}{\pi c^2} A(x) \quad \text{with} \quad x = ct/2 \tag{2}$$

where c is the speed of light in freespace, t the time variable, and x the space variable.

Using as target the example of Figure 1(a), Figure 1(b) compares "geometrical" and "physical" profile functions in 3 mutually orthogonal directions, x, y and z: The "geometrical" profile function is the transverse cross-sectional area, $A(x)$, along x direction. The "physical" profile function is calculated from its ramp response, $h_r(t)$, using (2).

3. IMAGE RECONSTRUCTION ALGORITHM

An analysis of profile functions of a target at several orientations can give information on its size and its approximate shape. This can be used directly as a signature for identification purposes. Furthermore, combining such responses so as to create a 3D image is an efficient means to represent the geometrical information on the target. The interesting property given by (2) have been first used by Young [1] for generating a 3D image of the target shape: his original algorithm uses profile functions from 3 mutually orthogonal viewing angles and applies a set of approximate surfaces limiting the contour of the object for each viewing angle independently. An iterative fitting of geometrical parameters of these enclosing surfaces permits to obtain an estimate of the final image as the volume common to the 3 set of such surfaces. Consequently, this technique is limited to single convex objects.

That is why we have proposed a new algorithm permitting to reconstruct non-convex objects, as well as separated objects [3, 4]. Our algorithm manages to exploit the information more effectively: it simultaneously uses the 3 profile functions through a 3D weighting function, which is equal to the product of these 3 profile functions accounting for the probability that a point belongs to the object. Considering 3 directions, x_1, x_2 and x_3, this weighting function is given by

$$A_{3D}(x_1, x_2, x_3) = A_1(x_1) \times A_2(x_2) \times A_3(x_3) \tag{3}$$

We scan successive slices along a given direction, x_3 for example. In each slice, we select points which have the highest values of $A_{3D}(x_1, x_2, x_3)$ so that the area of the resulting object in this slice (given by the sum of selected points) is equal to the profile function in this slice, $A_3(x_3)$. The 3D reconstructed object is finally composed of all selected points. Consequently, this algorithm is able to reconstruct the global shape of non-convex and/or separated objects, and to directly obtain a satisfactory estimate of these objects.

4. RESULTS FROM 3 MUTUALLY ORTHOGONAL DIRECTIONS

Figure 2 presents the 3D image of the stepcylinder reconstructed with this new algorithm, using geometrical profile functions. In this case of ideal profile functions and for mutually orthogonal directions, the original object is accurately reconstructed.

If we consider the realistic case of physical profile functions calculated from ramp responses, the resulting image (Figure 3) is distorted as compared to the original object, yet this result is still acceptable in the context of low frequency imaging where the goal is not to reconstruct a high resolution image but to identify a target from its approximate shape.

5. RESULTS FROM 3 ARBITRARY DIRECTIONS

We now consider non orthogonal directions, using the example of a stepcylinder along z direction. We use geometrical profile functions and we keep 2 orthogonal directions (direction 2 = y and

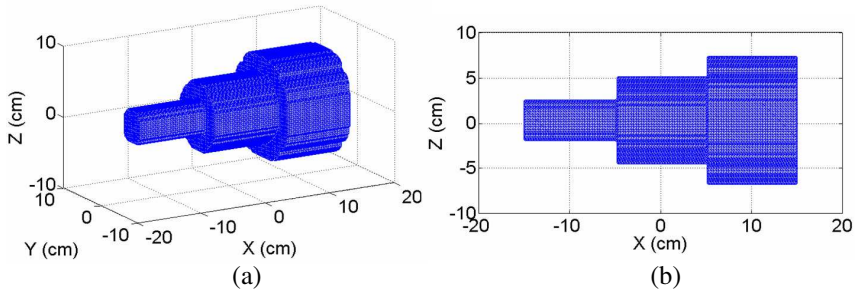

Figure 2: Reconstruction of the stepcylinder of Figure 1(a) from its 3 geometrical orthogonal profile functions. Scan direction: x. (a) 3D view. (b) (x-z) view.

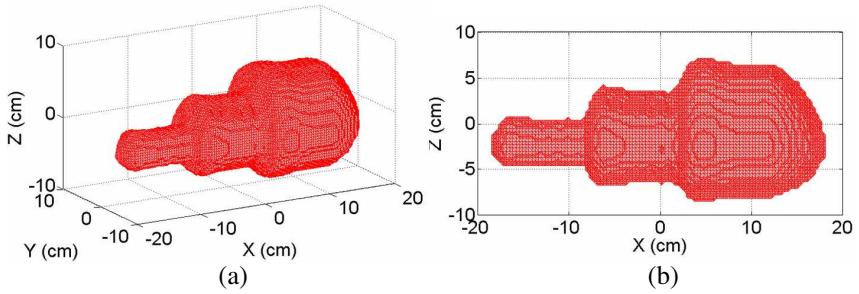

Figure 3: Reconstruction of the stepcylinder of Figure 1(a) from its 3 physical orthogonal profile functions. Scan direction: x. (a) 3D view. (b) (x-z) view.

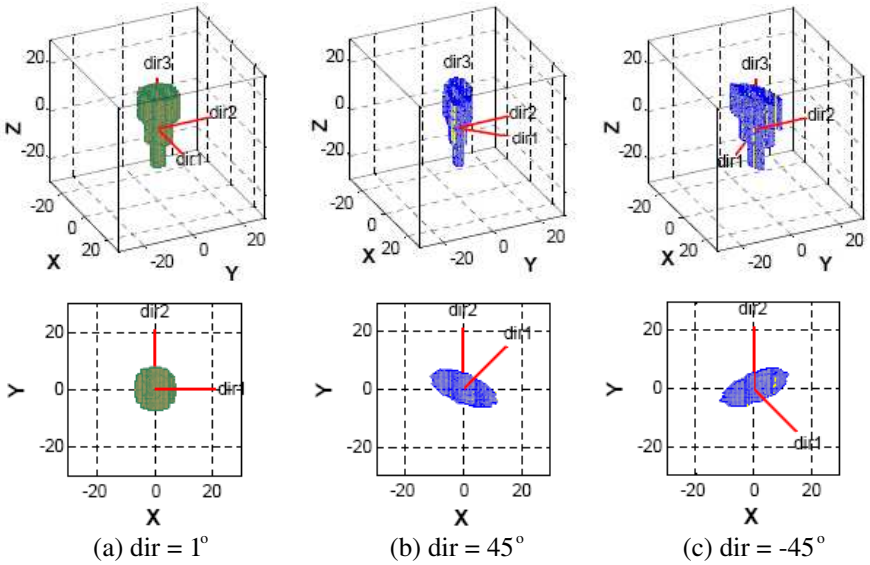

Figure 4: Reconstruction of a stepcylinder from its 3 geometrical profile functions. Scan direction: z. Top: 3D view, bottom: (x-y) view. dir 2 = y, dir 3 = z. (a) orthogonal direction (dir 1 = x), (b) and (c) arbitrary direction, dir 1 = $\pm 45°$.

direction $3 = z$), while the 3rd one (direction 1) is either at $\pm 45°$ in xy plane. We obtain the reconstruction in Figure 4. If we compare Figure 4(b) (case $+45°$) and Figure 4(c) (case $-45°$) to Figure 4(a) (case $0°$), we can see that the use of non-orthogonal observing directions results in a distortion of the reconstruct target: The object is elongated along the bisector of the non-orthogonal directions (directions 1 and 2 in this case).

6. CONCLUSIONS AND PERSPECTIVES

Low frequency radar target 3D imaging using ramp responses usually needs no more than 3 viewing angles to generate an image. We have developed a new algorithm able to directly reconstruct the global shape of non-convex and/or separated objects. For mutually orthogonal observing directions, this algorithm gives satisfactory target images, while its performance decreases in non-orthogonal cases.

However, radar equipments often have a limited observing view range for remote and/or large-scale targets. Therefore, the goal is to improve the performance of the algorithm for arbitrary observing directions. For that, we have developed an algorithm for calculating profile functions from a 3D object in arbitrary directions. Such reconstructed profile functions can be used as well for verifying the accuracy of a reconstructed image, as a new input for optimizing the reconstruction process.

REFERENCES

1. Young, J. D., "Radar imaging from ramp response signatures," *IEEE Transactions on Antennas and Propagation*, Vol. 24, No. 3, 276–282, 1976.
2. Kennaugh, E. M. and D. L. Moffat, "Transient and impulse response approximations," *Proc. IEEE*, Vol. 53, No. 8, 893–901, 1965.
3. Chauveau, J., N. de Beaucoudrey, and J. Saillard, "Low frequency radar targets 3-dimensional imaging using ramp response signatures," *International Radar Conference — Surveillance for a Safer World, RADAR*, Bordeaux, France, October 2009.
4. Chauveau, J. and N. de Beaucoudrey, "A new algorithm of 3D image reconstruction of radar targets from ramp responses in low frequency," *Progress In Electromagnetics Research M*, Vol. 16, 1–18, 2011.

A Wigner Ville Distribution Based Method for Detection of Gaussian Contaminated Sinusoidal Signal in Frequency Domain

Shahida G. Qadir[1], **Yangyu Fan**[1], **and Fathy M. Ahmed**[1, 2]

[1]School of Electronics and Information Processing, Northwestern Polytechnical University
Xi'an, Shaanxi, China
[2]Military Technical College, Cairo, Egypt

Abstract— Detection and frequency estimation of sinusoidal signals from a finite number of noisy discrete-time measurements have applications in several fields, e.g., in sonar and Radar for moving target detection. In, Pulsed Doppler radar, a bunch of Coherent Pulse Interval (CPI) is processed to detect and estimate the frequency of sinusoidal signal corresponding to the speed of target. With the advent of Fast Fourier Transform (FFT) algorithm, the Periodogram and its variants such as Bartlett's procedure and Welch method, have been extensively in use for spectral analysis.

In this paper a Wigner Ville Distribution (WVD) based new method is proposed for the detection and estimation of noisy sinusoidal signals in frequency domain. The Cross terms produced due to the bilinear nature of WVD are eliminated. The proposed method outperforms the Periodogram and its variants (Bartlett and Bartlett-based method proposed by reference [2]) for off-bin frequencies. The performance is found to be comparable in case of in-bin frequencies. Due to Low-sidelobes reported by WVD, no additional window operation is used, consequently the proposed method outperforms the windowed version of Periodogram and its variants for all 'in' and 'off' bin frequencies. Also, frequency resolution remains intact. However, the issue of increased computation of proposed method can be tackled by using high speed devices and many proposed real time WVD implementation algorithms. Performances of the proposed WVD based method and the other mentioned methods are evaluated through computer simulations by generating Receiver Operating Characteristics (ROCs) via Monte Carlo trials.

1. INTRODUCTION

Schuster's periodogram [3] is the first commonly used Detection and frequency estimation method. Later on, the windowed version of Periodogram of analytical signal $z(n)$ is proposed by Tukey, which is given as;

$$S_{Dz}(f_k) = \frac{1}{N}\left|\sum_{k=0}^{N-1} z(n)D(n)e^{-j2\pi n f_k}\right|^2, \quad k = 0, 1, 2, \ldots, N-1 \tag{1}$$

where frequency $f_k = k/N$. Periodogram is inconsistent because its variance does not decrease with sample size. In the Bartlett method, the variance in the periodogram estimate is reduced by a factor K by dividing the sequence $z(n)$ into K non-overlapping segments at the expense of reduction in the frequency resolution by factor K [1]. Reference [2] proposes another modification of Bartlett Periodogram. In this paper, we presented a new scheme derived from Wigner Ville Distribution (WVD); a well known tool used for analysis of signal in time and frequency domain [8]. The discrete version of WVD (DWVD) is given by Eq. (2) [6].

$$W'(n, 2f) = \sum_{m=-\infty}^{\infty} z\{(n+m)\Delta t\}z^*\{(n-m)\Delta t\}e^{-j2\pi m\Delta t} \tag{2}$$

It is a 2D operation. Windowed version of WVD is called Pseudo WVD [5–7]. However, for short length sequences (e.g., radar CPI), window operation can be avoided and PWVD can be represented by Eq. (3) with redefined Kernel and can be implemented by FFT operation as proposed by [7];

$$\mathrm{PWVD}(n, m) = \sum_{k=0}^{M-1} x(n, k)\exp(-j2\pi km/M),$$

$$\text{where} \qquad x(n, k) = \begin{cases} Q(n, k)Q^*(n, -k) & k = 0, \ldots, N/2-1 \\ Q(n, k-N)Q^*(n, -k+N) & k = N/2, \ldots, N-1 \end{cases} \tag{3}$$

where $Q(n,k) = z(n+k)$. For N odd, a zero has to be inserted, i.e., $Q(n,-N/2) = 0$.

In our proposed scheme, the WVD method is modified for calculating frequency spectrum of the signal (1D operation). The method is compared with standard periodogram. We also re-formulated the proposed method as SWVD and compared it with the variants of Periodogram given in [1, 2], through ROCs.

2. WIGNER VILLE DISTRIBUTION BASED PROPOSED METHOD

In our proposed method, WVD is used as a 1D operation to calculate only the frequency of signal. Cross-products are calculated for all time index $n = 0$ to $N-1$, then the summation is applied over time on complex cross-products to generate summed kernel, instead of calculating the kernel only at time $n = 0$ as suggested by [7]. The FFT of the summed kernel gives the frequency spectrum of the signal. The proposed method is mathematically described by Eqs. (4) & (5).

$$\mathrm{WVD}''(m) = \frac{1}{N}\left|\sum_{k=0}^{N-1} SR(k)\exp(-j2\pi km/N)\right|, m = 0,\ldots,N-1 \;\&\; n = 0,\ldots.N-1 \tag{4}$$

$$SR(k) = \begin{cases} \sum\limits_{n=k}^{N-k-1} x(n+k)x^*(n-k), & k = 0,\ldots,N/2-1 \\ 0, & k = N/2 \\ SR^*(N-k-1), & k = N/2+1,\ldots,N-1 \end{cases} \quad \text{for } N \text{ is even} \tag{5}$$

where, m is normalized frequency index and n is discrete time index. $SR(k)$ is the summed cross products of discrete signal $x(n)$ calculated in Eq. (3), which eliminates the problem of cross-terms of WVD generated due to bilinear nature of WVD. This also reduces the noise variance and boosts the level of energy of signal spectrum. Method also gives the reduction in sidelobe without using window operation. Hence, the frequency resolution remains intact. The twiddle factor requirement to calculate the WVD spectrum is twice in power than FFT's twiddle factor. Calculation of WVD through FFT algorithm gives advantage of 2f frequency scale (Eq. (2)), this increase frequency resolution and we got very good results at off-bin frequency of sinusoids without additional interpolation.

The proposed reformulated WVD based method for K segments of data is given by Eq. (6). This has further reduced the variance of spectrum at the expense of frequency resolution reduction by K.

$$SWVD''(m) = \frac{1}{N}\left|\sum_{i=0}^{K-1}\sum_{k=0}^{N-1} SR_i(k)\exp(-j2\pi km/M)\right|,$$

$$\text{where,}\quad SR_i(n) = SR(i\cdot M+n), i=0,1,\ldots,K-1;\quad m=0,\ldots,N-1 \;\&\; n=0,\ldots,N-1, \tag{6}$$

$$SR_i(k) = \begin{cases} \sum\limits_{n=k}^{M-k-1} x_i(n+k)x_i^*(n-k), & k = 0,\ldots,M/2-1 \\ 0, & k = M/2 \\ SR_i^*(M-k-1), & k = M/2+1,\ldots,M-1 \end{cases}$$

$$x_i(n) = x_i(i\cdot M+n),\ i = 0,1,\ldots,K-1 \text{ and } M \text{ is even} \tag{7}$$

3. COMPUTER SIMULATIONS

Computer simulations were carried out for the following two tests;

3.1. Cross Term Elimination Test of Proposed Method

WVD nature has cross-term problems due to bilinear nature. In our proposed method cross terms are eliminated. To show this, two sinusoids at $f_1 = 20\,\mathrm{Hz}$ and $f_2 = 40\,\mathrm{Hz}$ are added, and power spectrum of the signal is calculated by proposed WVD method (given by Eqs. (4) & (5)). Result presented in Figure 1 depicts that expected cross-term at $f = 30\,\mathrm{Hz}$ is completely eliminated. This reduces false alarm.

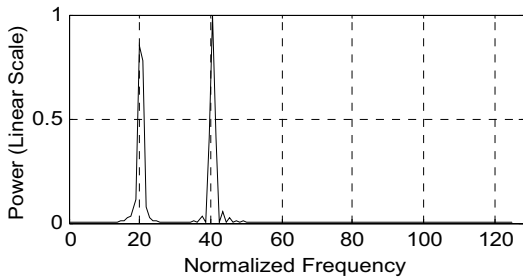

Figure 1: PSD of two tones ($f_1 = 20\,\text{Hz}$ and $f_2 = 40\,\text{Hz}$) by proposed method. (no cross term at $f = (f_1 + f_2)/2$).

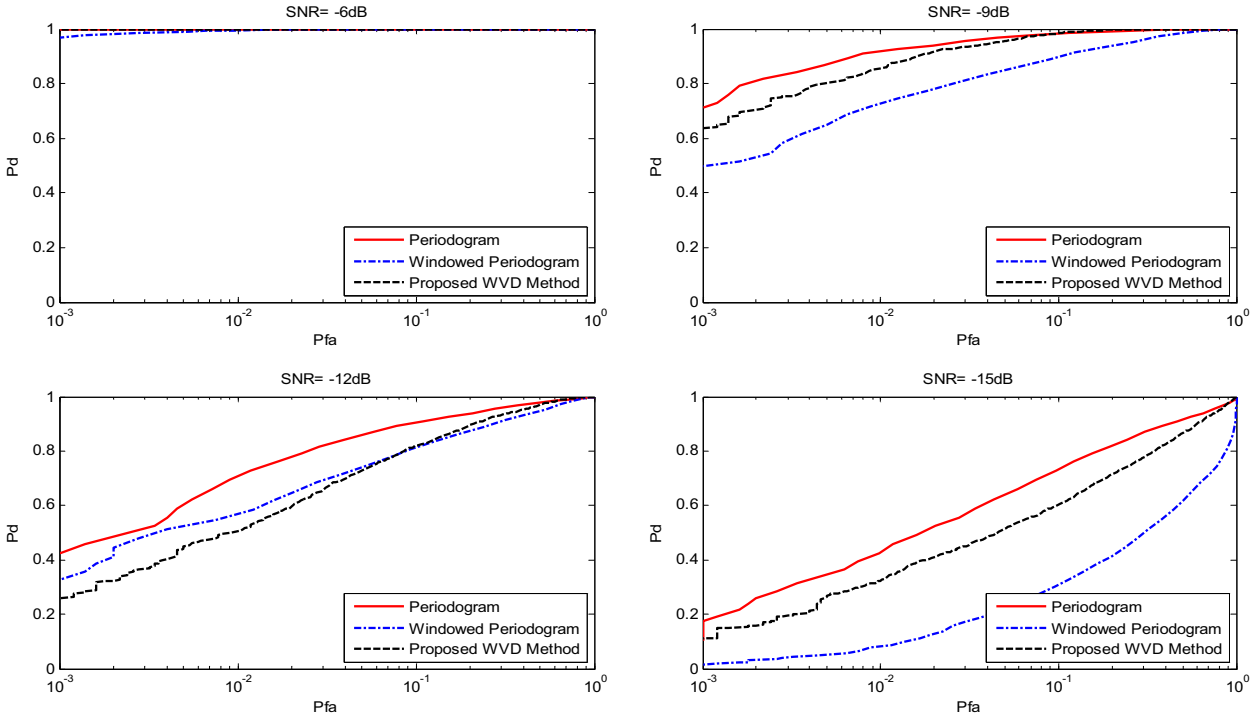

Figure 2: ROCs for detection of single sinusoid with frequency $f_0 = 0.25$ (in-bin) for different SNRs using Periodogram, windowed Periodogram and Proposed WVD method.

3.2. Single Tone Detection

In this test, the performances of Periodogram, its variants including the windowed periodogram, Bartlett method, method [2] and proposed WVD based method are analyzed. In this test, Single tone signal model and the Hypothetical analysis method ($H0$ & $H1$) described in detail under the heading of "Single Tone Detection" given in [1] is used. The receiver operating characteristic (ROC) are generated between false alarm probability $PFA = P(D1/H0)$ and detection probability $PD = P(D1/H1)$ [1]. White Gaussian noise with variance 1 was added to single tone signal having constant phase. Different SNRs were produced by properly scaling the signal power. The total sample size N was 256 and unless stated otherwise, the segment length M had a value of 64. The results for detection were averages of 50,000 independent runs. Validity of the test is confirmed by comparing ROCs (plotted by simulations only) of standard Periodogram and its variants with the results given in [1, 2] for same set of test parameters. The ROCs of the Proposed WVD method are compared with ROCs of following schemes;

- Standard Periodogram and Hamming Windowed Periodogram ($N = 256$, No segmentation)
- Bartlett Method & Bartlett Method proposed by [2] ($N = 256$, segments $K = 4, M = 64$)

Results are shown in Figures 2 to 4. Figure 2 shows the experimental ROCs in detecting a pure sinusoid in the presence of white Gaussian noise using the standard periodogram (with and without window) and our proposed method. Four values of SNR, namely, $-6\,\text{dB}$, $-9\,\text{dB}$, $-12\,\text{dB}$,

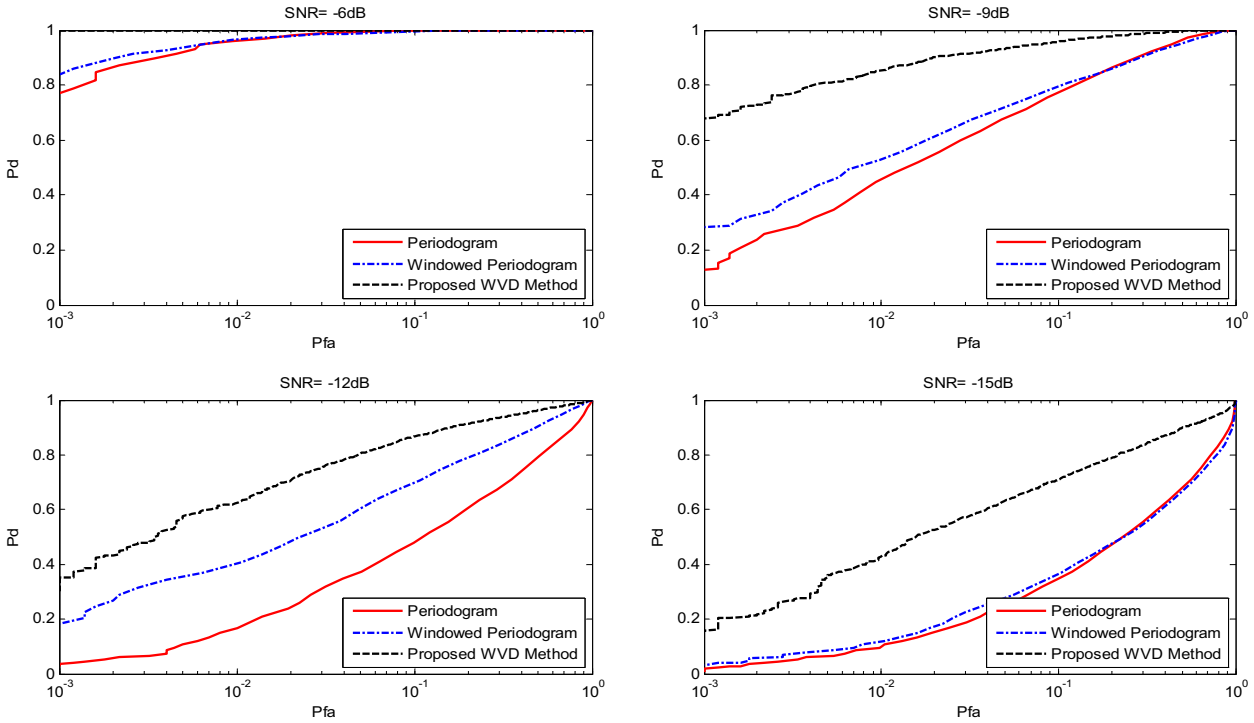

Figure 3: Comparison of ROCs for detection of single sinusoid with frequency $f_0 = 0.2578$ (off-bin) for different SNRs using Periodogram, windowed Periodogram and Proposed WVD method.

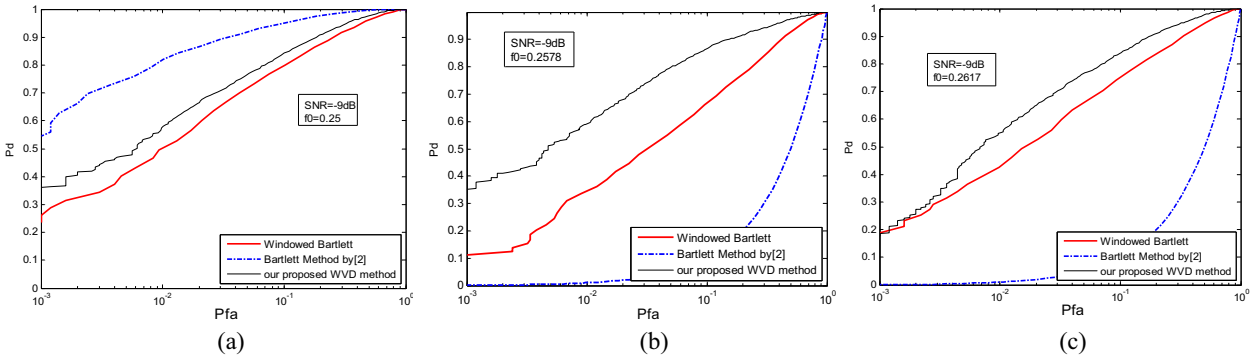

Figure 4: Comparison of ROCs for detection of single sinusoid by using windowed Bartlet, method [2] & Proposed SWVD″ Method (Segments $K = 4$, $SNR = -9\,\text{dB}$) with tone frequency. (a) $f_0 = 0.25$ (in-bin), (b) $f_0 = 0.2578$ (off-bin), (c) $f_0 = 0.2617$ (off-bin).

and $-15\,\text{dB}$ were tried. The frequency f_0 was chosen as 0.25 which corresponded to one of the FFT bins.

The test was repeated for off-bin frequency ($64.5/256 = 0.2520$) without interpolation and the results are shown in Figure 3. This shows our proposed method outperforms the windowed periodogram and gives a bit lower performance as compare to standard periodogram for in-bin frequency. However, the performance of proposed WVD based method is extremely promising for $f_0 = 0.2520$ (off-bin) frequencies than both standard and windowed periodogram for all SNRs. PD of our proposed method is about 72% for $PFA = 0.001$ at $SNR = -9\,\text{dB}$, while PD is only 15% for periodogram. Figure 4 shows the detection capability of our proposed segmented WVD method for segments $K = 4$. The method is compared with windowed Bartlett and method proposed by [2] for frequencies (0.25, 0.2578, 0.2617) at $SNR = -9\,\text{dB}$. Our proposed method gave promising results over Bartlett & method by [2] except for the case of $f_0 = 0.25$, where method by [2] performed better.

4. CONCLUSION

A Wigner Ville Distribution based new method is presented for detection of sinusoidal signal in white Gaussian noise. The cross-terms of WVD are eliminated through our proposed formulation to reduce the false alarms. The method is compared with standard Periodogram. The performance of reformulated proposed method (SWVD) for K data segments is compared with Periodogram variants (Bartlett & [2]) for the detection capability. The promising results obtained from the proposed method suggests it a better choice for use in radar systems for detection of moving targets. No use of windowing keeps the frequency resolution intact. The computational issue of the proposed method can be resolved by the use of high speed processing devices and techniques presented for real time implementation of WVD algorithm [4].

REFERENCES

1. So, H. C., Y. T. Chan, Q. Ma, and P. C. Ching, "Comparison of various Periodograms for sinusoid detection and frequency estimation," *IEEE Transactions on Aerospace and Electronic Systems*, Vol. 35, No. 3, July 1999.
2. Ahmed, F. M., K. A. Elbarbary, and A. R. H. Elbardawiny, "Anaytical performance evaluation of an enhanced frequency domain radar detector," *2008 IEEE Radar Conference, RADAR '08*, 1–5, May 2008.
3. Hero, A. (section wirtten by Alfred Hero), "Highlights of statistical and array signal processing," *IEEE SP Magazine*, submitted, June 1998.
4. Boashash, B. and P. J. Black, "An efficient real-time implementation of the Wigner-Ville distribution," *IEEE Transactions on Acoustics, Speech, and Signal Processing*, Vol. 35, No. 11, November 1987.
5. Chester, D., "Discrete Wigner implementation," *1986 Int. Symp. Circuit and Syst. Proc.*, 38–41, San Jose, CA, May 1986.
6. Abeysekera, S. S., "Computation of Wigner Ville distribution for complex data," *Electronics Letters*, Vol. 26, No. 16, 1315–1316, August 2, 1990.
7. Kumar, P. K. and K. M. M. Prabhu, "Simulation studies of moving target detection: A new approach with wigner-Ville distribution," *IEE Proc. — Radar, Sonar Navig.*, Vol. 144, No. 5, October 1997.
8. Debnath, L., "Recent development in the Wigner Ville distribution and time-frequency signal analysis," *PINSA*, Vol. 68, A, No. 1, 35–56, India, January 2002.

Effects of Millimeter Wave Exposure on Termite Behavior

A. Z. Tirkel[1], **J. C. S. Lai**[2], **T. A. Evans**[3], **and G. A. Rankin**[4]

[1]Scientific Technology, Australia
[2]University of New South Wales at the Australian Defence Force Academy, Australia
[3]CSIRO Entomology, Australia
[4]The University of Adelaide, Australia

Abstract— This paper presents experimental evidence, which demonstrates that resonant heating of termites at 28 GHz affects not only individual insects, but also their collective behavior. Termites have been attracted by, or repelled from the microwave beam. Collective behavior provoked by the beam included two modes: huddling by workers, and sacrificial exposure by soldiers.

1. INTRODUCTION

Termites cause billions of dollars of structural and cosmetic damage to buildings every year. A 24 GHz termite detector was developed by Scientific Technology, and commercialized by Termatrac© [1]. A third generation device with imaging capability is currently under development [2]. Apart from thermal effects, little is known about the effects that Termatrac© emissions have on the termites it senses. However, theoretical and experimental investigation of the interactions of millimeter and sub-millimeter waves with living things has a rich and varied history. This offers the intriguing possibility of termite provocation or control, using suitable emissions. Our experiments have confirmed that resonant heating of termites affects not only individual insects, but also their collective behavior. The paper is organized as follows. Section 2 discusses the state of knowledge about the non-thermal interactions of millimeter and sub-millimeter waves with living things, particularly insects. The discussion concerns interactions at a cellular level, and higher levels. None of these effects were observed in our experiments. Section 3 describes resonant heating experiments at 24 GHz and 28 GHz, their impact on individual insects, and on their collective behavior. This is followed by Section 4, the conclusions.

2. BACKGROUND

An understanding of the non-thermal effects of microwaves and millimeter waves on biological systems has far reaching consequences, whose impact cannot be underestimated. It encompasses the hazards of microwave exposure, its therapeutic use, biological control, sensing and weapons. It is also a complex problem, which has occupied many researchers, and perhaps that is why the debate has been clouded by emotion. Two types of interactions are pertinent to termites:

1. Cellular Interactions
2. Higher level interactions

2.1. Cellular Effects

A model of microwave-cell interactions was studied theoretically by Frohlich [3] in the 1960's and 1970's, who concentrated on the cell membrane. He calculated that the natural resonance of dipole charges on a typical cell membrane would be in the 50 GHz region, which was difficult to study experimentally at the time. 'How typical thought Frohlich for Nature to take advantage of our experimental incapabilities!' Frohlich's enthusiasm proved contagious, and a search for confirmation of the theory resembled the search for El Dorado, or the fountain of youth. The quest persists today.

Frohlich's evidence for such resonances was indirect. There was biological evidence that cell colonies synchronize their growth spurts, and this coincides with the appearance of sharp Raman absorption lines in the far IR. Lines below 6 THz are found in active (metabolizing) synchronized cells, whereas broad bands only are exhibited by both resting cells and nutrient solutions. The intensities of the Stokes and Anti-Stokes Lines were almost equal, so the process could not be attributed to a thermal effect. Frohlich concluded that living cells exhibited sharp energy states, which were pumped by a new metabolic process. The smallest separation of the levels which could be resolved at the time was 150 GHz, but Frohlich speculated that smaller separations must exist,

and that these should be commensurate with the natural frequencies of the oscillating dipoles of his model of the cell membrane.

An explanation of the narrowband nature of the absorption lines was needed. Frohlich postulated that this effect was due to a Bose condensation of the dipole oscillators, causing them to synchronize their frequencies, and therefore excite extremely narrow lines. Davydov [4] considered the effect to be due to soliton resonance. This led to the conclusion that metabolic energy may be used by biological systems to excite coherent vibrations in the millimeter and sub-millimeter region. Therefore, conversely, it should also be possible to use radiation at these frequencies to intervene in biological processes.

At a similar time, reports from the former Soviet Union indicated that narrowband absorption in many biological systems was observed, particularly around the 43 GHz, 51 GHz and 60 GHz regions, with some variation on that theme. This led to a frenzy of publications: experiments demonstrating the effects of narrowband absorption on cell growth and behavior, and modifications to the above theory justifying these results and vice versa. This has led to spin-offs, such as therapeutic use of specific millimeter wave frequencies as acupuncture treatment, specific cancer [5], and other pathology treatment, mimicking the Rife Machine [6], which purports to achieve such effects at lower frequencies. Millimeter wave therapy equipment and facilities are currently quite popular in the U.S.A., Russia and Eastern Europe.

A persistent issue is that of power density required for the effects to become apparent, i.e., a threshold. Belyaev et al. [7] claim to have demonstrated that exposure at the exact resonance frequency at power densities exceeding $10^{-19}\,\mathrm{W/cm^2}$ was sufficient to induce the "synchronization" effect in cell growth, therefore claiming that the threshold is practically zero. Osepchuk et al. [8] questioned the measurements as potentially flawed, a claim which was not addressed in Belyaevs subsequent rebuttal.

Numerous experimental papers give scant regard to the exact details of the equipment and measurement techniques, and thus, many results have not been successfully replicated, and must be called into question. This also applies to the theoretical papers justifying these results.

Clearly, this does not mean that the effects are not there, or that all experimental papers are flawed. A counter example, pertinent to insects is found in [9]. It was found that exposure of insects receiving ^{32}P orthophosphate to low-intensity (power density $0.5\,\mu\mathrm{W/cm^2}$) millimeter waves (42.2 GHz) changes the rate of label incorporation into their antennae. The magnitude of the effect is no less than 100–200%. The maximum response is reached 1.5–2 minutes after the onset of exposure.

2.2. Higher Level Effects

It has long been hypothesized that insects may use electromagnetic waves for sensing, navigation and communication. Pioneering work by Callahan, such as [10, 11] demonstrates that various moths are capable of modulating resonant IR emissions and presumably detecting such emissions. Callahan analyzed the performance of various anatomical parts of moths as dielectric waveguides and antennas, and constructed and characterized scale models at X band, demonstrating excellent performance. Gavan [12, 13] has extended this analogy to antenna arrays formed by spiked elements on the hornets cuticle. He speculated that hornets may use these arrays for navigation, deploying frequencies between 140 GHz and 600 GHz. His attempts to detect such emissions at 140 GHz were unsuccessful, but this was attributed to instrument limitations. An aspect of such investigations which appears to have been overlooked is the polarization of the transmissions, and the sensitivity of the detection to that polarization. It is known that insects with the ability of vision actively use polarization of skylight and reflected light for navigation [14], so it is also possible that any millimeter/sub-millimeter wave communication/navigation system might do so.

If it is true that insects employ millimeter and sub-millimeter wavelength emissions for communications, sensing and navigation, it offers the intriguing possibility of jamming their emissions or substituting false signals, in order to control them. This method has already been applied successfully by Evans et al. [15], who established that termites tap their food, and analyze its vibrational response, to assess its suitability as a food source. By recording various responses, and broadcasting them to termites, Evans et al. [15] managed to deceive termites, and induce them to sample wood that they would not normally eat, and conversely shun their favorite wood species.

A difficulty in assessing insect response to a given stimulus is that insects use other sensing methods, and their social interaction compounds the problem. Becker [16] has studied the effects of low frequency magnetic fields on termites. Recently, Esquivel et al. [17] have demonstrated, using

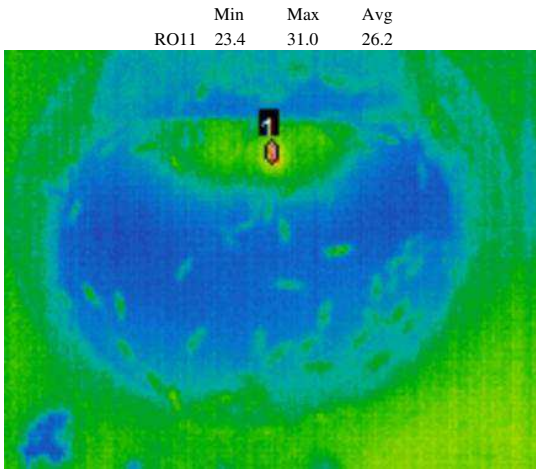

Figure 1: Termite "basking" under the horn.

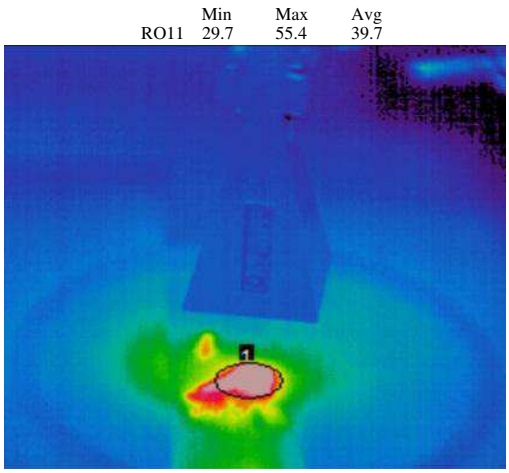

Figure 2: "Death huddle".

X band ferromagnetic resonance, that sufficient amounts of magnetite can accumulate in a termite body to act as a magnetic sensor.

Another aspect of this issue arises, because there exist commercial and exploratory termite sensors employing millimeter waves. The commercial sensor Termatrac©, operates in the ISM band at 24.125 GHz. An experimental sensor Fuji [18] operates at 100 GHz. As the millimeter wave spectrum becomes more congested, there are pressures to redistribute the ISM bands upwards in frequency. Concurrently, more devices are becoming available in these higher bands. Many of them involve components which generate harmonics, which are not easy to measure or control.

Therefore, it is important to establish whether exposure to these sensing frequencies, or any other critical millimeter wave frequencies can incidentally excite any of the non-thermal effects.

In view of this, it was decided to investigate termite response when exposed to 42 GHz and 60 GHz. No unusual effects were observed, although many more tests, as explained above, are required to confirm this.

3. THERMAL EFFECTS

It has been known that termites are affected by thermal and light gradients [19]. This paper demonstrates that individual and collective behavior of termites can be influenced by thermal effects induced by millimeter wave exposure. This offers the possibility of termite control. Three types of experiments were performed. First, termites in a Petri dish were exposed to 1.0 W of power at 24 GHz out of a pyramidal horn antenna (55×45 mm aperture) directly above the dish. The outlines of the dish and horn are visible in the thermal images taken by a NEC Thermo Tracer TH7102WV thermal camera, as shown in Fig. 1. The test worker termites (Mastotermes darwiniensis, approximately 12 mm long, and used in all three experiments) moved freely into and out of the beam and took turns in "basking" under the horn, achieving a maximum temperature of 31°C, which is within their thermal comfort zone and preferable to the ambient temperature of 22°C. The second experiment was also carried out in a Petri dish. Termites were exposed to 1.3 W at 28.24 GHz from a 30×30 mm pyramidal horn. It has recently been shown that 12 mm long termites exhibit resonant absorption near 25 GHz [20]. Individual termites exposed to the increased power density heated to 42°C. This was clearly uncomfortable for them, as evidenced by avoidance of the beam, and evasive behavior, such as reorienting their body to reduce the heating. Absorption is dependent on aspect angle and polarization [2]. In order to entice termites into the beam, a dead termite was placed in the center. This resulted in some termites venturing into the beam to investigate. These termites became distressed, and presumably sent distress signals to others, who followed, resulting in a huddle. This huddle proved suicidal, as shown in Fig. 2, where the peak temperature exceeded 55°C. Termites lack internal thermal regulation, and under the conditions in Fig. 2, lose most of their heat by radiation. The latter is proportional to ST^4, where S is the surface area and T is temperature in °K. By huddling, termites reduce their effective radiating surface area and increase the heat exchange between neighbors by radiation. This accounts for the extra 13°C rise in the huddle. Suicidal huddling behavior was also observed in termites "trying" to cross a water barrier, and it was also speculated that such huddles were also due to individuals

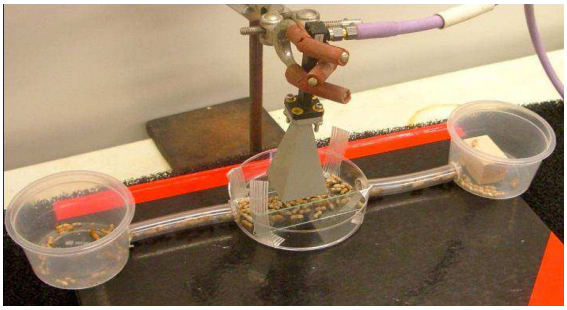

Figure 3: Mud tube simulation.

in distress (who fell into the water) attracting a crowd of other victims. Such social behavior for termites under distress has implications for termite control.

The setup involved in the third experiment is shown in Fig. 3. This simulates termites travelling to and from their nest via mud tubes. The "nest" with or without vermiculite is on the left, whilst the food (timber block) is on the right. In this case, no huddling was observed. However, after exposure, three soldier termites were observed in the beam, close to death, and unable to move. The soldiers did not attract the other caste termites, unlike what happened in the second experiment, Fig. 2. It is still not known why the soldiers did not save themselves. One possible reason is perhaps to stop workers from entering a danger zone as the job of the soldiers is to protect workers.

4. CONCLUSIONS

It appears that resonant absorption of millimeter wave radiation has the potential to kill, or to alter the social behavior of termites. In order to recreate a practical situation, a lens antenna is planned for the next experiment. This lens will increase the power density to compensate for the transmission losses through building materials.

ACKNOWLEDGMENT

This research was supported under the Australian Research Councils Linkage Projects funding scheme (project number LP0669638). The authors acknowledge the University of New South Wales at the Australian Defence Force Academy and CSIRO Entomology for research infrastructure support, Termatrac Pty Ltd and Scientific Technology Pty Ltd (industrial partners) for their facilities and equipment for this project.

REFERENCES

1. http://www2.termatrac.com/index.php?page=the-company.
2. Le Marshall, N. W. D., G. A. Rankin, and A. Z. Tirkel, "High resolution, wide coverage termite imager," *PIERS Proceedings*, 663–667, Xi'an, China, March 22–26, 2010.
3. Frohlich, H., "Coherent electric vibrations in biological systems and the cancer problem," *IEEE Transactions on Microwave Theory and Techniques*, Vol. 26, No. 8, 613–617, 1978.
4. Davydov, A. S., "Solitons and energy transfer along protein molecules," *Journal of Theoretical Biology*, Vol. 66, 379–387, 1977.
5. Makar, V. R., M. K. Logani, A. Bhanushali, M. Kataoka, and M. C. Ziskin, "Effect of millimeter waves on natural killer cell activation," *Bioelectromagnetics*, Vol. 26, 10–19, 2005.
6. http://www.electroherbalism.com/Bioelectronics/FrequenciesandAnecdotes/CAFL.htm.
7. Belyaev, I. Y., V. S. Shcheglov, Y. D. Alipov, and V. A. Polunin, "Resonance effect of millimeter waves in the power range from 10^{-19} to 3×10^{-3} W/cm^2 on escherichia coli cells at different concentrations," *Bioelectromagnetics*, Vol. 17, 312–321, 1996.
8. Osepchuk, J. M. and R. C. Petersen, "Comments on resonance effect of millimeter waves in the power range from 10^{-19} to 3×10^{-3} W/cm^2 on escherichia coli cells at different concentrations," *Bioelectromagnetics,* Vol. 18, 527–528, 1997.
9. Agafonova, N. K., N. E. Krassova, and E. E. Fesenko, "Rapid changes in phosphoinositide metabolism in antennae of insects exposed to low-intensity millimeter microwaves," *Biophysics*, Vol. 41, No. 2, 333–337, 1998. Translated from Biofizika, Vol. 41. No. 2, 353–357, 1998.

10. Callahan, P. S., "Insect antennae with special reference to the mechanism of scent detection and the evolution of the sensilla," *International Journal of Insect Morphology & Embryology*, Vol. 4, No. 5, 381–430, 1975.
11. Callahan, P. S., "Dielectric waveguide modeling at 3.0 cm of the antenna sensilla of the lovebug, plecia neartica hardy," *Applied Optics*, Vol. 24, No. 8, 1094–1097, 1985.
12. Gavan, J. and J. S. Ishay, "Hypothesis of natural radar tracking and communication direction finding systems affecting hornets flight," *Progress In Electromagnetics Research*, Vol. 34, 299–312, 2001.
13. Gavan, J., "Hypothesis of hornets biological thf radar for detection tracking and communication," *Asia-Pacific Conference on Environmental Electromagnetics*, 534–538, 2006.
14. Wehner, R., "Polarization vision — A uniform sensory capacity?," *The Journal of Experimental Biology*, Vol. 204, 2589–2596, 2001.
15. Evans, T. A., J. C. S. Lai, E. Toledano, L. McDowall, S. Rakotonarivo, and M. Lenz, "Termites assess wood size by using vibration signals," *Proceedings of the National Academy of Sciences*, Vol. 102, No. 10, 3732–3737, 2005.
16. Becker, G., "Communication between termites by biofields," *Biological Cybernetics*, Vol. 26, 41–44, 1977.
17. Esquivel, D. M. S., E. Wajnberg, G. R. Cernicchiaro, and O. C. Alves, "Comparative magnetic measurements of migratory ant and its only termite prey," *Journal of Magnetism and Magnetic Materials*, Vol. 278, 117–121, 2004.
18. Fujii, Y., Y. Fujiwara, Y. Yanase, S. Okumura, K. Narahara, T. Ngatsuma, T. Yoshimura, and Y. Imamura, "Nondestructive detection of termites using a millimeter-wave imaging technique," *Forest Products Journal*, Vol. 57, No. 10, 75–79, 2007.
19. Cabrera, B. J. and M. K. Rust, "Behavioral responses to light and thermal gradients by the western drywood termite (isoptera: kalotermitidae)," *Physiological and Chemical Ecology*, 436–445, 1996.
20. Tirkel, A. Z., J. C. S. Lai, T. A. Evans, and G. A. Rankin, "Heating and provocation of termites using millimeter waves," *PIERS Proceedings*, Marrakesh, Morocco, March 20–23, 2011.

Heating and Provocation of Termites Using Millimeter Waves

A. Z. Tirkel[1], **J. C. S. Lai**[2], **T. A. Evans**[3], **and G. A. Rankin**[4]

[1]Scientific Technology, Australia
[2]University of New South Wales at Australian Defence Force Academy, Australia
[3]CSIRO Entomology, Australia
[4]The University of Adelaide, Australia

Abstract— This paper presents thermal and non-thermal effects of millimeter wave exposure of various species of termites. Termites exhibit resonant absorption in the millimeter wave region, where Mie scattering dominates, and therefore direct heating of termites with minimal background heating is possible. Our experiments show that scatter and absorption simulations are confirmed at 24 GHz, 43.2 GHz and 60.2 GHz.

1. INTRODUCTION

This paper presents thermal and non-thermal effects of millimeter wave exposure of various species of termites. Conventional eradication uses an array of microwave horns powered by domestic 2.45 GHz magnetrons generating many kilowatts of power, see Fig. 1. This heats the surrounding building materials to above 55°C, which then causes mortality. Direct absorption is negligible, as termite dimensions are a small fraction of a wavelength, and so are well into the Rayleigh region. By contrast, typical termites exhibit resonant absorption in the millimeter wave region, where Mie scattering dominates, and therefore direct heating of termites with minimal background heating is possible.

2. PHYSICAL MODEL

The radar cross section of insect species has been modelled by treating them as drops of water of equivalent size and shape [1]. However, until now, very few scattering or absorption measurements of insects have been performed beyond 13 GHz. Liquid water exhibits dielectric relaxation at around 22 GHz causing significant dispersion and loss. Also, termites possess an exoskeleton, whose thickness is an increasing fraction of a wavelength as the frequency increases. Both these effects are considered in order to develop an appropriate physical model for frequencies between 10 GHz and 110 GHz.

Termites are composed of approximately 77% water [2]. The water component in living organisms is further divided into free water and bound water. The bound water molecules are attached to proteins, lipids etc. The combination is known as biological water. The dielectric properties of biological water have been studied extensively from DC to the IR. This has led to a model for the dielectric constant based on a frequency-dependent dielectric function, $\epsilon(z)$, (where $z = j\omega$) which includes n Debye relaxation processes and m vibrational modes [3]. $\Delta\epsilon_i$ is the weight of the ith Debye relaxation with relaxation time constant τ_i, and Δw_j is the weight of the jth vibrational

Figure 1: Termite eradication using an array of magnetrons heating surrounding materials.

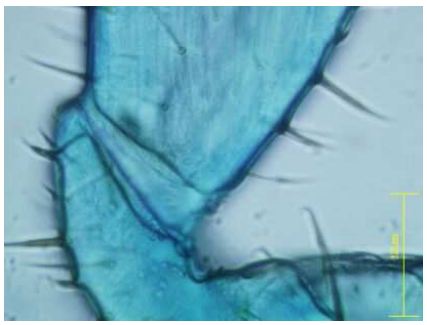

Figure 2: Leg of a Coptotermes acinaciformis (Courtesy of R. Ata Inta, UNSW@ADFA).

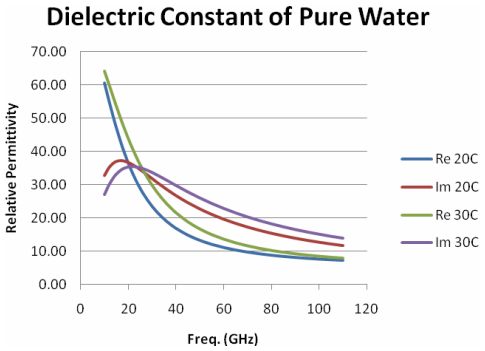

Figure 3: Relative permittivity of liquid water [9, 10].

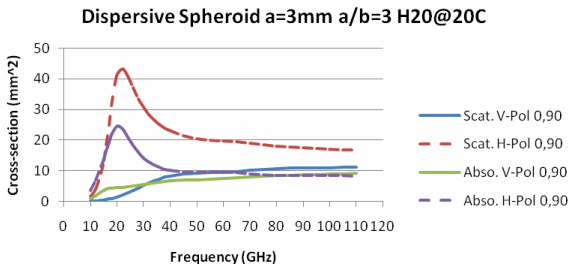

Figure 4: Scattering and absorption for 6 mm spheroid, aspect ratio 3, temperature 20°C.

Table 1: Effect of chitin layer on scattering, computed reflection and transmission.

Model		Reflection	Transmission
Layer 1	**Layer 2**		
Chitin [6]	**Water**	0.58	0.44
Chitin [7]	**Water**	0.58	0.44
None	**Water**	0.58	0.49

mode with vibrational moment correlation function Φ_j.

$$\epsilon(z) = \epsilon_0 + \sum_{i=1}^{n} \frac{\Delta\epsilon_i}{1 + z\tau_i^D} + \sum_{j=1}^{m} \Delta w_j (1 - z\Phi_j(z)) \tag{1}$$

It is clear that the major component of the relaxation spectrum due to water is between 8 and 10 ps with a weight of about 60 [4]. Other relaxation processes are far removed from this. There are two Debye absorption peaks around 100 MHz and 20 GHz for most biological materials. The low-frequency absorption is due to bound water, while the high-frequency absorption is due to free water and corresponds to the 8–10 ps relaxation time [5]. The bound water contribution at frequencies above 10 GHz is assumed to be negligible. Pure water and biological water have another much higher relaxation frequency around 850 GHz, and resonant absorption peaks between 2 and 20 THz.

Insect bodies are covered by an exoskeleton composed of a thin layer of chitin. A picture of a part of the leg of a typical termite is shown in Fig. 2. The scale marker is 125 µm. It indicates a chitin layer thickness of 5 µm. The dielectric properties of chitin have been studied extensively [6]. Insect exoskeleton is claimed to have a dielectric constant between 2.5 and 3 [7].

In order to evaluate the effect of the chitin layer on scattering, reflection and transmission were computed for pure water and for water coated with a 5 µm layer of chitin at normal incidence using Luxpop [8], see Table 1. The dielectric constant of water, derived from [9, 10], see Fig. 3, was varied to cover the 10 GHz to 100 GHz range.

It is clear from the computed reflection and transmission in Table 1 that the chitin layer reduces the transmission into water slightly. The effect appears to be independent of frequency from 10 GHz to 100 GHz. This is due to the small thickness of the layer compared to the wavelength. The errors due to the omission of the chitin layer from our scattering and absorption simulations is less than 10% and is therefore considered negligible.

3. SIMULATION OF SCATTERING AND ABSORPTION FROM TERMITES

The scattering and absorption of termites was investigated in a series of simulations using the software tool Mieschka [11], and a spheroid where the dielectric is liquid water. A dielectric spheroid is a representative object which can approximate the overall size, aspect ratio and composition of an actual termite. Mieschka computes, the total scattering of an incident plane wave from an object using Waterman's T-matrix method, which relates the incident field and the object geometry to the scattered field, and the absorption of an object based on the difference between the incident field and the scattered field. Mieschka's uniqueness lies in its ability to compute scattering estimates

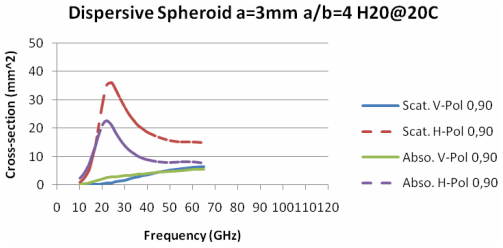

Figure 5: Scattering and absorption for 6 mm spheroid, aspect ratio 4, temperature 20°C.

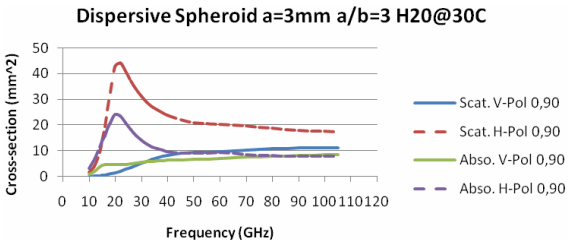

Figure 6: Scattering and absorption for 6 mm spheroid, aspect ratio 3, temperature 30°C.

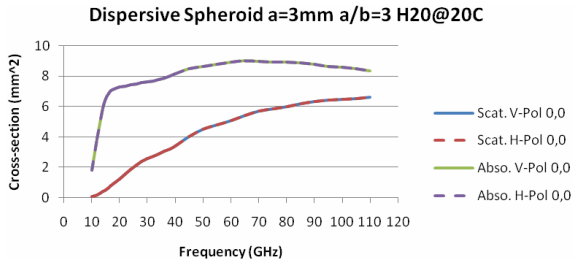

Figure 7: Scattering and absorption for 6 mm spheroid, aspect ratio 3, end-on, temperature 20°C.

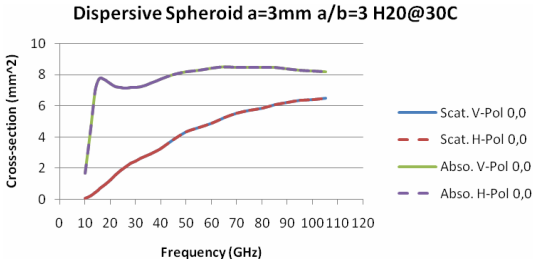

Figure 8: Scattering and absorption for 6 mm spheroid, aspect ratio 3, end-on temperature 30°C.

from objects in the resonant region, where approximations cannot be applied due to diffraction, and induced current effects. Mieschka was extensively validated against well-known results for resonant metallic and non-dispersive dielectric spheres.

Termites come in different sizes, depending on the species: the smallest termites are of the order of 4 mm in length and a typical termite may be 6 mm in length, although an upper limit is 12 mm. The simulations in this paper examine a spheroid with semi-major axis $a = 3$ mm, corresponding to a termite of length 6 mm, which is an average size. Scattering and absorption results for the broadside aspect ($\theta = 90°$, $\phi = 0°$) for the electric field parallel (H-Pol.) and perpendicular (V-Pol.) to the major axis for a 6 mm spheroid at 20°C with aspect ratio of 3 and 4 respectively are presented in Figs. 4 and 5.

These simulations show that near resonance the amount of scattering and absorption is much larger than the geometric cross-sections of the two spheroids (9.4 and 7.1 mm^2 respectively). They also show that the amount of scattering decreases with the increase in aspect ratio (43 to 35 mm^2) and that the absorption ratio also decreases with the increase in aspect ratio (24/4.4 vs 21/2.1). The resonant frequencies do not appear to be affected by the change in the aspect ratio.

Scattering and absorption results for the broadside aspect under the same conditions as Fig. 4 for a 6 mm spheroid at 30°C are presented in Fig. 6. These simulations show only minor variations in the amounts of scattering and absorption with a 10°C change in temperature. This suggests that the water resonance due to relaxation at 22 GHz and the object self-resonance are well separated under these conditions, whereas in Figs. 7 and 8, for the end-on aspect ($\theta = 0°$, $\phi = 0°$), the water resonance and object resonance are much closer together giving rise to a shift in resonances and anti-resonances in the range 15 to 20 GHz. This can be accounted for by the shift and broadening in the resonance in the imaginary part of the permittivity of liquid water, see Fig. 3.

4. EXPERIMENTS

Figure 9 shows thermal signatures of various termites exposed to 24 GHz obtained using a NEC Thermo Tracer TH7102WV thermal imaging camera. The temperature rise is directly related to size. The transmitter power was 1.5 W. Termites in a petri dish were exposed to a pyramidal horn antenna (55 mm × 45 mm aperture) directly above the dish. The outlines of the dish and horn are visible in the thermal images. Fig. 10 shows the polarization dependence of the temperature rise for two equal size termites. The termite oriented with its long axis parallel to the electric field shows much greater heating, indicating that absorption is greater. Thermal signatures of various termites exposed to 43.2 GHz (transmitter power into antenna +24 dBm, antenna aperture 35 mm × 26 mm)

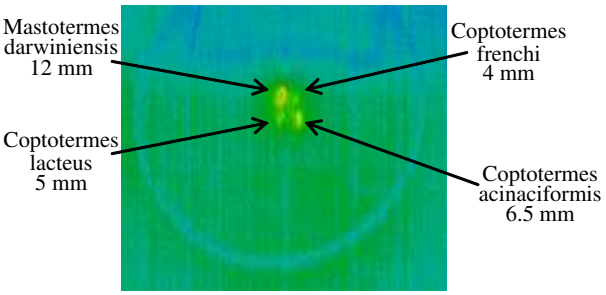

Figure 9: Size dependence of temperature rise.

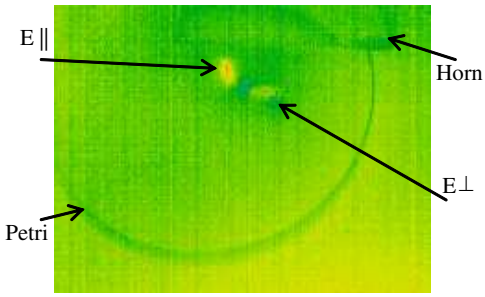

Figure 10: Polarization dependence of temp. rise.

and 60.2 GHz (transmitter power into antenna +18 dBm, antenna aperture 19 mm × 14.5 mm) showed high back scatter, consistent, with the second and third Mie resonance peaks, and negligible heating due to absorption.

5. CONCLUSIONS

Our experiments show that scatter and absorption simulations are confirmed at 24 GHz, 43 GHz and 60 GHz, which is in agreement with theory [12].

ACKNOWLEDGMENT

This research was supported under the Australian Research Council's Linkage Projects funding scheme (project number LP0669638). The authors acknowledge the University of New South Wales at the Australian Defence Force Academy and CSIRO Entomology for research infrastructure support, Termatrac Pty Ltd and Scientific Technology Pty Ltd (industrial partners) for their facilities and equipment for this project.

REFERENCES

1. Riley, J. R., "A millimetric radar to study the flight of small insects," *Electronics & Communication Engineering Journal*, Vol. 4, No. 1, 43–48, 1992.
2. Cooper, C. E. and P. C. Withers, "Termite digestibility and water and energy contents determine the water economy index of numbats (myrmecobius fasciatus) and other myrmecophages," *Physiological and Biochemical Zoology*, Vol. 77, No. 4, 641–650, 2004.
3. Nandi, N., K. Bhattacharyya, and B. Bagchi, "Dielectric relaxation and solvation dynamics of water in complex chemical and biological systems," *Chem. Rev.*, Vol. 100, 2013–2045, 2000.
4. Pickwell, E., B. E. Cole, A. J. Fitzgerald, V. P. Wallace, and M. Pepper, "Simulation of terahertz pulse propagation in biological systems," *Applied Physics Letters*, Vol. 84, No. 12, 2190–2192, 2004.
5. Satoru, M., K. Shinichi, Y. Shin, and H. Keniti, "Dielectric relaxation time and structure of bound water in biological materials," *J. Phys. Chem.*, Vol. 91, 6337–6338, 1987.
6. Lima, C. G. A., R. S. de Oliveira, S. D. Figueiro, C. F. Wehmannd, J. C. G'oes, and A. S. B. Sombra, "DC conductivity and dielectric permittivity of collagen-chitosan films," *Materials Chemistry and Physics*, Vol. 99, 284–288, 2006.
7. Callahan, P. S., "A High frequency dielectric waveguide on the antennae of night-flying moths (saturnidae)," *Applied Optics*, Vol. 7, No. 8, 425–1430, 1968.
8. http://www.luxpop.com/.
9. http://www.lsbu.ac.uk/water/microwave.html.
10. Meissner, T. and F. J. Wentz, "The complex dielectric constant of pure and sea water from microwave satellite observations," *IEEE Transactions on Geoscience and Remote Sensing*, Vol. 42, No. 9, 1836–1849, 2004.
11. Wauer, J., K. Schmidt, T. Rother, T. Ernst, and M. Hess, "Two software tools for plane-wave scattering on nonspherical particles in the german aerospace center's virtual laboratory," *Applied Optics*, Vol. 43, 6371–6379, 2004.
12. Barber, P. W., "Resonance electromagnetic absorption by nonspherical dielectric objects," *IEEE Transactions on Microwave Theory and Techniques*, Vol. 25, No. 5, 373–381, 1977.

Electromagnetic Information Transfer of Specific Molecular Signals Mediated through Aqueous Systems: Experimental Findings on Two Human Cellular Models

Alberto Foletti[1], **Settimio Grimaldi**[2], **Mario Ledda**[2], **and Antonella Lisi**[2]

[1]Independent Researcher, Lugano, Switzerland
[2]Institute of Neurobiology and Molecular Medicine, CNR, Rome, Italy

Abstract— Electromagnetic Information Transfer (EMIT) of Specific Molecular Signals according to previous report [3, 5] and ours [1] is having his serious experimental evidence.

The aim of the present work is to understand the possible role of water in mediating the electromagnetic information transfer of biological active molecules [5] such as retinoic acid (RA).

The electromagnetic information signals from the retinoic acid solution (RA-EMIT) was captured and transferred to the target as previously described by a commercially available oscillator (Vegaselect 719). In the present study the retinoic acid signals was first transferred to the cell's culture medium (RA-EMIT conditioned medium) then cells (LAN-5 neuroblatoma and NT2/D1 human teratocarcinoma) cells seeded with RA-EMIT off.

The same experiment was repeated culturing cells under continuous RA-EMIT conditions.

As an overall control the direct differentiating effect of RA solution on cell's culture was reported.

These experimental findings demonstrated that the RA-EMIT conditioned medium behave like retinoic acid thus inducing cell differentiation in both cell's lines.

1. TRANSMISSION APPARATUS

For transmission experiments (Fig. 1) to cells, the input coil coupled to wave generator VEGA select 719 was operated at room temperature, while the output coil was placed in cell incubator. The source tube containing 5 µM RA and target coil containing LAN-5 cells. The electronic signal corresponding to RA was superimposed to both a 7 Hz sinusoidal frequency carrier modulated at 3 KHz.

The oscillator was then turned on for 12 hrs a day for 5 days. During the experimental procedure, the various parameters such as power, voltage, capacitance and impedance remained constant.

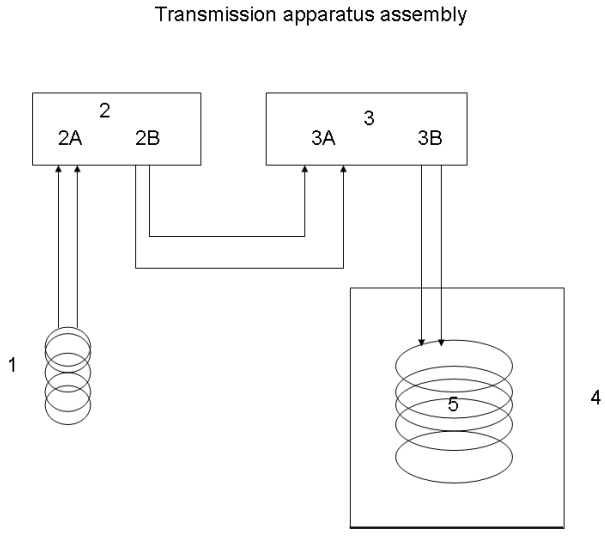

Figure 1: Experimental apparatus and assembly. 1: Source signal coil, 2: Electronic amplifier, 2A: input signal in the electronic amplifier, 2B: output signal from the electronic amplifier, 3: wave generator, 3A: input signal in wave generator, 3B: output signal from wave generator, 4: cell incubator, 5: target coil.

2. CONDITIONED EXPERIMENTS

For conditioned experiments cells medium were first continuosly exposed to RA-EMIT for 24 hrs, than RA-EMIT were turned off LAN-5 and NT2/D1cells were seeded and cultured to the end of the experiment.

3. CELLULAR METABOLIC ACTIVITY AND PROLIFERATION BY WST ASSAY

LAN-5 and NT2/D1cells were exposed to the electronically transmitted RA EMS by Vega select 719 and to conditioned medium. For each experiment LAN-5 and NT2/D1 cells were plated into 25 ml 4.2×5.2 cm base Corning flasks (2.0×10^5/ml cells in a total volume of 5 ml). The flasks were kept in the exposure system continuously for up to 5 days with or without RA-EMS with or without condizioned medium. Cells were then counted and metabolism determined by WST-1 method. The experiment was repeated three times.

The quantification of LAN-5 and NT2/D1 metabolic activity, as an index of cellular proliferation, was performed by a colorimetric assay based on oxidation of tetrazolium salts (Cell Proliferation Reagent water-soluble tetrazolium salt (WST)-1; Roche Diagnostics, Basel, Switzerland). Cells were cultured for up to 5 days in a normal humidified incubator (control) or in the presence of the RA-EMS (exposed), and they were analysed by means of the formazan dye every 24 h. WST reagent diluted to 1 : 10 was added in the wells at 4 h, 1, 2, 3 and 6 days after plating, and then incubated for 2 h in humidified atmosphere (37 8C, 5% CO2). Quantification of the formazan dye produced was performed by absorbance measurement at 450 nm with a scanning multiwell spectrophotometer (Biotrack II; Amersham Biosciences, Little Chalfont, UK).

4. STATISTICAL ANALYSIS

Statistics was performed with Student's t-test with $P < 0.05$ as the minimum level of significance.

5. RESULTS

5.1. Electronically Transmitted RA-EMIT and Conditioned Medium Effect on LAN-5 and NT2/D1cell Metabolism

The cell growth rate was analyzed by the WST-1 both in LAN-5 and NT2/D1cells as control (not exposed electronically transmitted RA) or exposed to the field with or without conditioned medium. An inhibition in the cell metabolism in the electronically transmitted RA (RA-EMIT) exposed and conditioned medium exposed was statistically ($p < 0.01$) significant after 5 days exposure (Table 1).

LAN-5 and NT2/D1 metabolic activity by WST-1 analysis in presence of RA-EMS and conditioned medium compared with RA as control.

6. DISCUSSION

Low frequency electromagnetic fields at 50 or 60 Hz indeed are reported to stimulate nerve regeneration, alter gene transcription [4] and they may also play a synergistic role in cellular processes that are already activated, such as cell proliferation. Despite an increasing number of publications demonstrate an effect of very low frequencies EM field on biological systems, other in vivo and in vitro studies suggest opposite results; in addition the possible interaction mechanism is not yet completely understood.

A possible mechanisms evoked to explain the mechanism of EM field action to biological system is involving Ca^{2+} transport across cell membrane, to trigger the signal transduction cascade.

Electromagnetic therapeutic potential can be seen in the proven efficacy of low-energy pulsed magnetic fields in non-union bone fracture healing, confirming that under certain conditions non-ionising electro-magnetic energy can influence physiological processes in organisms. Physiological

Table 1: Cellular metabolic activity and proliferation by WST assay.

LAN-5 and NT2/D1 metabolic activity by WST-1			
Cells line	Control	RA-EMIT	conditioned medium
Lan-5	1	0.7	0.5
NT2/D1	1	0.66	0.51
±S.D			

paradigms for non-ionising radiation effects are required. Clues may be found in the mechanisms by which EM field interacts with cultured cells under controlled laboratory conditions and by correlating in vivo evidence with in vitro data. Brain maturation depends on a sequence of postnatal events. The electromagnetic information signals from the retinoic acid solution (RA-EMIT) was captured and transferred to the target as previously described by a commercially available oscillator (Vegaselect 719). The retinoic acid signals was first transferred to the cell's culture medium (RA-EMIT conditioned medium) then cells (LAN-5 neuroblatoma and NT2/D1 human teratocarcinoma) cells seeded with RA-EMIT off.

As an overall control the direct differentiating effect of RA solution on cell's culture was reported.

These experimental findings demonstrated that the RA-EMIT conditioned medium behave like retinoic acid thus inducing cell differentiation in both cell's lines demonstrating a significant effects on cells proliferation leading to a 30% inhibition of cell metabolism.

Taken together all these data support an evident effect of the electronically transmitted retinoic acid (RA-EMS) electromagnetic field of driving LAN-5 and NT2/D1 cells toward a neuronal differentiation, which resembles the effect determined by morphogens, such as retinoic acid in its chemical form. The possibility to induce differentiation elicited by our system through extremely low frequency electromagnetic field represent an effective, minimally manipulating, and safe biotechnological tool to improve neurogenic differentiation in neurodegenerative diseases.

The physical nature of the nanostructures which support the EMS resonance remains to be determined. Several speculation at this time can proposed as a model to explain the effect of RA-EMIT conditioned medium on cells differentiation ranging from self maintained water structure due to RA-EMIT conditioned medium exposure as well as an alteration between free and bound calcium in RA-EMIT conditioned medium.

REFERENCES

1. Foletti, A. and S. Grimaldi, "Differentiation of human LAN-5 neuroblastoma cells by electronically trasmitted retinoic acid (RA)," *PIERS Online*, Vol. 6, No. 6, 518–522, 2010.
2. Lo, S. Y., X. Geng, and D. Gann, "Evidence for the existence of stable-water-cluster at room temperature and normal pressure," *Physics Letters A*, Vol. 373, 3872–3876, 2009.
3. Montagnier, L., J. Aissa, S. Ferris, J.-L. Montagnier, and C. Lavallée, "Electromagnetic signals are produced by aqueous nanostructures derived from bacterial DNA sequences," *Interdisciplinary Sciences Computational Life Sciences*, Vol. 1, 245–253, 2009.
4. Preparata, G., "QED and medicine," *Rivista di Biologia*, Vol. 93, 467–512, 2000.
5. Thomas, Y., M. Schiff, L. Belkadi, P. Jurgens, L. Kahhak, and J. Benveniste, "Activation of human neutrophils by electronically transmitted phorbol-myristate acetate," *Medical Hypotheses*, Vol. 54, 33–39, 2000.

Vectorial Electro-optic Sensors for Microwave Dosimetric Applications

P. Jarrige[1, 2], S. Kohler[3], N. Ticaud[3], L. Duvillaret[1], G. Gaborit[1, 2], P. Leveque[3], and D. Arnaud-Cormos[3]

[1]Kapteos SAS, rue Lac de la Thuile, F-73376 Le Bourget-du-Lac Cedex, France
[2]IMEP-LAHC, CNRS, University of Savoie, F-73376 Le Bourget-du-Lac Cedex, France
[3]XLIM Research Institute, CNRS, University of Limoges, F-87060 Limoges, France

Abstract— Fully dielectric pigtailed electro-optic sensors have been developed to quantify the energy absorbed by biological tissues exposed to radiofrequency telecommunication signals (GSM, UMTS, Wifi, WIMAX). Both applied electric field and temperature are simultaneously measured, leading to the specific absorption rate (SAR) which constitutes the reference parameter for microwave dosimetric applications. Measurements have been performed in the air and in a biological solution. In the frequency-domain, the electro-optic (EO) probe presents a dynamic range exceeding 70 dB and a sensitivity of 200 mV/m·Hz$^{1/2}$ in the biological medium. As it presents an intrinsic flat response from quasi DC to 20 GHz, electro-optic probes have also been used in the time-domain to perform first *in situ* measurements of ultrashort electric pulses in an electroporation cuvette. A temperature probe sensitivity of 3 mK has been reached.

1. INTRODUCTION

One purpose of dosimetric studies is to investigate potentiel effects of radiofrequency (RF) electromagnetic fields (EMF) on living tissues. Thus, SAR evaluation constitutes a major issue to quantify the power absorbed by living tissues exposed to RF EMF. Its evaluation is conducted using either the temperature increase induced by RF exposition or the electric (E) field within the biological medium. Many sensors dedicated to E-field or temperature measurements in biological media have been developed, like thermistors [1], devices based on thermo-optic effects [2], EO probes [3, 4] or sensors based on diode-loaded dipoles [5]. Due to their fully dielectric structure, EO probes are much less invasive than metal-based devices, limiting perturbations on the E-field to be measured.

The pigtailed EO probe presented in this paper can measure simultaneously, and at the same location, one E-field component over an ultra-wide frequency band (kHz-GHz frequency range) and the temperature variations [6]. The probe is based on Pockels' effect which traduces the linear variation of the refractive indices of an EO crystal with the applied E-field. We have developed an EO sensor based on the polarization state modulation of a laser beam probing a 7.1-mm long EO crystal of x-cut $LiTaO_3$. The relative phase shift $\Delta\varphi$ induced by the birefringence of the crystal is the sum of a relative phase shift $\Delta\varphi_0$ due to the intrinsic birefringence Δn_0 (varying with the temperature) and a relative phase shift $\Delta\varphi_E$ due to the RF E-field induced birefringence Δn_E. By compensating $\Delta\varphi_0$, it is possible to decorrelate the effects of temperature from those of applied E-field and thus to measure each of them. The EO probe is associated with a servo-controlled optical system that is continuously locked on an optimal working-point, corresponding both to highest sensitivity and linearity of the probe response. The EO crystal temperature variations are deduced from the values of the parameters that allow the system to compensate thermal drifts. Furthermore, the $LiTaO_3$ crystal presents a relative permittivity of 42 in the GHz range, closed to those of biological media. This leads to a relative low wave-impedance mismatch between the EO probe and the biological media, which is of major importance for high accuracy measurements.

The paper is divided in two parts. In the following section, we present a characterization of the EO probe in the frequency-domain: results on linearity, selectivity, sensitivity are discussed and lead to SAR evaluations. In the last section we present our first results in the time-domain.

2. RESULTS IN THE FREQUENCY-DOMAIN

The experimental setup for both E field and temperature measurements is presented in Fig. 1. A cuvette, filled with a 3 ml buffered salt solution ($\sigma = 1.77$ S/m and $\varepsilon_r = 80.3$ at 1.8 GHz) is placed in a TEM cell mounted on a rotation stage and loaded by a 50 Ω load. The cell is fed by a signal generator and followed by a 40-dB RF amplifier. A circulator is used for protection purpose. The output of the EO device is connected to a spectrum analyzer and the EO probe is inserted in

the cuvette. Linearity and selectivity measurements are done in air and in the biological medium. For temperature measurements, the EO probe is inserted in a Petri dish subjected to the same experimental conditions. All measurements have been done at 1.8 GHz (GSM carrier frequency).

2.1. E-field Measurements

In the air, the EO probe response is linear for a synthetizer output power ranging from −60 dBm (noise floor lower bound P_{low}) up to −1 dBm (microwave amplifier saturation upper bound P_{high}). In between the limits P_{low} + 3 dBm and P_{high} − 3 dBm, the best linear fit of the measurement data leads to a slope of 1.004 ± 0.004 with a standard deviation of 0.4 dB involving not only the EO measurement standard deviation but also standard deviations of nominal synthetizer output power and of nominal RF amplifier gain. Same measurements and data treatment have been realized with the EO probe submerged by the biological medium leading to a slope of 0.997 ± 0.007 with a dynamic range exceeding 70 dB. This latter one is limited by the RF amplifier saturation. A standard deviation of 0.7 dB is observed. The higher measurement dynamics (71.4 dB versus 60 dB) results from an increase of the EO probe sensitivity in the biological medium, this latter one being induced by the presence of a higher inner-probe E field, linked to the lower mismatch between EO crystal and ambiant medium permittivities. The distance between electrodes (12.8 mm) being much lower than the microwave signal wavelength (165 mm), an electrostatic model of the measurement apparatus (cuvette, solution and EO probe) has been used to give a first order estimation of the inner-probe E-field increase. The simulation leads to a gain of 10.4 dB in the biological solution. The small remaining difference (1 dB) between measurement and simulation could result from a resonance effect in the cuvette acting as a low Q-factor resonant cavity.

The EO probe selectivity has been evaluated via the measurement of the EO signal versus probe orientation in between the electrodes. The theoretical fit consists in a sinusoidal response to which

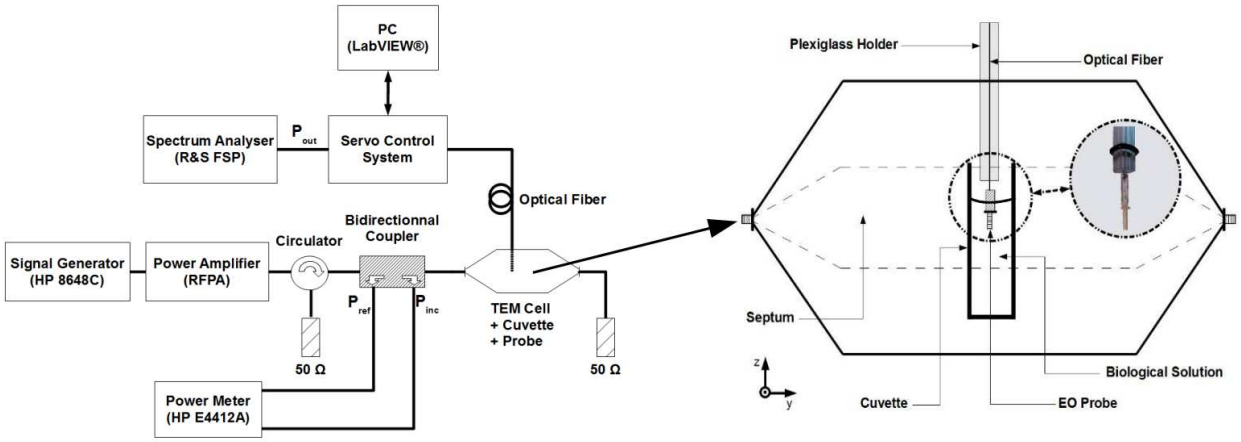

Figure 1: CW experimental set-up.

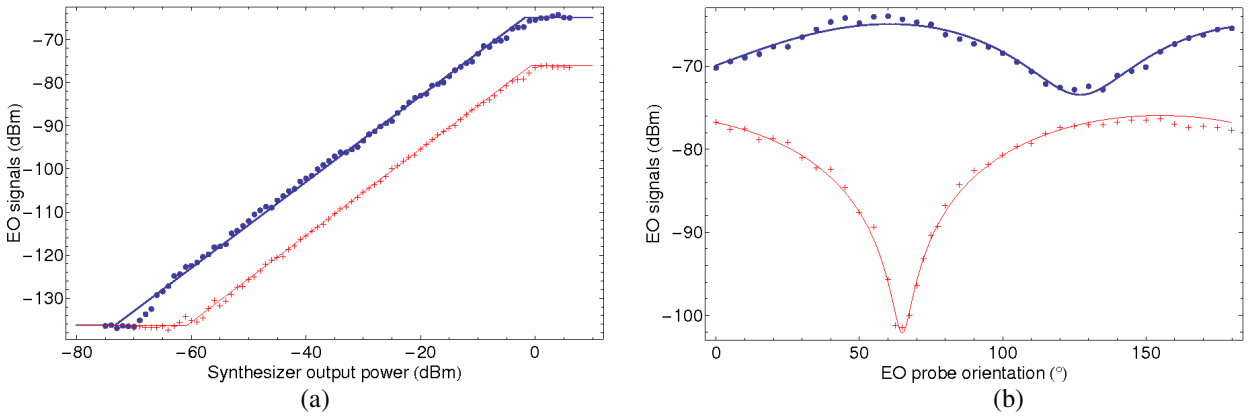

Figure 2: Responses of the EO probe in the air and in the biological solution with theoretical fits, (a) versus synthetizer output power, (b) versus orientation of the EO probe.

a residual signal (measurement floor of -102.1 ± 0.5 dBm) has been added, this latter one arising from direct electromagnetic coupling between generator and measurement apparatus. Indeed, both equipment being in the same room without Faraday cage, the EO probe selectivity is limited to 26 dB. A standard deviation of 0.6 dB is obtained. From the fit, the perpendicular to the EO probe sensitivity axis is determined with accurately: $\theta_{\min} = 64.9° \pm 0.2°$. Same measurement has been carried out with the EO probe placed in the biological solution. The angular response is no more sinusoidal and the 180°-periodicity is lost. Moreover, the dynamic range (8 dB) is greatly reduced compare to that obtained in air. On one hand the cuvette shape is rectangular, leading to a non homogeneous distribution of the E-field vector inside. On the other hand, rotation axis of the TEM cell and symmetry axis of the EO probe do not coincide. Such eccentric rotation movement in a non homogeneous E-field distribution leads to $\sin(2m(\theta - \theta_{\min}))$-type corrective terms in the fitting model ($m \in \mathbb{N}$). Considering only the dominating 2nd harmonic term ($m = 1$) leads to a satisfactory fit with a standard deviation of 0.5 dB. The 9.25 ± 0.35 dB E-field enhancement observed in the biological medium is consistent with the one observed for linearity measurements.

2.2. Temperature Measurements

A comparison of the EO probe with a standard optical probe (Luxtron®) has been made in a biological medium exposed to a 1.8 GHz microwave radiation. The raw data of probes temperature measurement are represented in Fig. 3. This curve represents the temperature evolution of both probes from their initial temperature (ambiant temperature). The exposition of the biological medium starts at time $t = 300$ s. As seen, an excellent agreement is observed between the two measures. However, a huge improvement of sensitivity is obtained with the EO probe. In order to quantify the sensitivity of the EO probe, we have modeled its temperature evolution considering a mono exponential temperature evolution at the begining and another one at the end of the microwave exposition. In order to get a better fit, we have added a linear drift (0.95°C/h) of the local ambiant temperature after the beginning of the microwave exposition. A perfect agreement is observed between the theoretical fit and the measurements. Values of 333 s and 2.45°C are obtained for the thermalization time constant and the amplitude of the microwave heating of the biological medium, respectively. The distribution of the difference between the theoretical fit and the EO measurement data is also ploted in Fig. 3. A gaussian-shape distribution is obtained with a standard deviation of 22 mK. For the Luxtron® probe, a standard deviation of 197 mK is obtained, i.e., a sensitivity ~ 10 times lower than Kapteos® EO probe.

2.3. SAR Evaluation in a Petri Dish

As seen previously, the EO probe has demonstrated its ability to measure both electric field and temperature with a high accuracy in biological media. As the SAR (expressed in W/kg) can be determined in two ways, one involving the thermic effect resulting from the RF exposition and the

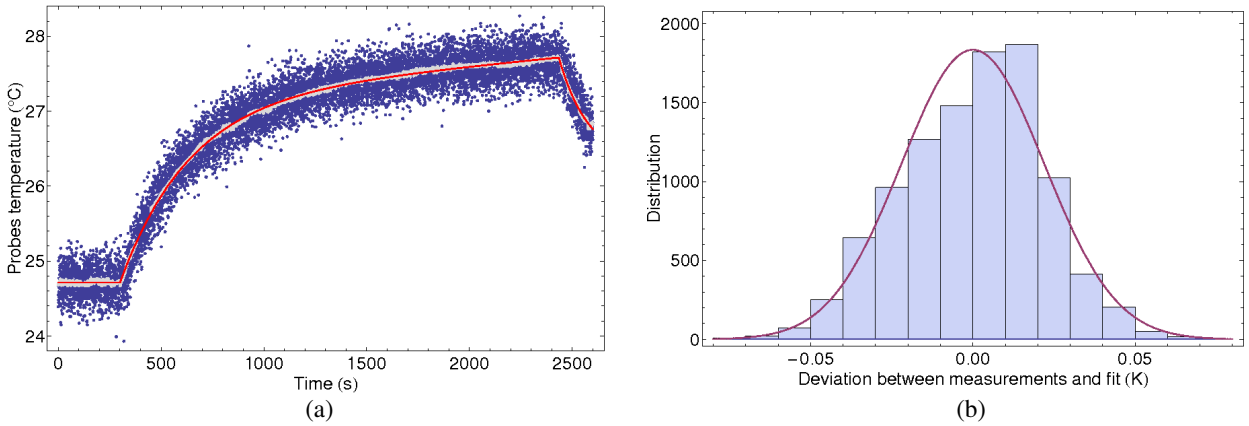

Figure 3: (a) Temperature measurements recorded by Luxtron® (blue dots) and Kapteos® (grey dots) probes and theoretical fit (red solid line). (b) Deviation between measurements and the theoretical fit (histogram) and best gaussian fit (red solid curve).

other one involving the E-field within the exposed biological medium, both definition can be used:

$$\mathrm{SAR} = C\frac{\partial T}{\partial t} = \frac{\sigma E^2}{\rho} \tag{1}$$

Specific heat C, temperature T, electric conductivity σ, density ρ and E field E are related to the studied biological medium. The experimental set-up is the same as the one used for temperature measurements. The probe is horizontally inserted in the center of a Petri dish filled with a biological solution. During the exposition, both E and T are simultaneously recorded allowing two different SAR determinations from (1). The calculated values of SAR, obtained from E and T measurements are 1.71 W/kg and 1.64 W/kg, respectively, thus differing of less than 5 percents.

3. INVESTIGATIONS IN THE TIME-DOMAIN

A characterization of the EO probe in the time-domain has been conducted using the experimental set-up depicted in Fig. 4. Ultra-short kV pulses are generated by photoswitches triggered by a pulsed laser. They are sent on the electroporation cuvette via a coaxial cable ending with two electrodes located on opposite sides of the cuvette. The active element of the EO probe, consisting of the EO crystal, is submerged by the biological solution filling the cuvette. Measurements have been performed with a fast sampling oscilloscope to which output of the EO device is connected. Electrical pulses are also measured upstream of the cuvette on a second channel of the oscilloscope.

3.1. E-field Measurement

Figure 5 shows the temporal profiles of both pulses generated and measured upstream of the electroporation cuvette and measured in situ by the EO probe. Several of the pulse echoes are observed on the curves. These echoes result from impedance mismatch within the propagation structure between the photoswitch and the cuvette. On the EO signal, half of echoes are observed due to the fact that there are also reflections on the sampling channel only visible on the pulse measured upstream. Fourier transform of each pulse (upstream and *in situ*) are also plotted in Fig. 5.

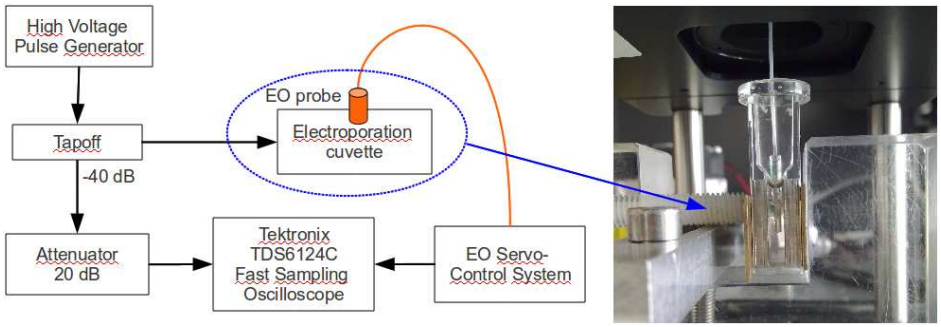

Figure 4: Kapteos EO probe inserted in an electroporation cuvette filled with a biological solution between two electrodes providing ultra-short kV electric pulses.

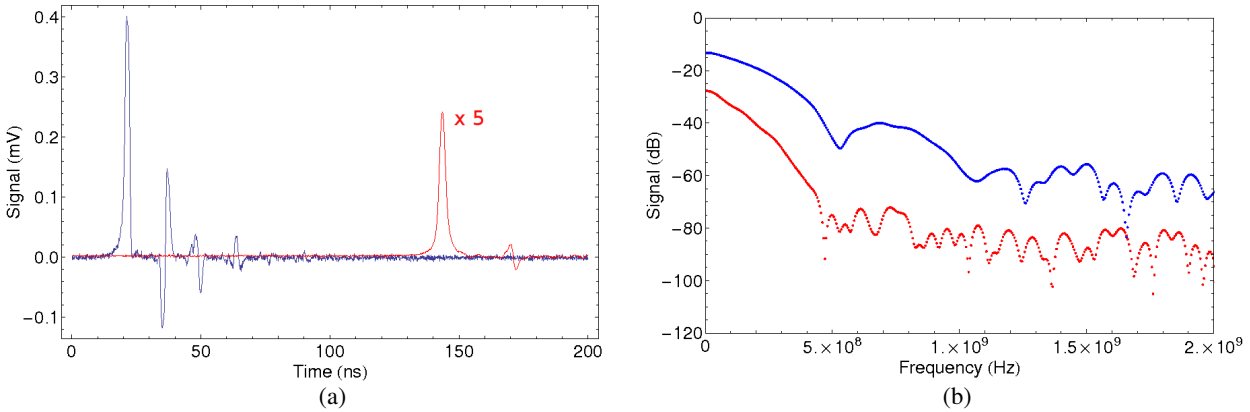

Figure 5: (a) Temporal profiles of both pulse measured upstream of the electroporation cuvette (in blue) and *in situ* measured by the EO probe (in red). (b) Fourier transform of each signal.

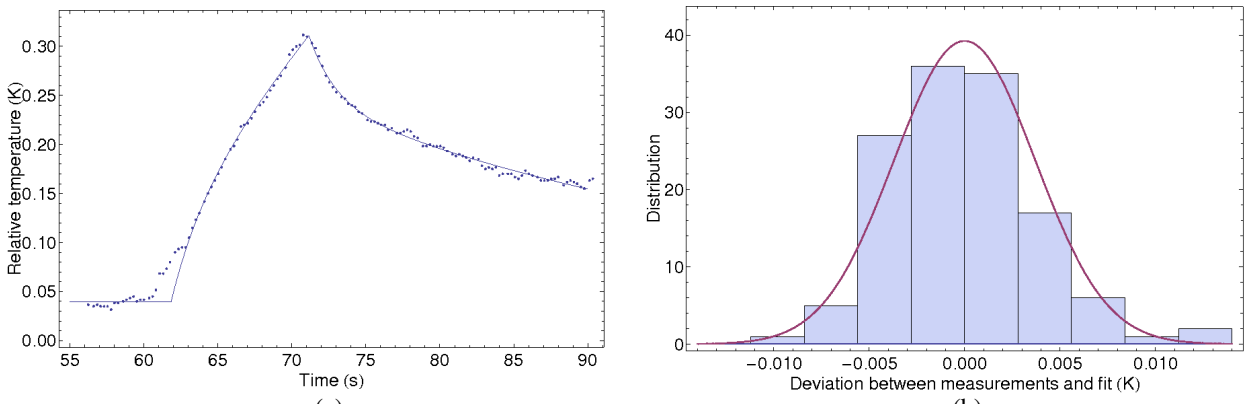

(a) (b)

Figure 6: (a) Relative temperature of a biological solution exposed to 10000 electric pulses and theoretical fit. (b) Gaussian-shape difference between fit and measurements.

3.2. Temperature Measurement

Figure 6 depicts the temperature evolution of the biological solution exposed to 10000 ultra-short kV electric pulses. As for CW temperature measurement, we have modeled the evolution of the EO probe temperature. We have considered that the biological medium acts as a thermostat for the EO crystal and that so does the air for the biological medium. We have also made the assumption that the 10000 electric pulses act as a continuous heat source during the exposition time window. Thus the thermal behaviors $T_{\mathrm{EO}}(t)$ and $T_{bio}(t)$ of both EO crystal and biological medium are governed by the following couple of differential equations (C, P: heat capacity and power):

$$\begin{cases} C_{bio}\, T'_{bio}(t) = -\lambda_{bio}(T_{bio}(t) - T_e) + P_{bio} \\ C_{\mathrm{EO}}\, T'_{\mathrm{EO}}(t) = -\lambda_{\mathrm{EO}}(T_{\mathrm{EO}}(t) - T_{bio}(t)) + P_{\mathrm{EO}} \end{cases} \tag{2}$$

Their resolution leads to three relations, each one being valid over a specific time window: before, during, and after the exposition. A very good agreement is observed between this model and the measurement (see Fig. 6). The distribution of the difference between the theoretical fit and the data, also ploted in Fig. 6, presents a gaussian shape with a standard deviation of only 3 mK. From this model, we have also obtained the thermalisation time constants of the EO probe and of the biological medium which are $\tau_{\mathrm{EO}} = 1.8\,\mathrm{s}$ and $\tau_{bio} = 33\,\mathrm{s}$, respectively.

4. CONCLUSION

We have presented novel EO probes able to simultaneously measure E-field and temperature inside biological media either in time-domain or in frequency-domain. For the first time to our knowledge, SAR has been determined by two different ways with the same single probe.

ACKNOWLEDGMENT

This work was supported by the French "Health and Radiofrequency" Foundation, under Biocapteo project and by the DGA (French Military Programs Management and Procurement Agency).

REFERENCES

1. Schuderer, J., T. Schmid, G. Urban, T. Samaras, and N. Kuster, "Novel high-resolution temperature probe for radiofrequency dosimetry," *Phys. Med. Biol.*, Vol. 49, N83–N92, 2004.
2. Baba, M., Y. Suzuki, M. Taki, K. Fukugana, and S. Watanabe, "Three dimensional visualization of the temperature distribution in a phantom for the assessment of localized exposure to microwave," *Bioelectromagnetic Society Annual Meeting*, June 2005.
3. Togo, H., N. Kukutsu, N. Shimizu, and T. Nagatsuma, "Sensitivity-stabilized fiber-mounted electrooptic probe for electric field mapping," *J. Lightwave Technol.*, Vol. 26, 2700–2705, 2008.
4. Lee, D. J., N.-W. Kang, J. Y. Kwon, and T. W. Kang, "Field-calibrated electro-optic probe using interferometric modulations," *J. Opt. Soc. Am. B*, Vol. 27, 318–322, 2010.
5. Faraone, A., D. O. McCoy, C. K. Chou, and Q. Balzano, "Characterization of miniature e-field probes for SAR measurements," *IEEE International Symposium on Electromagnetic Compatibility*, Vol. 2, 749–753, 2000.
6. Bernier, M., G. Gaborit, L. Duvillaret, A. Paupert, and J.-L. Lasserre, "Electric field and temperature measurement using ultra wide bandwidth pigtailed electro-optic probes," *Appl. Opt.*, Vol. 47, 2470–2476, 2008.

New Techniques to Reduce the Common-mode Signal in Multi-frequency EIT Applications

Mohamad Rahal[1], **Ibrahim Rida**[1], **Muhammad Usman**[1], **and Andreas Demosthenous**[2]

[1]Department of Electrical Engineering, University of Hail
P. O. Box 2440, Hail, Saudi Arabia
[2]Department of Electronic and Electrical Engineering, University College London
London, WC1E 7JE, UK

Abstract— Bio-impedance voltage measurements suffer from many potential errors. One of the key errors that affect the accuracy in medical impedance imaging and bio-impedance measurements is the common-mode error. In *electrical impedance tomography* (EIT) applications, where current is injected into the subject to make the measurements, the major problem is that the interference does not occur at the power supply frequency (50 or 60 Hz) but at the working frequency. Traditional techniques such as filtering or screening have little effect in reducing this common-mode interference. In this paper, we present a common-mode feedback topology which reduces these errors for use in EIT systems (10–200 kHz current injection frequency). A frequency-selective feedback network is described which reduces the common-mode voltage due to electrode impedance mismatch at the input of the differential amplifier. The circuit was designed and implemented in CMOS technology dissipating about 20 mW. Measured results show that the common-mode signal is reduced by 85%, 75%, 70% and 65% at 10 kHz, 50 kHz, 100 kHz and 200 kHz, respectively.

1. INTRODUCTION

Electrical Impedance Tomography (EIT) is an imaging technique that estimates the complex conductivities of the interior of an object from measurements made on its surface. In the medical field EIT has the potential for use in various applications such as breast, brain and lung imaging [1]. In particular, EIT has the ability to become a clinical tool for studying regional lung ventilation in particular for neonate applications, which can only be viably assessed through EIT due to the difficulty of applying traditional techniques such as X-ray and MRI. Although EIT suffers from poor resolution compared to traditional imaging techniques; it has advantages compared to these in terms of simplicity, cost, non-invasive, and the absence of ionizing radiation [3]. EIT data are collected via an array of electrodes (multiple electrodes) attached on the surface of the subject where the induced voltages are measured [1]. Fig. 1 shows a typical EIT application where a small alternating current (AC) (< 1 mA) at 50 kHz is commonly injected through one electrode pair and voltages differences are recorded from the remaining electrodes. Then, the current is injected using the next pair of electrodes until all the available electrodes have been switched. The speed of the switching determines the frame rate, with real time imaging requiring frame rates from a few Hz up to 30 Hz. Recent studies have shown that injecting multiple frequencies at the same time will produce better tissue characterization. In addition, injecting multiple frequencies simultaneously reduces the measurement time.

The sources of errors in bio-potential recording have been extensively studied in the recording of signals such as the electrocardiogram (ECG) or electromyogram (EMG). In addition, sources of errors in EIT have been discussed in various studies [2, 5, 6]. It was indicated in [5] that the common-mode errors in EIT measurement are due to the changes in stray capacitance and electrode impedance mismatches. Furthermore, the common-mode (CM) voltage is usually higher than the

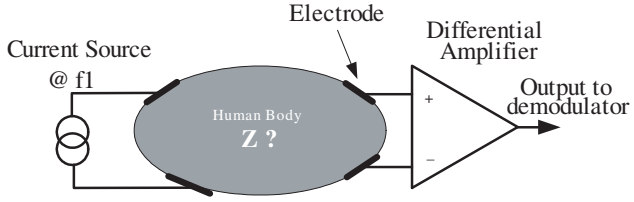

Figure 1: Simple EIT injection/recording system.

differential voltage (DV) at the recording electrodes and since this CM is of the same frequency as the DV, suppression of the CM by the differential amplifier is limited, in particular at high frequencies. Various studies [4, 8] have suggested the use of common-mode feedback (CMFB) to reduce the CM but no measured results are given. In [8], it was shown that using an extra electrode the use of common-mode feedback has the potential to obtain a significant improvement at 10 kHz, although it was suggested a large phase margin is required to guarantee the stability of the feedback system. However, no measured result was presented. In this work, we present an integrated topology for CMFB that is suitable for multi-frequency EIT. After this introductory part, Section 2 describes the theory and the operation of common-mode feedback. Section 3 presents measured results and conclusions are suitable drawn in Section 4.

2. METHODS

2.1. CMFB

Figure 2 shows the basic topology for the common mode feedback to suppress the common-mode error due to electrodes mismatches with the feedback path applied to one of the injecting electrodes. According to [8], there are two other alternatives, a) by applying feedback to an extra electrode, but this might change the current distributions, b) by using resistors/capacitors, feedback is applied to both terminals but this might reduce the output impedance. For the topology shown in Fig. 2 the initial CM is higher. In order for the feedback path to support multi frequency, it is desirable for the feedback network to be frequency selective and tunable.

Figure 3 shows the basic topology of the feedback network [4]. The CM is multiplied by the I/Q at the locking frequency, then its low-pass filtered. For example if the CM is in phase with the I signal, then the output from the low-pass filtered in the I path will give a maximum DC signal, whereas the output from the Q path will give a minimum. After that the outputs from the low-pass filter stages are then multiplied by the corresponding I/Q signals, then the outputs are summed, amplified and applied to the injecting electrode in a negative feedback loop. For single frequency injection the overall expression for the feedback network can be expressed as:

$$A_{FB}(s) = -\frac{1}{1 - jw_1\tau + s\tau} \tag{1}$$

where τ represents the time constant of the low pass filter and w_1 is at the locking frequency. The magnitude of the above expression can be expressed as:

$$|A_{FB}(s)| = -\frac{1}{s^2\tau^2 + 2\tau s + w_1^2\tau^2 + 1} \tag{2}$$

The frequency response of the feedback network has a sharp peak at the locking frequency (w_1). A small time constant causes inadequate phase margin (< 60 degrees), which causes ringing in the

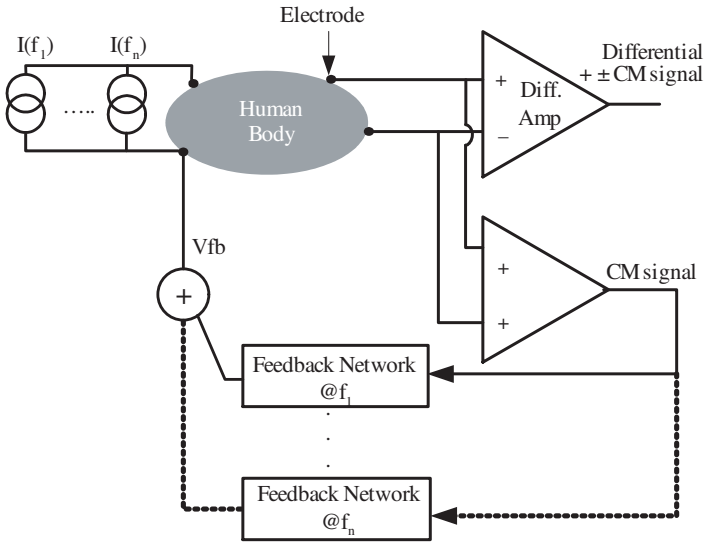

Figure 2: Multi-frequency CMFB to reduce the CM signal.

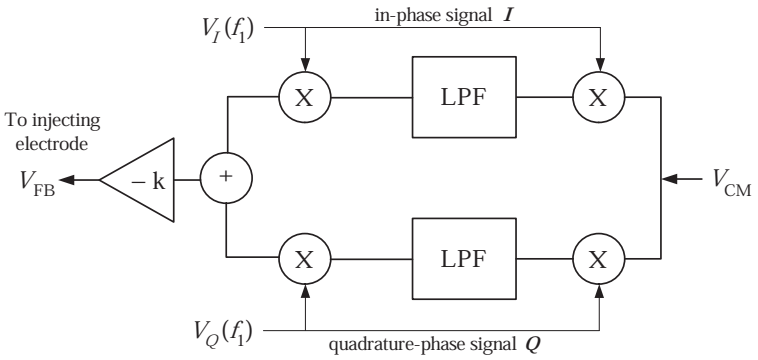

Figure 3: Common-mode feedback network.

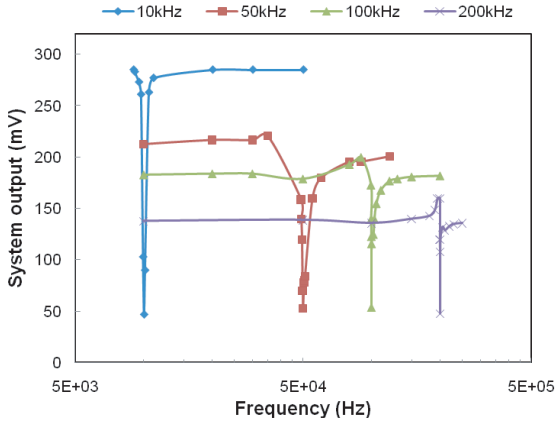

Figure 4: CM signal reduction as a function of the locking frequency for the RC model with different injection frequencies.

step response. Large time constant increases the phase margin; however the suppression of the CM will take longer.

3. RESULTS

An integrated solution was designed using a 5 V, 0.35-µm CMOS process technology. The simulations and layout were carried out using the Cadence design kit provided by the foundry. The closed loop response network was tested for various input frequencies when the locking frequency of the I/Q signals was varied from 10 kHz to 1MHz and the results is shown in Fig. 4. The output has as a band-reject filter response centred at the locking frequency. The bandwidth of the feedback network is about 250 kHz. The closed loop response was carried out using a realistic RC model of the electrodes [7]. The average reduction over 10 chips at 10 kHz, 50 kHz and 100 kHz were 86%, 63% and 45%, respectively.

4. CONCLUSIONS

In this paper, we have presented a practical implementation of a feedback technique to suppress the CM voltage present in EIT measurements. The topology used is frequency-selective and the feedback is applied to one of the injecting electrodes. Experiments were carried out using a RC model of the electrodes to demonstrate the suppression of the CM signal. Future work will concentrate in reducing the time constant of the feedback network in order to support high frame rates, in particular when large common-mode signals are present.

ACKNOWLEDGMENT

We would like to acknowledge the support of the UK Engineering and Physical Sciences Research Council (EPSRC) under grant numbers EP/E031633/1 and EP/E029426/1.

REFERENCES

1. Bayford, R., "Bioimpedance tomography (electrical impedance tomography)," *Annu. Rev. Biomed. Eng.*, Vol. 8, 63–91, 2006.
2. Boone, K. and D. Holder, "Current approaches to analogue instrumentation design in electrical impedance tomography," *Physiol. Meas.*, Vol. 17, 229–247, 1996.
3. Brown, B., D. Barber, and A. Seagar, "Applied potential tomography: Possible clinical application Clin," *Phys. Physiol. Meas.*, Vol. 6, 109–121, 1989.
4. Hwang, I., "Common-mode feedback amplifier for biomedical measurements," *Proc. IASTED International Conference Biomedical Engineering*, 453–455, 2005.
5. McEwan, A., G. Cuisk, and D. Holder, "A review of errors in multi-frequency EIT instrumentation," *Physiol. Meas.*, Vol. 28, S197–S215, 2007.
6. Petrova, G., "Influence of electrode impedance changes on the common-mode rejection ratio in bioimpedance measurements," *Physiol. Meas.*, Vol. 20, N11–N19, 1999.
7. Rahal, M., J. Moy Khor, A. Demosthenous, A. Tizzard, and R. Bayford, "A comparison study of electrodes for neonate electrical impedance tomography," *Physiol. Meas.*, Vol. 30, 11–14, S73–S84, 2009.
8. Rosell, J. and R Riu, "Common-mode feedback in electrical impedance tomography," *Clin. Phys. Physiol. Meas.*, Vol. 13, 11–14, 1992.

Human Exposure to Outdoor PLC System

Vicko Doric[1], **Dragan Poljak**[1], **and Khalil El Khamlichi Drissi**[2]

[1]University of Split, Croatia
[2]Blaise Pascal University, France

Abstract— In this paper, human exposure to a simple outdoor PLC system is assessed. An electric field irradiated by the PLC configuration is calculated using the wire antenna model. For the frequency range from 1 to 10 MHz the human body is represented by the equivalent thick cylindrical antenna, while in the range from 10–30 MHz a parallelepiped body model is used. The axial current density distribution induced along the body as well as the values of surface and whole body averaged SAR, are calculated and compared with limits defined by relevant international standards.

1. INTRODUCTION

The purpose of Power Line Communications (PLC) system is to ensure necessary communication means via existed power line network and electrical installations in houses and buildings. A serious shortcoming of this new technology is related to electromagnetic interference (EMI) problems, as overhead power lines at the PLC frequency range (1 MHz to 30 MHz) act as transmitting or receiving antennas, respectively.

There are significant number of papers dealing with different models for accurate EMC analysis of the PLC systems and their influence to radio and telecommunications equipment [1–4].

On the other hand, human exposure to the PLC electromagnetic radiation is almost entirely neglected EMC aspect of the PLC technology although the human body, when exposed to electromagnetic radiation, behaves as a receiving antenna in this frequency region.

In this paper, human exposure to a simple outdoor PLC system is assessed. An electric field irradiated by the PLC configuration is calculated using the accurate wire antenna model presented in [5]. In order to estimate effects of the PLC electromagnetic radiation on the humans, two simple body models are used.

For the frequency range from 1 to 10 MHz the human body is represented by the equivalent thick cylindrical antenna in order to calculate the axial current density distribution induced along the body. The values of the induced surface and whole body averaged SAR are, on the other hand, obtained in the frequency range from 10 to 30 MHz using parallelepiped body model. Obtained results are compared to the exposure limits proposed by ICNIRP [6, 7].

2. ANTENNA MODEL OF A SIMPLE PLC SYSTEM

The geometry of a simple PLC system analyzed within the scope of this paper is shown in Fig. 1. The system consists of two conductors placed in parallel above each other at the distance d. The conductors are suspended between two poles of equal height, thus heaving the shape of the catenary.

The geometry of a catenary is fully represented by such parameters as the distance between the points of suspension, L, the sag of the conductor, s, and the height of the suspension point, h, as shown in Fig. 1. The imperfectly conducting ground is characterized with the electrical permeability ε_r and conductivity σ, respectively. The conductors are modelled as thin wire antennas excited by the voltage generator V_g at one end, and terminated by the load impedance Z_L at the other end.

The current distribution over the multiple wires of arbitrary shape is governed by the set of coupled integro-differencial equations of the Pocklington type [5]. The influence of the lossy ground is taken into account by the Fresnel reflection coefficient.

Governing set of integral equations is numerically solved using the Galerkin-Bubnov scheme of the Boundary Element Method.

Once the equivalent current distribution over the wires is obtained, the values of the radiated electric and magnetic field at arbitrary point are readily obtained.

3. PARALLELEPIPED MODEL OF THE HUMAN BODY

The exposure of humans to RF electromagnetic radiation is quantified by Specific Absorption Rate (SAR). SAR is defined as the mass average rate of energy absorption in tissue:

$$SAR = \frac{dP}{dm} = \frac{d}{dm}\frac{dW}{dt} = \frac{d}{dt}\frac{dW}{dm} = \frac{d}{dt}\frac{dW}{\rho dV} \tag{1}$$

and it is expressed in W/kg.

If the human body is illuminated by the plane wave, SAR induced on the surface of the human body could be calculated analytically by following formula [8]:

$$SAR_{surf} = \frac{\sigma}{\rho}\frac{\mu\omega}{\sqrt{\sigma^2+\varepsilon^2\omega^2}}\left(1+\gamma_{pw}\right)^2\frac{\left|E^{inc}\right|^2}{Z_0^2} \tag{2}$$

where E^{inc} is root-mean-square value of the incident electric field, while γ_{pw} stands for simplified plane wave reflection coefficient given by:

$$\gamma_{pw} = \frac{2\left|\sqrt{\varepsilon_{eff}}\right|}{\left|\sqrt{\varepsilon_{eff}}+\sqrt{\varepsilon_0}\right|} - 1 \tag{3}$$

If the human body is approximated by the parallelepiped with dimensions: 180 cm×40 cm×20 cm (Figure 2), whole body average SAR induced inside the human body is given by [8]:

$$SAR_{WB} = \frac{1}{HD}\int_0^H\int_0^D SAR_{surf}e^{-\frac{2x}{\delta_{skin}}}dxdz = \frac{\delta_{skin}}{2D}\left(1-e^{-\frac{2D}{\delta_{skin}}}\right)SAR_{surf} \tag{4}$$

where δ_{skin} is skin depth defined by:

$$\delta_{skin} = \sqrt{\frac{2}{\omega\mu\sigma}}. \tag{5}$$

4. CYLINDRICAL MODEL OF A HUMAN BODY

The human body standing on the ground and exposed to electromagnetic radiation at the PLC frequencies can be represented by the conducting cylinder of the full length L and radius a, as it is shown in Figure 3.

The current distribution along the cylinder representing the human body can be obtained by solving the corresponding thick wire integral equation of the Pocklington type [8]:

$$E_z^{inc} = -\frac{1}{j4\pi\omega\,\varepsilon_0}\int_{-L}^{L}\left[\frac{\partial^2}{\partial\, z^2}+k^2\right]g_E(z,z')I(z')dz' + Z_L(z)I(z) \tag{6}$$

For the RF range of frequencies the load impedance Z_L is given by [8]:

$$Z_L(z) = \frac{1}{a^2\pi\sigma}\left(\frac{ka}{2}\right)\frac{J_0(j^{-1/2}ka)}{J_1(j^{-1/2ka})} + Z_c \tag{7}$$

and the corresponding induced current density is readily obtained using the following expression [8]:

$$J_z(\rho,z) = \frac{I(z)}{a^2\pi}\left(\frac{ka}{2}\right)\frac{J_0(j^{-1/2}k\rho)}{J_1(j^{-1/2}ka)}. \tag{8}$$

5. NUMERICAL RESULTS

The computational examples are related to the simple PLC circuit shown in Figure 1. The distance between the poles is $L = 200\,\mathrm{m}$, with the radii of wires $a = 6.35\,\mathrm{mm}$. The wires are suspended on the poles at heights $h_1 = 10\,\mathrm{m}$, and $h_2 = 11\,\mathrm{m}$ above the ground, respectively. The sag of the conductor is assumed to be $s = 2\,\mathrm{m}$ and ground parameters are $\varepsilon_r = 13$ and $\sigma = 0.005\,\mathrm{S/m}$. The impressed power is 1 mW (average power required for the PLC system operation) and operating frequency is changed from 1 MHz to 30 MHz. The value of the terminating load Z_L is $50\,\Omega$.

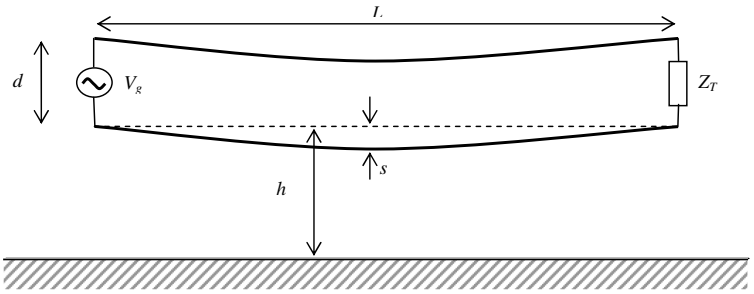

Figure 1: Simple outdoor PLC circuit.

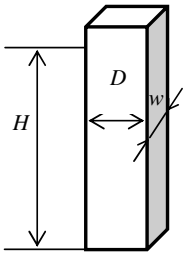

Figure 2: Parallelepiped body model.

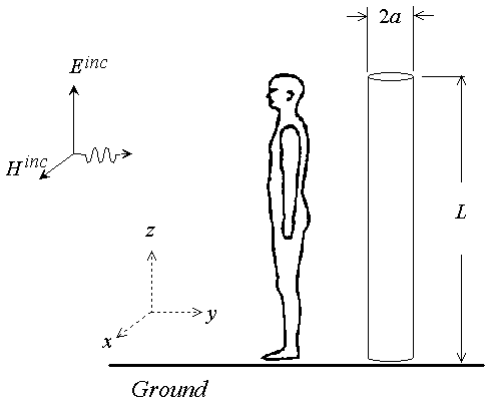

Figure 3: Cylindrical body model.

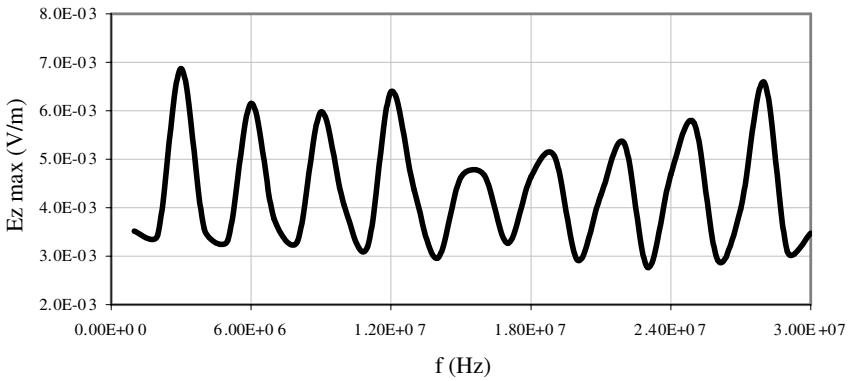

Figure 4: Maximal value of E_z component below the conductor ($z = 1.75\,\mathrm{m}$).

The maximum values of the z component of the radiated electric field for the worst case scenario (person standing directly under the power lines) for the frequency range from 1 MHz to 30 MHz and are calculated and shown in Figure 4.

Thus obtained values of the incident electric field are then used as an input data for the calculation of the induced current densities and SAR inside the human body.

First, the induced current distributions along the human body are calculated for frequency range from 1 MHz to 10 MHz with frequency step of 1 MHz using the cylindrical model of the human body. Obtained current distribution for the frequency $f = 4\,\mathrm{MHz}$ is shown in Figure 5. It is obvious from the picture that highest level of current is induced at the feet (connection with ground) while the current induced at the top of the head is equal to zero due to the applied boundary condition.

Furthermore, for the frequencies up to 10 MHz corresponding current densities inside human body are calculated using Equations (7) and (8) and compared with basic restrictions defined by ICNIRP [6]. The obtained results are shown in Table 1.

According to the ICNIRP for the case of simultaneous exposure to fields of different frequencies these exposures are additive in their effects. For the frequencies up to 10 MHz induced current

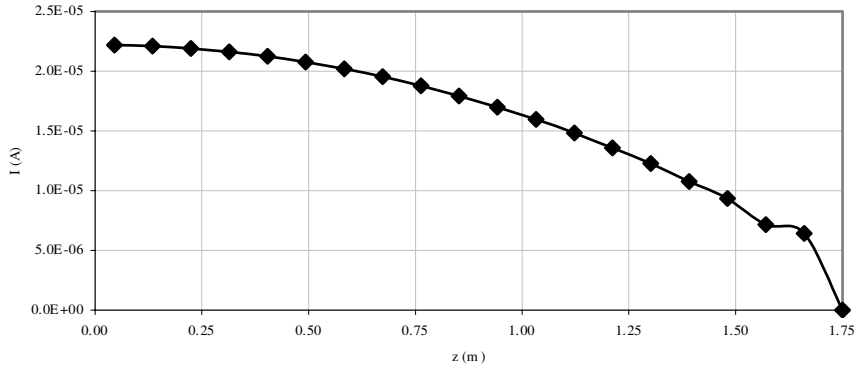

Figure 5: Current density induced along the body ($f = 4\,\mathrm{MHz}$).

Table 1: Maximum values of the induced current density inside the human body compared to the basic restrictions.

f [MHz]	$I_{\max}$ [A]	$J_{\max}$ [A/m^2]	$J_{\max}/J_{ref}$ workers	$J_{\max}/J_{ref}$ public
2	2.77E-06	4.60E-05	1.63E-06	8.13E-06
4	2.22E-05	3.74E-04	6.62E-06	3.31E-05
6	1.59E-05	2.73E-04	3.22E-06	1.61E-05
8	4.45E-06	7.78E-05	6.88E-07	3.44E-06
10	4.22E-06	7.50E-05	5.30E-07	2.65E-06

Table 2: Induced values of SAR inside the body.

f [MHz]	SAR_{surf} [nW/kg]	SAR_{WB} [nW/kg]	f [MHz]	SAR_{surf} [nW/kg]	SAR_{WB} [nW/kg]
5	0.0119	0.0068	20	0.0352	0.0129
10	0.0347	0.0162	25	0.1676	0.0560
15	0.0668	0.0272	30	0.0727	0.0225

$SAR_L = 0.4\,\mathrm{W/kg}$ (workers), $0.08\,\mathrm{W/kg}$ (public) [5].

densities should be added according to [6]:

$$\sum_{i=1\,\mathrm{Hz}}^{10\,\mathrm{MHz}} \frac{J_i}{J_{L,i}} = 1.31 \cdot 10^{-4} \ll 1$$

It is obvious that current densities levels induced inside human body due to radiation of the outdoor PLC system are for the couple orders of magnitude under the limits proposed by the international standards.

Next, based on the parallelepiped model of the human body induced values of surface SAR and whole body average SAR are calculated using Equations (1) and (4). Again, the previously calculated maximum values of the radiated electric field from the PLC system are used as input values for the incident field.

Obtained results are shown in Table 2. Compared to the basic restrictions ($SAR_L = 0.4\,\mathrm{W/kg}$ for workers, $0.08\,\mathrm{W/kg}$ for general public) induced levels are obviously insignificant (8 orders of magnitude smaller!).

Finally, the SAR values for all frequencies are added in order to assess the cumulative effect for the public population:

$$\sum_{i=1\,\mathrm{MHz}}^{30\,\mathrm{MHz}} \frac{SAR_i}{SAR_L} = 8.93 \cdot 10^{-9} \ll 1$$

The obtained results clearly show that heating effect due to the electromagnetic radiation of the outdoor PLC system is negligible.

6. CONCLUSION

In the scope of this paper, the originally developed wire antenna model, taking into account the conductor sag, is used for calculation of the spatial distributions of the radiated electric field in the frequency range from 1 to 30 MHz. Maximum levels of the calculated electric fields represent the worst case scenario incident values for the assessment of the human exposure to a simple outdoor PLC system electromagnetic radiation.

For the frequency range from 1 to 10 MHz the human body is represented by the equivalent thick cylindrical antenna, while in the range from 10 to 30 MHz the parallelepiped body model is used. The axial current density distributions induced along the body are calculated for a number of frequencies and some illustrative numerical results have been presented. Also, the assessment of both the surface and whole the body averaged SAR has been undertaken. The obtained values of both the current density and SAR stay well below the exposure limits proposed by ICNIRP.

However, if the PLC should become widely applied technology, the question about cumulative effects of the multiple signals should be raised.

REFERENCES

1. Luo, W. Q. and S. Y. Tan, "A distributed circuit model for power-line communications," *IEEE Transactions on Power Delivery*, Vol. 22, No. 3, 1440–1445, Jul. 2007.
2. Luo, W. Q. and S. Y. Tan, "A radiated emission model for power line communications," *IEEE Trans. Power Del.*, Vol. 21, No. 3, 1245–1249, Jul. 2006.
3. Am Amirshahi, P. and M. Kavehrad, "Medium voltage overhead power-line broadband communications; transmission capacity and electromagnetic interference," *Proc. International Symposium on Power Line Communications (ISPLC 2005)*, Vancouver, Canada, Apr. 6–8, 2005.
4. Karduri, M., M. D. Cox, and N. J. Champagne, "Near-field coupling between broadband over power line (BPL) and high-frequency communication systems," *IEEE Transactions on Power Delivery*, Vol. 21, No. 4, 1885–1891, Oct. 2006.
5. Doric, V. and D. Poljak, "EMC analysis of the PLC system based on the antenna theory," *Proceedings of ICECom 2010*, Dubrovnik, Croatia, Sep. 20–23, 2010.
6. International Commission on Non-ionizing Radiation Protection (ICNIRP): Guidelines for Limiting Exposure to Time-varying Electric, Magnetic, and Electromagnetic Fields (up to 300 GHz), *Health Phys.*, Vol. 74, No. 4, 494–522, 1998.
7. European Council Recommendation of 12 July 1999 on the limitation of exposure of the general public to electromagnetic fields (0 Hz to 300 GHz) — 1999/519/EC, *Official Journal of the European Communities*, 197, Jul. 30, 1999.
8. Poljak, D., *Human Exposure to Electromagnetic Fieds,* WIT Press, Southampton, Boston, 2003.

Analysis of Transmit Magnetic Field Homogeneity for a 7 T Multi-channel MRI Loop Array

M. Kozlov and R. Turner
Max Planck Institute for Human Cognitive and Brain Sciences
Stephanstrasse 1A , Leipzig D-04103, Germany

Abstract— Most MRI studies benefit from good homogeneity of the transmit magnetic field. We presented numerical investigation for a set of array/load configurations obtained by RF circuit and frequency domain 3-D EM co-simulation. This is a very powerful and fast method for array coil investigation, since one multi-port 3-D EM simulation, which can be calculated in a reasonable time, is sufficient for obtaining the array field homogeneity with any different tuning/feeding/decoupling conditions. We applied capacitor and inductor based decoupling networks and compared their array homogeneity obtained when the power reflected by the entire coil was minimized. The optimal separation between load and array giving best homogeneity without visible degradation of mean B_1+ over the center transverse slice is in the range of 30–45 mm. This result assists the design of transmit-only/receive-only (TORO) arrays, because about 40 mm separation provides adequate space for an RX-only coil.

1. INTRODUCTION

Most MRI studies benefit from good homogeneity of the transmit magnetic field. Due to the complexity of the problem at 300 MHz, where the wavelength in human tissue is comparable with the size of most human organs, experimental optimization alone is extremely time consuming and costly. Numerical simulation becomes an important tool for analysis and optimization of transmit magnetic field homogeneity. Our goal was to clarify how shape of load, distance between array and load, Z direction length of array, and loop coil angularity affect transmit field homogeneity, for a set of coil/load geometries. We extended our research to two MRI experimental situations: either the load is much longer than, or it is comparable to, the MRI array length. The latter is typical for MRI scanning of ex-vivo samples and most animal experiments.

2. METHOD

We investigated array MRI arrays comprising 8 channels with identical rectangular loops (length 80, 100, 120 mm), mounted on a cylindrical acrylic former with diameter ranging from 130 mm to 280 mm. The angular size of the loops was varied from 40 degrees (the closest element spacing) to 22.5 degrees (the largest gap between elements). Cylindrical loads with diameters 120, 155 and 190 mm, and a 120 mm diameter spherical phantom, were used in this investigation. Cylindrical loads were as long as 375 mm, to minimize the influence of load length on transverse slice homogeneity for arrays with different lengths. The electrical properties of the single component load were close to those of average human tissue at 300 MHz — permittivity 52 and conductivity 0.55 S/m. In this arrangement, the cylindrical symmetry of array and load rules out improvement of array performance by RF shimming (adjustment of amplitude and phase for excitation signals). All arrays were excited in circular polarization mode, applying 1 W power to each port (array transmit power — $P_{transmit} = 8$ W), with a sequential 45 degree phase increment. Q factor of all capacitors is equal 1000.

The scanner gradient shield (with diameter of 683 mm and length 1200 mm) was always included in the numerical domain for simulation of unshielded and shielded arrays. The distance between the array and a 300 mm long local shield was varied between 50 mm and 100 mm, to understand the effect of this distance on transmit field homogeneity.

Our investigation was performed using RF circuit and 3-D EM co-simulation [1]. The RF circuit simulator was Agilent ADS software, and Ansoft HFSS was chosen as the 3-D EM tool for its robustness in handling complex coil geometry. To increase reliability of simulation data and to accelerate simulation convergence, the 3D simulation domain was optimized and manual initial mesh definition was used (Fig. 1). This includes: a) the load is split between the field of view (FOV) and two remaining sections, in which different mesh resolutions were applied; b) 3D dummy objects (with electrical properties of vacuum) were placed in regions where the gradient of electrical and magnetic fields is expected to be large, and a finer mesh resolution was applied in

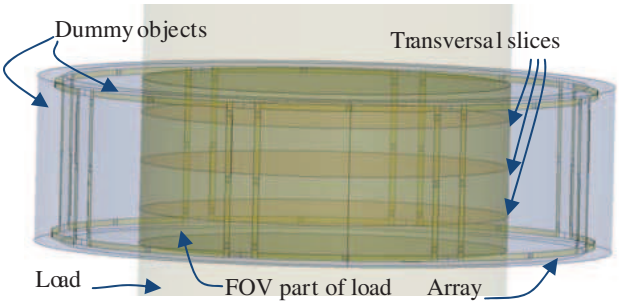

Figure 1: 3D EM simulation setup.

Table 1: Simulation data.

Coil length, mm				80					100					120				
Slice position, mm					0		+25			0		+25			0		+25	
				B_1+_c	B_1+_s	%	B_1+_s	%	B_1+_c	B_1+_s	%	B_1+_s	%	B_1+_c	B_1+_s	%	B_1+_s	%
Coil diameter, mm	300	Load diameter, mm	190	1.61	1.22	22	1.01	21	1.64	1.18	21	1.01	21	1.72	1.17	19	1.05	21
			155	2.11	1.19	19	1.17	20	2.13	1.34	19	1.18	21	2.16	1.31	21	1.18	21
	280		190	1.64	1.29	22	1.04	21	1.69	1.24	20	1.06	21	1.72	1.17	19	1.05	21
			155	2.22	1.49	18	1.26	20	2.28	1.45	19	1.26	20	2.28	1.39	20	1.25	21
	240		190	1.62	1.41	24	1.09	24	1.69	1.30	19	1.11	23	1.74	1.19	17	1.08	22
			155	2.38	1.70	17	1.35	19	2.43	1.61	17	1.36	19	2.66	1.50	19	1.34	20
	210		190	1.55	1.44	27	1.16	39	1.64	1.28	22	1.13	31	1.69	1.17	20	1.10	27
	200		190	1.51	1.46	30	1.23	48	1.61	1.30	25	1.17	37	1.72	1.18	23	1.13	31
			155	2.48	1.87	16	1.44	20	2.48	1.69	15	1.45	20	2.46	1.53	19	1.39	20
			120	3.64	2.43	18	1.97	22	3.63	2.27	22	1.95	23	3.54	2.12	25	1.90	25
	180		155	2.42	1.91	16	1.52	26	2.48	1.69	16	1.48	22	2.49	1.52	20	1.40	21
			120	3.77	2.55	16	2.04	21	3.71	2.34	21	2.02	22	3.64	2.16	26	1.95	24
	170		155	2.38	1.92	19	1.59	32	2.46	1.69	19	1.50	26	2.48	1.51	23	1.40	24
			120	3.81	2.61	16	2.08	20	3.74	2.39	21	2.05	21	3.66	2.18	25	1.97	23
	160		155	2.33	1.99	29	1.70	47	2.41	1.76	29	1.56	38	2.44	1.58	32	1.46	36
			120	3.84	2.67	15	2.13	18	3.78	2.42	21	2.09	20	3.72	2.20	26	2.00	23
	150		120	3.88	2.71	15	2.18	18	3.81	2.44	22	2.12	19	3.72	2.20	28	2.01	23
	140		120	3.87	2.75	16	2.25	18	3.80	2.44	24	2.15	22	3.73	2.21	28	2.01	23
	130		120	3.81	2.74	18	2.31	22	3.80	2.44	24	2.15	21	3.70	2.22	29	2.01	25

these regions than that used for other free space objects; c) all conducting elements were modeled as 3D objects, not as 2D resistive or PEC surfaces; d) at least 3 tetrahedra were placed within each current-conducting element cross section, because the RF current is well known to flow mostly on edges. This strategy results in convergence to $\Delta S < 0.002$ within not more than 3 adaptive iterations for the given investigation.

For all geometries, the array was tune/match/decoupled using capacitor and inductor based decoupling networks, or tuned only by minimization of power reflected by entire array. Transmit magnetic field inhomogeneity (calculated as the ratio of standard deviation to mean B_1+ over the given transverse slice (B_1+_s)) was computed at three transversal slices (center and $+/-25$ mm from the array/load center).

3. RESULTS

Array transmit field homogeneity strongly depends on the distance between array and load, as well as on the load diameter and shape, as shown in Table 1. For the smallest separation of array and load, the inhomogeneity increases with load diameter. There is an optimal distance between load and array giving the best homogeneity. The optimal distance and the slope of the inhomogeneity

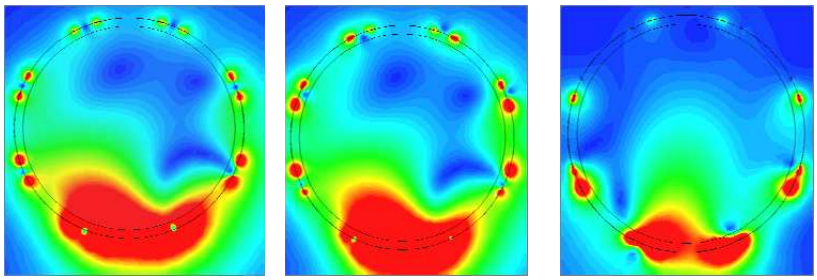

Figure 2: B_1+ on the center transverse slice for single channel excitation. 130 mm diameter and 120 mm length array with 120 mm diameter cylindrical load. From left to right: "C", "I" and "R".

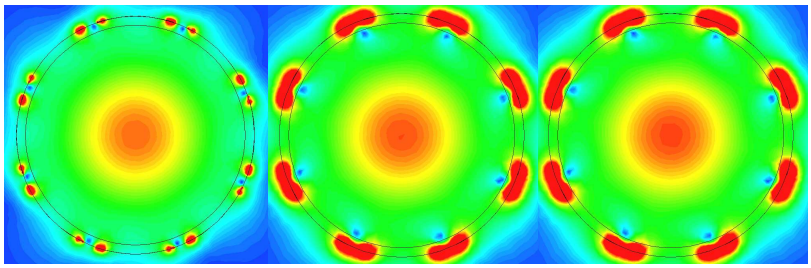

Figure 3: The same as Fig. 2 but the entire array is excited in circular polarization mode.

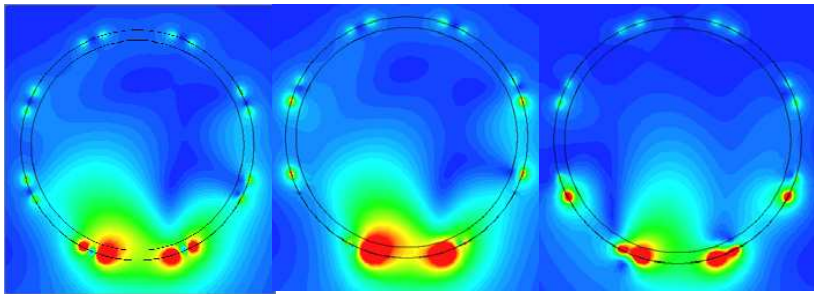

Figure 4: B_1+ on the central transverse slice for single channel excitation. 170 mm diameter and 120 mm length array with 155 mm diameter cylindrical load. From left to right: "C", "I" and "R"

curve versus distance both vary with load geometry. For the 80 mm long coil, optimization of homogeneity always entails a trade-off of the average value of transmit field for a given slice. Coil length plays an essential role in the degree of inhomogeneity only if the separation between array and load is small, or if the load diameter is 120 mm. For a load diameter of 155 mm, increasing the array length can either slightly reduce or increase the inhomogeneity, while simultaneously decreasing the mean value of this field for the central transverse slice. For a load diameter of 190 mm, increasing the array length only results in reducing the inhomogeneity.

The value of B_1+ in the centre of the load and array (B_1+_c) cannot be used to predict behavior (versus different factors) of the mean B_1+ over the center transverse slice. This is the case both when B_1+_c corresponds to the maximum value of B_1+ over the center transverse (tabulated in green) and when B_1+_c is smaller than maximum value of B_1+ over the central transverse slice (tabulated in purple). For a given setup, the constructive interference in the array centre is equal to 100%. Thus B_1+_c is bounded by the penetration of the magnetic field of a single array element to the array centre. The higher the value of B_1+_c, the higher the B_1+ produced by a single array element in the array centre. However, both the nonlinearity of the curve describing the magnetic field penetration versus distance to array element, and the constructive/destructive magnetic field interference versus position in slice, make it impossible to predict B_1+_s on the basis of the single quantity B_1+_c.

Due to limited space, Table 1 includes data for only one tuning condition, such that power reflected by the entire array was minimized. Although there can be significant variation of both B_1+_s and B_1+_c, the array tuning/decoupling conditions have little effect on homogeneity in most

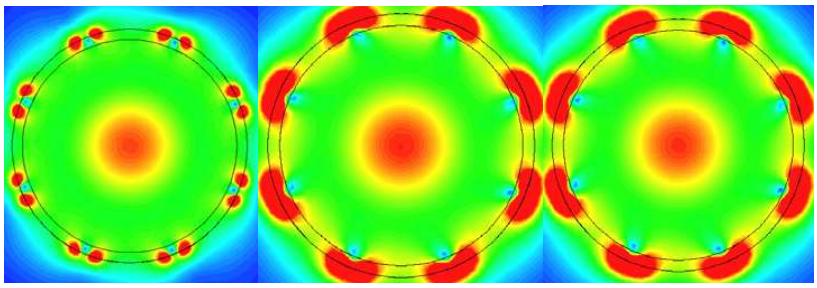

Figure 5: The same as Fig. 4 but the entire array is excited in circular polarization mode.

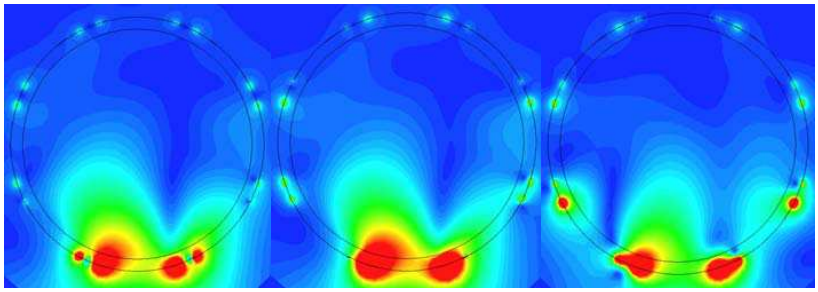

Figure 6: B_1+ on the central transverse slice for single channel excitation. 210 mm diameter and 120 mm length array with 200 mm diameter cylindrical load. From left to right: "C", "I" and "R".

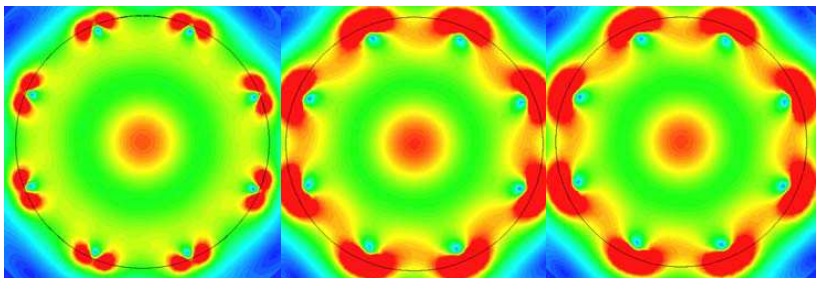

Figure 7: The same as Fig. 6 but the entire array is excited in circular polarization mode.

cases. Only when the separation between array and load is less than 20 mm can there be found some array/load configurations where the use of capacitor-based decoupling can increase homogeneity as much as 50%, at the expense of reduced average value over the slices and sometimes differing homogeneity for slices +25 mm and −25 mm from the array/load centre.

It should be noted that it is hard to predict nearly equal homogeneity of B_1+ over the central transverse slice (Figs. 3, 5, 7) for the cases of minimization of power reflected by entire array and inductor based decoupling network cases on the basis of the B_1+ slice profile for single channel excitation (Figs. 2, 4, 6). This result, and the observations mentioned above, imply that 3D EM simulation must be performed in order to obtain reliable data for the magnetic field distribution produced by the given array.

To shorten figure captions, we use the abbreviations "C" and "I" for the tune/match/decoupled condition corresponding to capacitor and inductor based decoupling networks respectively and "R" for configuration, where the power reflected by the entire coil was minimized.

For the configurations investigated, the effect of the local shield on transmit field homogeneity was less than 15%.

Decreasing the loop angular size can significantly degrade homogeneity if the separation between array and load is less than 20 mm. But if this is greater than 20 mm, for most coil/load geometries, changing angular size from 40 degrees to 22.5 degrees has little effect on slice homogeneity. As a result there is some design freedom for an entire transmit array if closely placed loop coils cannot be properly decoupled for a set of loads. Due to space restrictions, Table 2 only shows data for a 200 mm diameter array with 80 and 120 mm lengths and loaded by 120 mm ball and cylinder.

Table 2: Influence of loop angular size on homogeneity.

loop angular size	40				37.5				32.5				22.5			
Slice position, mm	0		+25		0		+25		0		+25		0		+25	
$\boldsymbol{B}_1+$, μT; Inhomogeneity, %	B_1+	%	B_1+	%	B_1+	%	B_1+	%	B_1+	%	B_1+	%	B_1+	%	B_1+	%
200x120 mm coil&120 mm ball load	3.63	26	2.85	21	3.61	26	2.84	21	3.55	26	2.79	21	3.34	26	2.63	21
200x120 mm coil&120 mm cylinder load	2.13	25	1.91	25	2.12	25	1.90	25	2.10	25	1.88	25	2.01	25	1.80	25
200x80 mm coil&120 mm cylinder load	2.44	18	1.98	22	2.43	18	1.97	22	2.40	18	1.94	22	2.28	18	1.84	22

The results reported were obtained in somewhat ideal array design conditions: a) values of fixed capacitors was not limited by the commercially available range of values, b) component value tolerance of zero was assumed, c) performance optimizations reach global minimum. The results can be considered as achieving the best possible homogeneity.

4. CONCLUSIONS

RF circuit and frequency domain 3-D EM co-simulation is a very powerful and fast approach for array coil investigation, since one multi-port 3-D EM simulation, which can be calculated in a reasonable time, is sufficient for investigation of the array behavior with different tuning/feeding/decoupling conditions. The optimal separation between load and array, giving the best homogeneity without visible degradation of mean B_1+ over the given transverse slice, is in the range of 30–45 mm. This result assists the design of transmit-only/receive-only (TORO) arrays, because about 40 mm load/array separation provides adequate space for an RX-only coil. To be able to adjust scanner transmit power for a given slice in real time may greatly affect the homogeneity optimization procedure for entire field of view, because such a transmit power adjustment avoids the need to minimize the difference between mean B_1+ for slices.

REFERENCES

1. Kozlov, M. and R. Turner, "Fast MRI coil analysis based on 3-D electromagnetic and RF circuit co-simulation," *Journal of Magnetic Resonance*, No. 200, 147–152, 2009.

Using Rectangular-shape Resonators to Improve the Far-end Crosstalk of the Coupled Microstrip Lines

Ding-Bing Lin[1], **Chen-Kuang Wang**[1], **Chi-Hao Lu**[1], **and Wen-Tzeng Huang**[2]

[1]Graduate Institute of Computer and Communication Engineering
National Taipei University of Technology, Taipei, Taiwan
[2]Department of Computer Science and Information Engineering
Minghsin University of Science and Technology, Hsinchu, Taiwan

Abstract— Modern electronic products must have high-speed, high-density layout, small size, faster rising time and lower voltages supply. With such design, signal integrity (SI) becomes a very important factor because sensitive equipment is affected by electromagnetic interference (EMI) and noise interference. Crosstalk is a major factor in SI from printed circuit boards (PCBs). Crosstalk noise is usually represented in terms of near-end crosstalk (NEXT) and far-end crosstalk (FEXT). In order to cost concerns, microstrip line is widely used for PCBs because it's easy to manufacture. In microstrip line structure, FEXT is induced by the difference between the capacitive coupling ratio (C_m/C_T) and inductive coupling ratio (L_m/L_S). In earlier research, however, many researchers had proposed solutions that are guard trace which are used to reduce NEXT and FEXT. Since a large number of shorting-via degrades the SI and reduces the flexibility of the circuit routing. Another technique to reduce the FEXT noise is serpentine guard trace, but this kind of guard trace requires to be terminated with matched resistances at both ends of guard trace. In this paper, we propose a method to reduce the far-end crosstalk by using rectangular-shape resonators (RSR) structure. In which, the shorting-via and resistance are not necessary to be used for improving the FEXT. The frequency-domain simulation of HFSS shows that the S_{41} of RSR structure is decreased more than 7 dB compared to the 3-W rule. The time-domain simulation of ADS shows that the peak of far-end crosstalk voltage of RSR structure is improved to 54% compared to the 3-W rule.

1. INTRODUCTION

In the modern generation of high information processing, electronic products must have high-speed, high-density layout, small size, faster rising time and lower voltages supply. With such designs, the signal integrity (SI) problem in a poor printed circuit board layout is affected by noise. SI is a critical factor in the design of a high-speed PCB [1]. Crosstalk is one noise source in PCBs and is of particular concern in high-density and high-speed circuits, is one major source of noise to interfere with SI. In recent years, the crosstalk noise problem is getting worse because layout density is increasing between connections of chips. Crosstalk noise is usually represented in terms of near-end crosstalk (NEXT) and far-end crosstalk (FEXT). FEXT is induced by the different of the inductive coupling ratio and capacitive coupling ratio, but in addition, it is proportional to the length of the parallel transmission lines and only exists in inhomogeneous environment, e.g., the microstrip structure [2]. In a parallel-terminated interface, the FEXT is more problematic than NEXT since it seriously affects the SI at the receiver side [3]. Therefore, decreasing FEXT is one of the most important goals in a PCB design.

In general, the electronic devices in order to prevent crosstalk interference are to be designed to three times the transmission line width, where the rules known as the 3 W [4]. The general method most commonly were to add guard trace structure between two coupled traces that the active trace to which the signal is applied is called the aggressor line, the passive trace to which no signal is applied is called the victim line. However, a guard trace is also a potential noise source because it is to like transmission line of open terminated [5]. In practice, guard trace with a lot of shorting-vias should be added to maintain a stable grounded potential. In a real layout, however, only a few plated vias can be used to connect the guard trace and ground plane due to circuit backside routing restriction [2, 6].

In this paper, we propose a method to reduce effectively the FEXT by using rectangular-shape resonators (RSR) structure. In which, the shorting-via and resistance are not necessary for improving the FEXT noise. Hence, compared to past method mentioned above, the proposed method own the advantage of the flexibility of the circuit backside routing.

2. FAR-END CROSSTALK

Crosstalk occurs due to the coupling effects caused by the mutual capacitance (C_m) and mutual inductance (L_m) of the victim and aggressor, driven by the transient signals in the aggressor. Crosstalk noise is usually represented in terms of NEXT and FEXT. The equivalent model of the two parallel traces is shown in Fig. 1(a), and the typical crosstalk signature of the victim without a guard trace is shown in Fig. 1 [1]. The end of the victim closest to the driver (receiver) of the aggressor is called the near (far) end. When the rise and fall times of the aggressor's transient logic states change continually, the signal operation of the victim will be destroyed, since the coupling effect of C_m and L_m transfer energy from the aggressor [9]. Since modern high-speed circuits have intensive of wiring layout caused by high C_m and L_m, crosstalk noise is a major issue in high-speed digital system design. In some cases, e.g., microstrip line, the inductive coupling ratio is always larger than capacitive coupling ratio because the dielectric constant of surrounding air is less than that of the PCB dielectric material [7]. This difference between inductive and capacitive coupling ratios can induce FEXT. Let L_S and C_S be the self-inductance and self-capacitance, respectively. The FEXT can be represented as [8]

$$V_{FEXT} = -\frac{V_{in}}{2T_r} \cdot TD \cdot \left(\frac{L_m}{L_S} - \frac{C_m}{C_T} \right) \tag{1}$$

where V_{in} is the input voltage, TD is the time delay and T_r is the rising time.

Based on Eq. (1), how to get lower difference of the inductive coupling and capacitive coupling is necessary to decrease FEXT.

3. RECTANGULAR-SHAPE RESONATORS STRUCTURE

In the following analysis structure which is placed on FR4 PCB substrate. Dielectric constant of the substrate is 4.4 and thickness is 1.6 mm. The thickness of copper (trace and ground) is 0.035 mm. The width of the microstrip line is designed to 3 mm to match 50 Ω. The length of trace is 50 mm. Figs. 2(a), (b) and (c) represent the three structures, 3-W rule, shorting-via guard trace and RSR structure, respectively. For the fair comparison, all of the above layout parameters are the same among these three approaches. In Fig. 2(b), we used seven shorting-vias to enhance FEXT, and distance between vias is 7.8 mm. Based on [10], between the two vias the resonant frequency can be determined. In the guard trace of seven shorting-vias, we can move the first resonant frequency of the bandwidth in interested frequency range.

Although shorting-via guard trace can reduce FEXT which takes a lot of via hole connected to the ground plane. In practice, however, we can't use a lot of via hole by circuit routing restriction [2, 5]. In this concerns of circuit backside routing restriction, the RSR structure is used to improve FEXT as Fig. 2(c), where $l_r = 8$ mm and $W_r = 1$ mm. In this method, it needn't use any shorting-via and resistance connected to ground plane. In order to compare the convenience, we use eleven RSR structure to reduce the FEXT. In practice, we can add more RSR structure to improve the FEXT because it does not need to use shorting-via.

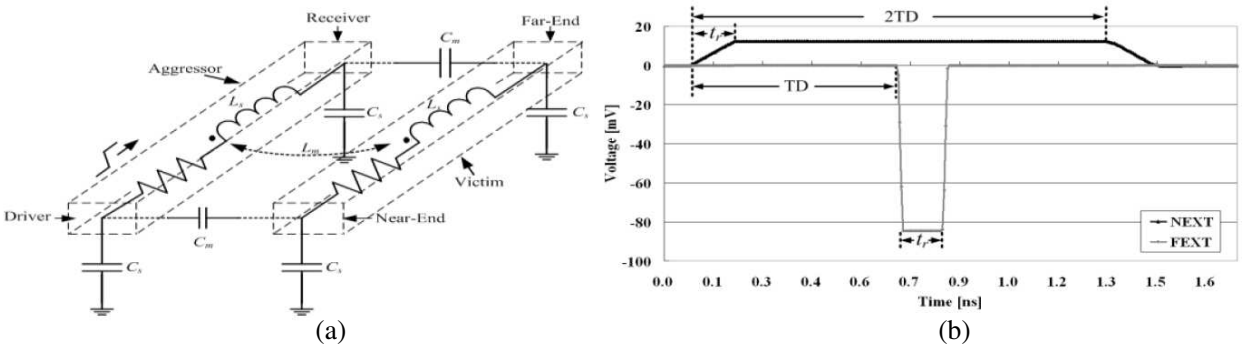

Figure 1: (a) Equivalent model of the two parallel traces [8]. (b) Typical crosstalk signature of the victim without a guard trace [1].

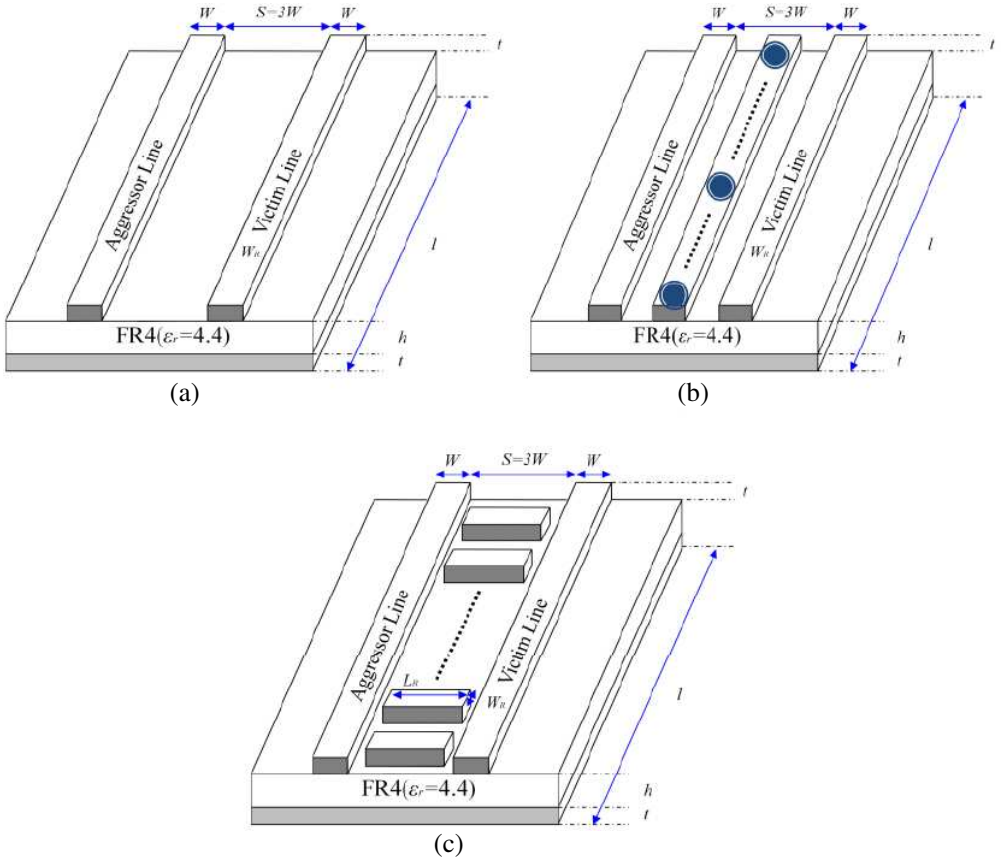

Figure 2: Comparison among three topologies. (a) 3-W Rule, (b) shorting-via guard trace, (c) RSR structure.

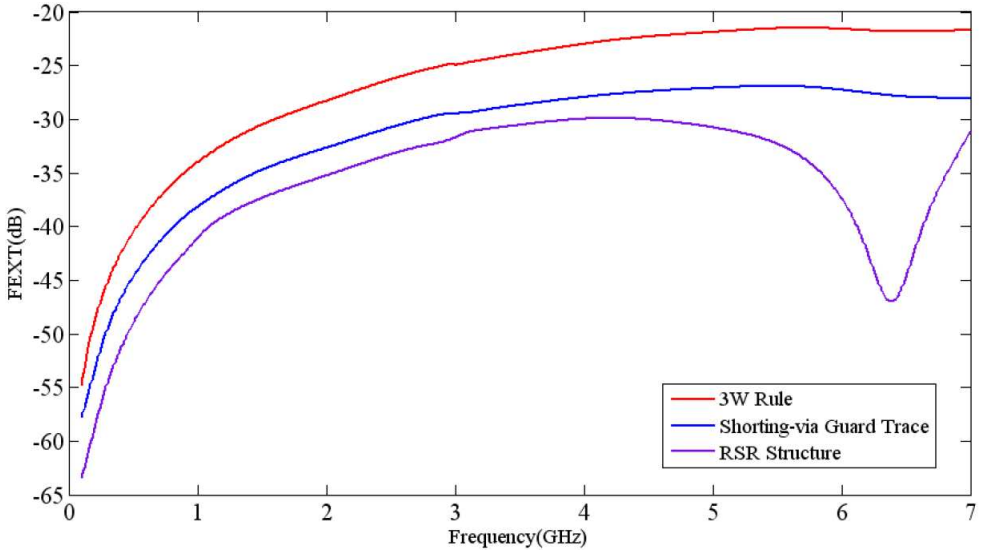

Figure 3: Comparison of frequency-domain simulation.

4. SIMULATION AND COMPARISON

Figures 2(a), (b) and (c) show the comparison of the three cases as 3-W, shorting-via guard trace and RSR structure, respectively. The parameter setup is the same as that in Fig. 2 and Section 3. In this work, frequency-domain simulation is based on using the field solver High Frequency Structure Simulator (HFSS) [11] and FEKO [12]. Comparison of three kinds of structure, the shorting-via guard trace and RSR are better than the 3-W rule. But in RSR structure, where needn't use shorting-via to enhance the FEXT. RSR structure can enhance 7 dB and 3 dB for 3 W and

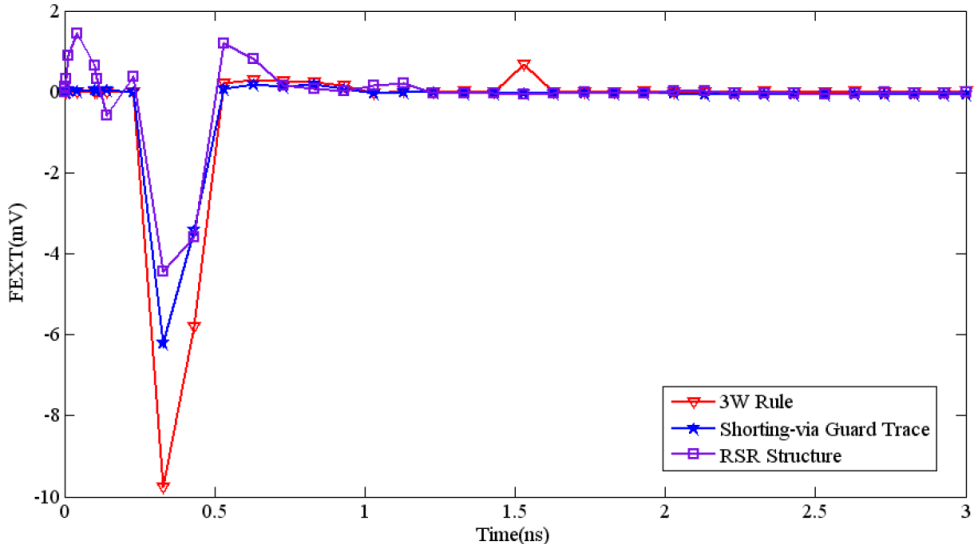

Figure 4: Comparison of time-domain simulation.

shorting-via structure. In Fig. 4, the time-domain simulation of Advanced Design System (ADS) shows that the peak of far-end crosstalk voltage of RSR structure is improved to 54% of that of 3-W rule, where input voltages is 1 V and rising time is 100 ps.

5. CONCLUSIONS

Verified in the frequency-domain simulation results, our approach of the rectangular-shape resonators structure can enhance far-end crosstalk by 7 and 3 dB compared to the three times of width rule and the shorting-via guard trace, respectively. In time-domain simulation, the rectangular-shape resonators structure can decrease 54% and 30% compared to the 3-W rule and the shorting-via guard trace, respectively. All results are showing that the proposed structure has a very good performance among these three approaches. In this method, it can reduce the FEXT, where needn't use shorting-via and resistance to enhance the FEXT noise. Hence, our method can be indeed employed to those products of the high-speed printed circuit board applications to suppress the far-end crosstalk and then increase their reliability and circuit routing flexibility.

ACKNOWLEDGMENT

This work was supported by the National Science Council of Taiwan under grant NSC 99-2515-S-027-001- and NSC 99-2220-E-027-006-.

REFERENCES

1. Bogatin, E., *Signal Integrity-simplified*, Prentice Hall, 2003.
2. Cheng, Y. S., W. D. Guo, G. H. Shiue, H. H. Cheng, C. C. Wang, and R. B. Wu, "Fewest vias design for microstrip guard trace by using overlying dielectric," *2008 IEEE-EPEP*, 321–324, San Jose, CA, Oct. 27–29, 2008.
3. Lee, S. K., K. Lee, H. J. Park, and J. Y. Sim, "FEXT-eliminated stub-alternated microstrip line for multi-gigabit/second parallel link," *Electron. Lett.*, Vol. 44, No. 4, 272–273, Feb. 2008.
4. Montrose, M. I., *EMC and the Printed Circuit Board: Design, Theory, and Layout Made Simple*, IEEE Press, 1998.
5. Huang, W.-T., C.-H. Lu, and D.-B. Lin, "The optimal number and location of grounded vias to reduce crosstalk," *Progress In Electromagnetics Research*, Vol. 95, 241–266, 2009.
6. Chiu, P. W. and G. H. Shiue, "The impact of guard trace with open stub on time-domain waveform in high-speed digital circuits," *Electrical Performance of Electric Package and System*, 219–222, Oct. 2009.
7. Lee, K., H. B. Lee, H. K. Jung, J. Y. Sim, and H. J. Park, "A serpentine guard trace to reduce the far-end crosstalk voltage and the crosstalk induced timing jitter of parallel microstrip lines," *IEEE Transactions on Advanced Packaging*, Vol. 31, No. 4, 809–817, Nov. 2008.

8. Hall, S., J. Hall, and J. McCall, *High Speed Digital Design: A Handbook of Interconnect Theory and Design Practice*, John & Sons, New York, 2000.
9. Sharawi, M. S., "Practical issues in high speed PCB design," *IEEE Potentials*, Vol. 23, No. 2, 24–27, Apr./May 2004.
10. Novak, I., B. Eged, and L. atvani, "Measurement by vector-network analyzer and simulation of crosstalk reduction on printed circuit boards with additional center traces," *Proc. IEEE Instrum. Meas. Technol.*, 269–274, Irvine, CA, May 1993.
11. Ansoft HFSS user's GuideHigh Frequency Structure Simulator, Ansoft Co., 2003.
12. FEKO User's Manual Suite 5.5, EM Software & Systems-S.A. (Pty) Ltd, South Africa, July 2009. http://www.feko.info.

Electromagnetic Model of In-wall Wiring of Indoor Powerline Communications

V. Arnautovski-Toševa[1, 2], **K. El Khamlichi Drissi**[1], **and K. Kerroum**[1]

[1]LASMEA Laboratory, University Blaise Pascal, Aubiere, France
[2]Electrical Engineering and IT, University Ss. Cyril and Methodius, Skopje, Macedonia

Abstract— Powerline Communications (PLC) represent technology that enables data transfer at narrow or broad band speeds through power lines by using advanced modulation technology. Although the PLC technology in the beginning was promising and was potentially easy to install and inexpensive, it is still not fully developed and standardized. One major concern related to these systems is the electromagnetic field radiation. This paper is aimed to present one approach within the EMC issue related to indoor PLC.

1. INTRODUCTION

To transmit signal between the transmitter and receiver, PLC technology works by coupling to the existing electrical wiring a modulated signal from 1–30 MHz, usually between phase and neutral line or between different phase wires, using appropriate inductive or capacitive couplers.

However, high frequency band from 1 to 30 Hz over power lines present various and quite complex EMC problems [1]. This refers to emissions and immunity of different systems that use the same high frequency band. Various numerical methods and simulation tools have been introduced to provide design assistance in such EMC problems [2]. In this paper the radiated electromagnetic field by an indoor PLC circuit has been analyzed using a three dimension Method of Moments (3D-MoM) on the antenna theoretical background. The low voltage circuit is modeled with equivalent thin-wires and the wall as a homogeneous conductive central layer of a three layer stratified media (air/wall/air). The software developed in Fortran offers great flexibility for parametric analysis, and may be linked to specialized software for circuit analysis, as Matlab. In this paper, the authors are focused on the investigations the electric radiation performance of a PLC indoor circuit when excited by signals in frequency range from 3 to 30 Hz.

2. MATHEMATICAL MODEL

An efficient yet adequately accurate approach by combining MoM and equivalent thin-wire modeling is proposed. The mathematical model is based on the assumption that such wiring at high frequencies behaves like a transmitting antenna. Considering the high frequency range the mathematical model is based on rigorous formulations derived from the full set of the Maxwell's equations and the theoretical background of microstrip antenna analysis [3]. It is developed in the frequency domain and tends to take into account the electromagnetic effects related to the geometry of the formed circuit and the influence of the media. The model is based on the MPIE integral equation of the electric field created by the currents and the loads presented in the segments. The exact Green's functions due to HED in stratified media involve Sommerfeld type integrals that are solved by direct numerical integration. The solution is obtained using the MoM with triangular basis and weighting functions in a similar way as in [4].

2.1. The Physical Model

The physical model of a simplified in-wall PLC wiring is shown in Fig. 1. The geometry of the circuit is assumed as rectangular with length L and width W. It is formed by the thin-wire conductors of radius a, and lies in the x-y plane. For the purposes of MoM application the conductors are based on the fictitious segmentation into straight tubular segments. The axial current along the conductors is approximated by a linear combination of overlapping triangle dipole expansions functions positioned along two neighbor segments of total length l_n [4].

The excitation is assumed by an ideal harmonic source generator V_S in frequency range from 3 to 30 MHz. The internal resistance and the load are represented by resistors R_S and R_L respectively. The circuit is placed at a depth h in the wall. The wall surfaces correspond to the plane $z = 0$ and $z = -d$. The wall is represented as a homogeneous central layer of a three layers stratified media, characterized by a relative permittivity ε_r, a permeability μ_0, and a conductivity σ.

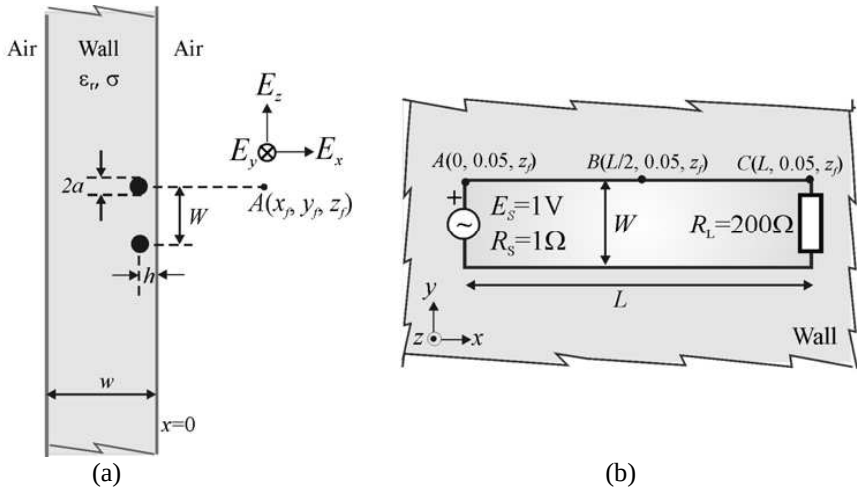

Figure 1: (a) A physical model of a PLC in-wall circuit: A wall/circuit cross-section, (b) a circuit geometry in the $z = -d$ plane with the observation pints A, B and C in the $z = +z_f$ plane in front of the wall.

2.2. The Impedance Matrix

The mathematical model that is based on mixed potential integral equation (MPIE) [5], that is solved by the method of moments. Herewith, the elements of the impedance matrix $[Z]$ that represent mutual impedances z_{mn} are calculated between pair of triangular dipoles: source dipole n of length l_n carrying current I_n, and test m of length l_m as

$$z_{mn} = -\frac{1}{I_n}\int_{l_n} \mathbf{E}_n \cdot I_m \mathbf{l}_m = \frac{1}{I_n}\int_{l_n} (j\omega \mathbf{A}_n + \nabla\phi_n) \cdot I_m \mathbf{l}_m, \tag{1}$$

where $\mathbf{E}_n$ is the electric field at the surface of the observation segment m. Here, the computation of the vector and scalar potentials involves appropriate Green's functions through the following integral form

$$\mathbf{A}_n = -\int_{l_n} \underline{G}_A \cdot I_n d\mathbf{l}_n \;\text{ and }\; \phi_n = \int_{l_n} G_\phi q_n dl_n \;\text{ with }\; q_n = \frac{-1}{j\omega}\frac{dI_n}{dl_n}. \tag{2}$$

In (2), $\underline{\mathbf{G}}_A$ is a dyadic Green's function for the magnetic vector potential, and G_ϕ is a scalar potential Green's function due to elementary horizontal electric dipole (HED) embedded in horizontal three-layer medium (air/wall/air). Above Green's functions are obtained by numerical integration of the following Sommerfeld-type integrals from their spectral expressions [3] given in general form as follows

$$\tilde{G}_A^{xx} = \frac{\mu_0}{j2k_z} T^{\mathrm{TE}} \;\text{ and }\; \tilde{G}_\phi = \frac{1}{\underline{\varepsilon}_r j2k_z}\left[T^{\mathrm{TE}} + \frac{k_z^2}{k_\rho^2}\left(T^{\mathrm{TE}} \pm \frac{1}{jk_z}\frac{\partial T^{\mathrm{TM}}}{\partial z}\right)\right]. \tag{3}$$

Here, T^{TE} and T^{TM} are plane wave transmission coefficients from the plane of the source to the plane of the observation; k_z is vertical wave number for the layer of the source and $k_z^2 + k_\rho^2 = \underline{\varepsilon}_r k_0^2 = (\varepsilon_r - j\sigma\omega\varepsilon_0)k_0^2$.

2.3. Calculation of the Electric Field Vector

When the solution of above equation due to all source current segments is evaluated, then a very accurate 3-D profile of the radiated electric field can be obtained. The vector components of the electric field can be deduced by using 'ghost' segments oriented along x, y and z axis, which captures the essence of Method of Moment as an 3-D electromagnetic solver. Here, the superposition principle is used to calculate the electric field in point $P(x_f,\, y_f,\, z_f)$ in front of the wall,

$$\mathbf{E}_P = \sum_{n=1}^{N} \mathbf{E}_{Pn} \;\text{ with }\; \mathbf{E}_{P_n} = -j\omega \int_{\ell_n} \bar{\mathbf{G}}_A \cdot I_n d\mathbf{l}_n + \nabla\frac{1}{j\omega}\int_{\ell_n} q_n G_\phi dl_n \text{ where} \tag{4}$$

$$E_{Pnx} = -j\omega A_{nx} - \frac{\partial}{\partial x}G_{n\varphi};\;\; E_{Pny} = -\frac{\partial}{\partial y}G_{n\varphi};\;\; E_{Pnz} = -j\omega A_{nz} - \frac{\partial}{\partial z}G_{n\varphi}. \tag{5}$$

3. NUMERICAL RESULTS

In this section, some numerical results that represent the radiated electric field in vicinity of an in-wall PLC circuit are presented. It is assumed that the circuit dimensions are: length $L = 5\,\mathrm{m}$, width $W = 5\,\mathrm{cm}$, conductor radius $a = 5\,\mathrm{mm}$. It is placed at depth $h = 3\,\mathrm{cm}$ in the wall of thickness $d = 20\,\mathrm{cm}$. The wall permittivity and conductivity are $\varepsilon_r = 10$ and $\sigma = 10^{-3}\,\mathrm{S/m}$. The voltage amplitude is $1\,\mathrm{V}$, $R_S = 1\,\Omega$ and $R_L = 200\,\Omega$.

Firstly, in Fig. 2 it may be observed the magnitude and the phase of the current in the source and in the middle of the conductor with length L, with respect to frequency.

Figure 3 shows a 2D and a 3D view of the electric field vector at distance $z = 10\,\mathrm{cm}$ from the wall surface calculated at 10 MHz. As may be observed in Fig. 3(a), the E_y component is completely dominating while E_x component is negligible in points parallel the wall surface. As may be observed in Fig. 3(b), the E_z component is significant in points that are parallel to the long conductors of length L.

Figure 4 shows respectively the magnitudes of the electric field components E_y and E_z at points A, B and C along a profile $y = 5\,\mathrm{cm}$ and distance $z = 10\,\mathrm{cm}$ in front of the wall surface. The x-coordinates of the points A, B and C along a profile correspond to: 0 m (close to the source V_S), 2.5 m (in the middle of the conductor with length L) and 5 m (close to the load R_L).

When increasing the distance from the wall surface the level of the electric field components rapidly decreases as may be observed in Fig. 5. Here, the magnitude only of the dominating E_y component is shown. The observation points A, B and C lie along the profile $y = 5\,\mathrm{cm}$ and distance $z = 25\,\mathrm{cm}$ and $z = 50\,\mathrm{cm}$ from the wall respectively. As may be observed, the magnitude of the electric field component E_y at 25 cm in front of the wall is about one-third of the value at 10 cm, whereas at distance of 50 cm in front of the wall the magnitude of the E_y component declines at

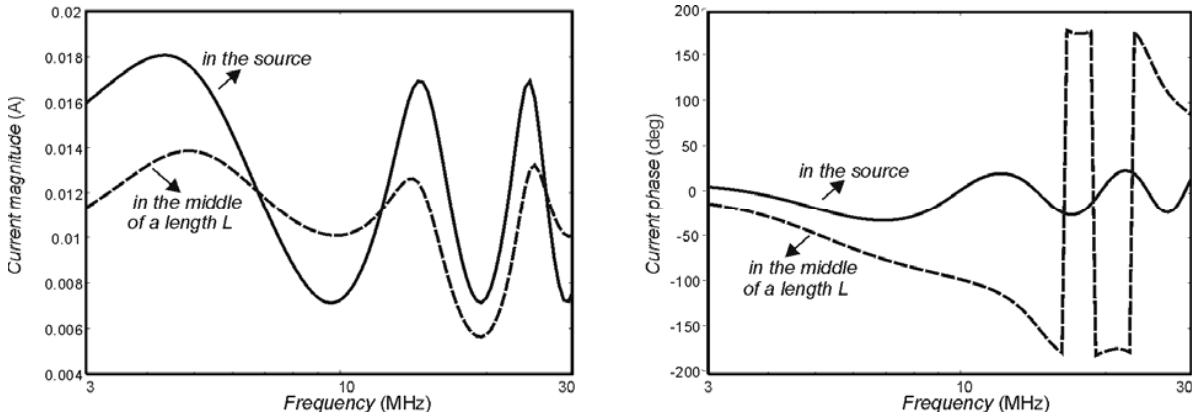

Figure 2: A magnitude and a phase of a current in the source and in the middle of a length L with respect to frequency.

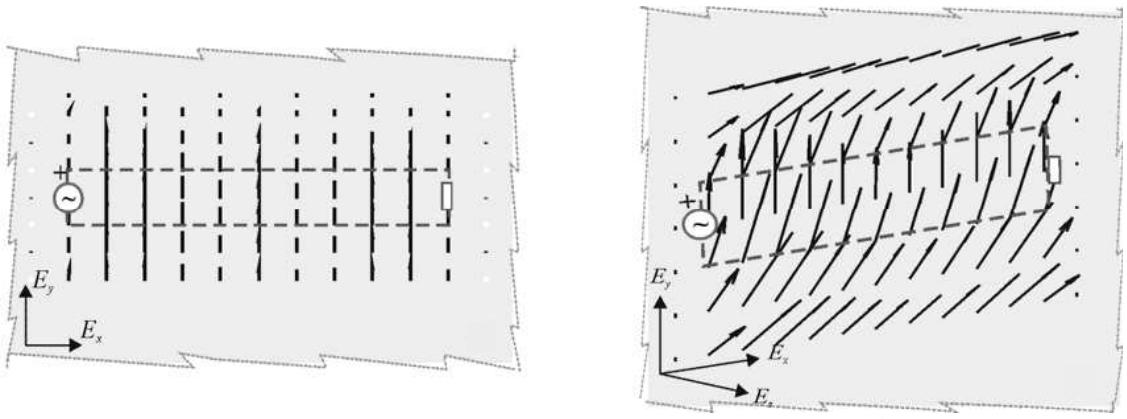

(a) (b)

Figure 3: A 2D and a 3D view of the electric field vector at distance: 10 cm from the wall surface calculated at 10 MHz.

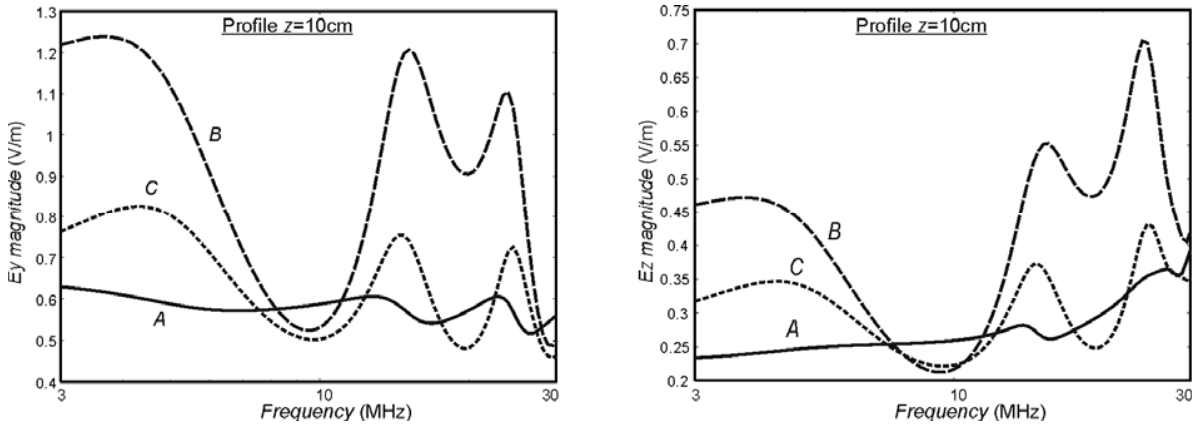

Figure 4: Magnitudes of the E_y and E_z electric field components at points A, B and C along a profile at distance of 10 cm from the wall surface in frequency range from 3 to 30 MHz.

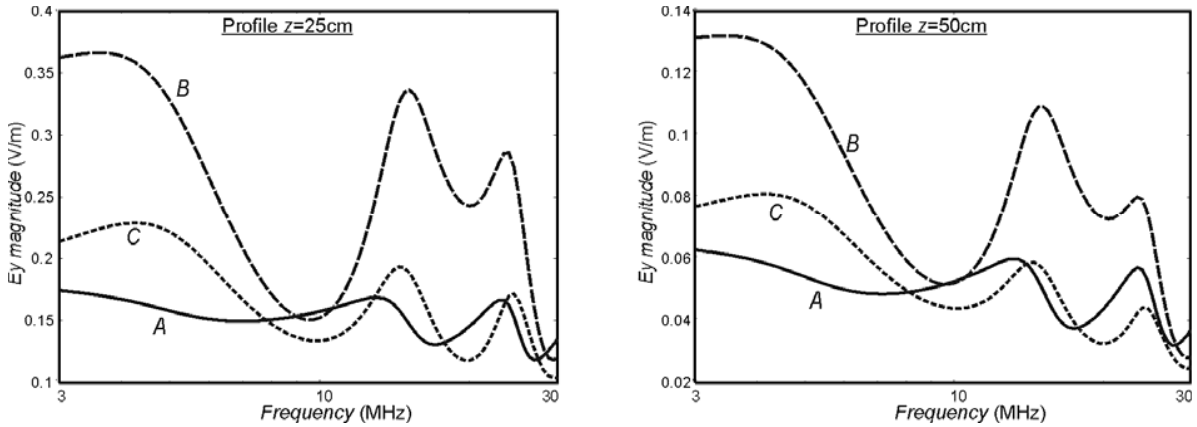

(a) (b)

Figure 5: Magnitude of the E_y electric field component at points A, B and C along a profile at distance of 25 cm (a) and 50 cm (b) in front of the wall in frequency range from 3 to 30 MHz.

only one-tenth the value at 10 cm. As may be observed, in all cases the shape of the curves of E_y and E_z follow the oscillations of current with respect to frequency.

4. CONCLUSIONS

In this paper the authors are focused on the analysis of the electric field radiated by the in-wall PLC circuit when excited by high frequency input signal. The proposed model is developed in frequency domain on the basis of antenna theory and uses the MoM method. The electric field radiated from an indoor low voltage circuitry excited by high frequency signals in frequency range from 3 to 30 MHz has been analyzed. The results show 3D view of the electric field vector distribution at points parallel to the wall surface. Also, some results of the frequency behavior of E_y and E_z components with respect to frequency and distance from the wall surface has been represented. The results lead to the following conclusions:

- The E_y component (parallel to the source) of the electric field is dominating while the E_x component is negligible. The E_z component (orthogonal to the wall) is significant in points parallel to the long conductors.
- The magnitude of the electric field at distance of 50 cm from the wall surface is about one-tenth of the value obtained at 10 cm from the wall.
- The frequency behaviour of the field components is strongly affected by the frequency oscillations.

ACKNOWLEDGMENT

This work has been realized within the FP7-PEOPLE-2009-IEF Project 253783.

REFERENCES

1. Zimmermann, M. and K. Dostert, *Power Line Communications: Theory and Applications for Narrowband and Broadband Communications over Power Lines*, John Wiley and Sons, 2010.
2. Teshe, F. M., M. Ianosz, and T. Karlsson, *EMC Analysis Methods and Computational Modems*, John Wiley and Sons, 1997.
3. Dural, G. and M. Aksun, "Closed-form Green's functions for general sources and stratified media," *IEEE Transactions on Antennas and Propagation*, Vol. 43, No. 7, 1545–1552, July 1995.
4. Arnautovski-Toseva, V. and L. Grcev, "Electromagnetic analysis of horizontal wire in two-layered soil," *Journal of Computational and Applied Mathematics*, Vol. 168, No. 1–2, 21–29, 2004.
5. Mosig, J. R. and F. E. Gardiol, "A dynamic model for microstrip structures," *Advances in Electronics and Electron Physics*, Vol. 59, 139–237, P. W. Hawkes, Ed., Academic, New York, 1982.

Analysis of Transmit Performance Optimization Strategies for Multi Channel MRI Array

M. Kozlov and R. Turner
Planck Institute for Human Cognitive and Brain Sciences, Leipzig, Germany

Abstract— Experimental optimization of MRI multi-channel arrays can be very time consuming and costly. We present an approach based on co-simulation of the RF circuit and frequency-domain 3-D electromagnetic fields (EM) which allows very powerful and fast investigation of array coils, since one multi-port 3-D EM simulation, which can be calculated reasonably quickly, is sufficient for obtaining the array behavior with any combination of tuning/feeding/decoupling conditions. We explored capacitor and inductor based decoupling networks, comparing their array performance in the condition of minimal power reflected by the entire coil. The necessary inclusion of all tuning/feeding/decoupling circuits enables accurate array performance data to be obtained. Especially for relative small coil loading, S_{xx} and S_{xy} alone provide insufficient guidance in regard to the decoupling required to optimize array performance. The power reflected by the entire coil must also be minimized.

1. INTRODUCTION

MRI multi channel arrays enable several novel applications such as B_1 shimming and transmit SENSE. Due to the complexity of the problem, experimental optimization alone is extremely time consuming and costly. Numerical simulation may be an important tool for array optimization and is required to predict the RF field distribution. However, the published simulation approaches, mainly based on finite difference time domain solvers, are insufficiently flexible for the analysis of multi-channel array decoupling, and cannot be applied for most tune/match/decoupling problems without many time-consuming 3D EM simulations. Our goal was to develop an approach for obtaining coil performance data over a range of tune/match/decoupling strategies, with only one 3D EM computation, to quantify coil performance realistically as B_1+ (in Tesla) versus the square root of the transmit power, for several coil and load geometries, and to map the predicted RF fields of the optimized coil.

2. METHOD

We investigated array MRI coils comprising 8 channels with identical rectangular loops (length 100, 120 mm), mounted on a cylindrical acrylic former with diameter ranging from 220 mm to 300 mm. The angular size of the loops was varied from 40 degrees (the closest element spacing) to 22.5 degrees (the largest gap between elements). Cylindrical loads with a range of diameters, and a 120 mm diameter spherical phantom, were used in this investigation. In this arrangement, the cylindrical symmetry of array and load rules out improvement of array performance by RF shimming (adjustment of amplitude and phase for excitation signals). The electrical properties of the single component load were close to those of average human tissue at 300 MHz — permittivity 52 and conductivity 0.55 S/m. All arrays were excited in circular polarization mode, applying 1 W power to each port (array transmit power — $P_{\text{transmit}} = 8$ W), with a sequential 45 degree phase increment. Q factor of all capacitors is equal 1000.

The scanner gradient shield (with diameter of 683 mm and length 1200 mm) was always included in the numerical domain for simulation of unshielded and shielded arrays. The distance between the shielded array and a 300 mm long local shield was varied to maintain approximately the same ratio of the distances of coil to load centre and shield to load centre.

We attached capacitor and inductor based decoupling networks and compared their array performance obtained when the power reflected by the entire coil was minimized. Our tune/match/decoupling approach relies on RF circuit and 3-D EM co-simulation [1]. The RF circuit simulator was Agilent ADS software, and Ansoft HFSS was chosen as the 3-D EM tool, for its robustness in handling complex coil geometry and fast multi-port simulation. In brief, the co-simulation approach entails substitution of all tune/match/decouple networks by ports during the 3D-EM simulation, and their reconnection during circuit simulation, followed by a simple computation (weighted sum of already calculated quantities) of the final 3D electromagnetic field distribution. Substitution

of an RF network by a lumped 3-D EM port requires equalization of entering and leaving currents, because such a port is not a true differential port. This condition applies automatically for some decoupling and most tune/match networks used for MRI coil design, but can be infringed by decoupling networks connected between different coil element, or having internal connection to ground.

For inductive decoupling within the loop array, a decoupling network inductor, placed in series with a loop radiative element, is usually accompanied by a distributed capacitor in series. Both elements have the same entering and leaving currents. This enables substitution of this sub-circuit by one port. The opposite case is the capacitive decoupling network, which includes capacitors connected between the different radiative elements comprising the 3D structure. Due to such cross-connections and a generally asymmetrical load (for example the human head), the entering and leaving currents are different for this network, treated as a single subcircuit. For this reason, the capacitor-based decoupling network must be substituted by 4 ports. These ports need not be closely co-located. Decoupling capacitors between radiative elements (and their port substitution) can be placed in arbitrary positions, in reality and in the numerical domain, provided that a 3D EM simulation is performed for each different independent position of decoupling capacitors. For the present investigation a) the position of decoupling capacitors is fixed at each end of the array elements (Fig. 1) and b) two inductor based decoupling networks (Fig. 2) placed at both ends of the array elements. The latter arrangement implies that 4 inductors are placed in series with each loop radiative element.

Because the decoupling network influences the value of distributed capacitors, for maximal flexibility, all distributed capacitors were also substituted by lumped ports. The values of distributed capacitors were then obtained by RF circuit optimization. The total number of ports amounts to 80, for an 8 element coil with 8 capacitors in the radiative loop and two connections for decoupling circuits.

If a simulated port does not correspond to any actual circuit element for a given array design (for example ports provided for decoupling capacitors when an inductive decoupling network is the subject of analysis) then a very high impedance (10 GOhm) resistor is connected across this port, for the purpose of circuit simulation.

The required values of fixed and adjustable multi-channel array lumped elements are obtained

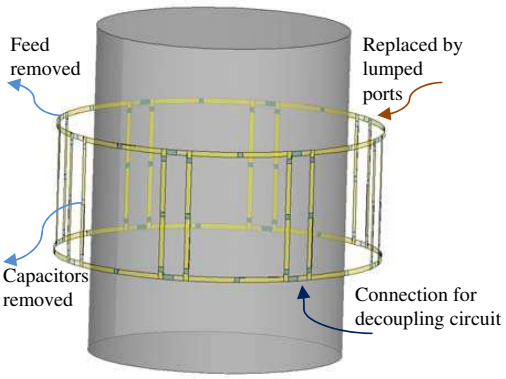

Figure 1: 3-D EM model setup.

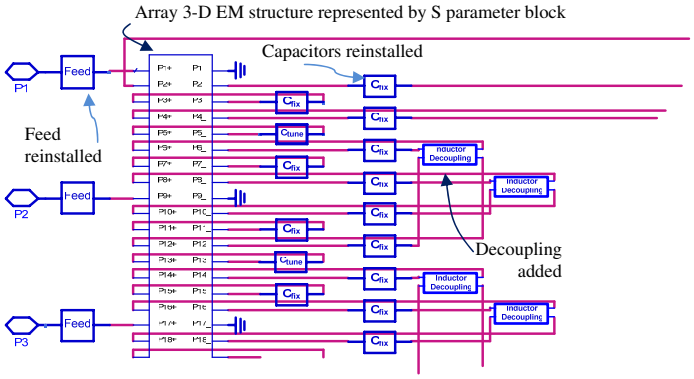

Figure 2: 3-D EM model setup.

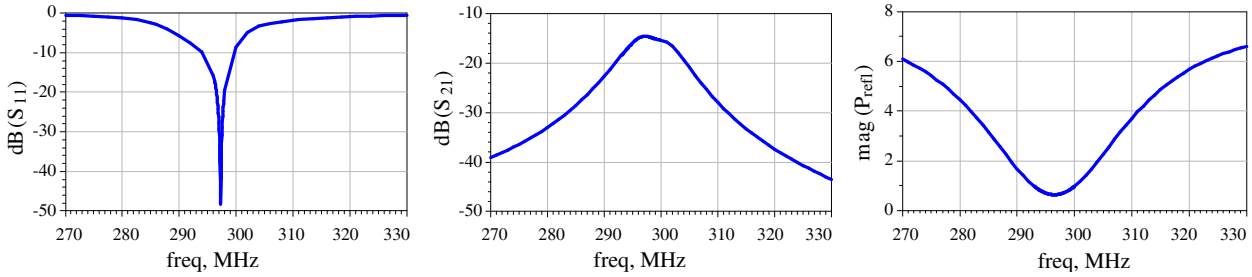

Figure 3: Data for an array with decoupling network.

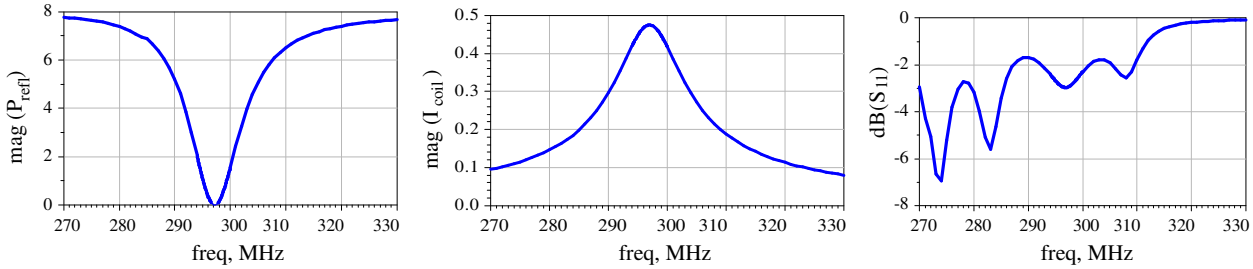

Figure 4: Data for an array for which the power reflected by the entire coil was minimized.

by a numerical domain RF circuit tuning/matching/decoupling procedure that is very close that used in real life, especially if this includes a computational step. For the array with capacitor and inductor based decoupling networks the procedure is guided by a set of criteria defined as a) the frequency at which S_{xx} approaches its minimum must be equal to the MRI resonance frequency, for each array element; b) S_{xx} must be $< -30\,\mathrm{dB}$, for each array element; c) S_{xy} must be $< -20\,\mathrm{dB}$, for each neighbouring pair. This results in as many as 24 criteria for an 8-channel loop array.

To minimize power reflected by the entire coil, criteria are defined such that the power reflected by each element must be equal to zero. Thus there are 8 criteria for an 8-channel loop array. It should be noted that this optimization approach is not concerned with S_{xx} and S_{xy} minimization. By contrast, in most cases our approach to transmit optimization yields highly coupled coil elements and pure S_{xx} matching. But here the maximum coil current is exactly at the MRI resonance frequency and transmit performance is optimal (Fig. 4 and Table 1).

In general, any other criterion can be incorporated in the procedure, and each criterion can be independently modified and weighted to adjust its influence on a optimization error function that is iteratively minimized by a software circuit optimizer.

Initial guesses are made, based on numeral simulation experience or available experimental data, for the values of fixed elements and the starting values of adjustable elements (tune and match capacitors/inductors/mutual inductance), as well as the range over which they can be varied. Then the RF circuit optimizer performs two steps: 1000 random tries, followed by gradient optimization to ensure that the global minimum condition has been found. If the initial guess is too inaccurate, or if the range of allowed variation of adjustable element values is too large, the circuit optimizer cannot find a converged solution. As in real life, the analysis of circuit simulation data (primary S parameter matrix and current in each array element) provides information for the direction of initial value adjustment. After this re-adjustment the RF circuit optimizer is restarted.

If this multiple criterion optimization cannot be handled as a single run setup, the multi-channel array tuning/matching/decoupling procedure can be rearranged, as in reality. A common approach is to tune and match each individual array element separately at the outset. To eliminate coupling to other array elements, these can be decoupled from the element of interest by substitution of lumped elements (for example distributed capacitors) by high impedance resistors. Individual element tuning and matching is then guided by the (a) and (b) criteria mentioned above. Because this is a simple setup for the software circuit optimizer, it converges in most cases, but the values of adjustable elements may be unrealistic. In such cases, the values of fixed elements must be reset, and the optimizer must be restarted. The values obtained for fixed and variable elements that are valid for individual element tuning and matching then serve as starting values when the element is used in the entire array. As already noted, the decoupling strategy affects the value of some fixed elements. For example, the value of distributed capacitors must be decreased when inductive decoupling is used, because this network increases the effective inductance of radiative loop.

The magnetic field generated by each coil element is defined by the current through it. At 300 MHz and higher frequencies, the current can vary across different locations within the array. By monitoring the power reflected by the entire coil and the currents through distributed capacitors, in some cases the values of distributed capacitors can be further adjusted to optimize current distribution and/or to minimize this power for the given geometry and tune/match/decouple conditions. This eliminates the need to calculate combined 3-D EM fields for each step during coil performance investigation, a feature that additionally reduces the investigation time.

3. RESULTS

The power balance calculation workflow is shown in Fig. 5. If the non-conservative RF electric field is generally dominant, the ratio of mean B_1+ over the load (B_1+_{brain}) to $\sqrt{P_{\text{load}}}$ is stable (with only $+/-5\%$ variation) for a given coil/load geometry. P_{load}, P_{radiated} and P_{coil} are closely interrelated. Therefore the ratio of power delivered to load to the power delivered to the entire coil varies also a little ($+/-10\%$) for different tuning/matching/decoupling conditions. Thus minimization of the power reflected by the entire coil, which S_{xx} and S_{xy} data alone do not reveal (Fig. 3), becomes one of the major target for array performance optimization.

An example of power balance data is shown in Table 1 for an array 200 mm in diameter and 120 mm high. The abbreviations C/I/R correspond to capacitor and inductor based decoupling networks, and the power reflected by the entire coil was minimized respectively. There are two very different behaviors for array performance optimization: large loading, where the power delivered to the load is more than 95% of transmit power; and relative small loading, where the latter quantity can be less than 70%. For the first case the distributed capacitor value and decoupling strategy have minimal influence on array performance, and neither does the type of decoupling.

For the second case, tuning based only on minimization of the power reflected by the entire coil provides array performance which is relatively insensitive to the values of distributed capacitors. For both inductive and capacitor decoupling approaches, adjustment of the distributed capacitor values can result in variation of the power reflected by entire coil, and thus improvement of the array performance can be obtained, as shown in Fig. 6. This is mostly the case for capacitor based decoupling networks.

For any geometry/load investigated, both capacitor and inductive based decoupling provide greater decoupling for the first neighbour than for the second neighbour coil element.

In some array/load configurations, it is impossible to minimize the power reflected by entire coil with any type of decoupling, mainly because the coupling to the second and third neighbours cannot be reduced.

Table 1: Power balance.

Load	Small			Medium			Large		
Tuning	C	R	I	C	R	I	C	R	I
$P_{absorbed}$, W	7.07	8	6.27	7.54	8	7.74	7.93	8	7.95
$P_{radiated}$, W	0.07	0.07	0.05	0.02	0.02	0.02	0.01	0.01	0.01
P_{volume}, W	0.17	0.43	0.40	0.12	0.28	0.33	0.07	0.19	0.20
$P_{resistive}$, W	0.20	0.42	0.33	0.14	0.29	0.27	0.09	0.19	0.18
P_{load}, W	6.63	7.08	5.49	7.26	7.41	7.12	7.76	7.61	7.56
B_1+, µT	2.75	2.84	2.50	1.65	1.67	1.64	0.83	0.84	0.84

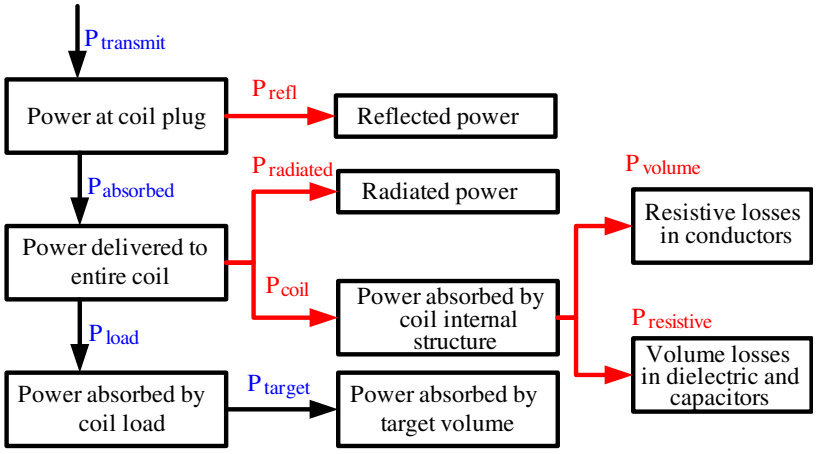

Figure 5: Power balance calculation workflow.

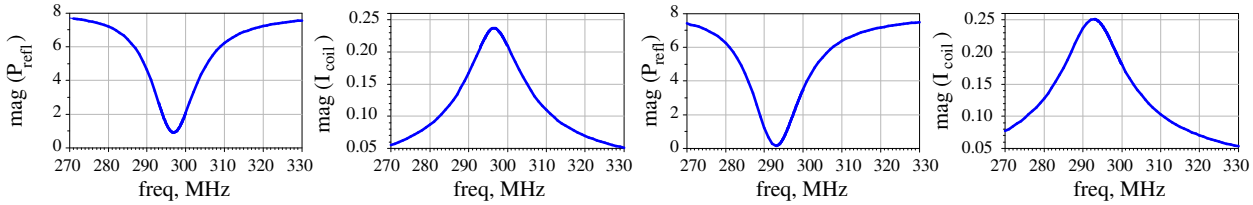

S_{xy}	11	21	31	41	51	61	71	81
dB	−44	−18.9	−9.6	−13.2	−19.3	−13.2	−9.6	18.9

S_{xy}	11	21	31	41	51	61	71	81
dB	−44	−15.7	−8.0	−12.0	−16.1	−12.0	−8.0	15.7

Figure 6: Left: data for distributed capacitors are equal to 7.4 pF, right: data for distributed capacitors are equal to 6.9 pF.

The results reported here were obtained in some sense for ideal array design conditions: a) values of fixed capacitors were not limited by the commercially available range of values, b) zero value tolerance was assumed, c) performance optimizations reached a global minimum. The results can be treated as the best possible optimization achievement. The approach presented for array investigation can straightforwardly incorporate lumped-element nominal values and tolerance ranges, and it can mimic the limited possibilities of actual (real) tune/match/decoupling procedure by adjusting the set of criteria and/or optimization sequence steps.

4. CONCLUSION

RF circuit and frequency domain 3-D EM co-simulation is a very powerful and fast approach for array coil investigation, since one multi-port 3-D EM simulation, which can be calculated in a reasonable time, is sufficient for investigation of the array behavior with different tuning/feeding/decoupling conditions. The necessary inclusion of all tuning/feeding/decoupling circuits enables accurate array performance data to be obtained. For small coil loading, S_{xx} and S_{xy} provide insufficient guidance in regard to the decoupling required to optimize array performance. The power reflected by the entire coil must also be minimized. The latter is provided by RF circuit simulation. This eliminates the need to calculate combined 3-D EM fields for each step during coil performance investigation, a feature that additionally reduces the investigation time.

REFERENCES

1. Kozlov, M. and R. Turner, "Fast MRI coil analysis based on 3-D electromagnetic and RF circuit co-simulation," *Journal of Magnetic Resonance*, No. 200, 147–152, 2009.

Harmonic-suppression Using Adaptive Surface Meshing and Genetic Algorithms

M. S. Bin-Melha[1], R. A. Abd-Alhameed[1], D. Zhou[1], Z. B. Zainal-Abdin[1], C. H. See[1], I. T. E. Elfergani[1], and P. S. Excell[2]

[1]Mobile and Satellite Communications Research Centre, University of Bradford, Bradford, UK
[2]Centre for Applied Internet Research, Glyndwr University, Wrexham, UK

Abstract— A novel design strategy for microstrip harmonic-suppression antennas is presented. The computational method is based on an integral equation solver using adaptive surface meshing driven by a genetic algorithm. Two examples are illustrated, all involving design of coaxially-fed air-dielectric patch antennas implanted with shorting and folded walls. The characteristics of the antennas in terms of the impedance responses and far field radiation patterns are discussed theoretically and experimentally. The performances of all of the GA-optimised antennas were shown to be excellent and the presented examples show the capability of the proposed method in antenna design using GA.

1. REVIEW AND SUMMARY OF THE METHOD

Harmonic suppression antennas (HSAs) are used to suppress power radiation at harmonic frequencies from active integrated antennas. An antenna that presents a good impedance match at the fundamental design frequency (f_o) and maximised reflection at harmonic frequencies is said to be a harmonic suppression antenna. In addition, the input impedance of any HSA design has to have minimised resistance at the harmonic frequencies and hence will be largely reactive [1, 2]. Several techniques have been proposed to control such harmonics, such as shorting pins, slots or photonic bandgap structures [3, 4]. In [5], the modified rectangular patch antenna with a series of shorting pins added to the patch centre line was applied to shape the radiated second harmonic from the active amplifying-type antenna, in order to increase the transmitter efficiency. Unfortunately, the proposed design does not provide the termination for the third harmonic. A circular sector patch antenna with 120° cut out was investigated and proved to provide additional harmonic termination for the third harmonic, also claiming a further enhancement in the transmitter efficiency [2]. Further, an H-shaped patch antenna was designed and applied in oscillator-type active integrated antennas for the purpose of eliminating the unwanted harmonic radiation [6, 7]. The present work presents a clear motivation to develop a coherent design strategy for microstrip HSA in active integrated applications. The technical work, adopts a computational technique using adaptive surface meshing driven by a genetic algorithm.

The benefit of applying GA methods is that they provide fast, accurate and reliable solutions for antenna structures. A genetic algorithm driver [8–10], written in Fortran, was adopted in this work in conjunction with the authors' Fortran source code [11], which was used to evaluate the randomly-generated antenna samples. Several antenna designs, derived using GA in previous work by the authors [12–14], have shown that the GA method to be an efficient optimiser tool that can be used to search and find rapid solutions for complex antenna design geometries.

An adaptive meshing program was also written in Fortran by the present authors and added as a subroutine to the GA driver, with the primary objective of simulating air-dielectric planar microstrip patch antenna designs: this used a surface patch model in cooperation with a GA. In addition to microstrip patch designs, the program can support the design of any 3D antenna geometry structure, including moderate amounts of dielectric materials. The present work is an extended version of preliminary work reported in [15]. The design of coaxially-fed air-dielectric microstrip harmonic-rejecting patch antennas for 2.4 GHz was investigated, enforcing suppression of the first two harmonic frequencies, using a genetic algorithm. The designs included patch antennas with shorted and folded walls.

2. SIMULATION AND RESULTS

Simple coaxially-fed air-dielectric patch antennas with shorted and folded walls, mounted on an infinite ground plane and operating at 2.4 GHz, were selected for this study as a simple exemplar to demonstrate acceptable harmonic rejection [5].

The proposed outline antenna designs are shown in Fig. 1. The full width shorted patch is subdivided into four trilaterals and two quadrilaterals, including the conducting shorted wall, as illustrated in Figs. 3(a) and 3(b). This design required six parameters to be defined. The second design example is similar to the first, but uses a modified folded wall, as shown in Figs. 3(c) and 3(d), in which the total surface area was subdivided into four trilaterals and three quadrilaterals. The fold in the wall means that it is no longer electrically connected to the ground plane, although the folded portion will provide strong capacitive coupling. In this model eight GA parameters were considered.

Table 1 presents the GA input parameters in which the possible range of values is shown for two examples considered. For this optimisation process, real-valued GA chromosomes were used. It should also be noted that the fundamental, first and second harmonic frequencies were considered within the GA cost function.

For validation, prototypes of the GA-optimised harmonic-suppression antennas (HSAs) of the two models were designed and tested. Copper sheet with thickness of 0.5 mm was used for the patch antenna, shorted/folded wall and the ground plane. The ground plane size was set to 140 mm × 140 mm, this relatively large size being chosen in order to attenuate the effect of the edges of the finite ground plane. The return losses were validated and measured results compared with calculations are shown in Fig. 2. As can be seen, the results for rejection levels of 2nd and 3rd harmonics were quite encouraging and no other resonances or ripples were found over the harmonic frequency bands.

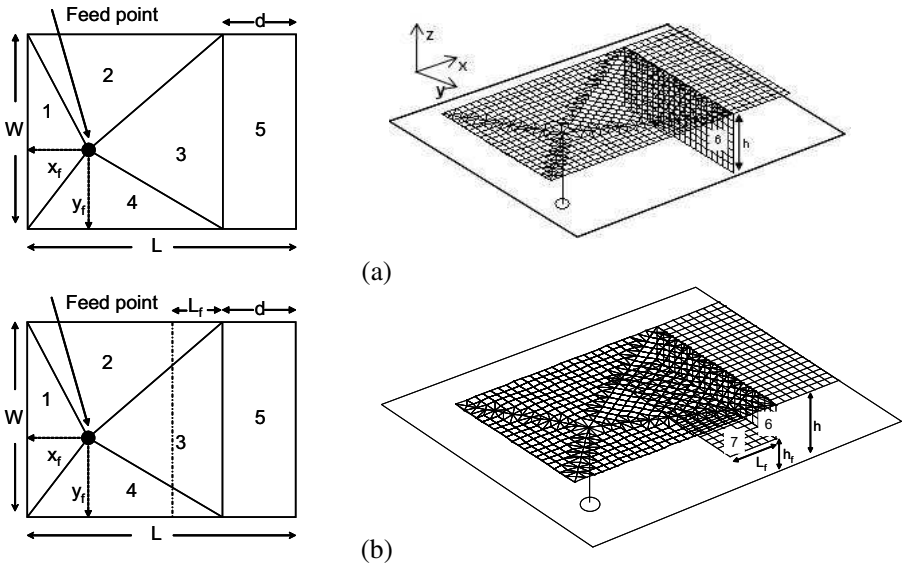

Figure 1: (a), (b) The proposed antenna models for full-width shorted wall; and (c), (d) folded wall. (a), (c): Top view; (b), (d): 3D view of surface patch meshing.

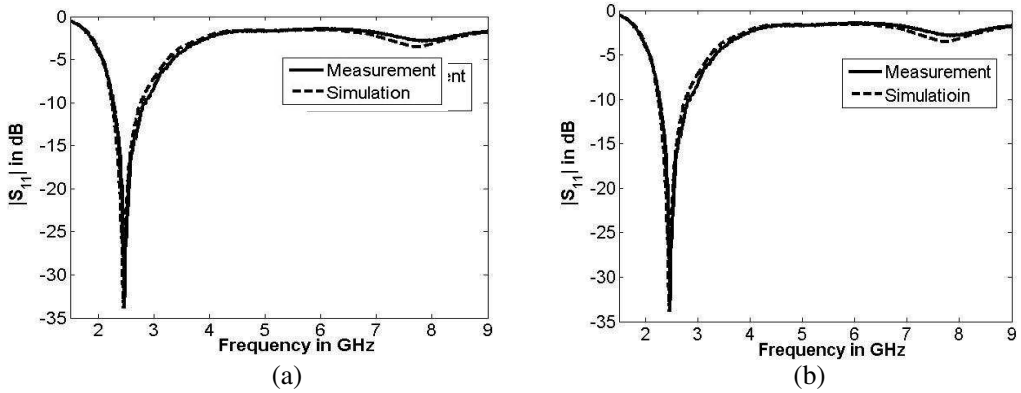

Figure 2: Performance of the measured and calculated return losses of the GA-optimised HSAs; (a) full-width shorted wall; and (b) folded wall.

Table 1: Summary of GA input parameters, antenna variables and best solutions for the proposed designs, including shorted and folded walls.

GA parameters	**Harmonic suppression antenna parameters**	**Fully shorted**	**Folded wall**
	Parameters (m)	Optimal (m)	Optimal (m)
	Antenna length (L) (0.03–0.06)	0.03950	0.04540
No. of population size = 4	Antenna width (W) (0.02–0.06)	0.03305	0.03006
No. of parameters: 6 (Figure 1(a1)), 7 (Figure 1(a2)), 8 (Figure 1 (a3))	Shorting or folded wall position (d) (0.002–0.03)	0.00972	0.00748
Probability of mutation = 0.02	Antenna height (h) (0.003–0.01)	0.0079	0.00989
Maximum generation = 500	Feeding point at x-axis (X_f) (0.004–0.02)	0.00723	0.00571
No. of possibilities = 32768	Feeding point at y-axis (Y_f) (0.004–0.02)	0.01752	0.01392
	Variable shorting wall width (W_s) (0.001–0.03)	-	-
	Extend folded wall length (L_f) (0.005–0.015)	-	0.01327
	Extend folded wall height (h_f) (0.001–0.0035)	-	0.00159

Table 2: Simulated and measured gain values at the fundamental frequency for the two antennas shown in Fig. 1.

Type of antenna		**Full shorted wall**		**Folded wall**	
Antenna gain (dBi)		Measured	Simulated	Measured	Simulated
Frequency (GHz)		$f_o = 2.47$		$f_o = 2.45$	
x-z plane	H.P.[1]	−8.35	−24.74	−13.45	−23.71
	V.P.[1]	4.14	4.06	5.01	5.03
y-z plane	H.P.	1.71	2.29	3.11	3.98
	V.P.	0.54	0.16	2.04	2.50

The input impedances of the prototype antennas were also measured over a wide frequency band as shown in Fig. 3. The measured input impedance of these antennas at the fundamental operating frequency and its first two harmonics shows that almost perfect matching to 50 Ω was attained at the fundamental frequency, while fairly small resistive impedances at harmonic frequencies were observed.

The simulated and measured radiation patterns in the z-x plane for the prototype antenna shown in Fig. 1 is presented in Fig. 4 the fundamental, second and third harmonic frequencies. The results are in good agreement and confirm viable levels of suppression of 2nd and 3rd harmonic levels. The fields for the second antenna design is quite similar thus are not shown here. These levels may be summarised as follows: for the fully-shorted wall design the maximum 2nd and 3rd harmonic radiation amplitudes were lower than 13 dB and 18 dB (respectively) below the fundamental for the z-x plane and 10 dB and 9 dB below for the z-y plane.

The simulated and measured gain values at the fundamental frequency for the two antennas shown in Fig. 1 are presented in Table 2. The simulated and measured co-polar gain values show reasonable agreement, although the differences in the cross-polar gain values are more significant. The cross-polar results are inherently weaker and hence more susceptible to minor deviations in the practical test implementation.

It was found that the full-width shorted-wall prototype antenna was resonant at 2.47 GHz and presents quite a wide bandwidth of around 500 MHz. The reflection coefficient level at the first and

second harmonic frequencies was found to be 1.71 dB and 2.45 dB, respectively. These results are quite acceptable, as compared with HSAs published in the open literature [15]. It is notable that the measured resonant frequency of the prototype antenna shows good agreement with the prediction. The third prototype exhibited approximately 380 MHz bandwidth, centred at a 2.45 GHz resonance frequency. The rejection levels of the 2nd and 3rd harmonics were about 1.5 dB and 1.9 dB respectively.

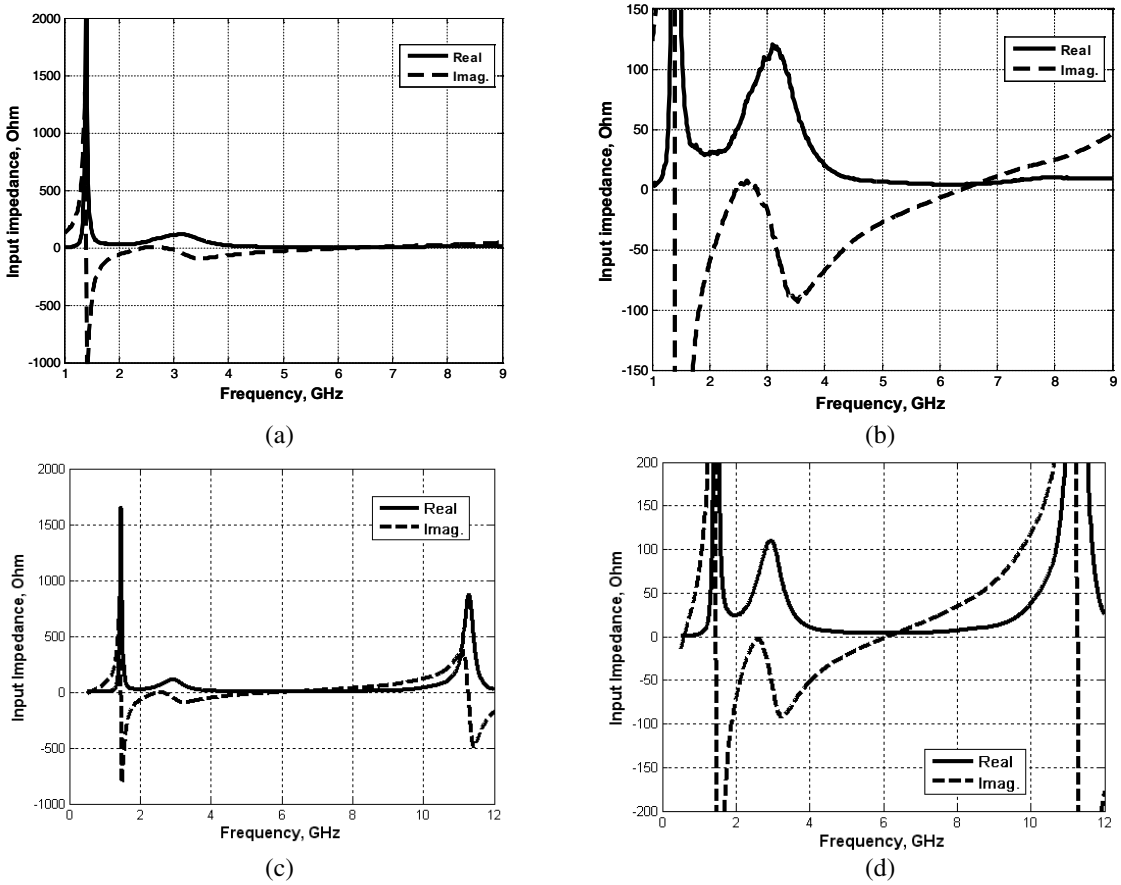

Figure 3: The overall measured input impedance of the patch antennas; (a), (b) full-width shorted wall; and (c), (d) folded wall. (b), (d) show detail expanded from (a), (c).

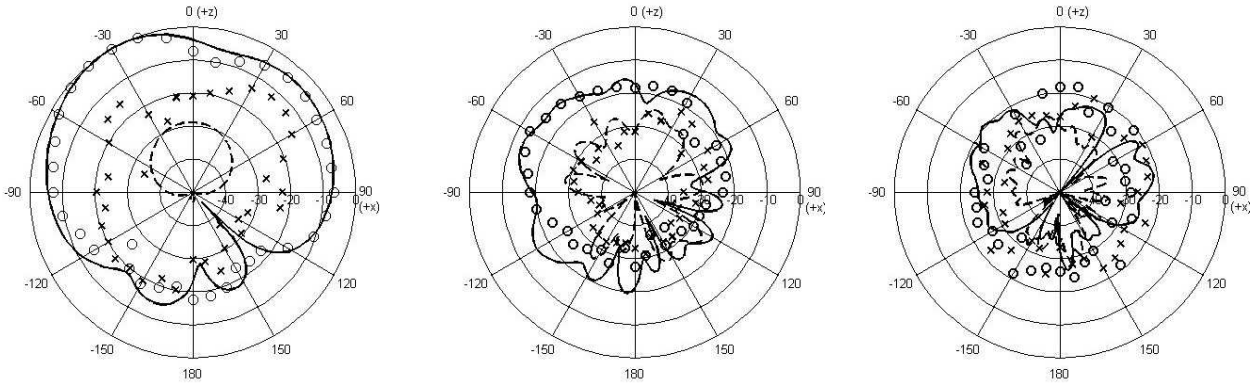

Figure 4: Measured and simulated radiation patterns of the proposed GA-optimised HSA with full-width shorted wall for 2.47 GHz, 4.94 GHz and 7.41 GHz over: z-x plane; ('—' measured E_θ, 'ooo' simulated E_θ, '- - -' measured E_ϕ, 'xxx' simulated E_ϕ).

3. CONCLUSIONS

A novel technique for the design and optimisation of harmonic-suppression patch antennas, applying adaptive surface patch models and genetic algorithms, has been presented. Hardware realisations of three coaxially-fed air-dielectric microstrip patch antennas were used to evaluate and validate the design theory. Comparison of return loss and far field radiation pattern measurements showed good agreement with the predictions. The examples presented confirmed the capability of the proposed method for antenna design using GA and adaptive surface meshing, showing reasonable stability and accuracy in the results.

REFERENCES

1. Elkhazmi, E., N. J. McEwan, and J. Moustafa, "Control of harmonic radiation from an active microstrip patch anrtenna," *Journees Internationale de Nice sur les Antennes*, 313–316, November 1996.
2. Radisic, V., Y. Qian, and T. Itoh, "Class F power amplifier integrated with circular sector microstrip antenna," *IEEE MTT-S Symposium Digest*, 687–690, 1997.
3. Kim, H., K. S. Hwang, K. Chang, and Y. J. Yoon, "Novel slot antennas for harmonic suppression," *IEEE Antennas and Wireless Components Letters*, Vol. 14, No. 6, 286–288, 2004.
4. Sung, Y. J. and Y.-S. Kim, "An improved design of microstrip patch antennas using photonic bandgap structure," *IEEE Transactions on Antennas and Propagation*, Vol. 53, No. 5, 1799–1804, 2005.
5. Radisic, V., S. T. Chew, Y. Qian, and T. Itoh, "High efficiency power amplifier integrated with antenna," *IEEE Microwaves and Guided Wave Letters*, Vol. 7, No. 2, 39–41, February 1997.
6. Sheta, A. F., "A novel H-shaped patch antenna," *Microwave and Optical Technology Letters*, Vol. 29, No. 1, 62–66, April 2001.
7. Chu, Q.-X. and M. Hou, "An H-shaped harmonic suppression active integrated antenna," *International Journal of RF and Microwave Computer-aided Engineering*, Vol. 16, No. 3, 245–249, May 2006.
8. Mangoud, M. A., R. A. Abd-Alhameed, and P. S. Excell, "Optimisation of channel capacity for indoor MIMO systems using genetic algorithm," *Proceedings of the Third International Conference on Internet Technologies and Applications (ITA 09)*, 431–439, Glyndwr University, Wrexham, Wales, UK, 2009.
9. Karamalis, P. D., A. G. Kanatas, and P. Constantinou, "A genetic algorithm applied for optimization of antenna arrays used in mobile radio channel characterization devices," *IEEE Trans. on Intrumentation and Measurements*, Vol. 58, No. 8, 2475–2487, 2009.
10. Carroll, D. L., FORTRAN Genetic Algorithm Driver, Version 1.7, Download from: http://www.staff.uiuc.edu/∼carroll/ga.html, 12/11/98.
11. Abd-Alhameed, R. A., P. S. Excell, and J. Vaul, "Currents induced on wired I.T. Networks by Randomly distributed phones — A computational study," *IEEE Trans. on Electromagnetic Compatibility*, Vol. 48, No. 2, 282–286, May 2006.
12. See, C. H., R. A. Abd-Alhameed, D. Zhou, P. S. Excell, and Y. F. Hu, "A new design of circularly-polarised conical-beam microstrip patch antennas using a genetic algorithm," *Proceedings of the European Conference on Antennas and Propagation: EuCAP 2006*, Session 4PA1, Paper No.100, Nice, France, 2006.
13. Zhou, D., R. A. Abd-Alhameed, and P. S. Excell, "Bandwidth enhancement of balanced folded loop antenna design for mobile handsets using genetic algorithms," *PIERS Online*, Vol. 4, No. 1, 136–139, 2008.
14. Zhou, D., R. A. Abd-Alhameed, C. H. See, P. S. Excell, F. Y. Hu, K. Khalil, and N. J. McEwan, "Quadrifilar helical antenna design for satellite-mobile handsets using genetic algorithms," *Microwave and Optical Technology Letters*, Vol. 51, No. 11, 2668–2671, November 2009.
15. Zhou, D., R. A. Abd-Alhameed, C. H. See, M. S. Bin-Melha, E. T. I. Elferganai, and P. S. Excell, "New antenna designs for wideband harmonic suppression using adaptive meshing and genetic algorithms," *Proceeding of Mosharaka International Conference on Communications, Propagation and Electronics*, Technical Session 1, 5–9, Amman, Jordan, March 5–7, 2010, ISBN: 978-9957-486-06-8.

A Reliable Lattice-Boltzmann Solver for Electrodynamics: New Applications in Non-linear Media

M. Mendoza[1] and J. D. Muñoz[2]

[1]ETH Zürich, Computational Physics for Engineering Materials, Institute for Building Materials
Schafmattstrasse 6, HIF, CH-8093 Zürich, Switzerland
[2]Simulation of Physical Systems Group, Ceiba-Complejidad, Departamento de Fisica
Universidad Nacional de Colombia, Crr 30 # 45-03, Ed. 404, Of. 348, Bogotá D.C., Colombia

Abstract— Hereby we summarize a recently developed 3D lattice-Boltzmann method for the simulation of Maxwell equations in materials, and we illustrate its performance by computing the time evolution of electromagnetic fields inside a non-linear dielectric medium. The model allows for both dielectrics and conductors with realistic parameters and has computed the most diverse electromagnetic problems (including micro-strips and antennas), all with 2% accuracy. Preliminary tests showed that it is one order of magnitude faster than the original finite-difference time-domain scheme formulated by Yee to reach the same accuracy. To illustrate the power of the new solver, we simulate the time evolution of a cylindrical electromagnetic wave through a non-linear and non-dispersive medium and the resonant modes of a cylindrical cavity filled with that medium. Our results are in excellent agreement with the analytic solutions by E. Y. Petrov and A. V. Kudrin for the same cases. The model constitutes, therefore, a valuable alternative to compute electromagnetic fields, even in non-linear media.

1. INTRODUCTION

Computer-based simulations play a central role in electrodynamics and, therefore, the development of new and powerful simulation methods has a direct impact on the field. Most time-dependent simulations are done with either finite-element or finite-difference methods like Finite-difference time-domain, FDTD [1–3]; in contrast, lattice-Boltzmann methods (LBM) have been traditionally taken as adequate just for fluids [4–6], plasmas [7–10] diffusion [11] and waves [12]. However, we have introduced a novel Lattice-Boltzmann method that reproduces in the continuous limit the whole Maxwell equations for media [13]. The model successfully computes for the most diverse electromagnetic problems within 2% accuracy. Even more, some preliminary results show that the new method is one order of magnitude faster than the FDTD original formulation by Yee [1] to reach the same accuracy. Therefore, this lattice-Boltzmann model shows to be a valuable alternative to simulate electrodynamics.

Hereby, we apply this model to the study of the time evolution of the electromagnetic fields inside a non-linear and non-dispersive medium in two cases: the propagation of a cylindrical electromagnetic wave and the resonant modes of a cylindrical cavity filled with that medium. So, we reproduce the numerical results and compare with the analytical solutions obtained by E. Y. Petrov and A. V. Kudrin for the same cases [14]. For this purpose, the procedure to compute the effective electric field in [13] has been slightly modified to account for the non-linear response of the medium. The electromagnetic fields obtained with our LBM are in excellent agreement with the analytical results, illustrating the possibilities of the new method to simulate electrodynamics, even with non-linear media.

2. THE LBM FOR ELECTRODYNAMICS

As in every LBM, the D-dimensional space is divided into a regular grid of cells. Each cell has Q vectors linking with the neighboring cells. We use the D3Q13 set of vectors: a null vector $\vec{v}_0 = (0,0,0)$ and twelve vectors $\vec{v}_i^p$ of length $\sqrt{2}$ ($p = 0,1,2$ indexes the plane of location and $i = 1,2,3,4$ indexes the direction inside the plane, Figure 1(a)). Associated to each non-zero velocity vector $\vec{v}_i^p$ there are two electric $\vec{e}_{ij}^p$ vector of length $1/\sqrt{2}$ and two magnetic $\vec{b}_{ij}^p$ auxiliary vectors of length 1, with $j = 0,1$ (Figure 1(b)), related by $\vec{b}_{ij}^p = \vec{v}_i^p \times \vec{e}_{ij}^p$. The picture is completed by the null vectors $\vec{e}_0 = (0,0,0)$ and $\vec{b}_0 = (0,0,0)$.

All the information on the fields is condensed into the so-called *distribution functions*. There are four distribution functions $f_{ij}^{p(r)}$ ($j = 0,1$ and $r = 0,1$) traveling with each velocity vector $\vec{v}_i^p$

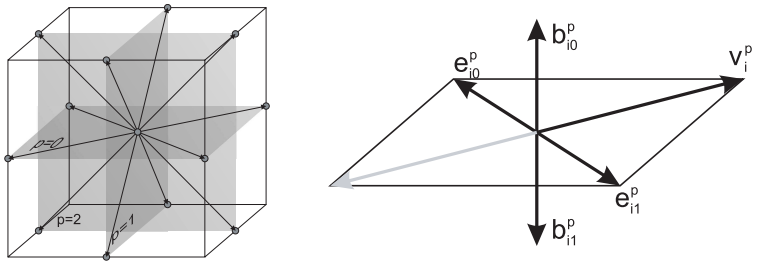

(a) (b)

Figure 1: (a) Velocity vectors D3Q13 to model the Maxwell equations, with p the plane of location. (b) Auxiliary electric and magnetic vectors associated to each velocity vector.

and two functions $f_0^{(r)}$ fixed to the null vector $\vec{v}_0$. The macroscopic fields are computed at each cell from the distribution functions by

$$\vec{D} = \sum_{i=1}^{4}\sum_{p=0}^{2}\sum_{j=0}^{1} f_{ij}^{p(0)}\vec{e}_{ij}^{p}, \quad \vec{B} = \sum_{i=1}^{4}\sum_{p=0}^{2}\sum_{j=0}^{1} f_{ij}^{p(1)}\vec{b}_{ij}^{p}, \quad \rho_c = f_0^{(0)} + \sum_{i=1}^{4}\sum_{p=0}^{2}\sum_{j=0}^{1} f_{ij}^{p(0)}, \tag{1}$$

$$\vec{E} = \frac{\vec{D}}{\epsilon_r}, \quad \vec{H} = \frac{\vec{B}}{\mu_r}, \quad \vec{J} = \sigma\vec{E}, \tag{2}$$

where $\vec{D}$, $\vec{E}$ and $\vec{J}$ are subsidiary fields representing the displacement field, the electric field and the total current density before external forcing, respectively (the actual mean fields, including external forcing, are described below). In addition, $\vec{B}$ is the induction field, $\vec{H}$ is the magnetic field, ρ_c is the total charge density and ϵ_r, μ_r and σ are the relative dielectric constant, the relative permeability constant and the conductivity for the medium, respectively.

At every time step, these functions evolve and travel to the next cell according to the Boltzmann equation in the Bhatnagar-Gross-Krook (BGK) approximation [15],

$$f_i(\vec{x}+\vec{v}_i, t+1) - f_i(\vec{x}, t) = -\frac{1}{\tau}\left(f_{ij}^{p(r)}(\vec{x}, t) - f_{ij}^{p(r)\mathrm{eq}}(\vec{x}, t)\right), \tag{3}$$

$$f_0^{(r)}(\vec{x}, t+1) - f_0^{(r)}(\vec{x}, t) = -\frac{1}{\tau}\left(f_0^{(r)}(\vec{x}, t) - f_0^{(r)\mathrm{eq}}(\vec{x}, t)\right), \tag{4}$$

with $\tau = \frac{1}{2}$. In other words, if not traveling they would exponentially decay to equilibrium functions, given by

$$f_{ij}^{p(0)\mathrm{eq}}(\vec{x}, t) = \frac{1}{16}\vec{v}_i^{p}\cdot\vec{J}' + \frac{\epsilon}{4}\vec{E}'\cdot\vec{e}_{ij}^{p} + \frac{1}{8\mu}\vec{B}\cdot\vec{b}_{ij}^{p}, \quad f_{ij}^{p(1)\mathrm{eq}}(\vec{x}, t) = \frac{1}{16}\vec{v}_i^{p}\cdot\vec{J}' + \frac{1}{4}\vec{E}'\cdot\vec{e}_{ij}^{p} + \frac{1}{8}\vec{B}\cdot\vec{b}_{ij}^{p}, \tag{5}$$

$$f_0^{(0)\mathrm{eq}}(\vec{x}, t) = f_0^{(1)\mathrm{eq}}(\vec{x}, t) = \rho_c. \tag{6}$$

The current density term in the Ampere's law is included as an external forcing term by following the proposal of Zhaoli Guo, Chuguang Zheng and Baochang Shi [16]. Thus, the electric $\vec{E}$ and current density $\vec{J}$ fields described in Eq. (2) are just subsidiary fields for the time evolution. The actual fields are given by

$$\vec{E}' = \vec{E} - \frac{\mu_0}{4\epsilon_r}\vec{J}', \quad \vec{J}' = \sigma\vec{E}' = \frac{\sigma}{1+\frac{\mu_0\sigma}{4\epsilon_r}}\vec{E}. \tag{7}$$

This lattice-Boltzmann model reproduces the Maxwell equations

$$\frac{\partial\rho_c}{\partial t} + \nabla\cdot\vec{J}' = 0, \quad \nabla\times\vec{E}' = -\frac{\partial\vec{B}}{\partial t}, \quad \nabla\times\vec{H} = \mu_0\vec{J}' + \frac{1}{c^2}\frac{\partial\vec{D}'}{\partial t}, \tag{8}$$

with second-order accuracy. The time step δt and the cell size δx are related by $\delta x = c\delta t$ (with c the speed of light in vacuum) and, therefore, the Courant-Fredericks-Levy criterion is automatically

fulfilled. This model reproduces the most diverse electromagnetic problems, like the propagation of electromagnetic waves (both in dielectric media and in waveguides), the skin effect, the radiation pattern of a small dipole antenna and the natural frequencies of a resonant cavity, all within 2% accuracy. Even more, some preliminary results show that the new method is one order of magnitude faster than the FDTD original formulation by Yee [1] to reach the same accuracy. For a detailed description of how the method works and why it reproduces the Maxwell equations in media, see Ref. [13].

3. APPLICATIONS IN A NONLINEAR AND NONDISPERSIVE MEDIUM

In order to illustrate the possibilities of the new method to simulate non-linear media, let us reproduce the numerical results and compare with the impressive analytical solutions obtained by E. Y. Petrov and A. V. Kudrin for two systems [14]. The first one consists on the propagation of a cylindrical electromagnetic wave in a non-linear and non-dispersive dielectric medium, and the second one studies the resonance modes of a cylindrical cavity filled with that medium. Because of the symmetry of both problems, we work only with the z-component of the electric and displacement fields, $\vec{E} = (0, 0, E)$ and $\vec{D} = (0, 0, D)$, respectively. The medium is characterized by a permittivity ϵ_r depending on the magnitude E of the electric field, as $\epsilon_r(E) = \epsilon_1 \exp(\alpha E)$, where ϵ_1 and α are constants. Because $dD = \epsilon_r(E)\epsilon_0 dE$, we obtain $D = D_0 + \alpha^{-1}\epsilon_0\epsilon_1[\exp(\alpha E) - 1]$ for the displacement field. Assuming $D_0 = 0$ and because $|\alpha E| \ll 1$ in many experiments, we expand up to second order to obtain

$$D = \epsilon_0\epsilon_1\left[E + \alpha\frac{E^2}{2}\right], \quad E = \frac{\sqrt{\epsilon_0\epsilon_1(2\alpha D + \epsilon_1\epsilon_0)} - \epsilon_0\epsilon_1}{\alpha\epsilon_0\epsilon_1}. \tag{9}$$

Therefore, in order to model this non-linear medium we just compute the electric field from Eq. (9) instead of the linear expression, Eq. (2).

To reproduce the propagation of a cylindrical electromagnetic wave we started with the following initial condition for the electric and magnetic fields [14]:

$$E = \beta[1 + \rho\exp(\alpha E)]^{-3/2}, \quad H = 0, \tag{10}$$

where β is a constant fixing the electric field strength, $\rho = r/a$, r is the cylindrical coordinate and a is a characteristic length scale. Eq. (10) is a non-explicit equation for the electric field; therefore, the initial configuration was computed with a numerical solver.

Figure 2(a) illustrates the evolution of the electromagnetic field for several times. The simulation was performed on a grid of $512 \times 512 \times 1$ cells with periodic boundary conditions, with $r = 0$ at the center of the array. The values for the constants are (in automaton units): $\mu_0 = 2.0$, $\epsilon_0 = 1.0$, $\epsilon_1 = 2.0$, $a = 25.6$, $\alpha = 0.1$, and $\beta = 10.0$. The figure uses the dimensionless time $\tau = t(\epsilon_0\epsilon_1\mu_0)^{-1/2}/a$ and the impedance of the vacuum $Z_0 = \sqrt{\mu_0/\epsilon_0}$. We achieved an excellent agreement between the analytical curves of Ref. [14] and the numerical results. The simulation spanned 60 seconds in a standard PC.

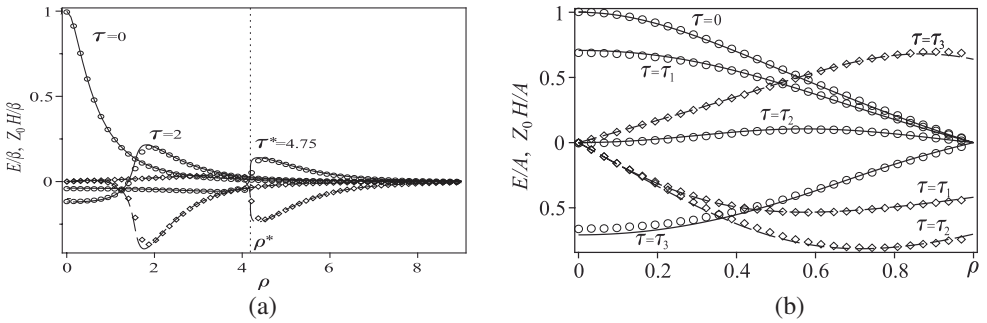

Figure 2: Radial distributions of the electric field (solid curves, circles) and the magnetic field (dashed curves, diamonds) for (a) a cylindrical wave propagating inside a non-linear medium at different time steps τ and (b) the $n = 1$ mode inside a cylindrical cavity at times $\tau = 0$, $\tau_1 = \pi/(4\kappa_1)$, $\tau_2 = \pi/(2\kappa_1)$ and $\tau_3 = 5\pi/(4\kappa_1)$. The curves represent the analytical solutions from Ref. [14], and the circles and diamonds denote the simulation results with the Lattice-Boltzmann model.

To simulate a resonant cavity, we imposed that the electric field vanishes for $r > a$, modeling a perfect conductor. The initial configuration for the electromagnetic fields was given by

$$E = AJ_0(\kappa_n \rho e^{\alpha E/2})\cos(\kappa_n \theta), \quad H = -AZ_0^{-1}\epsilon_1^{1/2} e^{\alpha E/2} J_1(\kappa_n \rho e^{\alpha E/2})\sin(\kappa_n \theta), \tag{11}$$

where A is an amplitude factor, $J_m(x)$ is the Bessel function of the first kind of order m and κ_n is the nth root of the equation $J_0(x) = 0$. The variable θ is defined by

$$\theta = \tau + \frac{\alpha Z_0 \rho H}{2\sqrt{\epsilon_1}}. \tag{12}$$

As before, the initial configuration is not explicit for E and H; thus, we used a numerical solver to find it.

Figure 2(b) shows the electric and magnetic fields for the first mode, $n = 1$ ($\kappa_1 \sim 2.4$), as a function of ρ for several time steps τ. For the simulation we used a grid of $256 \times 256 \times 1$ cells with periodic boundary conditions, with the center of the cylinder at the center of the array. The values for the constants are the same as before, but $a = 125.0$, and $A = 5.0$. The results show again an excellent agreement with the analytical results from Ref. [14].

One of the most interesting results for this non-linear resonant cavity is the time evolution of the magnetic field H in the mode $n = 2$, which oscillates with twice the frequency of the electric field. Figure 3 shows this intriguing phenomenon.

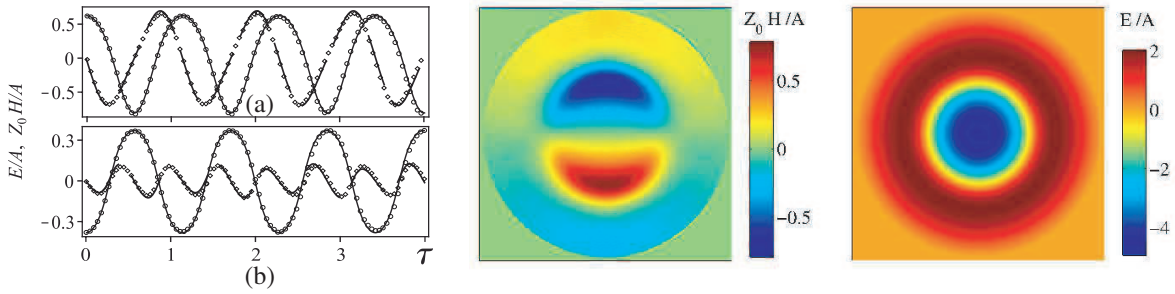

Figure 3: (left) Electric and magnetic fields as a function of time for the cylindrical cavity in the $n = 2$ mode at position (a) $\rho = 0.2$ and (b) $\rho = 0.7$. The results of the simulation are shown with the same symbols than Figure 2. Snapshots of the (center) electric and (right) magnetic fields at $\tau = 4$ for same mode.

4. CONCLUSION

We have summarized a recently developed lattice-Boltzmann method that reproduces the Maxwell equations in materials [13], and we have used it to simulate the time evolution of a cylindrical electromagnetic wave through a non-linear and non-dispersive medium and the resonant modes of a cylindrical cavity filled with that medium. Our results are in excellent agreement with the analytic solutions by E. Y. Petrov and A. V. Kudrin [14] for the same systems. These results enlarge the success of this lattice-Boltzmann model to compute for electromagnetic fields and show that even for non-linear media it is a valuable alternative to simulate electrodynamics.

ACKNOWLEDGMENT

The authors are deeply thankful to Hans J. Herrmann at the Institute for Building Materials at ETH-Zürich for hospitality and help. We also thank the Colombian Excellence Center for the Simulation and Modeling of Complex Systems, CeiBA-Complejidad for financial and travel support.

REFERENCES

1. Yee, K., "Numerical solutions of initial boundary value problems involving Maxwell's equations in isotropic media," *IEEE Transactions on Antennas and Propagation*, Vol. 14, 302, 1966.
2. Taflove, A. and S. C. Hagness, *Computational Electrodynamics — The Finite-difference Time-domain Method*, Artech House, Boston, 2000.
3. De Raedt, H., K. Michielsen, and M. T. Figgle, "Solving the Maxwell equations by the Chebyshev method: A one-step finite-difference time-domain algorithm," *IEEE Transactions on Antennas and Propagation*, Vol. 51, 3155, 2008.

4. McNamara, G. R. and G. Zanetti, "Use of the Boltzmann equation to simulate lattice-gas automata," *Phys. Rev. Lett.*, Vol. 61, 2332, 1988.
5. Higuera, F., S. Succi, and R. Benzi, "Lattice gas dynamics with enhanced collisions," *Europhys. Lett.*, Vol. 9, 345, 1989.
6. Mendoza, M., B. M. Bogoshian, H. J. Herrmann, and S. Succi, "Fast lattice boltzmann solver for relativistic hydrodynamics," *Phys. Rev. Lett.*, Vol. 105, 014502, 2010.
7. Succi, S., R. Benzi, and M. Vergassola, "Lattice Boltzmann scheme for two-dimensional magnetohydrodynamics," *Phys. Rev. A*, Vol. 4, 4521, 1991.
8. Chen, S., H. Chen, D. O. Martinez, and W. H. Matthaeus, "Lattice Boltzmann model for simulation of magnetohydrodynamics," *Phys. Rev. Lett.*, Vol. 67, 3776, 1991.
9. Dellar, P. J., "Lattice kinetic schemes for magnetohydrodynamics," *J. of Comp. Phys.*, Vol. 179, 95, 2002.
10. Mendoza, M. and J. D. Munoz, "Three-dimensional lattice Boltzmann model for magnetic reconnection," *Phys. Rev. E*, Vol. 77, 026713, 2008.
11. Flekkoy, E. G., "Lattice BGK model for miscible fluids," *Phys. Rev. E*, Vol. 54, 5041, 1993.
12. Chopard, B. and M. Droz, *Cellular Automata Modelling of Physical Systems*, Cambridge University Press, New York, 1998.
13. Mendoza, M. and J. D. Muñoz, "Three dimensional lattice Boltzmann model for electrodynamics," *Phys. Rev. E*, Vol. 82, 056708, 2010.
14. Petrov, E. Yu. and A. V. Kudrin, "Exact axisymmetric solutions of the maxwell equations in a nonlinear nondispersive medium," *Phys. Rev. Lett.*, Vol. 104, 190404, 2010.
15. Bathnagar, P. L., E. P. Gross, and M. Krook, "A model for collision processes in Gases. I. Small amplitude processes in charged and neutral one-component systems," *Phys. Rev.*, Vol. 94, 511, 1954.
16. Guo, Z., Ch. Zheng, and B. Shi, "Discrete lattice effects on the forcing term in the lattice Boltzmann method," *Phys. Rev. E*, Vol. 65, 046308, 2002.

Developing Sample Holders for Measuring Shielding Effectiveness of Thin Layers on Compound Semiconductor Substrates

Sz. Nagy and A. Fehér
Department of Telecommunications, Széchenyi István University, H-9026 Győr, Egyetem tér 1., Hungary

Abstract— Wavelet or multiresolution analysis (MRA) is widely applied in advanced data compression algorithms, solving differential equations, and some approaches have already applied this technique in describing electromagnetic fields. The main advantage of the application of MRA is its adaptivity and flexibility. Since the details of the electromagnetic field are not distributed equally over different parts of the system (i.e., the description of some parts need finer details, while others are easily represented at low resolution level), locally different resolution levels can be applied. Wavelet based adaptive solution possibilities of differential equations of electromagnetic field are investigated in the followings. The adaptivity of the method means in this case, that the refinement level of the solution can be increased locally, if the accuracy needs it, during the calculations.

The applicability of the eigenvalue-type differential equation solving method is illustrated by solution of microwave wave-equations of cavity resonators.

1. INTRODUCTION

The idea of applying multiresolution analysis (MRA) or wavelet analysis in electromagnetic field simulation is not completely new. Since wavelets are in the scope of numerical mathematics since the eighties, many applications arose related to electromagnetic fields. Most of these use wavelet transform as a data processing, analyzing method [1, 2]. Our article uses wavelet analysis as a tool of solving differential equations, i.e., we transform the partial differential equations of the electric (magnetic) field into matrix equations of the wavelet expansion coefficients of the same quantity. This kind of approximation has, however, rather wide literature. One of the earliest appearance of MRA in electromagnetic fields calculation [3] and their followers [4] expands the electronic and magnetic fields by means of wavelets and scaling functions in 3 spatial dimensions and the time is treated according to the finite differences method of [5]. Since then, many promising, wavelet based time-domain simulations were p in the literature [6–8]. Kaiser and his group used wavelets for many purposes in electrodynamics, from radar applications to "atomic" composition of electromagnetic waves [9–12]. Also a wavelet-finite element mixed method appeared [13]. Or method provides solution for those kind of partial differential equations, that can be represented as eigenvalue-type equations, such as the problem of waveguides and cavities [15].

2. ADAPTIVE WAVELET METHODS FOR SOLVING PARTIAL DIFFERENTIAL EQUATIONS

Multiresolution analysis of Hilbert space $L^2(\mathbb{R})$ is a sequence of its closed subspaces $\{V_m, m \in \mathbb{Z}\}$ that are embedded into each other. These subspaces are the resolution levels, and have special properties, namely, the basis functions of V_m (the so called scaling functions) are shifted versions of a given function $s_{m0}(x)$ on an equidistant grid of spacing b. if m, the resolution level increases, the scaling functions and the grid distance b are shrunk by a constant a. This means, that the (orthonormal) basis set of subspace V_m is $\{s_{m\ell}(x)|\ell \in \mathbb{Z}\}$, where $s_{m\ell}(x) = a^{m/2}s_0(a^m x - b\ell)$. Usually the values $a = 2$ and $b = 1$ are used.

The resolution levels V_m are embedded in each other, i.e., the basis functions of a rougher subspace V_m can be expressed as a linear combination of the scaling functions of the finer levels $n > m$. For $n = m + 1$,

$$s_{m\ell}(x) = \sum_{k=0}^{N_s} p_k s_{m+1\,k+2\ell}(x) \tag{1}$$

with $\sum_{k=1}^{N_s} p_k = 2$. This formula is called the two-scale equation or *refinement equation*. There exist such basis sets that the number N_s of the non-zero expansion coefficients p_k are finite, in these cases the mother scaling function s_0 has finite support: $s_0(x) = 0$ if not $x \in [0, N_s)$ [16, 17].

A function $f \in L^2(\mathbb{R})$ can be projected onto subspaces of any resolution level m, thus an mth approximation of the function is

$$P_m f(x) = f^{[m]}(x) = \sum_\ell c_{m\ell} s_{m\ell}(x), \tag{2}$$

with $c_{m\ell} = \langle s_{m\ell} | f \rangle$, and P_m being the projector to V_m.

The orthogonal complement of a rougher subspace V_m in the next finer subspace V_{m+1} is the *detail space* W_m

$$V_{m+1} = V_m \oplus W_m. \tag{3}$$

In these detail spaces W_m the basis set can be $\{w_{m\ell}(x) | \ell \in \mathbb{Z}\}$ with the basis functions $w_{m\ell}(x) = 2^{m/2} w_0(2^{-m}x - \ell)$. The elements of these basis sets $\{w_{m\ell}(x) | \ell \in \mathbb{Z}, m = 0, 1, \ldots\}$ are the wavelets, they can be also compactly supported, like the scaling functions. Their generation from the coefficients p_k and the scaling functions is

$$w_{m,\ell}(x) = \sum_{k=1-N_s}^{1} q_k s_{m+1\, 2\ell-k}(x), \tag{4}$$

where $q_k = (-1)^k p^*_{-k+1}$.

There exist a transformation that gives the finer resolution scaling functions from the lower level basis functions and can be summarized in the formula

$$s_{m+1\, 2L+z}(x) = 2^{-1/2} \sum_{K=0}^{(N_s-1)/2} p^*_{2K+z} s_{m\, L-K}(x) + 2^{-1/2} \sum_{K=-(N_s-1)/2}^{0} q^*_{2K+z}\, w_{m\, L-K}(x), \tag{5}$$

for $z = 0, 1$.

Using the multiresolution concept, the Hilbert space of the square integrable functions can be segmented as

$$L^2(\mathbb{R}) = \bigoplus_{m=m_0}^{\infty} W_m \oplus V_{m_0} \tag{6}$$

with any starting resolution level m_0. If an Mth level expansion is sufficient ($M > m_0$),

$$V_M = \bigoplus_{m=m_0}^{M-1} W_m \oplus V_{m_0} \tag{7}$$

holds, which means, that the Mth level approximation of a function $f \in L^2(\mathbb{R})$ can be given either in the basis $\{s_{Mk} | k \in \mathbb{Z}\}$ or in $\{s_{m_0 k}, w_{mk} | k \in \mathbb{Z}, m = m_0, m_0 + 1, \ldots, M-1\}$ as

$$f^{[M]}(x) = \sum_k c_{Mk} s_{Mk}(x) \tag{8}$$

$$f^{[M]}(x) = \sum_k c_{m_0 k} s_{m_0 k}(x) + \sum_{m=m_0}^{M-1} \sum_k d_{mk} w_{mk}(x). \tag{9}$$

Let us suppose, that the function f is compactly supported in the interval $\mathcal{J}$ of length $2^{-M}J$, $J \in \mathbb{N}$. The number of coefficients $\{c_{Mk}\}$ in (8) is the same as the total number of coefficients $\{c_{m_0 k}, d_{mk}\}$ in formula (9) (independent of starting level m_0). The basic idea behind the wavelet based compression algorithms is the following. In a given region it is not necessary to keep all the expansion coefficients d_{mk}, if already a lower resolution level is sufficient. Ignoring the small coefficients of type d_{mk} can lead to a manageable size of data sets. These considerations are valid for more dimensions, where the basis functions can be direct products of one dimensional scaling functions and wavelets.

Using the multiresolution analysis basis set, any function of the space $L^2(\mathbb{R})$ (or $L^2(\mathbb{R}^D)$) can be expanded as linear combinations of scaling functions and wavelets. If the components of our

electromagnetic field are square integrable functions, i.e., elements of Hilbert space $L^2(\mathbb{R})$, they can be exactly decomposed as

$$E(x) = \sum_{\ell\in\mathbb{Z}} c_\ell \, s_{0\ell}(x) + \sum_{m=0}^{\infty} \sum_{\ell\in\mathbb{Z}} d_{m\ell} \, w_{m\ell}(x). \tag{10}$$

Here E represents the electromagnetic field (component) which is the solution of the studied partial differential equations system. If $E(x)$ is compactly supported, the total number of expansion coefficients in a given resolution level m scales as $\sim 2^m$ (or in D dimensions $\sim 2^{mD}$), which makes the above expansion unapplicable. The exponential increase of number of the necessary basis functions can be avoided by an adaptive refinement strategy, including wavelets only in those regions, where the details of the electromagnetic field require it, and do not calculate the nearly zero expansion coefficients. But how can we know, if the coefficient would be near zero or not, before we would calculate them? The next few paragraphs will give the answer.

According to studies of model systems that are exactly solvable [15], the high resolution wavelets have exponentially small contribution in the solutions, thus probably they can be omitted completely. At lower m values only a fractional part of them have essential contribution in the expansion, mostly localized to quickly changing parts of the exact solutions, especially at singularities of the solution. According to these considerations, the resolution levels can be separated to necessary and not necessary wavelets, i.e., the resolution levels can be truncated.

Clearly, we need a method that gives the essential coefficients in (10), prior to calculating the complete resolution level. Let us suppose, that we have already calculated the solution of the equation (system) at resolution level Mth, thus the approximation on the above function $E(x)$ is

$$\tilde{E}^{[M]}(x) = \sum_{\ell\in\tilde{V}_0} \tilde{c}_\ell^{[M]} \, s_{0\ell}(x) + \sum_{m=0}^{M-1} \sum_{\ell\in\tilde{W}_m} \tilde{d}_{m\ell}^{[M]} \, w_{m\ell}(x). \tag{11}$$

Here the upper index of $\tilde{E}^{[M]}(x)$ means, that the solution is restricted to the spaces under resolution levels M, whereas $\tilde{}$ means that the resolution level is truncated. The notation $\ell \in \tilde{W}_m$, means, that the summation index ℓ is restricted to those wavelets $w_{m\ell}$ which are necessary for the mth resolution level, i.e., that belong to the truncated wavelet subspace $\tilde{W}_m$. Using only this knowledge, plus the partial differential equation to be solved this knowledge, the $(M+1)$th level coefficients can be predicted.

Let us denote the operator corresponding to the partial differential equation by D, and its representation in a finite resolution level M wavelet-scaling function basis by $\hat{D}^{[M]}$. Since $\tilde{E}^{[M]}$ denotes the eigenfunction of the restricted differential operator $\tilde{D}^{[M]}$, the eigenvalue equation that is solved at resolution level M is

$$(\tilde{D}^{[M]} - \tilde{\lambda}^{[M]})\tilde{E}^{[M]} = 0. \tag{12}$$

If one of $\tilde{D}^{[M]}$ or $\tilde{\lambda}^{[M]}$ is replaced by D or λ, the above equation will not hold any more. The quality of the Mth level approximation of the eigenvalues and eigenvectors can be characterized by the error function

$$\tilde{\Delta}^{[M]} = (D - \tilde{\lambda}^{[M]})\tilde{E}^{[M]} \neq 0. \tag{13}$$

The essential basis functions of the next wavelet subspace W_M can be approximated. (Note, that the resolution level M contains W_{M-1} as the highest level detail space (3).) If instead of the whole Hilbert space, $\tilde{\Delta}^{[M]}$ is measured in the next level subspace W_M, the value of the expansion coefficients of the error function

$$r_{M\ell} = \left| \int w_{M\ell}(x)(D - \tilde{\lambda}^{[M]})\tilde{E}^{[M]}(x)dx \right|^2 \tag{14}$$

gives a good approximation on the value of the error that can be caused if the wavelet $w_{M\ell}$ is omitted in the calculation. If $r_{M\ell}$ is large enough, the wavelet $w_{M\ell}$ should be included in the further calculations.

Calculating the $r_{M\ell}$ values for all the ℓ belonging to the support of E would be unnecessary in the regions where the Mth refinement level had already zero expansion coefficients. Here no further refinement is needed, thus no $r_{M\ell}$ values are to be calculated. This method is adaptive in the sense, that

Table 1: The deviation of the truncated wave function $\tilde{E}_0^{[M]}$ from the eigenfunction $E_0^{[M]}$ of the full Mth level problem with error tolerance $\eta = 10^{-8}$ in the detail spaces V_0, $W_0, \ldots, W_3$. The error where not given is less than the numerical precision of the computer arithmetics.

M	$\delta\|P_0\tilde{E}_0^{[M]}\|^2$	$\delta\|Q_0\tilde{E}_0^{[M]}\|^2$	$\delta\|Q_1\tilde{E}_0^{[M]}\|^2$	$\delta\|Q_2\tilde{E}_0^{[M]}\|^2$	$\delta\|Q_3\tilde{E}_0^{[M]}\|^2$
1	0.205×10^{-11}	-0.205×10^{-11}			
2	0.023×10^{-11}	-0.023×10^{-11}			
3	-5.933×10^{-11}	5.902×10^{-11}	3.2×10^{-13}		
4	-5.408×10^{-11}	5.457×10^{-11}	-5.1×10^{-13}	2×10^{-14}	
5	-3.550×10^{-11}	3.530×10^{-11}	1.8×10^{-13}	3×10^{-14}	-10^{-14}

- only those wavelet basis functions $w_{M\ell}$ are included into the diagonalization of the partial differential equation, for which the coefficient predicted from the previous level calculations is large enough,
- only those $r_{M\ell}$ values are predicted, for which the support of $w_{M\ell}$ overlaps with the essential wavelets of W_{M-1}.

The followings summarize the method

1. Use the set $\hat{W}_M$ of wavelets $w_{M\ell}$ for which the following condition holds

$$\text{support}(w_{M\ell}) \cap \text{support}(\tilde{W}_{M-1}) \neq \emptyset.$$

2. Calculate the predicted error components (14) for these chosen wavelets, and sort them to descending order of $r_{M\ell}$.
3. If the error tolerance is denoted by η, include the wavelets with large $r_{M\ell}$ into the truncated subspace $\widetilde{W}_M$, one by one until the following condition is satisfied

$$\sum_{\ell \in \hat{W}_M} r_{M\ell} - \sum_{\ell \in \tilde{W}_M} r_{M\ell} \leq \eta. \tag{15}$$

4. Solve the differential equation in the truncated Hilbert space $\tilde{V}_0 \oplus \bigoplus_{m=0}^{M} \tilde{W}_m$.

3. CALCULATIONS

Using this method, a quite large number of wavelets can be omitted from the calculation, e.g., for a simple harmonic oscillator's first eigenfunction includes $\dim W_6 = 646$ basis functions, whereas for the adaptive method only $\dim \tilde{W}_6 = 296$, if error condition $\eta = 10^{-9}$ is applied in both cases. In order to measure the error of this method, we have considered, how large the is the deviation between the full Mth level solution and the solution of our method. The results for a rather strict error tolerance are listed in Tab. 1. It can be seen, that with increasing resolution level, the errors decrease, even within the columns (i.e., the projections onto the same subspace). In case of less strict error limits, the deviation of the truncated and full solutions projected to one subspace saturates at lower resolution levels, e.g., for $\eta = 10^{-4}$, the error in the projected scaling function subspace does not chang significantly above $M = 4$.

4. SUMMARY

A wavelet based adaptive solution method is presented, that predicts the necessary wavelets of the finer, next resolution level from the results of the previous level calculations. One dimensional test calculations have been carried out, but the method can be straightforwardly extended to 2 and 3 dimensions.

ACKNOWLEDGMENT

This work was supported by the Bolyai János Research Fellowship of the Hungarian Academy of Sciences and by the Széchenyi István University under project TáMOP 4.2.1.B.

REFERENCES

1. Wei, X. C., E. P. Li, and C. H. Liang, "Fast solution for large-scale electromagnetic scattering problems using wavelet transform and its precondition," *IEEE Trans. Magn.*, Vol. 36, No. 9, 644–648, 2000.
2. Bilgic, W., A. Rennings, and P. Waldow, "Appropriate wavelets with compact support for the compression of FDTC calculated electromagnetic fields," *IEEE Trans. Magn.*, Vol. 36, No. 9, 644–648, 2000.
3. Krumpholz, M. and L. P. B. Katehi, "MRTD: New time-domain schemes based on multiresolution analysis," *IEEE Trans. Microw. Theor. Techinques*, Vol. 44, No. 4, 555–571, 1996.
4. Rickard, Y., "An efficient wavelet-based solution of electromagnetic field problems," *Appl. Num. Math.*, Vol. 58, 472–485, 2008.
5. Yee, K. S., "Numerical solution of initial boundary value problems involving Maxwell's equations in isotroic media," *IEEE Trans. Antennas Propagat.*, Vol. 14, No. 3, 302–307, 1996.
6. Pertz, O. and A. Beyer, "Applying wavelets to electromagnetic field simulation: The method of lines," *IEEE MTT-S Digest, Proc. of the MTT-S IMS*, TU2E-6, 129–132, Boston, USA, June 2000.
7. Pertz, O. and A. Beyer, "A novel wavelet-based method for EM field simulation," *IEEE Proc. of the 33rd European Microwave Conference*, 111–114, Munich, Germany, June 2003.
8. Werthen, M. and I Wolff, "A novel wavelet based time domain simulation approach," *IEEE Microw. Guided Wave Lett.*, Vol. 6, No. 12, 438–440, 1996.
9. Kaiser, G., "Wavelet electrodynamics II: Atomic decomposition of electromagnetic waves," *Appl. Comp. Harmonic Anal.*, Vol. 1, No. 1, 246–260, 1994.
10. Kaiser, G., *Short-pulse Radar via Eletromagnetic Wavelets, in Ultra-wideband, Short-pulse Electromagnetics 3*, Eds.: C. E. Baum, L. Carin, and A. P. Stone, Plenum Press, 1997.
11. Kaiser, G., *Eigenwavelets of the Wave Equation, in Harmonic Analysis, Signal Processing and Complexity*, Eds.: I. Sabadini, D. C. Struppa, and D. F. Walnut, Birkhauser, 2005.
12. Hansen, T. and G. Kaiser, "Generalized Huygens principle with pulsed-beam wavelets," *J. Phys. A: Math. Theor.*, Vol. 42, No. 475403, 2009.
13. Yang, S., S. L. Ho, P. H. Ni, and G. Z. Ni, "A combined wavelet-FE method for transient electromagnetic field computations," *IEEE Trans. Magn.*, Vol. 42, No. 4, 571–574, 2006.
14. Yang, S., G. Ni, S. L. Ho, J. M. Machado, M. A. Rahman, and H. C. Wong, "Wavelet-Galerkin method for computation of electromagnetic fields-computation of connection coefficients," *IEEE Trans. Magn.*, Vol. 36, No. 9, 644–648, 2000.
15. Pipek, J. and S. Nagy, "Refinement trajectory and determination of eigenstates by a wavelet based adaptive method," *J. Chem. Phys.*, Vol. 125, No. 174107, 2006.
16. Daubechies, I., *Wavelets*, *CBMS-NSF Series in Appl. Math.*, Siam Publ., Philadelphia, 1992.
17. Chui, C. K., *An Introduction to Wavelets*, Academic Press, San Diego, 1992.
18. Dahmen, W., *J. Comput. Appl. Math.*, Vol. 128, No. 1, 123, 2001.

Dissipative Losses Evaluation in Magnetic Power Devices with Litz-wire Type Windings

C. Carretero[1], **R. Alonso**[2], **J. Acero**[1], **Ó. Lucía**[1], **and J. M. Burdío**[1]

[1]Departamento de Ingeniería Electrónica y Comunicaciones, Universidad de Zaragoza, Spain
[2]Departamento de Física Aplicada, Universidad de Zaragoza, Spain

Abstract— Power electronics systems usually drive medium to high levels of electrical energy. Presently, Switching-Mode Power Supplies (SMPS) have been extensively used to improve the system performance. Additionally, working frequencies have been gradually increased in order to reduce device sizes. As a consequence, the optimization of different components required to obtain an appropriate efficiency keeping safety operation conditions has become more difficult. This work deals with the analysis of power losses in the magnetic devices, focused on those originated in the windings. The winding power losses can be classified into two different categories: conduction and proximity losses. The first ones are due to the currents driven by the windings, which are normally made with a low resistivity material, e.g., copper or aluminum, including skin effects. The second ones, proximity losses, are associated with the currents induced because the windings are immersed in a magnetic field, and may become more important than the conduction losses at high frequencies. This is especially important for windings made with solid wire. The last issue may be partly overcome by using Litz wires which consist of multiple small cylindrical strands properly braided to achieve the equivalence among them.

1. INTRODUCTION

Previous papers evaluate analytically conduction and proximity losses in windings made of wire composed by circular cross-section strands. Analytical expressions for both losses have been developed considering an infinite-length cylindrical strand with radius r_0 made of an electrical conductor immersed in a uniform longitudinal electric field $\mathbf{E}$ and a uniform transversal magnetic field $\mathbf{H}_0$ respectively [1–4].

The field evaluation has been performed in the frequency domain, where the exponential expression $e^{-j\omega t}$ is suppressed for simplicity. The Helmholtz potential decomposition is used to obtain the electromagnetic field. The scalar potential is neglected because no free charge densities are present in the system. As a result, the electromagnetic field is described by means of the magnetic vector potential $\mathbf{A}$. The quasi-static approach can be applied because the usual wire cross-section dimensions are smaller than the wavelength of the involved fields, considering that the frequencies range from *dc* to several tens of MHz. For this reason, the radiation effects have been neglected. As a result, both conduction and proximity power losses expressions are derived from the solution of the following diffusion equation

$$\nabla^2\mathbf{A} - j\omega\mu\sigma\mathbf{A} = 0. \tag{1}$$

A general solution for the equation expressed in a cylindrical coordinate framework is provided in [5] by means of an infinite set of eigenfunctions. Applying the correct boundary conditions, both expressions emerge, respectively, as the zero order and first order solution for the magnetic vector potential longitudinal component A_z. Additionally, a close relationship between the ratio r_0/δ, where r_0 is the strand radius and δ is the penetration depth, and both types of power losses can be established. Note that the frequency dependence of losses is accounted by means of δ.

2. POWER LOSSES IN A CYLINDRICAL WIRE

The laplacian considering cylindrical coordinates has the following expression

$$\nabla^2\mathbf{A} = \left(\nabla^2 A_\rho - \frac{2}{\rho^2}\partial_\varphi A_\varphi - \frac{A_\rho}{\rho^2}\right)\hat{\boldsymbol{\rho}} + \left(\nabla^2 A_\varphi - \frac{2}{\rho^2}\partial_\varphi A_\rho - \frac{A_\varphi}{\rho^2}\right)\hat{\boldsymbol{\varphi}} + \nabla^2 A_z\hat{\boldsymbol{z}}. \tag{2}$$

Combining this equation with (1), and extracting the $\hat{\boldsymbol{z}}$ component directed along the cylindrical wire, we obtain the following expression

$$\frac{\partial_\rho\left(\rho\partial_\rho A_z\right)}{\rho} + \frac{1}{\rho^2}\partial_\varphi^2 A_z + \partial_z^2 A_z - j\omega\mu\sigma A_z = 0. \tag{3}$$

In order to simplify the equation, the fields have been considered uniform along the axial direction of the cylinder, fulfilling the condition $\partial_z A_z = 0$, therefore, we have

$$\frac{\partial_\rho \left(\rho \partial_\rho A_z\right)}{\rho} + \frac{1}{\rho^2}\partial_\varphi^2 A_z - j\omega\mu\sigma A_z = 0. \tag{4}$$

2.1. Conduction Losses

An additional constraint is needed to obtain the conduction power losses which is obtained enforcing $\partial_\varphi A_z = 0$. Therefore, we have

$$\frac{\partial_\rho \left(\rho \partial_\rho A_z\right)}{\rho} - j\omega\mu\sigma A_z = 0. \tag{5}$$

Solving (5), as appear in [5], we obtain the following 0th order solution

$$A_z = \begin{cases} C_1 J_0\left(k\rho\right) + C_2 N_0\left(k\rho\right) & \rho < r_0 \\ C_1' ln\rho + C_2' & \rho > r_0 \end{cases}, \tag{6}$$

where $k = (-j\omega\mu\sigma)$, or, equivalently, $k = \frac{-1+j}{\delta}$, and, J_0 and N_0 are respectively the first kind and second kind Bessel functions of 0th order.

Applying the appropriate boundary conditions, we obtain [3]

$$\mathbf{E} = -\frac{V}{l}\frac{J_0\left(k\rho\right)}{J_0\left(kr_0\right)}\hat{\mathbf{z}}. \tag{7}$$

Inside the conductor medium, the current density obeys the expression $\mathbf{J} = \sigma\mathbf{E}$. Integrating the current density in the cross-section area, we obtain the current driven by the cylinder

$$I = \frac{V}{l}\frac{2\pi r_0 \sigma J_1\left(kr_0\right)}{kJ_0\left(kr_0\right)}. \tag{8}$$

Therefore, the conduction impedance per unit length $Z_{cond,u.l.}$ is provided by

$$Z_{cond,u.l.} = \frac{kJ_0\left(kr_0\right)}{2\pi r_0 \sigma J_1\left(kr_0\right)}. \tag{9}$$

The conduction resistance per unit length $R_{cond,u.l.}$ is equal to the real part of $Z_{cond,u.l.}$, hence

$$R_{cond,u.l.} = \frac{1}{\pi r_0^2 \sigma}\Phi_{cond}\left(r_0/\delta\right), \tag{10}$$

where the factor $\Phi_{cond}\left(r_0/\delta\right)$ is defined as

$$\Phi_{cond}\left(r_0/\delta\right) = \mathfrak{Re}\left(\frac{kr_0 J_0\left(kr_0\right)}{2J_1\left(kr_0\right)}\right). \tag{11}$$

2.2. Proximity Losses

The appropriate condition to obtain the proximity losses can be expressed as $\partial_\varphi A_z = 1$, therefore (4) is reduced to

$$\frac{\partial_\rho \left(\rho \partial_\rho A_z\right)}{\rho} - \frac{1}{\rho^2}A_z - j\omega\mu\sigma A_z = 0, \tag{12}$$

whose general solution is shown as follows [5]

$$A_z = \begin{cases} \left(C_1 J_1\left(k\rho\right) + C_2 N_1\left(k\rho\right)\right)\left(D_1 \sin\varphi + D_2 \cos\varphi\right) & \rho < r_0 \\ \left(C_1'\rho + C_2'/\rho\right)\left(D_1' \sin\varphi + D_2' \cos\varphi\right) & \rho > r_0 \end{cases}, \tag{13}$$

where J_1 and N_1 are respectively first kind and second kind Bessel functions of first order.

The regularity condition is fulfilled in this case. Therefore, C_2 is equal to zero. In order to simplify the development without loss of generality, D_2 is also null. Finally, the solution adopts the following form

$$A_z = \begin{cases} AJ_1\left(k\rho\right)\sin\varphi & \rho < r_0 \\ \left(B/\rho + C\rho\right)\sin\varphi & \rho > r_0 \end{cases}. \tag{14}$$

The constants A, B and C are defined by means of the system constraints. The magnetic field H is determined using the expression $\frac{1}{\mu}\nabla \times A_z\hat{z}$, obtaining

$$H = \begin{cases} \frac{J_1(k\rho)}{\rho}\frac{Acos\varphi}{\mu}\hat{\rho} + \left(\frac{J_1(k\rho)}{\rho} - kJ_0\left(k\rho\right)\right)\frac{Asin\varphi}{\mu}\hat{\varphi} & \rho < r_0 \\ \left(\frac{B}{\rho^2} + C\right)\frac{\cos\varphi}{\mu_0}\hat{\rho} + \left(\frac{B}{\rho^2} - C\right)\frac{\sin\varphi}{\mu_0}\hat{\varphi} & \rho > r_0 \end{cases}. \tag{15}$$

Considering the magnetic field H_0 at infinity, we obtain the following constraint

$$H_0 = lim_{\rho\to\infty}H = C\frac{\cos\varphi}{\mu_0}\hat{\rho} - C\frac{\sin\varphi}{\mu_0}\hat{\varphi} \quad \Rightarrow \quad C = \mu_0 H_0. \tag{16}$$

Moreover, from the magnetic vector potential continuity at radial position r_0, we have

$$B = Ar_0J_1\left(kr_0\right) - r_0^2\mu_0 H_0. \tag{17}$$

Finally, including the continuity of the tangential component of the magnetic field, we obtain

$$A = \frac{2\mu_0 H_0}{kJ_0\left(kr_0\right)}. \tag{18}$$

Introducing the coefficients in (14), we have

$$A_z = \begin{cases} 2\mu_0 H_0\frac{J_1(k\rho)}{kJ_0(kr_0)}\sin\varphi & \rho < r_0 \\ \mu_0 H_0\left(\frac{2J_1(k\rho) - kr_0J_0(kr_0)}{k\rho J_0(kr_0)} + \rho\right)\sin\varphi & \rho > r_0 \end{cases}. \tag{19}$$

The electric field $\mathbf{E}$ inside the conductor is defined using the previous expressions as follows

$$\mathbf{E} = 2\mu_0 H_0\frac{J_1\left(k\rho\right)}{kJ_0\left(kr_0\right)}\sin\varphi\hat{z}. \tag{20}$$

The power losses per unit length originated by the external transversal magnetic field $\mathbf{H}_0$ is obtained by integrating the dissipative power density $\frac{1}{2}E\cdot J^*$ arising from the induced currents. Performing the azimuthal integration, we obtain

$$P_{prox,u.l.} = \frac{4\pi H_0^2}{\sigma\delta^2}\frac{\int_0^{r_0} J_1\left(k\rho\right)J_1^*\left(k\rho\right)\rho d\rho}{J_0\left(kr_0\right)J_0^*\left(kr_0\right)}, \tag{21}$$

which leads to

$$P_{prox,u.l.} = \frac{2\pi}{\delta}\Phi_{prox}\left(r_0/\delta\right)H_0^2. \tag{22}$$

where it is defined the factor

$$\Phi_{prox}\left(r_0/\delta\right) = -\frac{r_0}{\delta}\frac{ber_2\left(\frac{\sqrt{2}r_0}{\delta}\right)\left(ber_1\left(\frac{\sqrt{2}r_0}{\delta}\right) + bei_1\left(\frac{\sqrt{2}r_0}{\delta}\right)\right) + ber_2\left(\frac{\sqrt{2}r_0}{\delta}\right)\left(ber_1\left(\frac{\sqrt{2}r_0}{\delta}\right) + bei_1\left(\frac{\sqrt{2}r_0}{\delta}\right)\right)}{ber_0^2\left(\frac{\sqrt{2}r_0}{\delta}\right) + bei_0^2\left(\frac{\sqrt{2}r_0}{\delta}\right)}. \tag{23}$$

If the total magnetic field is originated by a single-coil system carrying a current I, the proximity power losses can be defined using an equivalent proximity resistance per unit length $R_{prox,u.l.}$. It can be calculated from the definition $P_{prox,u.l.} = \frac{1}{2}R_{prox,u.l.}I^2$. As a result, considering (22) and (23), we have

$$R_{prox,u.l.} = \frac{4\pi}{\delta}\Phi_{prox}\left(r_0/\delta\right)\overline{H}_0^2. \tag{24}$$

where $\overline{H}_0^2$ is the square of the magnetic field arising from the coil carrying 1 ampere.

3. RESISTANCE OF A RING-TYPE COIL

The previous expressions can be applied to calculate the resistance of a circular coil with rectangular cross-section which is made with Litz wire. Litz wire consists of a bundle of cylindrical conductive strands which are braided in such way to have azimuthal and longitudinal transposition equivalence. As a consequence, each strand exhibits the same impedance and the current is equally distributed among the strands.

A ring-type coil is made wound n turns of n_0 strands with a r_0 radius uniformly in the cross-section. The geometry of the circular coil is determined by the internal radius r_{int}, the external radius r_{ext}, and the height h, as shown in Figure 1. The coil can be modeled as a uniform current density because the radius r_0 and the distance between strands are smaller than the coil dimensions. An ideal coil placed in air is electrically characterized by an inductance L which is independent of the frequency. The resistance of this kind of devices can be accounted by addition of conduction and proximity losses in the windings.

The conduction resistance R_{cond} can be calculated considering overall strands connected in parallel. Therefore, R_{cond} is equal to $R_{cond\,u.l.}$ multiplied by the wire length $n\pi(r_{ext} - r_{int})$ and divided by the number of strands n_0, as can be seen as follows

$$R_{cond} = \frac{1}{r_0^2 \sigma} \frac{n}{n_0} \Phi_{cond}\left(r_0/\delta\right)\left(r_{ext} - r_{int}\right). \tag{25}$$

The proximity resistance R_{prox} is calculated by means of the following expression

$$R_{prox} = \frac{8\pi^2}{\sigma} n n_0 \Phi_{prox}\left(r_0/\delta\right)\left\langle r \cdot \overline{H}_0^2 \right\rangle, \tag{26}$$

where r is the radial position with respect to the coil axis and $\langle r \cdot \overline{H}_0^2 \rangle$ is the coil cross-section average of the product between r and $\overline{H}_0^2$.

A comparison between experimental measurements and the resistance values obtained from (25) and (26) is shown in Figure 2. The calculation of the magnetic field used in (26) can be performed by means of both analytical methods [6] and numerical calculations [7, 8]. Frequency dependent resistance has been measured by means of a precision LCR meter (Agilent E4980A).

The coil characterized in Figure 2 is a toroid with internal radius r_{int} of 21.5 mm, external radius r_{ext} of 29 mm and height h of 4 mm. The coil is made wound 24 turns of Litz wire composed by 35 strands of radius $r_0 = 75\,\mu$m.

Figure 2 shows a good agreement between experimental data and resistance calculated from (25) and (26). At frequencies below 10 kHz, the resistance is determined by R_{cond} with a negligible frequency dependence, whereas, at frequencies over 100 kHz, the resistance increases sharply because the proximity effects dominate. From the calculations is inferred that R_{cond} is almost constant in the whole frequency range and R_{prox} becomes important above several tens of kHz.

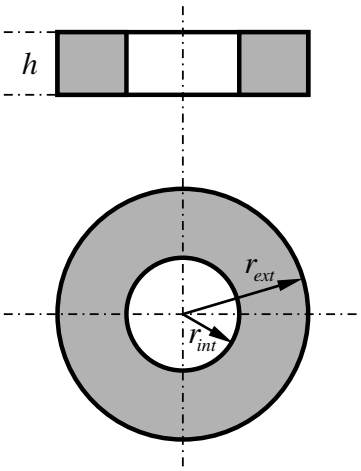

Figure 1: Lateral and top views of a ring-type coil.

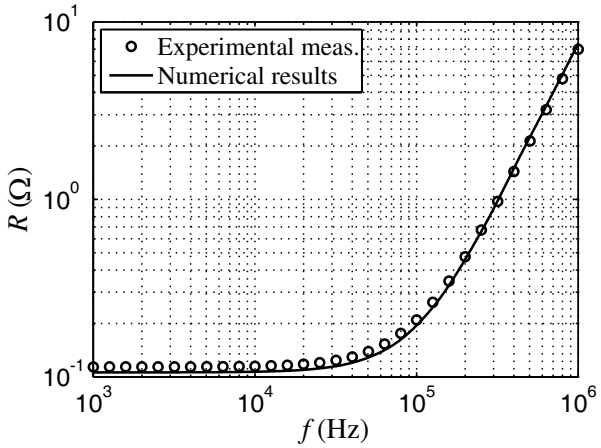

Figure 2: Resistance of a 24−turns coil made with Litz wire.

4. CONCLUSIONS

In this paper, a method to calculate power losses in multistranded wire-made devices is explained. A unified modeling of the two types of losses in the windings of power devices is performed. The expressions obtained has been experimentally validated. The experimental measurements shows a good agreement with the numerical calculations.

ACKNOWLEDGMENT

This work was partly supported by the Spanish MICINN under Project CSD2009-00046 and Project TEC2010-19207, by DGA under Project PI065/09, and by Bosch and Siemens Home Appliances Group.

REFERENCES

1. Acero, J., et al., "Frequency-dependent resistance in litz wire planar windings for domestic induction heating appliances," *IEEE Trans. Power Electron.*, Vol. 21, No. 4, 856–866, 2006.
2. Koertzen, H. W. E., J. D. van Wyk, and J. A. Ferreira, "An investigation of the analytical computation of inductance and AC resistance of the heat-coil for induction cookers," *in IEEE Industry Applications Society Conf. (IAS) Rec.*, 1113–1119, 1992.
3. Lammeraner, J. and M. Stafl, *Eddy Currents*, CRC Press, Cleveland, 1966.
4. Kazimierczuk, K., *High-Frequency Magnetic Components*, Wiley, Chichester, 2009.
5. Rothwell, E. J. and M. J. Cloud, *Electromagnetics*, CRC Press, Boca Raton, 2001.
6. Conway, J. T., "Exact solutions for the magnetic fields of axisymmetric solenoids and current distributions," *IEEE Trans. Magn.*, Vol. 37, No. 4, 2977–2988, 2001.
7. Gyselinck, J., R. V. Sabariego, and P. Dular, "Time-domain homogenization of windings in 2-D finite element models," *IEEE Trans. Magn.*, Vol. 43, No. 4, 1297–1300, 2007.
8. Sabariego, R. V., P. Dular, and J. Gyselinck, "Time-domain homogenization of windings in 3-D finite element models," *IEEE Trans. Magn.*, Vol. 44, No. 6, 1302–1305, 2008.

The Minimum Phase Nature of the Transfer Function of the Impulse Radiating Antenna

J. S. McLean[1], **R. Sutton**[1], **and H. Foltz**[2]

[1]TDK R&D Corp., USA
[2]University of Texas — Pan American, USA

Abstract— The Impulse Radiating Antenna, a reflector antenna employing a TEM feed, has been shown to provide excellent time-domain pulse reproduction on its principal axis. We examine the on-axis response of a representative, well-designed Impulse Radiating Antenna in the frequency- and time-domains and show that it is the existence of the pre-pulse in the time-domain response that causes the frequency-domain transfer function to be non-minimum phase in nature. Moreover, the hypothetical time-domain response corresponding to the minimum phase frequency domain transfer function derived in turn from the magnitude of the on-axis response of the impulse radiating antenna is essentially identical to the actual time domain response except that the pre-pulse occurs after the main pulse. That is, the time domain response associated with the minimum phase transfer function appears almost as a mirror image of the actual time domain response with the symmetry occurring around the center of the main pulse.

1. INTRODUCTION

The Impulse Radiating Antenna (IRA), a reflector antenna employing a TEM feed structure [1], has been shown to provide excellent time-domain pulse reproduction on its principal axis; more specifically as stated in [1], "a step-like signal into the antenna gives an approximate delta-function response in the far field." While this statement succinctly describes the ideal time domain behavior, the frequency domain counterpart is that perfect time domain pulse reproduction requires satisfaction of the distortionless transfer function criterion in the frequency domain. Distortionless transfer functions, in turn, are a small subset of a more general group, minimum-phase transfer functions. When a minimum-phase network exhibits a transfer function magnitude which is nearly constant with frequency, its associated phase function necessarily satisfies the distortionless transfer function criterion; however, many broadband antennas and other physical systems exhibiting flat or nearly flat transfer functions are not minimum-phase. An example of such a broadband, non-minimum phase antenna is the Log-Periodic Dipole Antenna (LPDA), the transfer function of which exhibits a nominally flat magnitude, but deviates greatly from minimum phase behavior [2]. It is well known that this antenna exhibits poor time domain pulse fidelity.

2. FREQUENCY DOMAIN TRANSFER FUNCTION

The frequency domain complex vector antenna transfer function $\vec{H}$ gives the far field radiated electric field $\vec{E}$ in terms of the power-normalized incident voltage a at the antenna input port [3]:

$$\frac{\vec{E}\left(R,\theta,\phi,\omega\right)}{\sqrt{\eta_0}} = -j\omega\vec{H}\left(\theta,\phi,\omega\right)\frac{e^{-j\beta R}}{2\pi R c_0}a\left(\omega\right). \tag{1}$$

This definition explicitly includes a differentiation of the transmitted signal through the $j\omega$ factor[1]. Thus, a hypothetical antenna with a unity transfer function for all frequency would still differentiate the incident signal in the sense that the radiated electric field would resemble the time derivative of the input voltage. Thus, the inverse Fourier transform of the antenna transfer function may be called antenna impulse response, but it actually gives the far field electric field due to a step incident voltage. Note that the definition for antenna transfer function given in Eq. (1) has units of meters and is identical to the frequency domain counterpart of the normalized impulse response defined in [4, 5].

However, the differentiation in Eq. (1) is distinct from the intrinsic high-pass nature of the impedance matching and power transfer characteristics of any finite-sized antenna. A finite size

[1]Strictly speaking, the antenna transfer function does not directly yield the electric field due to the incident voltage; therefore the "impulse response" derived from it does not give the electric field due to a voltage impulse at the input. The definition was arrived at by several different groups of researchers and is a compromise that provides some symmetry between forms for reception and transmission [3]. However, the authors note that there are other conventions that have been proposed.

antenna driven by a step input cannot sustain a DC electric field that decays as $1/R$ in the far-field; therefore, one can conclude from (1) that $\vec{H}$ must have at least one zero at $\omega = 0$. This can also be seen in the relationship between the complex vector effective length $\vec{h}_{eff}$ and the antenna transfer function:

$$\vec{H}(\theta, \phi, \omega) = \frac{\sqrt{\eta_0 Z_0}}{Z_0 + Z_A(\omega)} \vec{h}_{eff}(\omega) \tag{2}$$

where Z_0 is the normalizing impedance for the antenna input port and Z_A is the antenna input impedance. The frequency domain transfer function must exhibit at least one zero at DC. Some antennas (for example, a short monopole) have an effective height that is constant and finite in the limit as $\omega \to 0$; however, such antennas have an input impedance Z_A that becomes infinite at DC. The authors are unaware of any antenna that has both nonzero effective height and finite impedance at DC. The conclusion is that the relationship between electric field and input voltage must always have at least two zeroes at $\omega = 0$, and therefore the response to a step input must be zero average in the time domain.

The Impulse Radiating Antenna is primarily a reflector antenna. However, the TEM feed structure itself also radiates and behaves essentially as a $P \times M$ antenna. It can be shown that one type of canonical $P \times M$ antenna sometimes referred as a balanced transmission line wave (BTW) sensor [6], a backward-radiating, terminated uniform transmission line, has an asymptotic slope of 12 dB/octave in its gain, and thus has an asymptotic slope of 6 dB/octave in its transfer function, indicating a single zero at $\omega = 0$. The Impulse Radiating Antenna can also be shown to exhibit a single zero at DC in its effective length and transfer function. Both the balanced transmission line wave sensor and the IRA are very well matched due to the internal loads and the complex voltage division term in (2) is essentially frequency independent. Thus, when relating the incident input voltage to the far field radiated electric field the high-pass differentiation appears twice: once in the transfer function (and thus the effective height), and again due to the $j\omega$ factor in Eq. (1) for the electric field.

An antenna with a frequency-domain transfer function (as defined in [3]) of unity for all frequency would generate an electric field impulse in the far field in response to a step input, and is said to satisfy the distortionless transfer function criterion. The IRA *nearly* satisfies the distortionless transfer function criterion and thus is *nearly* minimum phase in the frequency domain. However, the small departure of its transfer function from minimum phase is quite interesting.

Close examination of the time domain response of the IRA reveals a pre-pulse as well as a long shallow tail following the main pulse [1]. The pre-pulse has been shown to be step-like in the time domain. It radiates from the TEM feed structure and necessarily precedes the main pulse from the reflector. It can be shown that having two radiation mechanisms (in this case direct feed radiation and the reflector radiation) with different delay times leads to non-minimum phase behavior if the

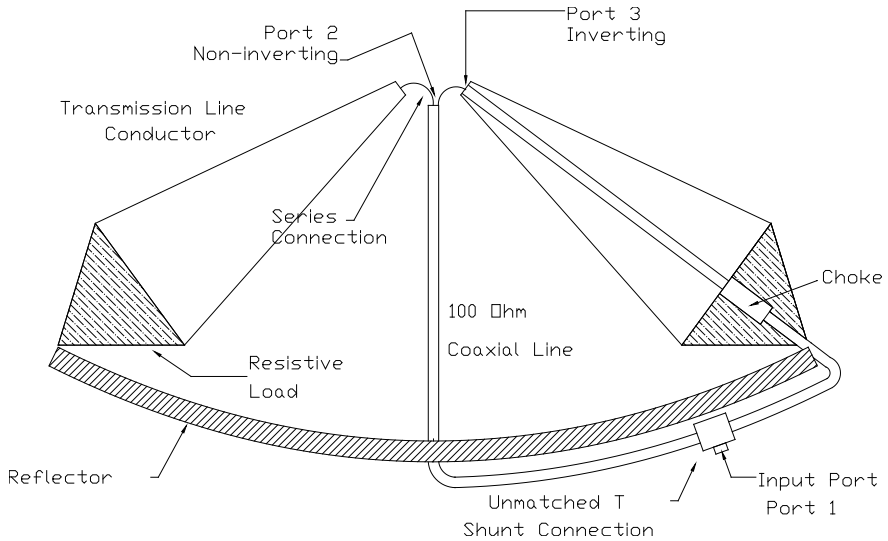

Figure 1: Schematic drawing of an impulse radiating antenna. The reflector employed by the Farr IRA-3 has a diameter of $D = 46$ cm and focal length of $F = 23$ cm and thus $F/D = 0.5$.

smaller signal is the first to arrive in the far-field. The lack of minimum phase behavior in turn implies that the distortionless criterion cannot be satisfied, and furthermore, that it cannot be corrected through passive equalization.

As discussed above, Eq. (1) relating the electric field to the incident voltage must contain at least two zeroes at DC, and the entire time domain response must average to zero. In [1] some discussion is given concerning how if the area of the pre-pulse could be made to equal that under the main impulse (thus giving zero DC average) then the tail of the response would be small. The area of the pre-pulse is tailored by adjusting the characteristic impedance of the TEM feed of the IRA. Thus, the canonical or ideal response of the Impulse Radiating Antenna is a step followed immediately by an impulse of equal area. The particular IRA characterized here, the Farr Research IRA-3, exhibits a very good on-axis, time-domain response with a very minimal tail.

3. MEASUREMENT

The port-to-port forward transfer scattering parameter of combination of a Farr Research IRA-3 impulse radiating antenna and a Farr Research TEM-1 TEM horn was measured in a fully anechoic chamber using an automatic vector network analyzer. The analyzer was calibrated using a so-called transmission calibration; that is, a full two-port calibration was not used due to the very long coaxial cables connecting the network analyzer, which was located outside the chamber, to the antennas. The magnitude of the measured transfer scattering parameter is shown in Fig. 3.

The TEM horn had been previously characterized as described in [8]. From the transfer scattering parameter measurement, the transfer function of IRA was then determined. The magnitude

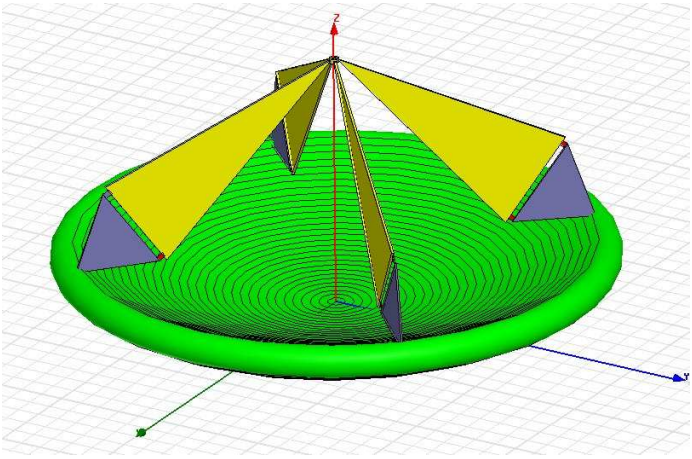

Figure 2: Solid model of impulse radiating antenna. A bifurcating ground plane located in the x-z plane has been omitted for clarity.

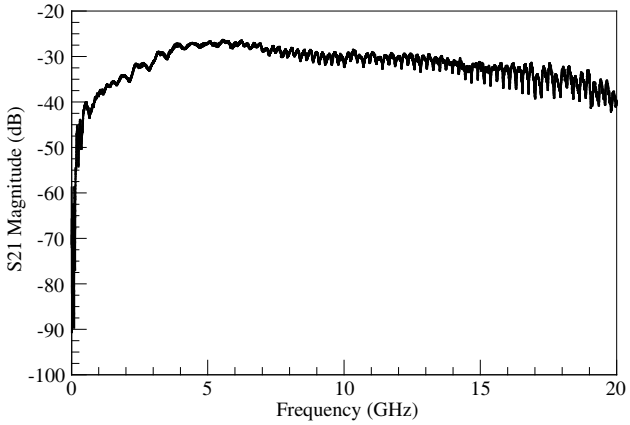

Figure 3: The magnitude of the measured transfer scattering parameter S_{21} of the 2-port network comprised by a Farr Research IRA-3 impulse radiating antenna and a Farr Research TEM-1 TEM horn situated in an anechoic chamber with principal axes aligned and with 3.5 meters separation.

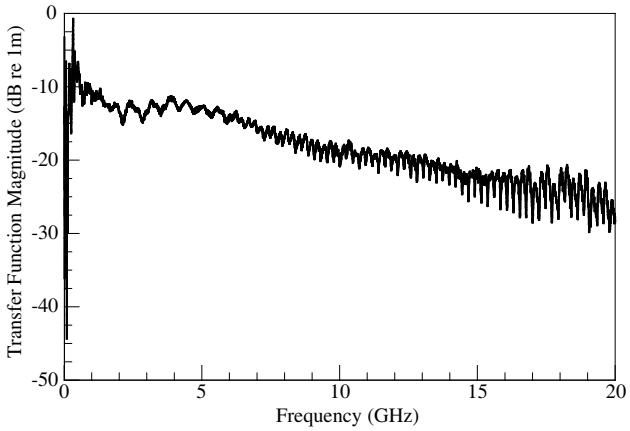

Figure 4: Magnitude of the frequency domain transfer function of the Farr IRA-3 impulse radiating antennas as derived measured port-to-port insertion loss data.

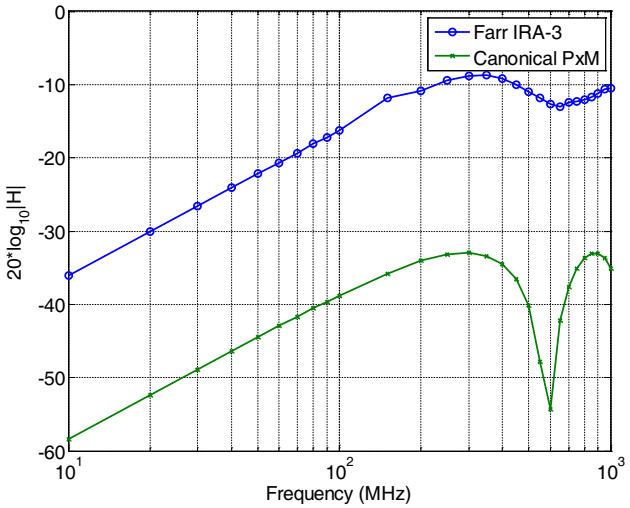

Figure 5: Magnitude on-axis transfer function of a canonical $P \times M$ antenna (length 23 cm) and a numerical model of the Farr Research IRA-3 impulse radiating antenna. As expected the slope of the transfer function is asymptotically = 6 dB/octave at the low end of the frequency range.

of the frequency domain transfer function is shown in Fig. 4. The transfer function data given here agrees reasonably well with the data provided by the manufacturer.

4. LOW FREQUENCY EXTRAPOLATION OF MEASURED DATA

The IRA transfer function magnitude shown in Fig. 4 appears to reach an approximately constant value at low frequency. However, as discussed in Section 2, it is known that there is at least one zero at DC, and therefore one can conclude that there is also a pole at a low but finite frequency. S_{21} in a two-antenna measurement has at least three zeroes at DC (one in each of the transfer functions plus the $j\omega$ factor in Eq. (1)), and thus the measured signal decreases very rapidly at low frequency. In the data presented here, unavoidable noise overcomes the measured signal before the pole in the IRA transfer function can be seen.

To study the minimum phase behavior of the IRA, a Hilbert transform is performed to derive the minimum phase function from the transfer function magnitude, which requires in principle integration over all frequency. Explicit or implicit (simple truncation) extrapolation of the finite frequency range is necessary. The value of the minimum phase function as $\omega \to 0$ is determined by the limiting slope at low frequency. Due to the noise problem described above, the low frequency behavior must be extrapolated.

The operation of the IRA in the lowest registers of its operating frequency range is similar to that of the so-called $P \times M$ antenna or Balanced Transmission Line Wave (BTW) sensor [6]. The

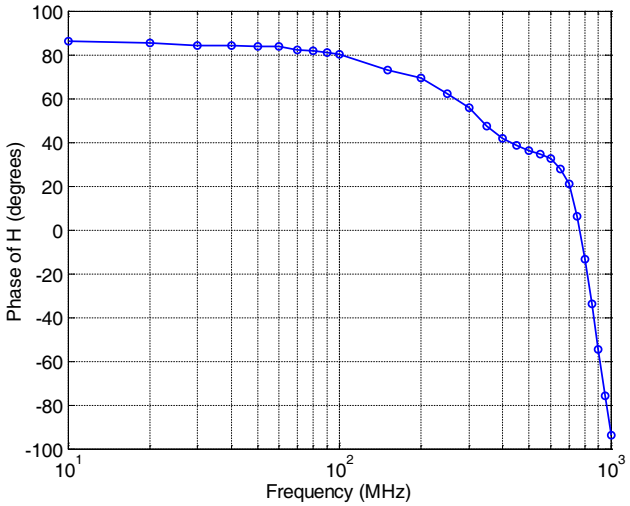

Figure 6: Simulated phase of far-field on-axis electric field of Farr IRA-3. A factor of $\exp(-jkR)$ has been removed from the data. As can be seen the phase of the transmitted electric field with respect to the source asymptotically approaches 90° at low frequencies. This is consistent with there being one zero at DC in the transfer function.

antenna exhibits a pattern which is a cardioid of revolution about the principal axis and has an effective length and transfer function the magnitudes of which increase 6 dB/octave asymptotically. The power gain increases 12 dB per octave asymptotically. Fig. 5 shows data for the Farr IRA-3 generated using a commercial FEM simulator, Ansoft's HFSS software, with comparison to a canonical $P \times M$ antenna. In this numerical simulation the equal-delay balun was not modeled. The canonical $P \times M$ antenna is a terminated two-wire transmission line with characteristic impedance of 450 Ohms and terminated in a matched load. The length of the line is 246 mm corresponding to the focal length and hence feed dimension of the Farr IRA-3. The data was obtained using a numerical model implemented using the Numerical Electromagnetics Code (NEC). Note that both antennas show 6 dB/decade slope in the magnitude of their transfer functions in low portion of the frequency range. Since both antennas are very nearly perfectly matched at the low ends of their respective operating frequency ranges, it can be shown that the antenna transfer function as well as the traditional effective height rolls off with 6 dB/octave. Thus, the extrapolation of the transfer function to DC requires that there be exactly one zero at the origin.

5. MINIMUM PHASE TRANSFER FUNCTION

The minimum-phase quality of the transfer function of an antenna is associated with the propagation of energy through the system. Having a single path through the network or system is a sufficient condition to have minimum-phase behavior. It was shown in [7] that the broadband, double-ridged horn is very nearly minimum phase on its principal axis, but deviates from this condition off-axis. It was surmised that this was due primarily to interference between the direct radiation from the horn's aperture and fields diffracted by the edge of the horn. In [8], it was shown that an asymmetric or half TEM horn such as the Farr Research TEM-3 exhibits a minimum phase response on its principal axis as well as off axis in the E-plane for angles below the ground plane, but is not minimum phase off-axis above the ground plane. This is because below the ground plane the radiation is essentially entirely due to a single mechanism, diffraction from the edge of the ground plane.

The question in this case is whether a similar multiple path effect applies to the IRA. In Fig. 7 we show the measured transfer function phase for the IRA in comparison with the minimum phase function for the antenna. The minimum phase function was computed using the Bode-Hilbert transform of the measured magnitude data, but with the data truncated at 300 MHz and replaced with extrapolated points computed using the 6 dB/octave slope as discussed in Section 4. It can be seen that there is good agreement above 5 GHz, but increasing non-minimum phase behavior below 5 GHz. This is evidence that there are multiple radiation mechanisms.

Figures 8 and 9 show, for the curves labeled "measured" data, the inverse Fourier transform of the measured transfer function. For these curves no extrapolation or windowing was used. The

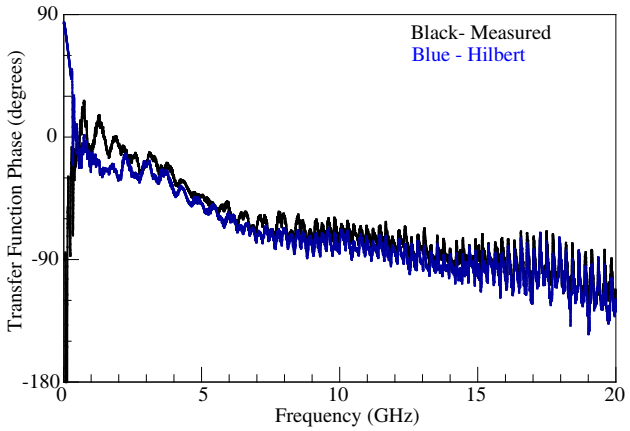

Figure 7: Measured phase of transfer function and minimum phase function computed from the magnitude of the measured transfer function.

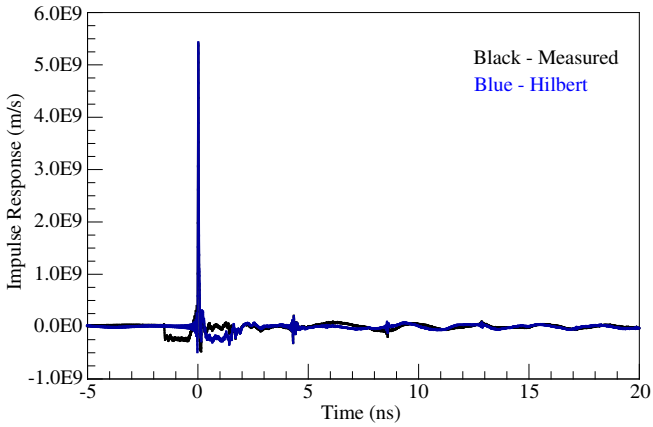

Figure 8: The impulse response of the IRA as derived from frequency-domain data measured in an anechoic chamber (black). For comparison, the impulse response derived from a hypothetical transfer function with the same magnitude but Hilbert minimum phase (blue).

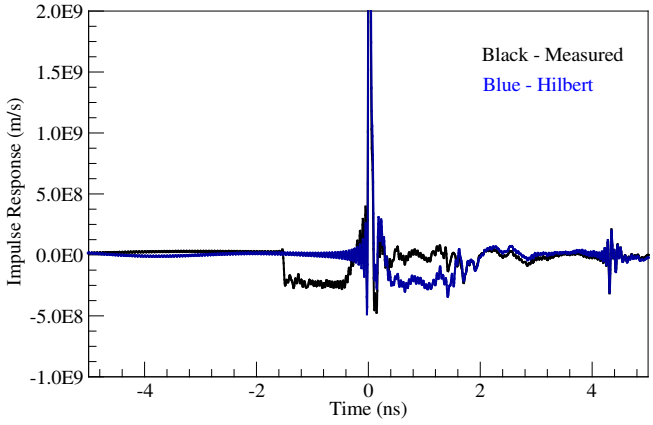

Figure 9: Same data as Figure 8, on an expanded scale. Note that the rectangular pre-pulse that precedes the main pulse in the measured data. If the transfer function is modified to be Hilbert minimum phase, the pre-pulse is transposed such that it follows the main pulse in the response derived from the minimum phase transfer function.

shapes correspond to the electric field that would be produced by a step input, which is the intended mode of operation for the IRA. The negative going pre-pulse is clearly evident starting 1.6 ns prior to the main pulse. The step-like appearance of the pre-pulse leads one to believe that it is associated

with a pole at low frequency. Since the deviation from minimum phase behavior is at low frequency, one might guess that the pre-pulse is the most important cause of the deviation.

As further confirmation, one can carry out a "thought experiment", in which a new hypothetical transfer function is generated, consisting of the actual magnitude from measurements, with the minimum phase function derived from the Hilbert transform. This hypothetical transfer function is then used to generate a time response via an inverse Fourier transform. The same procedure was used in [8] to analyze a TEM horn, and it was seen that in directions where the measured transfer function was not minimum phase, the new hypothetical time-domain response differed from the actual response in that the precursors to the main pulse in the actual data were transposed to the opposite (later) side of the main pulse, thus providing a clean onset to the main pulse. Thus the precursors could be seen to be directly responsible for the deviations from minimum phase.

A similar computation was carried out for the IRA. The results are the blue curves labeled as "Hilbert" in Figs. 8 and 9 It can be seen that in the time-domain response computed from the minimum phase function, the pre-pulse is transposed about the main impulse such that it later. This behavior can be qualitatively explained in terms of a simple model based on rays representing major sources of radiation. In general, the frequency-domain minimum-phase criterion will be satisfied only if the time-domain field from the strongest radiation source is the first to arrive at the observation point. Enforcing the minimum phase condition in the frequency domain re-orders the time-domain response such that the main impulse is first.

6. CONCLUSIONS

The impulse radiating antenna exhibits a transfer function that is essentially minimum phase at high frequency, but has a small but significant deviation from minimum phase at low frequency. By comparing the actual impulse response to a hypothetical impulse response for a transfer function that is modified to be minimum phase, it can be seen that the pre-pulse due to direct radiation from the feed is the most prominent cause of the non-minimum phase behavior.

ACKNOWLEDGMENT

This work was supported in part by the Army Research Office through grant W911NF-06-1-0420.

REFERENCES

1. Baum, C. E., E. G. Farr, and D. V. Giri, "Review of impulse-radiating antennas," *Review of Radio Science* (W. S. Stone, ed.), Chapter 12, 1996–1999, Oxford University Press, 1999; Also presented at the *1999 URSI General Assembly*, Toronto, Canada, Aug. 1999.
2. McLean, J. S. and H. Foltz, "Minimum-phase / all-pass decomposition of LPDA transfer functions," *Proc. of the 2009 IEEE International Conference on Ultra-Wideband, (ICUWB 2008)*, Vancouver, Canada, Sept. 2009.
3. McLean, J. S., R. Sutton, A. Medina, H. Foltz, and J. Li, "The experimental characterization of UWB antennas," *IEEE Antennas and Prop. Magazine*, Vol. 49, No. 6, 20–30, Dec. 2007.
4. Farr, E. G. and C. E. Baum, "Extending the definitions of antenna gain and radiation pattern into the time domain," *Sensor and Simulation Notes*, Note SSN 350, Nov. 1992.
5. Farr, E. G. and C. E. Baum, "Time domain characterization of antennas with TEM feeds," *Sensor and Simulation Note*, 426, Oct. 1998.
6. Farr, E. G. and J. S. Hofstra, "An incident field sensor for EMP measurements," *Sensor and Simulation Note*, 319, SSN 319, Nov. 6, 1989.
7. McLean, J. S., H. Foltz, and R. Sutton, "The directional dependence of the minimum-phase property of the antenna transfer function," *Proc. Loughborough Antenna Conference*, Loughborough, UK, Nov. 2009.
8. McLean, J. S., A. Medina, R. Sutton, and H. Foltz, "Directional dependence of the minimum phase property of the TEM horn transfer function," *2010 AMEREM Conference*, Toronto, Canada, Jul. 2010; Also submitted to *UWB-SP-2010*.

The Study on Electromagnetic Force Induced Vibration and Noise from a Normal and an Eccentric Universal Motors

K. Shiohata[1], **R. Kusama**[2], **S. Ohtsu**[3], **and T. Iwatsubo**[4]

[1]Ibaraki University, 4-12-1 Nakanarusawa, Hitachi, Ibaraki, Japan
[2]Toyota Ltd, Japan
[3]Yamagata, Hitachioomiya, Ibaraki 319-3111, Japan
[4]Kansai University, Japan

Abstract— There are many harmonic components in the electromagnetic force caused by electrical motors. The harmonic components induce the structural vibration and noise, frequently. The unbalanced electromagnetic pull force is generated between the rotor and the stator when the rotor is not corresponding to the center of the stator, that is, eccentric in the electrical motor. In the paper, first, the harmonic components of electromagnetic force caused from a normal and an eccentric universal motor are discussed numerically. Then, the effect of the difference of the harmonic components of electromagnetic force caused from a normal and an eccentric motor on the structural vibration are discussed numerically. From the numerical simulation, the spectrum distribution is different in the space region between a normal and an eccentric motor. And the 12^{th} time order components of electromagnetic force and an electromagnetic vibration and noise of eccentric motor are larger than those of a normal motor.

1. INTRODUCTION

Universal motors shown in Fig. 1 have been the major source of power for power tools and vacuum cleaners since their early days. Recently, the motors have become to run in very high speed and to generate much higher horsepower per unit weight and mechanical structure have become lighter and smaller. As a result of these trends, mechanical vibration and noise are increasing. The lightening of the motor core was also attempted, consequently the electromagnetic exciting force increased by magnetically saturating, and the vibration and noise became easy to be generated. The reason of noise and vibration is the harmonic components of electromagnetic force caused from a motor. The waveform of an electromagnetic stress is shown as Fig. 2. By FFT in the time and space domain of the waveform, many harmonic components are obtained at one point along the inner bore of the stator

In the production of the electrical motor, it is difficult that the center of the rotor always coincide with the center of the stator.

The unbalanced electromagnetic attractive force is generated between the rotor and the stator when the rotor does not coincide with the center of the stator, that is, eccentric in the electrical motor.

In the eccentricity, there are two patterns. One is static eccentricity which rotor center does not coincide with stator center, and the other is dynamic one which is generated by mass unbalances.

The unbalanced electromagnetic attractive force becomes a cause of the vibration and noise from the motor. Iwatsubo et al. [1] discussed the stability of induction motor. B. S. Rahman and D. K. Lieu discussed the relation between electromagnetic stress and radial offset [2].

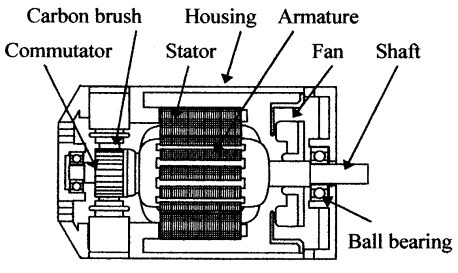

Figure 1: Schematic of universal motor.

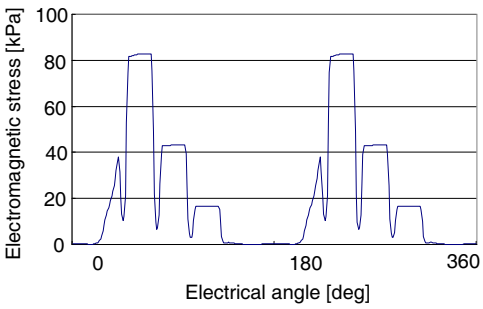

Figure 2: Waveform of electromagnetic stress at a position of rotational angle.

In this study, the electrical, vibration, and noise characteristics are studied for static eccentricity rotor of universal motor. Ohts et al. reported the test equipment of universal motor and reported the electrical, the vibration, and the noise characteristics of the normal condition of the motor [3].

In the paper, the harmonic components of electromagnetic force and an electromagnetic vibration and noise from universal motor with rotor eccentricity are numerically discussed comparing with normal rotor. The magnitude of eccentricity is 0.2 mm against air gap 0.4 mm and, angle of eccentricity is 0, 45, 90, and 135 degree.

2. ANALYTICAL METHOD

2.1. Harmonics Analysis of Electromagnetic Stress

This analytical method has been presented by Kobayashi, et al. [4]. In this study, a two-dimensional finite element method is used. The electromagnetic force is calculated in two steps.

Magnetic flux density along the stator inner bore is calculated, taking into account the motion of the rotor and the eddy current in the rotor bars.

From the above calculation results, electromagnetic force is calculated by using the Maxwell stress equation:

$$\sigma_r = \frac{1}{2\mu_0}\left(B_r^2 - B_t^2\right) \tag{1}$$

where B_r and B_t are radial and tangential magnetic flux density, respectively. In Fig. 2, the calculated distribution of radial electromagnetic force at one point along the inner bore of the stator is shown. These distributions are calculated at several points along the inner bore of the stator. The number of points depends on the meshes divided by using the finite element method. Radial electromagnetic force stress therefore consists of many frequency components along the inner bore of the stator. However, because the frequency is low, the fundamental component has only a small influence on the vibration and acoustic noise.

The electromagnetic density is expressed by the Fourier series as follows:

$$\sigma_r = \sum_k \sum_l a_{k,l} \sin(kx - l\omega\, t + \alpha_{k,l}) \tag{2}$$

where ω $(= 2\pi f)$ is frequency of the stator current (rad/s), k and l are the space and time harmonic order, respectively. And a_{kl} and α_{kl} are amplitudes and phases of the harmonic components and are calculated as follows:

$$c_{k,l} = \iint \sigma_r \sin(kx - l\omega\, t)dtdx \tag{3}$$

$$d_{k,l} = \iint \sigma_r \cos(kx - l\omega t)dtdx \tag{4}$$

$$a_{k,l} = \sqrt{c_{k,l}^2 + d_{k,l}^2} \tag{5}$$

$$\alpha_{k,l} = \tan^{-1}\left(\frac{c_{k,l}}{d_{k,l}}\right) \tag{6}$$

Figure 3 shows the example of the spectrum of electromagnetic stress Calculated harmonics are plotted in the k-l plane. A negative time-harmonic order indicates backward rotation of the electromagnetic waves. On the other hand, the space order k participates in the deformation in the radial direction along the stator circumference. The relation between circular mode order n and space order k is

$$n = k \times (p/2) \tag{7}$$

2.2. Transformation of Electromagnetic Stress into Exciting Force for the Structural Vibration Calculation

To calculate three-dimensional structural vibration, it is necessary to transform the electromagnetic force stress calculated by two-dimensional analysis into three-dimensional electromagnetic force. Figs. 4(a), (b) show this transformation. The electromagnetic stress is calculated along the inner bore in two dimensions as shown in Fig. 4(a) and the unit is Pascal. On the contrary, the exciting force on the structure is actually in three dimensions as shown in Fig. 4(b) and the unit is Newton.

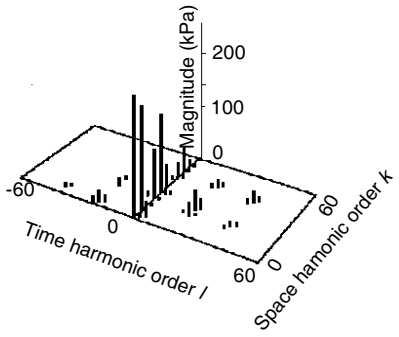

Figure 3: Spectrum of electromagnetic stress.

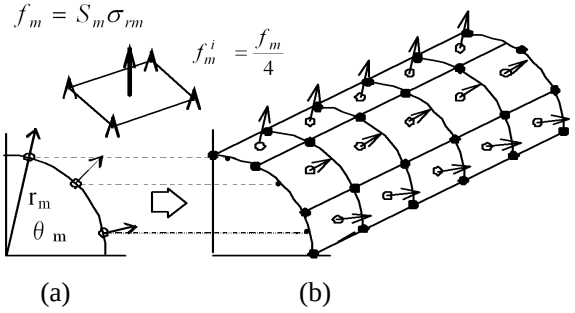

Figure 4: Transformation of electromagnetic force into structural exciting force. (a) Electromagnetic force stress (two dimensions). (b) Excting force of structure analysis (three dimensions).

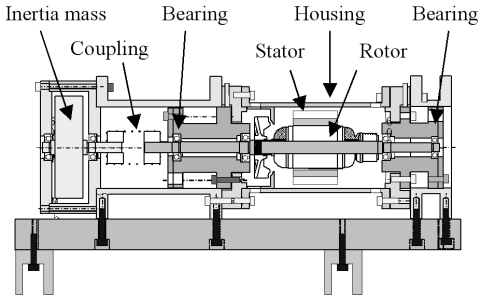

Figure 5: Configuration of the test apparatus.

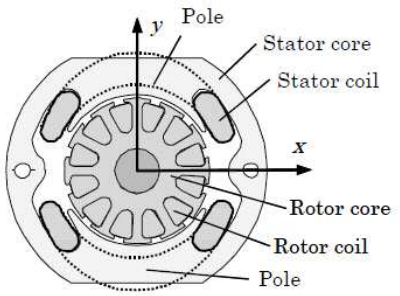

Figure 6: Cross section of the universal motor.

When the motor is not a skew structure, the electromagnetic stress in the axial direction is almost constant. The exciting force on the structure is therefore also assumed to be constant in the axial direction. When the structure is divided as shown in Fig. 4(b), it is necessary to calculate the exciting force on element m ($m = 1,\ldots, M$). First, the center of gravity of the element m (r_m, θ_m) is calculated in terms of polar coordinates. Then the electromagnetic stress σ_m is calculated by Eq. (2) at point (r_m, θ_m). And the electromagnetic force f_m is calculated by multiplying by area S_m of element m. Next, the electromagnetic force f_m is distributed at the nodes of element m. In this analysis, the electromagnetic force is distributed at the nodes of element m equally. The same calculation is carried out for all elements. Finally, the exciting force on the entire structure is determined.

3. ANALYSIS OF ELECTROMAGNETIC FORCE STRESS

3.1. Analytical Model

The rotational speed of rotor (armature) at no load condition is 24000 rpm, and the rated consumed electrical power is 1100 W. The air gap is 0.4 mm in the radial direction. The number of rotor (armature) slot is 12. It is possible to use the universal motor even in both of alternating current and direct current. The number of carbon brush is 2 and the number of segment is 24. Then, all iron cores laminate silicon sheet of the 0.5 mm thickness in order to decrease eddy current loss and exothermic reaction. Fig. 5 shows the configuration of test apparatus used in this study, including the universal motor. Fig. 6 shows the cross section of the universal motor.

3.2. Modeling of Electromagnetic Field Analysis

In the electromagnetic field analysis, 2-D FEM analysis is applied and ANSYS software is used. The elements are defined in the radial and circumferential directions and the 4-nodal point solid is used. Air-gap is divided especially in detail in consideration of the rotor eccentricity. Fig. 7 shows the FEM model for the electromagnetic field analysis. The degree of freedom is 14752.

It is defined for the amount of eccentricity ε and the angle of eccentricity ϕ based on a rotor center position in the state without the eccentricity as shown in Fig. 8.

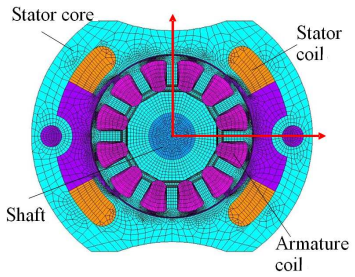

Figure 7: FEM model.

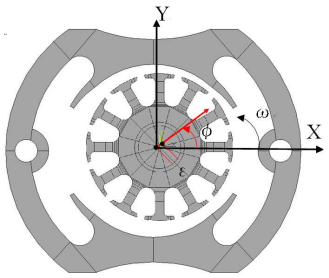

Figure 8: Definition of eccentricity.

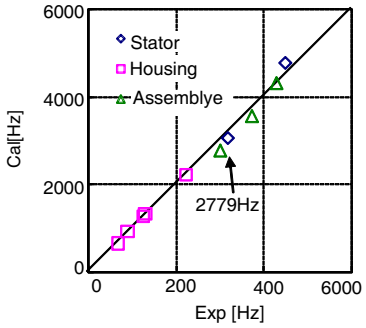

Figure 9: Comparison of natural frequency.

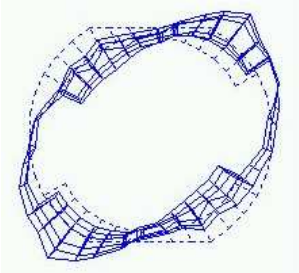

Figure 10: 2nd Circular mode of housing (2779 Hz).

3.3. Modeling of Structural Vibration Analysis

In the structural vibration analysis, 3-D FEM analysis is applied and ANSYS software is used. The degree of freedom is 54186. To make the model with high accuracy, the impact tests are done for stator, housing and motor assembly. From the tests, vibration modes, natural frequencies and modal damping are analyzed. The measured and calculated natural frequencies are shown in Fig. 9. Fig. 10 shows the 2nd circular mode of housing in the motor assembly at 2779 Hz. The difference between the measured and calculated natural frequency of the parts is about 7%. From the comparison, the accuracy of the structural vibration model is well.

4. MUMERICAL SIMYULATION

4.1. Electric Magnetic Force

By using FEM software ANSYS, magnetic flux is calculated. The contour of the magnetic flux density distribution for a normal and an eccentric motor is shown in Fig. 11. The magnitude and angle of the eccentricity is 0.2 mm and 45 degrees, respectively. The maximum of the magnetic flux density is about 2 T.

In the air-gap, the magnetic flux density is the maximum in the 45 degrees and 225 degrees. In the normal rotor, the magnetic flux density is symmetry in the original point. On the contrary, in the eccentric motor, the magnetic flux density is not symmetry in the original point.

By FFT analysis following Eq. (2), the harmonic components of the magnitude of the electromagnetic stress is obtained. Fig. 12 shows the spectrum of the electromagnetic stress for a normal rotor. From the Fig. 12, The electromagnetic stress of 0th, 12th, 24th time order component are particularly dominant. The 12th, 24th components influence the vibration and noise. The electromagnetic stress at 12th time order is fundamental component caused by the number of rotor slot. Fig. 13 shows the electromagnetic stress of the 0th to 10th space order component of 12th time order.

The electromagnetic stress at 12th time order when it is 0.1 mm, 0.2 mm, and 0.3 mm in the amount of eccentricity is shown in figure. From the Fig. 13, the following are discussed.

(1) The electromagnetic force component at the odd number of the space mode doesn't exist when the rotor is not eccentric.

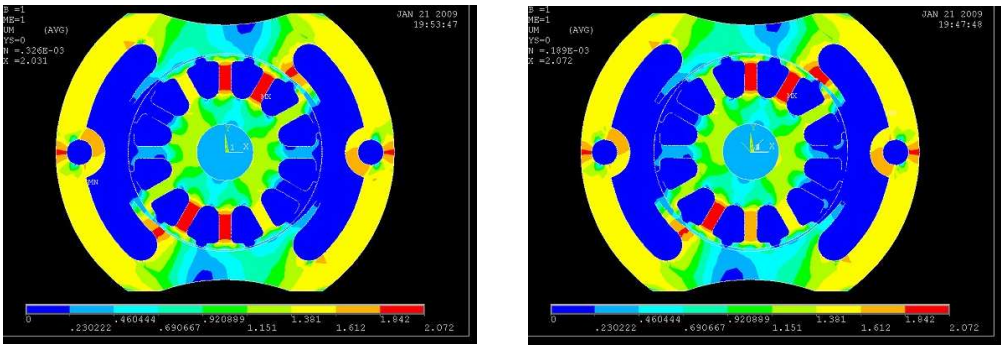

(a) Normal motor (ε=0) (b) Eccentric motor (ε=0.2, φ=45deg)

Figure 11: Contour of the magnetic flux density.

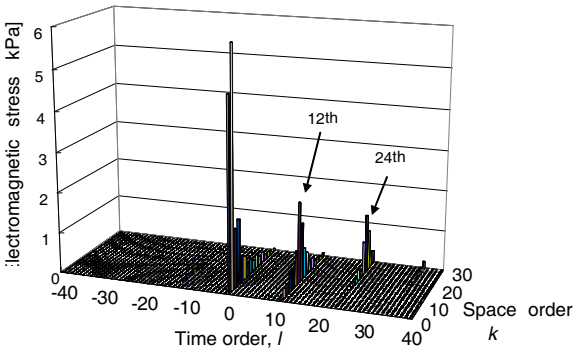

Figure 12: Spectrum of electromagnetic stress in the time and space region.

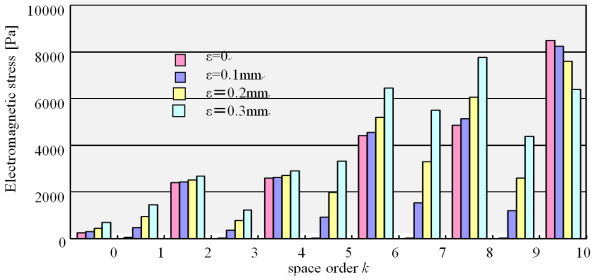

Figure 13: The harmonic components of the electromagnetic force stress at 12th time order in 45 degree direction.

(2) The magnitude of electromagnetic force at the space order depends on the amount of eccentricity, but the magnitude correlation is not constant.

(3) The magnitude of electromagnetic force depends on the space order, but the magnitude correlation is not constant.

4.2. Vibration Caused by Electromagnetic Force

The electromagnetic stress is transformed to structural exciting force by procedure in the Section 2.2. The exciting force is added to the housing in the motor model and the vibration of the surface is calculated. The displacement of the housing center of the normal and the eccentric motor ($\varepsilon = 0.2\,\text{mm}$, $\phi = 45\,\text{deg}$) at the natural frequency 2779 Hz is shown in Figs. 14(a), (b) by contours. Both contours are different a little. Then, the difference is compared quantitatively.

Then, the 8 positions are chosen to discuss the difference of the displacement between the normal motor and the eccentric motor. Fig. 15 shows the displacement of a normal rotor and eccentric motor ($\varepsilon = 0.2\,\text{mm}$, $\phi = 45\,\text{deg}$) in the 8 locations shown in Fig. 16. From the figure, the following are discussed.

(1) The displacement of the eccentric motor is larger than that of the normal motor.

(2) The ratio of the maximum displacement is about 1.23.

(3) Both displacement of the normal motor and the eccentric motor is larger at ③ and ⑦.

4.3. Noise Caused by Electromagnetic Force

The noise radiated from the surface of the motor housing is calculated by BEM (Boundary Element Method) which is named as the Acoustics contained in the software "LMS Virtual Lab.". In Fig. 17, the contours of noise of the normal and the eccentric motor ($\varepsilon = 0.2\,\text{mm}$, $\phi = 45\,\text{deg}$) are shown. The locations in the axial direction are the center of housing same as the Fig. 14. In Fig. 17, the magnitude of noise is shown. The locations in the circumferential are the same as Figs. 14 and 15, and the locations in the radial direction are 1m outside from the housing. The mean value of noise

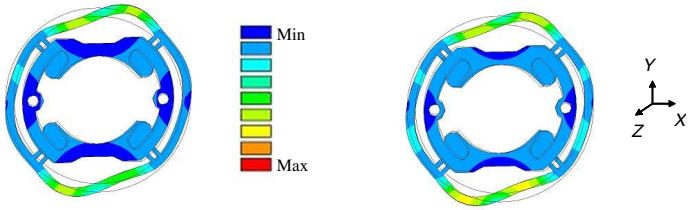

(a) normal motor (b) eccentric motor

Figure 14: Contour of displacement of the housing ($\varepsilon = 0.2\,\text{mm}$, $\varphi = 45\,\text{deg}$).

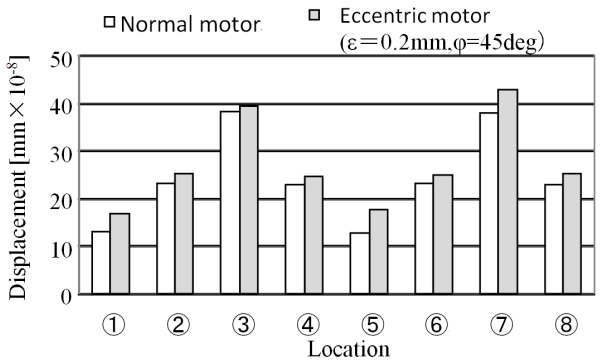

Figure 15: Displacement of housingcaused by electromagnetic force at 2779 Hz.

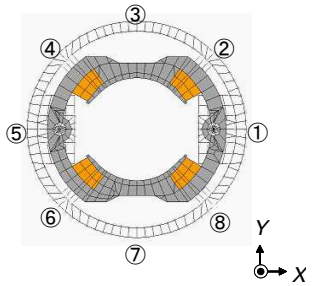

Figure 16: Location of calculation of vibration of the cross section of housing.

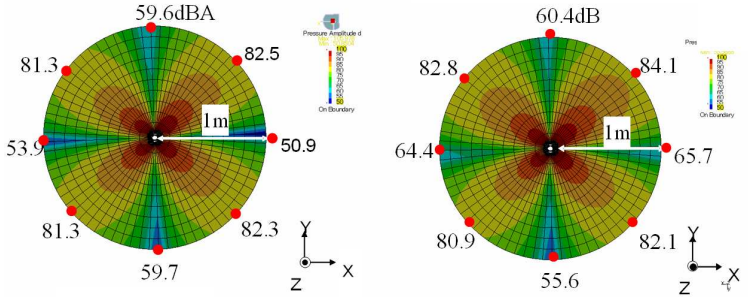

(a) Normal motor (b) Eccentric motor

Figure 17: Contour of noise of the motor.

of 8 positions of the normal motor and the eccentric motor is 69 dB and 72 dB respectively. From the figure, the following are discussed.

(1) The magnitude of noise in the 45 deg, 135 deg, 225 deg and 315 deg directions is dominant.
(2) The distribution of noise is almost the same between the normal motor and the eccentric motor.
(3) The distribution of noise in the eccentric direction is a little bit difference.
(4) The magnitude of noise from the eccentric motor is overall larger than that from the normal motor.
(5) The maximum of the mean value of noise of the normal motor is 3 dB larger than that of the eccentric motor.

5. CONCLUSION

The harmonic components of electromagnetic force and an electromagnetic vibration and noise from universal motor with eccentricity were numerically discussed comparing with those of normal universal motor and the following are concluded. From the results, the 12th time order components of electromagnetic force and an electromagnetic vibration and noise of eccentric motor are larger than those of a normal motor. In addition, although the electromagnetic force harmonic components

at the even number of the space mode exist when the rotor is non-eccentric or eccentric, that of the odd number of the space mode doesn't exist when the rotor is not eccentric.

REFERENCES

1. Iwatsubo, T., et al., "Vibration analysis of an induction motor under electromagnetic force," *Transactions of the Japan Society of Mechanical Engineers*, Vol. 60, No. 680, 103–108, 2003 (in Japanese).
2. Raman, B. S., "The origin of permanent magnet induced vibration in electrical machines," *ASME*, Vol. 113, 476–481, 1991.
3. Ohts, S., K. Shiohata, and T. Ogata, "A method for analyzing electromagnetic-force–induced noise from a universal motor," *APVC2005 Proceedings of the Asia Pacific Vibration Conference*, Malaysia, 2005.
4. Kobayashi, T., F. Tajima, M. Ito, and S. Shibukawa, "Effect of slot combination on acoustic noise from induction motors," *IEEE Transactions on Magnetics*, Vol. 33, No. 2, 2101–2104, 1997.

Engineering Students' Conceptual Understanding of Electro- and Magnetostatics

Johanna Leppävirta, Henrik Kettunen, and Ari Sihvola
Department of Radio Science and Engineering
Aalto University School of Science and Technology, Finland

Abstract— At the university level, the teaching of engineering students is often focused mostly on the development of procedural knowledge, that is, formulating and solving problems mathematically. Another very important factor associated with the enhancement of engineering skills is the conceptual knowledge, the actual comprehension of the physical concepts and the relations between them. Prior research has revealed that academically successful engineering students often lack deep understanding of the basic concepts and principles that underlie their training areas [1]. The aim of this study was to assess undergraduate engineering students' conceptual knowledge of electro- and magnetostatics and examine how these conceptions would change after instruction. The Conceptual Survey of Electricity and Magnetism (CSEM) [2] multiple-choice test was administered as a pre- and post-test to students (cumulative $N = 233$) enrolled on an elementary course on electromagnetics (Static Field Theory) at Aalto University School of Science and Engineering, Finland. The study shows that engineering students have considerably more difficulties with magnetostatics than with electrostatics. The instruction, although extensive, does not produce significant changes on students' initial conceptual understanding of magnetostatics. The study also found that the correlation between the students' conceptual and procedural knowledge was quite low. The result indicates that basic conceptual knowledge is a necessary but not sufficient condition for acquiring procedural skills in electrostatics and magnetostatics. The findings suggest that more instructional time should be spent on mathematically and conceptually demanding magnetostatics. Furthermore, we need to broaden the view of what type of knowledge is valued and assessed in engineering education. These results encourage us to develop and introduce new instructional practices for enhancing conceptual understanding of students during elementary engineering courses.

1. INTRODUCTION

Proficiency in problem-solving and calculation has long been one of the main goals in many domains of engineering education. Although teachers without doubt acknowledge the importance of the conceptual base, the approach to teaching and assessment has traditionally been procedurally dominated [3]. Recent studies, however, show that academically successful engineering students often have little understanding of the basic concepts and principles that underlie their areas of training [1].

Conceptual understanding makes the learning of procedural skills easier and frees capacity for learning more difficult procedures [4]. When skills are learned without understanding, they are learned as isolated bits of knowledge and it can be difficult to engage students in activities that help them understand the reasons underlying the procedures. On the other hand, without sufficient procedural fluency, students have trouble deepening their understanding of the basic ideas or solving problems mathematically [5].

Byrnes and Wasik [6] distinguish two approaches regarding the relationship between procedural and conceptual knowledge in the domain of mathematics. In the *simultaneous activation approach*, conceptual knowledge is seen as necessary and sufficient for correct use of procedures. This view argues that enriching students' conceptual knowledge enables the students to detect errors in their procedures [5]. Furthermore, if conceptual knowledge is low, procedures will be performed incorrectly. The contrasting view is the *dynamic interaction approach* [6]. The conceptual knowledge is seen as a necessary but not sufficient condition for acquiring procedural skills. Conceptual knowledge forms a basis for learning new procedures, but once acquired, procedures develop independently through proceduralization, discrimination and generalization. Moreover, conceptual and procedural knowledge seem to interact in diachronic cycles over time rather than simultaneously when student is engaged in problem-solving.

The aim of this study was to assess undergraduate engineering students' conceptual ideas of electrostatics and magnetostatics and examine how their conceptions change after instruction. We also examine the possible relations and correlations between students' conceptual and procedural understanding in electromagnetics.

2. METHODS

The conceptual learning gains were measured by using the Conceptual Survey of Electricity and Magnetism (CSEM) test [2]. The CSEM is a broad survey instrument that investigates the understanding of electric charge, potential, electric and magnetic field and force, and Newton's laws in the context of electromagnetics. The CSEM consists of 32 multiple-choice questions. In this study, the last four of these questions (29–32) were omitted since they deal with dynamic field theory, which was not covered in this studied elementary electromagnetics course focusing only in static fields. The test was translated into Finnish and was used as a pre- and post-test. The pre-test was administered to students during the first lecture and the post-test after the final lecture. The post-test data of autumn 2010 course has not yet been collected at the time this paper is written.

The CSEM test was conducted on students (cumulative $N = 233$) enrolling in the Static Field Theory course at Aalto University School of Science and Engineering, Finland, in autumn 2007 and 2010. Electromagnetic field theory is taught in two one-semester courses (Static and Dynamic Field Theory) to sophomore students participating in the electrical engineering program. The aim of the Static Field Theory course was to learn the basic concepts of electricity and magnetism: electric and magnetic field and force, electric potential, conductors, electric currents, and so on. The course consisted of lectures, complex multi-step homework exercises, a project work, and a final exam. Students could participate in tutorials, where they solved standard textbook problems with the help of an assistant. The multi-step homework exercises were compulsory and more complex than the exercises solved at tutorials. A Finnish textbook [7] about static field theory was used during the course and the language of instruction was Finnish.

The procedural knowledge of students was measured by assessing their performance in the final exam. The exam exercises were complex problems and similar to the homework exercises, which required an ability to identify and formulate the precise problem from the given scenario.

3. RESULTS

The overall success of undergraduate engineering students on the CSEM test was 57% and 59% of correct answers in years 2007 and 2010, respectively. The pre-test results indicate that the level of preliminary knowledge of the students was quite equal in both years. The CSEM score increased to 67% after instruction (2007). The normalized learning gain g, which is defined as the actual average gain divided by the maximum possible gain,

$$g = \frac{\%\text{post} - \%\text{pre}}{100 - \%\text{pre}}, \tag{1}$$

was 0.23. According to cut-off criteria of Hake [8], this score is considered as low-gain ($g < 0.30$). In traditional courses that have low interactive engagement, the average gain varies generally between 0.15 and 0.30. The overall results reveal a notable disparity between electricity and magnetism questions (see Fig. 1). In 2007, the pre-test scores were 62% (electrostatics) and 45% (magnetostatics), and the post-test scores 72% (electrostatics) and 54% (magnetostatics). In 2010, the pre-test scores were 64% (electrostatics) and 45% (magnetostatics). The electrostatic questions were considerably easier to students than the questions relating to magnetostatics. The engineering students performed 17 (2007) and 19 (2010) percentage units poorer on the magnetism questions compared to the electricity questions. Furthermore, the learning gain was different in the two topics: on magnetism questions, g was only 0.17 while on electricity questions the gain was 0.26.

To compare students' conceptual and procedural performance a scatter plot was constructed for the data. The graph area was divided into four quadrants (numbered anti-clockwise beginning with the top right quadrant) splitting the vertical and horizontal axes at the corresponding average value for all students for the relevant index. The relation between conceptual and procedural knowledge was investigated with the Pearson correlation coefficient.

The number of participants with matching CSEM post-test- and final exam data was 102 (year 2007). The average CSEM post-test score for this sample was 18.80 (standard deviation 7.54; scale 1–28) and the average final exam score 14.47 (standard deviation 5.75; scale 1–30). The correlation between conceptual and procedural performance was 0.49, which, although significant ($p < 0.01$), was not very high. The first quadrant in Fig. 2 contains students that perform well both conceptually and procedurally. One third of the participants entered into this group. An equal amount of students (33%) were in quadrant 3, which means that they performed poorly in both aspects. The second quadrant contains students that performed well conceptually but

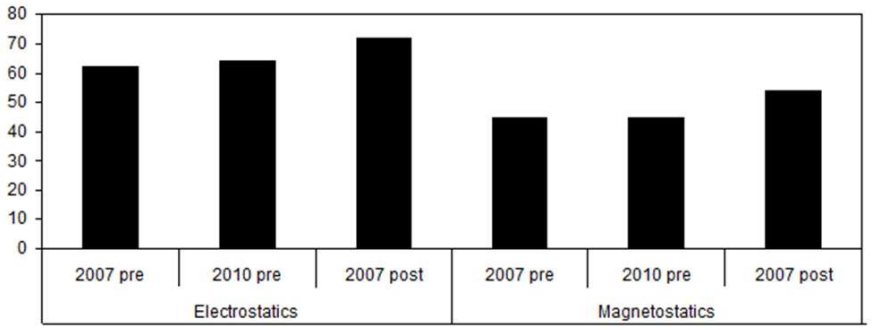

Figure 1: The average performance (%) in the CSEM conceptual areas.

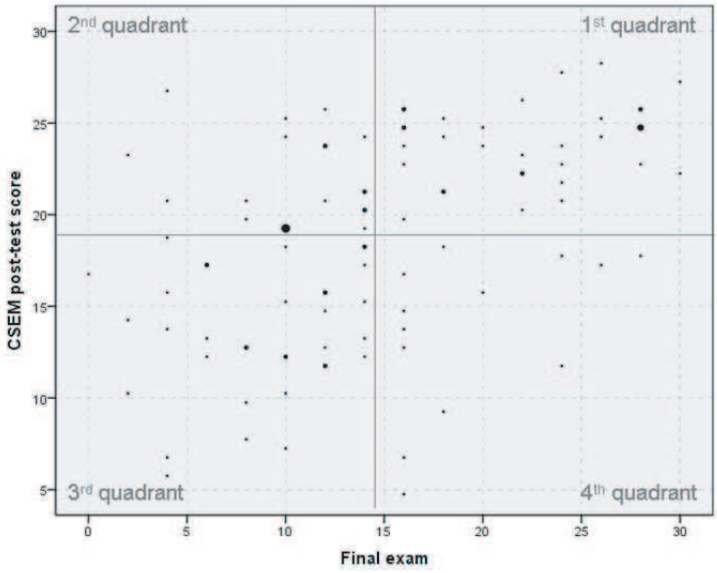

Figure 2: Comparison of scores on the CSEM post-test (scale 1–28) with scores on the final exam (scale 1–30).

poorly procedurally, and the fourth quadrant contains students performing well procedurally, but not well conceptually. It is interesting to note that more students were conceptually strong and procedurally weak (19%) than procedurally strong and conceptually weak (14%). This observation supports the dynamic interaction view which considers the conceptual mastery to be a necessary but not sufficient requirement for achieving expertise in the topic.

4. CONCLUSION

The results indicate that there is a relation between conceptual and procedural knowledge when learning electro- and magnetostatics. The findings of this study can be said to generally favour the dynamic interaction view that conceptual knowledge is a necessary but not sufficient condition for procedural knowledge. As seen in Fig. 2, 19% of students performed well conceptually, but did not succeed in the final exam. Fewer students (14%) lacked conceptual knowledge but were proficient in procedures and problem-solving. This suggests that some general knowledge of the basic concepts and relations are needed in order to succeed in complex problem-solving. The findings reveal, however, that in the context of electromagnetics, it is possible to have conceptual knowledge without considerable procedural skills but the reverse situation is less common. As the dynamic interaction view proposes, the conceptual knowledge forms the basis for learning new procedures but once acquired, procedures develop independently. Our other study [9] shows that prior conceptual knowledge predicts success in the final exam, but developing students' procedural skill with complex problem exercises during the course does not significantly enhance students' conceptual knowledge.

Our research findings, as well as prior studies [2], indicate that students have considerably more difficulties with magnetostatics than with electrostatics. This applies to both conceptual and procedural understanding. Even though the magnetostatic phenomena are more visible than the electrostatic ones, consider, for example, permanent magnets and compasses, the procedural mathematical treatment of magnetic quantities seems to be more problematic. There is, of course, a certain fundamental difference between electro- and magnetostatics. Whereas the electric field arises from charges, the magnetic field arises from current, the simplest magnetic source being a dipole.

The field theory course in the present study begins with electrostatics, which is a common tradition in electrical engineering curricula. The required mathematics, vector algebra and analysis, is mostly covered using electrostatic examples. Magnetostatics are taught in the end of the course and also less time is used for covering this topic. Many magnetostatic concepts can be taught by referring to their duality with electrostatics. However, due to the aforementioned difference between electric and magnetic sources, magnetic fields often are mathematically more complicated, considering, for example, the Coulomb's law in electrostatics and the Biot-Savart's law in magnetostatics. Therefore, the proficiency in manipulating vectors becomes essential. On this particular course, many students had problems especially with vector algebra. Moreover, considering the CSEM test, it seems that also the conceptual understanding of magnetic field is more difficult to achieve. In addition, the learning gain remained lower in the magnetostatics questions.

The study indicates the need for educational practice to broaden its view of what type of knowledge is valued and assessed in engineering courses. In order to be proficient in mathematics, science, and engineering, students need to deepen their understanding of the key concepts and relations within their areas of training. We would recommend practitioners to seek ways of introducing new instructional practices for enhancing engineering students' conceptual proficiency.

ACKNOWLEDGMENT

This work was supported in part by Aalto University School of Science and Technology, Lifelong Learning Institute Dipoli and Faculty of Electronics, Communications and Automation, and the Academy of Finland.

REFERENCES

1. Taraban, R., E. E. Anderson, A. DeFinis, A. G. Brown, A. Weigold, and M. P. Sharma, "First steps in understanding engineering students' growth of conceptual and procedural knowledge in an interactive learning context," *J. Eng. Educ.*, Vol. 96, No. 1, 57–68, 2007.
2. Maloney, D. P., T. L. O'Kuma, C. J. Hieggelke, and A. Van Heuvelen, "Surveying students' conceptual knowledge of electricity and magnetism," *Phys. Educ. Res., Am. J. Phys. Suppl.*, Vol. 69, No. 7, S12–S23, 2001.
3. McDermott, L. C., "Millikan Lecture 1990: What we teach and what is learned — Closing the gap," *Am. J. Phys.*, Vol. 59, No. 4, 301–315, 1991.
4. Hiebert, J. and P. Lefevre, "Conceptual and procedural knowledge in mathematics: An introductory analysis," *Conceptual and Procedural Knowledge: The Case of Mathematics*, J. Hiebert (Ed.), 1–27, Lawrence Erlbaum Associates, London, 1986.
5. Kilpatrick, J., J. Swafford, and B. Findell (Eds.), *Adding It up: Helping Children Learn Mathematics*, 115–155, National Academy Press, Washington, DC, 2001.
6. Byrnes, J. P. and B. A. Wasik, "Role of conceptual knowledge in mathematical procedural learning," *Developmental Psychology*, Vol. 27, No. 5, 777–786, 1991.
7. Lindell, I. V. and A. Sihvola, *Sähkömagneettinen kenttäteoria, Staattiset kentät*, Otatieto, Espoo, 2007 (in Finnish).
8. Hake, R. R, "Interactive-engagement versus traditional methods: A six-thousand-student survey of mechanics test data for introductory physics courses," *Am. J. Phys*, Vol. 66, No. 1, 64–74, 1998.
9. Leppävirta, J., H. Kettunen, and A. Sihvola, "Complex problem exercises in developing engineering students' conceptual and procedural knowledge of electromagnetics," *IEEE Trans. Educ.*, 2010, DOI: 10.1109/TE.2010.2043531, (early access).

A Physical Model of Electro-magnetism for a Theory of Everything

M. J. Underhill
Underhill Research, UK

Abstract— The objective is a physical model that links Electro-Magnetism or Electro-Magnetics (EM) to the rest of physics for a Theory of Everything (ToE). The proposed model postulates a real spatial 'ether' described by four partially coupled transmission line equations mapping classical fields into spatial potentials, charges and currents. 'EM coupling' and 'Process Capture' are the main links to the rest of physics. One outcome of EM coupling is the removal of all mathematical and physical singularities in EM and elsewhere in physics. Process Capture defines 'process regions' where only one physical process dominates. One outcome is 'heuristic EM simulation' requiring no matrix inversion. Maxwell's Equations and some of the existing tenets of physics are significantly revised. The outcome is a ToE allowing all physics to be described in EM terms. Some novel examples are given, namely: 'continuous relativity', 'dark matter' compared to normal matter, photon 'string arrows', and 'toroidal EM string loops' for particles. In this ToE mathematics is used as a language to describe but not dictate the physics.

1. INTRODUCTION

This paper originates from an unpublished seminar given to research students at the University of Surrey in 2004 [1]. Since then much of the originally speculative theory has been refined by matching against practical observations and experimental results. The proposed physical EM model gives the best agreement with the observations and practical results collected so far. The paper builds on from a Goubau line [2] EM string arrow photon model proposed in 2009 [3]. The stability of this photon model is related to the stability of oscillators with noise [4, 5] and the stability displays hysteresis as found in injection locked oscillators [6, 7]. Process Capture is an essential part of the EM ToE model, and it was originally observed in measurements of the multiple radiation mode resistances of a small tuned loop antenna [8]. Traditional mathematical formulations of Maxwell's Equations [9–11] have been found ignore EM coupling between fields and to lack evanescent wave solutions capable of representing Goubau line, surface wave, wave-tilt and ground constant measurements. The (new) mathematics here has been devised and chosen to make good these deficiencies.

2. THE LOCAL ETHER FOUR TRANSMISSION LINE MODEL OF EM

The chosen physical model is two low-pass and high-pass pairs of co-located transmission lines in a 'local ether' as shown in Figures 1(a) to (f). All the transmission lines are partially coupled. The lines are shown in lumped component equivalent circuit form. One LP/HP pair represents conventional and electric displacement current, with electric vector potential. (For this pair E is lamellar and H is solenoidal.) The other pair represents magnetic displacement current and magnetic vector potential. (For this pair H is lamellar and E is solenoidal.)

In free space the line pairs have equal velocity and nomnal characteristic impedance The 'local ether' properties are given by complex, frequency dependent, values of ε and π along the direction of power flow. E and H are defined as electric and magnetic vector potentials and are analogues of voltage on the lines. D and B are defined as electric and magnetic vector charge densities respectively. Electric and magnetic displacement current densities are defined as 'bi-vectors' with one vector component in the D or B field direction, and the other vector component in the direction of current flow. The current magnitudes are found by equating the energy of the currents to the energy of the charges (energy conservation). The currents are time domain Hilbert transforms of the charges, and vice versa. For travelling waves the currents and charges are co-local.

For standing waves the currents and charges are a quarter of a wavelength apart. In this model both the currents and the charge gradients in the local ether can radiate or receive. Positive quadrature potential of a current indicates radiation. Negative quadrature potential of a current indicates reception. The local ether acts as a focusing lens for receiving (wire) antennas. The local ether constants are altered (increased) by the local stored energy.

For the low-pass electric line, the specific series inductance (per reciprocal unit area and per unit length) is equated to μ and the specific shunt capacitance (per unit area and per reciprocal unit length) is equated to ε. The specific series reactance is $j\omega\mu$ and the specific shunt susceptance is

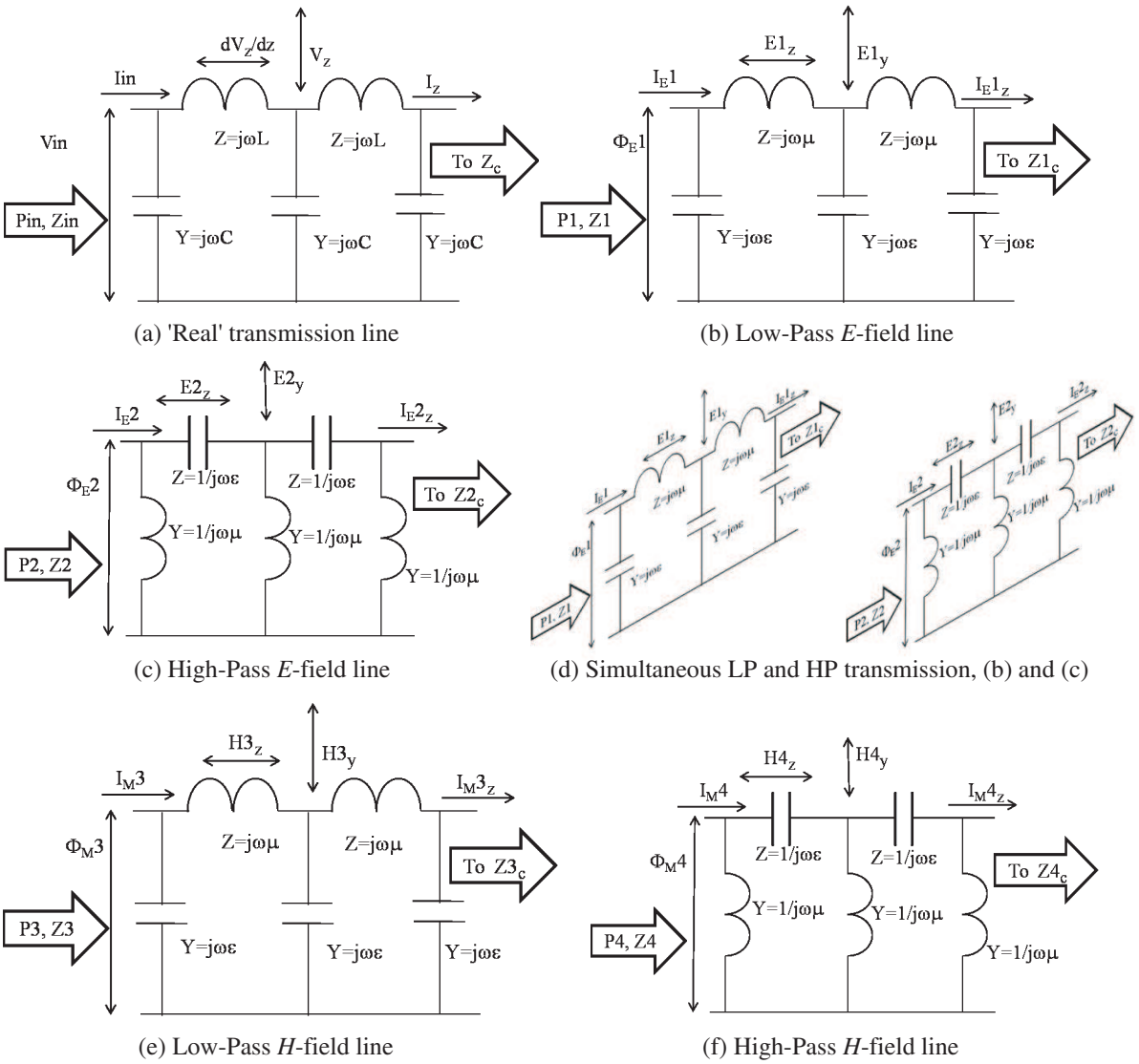

Figure 1: The four transmission line model of Electro-Magnetic (EM) waves in a local ether defined by permittivity ε and permeability μ. (a) is the basis transmission line lumped equivalent circuit, with voltage V and current I. L and C are values per unit length along the line. (b) is the free-space 'electric' transmission line low pass (LP) equivalent to the plane wave solution of Maxwell's equations, with L mapped to μ and C mapped to ε. V is mapped to the electric vector potential Φ_E and I is mapped to electric displacement current I_E. (c) is a novel discovery: it is the high-pass (HP) solution to Maxwell's equations that is found to dominate above about 47.75 MHz. (d) shows that both the HP and LP models are active around 47.75 MHz. (e) and (f) are the LP and HP magnetic current and magnetic vector potential equivalents, respectively of (b) and (c).

$j\omega\varepsilon$. The high pass electric line has specific series reactance of $1/j\omega\varepsilon$ and specific shunt susceptance of $1/j\omega\mu$.

At the critical frequency of 47.75 MHz the transmitted power becomes equally divided between the LP and HP modes, a few wavelengths away from a source. Initial measurements indicate that the power split changes over progressively bandwidth equivalent to at least two poles with a bandwidth equivalent to a Q of about 6 or perhaps 2π. There is also a possible weak resonance with a Q of about 40 or $(2\pi)^2$.

The EM model also explains the anomalous 'wave-tilt' (reversed at low frequencies) found over real ground. Above a critical frequency for the ground the high pass model dominates and captures most of the wave energy of the vertically polarised ground wave components in, and just above, the ground. The phase of E_z is then such as to tip the wave $E_y + E_z$ forward in the direction of travel. However below the critical frequency the low-pass model dominates, the phase of E_z is reversed

and the E-field of the wave $E_y - E_z$ tips backwards. The wave-tilt critical frequency is typically between 5.3 and 6.8 MHz.

3. THE EM MODEL FREE SPACE CRITICAL FREQUENCY

In free-space the low-pass transmission lines of the EM model are operative predominantly below 47.75 MHz and the high-pass lines above $f_c = 47.75$ MHz. We find that at $f_c = 47.75$ MHz (or $\omega_c = 300$ Mrad/s), $Z_0 = 120\pi = \omega\mu_0 = 1/\omega\varepsilon_0$. This is thought to be the origin of the critical frequency of 47.75 MHz.

4. ELECTRO-MAGNETIC COUPLING

In free-space we find that the co-local electro-magnetic (EM) coupling between the fields H and D/ε, and between H and B/μ is $\kappa = 1/2\pi$. This means that any field sensors for E, D, H, and B will always also measure respectively D, E, B, and H with reduced sensitivity of -16 dB. This also explains 'dark matter' properties. Induction is also a manifestation of EM coupling. Potentials (and potential gradients) are induced or created in the local ether surrounding charges and currents by a local induction process. Potentials also induce and create charges and currents. The induction strength is found to be inversely proportional to the square root of frequency. This form of EM coupling defines the profiles of evanescent waves, surface waves, photons, EM strings, and the edges of black holes.

4.1. Process Capture

Process capture is an observable fundamental law (originally seen in small tuned loop antennas). Overlapping distributed processes combine at any point according to the RSS (Root-Sum-of-the-Squares) law. The strongest process 'captures' and suppresses the weaker process. Over a short (coupling) distance the suppression is progressive. Propagation at 47.75 MHz could be metastable. We find bounded regions where one process is almost totally dominant. Fast and robust 'Analytic Region (AR) Modelling' is a consequence; no matrix inversion is required. Process capture explains observed 'ether dragging', and this leads to 'Continuous Relativity', which encompasses and joins Special and General Relativity. (Faster-than-light travel is possible.) Process capture reconciles Michelson-Morley results with the existence of a real physical ether.

4.2. Evanescent Wave Profiles

EM wave equations are separated into travelling wave and evanescent wave parts. Two prototype evanescent wave profiles $R1$ and $R3$ are proposed and are both given by:

$$R_n = \left(1 - e^{-\kappa_n/(\sqrt{f}\times r^n)}\right) \tag{1}$$

where $n = 1$ for potential around a source, and $n = 3$ for the profile of the 'substance' of a EM string or the edge of a black hole. The EM coupling factors κ_1 and κ_3 have different values for dark matter and ordinary matter. These profiles have finite size and no mathematical or physical singularities. The profile equations can be extended represent complex impedance around antenna surfaces and wires and absorption magnitude and height ($\propto 1/\sqrt{f}$) profile above real ground. EM strings have self-stable evanescent wave profiles. They have a single dominant line spectrum and obey a Schrödinger equation.

The various EM strings are shown in Figure 2.

4.3. Matter and Dark Matter

All charges, currents and potentials have (self-) energy. Energy is 'substance' (charge or current) times potential and *is* gravitational mass. Ordinary matter has point-like atoms and substance then dominates over self-potential. The self-potential has a time delay and an offset during acceleration, making inertial and gravitational masses equal. In dark matter the energy of the potential is greater than the substance energy. Dark matter is continuous and diffuse, and has very low inertia. Thermal radiation in space is dark matter. The Goubau single wire (non-radiating) transmission line displays the stable evanescent wave profiles of current filaments and proposed EM 'strings'. Photons are 'dark matter' EM string arrows. Particles are made from EM toroidal string loops of defined size, frequency and dimensionality. See Figure 2. String loop and black hole densities are similar. String loops obey a Schrödinger equation.

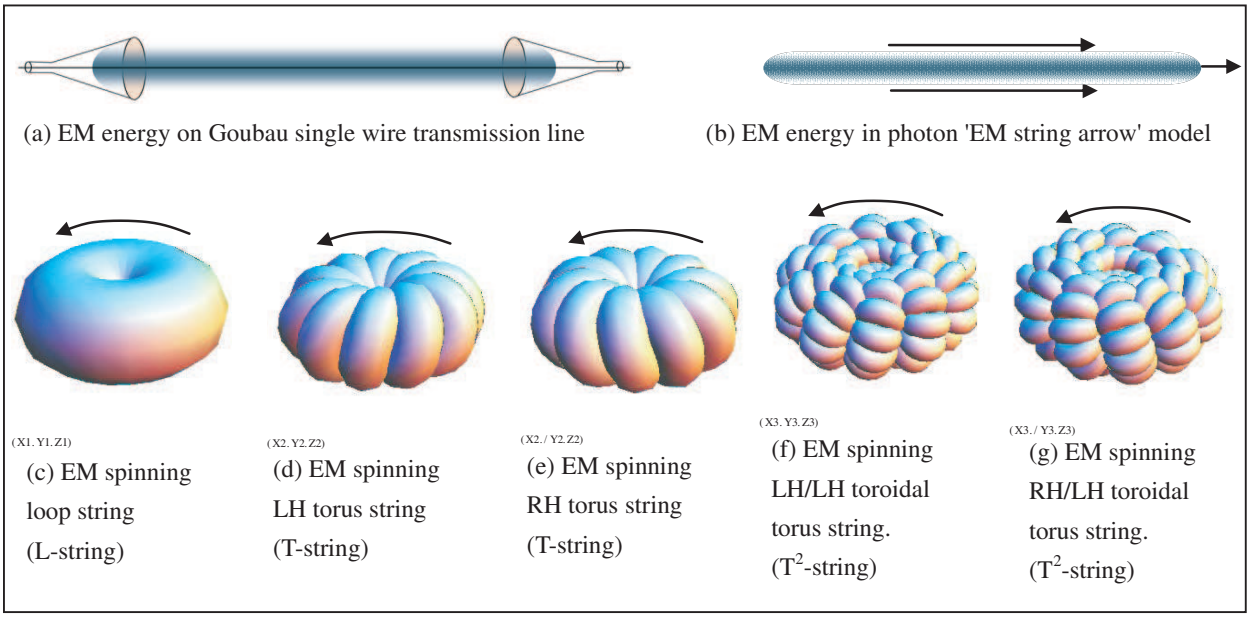

Figure 2: EM String models for photons and sub-atomic particles: (a) EM energy on Goubau single wire transmission line. (b) EM energy in photon 'EM string arrow' model, with similar energy distribution to (a). (c) EM spinning loop string; an L-string. (d) EM spinning LH torus string; a T-string. (e) EM spinning LH torus string; a T-string and a mirror image of (d). (f) EM spinning LH/LH toroidal torus string; a T^2-string. (g) EM spinning RH/LH toroidal torus string; a T^2-string and a mirror image of (f).

5. CONCLUSIONS

All physics can be described and modeled in Electro-Magnetic (EM) terms. A real physical ether is an essential part of the proposed EM model. 'Process capture' resolves any conflict with Michelson-Morley results. 'Continuous Relativity', based on the existence of a real ether, encompasses and unites Special Relativity and General Relativity. The proposed EM model has no physical or mathematical singularities. 'Analytic Region Modeling' promises to be the future of EM simulation.

ACKNOWLEDGMENT

This work has been undertaken as an unfunded amateur, but based on engineering and scientific research experience in industry, an SME, research consultancy, and as a part time and a full time academic at the University of Surrey. Thanks are due to many students, staff, friends and colleagues who have had a perhaps unwitting positive impact.

REFERENCES

1. Underhill, M. J., "From tuned loop antennas to loop strings and an EM Framework Theory of Everything," *ATI Research Seminar*, University of Surrey, March 25, 2004 (Unpublished but PDF available on request).
2. Goubau, G., "Surface waves and their application to transmission lines," *J.A.P.*, Vol. 21, 1119–1128, Nov. 1950.
3. Underhill, M. J., "The phase noise spectrum and structure of photons?" *Proc. 16th EFTF-2010*, 8 pages, Noordwijk, Netherlands, Apr. 13–16, 2010.
4. Underhill, M. J., "More fundamental instabilities in oscillators?" *Proc. 15th EFTF'09: IEEE-FCS'09*, 334–337, Besancon, France, Apr. 20–24, 2009.
5. Leeson, D. B., "A simple model of feedback oscillator noise spectrum," *Proc. IEEE*, Vol. 54, No. 2, 329–330, 1966.
6. Underhill, M. J., N. Siripon, and N. Christophorou, "Determination of the capture range and locking range of injection locked oscillators," *Proc. 15th EFTF*, 232–236, Neuchatel, Switzerland, Mar. 2001.
7. Underhill, M. J., "Fundamental limitations of oscillator performance," *The Second International Conference on Frequency Control and Synthesis*, No. 303, 18–31, IEE Publication, 1989.

8. Underhill, M. J. and M. Harper, "Small antenna input impedances that contradict the Chu-Wheeler Q criterion," *Electronics Letters*, Vol. 39, No. 11, May 23, 2003.
9. Hunt, B. J., *The Maxwellians*, Cornell University Press, 1991, ISBN 0-8014- 8234-8.
10. Maxwell, J. C., *A Treatise on Electricity and Magnetism*, 3rd Edition, Vol. 1, Dover reprint, ISBN 0-486-60636-8.
11. Maxwell, J. C., *A Treatise on Electricity and Magnetism*, 3rd Edition, Vol. 2, OUP reprint, ISBN 0-19-850374-1.

Space Constants of Auxiliary Waves

T. Koryu Ishii
Marquette University, Milwaukee, Wisconsin, USA

Abstract— Space constants of auxiliary waves are investigated. In this investigation, validity of space constants of auxiliary waves are examined by cross checking propagation constants and wave impedance under the same polarization. The principal wave considered is a uniform TEM mode electromagnetic plane wave. The auxiliary waves are associated with the principal wave, then various sets of space constants are derived from auxiliary waves based upon the propagation constants or wave impedance of various polarizations.

This approach suggests the existence of a new set of wave impedances for auxiliary waves. This set of space constants shows space constants for auxiliary waves are inhomogeneous and anisotropic for auxiliary waves even though these are homogenous and isotropic for the principal wave. As a numerical example, space constants for free space are sketched for the first time. The sketch shows indeed space constants of free space for auxiliary waves are inhomogeneous and anisotropic.

1. INTRODUCTION

Space for propagation of electromagnetic waves which are defined by permittivity ε_p, permeability μ_p, and conductivity σ_p, is considered. These constants are termed the space constants for convenience in this work [1, 2].

The principal wave is the electromagnetic wave which is originally launched into space for utilitarian purposes. The auxiliary waves are non-principal waves associated with the principal wave. The auxiliary waves are generated by the principal wave. The principal wave considered in this study is uniform TEM mode plane waves of both vertical and horizontal polarizations. Various sets of space constants are derived for auxiliary waves based upon the propagation constant or wave impedance and polarizations. In this study, the principal wave is propagating in the y direction with vertical or horizontal polarizations. In considering vertical polarization, the E field vector points towards the z direction. With horizontal polarization, E field vector points towards the $-x$ direction.

In this study, one of the auxiliary waves is considered propagating in the r direction. Propagation constant of the principal wave is represented by $\dot{\gamma}_p$. The propagation constant of the auxiliary wave is represented by $\dot{\gamma}_a$. The relationship between $\dot{\gamma}_a$ and $\dot{\gamma}_p$ is, by elementary geometrical observation,

$$\dot{\gamma}_a = \dot{\gamma}_p \sin\theta \sin\varphi \tag{1}$$

2. PROPAGATION CONSTANTS

Propagation constant $\dot{\gamma}_a$ is a projection of $\dot{\gamma}_p$ as seen in Equation (1). There is no information of polarization. Therefore, for both vertical and horizontal polarization of the principal wave,

$$\dot{\gamma}_a^2 = \dot{\gamma}_p^2 \sin^2\theta \sin^2\varphi \tag{2}$$

By association of telegrapher's equation and Helmhortz' wave equation [3],

$$\begin{aligned} \dot{\gamma}_a^2 &= j\omega\mu_p(\sigma_p + j\omega\varepsilon_p)\sin^2\theta\sin^2\varphi \\ \dot{\gamma}_a^2 &= j\omega\mu_p(\sigma_p + j\omega\varepsilon_p)(\sin^2\theta\sin^2\varphi)^{1-n}(\sin^2\theta\sin^2\varphi)^n \end{aligned} \tag{3}$$

where, n is a number.

This means that

$$\dot{\gamma}_a^2 = j\omega\mu_p(\sin^2\theta\sin^2\varphi)^{1-n}(\sigma_p + j\omega\varepsilon_p)(\sin^2\theta\sin^2\varphi)^n \tag{4}$$

or,

$$\dot{\gamma}_a^2 = j\omega\mu_p(\sin^2\theta\sin^2\varphi)^n(\sigma_p + j\omega\varepsilon_p)(\sin^2\theta\sin^2\varphi)^{1-n} \tag{5}$$

or, for $n = 0$

$$\dot{\gamma}_a^2 = j\omega\mu_p\sin^2\theta(\sigma_p + j\omega\varepsilon_p)(\sin^2\varphi) \tag{6}$$

or, for $n = 1$,

$$\dot{\gamma}_a^2 = j\omega\mu_p\sin^2\varphi(\sigma_p + j\omega\varepsilon_p)(\sin^2\theta) \tag{7}$$

Spaces of Equations (4) through (7) are respectively named Type I through IV Spaces.

3. WAVE IMPEDANCE

For a vertically polarized principal wave, by elementary geometrical observation, the wave impedance of auxiliary wave is

$$\dot{\eta}_a = \dot{E}_z \sin\theta / \dot{H}_x \sin\varphi = \dot{\eta}_p \sin\theta / \sin\varphi \tag{8}$$

where η_p is the wave impedance of the principal wave. In this case, it is known to be $\dot{\eta}_p = \sqrt{\frac{j\omega\mu_p}{\sigma_p + j\omega\varepsilon_p}}$ [3]. Similarly, the wave impedance for a horizontally polarized auxiliary wave is

$$\dot{\eta}_a = \dot{E}_x \sin\varphi / -\dot{H}_z \sin\theta = \dot{\eta}_p \sin\varphi / \sin\theta \tag{9}$$

4. SPACE CONSTANTS OF AUXILIARY WAVES

For Types I through IV Spaces, from Equations (4) through (7), space constants of different types for their respective spaces are obtained as follows.

Type I Space:

$$\varepsilon_a = \varepsilon_p \sin^{2n}\theta \sin^{2n}\varphi, \quad \mu_a = \mu_p \sin^{2(1-n)}\theta \sin^{2(1-n)}\varphi, \quad \sigma_a = \sigma_p \sin^{2n}\theta \sin^{2n}\varphi \tag{10}$$

Type II Space:

$$\varepsilon_a = \varepsilon_p \sin^{2(1-n)}\theta \sin^{2(1-n)}\varphi, \quad \mu_a = \mu_p \sin^{2n}\theta \sin^{2n}\varphi, \quad \sigma_a = \sigma_p \sin^{2(1-n)}\theta \sin^{2(1-n)}\varphi \tag{11}$$

Type III Space:

$$\varepsilon_a = \varepsilon_p \sin^2\varphi, \quad \mu_a = \mu_p \sin^2\theta, \quad \sigma_a = \sigma_p \sin^2\varphi \tag{12}$$

Type IV Space:

$$\varepsilon_a = \varepsilon_p \sin^2\theta, \quad \mu_a = \mu_p \sin^2\varphi, \quad \sigma_a = \sigma_p \sin^2\theta \tag{13}$$

Equations (10) through (13) are examined, using Equations of propagation constants (4) through (7), where ε_a, μ_a, and σ_a are equivalent permittivity, permeability, and conductivity of the space for auxiliary waves, and equations of wave impedance (8) or (9). For Type I Space, if Equation (10) is substituted in Equation (4) of propagation constant,

$$\dot{\gamma}_a^2 = \dot{\gamma}_p^2 \sin^2\theta \sin^2\varphi \tag{14}$$

If Equation (10) is substituted in Equation (8) of wave impedance,

$$\dot{\eta}_a^2 = \dot{\eta}_p^2 \sin^{2(1-2n)}\theta \sin^{2(1-2n)}\varphi \tag{15}$$

For Type II Space, if Equation (11) is substituted in Equation (7) of propagation constant

$$\gamma_a^2 = \gamma_p^2 \sin^2\theta \sin^2\varphi \tag{16}$$

If Equation (11) is substituted in Equation (8) or (9) of wave impedance,

$$\dot{\eta}_a^2 = \dot{\eta}_p^2 \sin^2\theta / \sin^2\varphi \quad \text{or} \quad \dot{\eta}_{\mathrm{a}}^2 = \dot{\eta}_{\mathrm{p}}^2 \sin^2\varphi / \sin^2\theta \tag{17}$$

For Type III Space, if Equation (12) is substituted in Equation (6) of propagation constant,

$$\dot{\gamma}_a^2 = j\omega\mu_p(\sigma_p + j\omega\varepsilon_p) \sin^2\theta \sin^2\varphi \tag{18}$$

If Equation (12) is substituted in Equation (8) or (9) of wave impedance,

$$\dot{\eta}_a^2 = \{j\omega\mu_p/(\sigma_p + j\omega\varepsilon_p)\} \sin^2\theta / \sin^2\varphi \quad \text{or} \quad \dot{\eta}_a^2 = \{j\omega\mu_p/(\sigma_p + j\omega\varepsilon_p)\} \sin^2\varphi / \sin^2\theta \tag{19}$$

For Type IV Space, if Equation (13) is substituted in Equation (7) of propagation constant,

$$\dot{\gamma}_a^2 = j\omega\mu_p(\sigma_p + j\omega\varepsilon_p) \sin^2\theta \sin^2\varphi \tag{20}$$

If Equation (13) is substituted in Equation (8) or (9) of wave impedance,

$$\dot{\eta}_a^2 = \{j\omega\mu_p/(\sigma_p + j\omega\mu_p)\} \sin^2\theta / \sin^2\varphi \quad \text{or} \quad \dot{\eta}_a^2 = \{j\omega\mu_p/(\sigma_p + j\omega\mu_p)\} \sin^2\varphi / \sin^2\theta \tag{21}$$

Equations (10) through (13) are confirmed to be correct by Equations (14) through (21). In contrast to Equations (10) through (13), the original space constants for the principal wave are ε_p, μ_p, and σ_p. This means that the space is homogenous and isotropic for the principal wave, but the same space is inhomogeneous and anisotropic for auxiliary waves.

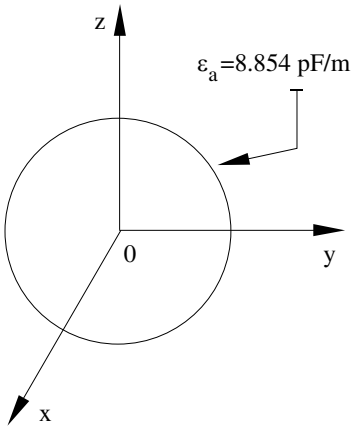

Figure 1: Permittivity pattern.

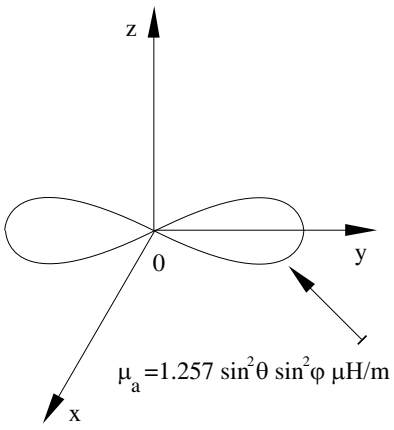

Figure 2: Permeability pattern.

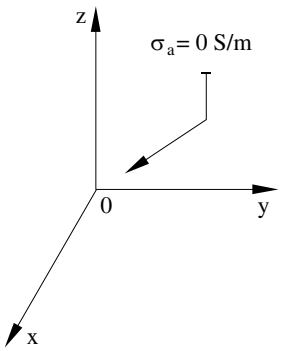

Figure 3: Conductivity pattern.

5. A SPECIFIC NUMERICAL EXAMPLE

As a specific numerical example, free space is considered:

For the principal wave TEM uniform plane wave,

$$\varepsilon_p = 8.854\,\mathrm{pF/m}, \quad \mu_\mathrm{p} = 1.257\,\mu\mathrm{H/n}, \quad \sigma_\mathrm{p} = 0\,\mathrm{S/m} \tag{22}$$

For auxiliary waves, and for Type I space,

$$\varepsilon_a = 8.854\sin^2\theta\sin^2\varphi\,\mathrm{pF/m}, \quad \mu_\mathrm{a} = 1.257\,\mu\mathrm{H/n}, \quad \sigma_\mathrm{a} = 0\,\mathrm{S/m} \tag{23}$$

For Type II Space,

$$\varepsilon_a = 8.854,\mathrm{pF/m}, \quad \mu_\mathrm{a} = 1.257\sin^2\theta\sin^2\varphi\,\mu\mathrm{H/n}, \quad \sigma_\mathrm{a} = 0\,\mathrm{S/m} \tag{24}$$

For Type III space,

$$\varepsilon_a = 8.854,\sin^2\varphi\,\mathrm{pF/m}, \quad \mu_\mathrm{a} = 1.257\sin^2\theta\,\mu\mathrm{H/n}, \quad \sigma_\mathrm{a} = 0\,\mathrm{S/m} \tag{25}$$

For Type IV space,

$$\varepsilon_a = 8.854\sin^2\theta\,\mathrm{pF/m}, \quad \mu_\mathrm{a} = 1.257\sin^2\varphi\,\mu\mathrm{H/n}, \quad \sigma_\mathrm{a} = 0\,\mathrm{S/m} \tag{26}$$

As an example, space constant patterns for Type II space are depicted as shown in Figs. 1–3.

6. CONCLUSION

Uniform homogenous isotropic and linear open space for electromagnetic principal wave propagation can be anisotropic and inhomogeneous for auxiliary waves. The space constant of auxiliary waves are examined using association of telegrapher's equation and Helmhortz' wave equation.

This study of propagation constant and space constant implies that the phase velocity of propagation of auxiliary waves is greater than the phase velocity of the propagation of the principal wave. This means that, in free space, propagation phase velocity of auxiliary waves is superluminal. It is also of interest to note that the wave impedance to the vertically polarized auxiliary wave is different from the wave impedance to the horizontally polarized auxiliary wave.

ACKNOWLEDGMENT

The author acknowledges the assistance of M.M. Ishii for preparation of the manuscripts and the members of the Marquette University Microwave Engineering Seminar for helpful discussions.

REFERENCES

1. Ishii, T. K., "Wave impedance of vertically polarized auxiliary waves," *Marquette University Microwave Engineering Seminar*, Milwaukee, Wisconsin, September 7, 2007.
2. Ishii, T. K., "Wave impedance of horizontally polarized auxiliary waves," *Marquette University Microwave Engineering Seminar*, Milwaukee, Wisconsin, January 25, 2008.
3. Ishii, T. K., M. R. Havey, and Y. W. Chen. "Equivalent circuit of unbound media," *Midwest Symposium on Circuit and Systems Conference Proceedings*, Vol. 28, 519–521, January 1986.

Characteristic Equations of Strip-slotted Structures

Seil Sautbekov and Gulnar Alkina
Eurasian National University, Kazakhstan

Abstract— This paper deals with further development of Wiener-Hopf-Fock method for obtaining the characteristic equation which follows from the solution of the boundary value problem of electromagnetic waves diffraction on the strip-slotted structures. The strip or an infinite grating is chosen in return for strip-slotted structures. The boundary value problem is consecutively solved by reducing to the system of singular boundary integral equations, then to the system of the second kind Fredholm equations, which effectively is solved by reducing to a system of the linear algebraic equations with the help of the etalon integral and of saddle point method. Setting the determinant of a system of the algebraic equations equal to zero, we find a characteristic equation, which determines the eigenfrequencies of the structures.

1. INTRODUCTION

To present time, basically only two rigorous analytical methods for solving diffraction problems are known: the Wiener-Hopf-Fock method (WHF) [1–3] and the method of Riemann-Hilbert [4, 5]. The WHF method is also known as the factorization method [6]. A canonical problem for plane finite structures is the diffraction of electromagnetic waves on a strip or slot. Many works are devoted to an asymptotic solution of diffraction problems on a strip (slot) [8–17]. In [7] the diffraction problem for a strip is considered by the WHF method and reduced to a system of integral equations. Unlike the results of D. S. Jones [8], in this paper the solution of this problem is reduced to a series having an asymptotic form that contains a resonant denominator [9]. Therefore, it is suggested to consider the characteristic equations by the WHF method.

2. REDUCING TO A SYSTEM OF THE INTEGRAL EQUATIONS

Let the plane wave impinges on ideally conducting strip $|z| \le a$, $y = 0$, $-\infty < x < \infty$:

$$E_x^o = -E_0 e^{ik(y\sin\vartheta_0 + z\cos\vartheta_0)}, \quad H_y^o = E_x^o\sqrt{\varepsilon/\mu}\cos\vartheta_0, \quad H_z^o = -E_x^o\sqrt{\varepsilon/\mu}\sin\vartheta_0, \tag{1}$$
$$H_x^o = 0, \quad E_y^o = E_z^o = 0, \quad k = \omega/c, \quad E_0 = const.$$

The direction of propagation of the incident wave is orthogonal to the x axis and makes an angle ϑ_0 with the z axis (Fig. 1). Further, the harmonic time factor $\exp(-i\omega t)$ is everywhere omitted.

The electromagnetic field

$$E_x = ikcA_x, \quad H_y = \frac{1}{\mu}\frac{\partial}{\partial z}A_x, \quad H_z = -\frac{1}{\mu}\frac{\partial}{\partial y}A_x, \tag{2}$$

is expressed by means:

$$A_x(y,z) = \frac{i\mu}{4\pi}\int_{-\infty}^{\infty}\frac{1}{v}\exp\{i(wz + v|y|)\}F(w)dw, \quad v = \sqrt{k^2 - w^2}. \tag{3}$$

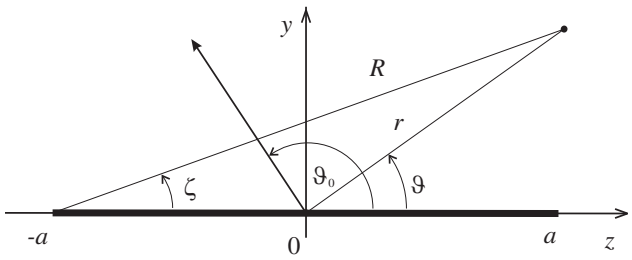

Figure 1: Diraction of plane wave at a strip.

From the boundary condition for the electric field on the strip

$$E_x + E_x^o = 0 \quad \text{at} \quad |z| \le a \quad (y = 0,\, -\infty < x < \infty),$$

and (2) and (3) we obtain an integral equation

$$\int_{-\infty}^{\infty} \exp(iwz)\frac{1}{v}F(w)dw + A_0 \exp(ihz) = 0 \quad \text{at} \quad |z| \le a, \tag{4}$$

where $A_0 = 4\pi E_0/(\omega\mu)$ and $h = k\cos\vartheta_0$.

We have the following integral equation from the continuity condition of the magnetic field (H_z) on the continuation of the strip:

$$\int_{-\infty}^{\infty} \exp(iwz)F(w)dw = 0 \quad \text{at} \quad a < |z|, \tag{5}$$

which follows immediately from absence of currents on the prolongation of the strip.

Let k have a small positive imaginary part that will vanish in the final formulas. Taking into account that the edges of a strip are secondary sources of waves, the Fourier-component of the current density is written as a sum from two analytical sources:

$$\begin{aligned} F(w) &= F_1 + F_2, \\ F_2(w) &= \sqrt{k-w}\left(A_2(w) + B^+(w)\right)\exp(iwa), \quad F_1(w) = \sqrt{k+w}\left(A_1(w) + B^-(w)\right)\exp(-iwa). \end{aligned} \tag{6}$$

The fields from the analytical sources must satisfy Meixner's condition, i.e., behaving at infinity as $w^{-1/2}$. The terms F_1 and F_2 are constructed by the Wiener-Hopf-Fock method such that A_1 and A_2 correspond to plane wave amplitudes; B^+ and B^- correspond to the amplitudes of the reflected waves from the strip edges. From this follows, that A_1 and A_2 should be analytical functions on the entire complex w plane except for a simple pole at $w = h$. As the singular points in the upper half plane (UHP) correspond to traveling waves to the right along the z axis, B^- should be analytical in the LHP, and B^+ in the UHP.

Thus, a system of singular integral Equations (4), (5) is reduced to a system of Fredholm integral equations of the second kind:

$$B^-(w) = \frac{1}{2\pi i}\int_{C^+} \frac{\exp(i2au)}{u-w}\sqrt{\frac{k-u}{k+u}}\left(A_2(u) + B^+(u)\right)du, \tag{7}$$

$$B^+(w) = \frac{1}{2\pi i}\int_{C^+} \frac{\exp(i2au)}{u+w}\sqrt{\frac{k-u}{k+u}}\left(A_1(-u) + B^-(-u)\right)du, \tag{8}$$

where

$$A_1(w) = \frac{A_o}{2\pi i}\frac{\sqrt{k-h}}{w-h}\exp(iha), \quad A_2(w) = -\frac{A_o}{2\pi i}\frac{\sqrt{k+h}}{w-h}\exp(-iha). \tag{9}$$

By introducing the integral operator

$$\mathbf{I}(w,u) = \frac{1}{2\pi i}\int_{C^+} du\frac{\exp(i2au)}{u-w}\sqrt{\frac{k-u}{k+u}},$$

the system of Equations (7) and (8) may be represented compactly as

$$\begin{aligned} B^+(w) &= \mathbf{I}(-w,u)\left(A_1(-u) + B^-(-u)\right), \\ B^-(w) &= \mathbf{I}(w,u)(A_2(u) + B^+(u)). \end{aligned} \tag{10}$$

Thus, for the solution of a boundary value problem it is necessary to find $F(w)$ that satisfies the system of integral Equations (4) and (5).

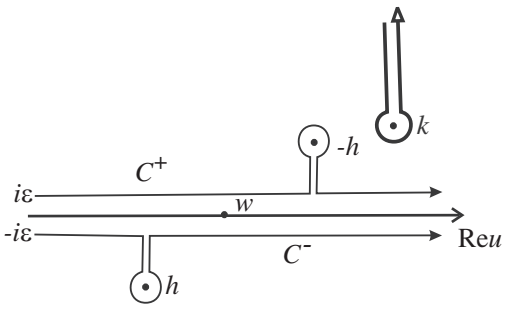

Figure 2: A plane of a complex variable w (or u).

3. CHARACTERISTIC EQUATION FOR STRIPS

The short-wave asymptotic behavior is achieved by means of the etalon integral

$$I(w) \equiv \mathbf{I}(w,u)\cdot 1,$$

using the stationary phase method. Here, the integration path in (10) is deformed up to the edge of the cut C_1, (Fig. 2) to get the contour of steepest descent that is a line parallel to imaginary axis upwards from the branch point. The result is

$$\begin{aligned} B^+(w) &\cong \mathbf{I}(-w,u)A_1(-u) + B^-(-k)I(-w),\\ B^-(w) &\cong \mathbf{I}(w,u)A_2(u) + B^+(k)I(w). \end{aligned} \tag{11}$$

The functions in (11) are found by solving the system of linear algebraic equations:

$$B^+(k) = \big(1 - I^2(-k)\big)^{-1}\big(\mathbf{I}(-k,u)A_1(-u) + I(-k)\mathbf{I}(-k,u)A_2(u)\big), \tag{12}$$

$$B^-(-k) = \big(1 - I^2(-k)\big)^{-1}\big(\mathbf{I}(-k,u)A_2(u) + I(-k)\mathbf{I}(-k,u)A_1(-u)\big), \tag{13}$$

Thus, the above-stated expressions give the dominant contribution to the solution of (10). Zeroing a denominator in (12), (13) gives a characteristic equation in the first approximation:

$$\det_1 = 1 - I^2(-k) = 0, \tag{14}$$

which determines the complex resonance frequencies of a strip, i.e., frequencies of self oscillations in absence of external incident waves. Here

$$I(-k) = \frac{1}{2i}\mathrm{H}_0^{(1)}(2ka) - 2ak\big(\mathrm{H}_0^{(1)}(2ka) - i\mathrm{H}_1^{(1)}(2ka)\big).$$

In order to take a account of the corrections of higher order it is necessary to expand the required functions B^+ and B^- in (10) in a Taylor series in the neighborhood of the point $u = k$ with the result:

$$\mathbf{I}(-w,u)B^-(-u) \;=\; e^{i2ak}\sum_{n=0}^{N}\frac{(i)^n}{n!}B^{-(n)}(-k)\frac{\partial^n}{\partial(2a)^n}\big(e^{-i2ak}I(-w)\big), \tag{15}$$

$$\mathbf{I}(w,u)B^+(u) \;=\; e^{i2ak}\sum_{n=0}^{N}\frac{(-i)^n}{n!}B^{+(n)}(k)\frac{\partial^n}{\partial(2a)^n}\big(e^{-i2ak}I(w)\big). \tag{16}$$

Now we will consider the characteristic equation in the second approximation for the estimation of the precision of the basic contribution of the integration by the saddle point method taking into account only the first derivatives in (15), (16) ($N = 1$):

$$\begin{aligned} \mathbf{I}(-w,u)B^-(-u) &\simeq B^-(-k)I(-w) + B^{-(1)}(-k)\big(kI(-w) + iI_a(-w)\big),\\ \mathbf{I}(w,u)B^+(u) &\simeq B^+(k)I(w) - B^{+(1)}(k)\big(kI(-w) + iI_a(-w)\big), \end{aligned}$$

where the following notation for the derivatives in the indicated points with respect to w and the parameter $b = 2a$ is introduced:

$$I_a(-w) \equiv \frac{\partial}{\partial b} I(-w), \quad B^{-(1)}(-k) \equiv \frac{\partial}{\partial w} B^-(w)\big|_{w=-k}, \quad I_a \equiv I_a(-k), \quad B^{+(1)}(k) \equiv \frac{\partial}{\partial w} B^+(w)\big|_{w=k}.$$

Substituting these expressions in (10) we find the matrix

$$\begin{pmatrix} 1 & 0 & -I(-k) & -kI(-k) - iI_a \\ 0 & 1 & -I_w & -kI_w - iI_{wa} \\ -I(-k) & kI(-k) + iI_a & 1 & 0 \\ -I_w & kI_w + iI_{wa} & 0 & 1 \end{pmatrix}$$

for the system of algebraic equations, where the following notation is introduced:

$$I_w \equiv \frac{\partial}{\partial w} I(w)\big|_{w=-k}, \quad I_{wa} \equiv \frac{\partial}{\partial b} I_w.$$

We get the characteristic equation in the second approximation by equating the determinant of the matrix to zero:

$$\begin{aligned} \det_2 \;=\; & 1 - \frac{H_0^4}{16} + \frac{ka}{12}\big(8H_0H_1(1+H_0^2) + iH_0^2(24+9H_0^2+H_1^2)\big) + \frac{(ka)^2}{36}\big(H_1^2(H_1^2-112) \\ & + 2H_0^2(312-47H_1^2) + 129H_0^4 - i16H_0H_1(H_1^2+15H_0^2+42)\big) + \frac{8(ka)^3}{9}(H_1+iH_0)\big(H_0(7H_1^2 \\ & - 9H_0^2-48) + iH_1(H_1^2+17H_0^2+32)\big) - \frac{64(ka)^4}{9}(H_1+iH_0)^2\big((H_1+iH_0)^2-4\big) = 0, \end{aligned} \tag{17}$$

where for brevity the values of the Hankel functions are designated as

$$H_0 \equiv \mathrm{H}_0^{(1)}(2ak), \quad H_1 \equiv \mathrm{H}_1^{(1)}(2ak).$$

The following values of the derivatives of I have been used in the characteristic equation:

$$\begin{aligned} I_w(-k) \;&=\; a(H_0 - \frac{i}{3}H_1) - \frac{8}{3}ika^2(H_0 - iH_1), \quad I_a = -\frac{1}{2}kH_0 + \frac{i}{2}kH_1 - ikI(-k), \\ I_{wa} \;&=\; \frac{1}{2}H_0 - 3ak(iH_0 + \frac{7}{9}H_1) - \frac{8}{3}(ak)^2(H_0 - iH_1). \end{aligned}$$

The variation of $\det_1$ and $\det_2$ with real k is presented in Fig. 3 using the basic contribution of the solution (10) with the saddle point method.

The behavior of the real part of the characteristic function for real values of k is maintained if $2ak$ is larger than about 0.04 in the first and in the second approach (Fig. 3). The behavior of the imaginary part of the characteristic functions for real values k are basically identical both in the first and in the second approximation.

Hence, on solving similar diffraction problems with the saddle point method and an etalon integral, the basic contribution of the integration should be restricted to the frequency band $2ka > 0.4$.

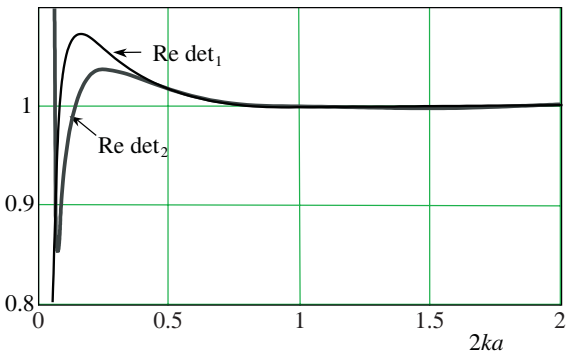

Figure 3: Real part of $\det_1$, $\det_2$ ($\mathrm{Im}ka = 0$).

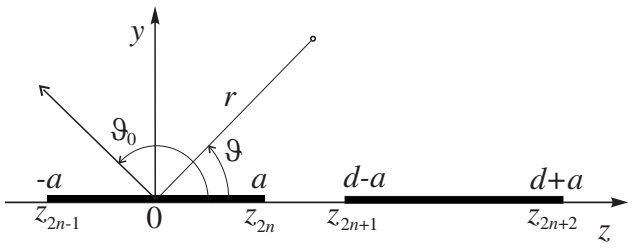

Figure 4: Diffraction of a plane wave on a grating.

The imaginary and real parts of the roots of the characteristic Equation (14) approach asymptotically

$$\mathrm{Im}(2ak) = -2.305 - 1.5\ln \mathrm{Re}(2ak), \quad \mathrm{Re}(2ak) \simeq \pi(n+1/4)\ (n=1,2,\ldots). \tag{18}$$

at Re$k \gg 1$. The obtained asymptotic formulas coincide with the result of [16]:

$$2ak \simeq (n+1/4)\pi - i1.5\ln\left(2\sqrt[3]{4\pi}(n+1/4)\pi\right).$$

4. CHARACTERISTIC EQUATION FOR GRATINGS

By analogy previous problem the boundary problem of a plane electromagnetic wave incident on an ideally conducting grating is reduced to a system of linear algebraic equations by means of integrating the system by the saddle point method and using etalon integrals. Then the solution of the system can be presented in the form

$$\begin{cases} B^+_{2n+1}(w) = I(-w)\big(A_{2n+2}(-k) + B^+_{2n+2}(-k) + B^-_{2n+2}(-k)\big), \\ B^-_{2n+1}(w) = J(w)\big(A_{2n}(k) + B^+_{2n}(k) + B^-_{2n}(k)\big), \\ B^+_{2n}(w) = J(-w)\big(A_{2n+1}(-k) + B^+_{2n+1}(-k) + B^-_{2n+1}(-k)\big), \\ B^-_{2n+2}(w) = I(w)\big(A_{2n+1}(k) + B^+_{2n+1}(k) + B^-_{2n+1}(k)\big), \end{cases} \tag{19}$$

where

$$\mathbf{J}(w,u) = \frac{1}{2\pi i}\int_{C^+} du \frac{\exp(i(d-2a)u)}{u-w}\sqrt{\frac{k+u}{k-u}}, \quad J(w) = \mathbf{J}(w,u)\cdot 1,$$

the coefficients are defined from the following system of algebraic equations:

$$\begin{pmatrix} e^{-ihd} & 0 & 0 & 0 & 0 & -I_- & 0 & -I_- \\ 0 & e^{-ihd} & 0 & 0 & 0 & -I_+ & 0 & -I_+ \\ 0 & 0 & 1 & 0 & -J_+ & 0 & -J_+ & 0 \\ 0 & 0 & 0 & 1 & -J_- & 0 & -J_- & 0 \\ 0 & -J_- & 0 & -J_- & 1 & 0 & 0 & 0 \\ 0 & -J_+ & 0 & -J_+ & 0 & 1 & 0 & 0 \\ -I_+ & 0 & -I_+ & 0 & 0 & 0 & e^{ihd} & 0 \\ -I_- & 0 & -I_- & 0 & 0 & 0 & 0 & e^{ihd} \end{pmatrix} \begin{pmatrix} B^+_{2n+1}(k) \\ B^+_{2n+1}(-k) \\ B^-_{2n+1}(k) \\ B^-_{2n+1}(-k) \\ B^+_{2n}(k) \\ B^+_{2n}(-k) \\ B^-_{2n}(k) \\ B^-_{2n}(-k) \end{pmatrix} = \begin{pmatrix} A_{2n}(-k)I_- \\ A_{2n}(-k)I_+ \\ A_{2n}(k)J_+ \\ A_{2n}(k)J_- \\ A_{2n+1}(-k)J_- \\ A_{2n+1}(-k)J_+ \\ A_{2n+1}(k)I_+ \\ A_{2n+1}(k)I_- \end{pmatrix}. \tag{20}$$

The following notations are introduced here for brevity:

$$I_- \equiv I(-k),\ I_+ \equiv I(k) = \frac{1}{2i}\mathrm{H}^{(1)}_0(2ak),\ J_- \equiv J(-k) = -\frac{1}{2i}\mathrm{H}^{(1)}_0(k(d-2a)),\ J_+ \equiv J(k) = e^{i(d-2a)k}.$$

Further, the periodic conditions

$$\begin{aligned} &B^-_{2n+2}(w) = e^{ihd}B^-_{2n}(w), \quad B^+_{2n+2}(w) = e^{ihd}B^+_{2n}(w), \\ &B^\pm_{2n-1}(w) = \mathrm{e}^{-\mathrm{i}hd}B^\pm_{2n+1}(w), \quad B^\pm_{2n-2}(w) = \mathrm{e}^{-\mathrm{i}hd}B^\pm_{2n}(w) \end{aligned} \tag{21}$$

follows from the substitutions $n \to n+1$ and $z \to z+d$, remembering to use $K \to \mathrm{e}^{-\mathrm{i}hd}K$ for the amplitude of the incident wave.

As the amplitude of a plane wave is equal to zero for self oscillations, it is necessary to note that in periodic conditions $h = 0$. Setting the denominator equal to zero, we find a characteristic equation that follows immediately from the solution (19) and (20):

$$\det = \begin{vmatrix} 1 & 0 & 0 & 0 & 0 & -I_- & 0 & -I_- \\ 0 & 1 & 0 & 0 & 0 & -I_+ & 0 & -I_+ \\ 0 & 0 & 1 & 0 & -J_+ & 0 & -J_+ & 0 \\ 0 & 0 & 0 & 1 & -J_- & 0 & -J_- & 0 \\ 0 & -J_- & 0 & -J_- & 1 & 0 & 0 & 0 \\ 0 & -J_+ & 0 & -J_+ & 0 & 1 & 0 & 0 \\ -I_+ & 0 & -I_+ & 0 & 0 & 0 & 1 & 0 \\ -I_- & 0 & -I_- & 0 & 0 & 0 & 0 & 1 \end{vmatrix} = (1 + I_- J_- - I_+ J_+)^2 - (I_- + J_-)^2 = 0. \quad (22)$$

REFERENCES

1. Noble, B., *Methods Based on the Wiener-Hopf Technique*, 2nd Edition, Chelsea, New York, 1988.
2. Wiener, N. and E. Hopf, "Über eine klasse singulärer integralgleichungen," *S. B. Preuss. Akad. Wiss.*, 696–706, 1931.
3. Weinstein, L. A., *The Theory of Diffraction and the Factorization Method*, Golem Press, Boulder, Colorado, 1969.
4. Shestopalov, V., *Method of Rieman-Hilbert Problem in Diffraction and Electromagnetic Wave Propogation Theories,* Publishing House of Kharkov University, Kharkov, 1971.
5. Agranovich, Z. S., V. Marchenko, and V. Shestopalov, *Zhornal Techn. Fiziki*, Vol. 32, 381–394, 1962.
6. Abragams, I. D. and J. B. Lawrie, *IMA Journal of Applied Mathematics*, Vol. 55, 35–37, 1995.
7. Sautbekov, S. S., "Factorization method for finite fine structures," *Progress In Electromagnetics Research B*, Vol. 25, 1–21, 2010.
8. Jones, D. S., *Acoustic and Electromagnetic Waves*, Clarendon Press, Oxford, 1986.
9. Ufimtsev, P. Y., *Fundamentals of the Physical Theory of Diffraction*, SciTech Publishing, Encino, 2007.
10. Brovenko, A. V., E. D. Vinogradova, P. N. Melezhik, A. Y. Poyedinchuk, and A. S. Troschylo, "Resonance wave scattering by a strip grating attached to a ferromagnetic medium," *Progress In Electromagnetics Research B*, Vol. 23, 109-129, 2010.
11. Imran, A., Q. A. Naqvi, and K. Hongo, "Diffraction of electromagnetic plane wave by an impedance strip," *Progress In Electromagnetics Research*, Vol. 75, 303–318, 2007.
12. Millar, R. F., "Diffraction of a wide slit and complementary strip," *Proc. of the Cambridge Philosophical Society*, Vol. 54, No. 4, 476–511, 1958.
13. Luneburg, E. and K. Westpfahl, "Bengung am streifen. hoch frequenz asymptotik and kleinmasche losung," *Annalen der Physik*, Vol. 21, Nos.1–2, 12–25, 1968.
14. Kieburts, R. B., "Constraction of asymptotic solutions to scattering problems in the Fourier transform representation," *Applied Scientific Research*, Vol. 12, No. 3, 221–234, 1965.
15. Stockel, H., "Bengung am spalt," *Annalen der Physik*, Vol. 16, Nos. 5–6, 209–219, 1965.
16. Nefyodov, E. I. and A. T. Fialkovski, *Asymptotical Theory of Diffraction of Electromagnetic Waves on Finite Structures*, Soviet. Radio, Moscaw, 1972.
17. Grinberg, G. A., "Diffraction of electromagnetic waves on a strip of finite width," *DAN USSR*, Vol. 129, No. 2, 295–298, 1959.

Self-field Theory a Mathematical Description of Physics

A. H. J. Fleming
Biophotonics Research Institute, Melbourne, Australia

Abstract— SFT is a new description of electromagnetic interactions applying across physics. At its heart are bispinorial motions for both the electromagnetic fields and the interacting particles. SFT is intimately related to quantum theory; instead of the single inequality uncertainty relationship, there are two exact equations one applying to electric currents, the other to magnetic currents. SFT is formulated in terms of the E- and H-fields rather than the potentials The mathematics of SFT applies to the 1st order Maxwell Lorentz equations rather than the 2nd order Lagrangian formulation. It has been used to solve a simple Bohr-like model of the hydrogen atom, obtained an analytic estimate for the mass of the photon, and provided the first glimpse of structure within the photon. This may yield an organizational structure for bosons reminiscent of the chemical table first noted by Mendeleev in 1860 via a two-dimensional array of elemental properties. The self-field formulation obtains an analytic expression for Planck's number providing a basis for its understanding as a variable of motion applying equally to the electron, the proton and the photon. SFT appears to apply equally to cosmology as to sub-photonic physics.

1. INTRODUCTION

In the electromagnetic (EM) version of SFT the Maxwell-Lorentz equations can be algebraically rewritten in matrix form as in (1) where each particle has two spinorial motions σ_i^{EM} and the corresponding currents κ_j^{EM}.

$$\mathbf{M}_{ij}^{EM}\sigma_i^{EM} = \kappa_j^{EM} \tag{1}$$

The motion of the electron is an exact EM self-field solution, its position at any time is the sum of two spinors forming a bispinorial motion $\sigma_o^{EM}(\mathbf{r}_o, \omega_o)$ and $\sigma_c^{EM}(\mathbf{r}_c, \omega_c)$ where the distance of the electron is written as a sum of the spinors not a Pythagorean root mean square but a function of orthogonal orbital and cyclotron spinors:

$$\mathbf{r}^{EM}\left(\mathbf{r}_o^{EM}, \omega_o^{EM}, \mathbf{r}_c^{EM}, \omega_c^{EM}\right) = \mathbf{r}_o^{EM}e^{j\omega_o t} + \mathbf{r}_c^{EM}e^{j\omega_c t} \tag{2}$$

Quantum theory as it applies to EM begins with the Heisenberg uncertainty relationship which is identical to (1) except that instead of one inexact equation there are two exact equations. SFT thus provides the analytic origins for the heuristic eigenvalue formulation of quantum theory.

If the intrinsic energy of the complete system changes the EM fields within an atomic array each atom can adjust altering the atomic and molecular binding structures. In effect this means that the radial and spin states of the two photons involved in the atomic binding energy can adapt to the energy change where the photons themselves are assumed to have a composite structure. Now the system has six degrees of freedom including the E- and H-fields in response to the change in ambient energy. The two extra variables give a range of variation orthogonal to the phase diagrams of atoms. A typical phase diagram shows only a solid line separating the various phases. SFT indicates a small range of binding structures that depend on the intrinsic energy of the system.

There are major differences between the SFT time-variant field motion and the time-invariant classical electromagnetics (CEM) where the field ubiquitously covers all solid angles with no definition other than its vector nature as to the actual field motion, field flux being the only indicator of field motion. Similarly the uncertainty of the field within quantum field theory (QFT) is related to its lack of a complete and coupled EM bispinorial field form. Other differences include an absence of HUP within SFT. As the photon is modeled via bi-spinors uncertainty is obviated. In SFT the electron's self-fields are modeled via a complete EM function that explicitly includes both E- and H-fields, enabling the complete analysis of the mutual self-field effect between two particles. Unlike the quantum potentials that are expectations yielding probabilistic solutions, the bi-spinorial field variables of SFT are deterministic. Quantum theory does not use the Lorentz equations thus it finds other ways (equations) to solve in terms of the expectations. The method invariably used is to apply the uncertainty equations as commutation relationships within the interaction matrices. Note that gauge theory that forms a large part of quadratic Lagrangian theory is not involved in SFT as there are fields not potentials in first order Maxwellian theory. The differences are mathematical but have major implications for the physical information and the predictions that can

be determined. Uncertainty applies only to the *model* of the physical interaction and not to the physics itself. It is a modeling error associated with way the field is incorporated into quantum theory (in quantum field theory the 'fields' are actually potentials or differential functions of the true fields).

A short summary of the mathematical and basic physical findings of SFT is as follows. SFT can be used to derive actual motions of the electron and proton within the hydrogen atom in the form of eigensolutions to the system of partial differential equations based on the ML equations. The atom is modeled via two point-mass particles, the electron, and the proton, an extension to the Bohr model. Planck's number $\hbar = \frac{q^2}{4\pi\varepsilon_0 v_e}$ is observed to be the energy per cycle of the principal eigenstate that depends on the motions of the electron, proton, and photon, all involved in the dynamic balance of the atom. The photon performs many relativistic transitions back and forth between the proton and electron within each cycle of the electron and proton that rotate coherently about their centre of mass. The phase length of the photon each time it transits $\pi/2$ maintains the overall coherency of the atom's periodicity providing a method for analytically comparing the energy of the photon with that of the electron $m_\gamma c^2 = \frac{\hbar\omega_\gamma v_e}{4c}$, where ω_γ is the collision frequency of the photon. Assuming some non-linear polygonal motion circumscribes a circle representing the Bohr mageton, the photon collision frequency is estimated as 54 using the known values of the fine-structure constant. $\alpha = \frac{v_e}{c} = \frac{4m_\gamma c^2}{\hbar\omega_\gamma}$ and the Landé g-factor. Thus m_γ evaluates to 0.396×10^{-55} kg (0.221×10^{-19} eV). Since the photon must perform a discrete number of transits per cycle this suggests collisional based polygonal rotations for both the electron and proton rather than the assumed circular rotations given by spinor theory used by both SFT and QFT. This suggests a way to check more detailed SFT models of the hydrogen atom that include a structured nucleus. Within molecules photon substructure introduces two previously unknown quantum numbers by which molecular bonds can range between strong and weak atomic structures. This photon mechanism appears involved in a number of energy/temperature dependent molecular processes. The cell cycle and other biological processes may well depend on the various hydration structures found within and around DNA and other biological protein structures. Physical phenomena show dependence on hydrogen bonding as in avalanches and the formation of cloud layers within the ionosphere or on the innate spectroscopy of bosons such as the magnetic flips of the Sun and Earth. SFT applies to gravitation as a form of bonding between molecular arrays. This is the basis of Einstein's EPR gedanken (thought experiment) that showed that quantum theory was incomplete. Gravitation at the Solar System level is a differential form of (1); there are long range forces between electric and magnetic dipoles causing the spin and orbit of the planets and the Sun. SFT is compatible with both special and general relativity except part of the dilations of time and distance are due to the hidden variables of the internal motion of the photon that are an outcome of its composite structure.

2. STRONG NUCLEAR FIELDS

Like the EM interaction the strong nuclear fields controlling the motions of charged particles satisfy the following adaptation of the ML equations.

$$\nabla \cdot \vec{\mathbf{E}} = \frac{\mathbf{q}_q}{\mathbf{v}_q} \tag{3a}$$

$$\nabla \cdot \vec{\mathbf{H}} = 0 \tag{3b}$$

$$\nabla \cdot \vec{\mathbf{N}} = 0 \tag{3c}$$

$$\nabla \times \vec{\mathbf{E}} + \mu_n \frac{\partial \vec{\mathbf{H}}}{dt} = 0 \tag{3d}$$

$$\nabla \times \vec{\mathbf{H}} - \varepsilon_n \frac{\partial \vec{\mathbf{E}}}{dt} = \frac{\pi}{s_q} \mathbf{q}_q \vec{\mathbf{v}} \tag{3e}$$

$$\nabla \times \vec{\mathbf{N}} + \mathbf{v}_n \frac{\partial \vec{\mathbf{E}}}{dt} = 0 \tag{3f}$$

where $\vec{\mathbf{N}}$ and $\vec{\mathbf{M}}$ are the nuclear field and flux density and the modified Lorentz equation for the forces acting on the quarks is

$$\vec{\mathbf{F}} = \mathbf{q}_q \vec{\mathbf{E}} + \mathbf{q}_q \vec{\mathbf{v}} \times \vec{\mathbf{B}} + \mathbf{q}_q \vec{\mathbf{v}} \times \vec{\mathbf{M}} \tag{3g}$$

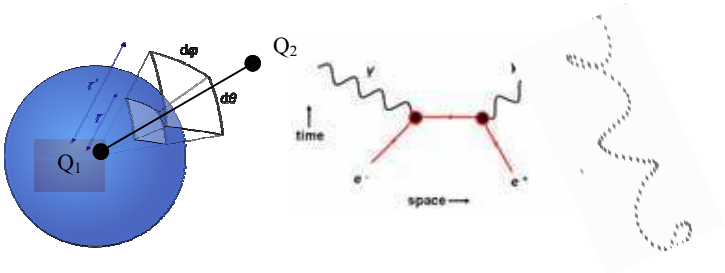

Figure 1: Field forms. (a) CEM (Credit Wikimedia), (b) QFT, (c) SFT.

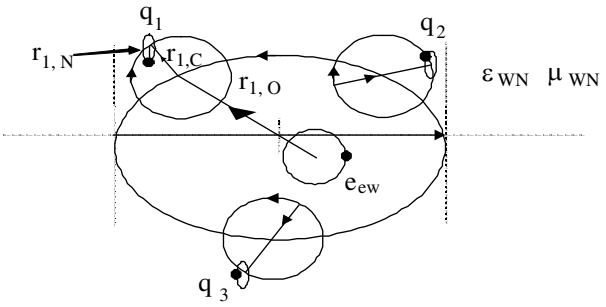

Figure 2: Electroweak Nuclear Shell Structures. Analogous to the EM electron shifting shell as energy density is raised via $\varepsilon_0\mu_0$, so too the weak electron moves its inner shell if $\varepsilon_{WN}\mu_{WN}$ is raised, at the same time the proton shifts its nuclear shell.

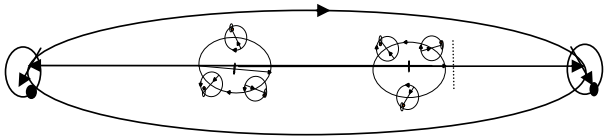

Figure 3: Pauli exclusion principle: Hydrogen molecule modeled as two protons with composite quark structure and two electrons.

and constitutive equations $\vec{\mathbf{B}} = \mu_n\vec{\mathbf{H}}$, $\vec{\mathbf{D}} = \varepsilon_n\vec{\mathbf{E}}$ and $\vec{\mathbf{M}} = v_n\vec{\mathbf{N}}$ where ε_n, μ_n and v_n are invariant scalars, the nuclear constitutive parameters similar to those of free space, ε_0 and μ_0, except the energy density within the nucleus now depends upon the three gluon fields

$$\mathbf{dU}_N = \rho_N\mathbf{dV} = \frac{1}{2}\left(\varepsilon_0\tilde{\mathbf{E}}\cdot\tilde{\mathbf{E}} + \mu_0\tilde{\mathbf{H}}\cdot\tilde{\mathbf{H}} + v_0\tilde{\mathbf{N}}\cdot\tilde{\mathbf{N}}\right)\mathbf{dV} \tag{3h}$$

The system of equations given in (3) can be used to model the SN interaction within the nucleus of the atom where the motions of quarks are trispinorial in comparison to the bispinorial motions of the electron and proton in EM theory. A similar trispinorial mathematics applies to galactic motions.

3. PAULI PRINCIPLE AND PHOTONIC STATES

Two most important findings of SFT are (1) a qualitative understanding and widening of the Pauli Principle and (2) there is a series of transitional chemical changes from liquid state to liquid crystal states that occur to macromolecular arrays as observed in the various structural forms of DNA linked to photon binding and its length.

SFT reveals a shell structure for the weak nuclear electrons and their complementary proton shell structures within the nucleus. As shown in Fig. 2 an internal SFT balance can be achieved between a weak electron and a proton within the central core or inner spherical region of the nucleus. In this region elevated energy densities are present via the electroweak constitutive parameters $\varepsilon_{WN}\mu_{WN}$. What this implies is that the strong nuclear effect occurs within an annular region where the quarks and gluons move (orbitals). Associated with this the electroweak orbits can be seen to be similar to their EM counterparts having spherical orbitals (s shells).

In SFT electrons and protons orbit as EM binaries in a stable double rotation (bispinor). If a second paired electron and proton are displaced in phase by π radians the combined motion and structure is also stable. Underpinning this is a physical principle in the way the photons cannot stream between more than two charges particles at the sub-atomic level simultaneously in a stable fashion. While photons transit between an electron and its paired proton as a pair of streams, they do not move as bispinors between other EM electrons or protons. While the three quarks in a proton connect to an electron this happens via combination of streams into a single stream and

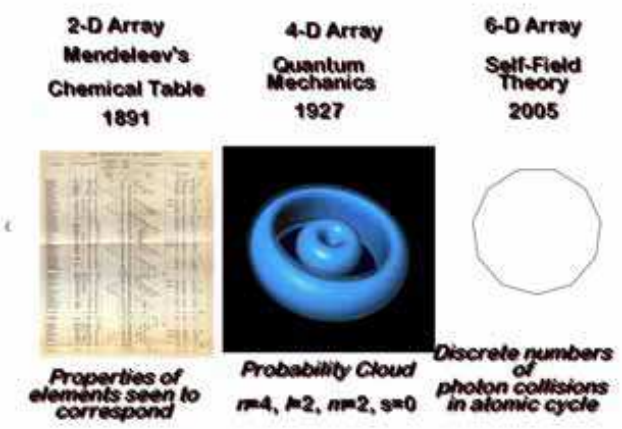

Figure 4: Historical perspective of two extra SFT quantum numbers related to photon in its role as binding energy (Credit Wikimedia).

the inverse separation. This photon bonding mechanism simplifies the mathematics of atomic and molecular structures. The four EM particles shown in Fig. 3 are connected by only two pairs of EM photon streams, two E-field streams and two H-field streams that rotate in synchronous fashion with the electrons and protons.

This synchronous motion also applies to multi-atom configurations including solid crystal arrays. Modern versions of the double-slit experiment can be easily understood where the two slits are made of the same solid piece of material. If the two slits are synchronous versions of each other then the slow build up of the final diffracted image photon by photon is no longer enigmatic. Hence arrays of matter appear synchronous in their motions in the same way as shown in Fig. 3.

The difference between a solid and a range of less rigid arrays of atoms can also be understood via the resonance of the binding photons. As these binding photons change their resonant phase length over integer multiples of $\pi/2$ the whole array becomes less and less rigid until the array can resemble a liquid. This process can continue until the whole array becomes disassociated and forms a gas.

While the gravitation force is not incorporated into the mathematics of CEM or QFT, the extension from molecular arrays to gravitational systems is a small mathematical extension within the SFT formulation. What emerges is a corresponding system of boson streams that link atomic arrays and gravitational arrays alike. Thus SFT applies to the four known forces currently known to physics.

REFERENCES

1. Fleming, A. H. J., "Electromagnetic self-field theory and its application to the hydrogen atom," *Physics Essays*, Vol. 18, No. 3, 265–285, 2005.
2. Fleming, A. H. J., "Self-field theory, analytic spectroscopy of the ordinary photon," *Proc. 2nd Electromagnetics Health and Environment Intl Conf.*, Wroclaw, Poland, 18–23, 2007.
3. Fleming, A. H. J., "Self-field theory — Biodiversity may be a resonance process," *PIERS Proceedings*, 828–831, Cambridge USA, July 5–8, 2010.
4. Fleming, A. H. J., "Self-field theory — A possible gravitational structure for galaxies," *PIERS Proceedings*, 823–827, Cambridge, USA, July 5–8, 2010.
5. Fleming, A. H. J., *Self-field Theory — A New Mathematical Description of Physics,* Pan Stanford Publishing, 2010.

Self-field Theory: Cosmological and Biological Evolution May Be Linked

A. H. J. Fleming
Biophotonics Research Institute, Melbourne, Australia

Abstract— Recently Self-Field Theory (SFT) was used to propose a link between cycles of biodiversity and galactic gravitational structure. This hypothesis provides a new form of gravitation applicable to galaxies different to solar systems that includes both photons and phonons. According to SFT photons and phonons react to form gluons in regions where the energy density is sufficiently high. The Maxwell-Lorentz (ML) equations appear able to be modified to provide a Maxwellian mathematics applicable to strong nuclear regions. Consequently, solidification can occur in galactic structures corresponding to findings of fairly constant galactic orbital speed variation with radial distance known since the 1930's. Universal expansion follows the work of Hubble in the 1920's in identifying a redshift applying to matter within the Universe. Biological evolution may correlate with cosmological evolution. It is known that the first simple forms of life around 4 billions years ago in the case of our own Milky Way Galaxy had single-celled structures. It was around this point in cosmological time that the Solar System is thought to have first formed. The small size of early proto-life forms and their bulk modulus relative to mammals corresponds to the fact that the energy density within the early Milky Way Galaxy would have been relatively higher than during later epochs when mammals of varying size evolved. Life-forms would be expected to grow larger and be more solidified via phonon resonance within the evolving galaxy as the photon energy density fell with inflation. Thus there may be an identifiable correspondence (perhaps similar to dendrochronology) between the phylogenetic tree of life and the inflationary processes of cosmological evolution into gravitational structures able to sustain the various life-forms.

1. INTRODUCTION

The mathematical description of physics given by SFT includes molecules and macromolecules such as DNA. Molecular motions involve the eigensolutions of the ML equations with six degrees of freedom and can be extended to include gravitational arrays consisting of dielectric and diamagnetic forces. At the solar system level this like general relativity involves Newtonian gravitation and planetary spins. Other forms of gravitation apply to other structures including galaxies and a possible structure connecting 'strings' of galaxies and super clusters at the domain above galaxies. This cosmological structure may have a super cluster core with 'tubes' or filamentary strings of galaxies orbiting around the super clusters. These strings are observed at the largest cosmological level.

The gravitational model of the Universe shown in Fig. 1 is based on the four levels of structure observed to hold across the universe. It is also based on the fact that there are distinct levels of gravitation given by SFT; each one a balance between matter and fields (bosons) of different types. The Solar System involves bispinorial motions, while the Galaxy involves trispinorial interactions. The proposed gravitational structure connecting galactic strings and super clusters may involve

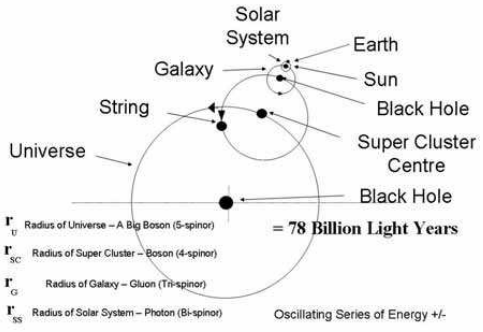

Figure 1: SFT model of the universe.

'quadrospinors' (4-spinors). Each gravitational domain therefore has its own unique structure. While the fields and their associated forms of matter of SFT are identifiably fractal, so too are life forms. Human life is based on many levels of biological organization including the whole body, organs, tissues, cells, proteins, DNA, and biophotons. These fractal domains whether gravitational or biological interact in harmony and synergy. It may be that all life forms evolved in a time sequence that depended on the cosmological evolutionary process. This cosmological evolution involved the various gravitational structures that can be observed, and the evolutionary process in general occurred as a 'top-down' sequence of events. In the sequence of events of inflationary cosmology the various bosons involved within their gravitational structures also evolved and dependent on both the various life forms also took shape and were formed within this framework.

2. GRAVITATIONAL STRUCTURE OF GALAXIES

Historically a widespread and considered opinion existed from 1687 till the 1930s that gravitation throughout all levels of interaction within the Universe was similar to that in the Solar System as proposed mathematically by Newton. Lagrange in the late 1700's followed the mechanical and astronomical paths in Newton's footsteps confirming and extending the application of Newton's gravitational laws to the full extent of the then known Universe. This was a time pre-quantum physics and pre-relativity during the 18th century when the Universe was thought of as a nebula, the term 'galaxy' did not appear in any index, and 'cosmogony' was used in discussing how the Solar System formed out of the Universe. In 1915 Einstein extended Newton's inverse square law to a system of geodesic equations that took into account the speed of light treated as an observable constant; this in effect was an extension to a second degree of freedom within gravitation at the level of the Solar System. In the 1920's Hubble used the 100 inch telescope at Mount Wilson to discover that the local 'star groups' were in fact other galaxies. He subsequently discovered cosmological redshift, a discovery that lead eventually to the theory of the Big Bang. In 1931 Oort observed the red-shift of stars near the Galactic Plane (GP). He found that the variation of orbital speeds with radial distance away from the Galactic Centre (GC) were fairly invariant unlike the Solar System where orbital speeds diminish. Zwicky in 1932 extended this finding by studying galaxies within the Coma Cluster measuring similar results. If gravitation were Newtonian, the stars should fly apart; the Milky Way Galaxy and its myriad counterparts within the Universe were thus now problematic in terms of their gravitational structure. Over the intervening years to the present one hypothesis is that dark matter including Massively Compact Halo Objects, and Weakly Interacting Massive Particles supplies the missing matter. Another hypothesis is MOdified Newtonian Dynamics that heuristically changes Newton's constant of gravitation to match the observed rotational speeds.

$$M_{ij}^{DSN}\sigma_i^{DSN} = \kappa_j^{DSN} \tag{1}$$

According to SFT galactic gravitation is a differential form of the strong nuclear (SN) ML equations given by (1): The internal three-particle structure of the gluon, and the tri-rotational dynamics of quarks within atomic nucleus, corresponds to the tri-rotational gravitational dynamics (Fig. 3). Looking at the picture that emerges from SFT, the bosonic structures involved, and observing the evidence from cosmology, it seems the Universe is segmented into layers of structure that depend on the spatial variation of energy density to form Solar Systems, Galaxies, and Super Clusters. Each layer has its own gravitational structure depending on the energy density and the bosons available as a function of space-time. Similar to photon streams within atoms the various bosons

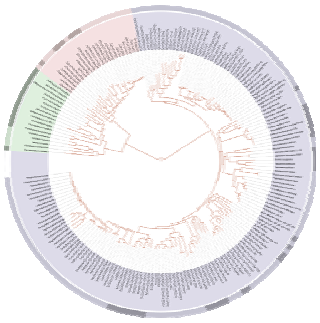

Figure 2: Tree of life based on genomes (Credit Wikimedia).

stream to and fro between conglomerates of various forms of mass, losing and regaining energy within transits.

If the energy density at the Earth's surface were constant, this would imply an infinite and possibly homogeneous region surrounding the Solar System and the Earth. In fact the Galaxy is observed to resemble a thin ellipsoid. Unlike the Solar System there has evolved a depth and structure orthogonal to the GP. The Galaxy also has a reasonably constant orbital speed unlike the orbital speed relationship found within the Solar System. The Galaxy therefore rotates approximately like a solid. Acoustic fields are known to be involved in structural integrity. Hans Jenny (1904–1972) studied the interaction of acoustics on the formation of structure within particulate substances such as sand, liquid, and iron filings examining the resonant acoustic modes on a sheet of metal. As the Earth and Solar System move up and down orthogonal to the Galactic Plane, the E-, H-, and A-fields on the Earth's surface vary. The Galaxy may be modeled as particles, the Solar System and the Black Hole near the GC moving within a galactic structure. It can be seen that the electric (E-), magnetic (H-), and acoustic (A-) fields on the Earth's surface will vary with distance above and below the GP. This cyclic variation is partly due to the falling-off in energy density near the upper and lower edges of the Galaxy as the mass density changes abruptly to that of intergalactic space. This wavelike variation in the fields may be involved in the observed cycles of biodiversity investigated recently by Medvedev and Melott.

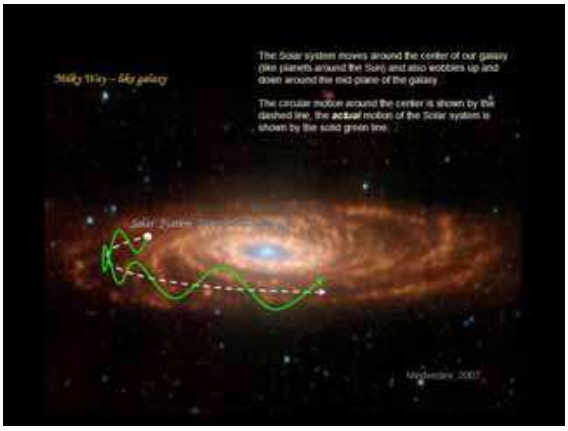

Figure 3: Galactic dynamics: a sun orbiting in a galaxy (Credit: Medvedev M. V. & A. L. Melott, "Do extragalactic cosmic rays induce cycles in fossil diversity?" *Astrophysics J.*, Vol. 664, 879–889, 2007).

3. COSMOLOGICAL AND BIOLOGICAL EVOLUTION MAY BE LINKED

In the same way the structure of a galaxy and its solar systems evolve so too does the structure of the life-forms it sustains at any point in time. The three-dimensional forces holding a galaxy together create the pressure within gas, solid, and liquid matter inside the galaxy. As well the radiation energy received from a sun is involved in mitosis and replication of any life forms. As the galactic three-dimensional structure evolves so too the gravitational forces evolve within the galaxy. This concerns both the photon and phonon energy densities as a function of the shape of the galaxy. As the galaxy grows, the height in the plane orthogonal to the GP grows. This increase in galactic size and height gives more three-dimensional solidification to the life-forms it can sustain. If a species can use this added solidity to its advantage then there is no reason why it will not evolve to a more solid entity. So too as the Big Bang expansion process continues a solar system expands and there is an associated lowering of photon energy within it lowering the EM energy density and a consequent. Increase in wavelength available via EM radiation. Hence size of life-forms can expand in a similar way to the solidification process. We would thus expect to observe biological evolution follows a path towards more solid and larger species as the galaxy and its solar systems evolve. This is generally what we do see when examining the various phylogenetic trees of life. In all there may be a correspondence across the evolutionary processes and energy densities needed within particle physics, the universal expansion, gravitational evolution and the phylogenetic tree of life.

4. ROLE OF ACOUSTIC AND EM RESONANCE IN BIODIVERSITY

As the Earth bobs up and down to its maxima in its motions within the Solar System around the Galactic Centre, it moves to regions where the acoustic fields are diminished and the structural integrity of matter on Earth is reduced limiting the ability of species to maintain their physiological integrity. Physiological integrity refers in part to the mechanisms a body uses to reach a state of constancy, homeostasis, and adaptation, and includes perfusion, nutrition and oxygenation. Tissues that were solid at or near the GP will be less solidified, and may not have the required structural integrity for life to be as viable at the maxima points in the galactic motion. There is a link between fluid dynamics and acoustics that is pertinent to the current discussion. As is known the speed of sound is given by $c_s = \sqrt{\kappa/\rho_0}$ where ρ_0 is the mean density and κ is the bulk modulus measuring a substance's resistance to compression. Similar equations hold for gases, liquids, and solids as well as biological tissues. If the bulk modulus of tissues falls below a certain threshold the tissue will lose its structural integrity. This is similar to the observation of space sickness that astronauts enduring prolonged stays in free space can suffer deleterious effects to bone, muscle, perfusion and blood pressure. This might especially be the case for large structures such as the dinosaurs that roamed the Earth some 60 Myr ago, a time of near maximum excursion from the GP.

Similar to the variation in the phonon field near the upper and lower edges of the Galaxy, a related effect happens with the E- and H-fields that are also involved in the galactic gravitational structure. The energy density of matter falls off near these edges. In this case, the Galaxy's Black Hole near the centre of the Galaxy is a negative source of energy unlike the Sun near the centre of the Solar System which is a positive source of energy. SFT indicates a fractal view of the Universe and its gravitational structures. This includes an oscillating series of gravitational forces going beyond the galactic level. Energy density in the bulk medium within the Universe, free-space, is observably convergent rather than divergent. As the Solar System bobs up and down, the relative energy due to the Galaxy is reduced and the Solar System will become slightly warmer than while moving near the GP. Longer wavelengths, and larger species, are associated with galactic dynamics closer to the GP as the ambient temperature deep inside the Galaxy would be expected to be cooler. Reproductive processes including mitosis within large species may become less viable as the frequencies of the energy required during the cell cycle increase away from their values within a more habitable and cooler zone. 'Goldilocks Zones' are thought necessary to sustain life both at the Solar System and the Galactic levels.

As the Galaxy radiates phonons and low energy photons, the Solar System radiates photons within the UV and visible range suitable for life. Popp studied the spectral emissions from the DNA of numerous life forms finding wavelengths from 200–800 nm. Thus life appears to receive its spectrum of energy from both the Galaxy and the Solar System as shown in the blackbody energy in Fig. 4. Interestingly the maximum of the blackbody curve for our Sun occurs near the midpoint of the range of DNA frequencies observed by Popp. Like the geodesics of gravitation within space-time, a similar 'geodesics' may apply to evolution of life in a parametric 'life-space-time'.

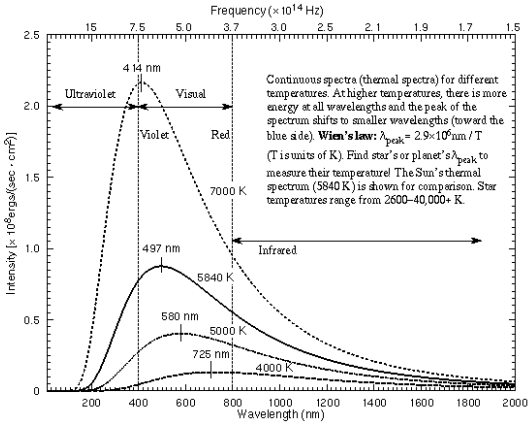

Figure 4: Blackbody for the Sun emits photons at around 500 nm suitable for eyes and DNA (Credit: Nick Strobel, www.astronomynotes.com).

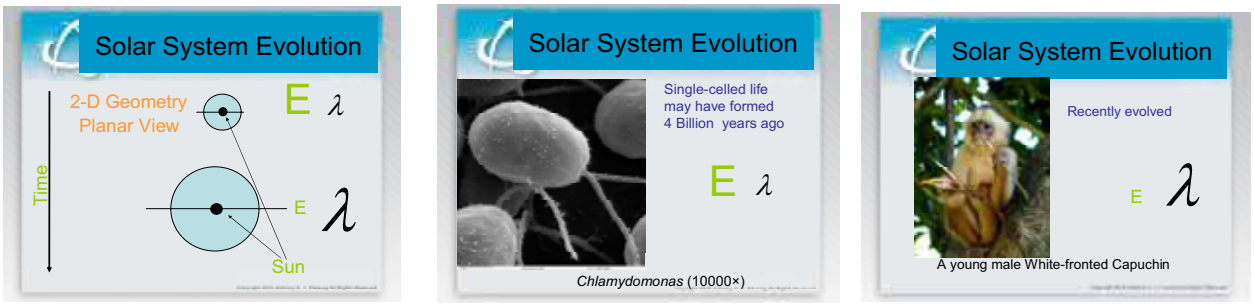

(a) (b) (c)

Figure 5: (a) Solar System and Galaxy (not shown) grow in size as inflation proceeds, (b) early life forms are small with lower bulk modulus (invertebrates), (c) while recent species are larger with higher bulk modulus (vertebrates).

5. CONCLUSIONS

Biological evolution may be related to cosmological effects: (1) Biodiversity varied with the phonon energy of the Galaxy which expanded during the inflationary process. In general as expansion proceeded there was a steady increase in bulk modulus of life forms over time. (2) There was reduced viability of biological tissues to withstand the drop-off in bulk modulus at maximum excursions from the GP leaving tissues less resistant to the forces wanting to implode their structure, especially large vertebrates. This reduction in bulk modulus may have left the largest of these species (dinosaurs) unable to function at a primary level. (3) Biodiversity also depended on the energy density within the Solar System as it evolved during inflation. Cells, tissues, organs and bone tissue and teeth evolved within available energy density over time. Thus as the Solar System evolved it expanded and the energy the Sun emitted dropped off over time. Life forms evolved as shown in Fig. 5. Biophotons that control mitosis and 'biophonons' that control bone growth originate from far outside the body from celestial and galactic sources. This may form the basis of a spectroscopic test for extraterrestrial life given that the next generation space-based optical telescopes may be capable of looking directly at exoplanets.

REFERENCES

1. Fleming, A. H. J., "Electromagnetic self-field theory and its application to the hydrogen atom," *Physics Essays*, Vol. 18, No. 3, 265–285, 2005.
2. Fleming, A. H. J., "Self-field theory, analytic spectroscopy of the ordinary photon," *Proc. 2nd Electromagnetics Health and Environment Intl Conf.*, 18–23, Wroclaw, Poland, 2007
3. Fleming, A. H. J., "Self-field theory-biodiversity may be a resonance process," *PIERS Proceedings*, 828–831, Cambridge, USA, July 5–8, 2010.
4. Fleming, A. H. J., "Self-field theory — A possible gravitational structure for galaxies," *PIERS Proceedings*, 823–827, Cambridge, USA, July 5–8, 2010.
5. Fleming, A. H. J., "Self-field theory — A new mathematical description of physics," Pan Stanford Publishing, 2010, to be published.

Self-field Theory and General Physical Uncertainty Relations

A. H. J. Fleming[1], **V. N. Matveev**[2], **and O. V. Matvejev**[2]

[1]Biophotonics Research Institute, Melbourne, Australia
[2]Sinerta Closed Joint-Stock Company, Vilnius, Lithuania

Abstract— The equations of Self-Field Theory (SFT) applying to the hydrogen atom are almost identical to the inequality relationship known as Heisenberg's Uncertainty Principle (HUP), the only differences being that the inequality sign of HUP is replaced by an equality relationship and there being two such equations in SFT. This duality is due to the bispinorial motions of the electron and proton, in the form of both electric and magnetic currents. This relativistic double motion can be compared with the single rotations of the Bohr Theory. In this regard SFT completes the Bohr Theory solution of the hydrogen atom. Although it has revealed a photonic level interaction within and between atoms SFT is seen as a mathematics that applies across physics and not just at the atomic level. Various SFT applications have emerged including a gravitational model for the Galaxy, and a new mathematics applying to the weak and strong nuclear forces. Recently Matveev and Matvejev have uncovered a general macroscopic form of HUP. A macroscopic rod incorporating a pair of synchronized clocks and a macroscopic object performing the function of an ideal physical clock were examined and its motions found to take the form $\Delta p_x \Delta x \geq h$ and $\Delta E \Delta t \geq h$, where h is Planck's constant where the precision and properties of all clocks must be considered. This general form of HUP provides a mathematical basis for the wide application of SFT. Up to the present time quantum theory has stood apart from macroscopic computations. Now quantum theory can be seen to be part of a more general mathematics applying to macroscopic domains.

1. INTRODUCTION

Over much of the 20th century many areas of science have depended for their underlying theoretical model on quantum theory with its uncertainty. Since before 1927 when quantum theory was introduced there has been an ongoing search for a general mathematics applicable across macroscopic and microscopic domains as well as the atomic and nuclear domains where probabilistic quantum methods have been the only available methods. Einstein rejected the probabilistic basis of quantum theory and searched unsuccessfully for a deterministic, relativistic and unifying field theory that might be applicable across physics.

A leading figure in this search was Herbert Fröhlich who along with Albert Einstein can be considered the scientific forebears of all who have searched for such a general mathematics. Fröhlich was involved in many areas of science including particle physics with contributions to nuclear forces and meson theory, and biology including dielectric theory and coherence. The first author is grateful to Dr Peter Rowlands of the Oliver Lodge Laboratory, Department of Physics at the University of Liverpool for a copy of the biographical book "*Herbert Fröhlich FRS — A Physicist Ahead Of His Time*". Fröhlich was Chair of Theoretical Physics at the University of Liverpool from 1948 till retiring in 1973 (from the position of Chair but not from further scientific endeavours) until his death in 1991 aged 85. Fröhlich had used quantum theory in the area of semiconductors to great effect writing his first book *Elektronentheorie der Metalle*, Springer, in Berlin, 1936. Like many other German and Eastern European scientists of this era he fled persecution. He escaped St Petersburg (then Leningrad) and the Stalinist purges of 1935 being interned as an 'alien' in London in 1940. Many of his ideas including biological coherence have been taken up by others including the first author whose work on diffusion within the cell membrane had its genesis in Fröhlich's ideas. Of particular interest to SFT in this biographical text is Fröhlich's unpublished 'bilocal' extension of the Dirac Theory to take into account the magnetic currents in quantum theory as well as the electric currents. This is equivalent to SFT's kernel discovery that also takes into account the magnetic currents of the electron providing a completion of the early Bohr Theory. Thus the work of Bohr, Fröhlich, and Hertz whose potentials in application to the far-fields of a half-wave dipole antenna were the original motivation for the bispinorial basis and can be seen to be part of the historical roots of SFT.

On a recent trip to St Petersburg, Russia, the first author met Vadim Matveev and his son Oleg Matvejev who have recently discovered a macroscopic version of HUP indicating the existence of a macroscopic version of quantum theory. Their work vindicates the overall thrust of Fröhlich's

lifelong efforts some decades earlier. Their work is presented in another talk in this session. The only difference between their work and SFT is the inclusion of the magnetic currents in SFT as mentioned above. The existence of a macroscopic quantum theory demonstrates the wide applicability of both quantum theory and SFT.

In the following, Heisenberg's original uncertainty as applied to a wave packet and Fröhlich's quantum method involving both electric and magnetic currents are seen to be theoretically very closely related to the deterministic and bispinorial SFT. Taken together with the general physical uncertainty relationship of Matveev and Matvejev, this provides a basis to understand that both quantum theory and SFT are applicable in general from macroscopic to atomic domains.

2. UNCERTAINTY FOR A WAVE PACKET

The uncertainty principle was first proposed by Heisenberg in 1927. HUP is presented in the original form given by Heisenberg. Assume the wave packet illustrated by Fig. 1 consists of sinusoidal plane waves of wavelengths close to λ_0. There are approximately $n = \Delta x/\lambda_0$ wavelengths within the packet. Outside the limits of the wave packet the waves must cancel each other by interference. This only occurs if at least $n + 1$ waves fall inside the limits of the wave. Thus we may write

$$\frac{\Delta x}{\lambda - \Delta\lambda} \geq n + 1 \tag{1}$$

In (1), $\Delta\lambda$ is the approximate range of wavelengths. Thus

$$\frac{\Delta x \Delta\lambda}{\lambda_0^2} \geq 1 \tag{2}$$

The group velocity of the wave can be written

$$v_g = \frac{h}{m_p \lambda_0} \tag{3}$$

The spreading of the wave is thus characterized by a range of velocities

$$\Delta v_g = \frac{\hbar}{m_p \lambda_0^2} \Delta\lambda_0 \tag{4}$$

By definition $\Delta p = m_p \, \Delta v_{gx}$ hence

$$\Delta p_x \Delta x \geq \hbar \tag{5}$$

HUP may also be written in the corresponding form

$$\Delta t \Delta E \geq \hbar \tag{6}$$

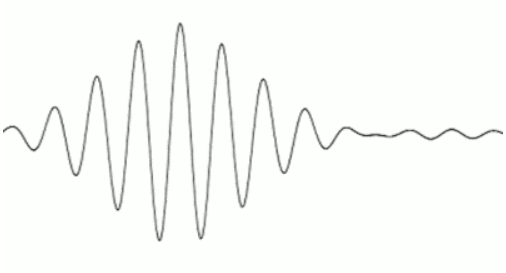

Figure 1: Wave packet with uncertainty Δx in position and Δp in momentum.

3. ELECTRON AND PROTON PERFORM BISPINORIAL MOTIONS IN HYDROGEN ATOM

In general both the particles and the EM fields that control the motions of charged particles satisfy the Maxwell-Lorentz equations. For application to atomic physics, regions where particle-field

interactions occur are assumed isotropic and homogeneous and the constitutive parameters, ε_0 and μ_0 the permittivity and permeability of free-space, are scalars. Where discrete particles carrying units of elementary charge q of opposite polarity are studied, in the absence of nebular regions of charge and current density, the ML equations are written

$$\nabla \cdot \vec{E} = \frac{q}{v_q} \tag{7a}$$

$$\nabla \cdot \vec{H} = 0 \tag{7b}$$

$$\nabla \times \vec{E} + \mu_0 \frac{\partial \vec{H}}{dt} = 0 \tag{7c}$$

$$\nabla \times \vec{H} - \varepsilon_0 \frac{\partial \vec{E}}{dt} = \frac{\pi}{s_q} q\vec{v} \tag{7d}$$

The Lorentz equation for the field-forces acting on the particles is written

$$\vec{F} = q\vec{E} + q\vec{v} \times \vec{B} \tag{7e}$$

The constitutive equations in free-space are

$$\vec{B} = \mu_0 \vec{H} \tag{7f}$$

$$\vec{D} = \varepsilon_0 \vec{E}. \tag{7g}$$

The relationship between the speed of light[1] and the ratio of the fields

$$c = (\varepsilon_0 \mu_0)^{-1/2} \tag{7h}$$

The atomic energy density per volume is

$$dU = \rho dV = \frac{1}{2}\left(\varepsilon_0 \tilde{E} \cdot \tilde{E} + \mu_0 \tilde{H} \cdot \tilde{H}\right) dV \tag{7i}$$

depends upon the E- and H-fields in the atomic region. (2.1a–d) are termed the EM field equations. In these equations, v is the particle velocity, m is its mass. It is assumed that the volume of integration v_q over which the charge density is evaluated, and the area the charge circulates normal to its motion s_q, are calculated during successive periods over which the internal motions of the atom take place (Fig. 2(b)).

The motion of the electron and proton are exact EM self-field solutions, their position at any time is the sum of two spinors forming a bispinorial motion $\sigma_o^{\mathrm{EM}}(r_o, \omega_o)$ and $\sigma_c^{\mathrm{EM}}(r_c, \omega_c)$ where the distance of the electron is written as a sum of the spinors not a Pythagorean root mean square but a function of orthogonal orbital and cyclotron spinors:

$$r^{\mathrm{EM}}\left(r_o^{\mathrm{EM}}, \omega_o^{\mathrm{EM}}, r_c^{\mathrm{EM}}, \omega_c^{\mathrm{EM}}\right) = r_o^{\mathrm{EM}} e^{j\omega_o t} + r_c^{\mathrm{EM}} e^{j\omega_c t} \tag{8}$$

The Maxwell-Lorentz equations can be algebraically rewritten in matrix form (7) where each particle has two coupled spinorial motions σ_i^{EM} and the corresponding coupled currents κ_j^{EM}.

$$\mathrm{M}_{ij}^{\mathrm{EM}} \sigma_i^{\mathrm{EM}} = \kappa_j^{\mathrm{EM}} \tag{9}$$

(9) has an analytic form remarkably similar to Heisenberg's uncertainty inequality relationship given by (5) or (6) except that there are two such equations, one relating to electric currents and the other to magnetic currents.

$$m_e v_o^2 = 2\hbar\omega_o \tag{10a}$$

$$m_e v_c^2 = 2\hbar\omega_c \tag{10b}$$

[1]In SFT, the speed of light is not proscribed from being variable. Depending on the energy density of the region under investigation, and the photon state, c can vary. Note also that the bispinorial basis is electromagnetically relativistic a priori. There is no need to insert explicit terms as was added to the Lagrangian in Dirac Theory.

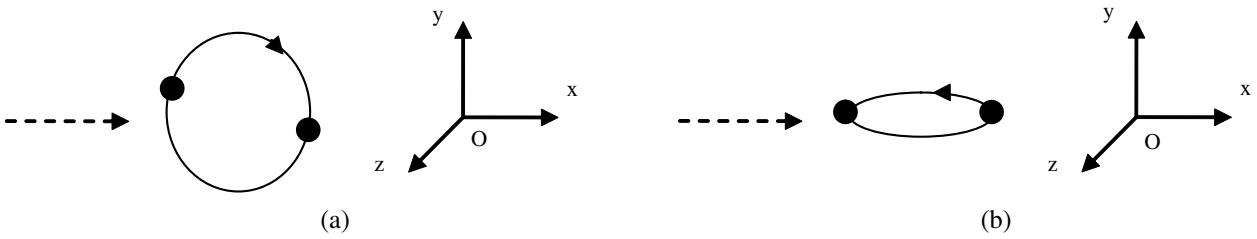

Figure 2: (a) Composite photon moving past point O along X axis rotating in X-Y plane. (b) Composite photon moving past point O along X axis rotating in Z-X plane.

These electric and magnetic currents take the form of a double rotation (bispinor) in the dynamic motions of the electron and proton. In regard to the photons which 'mediate' the electric and magnetic forces within the atom, there are thus two streams of photons, one relating to the orbital motions the other to cyclotron motions of both the electron and the proton. Hence there is an electric field and a magnetic field that form a coupled EM field that acts between the electron and proton. Shown in Figs. 2(a), (b) the photon for both the electric and magnetic field is modeled as a composite system of charges that can be observed by a loop detector in the two transverse planes as wave packets. This demonstrates the wave-particle nature of the EM field. There are situations where this coupled EM system of fields is not significant such as electrostatic and magnetostatic effects. In the atomic and molecular domains as in the terrestrial and gravitational domains such coupled electric and magnetic effects correspond to the findings of Matveev and Matvejev that there exists a general uncertainty relationship existing at both microscopic and macroscopic domains.

4. CONCLUSIONS

Over the long history of quantum theory it has been known that the uncertainty relationships have a wide applicability, although it has not been realised why this is the case. Rather HUP was a 'rule of thumb', a 'part of the fabric of reality' that physicists and engineers applied with partial success to many physical situations. While it has also been used at the gravitational domains 'quantum gravity' did not eventuate. In retrospect it can be seen that this was due to the incomplete nature of quantum theory, specifically the lack of consideration of the effects due to the magnetic currents. Einstein felt intuitively that quantum theory was incomplete and tried to demonstrate this via the EPR gedanken in 1935. As has been demonstrated in this report and in the report of Matveev and Matvejev the mathematics of uncertainty and the equations of SFT are remarkably similar and are general. It thus remains a historical quirk of fate that this generality and SFT did not emerge before WWII. It may be that the scientific world does not move with any haste. That may be seen as both a good and a bad thing — good in that no presumptuous errors are made but bad in that the world had to wait 75 years to finally begin to peer inside the photon with all the physical and biophysical knowledge that this contains.

REFERENCES

1. Hyland, G. J. and P. Rowlands, *Herbert Frohlich FRS: A Physicist Ahead of His Time*, 2nd Edition, University of Liverpool, 2008.
2. Matveev, V. N., *Into the Third Millennium without Physical Relativity*, CheRo Publishing House, Moscow, 2000.
3. Matveev, V. N. and O. V. Matvejev, "General physical uncertainty relations as a consequence of the lorentz transformation," *PIERS Proceedings*, Marrakesh, Morocco, March 20–23, 2011.
4. Fleming, A. H. J., "Electromagnetic self-field theory and its application to the hydrogen atom," *Physics Essays*, Vol. 18, No. 3, 265–285, 2005.
5. Fleming, A. H. J., "Self-field theory, analytic spectroscopy of the ordinary photon," *Proc. 2nd Electromagnetics Health and Environment Intl. Conf.*, 18–23, Wroclaw, Poland, 2007.
6. Fleming, A. H. J., *Self-field Theory — A New Mathematical Description of Physics*, Pan Stanford Publishing, to be published 2011.

General Physical Uncertainty Relations as a Consequence of the Lorentz Transformation

V. N. Matveev and O. V. Matvejev
Sinerta Closed Joint-Stock Company, Vilnius, Lithuania

Abstract— The uncertainty relations fall into the ranks of the most important quantum relations. It is believed that the uncertainty relation of momentum and coordinates, as well as the uncertainty relation of energy and time in practice are not observed in the macrocosm. The objective of the work at hand was to demonstrate the existence of general physical uncertainty relations that extend to macrobodies. A macroscopic object consisting of a rod equipped with a pair of synchronized clocks and a macroscopic object in and of itself performing the function of an ideal physical clock are examined. General physical relations are directly derived from Lorentz transformations for the case of the object's one-dimensional motion (along the X axis) — the uncertainty relation of the object's x coordinate and the projection of its impulse along the X axis, p_x, and the uncertainty relation of the object's observation time, t, and its energy, E. The relations take the form: $\Delta p_x \Delta x \geq H$ and $\Delta E \Delta t \geq H$. The H value in the relation has action dimensions and is dependent upon the precision of the object's clocks and/or upon the properties of the physical clock. Despite the interpretation of the concept of uncertainty being different from that in quantum mechanics, the relations derived in the limiting case with ideal physical clock take the form of $\Delta p_x \Delta x \geq h$ and $\Delta E \Delta t \geq h$, where h is the Planck constant.

1. INTRODUCTION

Uncertainty is a notion, which is not always interpreted identically [1, 2]. In physics of the macroworld there are inaccuracies of measurement results that cannot be eliminated by means of increasing measurement instrument accuracy. The uncertainty of the distance between two spheres that are located close to one another can serve as an example of this uncertainty. This distance remains uncertain with an accuracy of up to the dimensions of the spheres, even in the presence of ideal measurement accuracy, while the thing that remains unclear is what is meant by the sought distance — the distance between the centers of mass of the spheres, the distance between their geometric centers, the distance between the closest points of the spheres, or something else. Construing uncertainty in this manner is mentioned in extant literature, albeit in general terms. In this vein, for example, taking into account the fact that it is only possible to specify the location of a spatially extended body by determining the position of a single solitary point that belongs to it with some degree of uncertainty, the uncertainty of the position of a sphere determined by the position of its center, which equals the radius of this sphere, is written about in reference [3]. The uncertainty of specifying the moment in time of a process that does not occur instantaneously, but rather occupies a certain time interval, can serve as another example of an uncertainty of this type. These coordinate and time uncertainties, Δx and Δt, are precisely the ones that play a part in the uncertainty relations we derived.

2. MACROSCOPIC UNCERTAINTY SINGLE-TIME DATE

We will visualize a thin rod of proper length, L, at two points, a and b, on which synchronously running clocks, A and B, are installed at a distance of d from one another.

Let's say that clocks A and B, like the clocks appurtenant to the K^0 reference system, where the rod is at rest, show this system's time; i.e., the readings of clocks A and B are always in agreement with the readings of the K^0 system's clocks. The length, d, of section ab, which is located between points a and b, may be equal to or less than the rod length, L; i.e., the condition $L \geq d$ holds true in the general case. If $L > d$, then the rod will look something like this:

$$---------- A ----------B ----------$$

Here, the A and B characters conditionally designate clock A and clock B, while the broken line shows the body of the rod. If the distance, d, is equal to the rod length, L — i.e., if $L = d$, clocks A and B are then found at the ends of the rod. Let's say that rod R, which is positioned parallel to the X^0 axis of inertial system K^0, is at rest relative to this system and moves at a constant velocity, V', along the X' axis of another reference system, K' (the X^0 and X' axes of the K^0 and

K' systems slide along one another over the course of their relative motion). As follows from the Lorentz transformations, the difference in the readings $x'_{A,\,t'}$ and $x'_{B,\,t'}$ of clocks A and B situated in the points with cordinates $x'_{A,\,t'}$ and $x'_{B,\,t'}$ at a moment in time of t' for system K' equals

$$\tau_{B,\,t'} - \tau_{A,\,t'} = \frac{(x'_{B,\,t'} - x'_{A,\,t'})V'}{c^2\sqrt{1-(\frac{V'}{c})^2}}. \tag{1}$$

Introducing the notation $U' = V'/\sqrt{1-(\frac{V'}{c})^2}$ from formula (1) we obtain:

$$U' = \frac{c^2(\tau_{B,\,t'} - \tau_{A,\,t'})}{x'_{B,\,t'} - x'_{A,\,t'}}. \tag{2}$$

Thus, formula (2) can be used to find the value of U' and then the velocity V'. So far we tacitly proceeded on the basis of the assumption that clocks A and B of rod R run ideally. If the rate of the K' system clocks, the measured $x'_{B,\,t'} - x'_{A,\,t'}$ value, and the speed of light c value are as accurate as desired, the error in the U' value calculated using formula (2) will then be solely due to the existence of an absolute error, $\Delta(\tau_{B,\,t'} - \tau_{A,\,t'})$, in the difference of the $\tau_{B,\,t'} - \tau_{A,\,t'}$ readings of clocks A and B. In this instance, the $\Delta U'$ error, with allowance for formula (2), is expressed by the equality

$$\Delta U' = \frac{c^2\Delta(\tau_{B,\,t'} - \tau_{A,\,t'})}{x'_{B,\,t'} - x'_{A,\,t'}} \tag{3}$$

When the maximum absolute error of the difference in the readings of clocks A and B consists of the $\Delta\tau$ errors of each of these clocks — i.e., when $\Delta(\tau_{B,\,t'} - \tau_{A,\,t'}) = 2\Delta\tau$, it follows from equality (3) that:

$$(x'_{B,\,t'} - x'_{A,\,t'})\Delta U' = 2c^2\Delta\tau. \tag{4}$$

We will now imagine that the requirement of the single-coordinate nature of the specification of the location where rod R is situated at a moment in time of t' is satisfied. Let's say the essence of this requirement consists of using a single solitary x'_R coordinate to specify the location of the projection of rod R on the X' axis. This requirement can only be satisfied in part. For example, the coordinate of any point appurtenant to rod R can be specified as its x'_R coordinate and a reference to its uncertainty can accompany the specification of this coordinate. In particular, the coordinate of the geometric center of rod R, or the coordinate of its center of mass, can serve as the coordinate of this point. In such cases, the distance from the point with a coordinate of x'_R to the point of the rod's projection on the X' axis farthest away from it can be regarded as the uncertainty, $\Delta x'_R$, of the x'_R coordinate. When the position of rod R is specified in this manner, the x'_R coordinate indicates the location of one of a set of points of the projection of rod R that lies on the X' axis. If we give this point preference for one reason or another, the $\Delta x'_R$ uncertainty will then determine a range of point coordinates that, in the presence of other considerations, could also be regarded at the point coordinates of rod R. Since the length, $d' = d\sqrt{1-(V'/c)^2}$, of the rod's moving ab section within the K' system equals $x'_{B,\,t'} - x'_{A,\,t'}$, the uncertainty, $\Delta x'_{ab}$, of the x'_{ab} coordinate of section ab of rod R then equals $1/2(x'_{B,\,t'} - x'_{A,\,t'})$. Thus, formula (4) can be presented in the form

$$\Delta U'\Delta x'_{ab} = c^2\Delta\tau \tag{5}$$

Because $L \geq d$ in the general case, the $\Delta x'$ uncertainty of the x' coordinate of rod R within the arbitrary positioning of clocks A and B thereon ($\Delta x' = 1/2L'$) can then generally both equal and exceed the $\Delta x'_{ab}$ value. And since the relation $\Delta x' \geq \Delta x'_{ab}$ holds true, then in the general case of the arbitrary positioning of the clocks on the rod, formula (5) takes for an arbitrary system the form:

$$\Delta U_x\Delta x \geq c^2\Delta\tau \tag{6}$$

If the mass of rod R with clocks A and B is known without a doubt and equals M_R (here and further on, the concepts of Lorentz-invariant mass [4] will be used), relation (6) can be transformed into the relation $M_R\Delta U_x\Delta x \geq M_Rc^2\Delta\tau$ by multiplying its left-hand and right-hand members times M_R, whence, taking into account the fact that $M_RU_x = p_x$, we obtain $\Delta p_x\Delta x \geq M_Rc^2\Delta\tau$. Introducing the notation $H = M_Rc^2\Delta\tau$, then we obtain

$$\Delta p_x\Delta x \geq H. \tag{7}$$

3. MACROSCOPIC UNCERTAINTY SINGLE-POINT DATE

As follows from the Lorentz transformations, the difference in the readings $\tau_{A,x'}$ and $\tau_{B,x'}$ of clocks A and B of rod R coming to the point with coordinate x' at moments in time of $t'_{A,x'}$ and $t'_{B,x'}$ for system K' equals

$$\tau_{B,x'} - \tau_{A,x'} = \frac{t'_{B,x'} - t'_{A,x'}}{\sqrt{1 - (\frac{V'}{c})^2}}. \tag{8}$$

Introducing the notation $\Gamma' = 1/\sqrt{1 - (V'/c)^2}$ from formula (8) we obtain:

$$\Delta\Gamma' = \frac{\Delta(\tau_{B,x'} - \tau_{A,x'})}{t'_{B,x'} - t'_{A,x'}}$$

and then for the general case of the arbitrary positioning of the clocks on the rod $\Delta\Gamma\Delta t_x \geq \Delta\tau$, where Δt_x is an uncertainty of the moment of time t_x of location of rod R in the point with coordinate x'. By analogy with the uncertainty Δx of coordinate x we define here the uncertainty Δt_x as the value equal to $1/2(t'_{B,x'} - t'_{A,x'})$. Multiplying the left-hand and right-hand members of the inequation $\Delta\Gamma\Delta t_x \geq \Delta\tau$ times $M_R c^2$, bearing in mind that $\Delta\Gamma M_R c^2 = \Delta E$ and $M_R c^2 \Delta\tau = H$ we obtain

$$\Delta E \Delta t_x \geq H \tag{9}$$

4. PHYSICAL CLOCS AND THE CASE OF MICROSCOPIC UNCERTAINTY

Let's imagine that each of clocks A and B consists of two components, one of which, being artificial ("manmade"), performs the function of a display and provides discrete time readings, changing them in a keeping with external signals, while the other one — we will call it a physical clock — generates these signals in a natural, easy manner and controls the change in the display's readings. For the sake of clarity, we will visualize the second part of the physical clock as a piece of radioactive material with a long half-life (the material's radiant power can be regarded as constant for a sufficiently long time frame). If the display reacts to a specific portion, ε, of the physical clock material's absorbed gamma-radiation energy by changing its readings, then in the presence of a material radiant power than equals P, the frequency, v, of the change in the display readings will equal P/ε. We will call the portion the energy of the perceived physical clock signals. We will assume that, regardless of the quantity of the physical clock material, the display absorbs all of the energy radiated, and that each portion of the energy absorbed performs the function of a reading change signal that is perceived by the display. The frequency, v, of the physical clock materials signals perceived by the display, and accordingly the frequency of the change in the physical clock's readings, will then be proportional to the quantity of the physical clock's material. This means that if the frequency of the perceived signals equals v_0 in the presence of a physical clock material unit mass of m_0, it will then equal $M_0 v_0/m_0$ in the presence of a mass of M_0; i.e., $v = M_0 v_0/m_0$. Since the maximum absolute $\Delta\tau$ error of the readings of each of the clocks equals $1/v$, the following expression can be then derived:

$$\Delta\tau = \frac{m_0}{M_0 v_0}. \tag{10}$$

Taking the mass of the rod without the clocks to be negligible as compared to the mass of the physical clock material concentrated in clocks A and B, or assuming that the rod R consists entirely of the physical clock's material, the $2M_0$ value (since the mass of the material in both clocks equals $2M_0$) can be set to equal the mass, M_R, of rod R with clocks A and B. Taking this into account, it follows from the notation $H = M_R c^2 \Delta\tau$ and formula (10) that

$$H = \frac{2c^2 m_0}{v_0} \tag{11}$$

the relations (7) and (9) are formally transformed into the relations $\Delta p_x \Delta x \geq 2h$ and $\Delta E \Delta t_x \geq 2h$ via the simple substitution of the energy, hv_0, of a photon with a frequency of v_0 in place of the unit energy, $m_0 c^2$, of the physical clock in formula (11); i.e., by taking the unit mass of a photon, the v_0 frequency of which numerically equals the v_0 frequency of the signals of a hypothetical change in the clock readings as the physical clock. By the synchronous discrete stepped change of readings of

clocks A and B the error $\Delta(\tau_{B,t'} - \tau_{A,t'})$, taken as $2\Delta\tau$, can be reduced by half. In this instance, uncertainty relations take the form

$$\Delta p_x \Delta x \geq h \quad \text{and} \quad \Delta E \Delta t_x \geq h$$

The received relations do not reflect the statistical nature of the generation of the clock reading change signals; thus, when using this approach, reference can only be made to the order of the parameter present in the right-hand member of the relations and not its precise value.

5. CONCLUSIONS

The general physical relations derived are externally reminiscent of the known uncertainty relations of quantum mechanics; however, the physical essence of the values that go into the relations and that contain the relations themselves are different than those in quantum mechanics. However the relations prove to be connected to the Heisenberg relation, not only externally, but also internally. At first glance, the relations derived only hold true for the techniques of instantaneous and point observations of an object, and the uncertainties going into these relations consist exclusively of the uncertainties inherent in these techniques. In actuality, however, it is impossible to measure even the constant velocity of this rod R, equipped with clocks A and B, with absolute accuracy using conventional methods (based on the path traversed and the time), if the word combination "rod R with clocks A and B" is taken to mean a specific [5] object, the complement of characteristic traits of which includes the difference in the readings of clocks A and B (or the events that characterize this object).

REFERENCES

1. Tarbeyev, Y. V., V. A. Slayev, and A. G. Chunovkina, "Problems with using the international guide to the expression of uncertainty in measurement in Russia," *Izmeritelnaya Tekhnika [Measurement Techniques]*, No. 1, 69–72, 1997.
2. European Society for Analytical Chemistry/International Cooperation on Traceability in Analytical Chemistry (EURACHEM/CITAC) Guide Entitled "A quantitative description of uncertainty in analytical measurement" (2nd Edition, 2000) — Translated From the English. D. I. Mendeleyev Russian National Metrology Research Institute (RNMRI), St. Petersburg, 2002.
3. Sukhanov, A. D. and O. M. Golubeva, *Lectures on Quantum Physics*, Vysshaya Shkola [Higher School] Publishing House, Moscow, 54, 2006.
4. Okun, L. B., *Advances in the Physical Sciences (APS)*, No. 178, 541–555, 2008.
5. Matveev, V. N., *Into the Third Millennium without Physical Relativity*, CheRo Publishing House, Moscow, 2000.

Complete Imitation of the Special Theory of Relativity by the Means of the Classical Physics

V. N. Matveev and O. V. Matvejev
Sinerta Closed Joint-Stock Company, Vilnius, Lithuania

Abstract— Based on pre-Einstein classical mechanics, a theoretical model is constructed that describes the behavior of objects in a liquid environment that conduct themselves in accordance with the formal laws of the special theory of relativity. This model reproduces Lorentz contraction, time dilation, the relativity of simultaneity, the Doppler effect in its symmetrical relativistic form, and the twin paradox effects. The model makes it possible to obtain Lorentz transforms and to simulate Minkowski four-dimensional space-time. All the effects that simulate the effects of the special theory of relativity appear to be absolute in content, but relativistic in form. The relativistic nature of the model and the relativity of the physical effects within the framework of the proposed model are achieved by means of refusing to take the presence of an environment into account and introducing additional conditions. Once such condition consists of replacing the fact of the inequality of the speeds of information dissemination in opposite directions within a moving environment with the assumption of the equality of these speeds.

1. INTRODUCTION

From the moment that it first appeared [1] on up through the present time, Einstein's special theory of relativity has not been viewed as a direct consequence of classical mechanics, and for this reason, no serious attempts have been made to develop a special theory of relativity based on the principals of classical mechanics. True, formal techniques were presented in reference [2] — manipulations or machinations, as the author of this book himself calls them — that make it possible to obtain Lorentz transforms in acoustics. In the work at hand, we demonstrate that a significant number of relativistic effects can be simulated in an environment without manipulations and machinations, the fundamental means for which consist of classical mechanics.

2. SIMULATION OF TIME DILATABILITY WITHIN MOVING ELEMENTS

We will mentally picture a group of barges, R, at rest on the surface of a flat-bottomed water body with a depth of h. Let us suppose that there is a high-speed underwater shuttle with a speed of V that delivers sand from the floor to each of the barges. We will assume that the time required to move sand from the floor onto a boat and to offload it from the boat onto a barge is negligible as compared the shuttle's time of movement from the barge to the floor and back. Thus, the time required to deliver k shuttles of sand to the barge, Δt, is fixed using the simple formula $\Delta t(k) = 2\,\mathrm{kh/V}$. We will further assume that a group of barges, R', is also present on the surface of the water body that are drifting on the water in the same direction at a speed of $v\,(v < V)$. A high-speed shuttle is also delivering sand from the floor to each of the drifting barges via the shortest route. In this instance, the vertical component, V_Z (the shuttle submersion and surfacing speed), of the V velocity value is fixed using the formula $V_Z = V\sqrt{1-(v/V)^2}$; thus, to deliver k' boats of sand to a barge moving at a speed of v requires a time of:

$$\Delta t(k') = \frac{2k'h}{V\sqrt{1-(v/V)^2}}. \tag{1}$$

Let us suppose that meters of the quantities of sand reaching the barges and identical clocks with identical faces are placed on the barges. The clocks are set into operation by the sand quantity meters, so that they "tick" at a frequency that is proportionate to the frequency of shuttle movement. The clock hands on the barges drifting at a velocity of v move $1/\sqrt{1-(v/V)^2}$ time more slowly than the clock hands on the barges at rest. We will assume that the speed of movement of the clock hands on the barges at rest equals the speed of movement of the hands on "land-based" clocks — the clocks of outside observers — i.e., we find that the time of t, including its numeric values, also passes identically on the barges at rest. In this instance, we suppose that the clock readings on different barges at rest can differ from one another at a given moment in time (similar to the way that the readings of "land-based" clocks can differ in different time zones) until these

readings are no longer synchronized. We will designate the clock reading on a specific barge at rest, r, using the attribute t_r. Unlike our time, t, and the time on the barges at rest, t, we will call the time fixed by the clock readings on barges moving at a speed of v simulated time and will designate it using the attribute t' (with a prime sign). Concerning the simulated time on the drifting barges, t', we will say that it passes more slowly than the time on the barges at rest, t. We will designate the t' clock reading on a specific barge in motion, r', using the attribute $t'_{r'}$ (with prime signs), assuming that, as in the case of the barges at rest, the clock readings on the other drifting barges may differ from one another and from the $t'_{r'}$ readings up until the moment that they become synchronized. We will assume that the signals from the sand quantity meters in the form of timing pulses proceed not only to the clocks, but also to all the hardware without exception that it located on the barges, thereby setting them into operation at the same rate. The rate of operation (the response rate) of all the hardware on the barges in motion will then be slower than the rate of operation of the hardware on the barges at rest by $1/\sqrt{1-(v/V)^2}$ times.

Let us assume that time intervals of $\Delta t(\Delta n_{time})$ and $\Delta t'$ $(\Delta n'_{time})$ are used as the units of measurement on the barges at rest and the barges in motion, over the course of which the sand quantity meter readings are increased by Δn_{time} and $\Delta n'_{time}$, respectively, so that, being unified and standard, $\Delta n_{time} = \Delta n'_{time}$. In this case, based on our observation results, the Δt time interval and the $\Delta t'$ simulated time interval for any pair of barges in motion relative to one another between two identical events that we recorded will be linked by the correlations

$$\Delta t' = \Delta t\sqrt{1-(v/V)^2} \quad \text{and} \quad \Delta t = \Delta t'/\sqrt{1-(v/V)^2} \tag{2}$$

If the unit of measurement of the Δt (Δn_{time}) time on the barges at rest has the same name as the unit of measurement of the $\Delta t'$ $(\Delta n'_{time})$ simulated time on the barges in motion, for example, if both units are called a minute, then according to our observations, it can be said that a minute of simulated time on the barges in motion lasts $1/\sqrt{1-(v/V)^2}$ times longer than a minute of time on the barges at rest. Let us suppose that accurate documented information (on tangible media) concerning the clock readings on one barge are transmitted to another barge, either directly when these barges meet or by high-speed support boats that cruise on the water surface at a speed of V. Let us assume that one of the tasks of the hardware on the r and r' barges consists of experimentally confirming the fact of the movement of the r' barge without making contact with the water environment and having information concerning the slowness of the processes on the barge moving through the water environment by means of comparing the passage of time or the rates of hardware operation on the r and r' barges. As strange as it may be, it is impossible to solve this seemingly simple problem under the conditions specified. First of all, it is not possible to ascertain the slowness of the rate of operation on the barge in motion using any of the instruments that are a part of the hardware on each barge in motion due to the synchronism of the operation of these instruments with the operation of the other instruments and devices. Neither is it possible to ascertain slowness by documentarily tracking the processes on a barge in motion from a barge at rest when a speedboat is used to transfer documented information on operations from barge to barge. If the barges are inertial and they generally do not meet directly, or they only meet once, it is then necessary to transfer information at a distance using a boat at least one time. However, due to the finiteness of the boat's speed, there is a delay in receiving information from the other barge, and a document indicating, for example, the clock reading on the other barge reaches this barge when the clock reading on that other barge is not the same as it was at the time that the boat was dispatched from it. The consequence of this effect is such that, during the transfer of information by boat, it is only possible to obtain symmetrical results that do not make it possible to detect the difference in the clock running rates on the barge at rest, r, and the barge in motion, r'. For example, in making one of the r and r' barges noninertial, if a repeat meeting is ensured for the barges, time dilation then occurs on the noninertial barge, which may also be the r barge, and does not univocally confirm the fact of the r' barge's movement. Or, if boats are dispatched from the r barge to the r' barge with a frequency of f_r, and boats are dispatched from the r' barge to the r barge with a frequency of $f'_{r'}$ (in simulated time) that numerically equals the f_r frequency, then, as is easy to demonstrate, when the barges draw close, the $f'_{r'\leftarrow r}$ and $f_{r\leftarrow r'}$ boat arrival frequencies for the r' and r barges, respectively, are fixed by the symmetrical formulas $f'_{r'\leftarrow r} = f_r\sqrt{1+v/V}/\sqrt{1-v/V}$ and $f_{r\leftarrow r'} = f'_{r'}\sqrt{1+v/V}/\sqrt{1-v/V}$. Being similar to the formulas for the relativistic Doppler effect, these formulas do not make it possible to detect the difference in the clock rate on the r and r' barges.

3. SIMULATION OF THE CONTRACTION OF THE DISTANCE BETWEEN MOVING ELEMENTS

We will tie the Σ and Σ' Cartesian coordinate systems to the groups of barges at rest, R, and in motion, R', respectively, with mutually parallel axes of X and X', Y and Y', and Z and Z'. We will align the Z and Z' system axes perpendicular to the water surface and the X and X' in the direction of movement of the group in motion, R', while we will trace the Y and Y' axes perpendicular to the X, X' and Z, Z' axes, which it is acceptable to do in orthogonal Cartesian coordinate systems. We will assume that the hardware of each of the barges, the makeup of which includes the boats attached to each barge, is capable of independently measuring the distance from a given barge to specific points of the coordinate system tied to it without the involvement of the hardware of the other barges and without the synchronization of the clocks on the different barges. The distance is measured using long rulers and tape measures. Let us suppose that, within the Σ coordinate system, the hardware of a barge, r, located at the origin of coordinates, O, determines the distance from the O coordinate origin to a certain arbitrarily positioned point, a, within the Σ system in the following manner. A speedboat is dispatched from barge r to point O, which, upon arriving at point a, goes back to point O. The boat trip time there and back, Δt_{OaO}, is determined using the clock readings on barge r at the moments of the boat's departure and return, then the distance is calculated using the expression $\frac{1}{2}\tilde{V}\Delta t_{OaO}$, where $\tilde{V}$ is the average speed of the boat along the route from point O to point a and back. It stands to reason that, within the Σ system, the average speed, $\tilde{V}$, equals the V velocity value. We will designate the distance between point O and point a that the hardware of barge r measures in this manner using the attribute $l(\frac{1}{2}\Delta t_{OaO})$. We will designate this same distance, but one that we measured or calculated by any available means, using the attribute l_{Oa}. The $l(\frac{1}{2}\Delta t_{OaO})$ distance and the l_{Oa} distance only differ from one another in the means by which and the location at which they are determined.

We will assume that, within the Σ' coordinate system, the hardware of barge r', which is located at a coordinate origin of O', determines the distance from the O' coordinate origin to point a' of the Σ' system in precisely the same way that this is done in the Σ system. Let us suppose that a value equaling the product of $\frac{1}{2}\tilde{V}'\Delta t'_{O'a'O'}$ is by definition regarded as the distance measured in this way in the case at hand, $l'(\frac{1}{2}\Delta t'_{O'a'O'})$. Here, $\tilde{V}'$ is simulated; i.e., it is expressed by way of the simulated time, t', the average speed of the boat en route from point O' to point a' and back numerically equals the $\tilde{V}$ velocity value, and consequently the V velocity value, while $\Delta t'_{O'a'O'}$ is the simulated time of movement of the boat along the $O'a'O'$ route. We will call the distance that the hardware of barger' determines in this manner the simulated distance, $l'(\frac{1}{2}\Delta t'_{O'a'O'})$. If a speedboat moves along the Y' axis between point O' and a point lying on the Y' axis with a coordinate of y' (we will call this point the y' point), the V_Y component of the boat's speed, V (the speed of movement of the boat along the segment of a straight line that connects points O' and y'), which we extrinsically fix, will then equal $V\sqrt{1-(v/V)^2}$. Based on our calculations, the conventional distance, $l_{O'y'}$, that we fix between points O' and y' of the moving system, Σ', equals $\frac{1}{2}V\sqrt{1-(v/V)^2}\Delta t_{O'y'O'}$, while according to data from the hardware of barge r', the simulated distance, $l'(\frac{1}{2}\Delta t'_{O'y'O'})$, between points O' and y' equals $\frac{1}{2}\tilde{V}'\Delta t'_{O'y'O'}$. Since $\Delta t'_{O'y'O'} = \Delta t_{O'y'O'}\sqrt{1-(v/V)^2}$ according to formula (2), while $\tilde{V}'$ by definition equals V, then

$$l'\left(\frac{1}{2}\Delta t'_{O'y'O'}\right) = l_{O'y'}. \tag{3}$$

According to our data, during the movement of a speedboat between point O' and a point with a coordinate of x' that lies on the X' axis (the x' point), the speeds of movement of the boat in the opposite directions relative to these points equal $V-v$ and $V+v$. When the conventional distance between points O' and x' equals $l_{O'x'}$, the time of movement of the boat from point O' to point x' and back, $\Delta t_{O'x'O'}$, equals $l_{O'x'}/(V-v) + l_{O'x'}/(V+v)$; i.e.,

$$\Delta t_{O'x'O'} = \frac{2l_{O'x'}}{V(1-v^2/V^2)}. \tag{4}$$

The conventional average sped of movement of the boat along the X' axis relative to points O' and x' along the route there are back, $\tilde{V}_{X'}$ equals $2l_{O'x'}/\Delta t_{O'x'O'}$, or taking the previous equation

into account,

$$\tilde{V}_{X'} = V(1 - v^2/V^2). \tag{5}$$

According to our calculations, the conventional distance between points O' and x' of the moving system Σ, $l_{O'x'}$, equals $\frac{1}{2}\tilde{V}_{X'}\Delta t_{O'x'O'}$, while according to the calculations of the hardware on barge r', the simulated distance between them, $l'(\frac{1}{2}\Delta t'_{O'x'O'})$, equals $\frac{1}{2}\tilde{V}'\Delta t'_{O'x'O'}$. Since $\tilde{V}_{X'} = V(1-v^2/V^2)$ according to formula (5) and $\Delta t_{O'x'O'}$ equals $\Delta t'_{O'x'O'}/\sqrt{1-(v/V)^2}$ according to formula (2), then

$$l'\left(\frac{1}{2}\Delta t'_{O'x'O'}\right) = l_{O'x'}/\sqrt{1-(v/V)^2}. \tag{6}$$

4. SYNCHRONIZATION OF R AND R' GROUP (Σ AND Σ' SYSTEM) CLOCKS

We will imagine that the readings of the R group clocks are synchronized in such a manner that they are identical at any moment of our time, t. We will designate the group R time fixed by these readings that are identical for all the group R barges using the attribute t_R. Let us assume that the group R' clocks are also synchronized in such a manner that the sameness of the clock readings on the various R' group barges is ensured at any moment in our time. We will designate the group R' synchronized time using the attribute $t'_{R'}$. Furthermore, we will assume that at a moment in time when the O and O' coordinate origins of the Σ and Σ' systems are located at a single point, the clocks of the barges in both groups will have a zero reading. Thus, it follows from formula (2) that the R and R' group clock readings at any subsequent moment in time at any point within the water body will be linked to one another by the correlations

$$t'_{R'} = t_R\sqrt{1-(v/V)^2} \quad \text{and} \quad t_R = t'_{R'}/\sqrt{1-(v/V)^2} \tag{7}$$

Not being dependent upon coordinates and unequivocally corresponding to one another, the t_R and $t'_{R'}$ clock readings ensure the single-valuedness (the "absoluteness") of simultaneity in both barge groups. When synchronized clocks are present in the R and R' groups, it is possible to measure distances, lengths, and coordinates in each of these groups not only using the pseudolocation method, but also via the conventional means of combining and comparing them to one another, or using proper length units. Taking into account the fact that $l(O'x') = x - vt$, where x is the coordinate of point x' in the Σ system, and assuming that $l'(\frac{1}{2}\Delta t'_{O'x'O'}) = x'$, then from Equation (6) we obtain the forward transform of the coordinates

$$x' = (x - vt_R)/\sqrt{1-(v/V)^2} \tag{8}$$

The simulated velocity, v', of point O in the Σ' system equals $-x'_O/t'_{R'}$, where x'_O is the coordinate of point O in the Σ' system. Hence, taking x' and $t'_{R'}$ from formulas (7) and (8), we obtain the correlation $v' = v/(1 - v^2/V^2)$. Substituting $v = v'(1 - v^2/V^2)$ in formula (8), we obtain the transform

$$x/\sqrt{1-(v/V)^2} = x' + v't'_{R'}. \tag{9}$$

Let us suppose that in the groups at rest and in motion, R and R', the distances $l(\frac{1}{2}\Delta t_{space})$ and $l'(\frac{1}{2}\Delta t'_{space})$ of the standards constructed from pairs of barges are respectively used as the distance measurement units. We will assume that time intervals of Δt_{space} and $\Delta t'_{space}$ are required in order for a speedboat to traverse each of these distances there and back, so that the numerical values of these intervals are standardized and equal one another. If the $l(\frac{1}{2}\Delta t_{space})$ distance unit of the standard at rest has the same name as the $l'(\frac{1}{2}\Delta t'_{space})$ simulated distance unit of the standard in motion, for example, if both units are called a kilometer, then by analogy with formulas (3) and (6), the simulated and conventional lateral kilometers will equal one another, while the simulated longitudinal kilometer in motion will be $1/\sqrt{1-(v/V)^2}$ times shorter than the conventional kilometer at rest.

5. SIMULATION OF THE SYMMETRY OF RELATIVISTIC EFFECTS

In order to ensure the conditions of synchronism that are accepted in the special theory of relativity, it is necessary to simulate the synchronization of the R' group (Σ' system) clocks in such a manner that the speeds of movement of a boat from the O' coordinate origin to point x' and back to the O' coordinate origin are identical. It is not difficult to demonstrate that the equality of the boat's

speeds in opposite directions within the Σ' system can be achieved if, at the moment of the boat's arrival at point x', $t'_{R'}$, the reading of the clocks at this point equal not $t'_{R'}$, but rather $t''_{R'}$, which is $x'v/V^2$ shorter than $t'_{R'}$; i.e., if the equality $t''_{R'} = t'_{R'} - x'v/V^2$ is ensured. In this instance, the v'' and V'' velocities expressed through a time of $t''_{R'}$ will respectively equal the v and V velocities; i.e., $v'' = v$ and $V'' = V$. Taking this into account, from formula (9) and the previous arguments, it is easy to obtain the transforms

$$x = (x' + v''t''_{R'})/\sqrt{1-(v''/V'')^2}, \quad y = y', \quad \text{and} \quad t = (t''_{R'} + x'v/V^2)/\sqrt{1-(v''/V'')^2}, \tag{10}$$

then the transforms

$$x' = (x - vt)/\sqrt{1-(v/V)^2}, \quad y' = y, \quad \text{and} \quad t''_{R'} = (t - xv/V^2)/\sqrt{1-(v/V)^2}. \tag{11}$$

Transforms (10) and (11) do not differ from the Lorentz transforms, producing all the consequences that stem from this. The R and R' group hardware, which perceives its own proper longitudinal kilometer and its own proper second as representative, perceives the geometric dimensions of the objects of another group, including the dimensions of the kilometer standard, as contracted and the time as dilated.

6. CONCLUSION

The model proposed in the work at hand for simulating the special theory of relativity reveals the possibility of using the fundamentals of classical mechanics to simulate relativistic laws in an environment, which are described using constructs taken from the world environment. The question of the existence of a world environment itself is not addressed in this work, since the possibility of simulating the relativistic phenomena of a nonether world in an environment does not serve as proof of the existence of ether.

REFERENCES

1. Einstein, A., "Zur elektrodynamik bewegter Körper," *Annalen der Physik*, Vol. 4, No. 17, 891–921, 1905.
2. Boss, B., "Lectures on mathematics," *The Equations of Mathematical Physics*, Vol. 11, Publishing House, Librocom, Moscow, 2008.

FET-based Frequency Multiplier S-MMICs up to 440 GHz

I. Kallfass[1, 2], **H. Massler**[2], **A. Tessmann**[2], **and A. Leuther**[2]

[1]Karlsruhe Institute of Technology, Institut für Hochfrequenztechnik und Elektronik, Karlsruhe, Germany
[2]Fraunhofer Institute for Solid State Physics, Tullastraße 72, Freiburg, Germany

Abstract— We report on the design and performance of frequency multiplier submillimeter-wave monolithic integrated circuits (S-MMICs) that operate up to 440 GHz. The S-MMICs are based on state-of-the-art metamorphic high electron mobility transistor technology (mHEMT) with gate lengths down to 35 nm and cutoff frequencies f_T and $f_{\max}$ of 515 and 900 GHz, respectively. A class-B FET doubler circuit achieves −14.6 dBm of output power at 400 GHz, when driven with 2.5 dBm input power. An overview of mHEMT-based frequency multiplier performance in the entire millimeter-wave range is given.

1. INTRODUCTION

Active electronic integrated circuits have today reached operating frequencies well into the submillimeter-wave frequency range [1, 2]. Such S-MMICs, based on HEMTs exploiting the high-speed characteristics of InAlAs/InGaAs channels on InP substrates or, in the metamorphic approach, on GaAs substrates, offer such important advantages as the on-chip integration with other functional blocks like e.g., amplifiers, together with high conversion efficiency and ease of module integration. Frequency sources are required to provide the transmit signal of active systems as well as the local oscillator signal for frequency conversion in heterodyne topologies comprising mixers. As an advantageous alternative to fundamental oscillators, frequency multiplier chains in combination with high-quality oscillators can be employed to generate signals at high millimeter-wave and submillimeter-wave frequencies. The highest reported output frequencies to-date obtained by transistor-based frequency multipliers is 300 GHz at Jet Propulsion Laboratories [3]. In this paper, the design and performance of a frequency doubler utilizing mHEMT transistor technology for submillimeter-wave frequency generation is discussed.

2. THE 35 NM METAMORPHIC HEMT TECHNOLOGY

The frequency doubler S-MMIC to 440 GHz is designed and realized in a 35 nm gate length mHEMT technology using an $In_{0.52}Al_{0.48}As/In_{0.80}Ga_{0.20}As$ single channel on a linearly-graded metamorphic $In_xAl_{0.48}Ga_{0.52-x}As$ ($x = 0 \ldots 0.52$) buffer on 100 mm semi-insulating GaAs wafers [4]. The active devices consist of e-beam defined 35 nm Pt-Ti-Pt-Au T-gates. Their maximum channel current $I_{d,\max}$ is 1600 mA/mm. At a drain voltage of $V_D = 1$ V, a peak transconductance of more than 2500 mS/mm is measured. An extrinsic transit frequency of $f_T = 515$ GHz is extrapolated from the on-wafer measured current gain for a 2×10 µm common source HEMT. For the same device size, we calculate a maximum oscillation frequency $f_{\max}$ of approximately 900 GHz from both, the measured Mason's unilateral gain (MUG) and the maximum stable gain (MSG). Circuits are designed in a grounded coplanar (GCPW) environment, where transmission lines are realized within a reduced ground-to-ground plane spacing of 14 µm. After frontside processing, the GaAs substrates are thinned to 50 µm and provided with 20 µm dry-etched via holes for the suppression of parasitic substrate modes.

3. FREQUENCY MULTIPLIER DESIGN

The frequency doubler uses a single field-effect transistor (FET) device biased under class B conditions, i.e., the gate voltage is set close to the threshold voltage, such that a strong second-order harmonic component is present in the output current waveform of the transistor. The drain voltage is set to a typical active operating point at $V_D = 1$ V. The input of the transistor is matched to the fundamental input frequency f_{in} by a three-element matching network, comprising a series stub line, a shunt stub line and a series capacitance. At the transistor output, the fundamental frequency is suppressed by an open-ended $\lambda/4$ stub for the fundamental frequency. The purpose of the remaining elements in the output matching network is to guarantee the impedance match to the desired second-order harmonic frequency and to provide the drain bias voltage. Figure 1 shows a simplified schematic and the chip photograph of the frequency-doubler employing a transistor with 2×10 µm gate width. The S-MMIC is realized in 35 nm mHEMT technology and has a chip size of 0.5×0.5 mm^2, limited mainly by the probe pad dimensions.

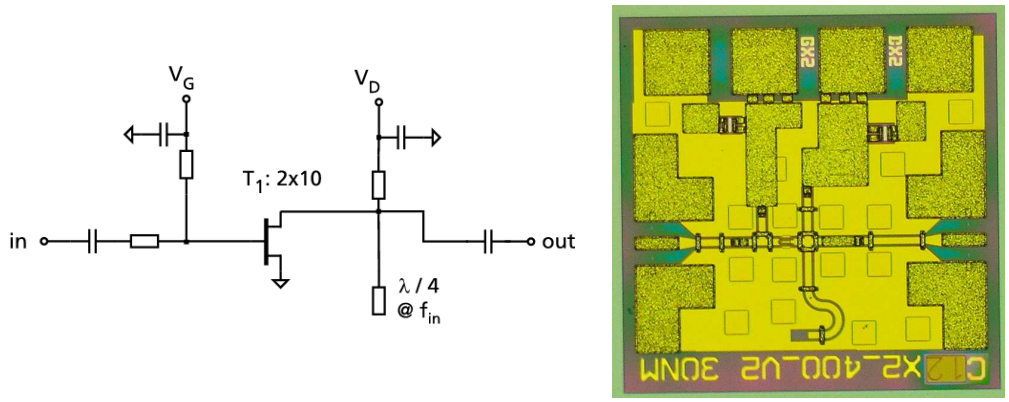

Figure 1: Simplified circuit schematic and chip photograph of the class-B FET frequency doubler to 440 GHz, realized in 35 nm mHEMT technology with a chip size of $0.5 \times 0.5\,\mathrm{mm}^2$.

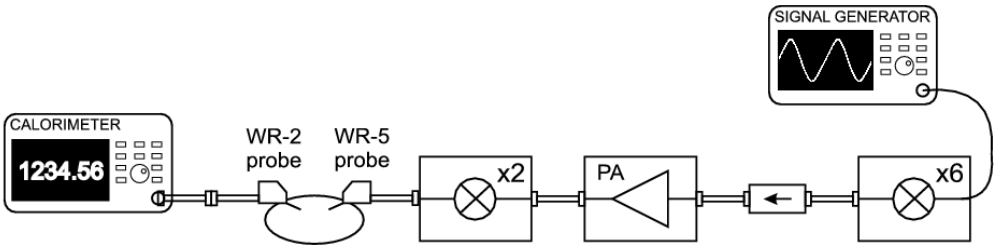

Figure 2: On-wafer measurement setup for the 440 GHz frequency doubler.

4. MEASUREMENT SETUP AND MULTIPLIER PERFORMANCE

The S-MMIC's on-wafer characterization involves careful power level normalization, taking into account losses in the coplanar measurement probes in WR-2 band (325–500 GHz). S-parameter measurements for probe characterization are carried out using two Oleson WR-2 frequency extensions to a standard network analyzer.

The measurement setup to characterize the frequency doubler in terms of its output power is sketched in Figure 2. The input power to the device under test is created by a commercial WR-5 (140–220 GHz) frequency doubler, who in turn is driven by an in-house power amplifier in W-band. The W-band signal is generated by a commercial source module. At the output, we employ an Erikson calorimeter to measure the total power generated at the output of the frequency doubler. The fundamental power component around 200 GHz lies below the cutoff frequency of the WR-2 waveguide. Higher order products at around 300 GHz and higher can propagate in the waveguide and will be registered by the calorimeter, but typically the most important unwanted component in this type of frequency multiplier is the fundamental frequency.

The measured output power P_{out} at different frequencies is shown as a function of the input power P_{in} in Figure 3. At 400 GHz, the doubler generates a P_{out} of -14.6 dBm when driven with 2.5 dBm P_{in}. The same output power is reached at 380 and 420 GHz, albeit at different input power levels. At 440 GHz, we are able to generate a maximum P_{in} of -2.5 dBm and the doubler reaches -15 dBm P_{out}. However, this P_{in} is not sufficient to drive the doubler into compression. The required input power for maximum output power decreases with increasing frequency in the observable frequency range. This indicates that the most favorable impedance matching conditions of this S-MMIC are met at 440 GHz or higher, and better performance can be expected still at frequencies above 440 GHz. As shown in the next chapter, an mHEMT-based frequency doubler to 200 GHz achieves an output power of about 1 dBm without post-amplification. This level is enough to drive the frequency doubler into saturation at 400 GHz and above.

5. OTHER MHEMT-BASED FREQUENCY MULTIPLIERS

A number of frequency multiplier MMICs for other millimeter-wave frequency ranges have been realized in IAF mHEMT technology. A compilation of the achieved output power versus frequency is shown in Figure 4. Table 1 summarizes their performance in terms of frequency range, mul-

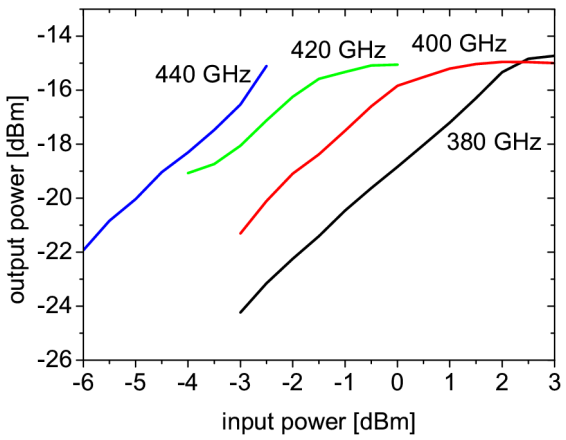

Figure 3: Measured output power versus input power and at different output frequencies.

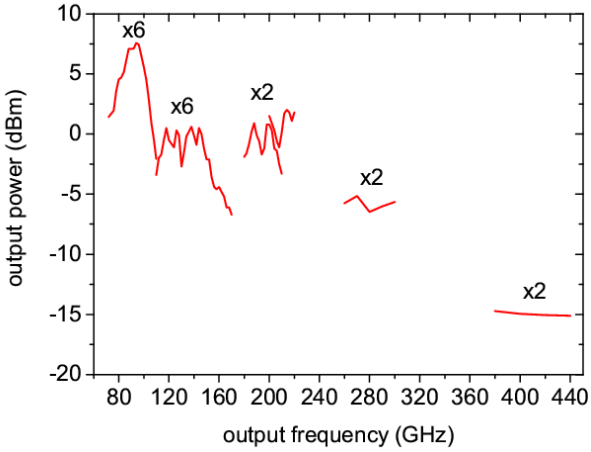

Figure 4: Comparison of the obtained output power versus output frequency from even-order frequency multiplier MMICs realized in IAF mHEMT technology.

Table 1: Summary of mHEMT-based frequency multiplier performance.

f_{out}/GHz	n	P_{out}/dBm	G_{conv}/dB
78–104	6	7.0	6.6
105–152	6	0	−10
160–210	2	1	−16
260–300	2	−6	−9
380–440	2	−14.6	−17.1

tiplication factor n and conversion gain. Balanced active multipliers-by-six [5, 6] achieve 7 and 0 dBm in the range from 78–104 and 105–152 GHz, respectively. Stand-alone frequency doublers without post-amplification and a similar circuit architecture to the one presented above achieve 1 and −6 dBm at 160–210 and 260–300 GHz, respectively. Up to 200 GHz, the MMICs are realized in either 100 or 50 nm mHEMT technology, featuring cutoff frequencies $f_T/f_{\max}$ of 220/300 and 375/600 GHz, respectively.

6. CONCLUSIONS

A class-B FET frequency doubler reaching submillimeter-wave frequencies in the range from 380 to 440 GHz with more than −15 dBm output power was presented. Further mHEMT-based frequency multiplier MMICs include active multipliers into W-band and frequency doublers to 200 and 300 GHz, completing a full MMIC-based multiplier chain for frequency generation up to 440 GHz.

ACKNOWLEDGMENT

We express our gratitude to our colleagues in the IAF technology department for their excellent contributions during epitaxial growth and wafer processing. This work was supported by the German Federal Ministry of Defense (BMVg) and the Bundeswehr Technical Center for Information Technology and Electronics (WTD81).

REFERENCES

1. Deal, W. R., K. Leong, X. B. Mei, S. Sarkozy, V. Radisic, J. Lee, P. H. Liu, W. Yoshida, J. Zhou, and M. Lange, "Scaling of InP HEMT cascode integrated circuits to THz frequencies," *Proc. IEEE Compound Semiconductor IC Symposium*, 195–198, Monterey, Oct. 2010.
2. Tessmann, A., A. Leuther, V. Hurm, H. Massler, M. Zink, M. Riessle, and R. Loesch, "High-gain submillimeter-wave mHEMT amplifier MMICs," *Proc. IEEE MTT-S Int. Microwave Symp.*, 33–36, Anaheim, May 2010.

3. Samoska, A. P. L., "Advanced HEMT MMIC circuits for millimeter and submillimeter-wave power sources," *Proc. Far Infrared, Submillimeter, and Millimeter Detector Technology Workshop Monterey, CA, USA*, Apr. 2002.
4. Leuther, A., A. Tessmann, I. Kallfass, H. Massler, R. Loesch, M. Schlechtweg, M. Mikulla, and O. Ambacher, "Metamorphic HEMT technology for submillimter-wave MMIC applications," *Proc. 22nd International Conference on Indium Phosphide and Related Materials*, 425–429, Piscataway, NJ, May 2010.
5. Kallfass, I., H. Massler, A. Tessmann, A. Leuther, M. Schlechtweg, and G. Weimann, "A broadband frequency sixtupler MIMIC for the W-band with > 7 dBm output power and > 6 dB conversion gain," *Proc. IEEE MTT-S Int. Microwave Symp.*, 2169–2172, Honolulu, Hawai, Jun. 2007.
6. Kallfass, I., A. Tessmann, H. Massler, P. Pahl, and A. Leuther, "An all-active MMIC-based chip set for a wideband 260–304 GHz receiver," *Proc. 5th European Microwave Integrated Circuit Conf.*, Paris, Sep. 2010.

Compact Non-degenerate Dual-mode Filter with Adjustable Transmission Zero

Abdel Fattah Sheta, Majeed Alkanhal, and Zeyad Alhekail
Department of Electrical Engineering and Prince Sultan Advanced Technologies Research Institute (PSATRI), King Saud University, P. O. Box 800, Riyadh 11421, Saudi Arabia

Abstract— In this paper, a band pass filter with adjustable transmission zeros is presented. The proposed filter structure is based on a non-degenerate dual-mode resonator loaded by either varactor diodes or open circuit stubs at its opposite corners. These loading techniques allow adjusting the transmission zeros either on the upper stopband or on the lower stopband. The effect of open stubs and varactor diodes loading is inspected and design curves for the proposed structure are deduced. Based on that, a filter is designed and implemented on Duroid substrate with 10.3 dielectric constant and 0.635 mm thickness to validate the proposed concept. Simulation and experimental results are, then, analyzed and compared.

1. INTRODUCTION

Compact, light weight, low cost and high selective filters attract much attention for recent wireless systems. In many applications, sharp cutoff rate filter response is usually required. The conventional way to achieve such response is to use higher order filters which lead to large, complex, and expensive structures. However, sharp cutoff rate can also be achieved using transmission zero concept [1–6]. In some cases, such as in cellular communications, microwave filters should be more selective on one side of the passband than the other [7]. On other word, a transmit filter should have high attenuation in the receive band and a receive filter should have high attenuation in transmit band. For this case, transmission zero concept would be the best suited.

Non-degenerate dual-mode filter [8] has asymmetric frequency response with the transmission zero located on the upper stopband. The fractional bandwidth can be adjusted from about 5% to 25%. The filter can be fed asymmetrically at opposite corners.

In this paper, two methods to control the filter transmission zero are proposed and investigated. The first is the use of open circuit stubs loading with appropriate stub lengths. The second is to control the position of the trasnmision zero electronically using varactor diode loading. The concept of the non-degenerate dual-mode filter is briefly introduced in the next section. The analysis of the non-degenerate dual-mode resonator loaded with open circuit stubs for transmission zero adjustment is also presented in this section. The effect of varactor loading is studied in Section 3. Experimental results are discussed in Section 4 followed by concluding remarks in Section 5.

2. FILTER CONFIGURATION AND OPEN CIRCUITED STUBS LOADING

The proposed structure is simply a dual-mode square-patch resonator, with four slots etched in a symmetrical shape loaded at opposite corners by open circuit stubs as shown in Fig. 1. The square patch length is W, while the slots have equal lengths L and widths S. The fields within the conventional square patch resonator can be expanded by the TM^z_{mn0} modes, where z is perpendicular to the ground plane [10]. The two fundamental degenerate modes correspond to TM^z_{100} and TM^z_{010} and the first higher order mode is the TM^z_{110}. These three modes can be excited simultaneously by asymmetrical non-orthogonal feed lines. The resultant modes of the slotted patch can be considered as perturbed types of that of the unslotted square patch [8]. It has also been reported that cutting slots in symmetrical shape as shown in Fig. 1 will decreases the resonance frequencies of the three modes but the resonance frequency of the mode TM^z_{110} decreases faster. Therefore bandpass filter behavior with fractional bandwidth up to 25% can be obtained using specific slots dimensions [8, 9]. The resultant size and bandwidth decrease as the slots length increases.

The modes TM^z_{100} and TM^z_{010} have an electric wall along the diagonal between the non-feeding corners. However, the mode TM^z_{110} has a magnetic wall along the same diagonal. Therefore loading the patch at this diagonal will affect only the resonance frequency of the mode TM^z_{110} (f_2) and has almost no effect on the resonance frequency of the modes TM^z_{100} and TM^z_{010} (f_1). The analysis is carried-out for a resonator designed on a Duroid dielectric substrate of 10.3 dielectric constant and 0.635 mm thickness. The dimensions of the simulated patch are $W = 14$ mm, $L = 5$ mm, and $S = 0.5$ mm. Denote f_1 as the resonance frequency of the degenerate modes TM^z_{100} and TM^z_{010}

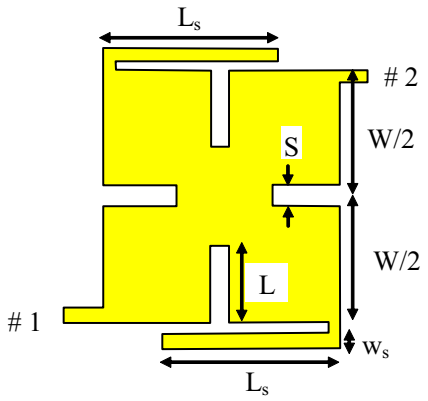

Figure 1: Non-degenerate dual-mode microstrip square patches resonator loaded at its opposite corners.

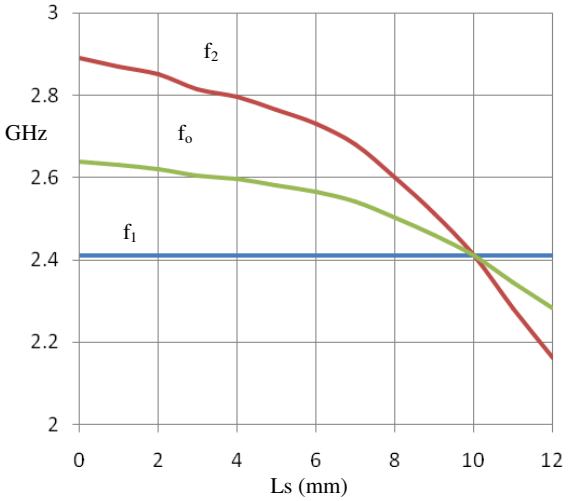

Figure 2: Effect of stubs loading on the resonance frequencies f_1 and f_2 of the structure in Fig. 1 with $W =$ 14 mm, $L = 5$ mm, $S = 0.5$ mm, on Duroid substrate with $\varepsilon_r = 10.3$ and thickness 0.635 mm, $Ls = 0.5$ mm.

and f_2 as the resonance frequency of the mode TM^z_{110}. Therefore, the open circuit stubs-loading increases the effective length of the mode TM^z_{110} and hence lowers its resonance frequency f_2 and also controls the position of the transmission zero accordingly. The effect of the stubs length Ls on the resonance frequencies f_1 and f_2 is shown in Fig. 2. This effect is studied using the IE3D simulation of the structure whose parameters are just mentioned. The stub width is selected to be 0.5 mm. The excitation technique proposed in [8] is used here to predict the resonance frequencies, f_1 and f_2.

No effect is observed on the resonance frequency of the modes TM^z_{100} and TM^z_{010}. Their resonance frequency f_1 is constant and equal to 2.41 GHz for stubs length change from 0 to 12 mm. However, the first higher order mode TM^z_{110} is highly affected and its resonance frequency, f_2, decreases from 2.89 GHz for $Ls = 0$ mm to 2.17 GHz for $Ls = 12$ mm. It is observed that the transmission zero remains on the upper stopband whenever the resonance frequency f_2 is greater than f_1 and become on the lower stopband when f_2 is less than f_1. The center frequency of the filter can be approximated as the geometric mean of f_1 and f_2. Bandwidth selection can be approximately chosen around the center frequency fo from Fig. 2. The procedure given in [8, 9] can also be used for this selection. A design case is considered herein in order to validate this concept. In this design the dimensions mentioned above are used with Ls equals 9 mm for transmission zero in the upper stopband and 10.7 mm for transmission zero on the lower stopband. The structure is simulated using the IE3D software. The simulated S_{21} and S_{11} are shown in Figs. 3(a) and 3(b), respectively. Quarter wave transformer is used for matching purposes.

The 3 dB bandwidth in the case of $Ls = 9$ mm is 160 MHz; from 2.35 to 2.51 GHz. For the case of $Ls = 10.7$ mm, the 3 dB bandwidth is also 160 MHz; from 2.32 to 2.48 GHz. The midband insertion loss of both cases is 1.4 dB. The design can be elctronically controlled using two switches

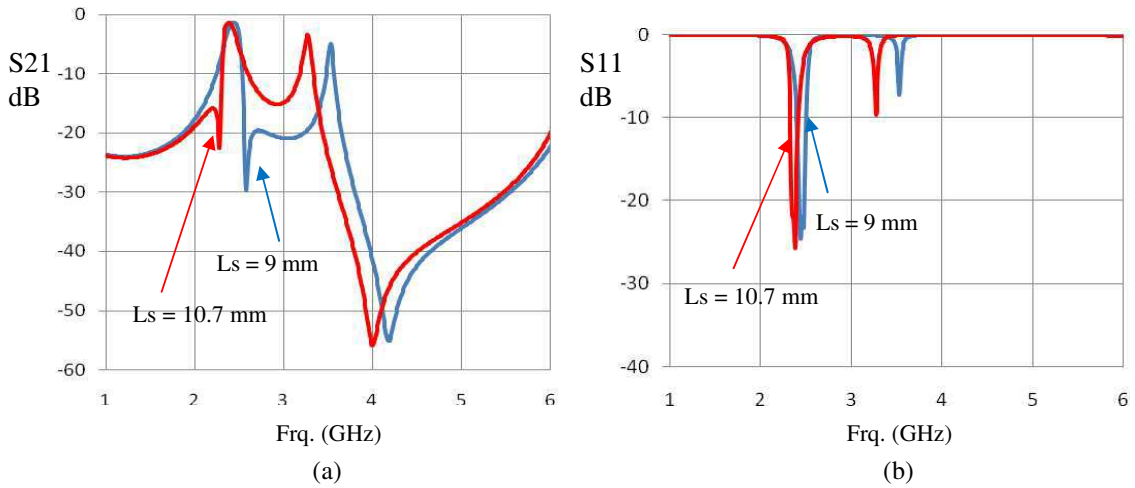

Figure 3: Simulation results of two filters designed based on the structure in Fig. 1 with physical parameters mentioned in the text. (a) S_{21}, (b) S_{11}.

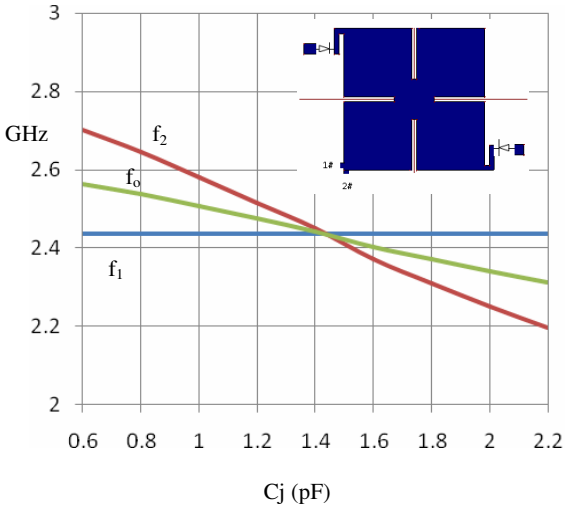

Figure 4: Effect of varactor diodes loading on the resonance frequencies f_1 and f_2. $W = 14\,\text{mm}$, $L = 5\,\text{mm}$, $S = 0.5\,\text{mm}$, on Duroid substrate with $\varepsilon_r = 10.3$ and thickness 0.635 mm, $Ls = 2.5\,\text{mm}$ and $Ws = 0.5\,\text{mm}$.

to connect or disconnect a differentail length ΔL which is 1.7 mm in our case. It has to be noted that, the design based on open circuit stubs is sensitive to the physical parameters of the open circuited stubs. Varctor loading can be used to offer very good control with less sensitivity as described in the next section.

3. FILTER DESIGN USING VARCTOR DIODES LOADING

The transmission zero of the filter shown in Fig. 1 can be electronically controlled using varactor diodes loading mechanism. Varactor diodes can be connected directly at the patch corners or at the end of short open circuited lines. In our case short lines of width 0.5 mm and length 2.5 mm are used. The varactor diode used for this application is the SMTD3001 silicon-based surface mounted structure that can be easily used up to 3 GHz. The diode can operate well in temperature range from $-65°$ to $150°$. The junction capacitance of the diode is approximately changes from 2.2 pF at 0 V reverse bias to about 0.6 pF at 30 V reverse voltage. In our analysis we will assume ideal diodes and we will only consider the junction capacitance. The effect of the junction capacitance on the resonance frequencies f_1 and f_2 is shown in Fig. 4. This effect is studied using the IE3D simulator based on the structure whose parameters are just mentioned in the previous section.

It is observed that large change in junction capacitance leads to little change in the resonance frequency and so very accurate bandwidth selection can be achieved. A bandpass filter is designed with a junction capacitance of 0.7 pF for a transmission zero in the upper stopband and 2 pF for a transmission zero in the lower stopband. These values have been chosen to maintain the same

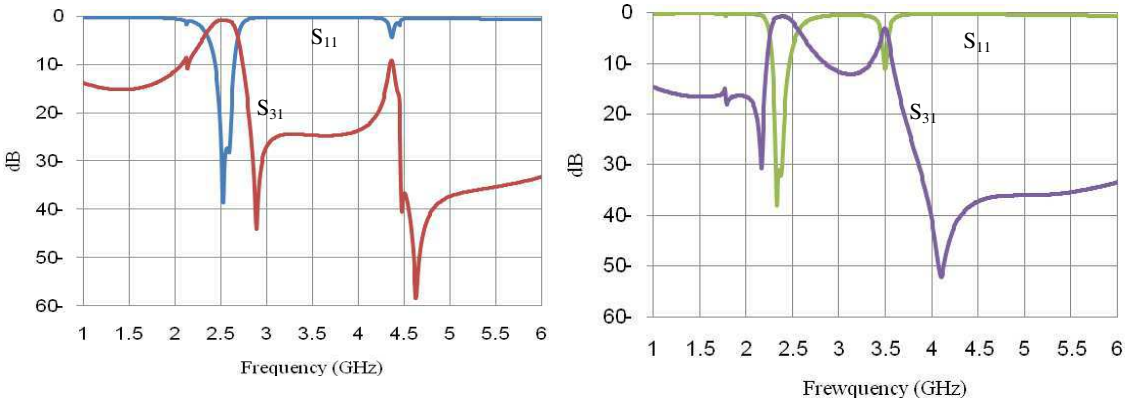

Figure 5: Simulation results of a tunable filter designed based on varactor loading technique with (a) $Cj =$ 0.7 pF and (b) 2 pF.

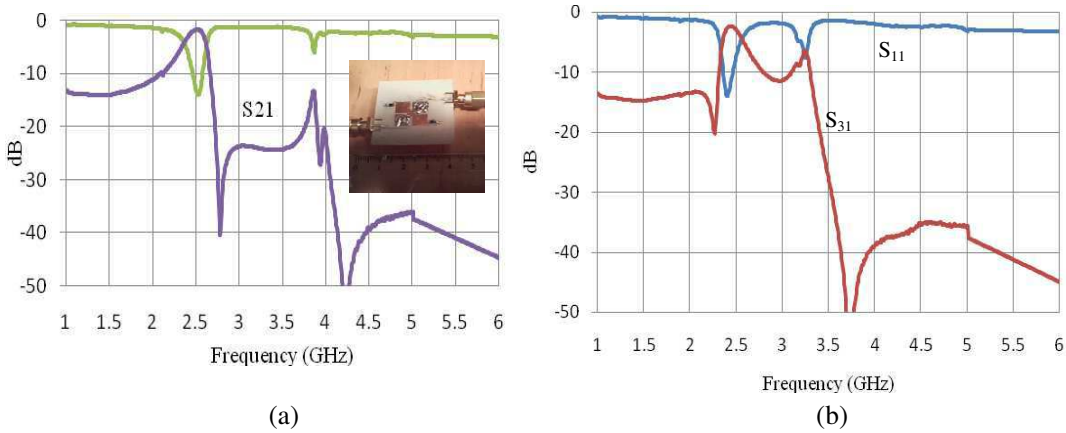

Figure 6: Experimental results of a tunable filter designed based on varactor loading technique with (a) $Cj = 0.7$ pF and (b) 2 pF.

filter bandwidth. Quarter wave transformer is also used to match the filter to 50 Ohms termination. The simulated S_{21} and S_{11} are shown in Figs. 5(a) and 5(b), respectively. The 3dB bandwidth in the case of 0.7 pF is 350 MHz; from 2.33 to 2.68 GHz. For the case of 2 pF, the 3 dB bandwidth is 320 MHz; from 2.26 to 2.58 GHz. The midband insertion loss of both cases is about 0.85 dB. A spurious response appears close to the passband in the case of large capacitance value. It has been shown that, this effect can be reduced by adding open circuit stubs on appropriate locations across the feed line.

4. EXPERIMENTAL RESULTS

The filter designed in the previeous section is implemented and tested. The feeders are moved just to simplify the matching. The measured results are shown in Fig. 6. The measured 3 dB bandwidth for the higher capacitance case is 320 MHz; from 2.28 to 2.6 GHz. For the lower capacitance case, the 3 dB bandwidth is 270 MHz; from 2.35 to 2.62 GHz. The midband insertion loss is about 1.8 dB for both cases which is more than the simulated results by about 1 dB. The differences between simulations and measurments can be attributed to the accuracy of the fabrication tools. A photograph of the fabricated filter is shown in the inset of Fig. 6(a). Investigation based on simulations show that the spurious response appears at the higher capacitance (Fig. 6(b)) near the pass band can be overcomed using shunt stub near the feed line. Other techniques to suppress spurious responses are underway.

5. CONCLUSION

A band pass filter with adjustable transmission zero has been proposed. The proposed filter-structure is based on non-degenerate dual mode resonators loaded by either varactor diodes or open

circuit stubs placed at opposite corners of the resonator. Two filters have been investigated and designed. The first one is designed based on open circuit stubs to show how stub lengths position the transmission zero in the upper stopband or on the lower stopband. The second filter has been designed using varactor diodes loading. The transmission zero in this case can be positioned electronically by applying appropriate reverse bias voltage across the varactors. The latter filter has been fabricated on Duroid substrate with 10.3 dielectric constant and 0.635 mm. Experimental results agree with the simulations results and demonstrate the concept of the proposed filter.

ACKNOWLEDGMENT

This work is supported by the National Plan for Science and Technology Program, Kingdom of Saudi Arabia, Research Grant: 08-ADV210-2.

REFERENCES

1. Tsai, C. M., S. Y. Lee, and C. C. Tsai, "Hairpin filters with tunabletransmission zeros," *IEEE MTT-S Int. Microwave Symp. Dig.*, 2175–2178, 2001.
2. Hsieh, L. H. and K. Chang, "Tunable microstrip bandpass filters with two transmission zeros," *IEEE Trans. Microw. Theory Technol.*, Vol. 51, No. 12, 520–525, 2003.
3. Shih, E. and J. T. Kuo, "A new compact microstrip stacked-SIR bandpass filter with transmission zeros," *IEEE MTT-S Int. Microwave Symp. Dig.*, 1077–1080, 2003.
4. Chang, C. Y. and C. C. Chen, "A novel coupling structure suitable for cross-coupled filters with folded quarter-wave resonators," *IEEE Microw. Wirel. Compon. Lett.*, Vol. 13, No. 12, 517–519, 2003.
5. Amari, S. and U. Rosenberg, "Synthesis and design of novel in-line filters with one or two real transmission zeros," *IEEE Trans. Microw. Theory Technol.*, Vol. 52, No. 5, 1464–1478, 2004.
6. Wu, C. H., Y. S. Lin, C. H. Wang, and C. H. Chen, "Compact microstrip coupled-line bandpass filter with four transmission zeros," *IEEE Microw. Wirel. Compon. Lett.*, Vol. 15, No. 9, 579–581, 2005.
7. Hunter, I., *Theory and Design of Microwave Filters*, ser. Electromagn. Wave, IEE, London, U.K., 2001.
8. Sheta, A. F., N. Dib, and A. Mohra, "Investigation of new nondegenerate dual-mode microstrip patch filter," *IEE Proc.-Microw. Antennas Propag.*, Vol. 153, No. 1, February 2006.
9. Sheta, A. F., "A small size dual-mode patch filter," *International Journal of Applied Electromagnetics and Mechanics (JAEM)*, Vol. 28, No. 1–2, 117–122, 2008.
10. Hong, J. S. and M. J. Lancaster, *Microstrip Filters for RF/Microwave Applications*, John Wiley & Sons, Inc., 2001.

6×3 Microstrip Beam Forming Network for Multibeam Triangular Array

A. Novo-García[1], **M. Vera-Isasa**[1], **Javier García-Gasco Trujillo**[2], **and M. Sierra-Pérez**[2]

[1]Universidad de Vigo, Spain
[2]Universidad Politécnica de Madrid, Spain

Abstract— A six inputs and three outputs structure which can be used to obtain six simultaneous beams with a triangular array of 3 elements is presented. The beam forming network is obtained combining balanced and unbalanced hybrid couplers and allows to obtain six main beams with sixty degrees of separation in azimuth direction. Simulations and measurements showing the performance of the array and other detailed results are presented.

1. INTRODUCTION

Nowadays, earth stations which integrate the ground segment in satellite communications use to be based on large reflector antennas for downloading data from the satellites. These reflector antennas, however, have some drawbacks regarding their high cost, mechanical complexity and low flexibility. For this reason, other antenna configurations have been studied.

Antenna arrays have some advantages over large dishes: capability to track several satellites simultaneously, higher flexibility, modularity and lower production and maintenance cost are the most important of them. GEODA [1] is a smart dome antenna composed of triangular phased arrays designed to receive signals from low orbit satellites. Its structure is shown in Fig. 1. It is composed of two different parts: a 1.5 meters high cylinder and a semisphere situated upon it. For the construction of these two pieces 60 triangular panels are required, each of them composed of 15 subarrays of three circular patches referred to as cells.

2. RADIATING ELEMENT

The basic radiating element of the structure is a circular patch. The patches are arranged in cells of three elements, as was explained in previous section. We can see in Fig. 2 an image of one of these cells.

The radiation of any of these cells will be given by the array factor of the set, whose expression is

$$AF(\theta, \varphi) = \sum_{n=1}^{3} A_n \, e^{j[ka \sin\theta \cos(\varphi - \varphi_n) + \alpha_n]} \tag{1}$$

where k is the wave number, a is the distance from the center of each patch to the center of the array, θ is the elevation angle, ϕ is the azimuth angle, $\phi_n = 2\pi\ (n/3)$ is the angular position of the element n in the plane which contains the three patches and A_n and α_n are the amplitude and phase of the excitation for this element. The working frequency for the cells will be $f_0 = 1.7\,\text{GHz}$ and the separation between patches is $d = 10\,\text{cm}$.

If the cell is properly fed, we could obtain main beams in the azimuth directions $\phi = 0°$, $60°$, $120°$, $180°$, $240°$ and $300°$ [2]. Phase relations needed to accomplish this are shown in Table 1.

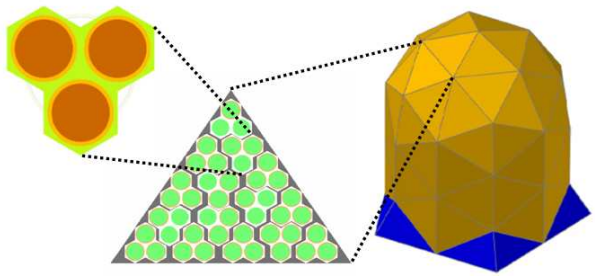

Figure 1.

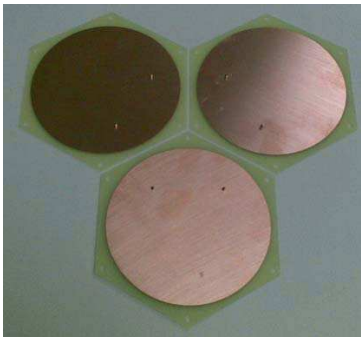

Figure 2.

3. BEAM FORMING NETWORK

The design is based on Butler networks [3], but with an odd number of inputs and outputs, as Shelton studied [4, 5]. In this paper, we use a set of equations which provide a relation between the lengths of the connection transmission lines in the network and the desired phase relation between the outputs [2]. These equations allow a flexible calculation of the transmission lines, and so a more flexible design of the BFN.

The design of a 3×3 lossless beam forming network has been carried out in [2]. The resulting structure (from now board A) is shown in Fig. 3 and it is composed by two balanced hybrid couplers (in red squares) and one unbalanced (in blue square). This network is able to provide phase relations at outputs suitable of obtaining radiation beams in the directions $\phi = 0°$, 120° and 240°.

With the use of a $4\pi/3$ fixed phase shifter, we can obtain a second network which can be used to get three simultaneous beams in the complementary directions of the first network, that is, in the azimuth directions $\phi = 60°$, 180° and 300°. Both circuits can be combined with three microstrip Wilkinson combiners at each of the outputs of the individual boards, following the scheme shown in Fig. 4, and this way a 6 inputs 3 outputs BFN is obtained. With this scheme each of the inputs will provide one phase relation at the outputs which can be used to obtain a beam in a given direction once these outputs are connected to the cell of three patch antennas.

Table 1.

Phase relation	Beam azimuth direction
$\alpha_1 = \alpha_2 = \alpha_3 + 120^o$	$\varphi = 0^o$
$\alpha_2 = \alpha_3 = \alpha_1 + 120^o$	$\varphi = 120^o$
$\alpha_3 = \alpha_1 = \alpha_2 + 120^o$	$\varphi = 240^o$
$\alpha_1 = \alpha_2 = \alpha_3 - 120^o$	$\varphi = 180^o$
$\alpha_2 = \alpha_3 = \alpha_1 - 120^o$	$\varphi = 300^o$
$\alpha_3 = \alpha_1 = \alpha_2 - 120^o$	$\varphi = 60^o$

Table 2.

	P1 (dB)	P2 (dB)	P3 (dB)	P1' (dB)	P2' (dB)	P3' (dB)	A1 (dB|deg)	A2 (dB|deg)	A3 (dB|deg)
P1	-25.11	-36.73	-30.25	-85.99	-52.96	-80.21	-8.78|-102.4	-8.66|141.3	-9.05| 101.4
P2	-36.73	-24.59	-30.4	-52.96	-77.65	-88.28	-8.98|-106.2	-9.47|15.2	-9.60|14.72
P3	-30.25	-30.4	-29.02	-79.62	-89.03	-53.54	-9.98|162.7	-9.20|164.6	-8.99|46.55
P1'	-85.99	-52.96	-79.6	-24.42	-42	-30.5	-8.79|-102.6	-8.67|141.2	-9.21|138.2
P2'	-52.96	-77.65	-89.03	-42	-25.49	-32.19	-8.97|-106.4	-9.45|15.05	-9.82|-105.9
P3'	-80.21	-88.28	-53.54	-30.5	-32.19	-30.98	-9.98|162.6	-9.21|164.4	-9.15|-74.38

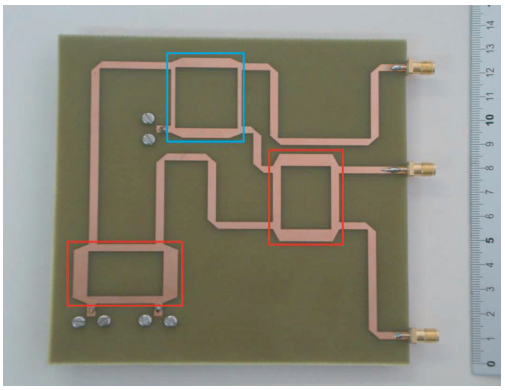

Figure 3. Board A.

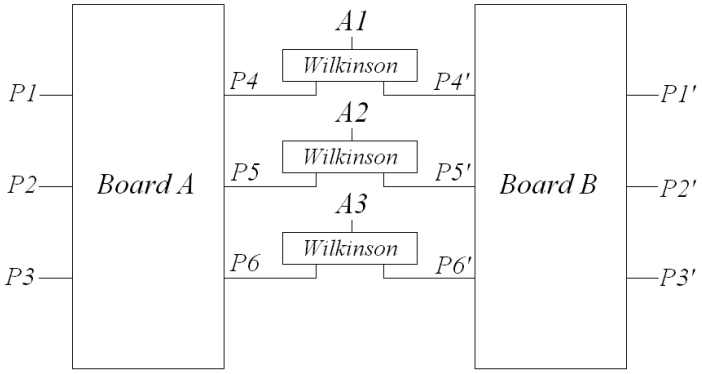

Figure 4. BFN.

4. RESULTS

Results obtained with *IE3D* software at 1.7 GHz are shown at Table 2 for each input of the 6×3 design. Each row shows the S parameters for each of the inputs shown in the first column. Phase relations for inputs P1, P2 and P3 are suitable of providing main beams in azimuth directions $\phi = 240°$, $120°$ and $0°$, while phase relations for inputs P1', P2' and P3' can be used to point the main beam in directions $\phi = 300°$, $60°$ and $180°$, respectively.

A prototype of board A was built (Fig. 3) and performance was measured for a signal at each of the inputs as can be shown in Fig. 5, where P1, P2 and P3 are signals at input ports, and P4, P5 and P6 are signals at output ports. Phase relations at outputs agree with those presented in the

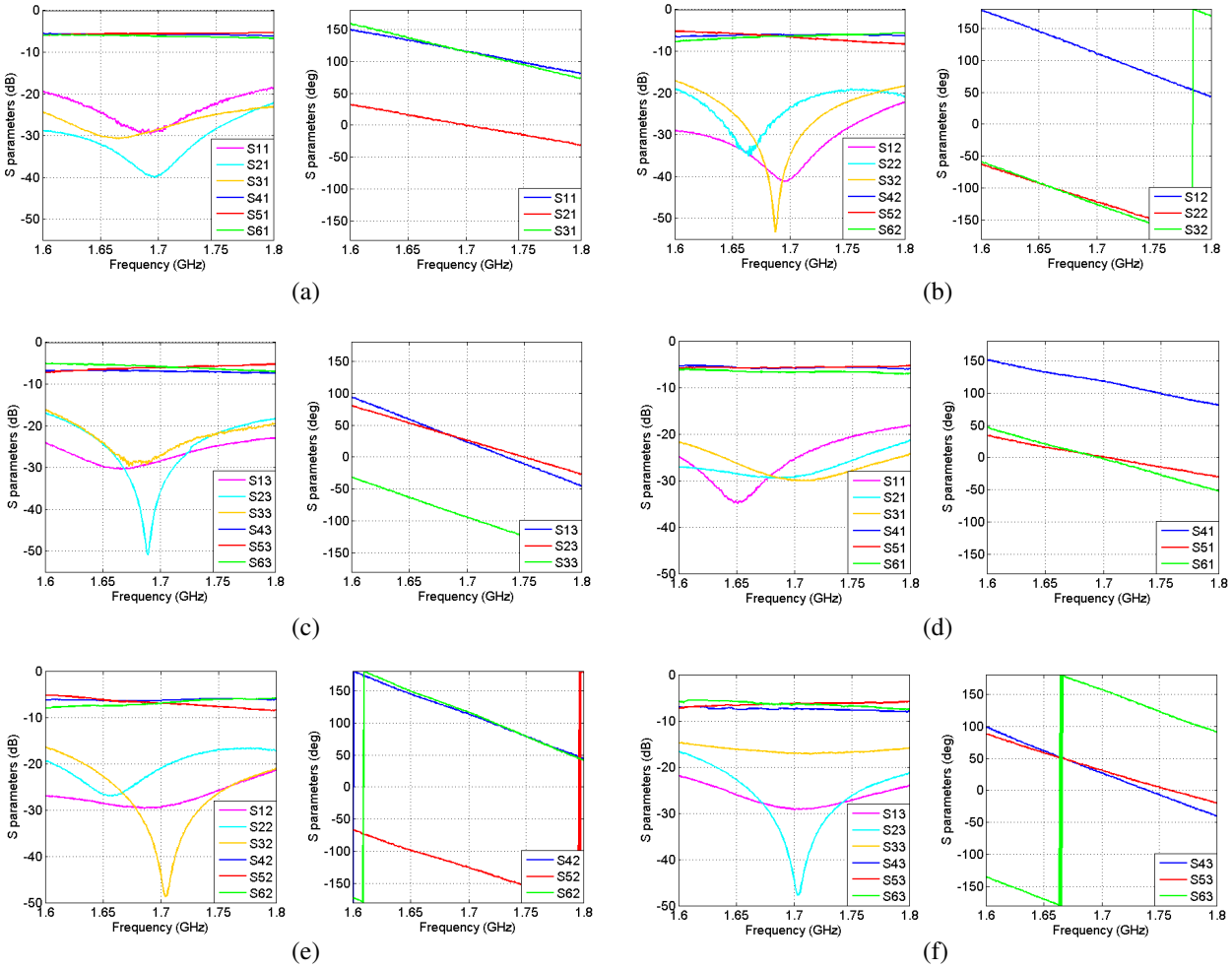

Figure 5. Measurements for board A: (a) Input 1, (b) Input 2, (c) Input 3 and measurements for board B: (d) Input 1, (e) Input 2, (f) Input 3.

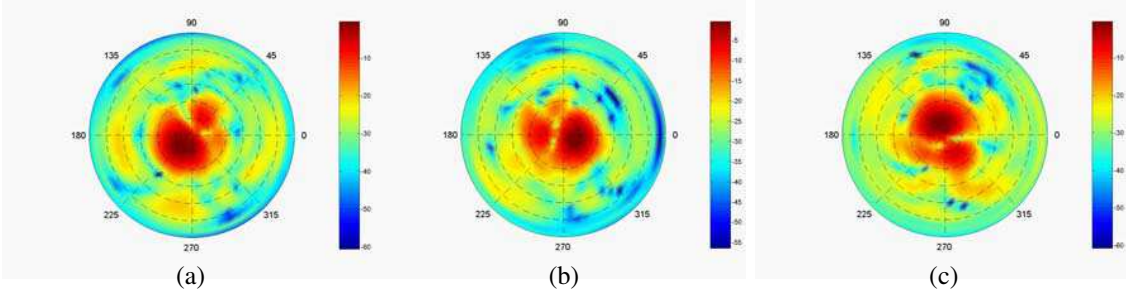

Figure 6. Radiation diagram with board A feeding a cell: (a) Input 1, (b) Input 2, (c) Input 3.

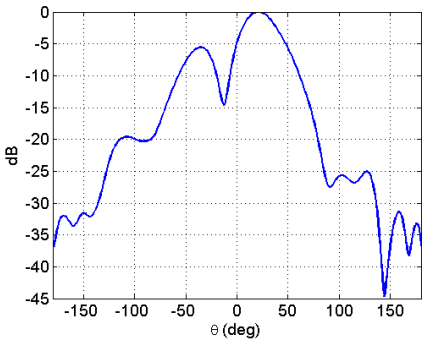

Figure 7.

first three rows of Table 1. Board B was also built and its performance is shown in Fig. 5, where it can be seen that phase relations coincide with the three final rows of Table 1.

The measured normalized radiation pattern in dB when each one of the inputs of the network A is selected is shown in Fig. 6. If signal is at input 1, the main radiation beam points at $\phi = 240°$; if it is at input 2, the main beam direction is $\phi = 0°$; if it is at input 3, we can see the main beam pointing at $\phi = 120°$.

The elevation pattern is similar for the three beams. In Fig. 7 it is shown for $\phi = 120°$.

5. CONCLUSIONS

A 6×3 beam forming network which can provide the phase relations needed to feed a circular array of 3 elements to obtain 6 simultaneous beams is presented in this paper. The network is composed of two 3×3 boards which have been built and measured, showing the desired performance at the working frequency. The combination of such boards with three Wilkinson dividers presented in this paper has been simulated and has shown the expected magnitude and phase relations at outputs.

ACKNOWLEDGMENT

This work was supported by MCI under TEC2008-06736-C03-02.

REFERENCES

1. Sierra-Pérez, M., A. Torres, J. L. Masa, M. Gómez, and I. Montesinos, "GEODA: Adaptive antenna array for satellite signal reception antennas and propagation," *Proceedings of the Second European Conference on Antennas and Propagation, EuCAP 2007*, 1–4, Edinburgh, Scotland, November 2007.
2. Novo-García, A., M. Vera-Isasa, and M. Sierra-Pérez, "3×3 microstrip beam forming network for multibeam triangular array," *Proceedings of 10th Mediterranean Microwave Symposium*, 166–169, Güzelyurt, Northern Cyprus, August 2010.
3. Butler, J. and R. Lowe, "Beam-forming matrix simplifies design of electronically scanned antennas," *Electronic Design*, Vol. 9, 170–173, 1961.
4. Shelton, J. P. and K. Kelleher, "Multiple beams from linear arrays," *IRE Transactions on Antennas and Propagation*, Vol. 9, No. 2, 154–161, 1961.
5. Shelton, J. P., "Multibeam, hexagonal, triangular-grid, planar arrays," *Antennas and Propagation Society International Symposium*, Vol. 3, 90–97, 1965.

Comparative Study of Two Microstrip Beam Forming Networks for Multibeam Triangular Array

A. Novo-García[1], **M. Vera-Isasa**[1], **and M. Sierra-Pérez**[2]

[1]Universidad de Vigo, Spain
[2]Universidad Politécnica de Madrid, Spain

Abstract— A comparative study between two beam forming networks for 3×3 multibeam operation is presented. The first one combines three 2×2 hybrid couplers and the second is based on a symmetrical 3×3 hybrid coupler. Both circuits have been designed and simulated, and two prototypes have been built and measured in microstrip technology. Their performances have been compared and the results are presented.

1. INTRODUCTION

Classical antennas for satellite communications are large reflector antennas fed by horns. These antennas can be used to receive satellite signals from any direction with a mechanical procedure. This is a drawback when tracking low orbit satellites, where the antennas must have a tracking system to accurately move it in a short time. Also, more than one horn must be used if it is desired to obtain a multibeam antenna.

An alternative would be to use planar arrays. These antennas use to be fed using a set of circuit elements, such as phase shifters, couplers and amplifiers in order to build a proper beam forming network (BFN) which can provide the desired multibeam response. In [1] the BFN needed to get three simultaneous beams for the case of a triangular array antenna of three elements has been studied. That study, based on Butler's and Shelton's works [2–4], allowed to design a network where transmission lines lengths were calculated with a set of three equations so that three simultaneous beams separated 120° in azimuth were obtained. These lines were connected with three 2×2 hybrid couplers, and a 3 inputs and 3 outputs structure was presented.

Similar response could also be obtained with a circular 3×3 structure proposed in [5]. That design consists of 2 concentric circles with 3 segments of length $\lambda/3$ connected by 3 lines of length $\lambda/12$.

In Sections 2 and 3, a brief description of the first and the second networks, respectively, is presented. Both of them were designed and simulated in microstrip technology to obtain the simultaneous beams at 1.7 GHz. Two prototypes were constructed and their performance measured and compared. The results obtained and the comparison between them can be found in Section 4. In this paper not only that performance was analyzed, but also considerations regarding their size, complexity and flexibility were discussed.

2. THREE 2×2 HYBRIDS NETWORK

The network is composed by two balanced 3 dB hybrids and one unbalanced in order to obtain uniform amplitude at the three outputs. In addition, the following condition must be observed:

$$l_1 - l_2 + l_3 = \lambda/4 \tag{1}$$

A more detailed description of the design process can be found in [1]. Phase relation obtained between the outputs can be seen in Table 1, where α_i is the phase at output i, These phase relations allows to obtain, with a triangular array, three simultaneous beams separated 120° in azimuth. The layout of the board (from now Board A) can be observed in Fig. 1.

Table 1.

Input	Phase relation at outputs	Beam azimuth direction
I_1	$\alpha_2 = \alpha_3 = \alpha_1 - 120°$	$\varphi = 300°$
I_2	$\alpha_1 = \alpha_3 = \alpha_2 - 120°$	$\varphi = 60°$
I_3	$\alpha_1 = \alpha_2 = \alpha_3 - 120°$	$\varphi = 180°$

Table 2: Transmission lines dimensions.

Transmission line	Length	Transmission line	Length
tl_1	λ	tl_4	$7\lambda/6$
tl_2	λ	tl_5	$\lambda/4$
tl_3	$\lambda/4$	tl_6	$2\lambda/3$

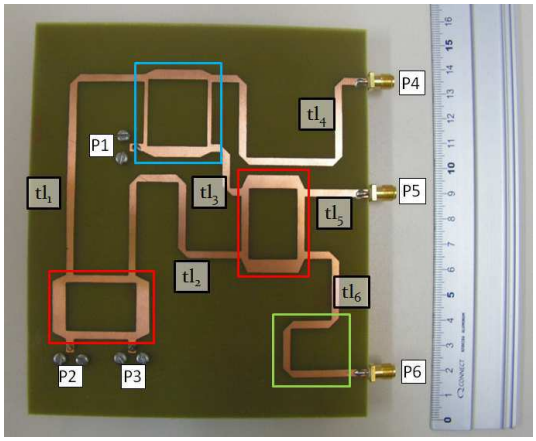

Figure 1: Board A.

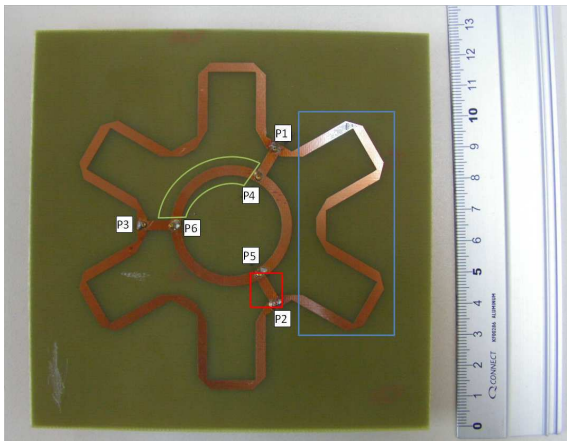

Figure 2: Board B.

The red squares surround the balanced hybrid couplers, while the blue square surrounds the unbalanced coupler and the green one marks the position of the phase shifter at output 3. Ports are displayed as Pi, where inputs are P1, P2 and P3, and outputs are in the right side as P4, P5 and P6. Transmission lines are named as tl_i, and their lengths are shown in Table 2.

3. 3×3 HYBRID NETWORK

A symmetrical 3×3 hybrid coupler can be derived from [5]. In Fig. 2, the representation of the circuit is shown. It consists of two concentric circles of length λ connected by 3 lines of length $\lambda/12$. Ports are located at the intersections between the three lines and both circular structures. Interior and exterior ports can be used as input or output ports. With that specifications in the dimensions of the design it is possible to obtain the desired phase response (Table 1).

A microstrip board was designed with the previous guidelines. Exterior circle segments were lengthened to make possible the fabrication of the structure, so that the segments of that circle between the interconnections of $\lambda/12$ are now of length $4\lambda/3$, while the inner circle segments have a length of $\lambda/3$. Outer circle was bended in order to reduce the dimensions of the design, which can be seen in Fig. 2 (from now Board B).

Segment of outer structure is surrounded by blue rectangle, while segment of inner circle is emphasized by a green arc. One of the three straight segments which join inputs and outputs is surrounded by a red square. Inputs were chosen to be at the outer structure (ports P1, P2 and P3), while outputs are at the inner ring (ports P4, P5 and P6). It can be noticed that the design presents three symmetry axes. A signal at a given input divides its power equally at the outputs, and the phase relation obtained is the same as obtained by the previous section network (Table 1).

4. PERFORMANCE AND COMPARISON

Prototypes of both boards designed have been built in microstrip technology with a FR-4 substrate with height $h = 1.5\,\text{mm}$ and relative permittivity $\xi_r = 4.25$. Magnitude and phase at each output have been measured when input signal is at input 1, input 2 and input 3. Those results are shown in Figs. 3 and 4 for board A and board B respectively.

Return losses measured for board B are considerably greater than those measured for board A, with a value near $-17\,\text{dB}$ at $1.7\,\text{GHz}$. That drawback is common for each of the 3 inputs for board B.

Performance of board A shows a bigger amplitude bandwidth. It can be noticed that at $1.75\,\text{GHz}$ for board B we have same magnitude for return losses and output signals for any of the inputs.

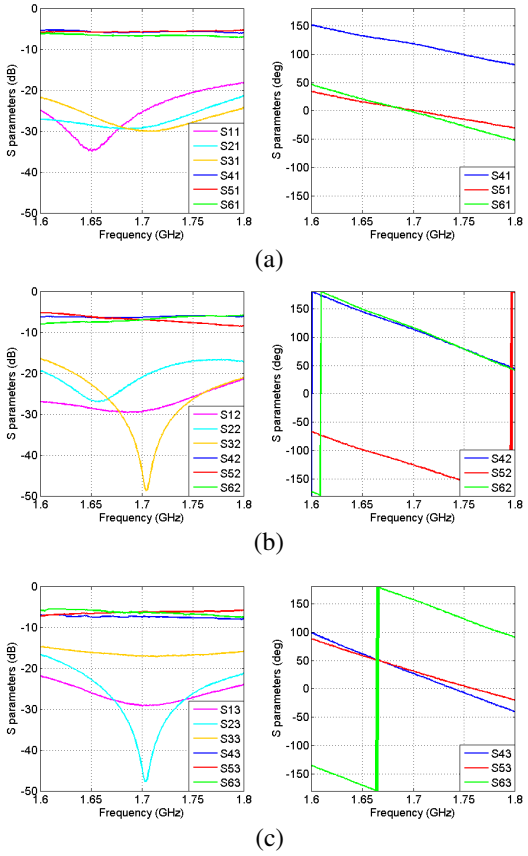

Figure 3: Measurements for board A: (a) Input 1, (b) Input 2, (c) Input 3.

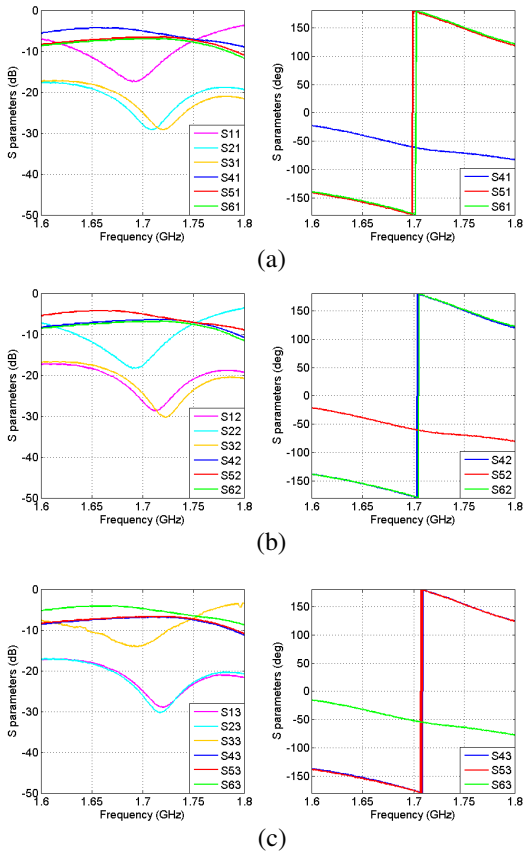

Figure 4: Measurements for board B: (a) Input 1, (b) Input 2, (c) Input 3.

Power at each output, isolation of the other inputs and return losses are in general more stable when we move from central frequency of 1.7 GHz in the case of using board A.

On the other hand, board B presents a bigger phase bandwidth at outputs. We can see that for board A phases at the outputs which should be the same only are equal at central frequency, since they present a slightly different slope. Phases of board B coincide for different frequencies..

It can also be noticed that output signals are not of the same amplitude at the frequency of interest when we are working with board B. Output signal at port opposite to the input port (O_i when signal at I_i) is bigger than other outputs until 1.75 GHz. Those signals also present a non-linear dependence with frequency.

Other comparisons can be done besides performance. Board B prototype is smaller than board A. This last one could be redesigned in order to obtain a smaller board, but moving the lines closer would make couplings to appear and performance would be worse.

Board A has a more flexible design. The use of the three equations presented in [1] allows the designer to obtain a network with given lengths, which also can be bent to have the outputs and inputs at the desired position. Board B, on the other hand, is a fixed structure. Its design is given in [5] and cannot be modified, and only panel connections can be used to build the ports.

Finally, the process of designing board B is easier. Structure has three symmetry axes, so that network can be divided in 3 exactly equal parts. This way, the correct design of one of these three parts is enough to obtain the complete structure.

5. CONCLUSIONS

Both boards can be used to obtain magnitude and phase at outputs needed to properly feed a triangular array which could provide three 120° separated beams. However, performance comparison carried out in last section showed differences which could make more suitable to select one board or another.

Board A should be used when a flexible network is needed. Other phase relations at outputs can be obtained modifying the transmission line lengths to obtain other beam pointing directions.

Board B, however, is a fixed design, where only the use of lengths presented in [5] will provide the desired phase relation at outputs. A different relation cannot be achieved by modifying these lengths.

Power performance of board B is constrained by return losses, which strongly limits its useful bandwidth. On the other hand, board A shows a good response for any input with independence of the frequency in the band between 1.6 and 1.8 GHz. The output responses are linear and do not vary considerably, unlike the output responses at board B. Nevertheless, when phase is analyzed, the relation at outputs for board B is more stable than at board A outputs.

ACKNOWLEDGMENT

This work was supported by MCI under TEC2008-06736-C03-02.

REFERENCES

1. Novo-García, A., M. Vera-Isasa, and M. Sierra-Pérez, "3×3 microstrip beam forming network for multibeam triangular array," *Proceedings of 10th Mediterranean Microwave Symposium*, 166–169, Güzelyurt, Northern Cyprus, August 2010.
2. Butler, J. and R. Lowe, "Beam-forming matrix simplifies design of electronically scanned antennas," *Electronic Design*, Vol. 9, 170–173, 1961.
3. Shelton, J. P. and K. Kelleher, "Multiple beams from linear arrays," *IRE Transactions on Antennas and Propagation*, Vol. 9, No. 2, 154–161, March 1961.
4. Shelton, J. P., "Multibeam, hexagonal, triangular-grid, planar arrays," *Antennas and Propagation Society International Symposium*, Vol. 3, 90–97, August 1965.
5. Roeder, A. and M. P. C. Maximo, "Microwave hybrid coupler having $3 \times N$ inputs and $3 \times N$ outputs," U. S. Patent 5,237,294, August 17, 1993.

Automatic Design and 3D Electromagnetic Simulation of Sub-nH Spiral Inductors

L. Aluigi, **F. Alimenti**, **and L. Roselli**
Department of Information and Electronic Engineering, University of Perugia, Perugia, Italy

Abstract— The design of modern radiofrequency integrated circuits on silicon operating at millimeter-waves typically requires the integration of several spiral inductors. At such high frequencies, a typical design requires inductors with sub-nH values, which are traditionally not available in the design-kits of the technology processes. In this work, we present a tool based on VbScripts that automatically executes three-dimensional layout editing and electromagnetic simulating commands. In detail, it draws the inductor masks for the specific microelectronic process, including vias and underpasses, in less than one minute, and then performs the electromagnetic simulations. The outputs are the exportable DRC-errors free layout (GDS-II format) and the 2π-model parameters to be included in the schematic editor. This tool allows significant design automation compatible with traditional commercial CAD tools.

1. INTRODUCTION

The implementation of high-performance radiofrequency integrated circuits (RFICs) is affected by the quality factor (Q) of passive components and their design accuracy. In particular, in the millimeter frequency range, the designers have to face with the lack of adequate spiral inductors with sub-nH inductance value, high-Q and high design accuracy [1]. Layout editing, electromagnetic simulations, (typically three-dimensional, or 3D), and design optimizations lead to extend considerably the design phase and hinder the automated design of mixed-signal systems.

In this paper, we propose a software tool based on VbScripts which contributes to the microelectronic design automation of sub-nH spiral inductors within the traditional commercial CAD environments. The paper is organized as follows. Section 2 highlights the design automation procedure proposed and describes the script code and the issues related to the simulation. Section 3 reports the results of a case of study.

2. AUTOMATIC DESIGN METHOD

The design-flow proposed herein is based on the 3D electromagnetic (EM) simulator HFSS (High frequency Structure Simulator) by Ansoft^{TM}. The latter is a high performance full wave electromagnetic field simulator for arbitrary 3D volumetric passive device modelling which integrates simulation, visualization, solid modeling and automation. HFSS employs the FEM (Finite Element Method) with adaptive meshing based on tetrahedrons. It solves the EM problem (i.e., the E and H fields in every mash cell) and provides the typical N-port descriptions, typically S-parameters, but also currents and field animations, radiation patterns, etc.

The overall flow chart illustrating the design procedure proposed is shown in Fig. 1, which includes both automatic and manual operations. As a first step the designer specifies the equations for geometric sizing of the spiral. Equation (1) is optimized for sub-nH spiral inductors. Instead of the classic approach of using an adaptation of the Wheeler's formula [2], we used the expression proposed in [3], which can be potentially extended to inductances as low as 0.1 nH,

$$L_s = \mu/2 \cdot c_1 \cdot n^2 \cdot d_{avg} \cdot f(\rho) \tag{1}$$

where n is the number of turns, $d_{avg} = 0.5(d_{in} + d_{out})$ is the average diameter, $f(\rho) = \ln(2.29/\rho) + 0.19\rho^2$, $\rho = (d_{out} - d_{in})/(d_{out} + d_{in})$ is the fill factor.

The output of the first step is a set of four first-guess values, w, s, N, d_{out}, which are introduced as inputs to the script. In the subsequent step, the tool automatically edits the layout and simulates the spiral inductor with a custom polysilicon pattern ground (PSG) in a full 3D EM simulator environment. Some portions of the code are shown in Fig. 2. The use of VbScript programming language allows interacting with the HFSS environment. Based on the technology description, the tool draws the cross section of the layer stack and adds a layer of air on top. The box sizes (x, y, and z) are proportional to the outer diameter of the spiral drawn.

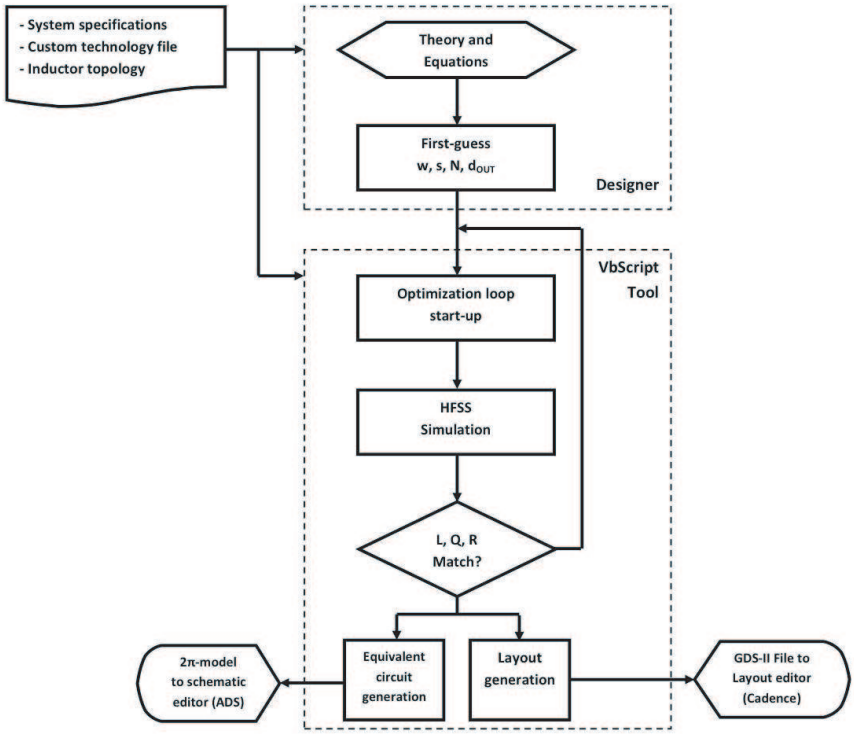

Figure 1: Flowchart illustrating the automated design method adopted.

```
` AUTOMATIC GENERATION OF AN OCTAGONAL, PLANAR, SYMMETRICAL COIL
` WITH HFSS Version 11.0 USING THE IHP's SG25 DESIGN-KIT
` v 4.04 – jul 29, 2010 upgrade of ver. 1.09
[...]
` TECHNOLOGY DEFINITION – METALS and LAYERS
[...]
oProject.AddMaterial Array ("NAME: METAL3", "conductivity: "24900000")
oProject.AddMaterial Array ("NAME: TM1", "conductivity: "31250000")
[...]
oProject.AddMaterial Array ("NAME: oxide", "permittivity: "4.1")
oProject.AddMaterial Array ("NAME: passivation", "permittivity: "5")
```

```
[...]
` COIL GEOMETRY DEFINITION WIZARD
[...]
outer_diameter = InputBox ("Outer Diameter [um]?", "STEP 1-5", "0")
width = InputBox ("Width [um]?", "STEP 2-5", "0")
[...]
` TURNS CONTROL
If x > 2 Then din_min = x Else din_min = 2
N =1
Z = (w + s)*2
[...]
```

Figure 2: Portions of the VbScript code.

This first version of the tool is capable of editing planar, octagonal and symmetric inductors realized by using the topmost metal layer, i.e., the thickest one. In fact, metal stacking, usually results in poorer self-resonance frequency performance than using the top one or two thick metals, except for spirals fabricated on highly resistive substrates (e.g., SOI). The octagonal shape represents a reasonable trade-off between square spirals, typically characterized by higher losses, and circular spirals, characterized by a higher drawing complexity in regard of matching to the layout rules.

Once the step above has been completed, the designer must set up the excitation ports before the EM simulation has place. HFSS allows the use of two kinds of ports: wave-port and lumped-port. In the case of lumped-port the excitation is applied at a point/cell as a voltage or current, whereas in wave-ports the excitation is so-called eigen-wave, such as the quasi-TEM wave supported by a microstrip line. The latter is applied to a proper lateral area of the simulation box which includes

the metal layer and the reference ground plan. Voltage is scalar while a wave is a vector, hence there are substantial differences between these two. If the excitation can be applied on some locally uniform region, the use of wave-ports is recommended, otherwise if geometry or material discontinuities are near to the application point of the excitation, like in our case, the use of lumped-ports is suggested. Finally, it is worth noticing that we introduce a ground shield below the inductors in order to improve the reproducibility [4]. The problem of ground returns has been accurately studied in [5].

When the EM simulation has been completed, the tool presents the resulting graphs for Q, L and R. If the results match the expected values it is possible to go to the final step: the equivalent circuit's parameters extraction and the layout file generation.

There is really a great variety of equivalent models for inductors reported in literature. These methods are generally categorized into numerical techniques [6], parameter fitting [7, 8] and physical models [8–10]. Numerical techniques are typically very time consuming, whereas parameter fitting models lack of flexibility in layout and process parameters variations. In order to satisfy the requirements in terms of accuracy, scalability and simulation time, wideband physics-based circuit models seem to be the best choice. For this reason we have chosen the 2π-model which seems to us a good compromise between high accuracy and low complexity. In particular, for the extraction of the 2π-model parameters we used the methods described in [9, 10]. An excellent agreement can be found over the whole frequency range (up to the self-resonance frequency).

The generation of a GDS-II file for the layout editor is a fairly straightforward task, thanks to the use of a *layermap* type file. It is worth mentioning that the inductor drawing layers imported into Cadence Virtuoso by using the GDS-II file generated by the tool are DRC error-free.

3. RESULTS

To illustrate the effectiveness of the developed tool, we refer in this section to a case study on the design of a 31.4 GHz low-noise amplifier (LNA) in a 250 nm SiGe BiCMOS technology. In this circuit, a 2-stage cascode LNA, we needed four inductors used for input, output and interstage matching, with values of inductance required ranging from 0.15 to 0.5 nH. Here we present the results for the 0.27 nH inductor.

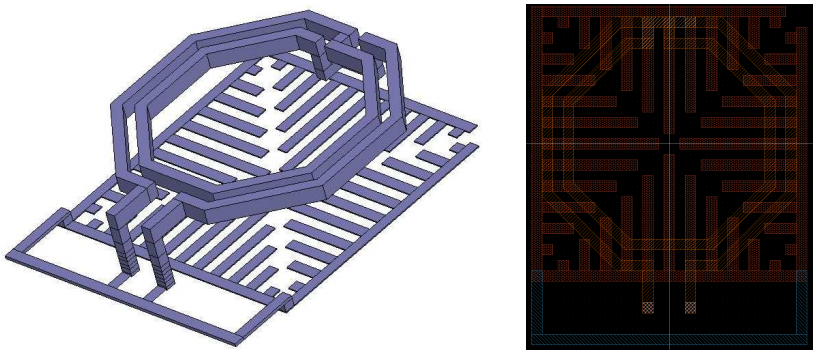

(a) (b)

Figure 3: (a) HFSS and (b) Cadence-Virtuoso layout of the 0.27 nH inductor. Diameter equal to 48 µm, track width equal to 2 µm, track spacing equal to 2 µm.

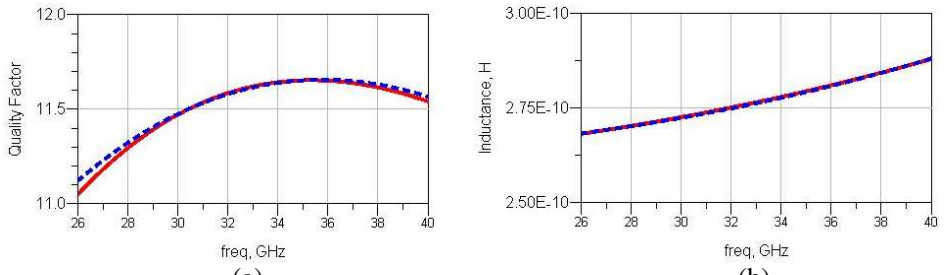

(a) (b)

Figure 4: EM simulation (dotted line) and the 2π-model simulation (solid line) of the 0.27 nH inductor. Comparison of (a) Quality Factor and (b) Inductance.

In Fig. 3(a), it is shown the 3D view of the structure created by the script. It is worth noticing that this step done manually would take about half an hour, while using the script it takes less than one minute. Fig. 3(b) shows the inductor drawing layers imported into Cadence Virtuoso which, as mentioned above, are DRC error-free as the script has been optimized for this purpose.

Figure 4 shows the results of the EM simulation (dotted line) and the 2π-model simulation (solid line) of the 0.27 nH inductor. It shows a comparison of (a) Quality Factor and (b) Inductance. It can be seen that the model is very accurate, not only at the center frequency of 31.4 GHz but over the entire K_a-band.

4. CONCLUSIONS

Accurate characterization of on-chip inductors is very crucial. One way to accurately characterize them is to perform RF measurements on a certain number of fabricated inductors. To find the inductor that meets the specifications a large number of inductors have to be included on the test wafer. This process is neither economic nor flexible and, especially for research purposes, is not always easily available. A reliable alternative, thanks to the advances offered by the software technology, is to use full-wave EM simulations. These have proven to have an accuracy in the modeling of the EM fields, of near 100% as compared with the measurements based-models. This approach is certainly more cost-effective than wafer runs, but still remains quite time consuming if a proper design strategy is not pursued. The aim of this paper is precisely to demonstrate an automatic procedure that drastically reduces the design time for RF inductors on silicon. At present, after having successfully used the tool for a project with the 250 nm BiCMOS technology, we are adapting it for use with a 65 nm CMOS technology.

ACKNOWLEDGMENT

The authors acknowledge IHP for having provided the employed design kit.

REFERENCES

1. Ytterdal T., Y. Cheng, and T. A. Fjeldly, *Device Modeling for Analog and RF CMOS Circuit Design*, John Wiley and Sons, 2003.
2. Wheeler, H. A, "Formulas for the skin effect," *Proceedings of the IRE*, Vol. 30, No. 9, 412–424, Sep. 1942.
3. Biondi, T., A. Scuderi, E. Ragonese, and G. Palmisano, "Sub-nH inductor modeling for RFIC design," *IEEE Microwave and Wireless Components Letters*, Vol. 15, No. 12, 922–924, Dec. 2005.
4. Lacaita, A., S. Levantino, and C. Samori, *Integrated Frequency Synthesizers for Wireless Systems*, Cambridge University Press, 2007.
5. Kraemer M., D. Dragomirescu, and R. Plana, "Accurate electromagnetic simulation and measurement of millimeter-wave inductors in bulk CMOS technology," *Proc. of the IEEE Topical Meeting on Silicon Monolithic Integrated Circuits in RF Systems (SiRF)*, 61–64, New Orleans, LA, Jan. 2010.
6. Long, J. R. and M. A. Copeland, "The modeling, characterization, and design of monolithic inductors for silicon RF IC's," *IEEE Journal of Solid-State Circuits*, Vol. 32, No. 3, 357–369, Mar. 1997.
7. Ashby, K. B., I. A. Koullias, W. C. Finley, J. J. Bastek, and S. Moinian, "High Q inductors for wireless applications in a complementary silicon bipolar process," *IEEE Journal of Solid-State Circuits*, Vol. 31, No. 1, 4–9, Jan. 1996.
8. Zito, D., D. Pepe, and B. Neri, "Wide-band frequency-independent equivalent circuit model for integrated spiral inductors in (Bi) CMOS technology," *13th IEEE International Conference on Electronics, Circuits and Systems, 2006, ICECS'06*, 478–481, Dec. 10–13, 2006.
9. Dickson, T. O., M. LaCroix, S. Boret, D. Gloria, R. Beerkens, and S. P. Voinigescu, "30–100-GHz inductors and transformers for millimeter-wave (Bi) CMOS integrated circuits," *IEEE Transactions on Microwave Theory and Techniques*, Vol. 53, No. 1, 123–133, Jan. 2005.
10. Oung-Ghyu, A., S.-K. Kim, J.-H. Chun, and B.-S. Kim, "Efficient scalable modeling of double-document equivalent circuit for on-chip spiral inductors," *IEEE Transactions on Microwave Theory and Techniques*, Vol. 57, No. 10, 2289–2300, Oct. 2009.

A Novel Dual-mode Dual-band Bandpass Filter with DGS

Chang Chen[1], **Weidong Chen**[1], **and Zhongxiang Zhang**[2]

[1]Department of EEIS, University of Science And Technology of China, Hefei, Anhui 230027, China
[2]Department of PEE, Hefei Normal University, Hefei, Anhui 230061, China

Abstract— A novel dual-mode dual-band bandpass filter with simple defected ground structure (DGS) is proposed. A dual-mode dual-band bandpass filter is obtained by combining the microstrip square loop on the top layer and another square loop constructed with DGS on the bottom layer, which achieve dual-mode single-band bandpass characteristic, respectively. Excited with common feed lines, the proposed filter is compact and easy fabrication. The design is confirmed by simulation and experiments with good agreement.

1. INTRODUCTION

Bandpass filter is a key component for modern communication systems. Recently, quick developments in communication systems require the radio frequency (RF) devices operating in multiple separated frequency bands, such as working on 1800 MHz and 1900 MHz for GSM and WCDMA mobile communications. Therefore, there has been growing interest in design of dual-band bandpass filter. Taking advantages of small size, low cost and easy fabrication [1] various microstrip structures are widely applied for realizing dual-band filters. In [2–4], a stepped-impedance resonator (SIR) is used for the design of dual-band bandpass filter as it can easily control the second pass band frequency. In [5], a dual-band bandpass filter is achieved by cascading a broadband filter with a bandstop filter. Meanwhile, due to compact and flexible characteristics, defected ground structure (DGS) is widely used to introduce the bandstop performance by collocating with a transmission line [6] or bandpass performance by coupling with a transmission line [7], respectively in filter design.

As is well known, a dual-mode bandpass filter with elliptic response can be realized by using square loop structure [8]. In [9], dual-mode stacked-loop structure with stacked dielectric layers is designed to achieve dual-band performance and there is a good isolation between two closely adjacent passbands, but two dielectric layers make the design complicated. In this paper, by combining the square loop on top layer and the other loop constructed with DGS on the bottom layer, a novel and simple dual-mode dual-band bandpass filter is thus achieved, and only one dielectric layer is required, smaking this filter compact and low cost. Rather good agreement has been seen between the simulation and experiment results, which validate the design.

2. CONVENTIONAL DUAL-MODE SQUARE LOOP FILTER

Figure 1(a) is the layout of a conventional dual-mode bandpass square loop filter with elliptic function, and it is easy to be integrated with the other circuits. The resonator can be treated as waveguide cavity with magnetic walls on the sides. The first two functional degenerate modes are TM^z_{100} and TM^z_{101}, where z direction is perpendicular to the ground plane. Due to the perturbation part, two orthogonal modes charactered by f_1 and f_2 couple and generate passband, which is shown in Fig. 1(b). The coupling coefficient k is

$$k = (f_1^2 - f_2^2)/(f_1^2 + f_2^2) \tag{1}$$

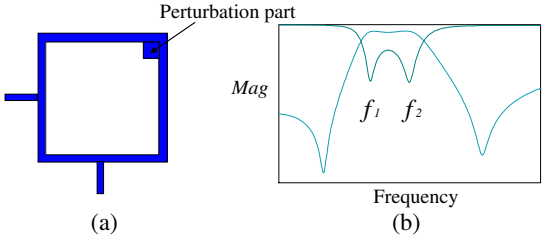

Figure 1: (a) Layout of the conventional dual-mode filter. (b) Resonance characteristic of the conventional dual-mode filter.

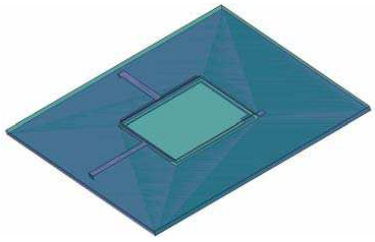

Figure 2: 3D drawing of the proposed filter.

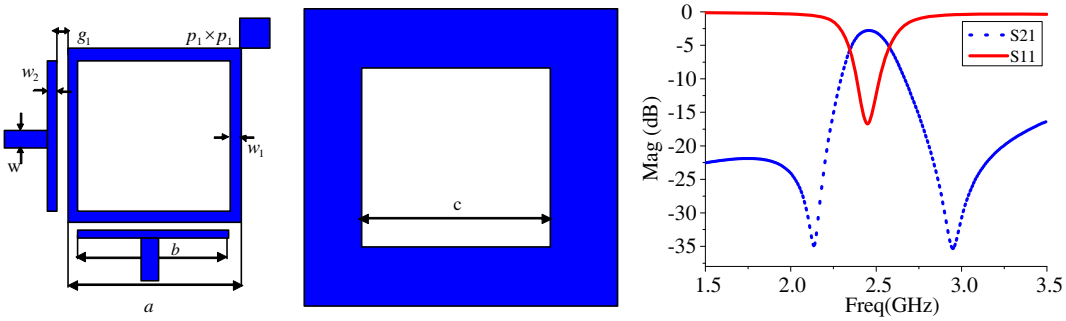

Figure 3: (a) Top view. (b) Bottom view. (c) Simulation results.

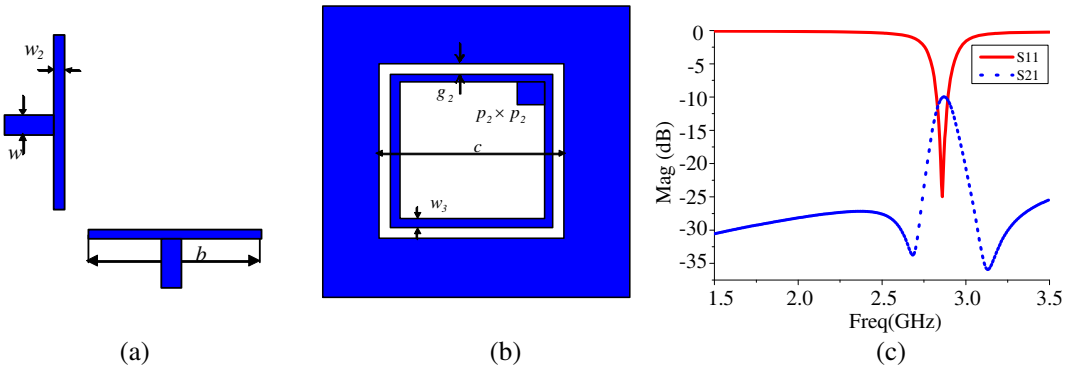

Figure 4: (a) Top view. (b) Bottom view. (c) Simulation results.

Without the perturbation part, there is no response even when the input is excited at resonance frequency for signals counteraction.

3. DESIGN OF DUAL-MODE DUAL-BAND FILTER

The proposed filter is obtained by combining the square loop on top layer and the other loop constructed with DGS on the bottom layer, and the units on the top layer and on the DGS are excited by the common feed lines on the top layer. The 3D drawing of the proposed filter is shown in Fig. 2. The substrate used in the design has a thickness $h = 0.8\,\text{mm}$ and a relative dielectric constant of 6.15.

In order to find out the resonance characteristic of the proposed filter, the two resonance units on top layer and on DGS are investigated, individually.

3.1. Single bandpass Filter on Top Layer

The structure of the resonance unit on the top layer is shown in Figs. 3 (a) and (b), which is similar to the conventional ones, except for the cut patch on ground. The other dimensions of the unit are as follows: $a = 15\,\text{mm}$, $b = 14.2\,\text{mm}$, $c = 15.4\,\text{mm}$, $w_1 = 0.2\,\text{mm}$, $w_2 = 0.3\,\text{mm}$, $g_1 = 0.2\,\text{mm}$, $p_1 = 1.2\,\text{mm}$ and $w = 1.15\,\text{mm}$ is the width of $50\,\Omega$ feed lines. The simulation results shown in Fig. 3(c) indicate it is a bandpass filter with elliptic function. The center frequency of the passband is $f_{c1} = 2.47\,\text{GHz}$ with two attenuation poles at 2.17 GHz and 2.94 GHz.

3.2. Single Bandpass Filter on DGS

Figures 4(a) and (b) exhibit the detailed structure of the single bandpass filter on defected ground structure. The corresponding dimensions are respectively: $c = 15.4\,\text{mm}$, $w_3 = 0.3\,\text{mm}$, $g_2 = 0.4\,\text{mm}$ and $p_2 = 1.3\,\text{mm}$. Fig. 4(c) shows the simulation results and the center frequency $f_{c2} = 2.87\,\text{GHz}$ with two attenuation poles at 2.73 GHz and 3.20 GHz. It is obvious that there is coupling between the square loop and ground. The coupling strength is determined by gap width g_2. In conventional design of square loop filter, the used method to tune the resonance frequency f is to change the mean circumference L. From [1],

$$f = \frac{c}{L\sqrt{\varepsilon_{eff}}} \tag{2}$$

f decreases when L increases. While in the present design, besides changing L, the resonance frequency f can be shifted by altering the gap width g_2. It should be noticed that the resonance

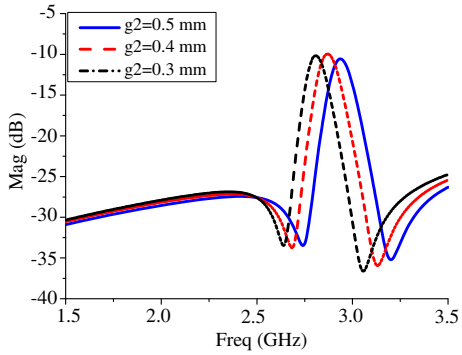

Figure 5: Passband shifts by altering g_2.

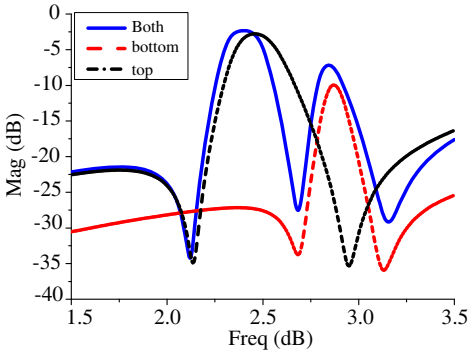

Figure 6: Comparision results of Case a, b and combination unit.

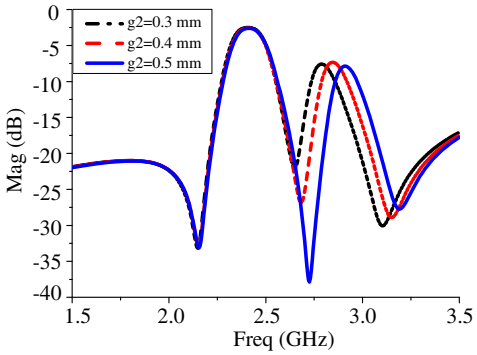

Figure 7: Operating passband of the proposed dual-mode dual-band filter versus changing g_2.

frequency f decreases with coupling strength and L increases caused by the decrease of g_2 while IL keeps almost the same. Fig. 5 demonstrates the passband shifts from 2.93 GHz to 2.81 GHz by altering g_2 from 0.5 mm to 0.3 mm.

After discussing the resonance characteristics of the top and bottom units, a novel dual-band filter is realized by combining the two filters together without changing any parameters. There are two transmission paths for RF signal, and the simulation results are shown is Fig. 6 and the center frequencies are 2.30 GHz and 2.80 GHz, respectively. The center frequencies of the filters shift a little after combination, while the insertion loss (IL) are both improved, especially the IL of the filter on the bottom. It indicates that for the proposed filter, the resonance frequencies lie on the self intrinsic structure, so the passbands of the filter can be tuned by changing the correspond dimensions. This characteristic is convenient for the design. Furthermore, the couplings among the structures on the top and bottom and feed lines occur thus the filter can be optimized by adjusting some relevant dimensions, such as w_2, w_3 and g_2 etc.

According to former discussion, it can be easily realized to tune one passband frequency while the other one almost keeps the same by changing g_2. The relevant simulation results are shown in Fig. 7.

4. SIMULATION AND EXPERIMENT RESULTS

In order to demonstrate the performance of the proposed novel dual-mode dual-band bandpass filter with DGS, the present filter is simulated by high frequency structure simulator (HFSS) and fabricated. Rogers R03006 is chosen for the dielectric substrate with the relative dielectric constant of 6.15, thickness of 0.8 mm, and the loss tangent 0.0025. Photographs of the fabricated filter are shown in Fig. 8.

From the simulation and experiment results showed in Fig. 9, the two passbands centered around 2.30 GHz and 2.80 GHz, respectively, are realized with several attenuation poles. It should be pointed out that the two attenuation poles between the two passbands are combined into one for the two adjacent passbands are too close.

The total size of the filter is only 27 mm×27 mm and is about $0.5\lambda_g \times 0.5\lambda_g$, where λ_g is the guided wavelength in the substrate at 2.5 GHz. As compared to the dual-mode dual-band bandpass filter using stackedCloop structure given in [9], in the present filter, only one layer substrate is needed, so the filter achieves almost 50% volume reduction and then the lower cost. The simulation and experiment results are shown in Fig. 9. Simulation agrees with experiment results rather well, and

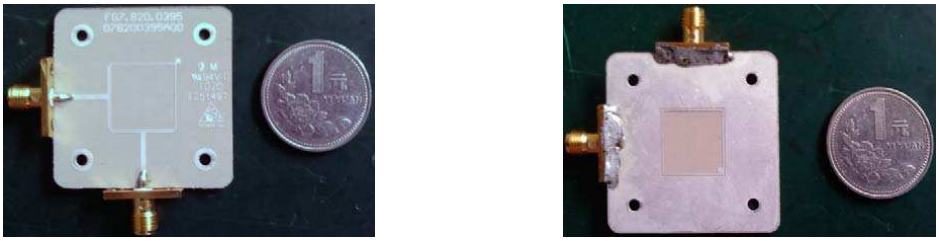

(a) (b)

Figure 8: Photographs of the filter. (a) Top view. (b) Bottom view.

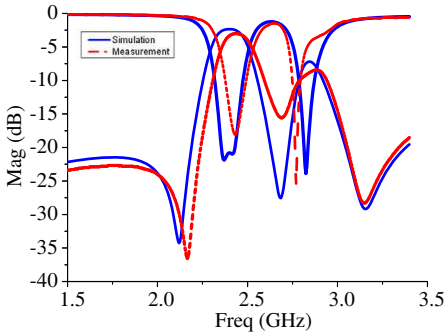

Figure 9: Simulation and experiment results.

a little higher insertion loss of the measurement is due to radiation of the slot on DGS.

5. CONCLUSION

A novel simple structure of microwave dual-mode dual-band bandpass filter is described. The proposed filter is constructed by combining the square loop on top layer and the other loop constructed with DGS on the bottom layer As a result, two adjacent elliptic function passbands are obtained. It makes the filter not only simple, compact, but also low cost. The effectiveness of the design and the practicality of the filter are confirmed by both simulation and experiment results.

REFERENCES

1. Hong, J.-S. and M. J. Lancaster, *Microwave Filters for RF/Microwave Applications*, Wiley, New York, 2001.
2. Kuo, J.-T. and E. Shih, "Microstrip stepped impedance resonator bandpass filter with an extended optimal rejection bandwidth," *IEEE Trans. Microw. Theory Tech.*, Vol. 51, No. 5, 1554–1559, May 2003.
3. Chang, S.-F., Y.-H. Jeng, and J.-L. Chen, "Dual-band step-impedance bandpass filter for multimode wireless LANs," *Electron. Lett.,* Vol. 40, No. 1, 38–39, January 2004.
4. Jiang, M., L.-M. Chang, and A. Chin, "Design of dual-passband microstrip bandpass filters with multi-spurious suppression," *IEEE Microw. Wireless Compon. Lett.*, Vol. 20, No. 4, 199–201, April 2010.
5. Tsai, L.-C. and C.-W. Hsue, "Dual-band bandpass filter using equal-length coupled-serial-shunted lines and Z-transform technique," *IEEE Trans. Microw. Theory Tech.*, Vol. 52, No. 4, 1111–1116, April 2004.
6. Promprathom, S., S. Chaimool, and P. Akkaraekthalin, "A microstrip two-layer dual-passband filter using aperture-coupled SIRs with wide rejection bandwidth by defected ground structure(DGS)," *Microwave Conference 2007, APMC 2007*, 1–4, Asia-Pacific, December 2007.
7. Ren, L. and H. Huang, "Dual-band bandpass filter based on dual-plane microstrop / interdigital DGS slot structure," *Electron. Lett.*, Vol. 45, No. 21, 1077–1079, January 2009.
8. Hong, J.-S. and M. J. Lancaster, "Realization of quasielliptic function filter using dual-mode mirostrip square loop resonators," *Electron. Lett.*, Vol. 31, No. 24, 2085–2086, November 1995.
9. Chen, J.-X., T. Y. Yum, J.-L. Li, and Q. Xue, "Dual-mode dual-band bandpass filter using stacked-loop structure," *IEEE Microw. Wireless Compon. Lett.*, Vol. 16, No. 9, 502–504, September 2006.

New Compact Dual-band Filter Using Common Resonator Sections and Double-diplexing Structure

Pu-Hua Deng[1], **Jyun-Hao Jheng**[2], **and Wen-Chi Kuo**[1]

[1]Department of Electrical Engineering, National University of Kaohsiung, Taiwan, R.O.C.
[2]Department of Graduate, Institute of Electrical Engineering
National University of Tainan, Taiwan, R.O.C.

Abstract— In this paper, a new compact size dual-band filter based on double-diplexing structure and shared common resonator sections is proposed. The basic configuration is composed of two shared stepped-impedance resonators (SIRs), four separate SIRs, and two T-junction circuits for two passbands. The shared SIRs can adjust fundamental resonant frequency and second harmonic resonant frequency thereof by designing the impedance ratio carefully, and therefore the fundamental resonant frequency and the second harmonic resonant frequency can be used to indicate the required frequencies of the two passbands, respectively. This property will be utilized to design the shared SIRs in the proposed structure. In conventional dual-band filters using single impedance ratio SIRs for dual passbands, the external quality factors of the two passbands cannot be extracted separately due to obstacles such as designing two external quality factors simultaneously with only one feed point. Thus, by adding the SIRs of two different impedance ratios near input port or output port, the fundamental frequencies thereof are designed at the center frequencies of two passbands, respectively, and the two feed points near input port or output port can be utilized to design the external quality factors of two passbands independently. Finally, the double-diplexing structure, i.e., the two T-junction circuits utilized in conventional diplexers, are located near the input and output ports and connected via the SIRs in a back-to-back fashion, and can achieve the required matching conditions at the input and output ports as well as mutual isolation between the two passbands concurrently. Specifically, a fourth-order dual-band filter with a Chebyshev response and 0.1-dB equal ripple is implemented on a substrate with a thickness of 0.508 mm, a relative dielectric constant of 3.55, and a loss tangent of 0.0027. The designed center frequencies of two passbands are 2.4 GHz and 4.1 GHz, respectively. The first and second fractional bandwidths are 11% and 9%, respectively. In conclusion, agreement between measured and simulated results is achieved and the proposed design concept is thereby verified.

1. INTRODUCTION

In modern wireless communication system, the applications of the multi-server and multi-band frequencies are important. Many circuits have been developed to select multi-band responses such as diplexers [1–3] and dual-passband filters [4–8]. In [1], the stepped-impedance resonators (SIRs) were used to implement a compact diplexer structure. Besides, the isolation is also the concerned problem for the design of diplexer. A wide-band diplexer using periodic stubs to realize a high isolation performance was proposed in [2]. In [3], the common resonator sections were used to design diplexers for compact size and high isolation.

For dual-band bandpass filter designs by using a single-circuit filter [4–7] to synthesis the dual-band response, the circuit size can be reduced effectively. However, the external quality factors for two passbands in [4–7] may not be extracted independently, i.e., the fractional bandwidths of two passbands may not be designed separately, which may be a challenge for a dual-band filter design.

In [8], a dual-band filter based on a double-diplexing structure was proposed a helpful design procedure for each band filter, which can simplify the overall design process. In this study, a new dual-band filter combined the double-diplexing structure [8] and the concept of the diplexer [3] using common resonator sections is presented, which has a compact circuit size and a simple design procedure for each band filter.

2. FILTER DESIGN

The proposed dual-band filter was based on the concept of the diplexer [3] utilizing common resonator sections.

To begin the proposed filter design, a conventional diplexer structure may be considered first, as shown in Figure 1. Here, the lengths of the T-junction lines l_A and l_B whose impedances are

both set to be 50 Ω, are chosen to meet the following conditions:

$$Z_A(f_A) \approx 50\,\Omega, \quad Z_A(f_B) \approx \infty \tag{1}$$
$$Z_B(f_B) \approx 50\,\Omega, \quad Z_B(f_A) \approx \infty \tag{2}$$

where $Z_i(f_j)$ expresses the input impedance from the point i at the center frequency of the bandpass filter j. By using the structure [3] based on the common resonator sections, a compact diplexer can be implemented, as shown in Figure 2, wherein the lengths of the T-junction lines l_A and l_B are required to satisfy the conditions (1) and (2). Besides, the same T-junction circuits of the Figure 2 can be connected to the port 2 and port 3, which make the two ports become one output port (port 2 in Figure 3). The proposed dual-band filter in Figure 3 is combined the double-diplexing structure [8] and the filter in the diplexer structure [3], which can simplify the filter design and reduce the circuit size simultaneously. Figure 3 shows the coupling paths and the matching lines of the proposed compact dual-band filter. The resonators $R1^A$ and $R1^B$ (the low-band and high-band resonators near input port) or the resonators $R4^A$ and $R4^B$ (the low-band and high-band resonators near output port) play important roles which facilitates extracting the external quality factor for each band independently. Besides, the resonators $R2^{AB}$ and $R3^{AB}$ are shared by the two passbands, the total filter size can be further reduced. The realized circuit of Figure 3 is shown in Figure 4. The detailed dimensions in Figure 4 are also found in Table 1. Note that the well-known coupled-resonator theory [9] is used to design each band filter response. The proposed filter is realized on a substrate with a thickness of 0.508 mm, a relative dielectric constant of 3.55, and a loss tangent of 0.0027. Figure 5 shows the measured and simulated results. For the first passband, the measured center frequency is 2.4 GHz, the minimum insertion loss is 2.34 dB, and the 3-dB fractional is 11%. For the second passband, the measured center frequency is 4.1 GHz, the minimum insertion loss is 3.16 dB, and the 3-dB fractional is 9%.

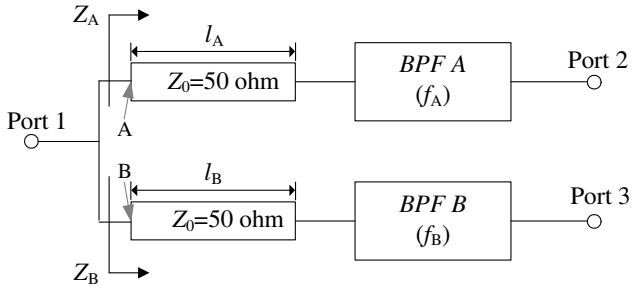

Figure 1: Conventional diplexer architecture.

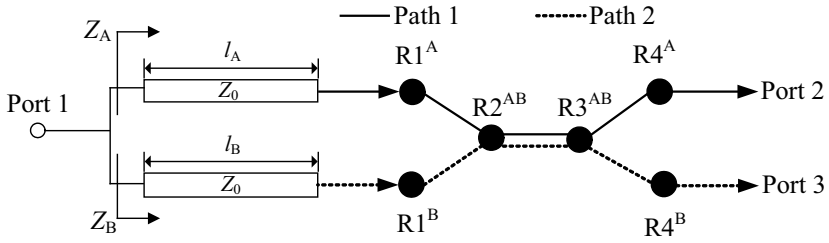

Figure 2: The diplexer structure in [3].

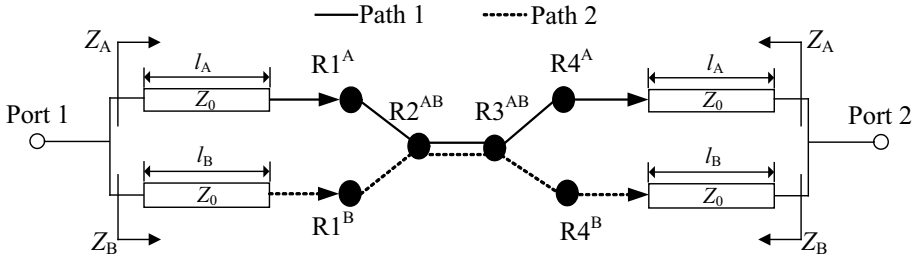

Figure 3: The proposed filter structure.

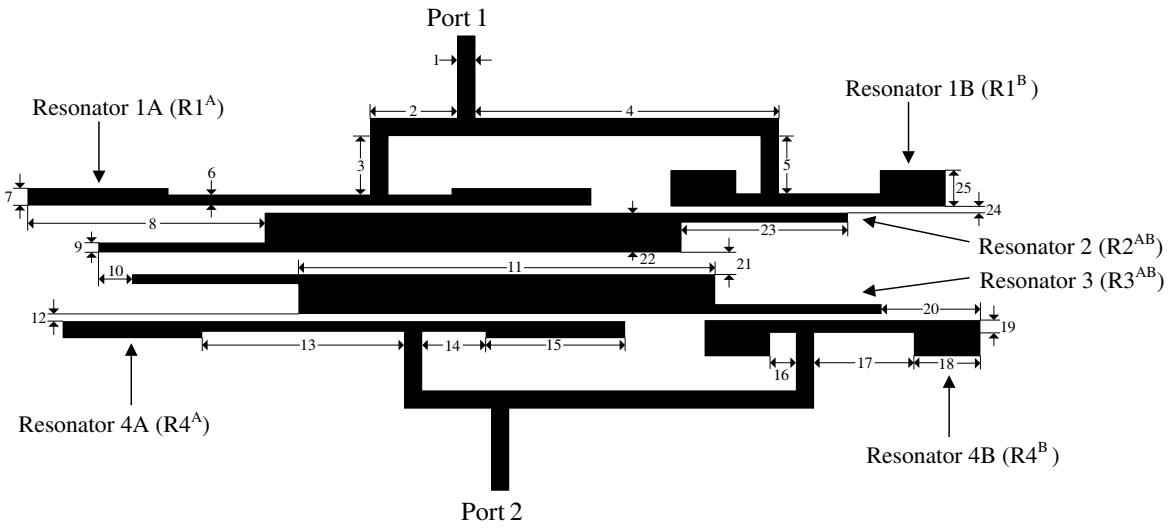

Figure 4: Layout of the proposed dual-band filter structure.

Table 1: Dimensions (in mm) of each part in the proposed structure (Figure 4).

Part number	1	2	3	4	5	6	7	8	9	10
Dimension	1.1	5.2	3.5	18.2	3.5	0.6	1	14.2	0.6	2.02
Part number	11	12	13	14	15	16	17	18	19	20
Dimension	25	0.45	12.1	3.8	8.4	1.5	6	4	0.8	5.88
Part number	21	22	23	24	25					
Dimension	0.6	2.4	10	0.34	2.2					

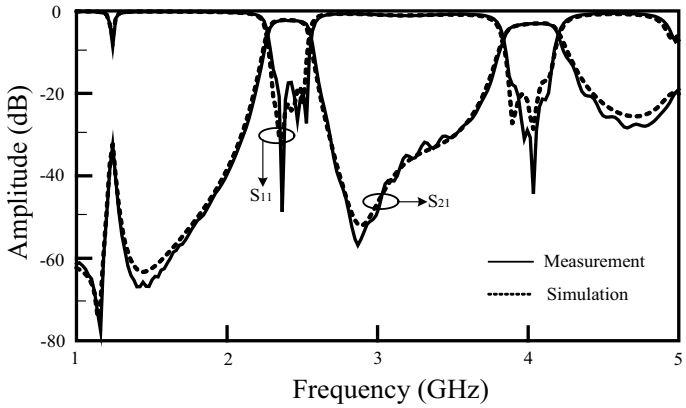

Figure 5: Simulated and measured results for the proposed filter in Figure 4.

3. CONCLUSIONS

A new dual-band filter based on double-diplexing structure and sharing SIRs is presented. The double-diplexing configuration can help designer to extract the external quality factors of high-band and low-band circuits independently. Then, the structure of shared SIRs can not only control the center frequencies of the two passbands but also to reduce the total circuit area. In this study, a microstrip fourth-order dual-band filter has been realized. Besides, the measured and full-wave simulated responses are in good agreement.

ACKNOWLEDGMENT

This work was supported by the National Science Council of Taiwan under Grant NSC 98-2218-E-390-001, Grant NSC 98-2221-E-390-041, and Grant NSC 99-2221-E-390-007. Besides, we are also grateful to the National Center for High-performance Computing for computer time and facilities.

REFERENCES

1. Srisathit, S., S. Patisang, R. Phromloungsri, S. Bunnjaweht, S. Kosulvit, and M. Chongcheawchamnan, "High isolation and compact size microstrip hairpin diplexer," *IEEE Microw. Wireless Compon. Lett.*, Vol. 15, No. 2, 101–103, 2005.
2. Strassner, B. and K. Chang, "Wide-band low-loss high-isolation microstrip periodic-stup diplexer for multiple-frequency applications," *IEEE Trans. Microw. Theory Tech.*, Vol. 49, No. 10, 1818–1920, 2001.
3. Chen, C. F., T. Y. Huang, C. P. Chou, and R. B. Wu, "Microstrip diplexers design with common resonator sections for compact size, but high isolation," *IEEE Trans. Microw. Theory Tech.*, Vol. 54, No. 5, 1945–1952, 2006.
4. Chen, C. F., T. Y. Huang, and R. B. Wu, "Design of dual- and triple-passband filters using alternately cascaded multiband resonators," *IEEE Trans. Microw. Theory Tech.*, Vol. 54, No. 9, 3550–3558, 2006.
5. Kung, C. Y., Y. C. Chen, C. F. Yang, and M. P. Houng, "The miniature 2.4/5.2 GHz dual-band bandpass filter with modified hairpin structure," *Proceedings of Microwave Conference*, 1–4, Asia-Pacific, 2007.
6. Chu, Q. X. and F. C. Chen, "A compact dual-band bandpass filter using meandering stepped impedance resonators," *IEEE Microw. and Wireless Compon. Lett.*, Vol. 18, No. 5, 320–322, 2008.
7. Chen, F. C. and Q. X. Chu, "A compact dual-band filter using S-shaped stepped impedance resonators," *Proceedings of International Microwave and Millimeter Wave Technology Conference*, Vol. 3, 1255–257, 2008.
8. Hsu, C. L. and J. T. Kuo, "Design of microstrip dual-band filters using a double Diplexing configuration," *Proceedings of Microwave Conference*, 1241–1244, Asia-Pacific, 2006.
9. Hong, J. S. and M. J. Lancaster, *Microstrip Filters for RF/Microwave Applications*, Wiley, New York, 2001.

Comparative Study of RF Dual-band-pass Filter

L. Bousbia, M. Mabrouk, and A. Ghazel
CIRTACOM-SUPCOM-ISETCOM de Tunis
Cité Technologique des Communications, Raoued 2088, Tunisia

Abstract— In this paper, the performances of RF dual-band-pass filter are studied using ADS and HFSS simulators. Comparative studies between both simulators results are considered. Based on such comparison, the reflection coefficient magnitude S_{11} result from ADS simulation is of 32.0 dB and is better than the obtained one from HFSS simulation which is of 8.0 dB. Insertion loss less than 0.4 dB from ADS simulator result. However the insertion losses obtained by HFSS simulation are about 0.9 dB. The template filter obtained with both methods is not substantially different in general.

1. INTRODUCTION

The demand for advanced filtering especially multi-band RF filters has significantly increased with the development of wireless communications standards and telecommunications equipments. Microstrip planar technology is the one of the suitable techniques to the design of RF filters [1]. Advancements in wireless communications require RF circuits with a dual band-pass operating. Therefore, the band pass filter is necessary to generate two or more transmission frequency bands [2]. Low insertion losses, low reflected power and small size for high level integration are essential criteria for satisfying band pass filtering [2, 3]. For designing this kind of filters, several techniques and methodologies are available. Nowadays, the trend is to take advantage of the accessible full wave electromagnetic (EM) simulators, which can provide complete analyses of physical structure of filters [2]. Full wave electromagnetic EM simulators such ADS or HFSS are used to solve practical and complex design problems [2]. The first simulator is based on the method of Moments (momentum) which converts the functional expressions to matrix equations. Momentum is numerical method which solves Maxwell's equation for the design. The MOM is a numerical technique that can be used to solve differential and integral equations. It is mainly used for solution of integral equations in EM problems [3].

The second simulator uses Finite Elements Method (FEM) which is mathematically used for finding approximate solution of partial differential equations as well as of integral equations. The FEM is a general numerical technique to find the approximate solutions to the boundary value problems. In the application of FEM, the entire volume is divided into sub-volumes in which the unknown functions are represented by simple interpolating functions [4]. This method splits surface into sub-regions most often triangular. The structure contains N number of triangle vertices of in the inner limits; we obtain a set of N equations with N variables. Both methods are the most widely used and the most often cited for filters simulation. In this paper, Comparison between both (ADS and HFSS) simulators results is made. The design process, as explained in Section 3, relies on simulations carried out using Advanced Design System (ADS) of Agilent and HFSS of ANSOFT [4].

2. DESIGN OF MICROSTRIP FILTER

The studied filter is composed of two ring-resonators loaded with two open-stubs. The used method is consisting of adding a half-wave length ($\lambda/2$) microstrip-line with an open-stub [5]. The principle of method is based on a total length of $\lambda/2$ for all of the sides of each ring resonator. Figure 1 illustrates the principle of the studied filter.

Figure 2 shows the physical layout of the dual band pass filter using uniform microstrip lines. This filter consists of two microstrip open loops. Two open circuited stubs are attached at the center of the respective microstrip lines [5]. The total length of the resonator is around a half wave length ($\lambda/2$). The design parameters dimensions are chosen as following and illustrated below: $W = 1.2\,\text{mm}$; $W_1 = 1.5\,\text{mm}$; $W_2 = 0.9\,\text{mm}$; $L = 11.2\,\text{mm}$; $L_1 = 6.7\,\text{mm}$; $g_1 = g_2 = 0.3\,\text{mm}$.

The structures of open loop resonators filter with center frequency 1.68 GHz and 2.81 GHz are designed on RT/duroid 6006 substrate with a thickness $H = 0.635\,\text{mm}$ and a relative dielectric constant $\varepsilon_r = 6.15$.

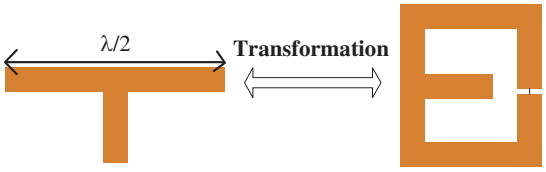

Figure 1: Principle of ring resonator design.

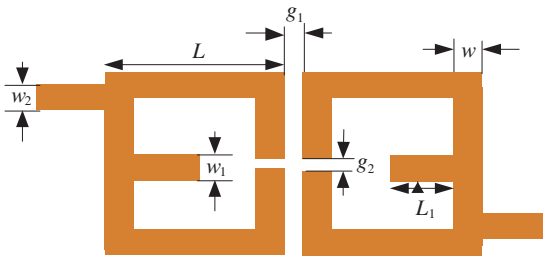

Figure 2: Topology of the studied dual band filter.

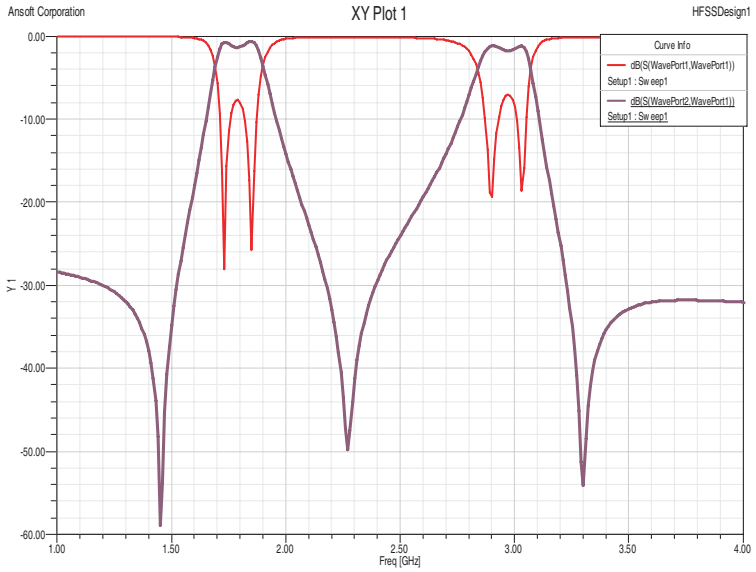

Figure 3: HFSS Simulated S_{21} and S_{11} parameters for the studied dual band filter.

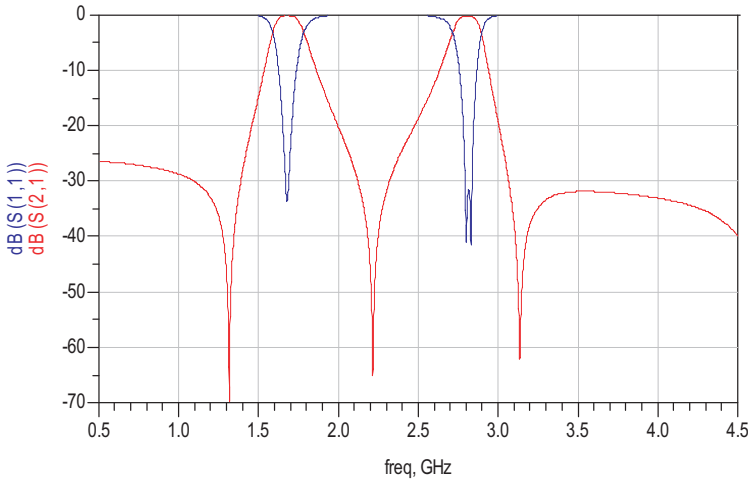

Figure 4: ADS Simulated S_{21} and S_{11} parameters for the studied dual band filter.

3. NUMERCAL STUDY: ADS AND HFSS SIMULATIONS

The full wave simulators are now inescapable in the design cycle of modern RF and microwave circuits. These simulators are making possible the design of several complex architectures operating in high frequency bands. The performances of the dual band RF filter have been studied using two full wave simulators, ADS and HFSS. The obtained S-parameters using both simulators are shown in Figure 3 and Figure 4 respectively.

The obtained characteristics of our studied filter with both methods are not substantially differ-

ent in overall. We can note that the obtained ADS simulated S-parameters are better than those obtained by HFSS. The major difference between simulation trials is the return loss values at the resonant frequencies. From the reflection magnitude we can deduce that S_{11} results from ADS simulation is of 32.0 dB and is better than the obtained one from HFSS simulation which is of 8.0 dB. The S_{21} obtained result from ADS simulator shows that the proposed filter has an insertion loss of 0.18 dB and 0.3 dB at the first resonant frequency 1.68 GHz, and the second resonant frequency 2.81 GHz respectively. However the insertion losses obtained by HFSS simulation are about 0.4 dB and 0.9 dB respectively therefore they are not so impressive compared to those obtained by ADS. ADS momentum simulation tool is the best for this kind of filter, and seems it is far more efficient than HFSS. The ADS simulation has a much shorter simulation run time (typically 2 s) than the HFSS (10 s), which solves each frequency point separately but consumes far more system memory.

4. CONCLUSIONS

The EM simulators offer several advantages and disadvantages, depending on the parameters that must be simulated. For our studied dual band filter, ADS offered most accurate, efficient and fast solution. For the S-parameters, especially S_{11} and S_{21}, neither program will offer fully accurate results, but ADS appears to be more accurate compared to HFSS. We are seeing significant reductions in the level of return losses obtained by ADS which have decreased fourfold compared to those fined by HFSS. The obtained S_{21} result from ADS simulator shows that the proposed filter has an insertion loss of 0.18 dB and 0.3 dB at the first resonant frequency 1.68 GHz, and the second resonant frequency 2.81 GHz, respectively. However, the obtained insertion losses by HFSS simulation are about 0.4 dB and 0.9 dB respectively. So ADS has been successfully used for the design of planar filter especially dual-band RF filters.

REFERENCES

1. Hong, J. S. and M. J. Lancaster, *Microstrip Filters for RF/Microwave Applications*, Wiley, New York, 2001.
2. Chen, Z.-X., X.-W. Dai, and C.-H. Liang, "Novel dual-band bandpass filter using double square loop structure," *Progress In Electromagnetics Research*, Vol. 77, 409–416, 2007.
3. Kinayman, N. and M. I. Aksum, *Modern Microwave Circuits*, Boston, London, 2005.
4. Yu, M., A. Panariello, M. Ismail, and J. Zheng, "3-D EM simulators for passive devices," *IEEE Microwave Magazine*, Vol. 9, No. 6, 50–61, December 2008.
5. Zhang, Y., J. X. Chen, and Q. Xue, "Dual-band bandpass filters using stub-loaded resonators," *IEEE Microwave and Wireless Components Letters*, Vol. 17, No. 8, 583–585, August 2007.

Vectorial Remote Sensing of Guided Electric Field with Pigtailed Electro-optic Microcavities

A. Warzecha[1], **G. Gaborit**[1,2], **and L. Duvillaret**[2]

[1]IMEP-LAHC, UMR 5130, Université de Savoie, bât. Chablais, Le Bourget-du-Lac Cedex 73376, France
[2]Kapteos, bât. Chablais, rue Lac de la Thuile, Savoie Technolac, Le Bourget-du-Lac Cedex 73376, France

Abstract— We present the applicability of pigtailed non-linear optical microcavities to perform non invasive vectorial characterization of electric (E) field, especially in guided configuration. Those sensors are based on Pockels' effect, which consists in additional birefringence induced by an applied E field in certain non-centrosymetric crystals [1], called electro-optic (EO) crystals. By sandwiching the EO crystal between two dielectric mirrors, the E-field induced phase modulation of the laser beam is then enhanced thanks to the resonance of the Fabry-Pérot (FP) cavity [2, 3]. Moreover, choosing a working wavelength on the steepest slope of one of the cavity resonance peaks leads to a direct amplitude modulation of the laser, this latter one being directly proportional to the applied E field. The vectorial behavior of the measurement (measurement of a given E field component) is intrinsically linked to the relation that links the crystal refractive indices variation to the applied E field through a scalar product with the sensitivity vector of the EO crystal [4]. Developed sensors are based on $LiNbO_3$ optical waveguides obtained by titanium diffusion along to the Y axis of the crystal. The waveguide is finally embedded between two multilayer dielectric mirrors to obtain the FP microcavity ($\sim 1\,mm^3$), coupled to a polarization maintaining fiber to perform remote measurements (up to a few 10 meters). Those transducers have already been studied in term of sensitivity and a lowest measurable E field of $1\,V{\cdot}m^{-1}{\cdot}Hz^{-1/2}$ has been achieved. They are also suitable for very high field strength measurement and we here demonstrate some time domain measurements of disruptive E field. Longitudinal spatial resolution is determinate by the length of the microcavity. Transversal spatial resolution has been estimated to less than $50\,\mu m$ by measuring fringing E-field above interdigitated strip lines. The bandwidth is linked to the inner-cavity photons life time and reaches a few tens of GHz. Two dimensional E-field mapping of fringing fields have been achieved in the frequency domain. Invasiveness of the sensors (influence of the probe on the electric signal propagation) is very low and quantitative estimations of this latter one are in progress. They are measured using common microwave differential techniques exploiting the EO-sensor induced variation of phase and amplitude of both transmitted and reflected microwave signals.

1. INTRODUCTION

E-field vectorial characterization is required for numerous applications: on chip diagnostic in electronics, antenna pattern measurements, electromagnetic compatibility, bioelectromagnetism dosimetry. Many tools or sensors are already available for these different applications. Monopoles, dipoles and patch antennas are actually very convenient although they are bandwidth limited. Moreover, the main drawback of these commonly used sensors is the invasiveness induced on the field to be measured, due to their metallic structure. The present sensor is based on the Pockels' effect which consist in an additional birefringence induced by the electric field. This modification on the optical properties takes place into non-centrosymmetric crystals and leads to highly compact and fully dielectric sensors. Furthermore, the sensor can be deported thanks to a polarization maintaining fiber insensitive to outer electromagnetic perturbation. The modification induced on a laser probe beam crossing the crystal is here enhanced within an optical cavity. The Fabry-Pérot (FP) effect increases the effective interaction length between the electric field to be characterized and the laser probe beam.

The cavity act as a multiple wave interferometer and it linear response exhibit transmission peaks for some particular optical wavelength. Any modification of the refractive index will lead to a spectral shift of those peaks. If the operating wavelength is set on one side of the peak, more precisely on the inflexion point of the response, any weak modification of refractive index induces the strongest and the most linear response of the transmitted (reflected) optical power. The laser beam intensity carries the image of the electric field via an optical fiber to a photodiode. The signal is finally visualized on oscilloscope for time domain measurements or on a spectrum analyzer for frequency domain measurements.

This paper is divided in four parts. The first section remind the sensor based theory, the second one explains the structure of the probe and the whole setup. We then present some characterization of disruptive electric field as an example of sensor potentialities. The last section is dedicated to quantitative estimations of the EO probe disturbance on guided microwave measurements.

2. THEORETICAL BACKGROUND

The whole form of the spectral behavior of a FP cavity is given in Equation (1).

$$R_{FP} = \left(1 - \frac{1}{\frac{8e^{2L\alpha}F^2\left(2F^2+\pi\left(\sqrt{4F^2+\pi^2}+\pi\right)\right)\sin^2\left(\frac{2L\pi n_{opt}}{\lambda}+\varphi_r\right)}{\left(2(-1+e^{2L\alpha})F^2+e^{2L\alpha}\pi\left(\sqrt{4F^2+\pi^2}+\pi\right)\right)^2}+1} \right) \tag{1}$$

This equation gives the normalized cavity response in reflexion as a function of it actual length L, the refractive index n_{opt} and its finesse $F = \frac{\pi e^{-\alpha L}\sqrt{R}}{1-Re^{-2\alpha L}}$. It also includes the propagation losses α in the cavity. If the inner cavity material is EO, its refractive indices depends vectorially on the applied electric field. The n_{opt} term becomes $n_z - n_z^3 r_{33} E_z$ in case of a Y-cut $LiNbO_3$ crystal (3 m symmetry) probed by an optical wave linearly polarized along the Z-axis [3]. r_{33} is one of the EO coefficient of the $LiNbO_3$ tensor. This refractive index variation leads to a phase shift of the optical beam and finally to a spectral shift of the reflexion and transmission peaks. The free spectral range FSR of the cavity (frequency separation between transmission peaks) writes :

$$FSR = \frac{c}{2n_{opt}\left(\vec{E}\right)L} \tag{2}$$

We here exploit this electric field dependence using a working wavelength on a side of a reflexion peak. This wavelength is accurately chosen at the inflexion point of the cavity response to obtain maximum linearity and sensitivity. This working point validates $\frac{\partial^2 R_{FP}}{\partial \lambda^2} = 0$ and corresponds to a normalized transmitted power of $(1 - \frac{2\pi^2}{6F^2-\sqrt{36F^4+4\pi^2F^2+\pi^4}+3\pi^2})$ corresponding to 0.25 for high finesse. The optical modulation depth d, given by the ratio between the modulated intensity for this working point and the mean intensity, is finally given by:

$$d \cong \sqrt{3} F n_z^3 \frac{L}{\lambda} r_{33} E_z \tag{3}$$

L is the actual length of the cavity. Let us notice that the effective length seen by the optical wave introduce the factor F. This latter equation summarize the linear and vectorial behavior of the FP cavity electric field sensor. Moreover, this electric field induced modification of the optical intensity is directly taken back from the sensor output without any modulation treatment. This leads to a compact and easy to use measurement bench.

3. DEVELOPED SENSOR AND ASSOCIATED MEASUREMENT BENCH

In order to exploit the previously explained effect, we have designed and realized a cavity based on a Y-cut $LiNbO_3$: Ti waveguide obtained by Titane diffusion. This waveguide is sandwiched between two multilayer dielectric mirror to obtain the cavity effect. The FP structure stability is obtained thanks to the transversal confinement of the beam into the waveguide. The device is fully dielectric and connected to a polarization maintaining fiber to allow deported measurement. Schematic and picture of the realized electric field probe are shown on Fig. 1. As the optical wave is also longitudinally confined, the sensor remains very small (millimeter sized) compared to the common wavelength of the E-field to be measured.

The full setup allowing to measure the electric field is depicted on Fig. 2(a)).

The optical source is a DFB laser @ 1.55 µm with 5 nm tuneability via temperature modulation thanks to TEC (temperature controler) and Peltier module (slow modulation < 0.1 Hz, high accuracy). A 0.5 nm wavelength range is also achievable thanks to regulating supply of the diode current (speed modulation > 10 Hz, low accuracy). A half-wave plate is used to align the laser probe beam polarization to select TE cavity mode and the probe the Z-axis of the crystal. The signal is measured in transmission and also in reflexion thanks to a non-polarizing beam splitter

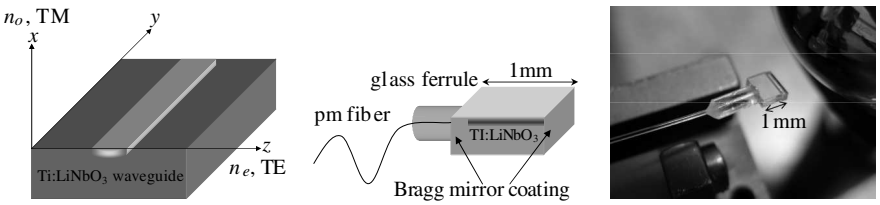

(a) (b) (c)

Figure 1: (a) Schematic of the $LiNbO_3 : Ti$ wave guide. (b) Structure of the microcavity based pigtailed EO sensor. (c) Picture of the realized probe.

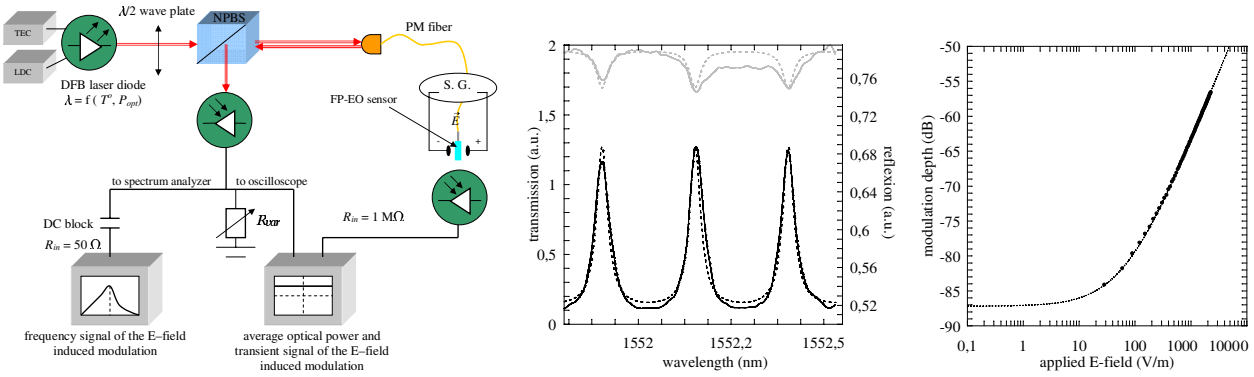

(a) (b) (c)

Figure 2: (a) Schematic of the optoelectronic setup dedicated to EO characterization of electric field. (b) Measured linear response of the probe with theoretical fit (dashed lines). (c) Non linear response of the probe obtained in CW configuration, with an applied E-field at 84 kHz.

(NBPS). These two spectra are visualized using an oscilloscope. From this measurements we obtain the finesse of the cavity and the coupling efficiency of the sensor. E-field to be measured is applied via parallel electrodes (E-field along z axis of the probe). This structure is fed by a signal generator which applies alternative E field on the FP cavity. Transmitted and reflected beams are detected by two photodiodes. Average signal is obtained on oscilloscope. it allows to determine the optimal working point, which is controlled thanks to the wavelength accordability. A spectrum analyzer is used to extract the amplitude modulation in case of a CW E-field (configuration for the FP-EO sensor studies). Fig. 2(b) present the experimental result concerning the EO probe linear response, i.e., reflexion and transmission of the cavity with respect to the wavelength. We can extract the finesse of the cavity also given by $\frac{FSR}{FWHM} = 7$, $FWHM$ beeing the full width of the peak at half maximum. Once the working wavelength fixed to the highest slope of the peak (inflexion point), we perform some non linear measurement in reflexion and result is shown on Fig. 2(c). The measured modulation depth extract from the fitting curve, including noise contributions, is $d = 6.4\ 10^{-7} E_z\,\mathrm{m} \cdot \mathrm{V}^{-1}$. The minimum detectable field is lower than $1\,\mathrm{V} \cdot \mathrm{m}^{-1} \cdot \mathrm{Hz}^{-1/2}$.

The vectorial properties of this sensor has also been investigated. We have extracted a selectivity to one component of the electric field greater than 30 dB. Furthermore, two dimensional electric field mapping has been achieved onto coplanar waveguides and the transverse spatial resolution of the measures is 30 µm, limited by the number of acquisition points.

4. TRANSIENT MEASUREMENTS OF VERY HIGH FIELD STRENGTH

The aim of this section is to give the potentiality of this kind of EO probe for very high electric field characterization. We here present transient measurements of lightning associated E-field. The field is here generated by a hammered piezo which feeds two electrodes. First experiment is shown on Fig. 3. The probe is directly placed between the two electrodes. Let us notice, on the bottom Fig. 3(a)), that the lightning channel surrounds the probe and follow the most ionizable way, i.e., where the electric field is maximum together with a disruptive E-field minimum. This leads to a measurement at the closest vicinity of the sensor. The transient evolution of the E-field is given on Fig. 3(b). Nevertheless, the repeatability of this single shot lightning is very poor. If the probe is well centered, the ionization channel can travel either up or down or in front of the sensor. The measurements can be dramatically different as the field orientation varies from one measure to

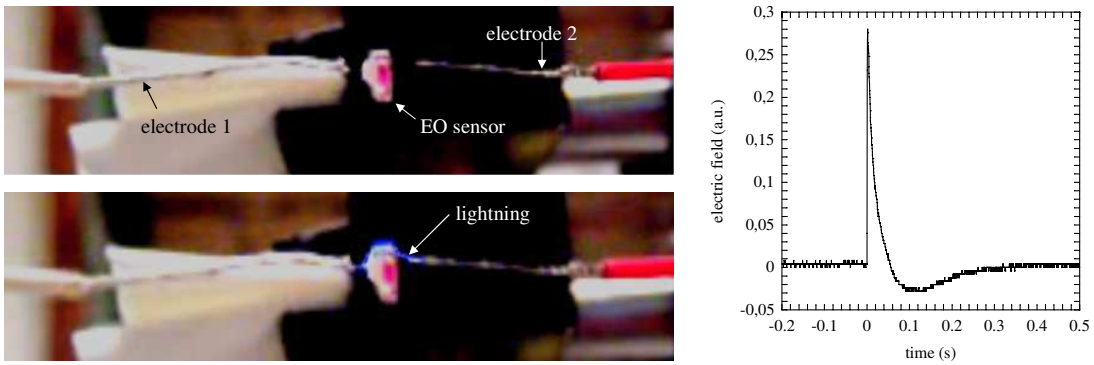

Figure 3: (a) Pictures of the electrodes and of the probe (top), then surrounded by the breakdown E-field (bottom). (b) Typical form of the E-field associated to the lightning, measured with the FP-EO probe.

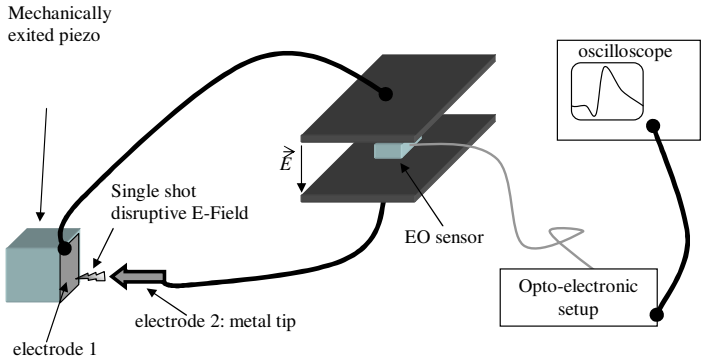

Figure 4: Experimental setup of the temporal evolution of a disruptive E-field.

another, and is not parallel to the EO probe sensitivity axis in general.

To increase the reproducibility, we deport the electric field toward two other remote parallel electrodes (Fig. 4). The electric arc is no more influenced by the probe and take always the same way from the fixed sharp tip. The spatial distribution of the field remains stable and do not influence the transient evolution.

The result on Fig. 5 is obtained for four successive electric arcs and the four acquisitions zoom to the E-field inducing the lightning (constant negative slope on Fig. 5(d)). Those four measures correspond to the convolution between the piezo associated electric field and the electric arc propagation. Let us notice on Fig. 5(d), the Corona effects (ionization without any leader channel), illustrated by the fast disturbance on the transient evolution (particularly at the bottom of the curve, where the field is maximum in the negative, just before the arc generation).

5. INVESTIGATION ON THE PROBE INVASIVENESS

We here propose to extract the variation of the effective permittivity seen by the microwave signal propagated along a Crawford cell. This measurement is performed in the frequency domain with a vectorial network analyzer. The TEM cell is here considered as a low-pass filter RC with R the real part of the cell impedance and C, the parallel capacitance between the fed line and the ground plates. The cut-off frequency of the filter is given by $F_c = \frac{1}{2\pi RC}$, with $C = \frac{\epsilon_0 \epsilon_r S}{e}$, S being the effective surface on the central line and e, the inter-electrode distance. We can deduce $\frac{\Delta\epsilon_r}{\epsilon_r} = -\frac{\Delta F_c}{F_c}$. The S_{21} parameter allow to extract F_c with and without the sensor placed in between the plates. The measured variation of effective permittivity is about 0.5% (Fig. 6(a)).

The phase of the S_{21} parameter leads to another equation for the effective permittivity variations: $\frac{\Delta\epsilon_r}{\epsilon_r} = 2\frac{\Delta\phi_{S21}}{\phi_{S21}}$. The relative phase shift $\frac{\Delta\phi_{S21}}{\phi_{S21}}$ is deduced from the result shown on Fig. 6(b) and reach once again to about 0.5%.

Let us finally exploit the reflective coefficient S_{11}. The resonance frequencies of the propagation line are defined by $F_r = m\frac{c}{2\sqrt{\epsilon_r}L}$, with m, the resonance order and L the length of the Crawford

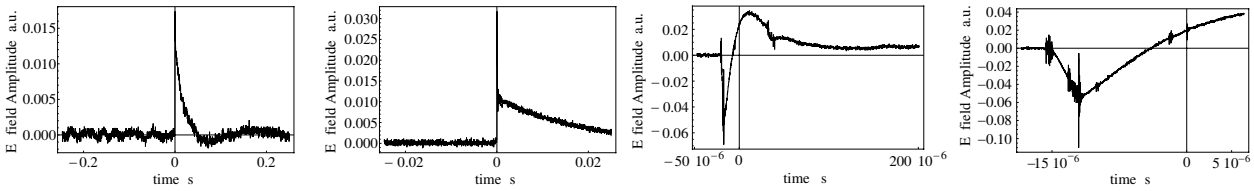

Figure 5: Transient evolution of the lightning associated E-field with different time scale, from (a) second to (d) microsecond.

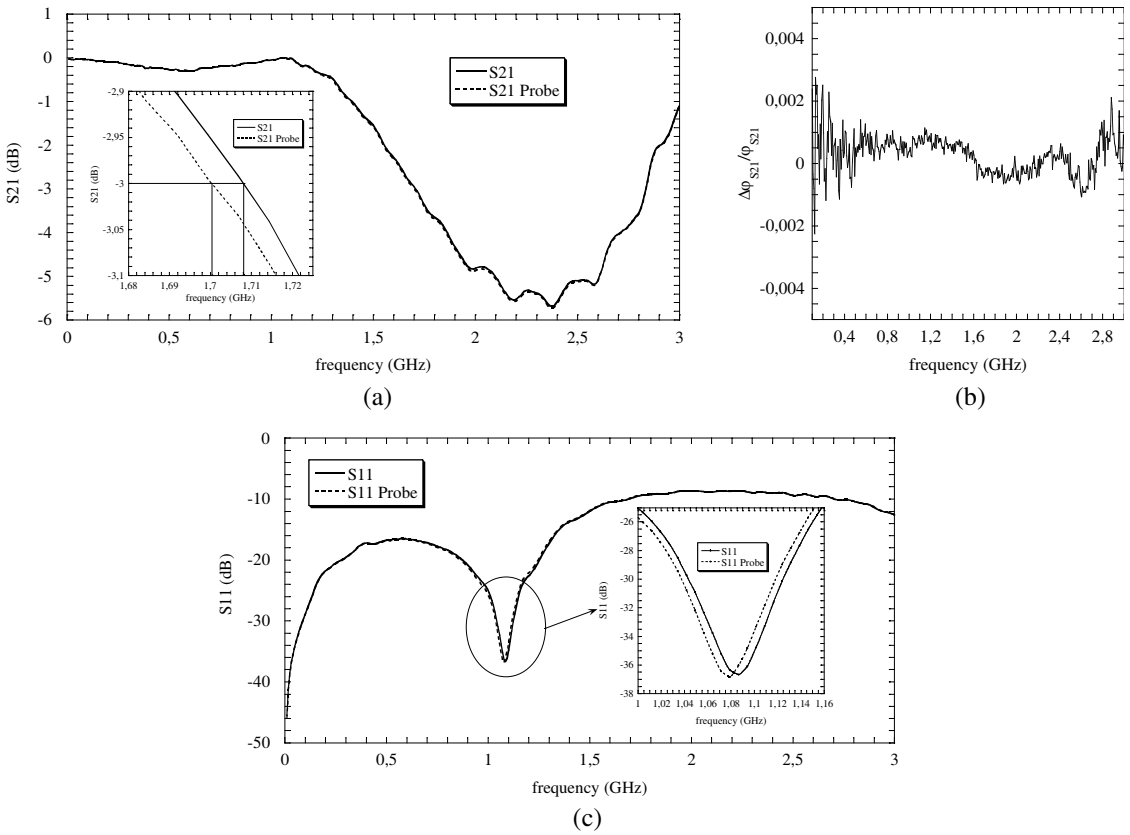

Figure 6: (a) Magnitude of the S_{21} parameter and (b) the crystal induced relative phase variation of S_{21}. (c) Magnitude of the S_{11} parameter.

cell. The link between the relative variations of ϵ_r and F_r is given by $\frac{\Delta\epsilon_r}{\epsilon_r} = -2\frac{\Delta F_r}{F_r}$. The F_r shift leads to a value of 1.4% for $\frac{\Delta\epsilon_r}{\epsilon_r}$.

We can compare the three previous values for the probe induced modification with the volume ratio R_v between the EO probe and the inner cell E-field volume distribution. This ratio have to be weighted with respective permittivity. We obtain $R_v \simeq 1.6\%$. This latter value maximize the invasiveness of the sensor.

6. CONCLUSION

We have realized a fully dielectric pigtailed sensor based on the EO effect enhanced thanks to a FP cavity. This sensors exhibits a sensitivity greater than $1\,\mathrm{V}\cdot\mathrm{m}^{-1}\cdot\mathrm{Hz}^{-1/2}$. This sensor is also suitable for very high E field measurement: we have performed some transient characterizations of disruptive E field in the air. Even if this sensor is very small sized and fully dielectric, we here evaluate the weak disturbance induced by sensor on the field to be measured, in the GHz range. The invasiveness of the probe is about 1% in our experimental configuration.

ACKNOWLEDGMENT

The authors acknowledge the DGA (French Military Programs Management and Procurement Agency) for its support.

REFERENCES

1. Yariv, A., *Optical Electronics*, Saunders College Publishing Ed., 1991.
2. Duvillaret, L., S. Rialland, and J. L. Coutaz, "Electro-optic sensors for electric field measurements. I. Theoretical comparison among modulation techniques," *J. Opt. Soc. Am. B*, Vol. 19, 2692–2703, 2002.
3. Gaborit, G., G. Martin, J. L. Coutaz, and L. Duvillaret, "High-finesse Fabry-Perot electro-optic sensors with enhanced sensitivity and high spatial resolution," *Appl. Opt.*, Vol. 47, 2001–2009, 2007.
4. Duvillaret, L., S. Rialland, and J. L. Coutaz, "Electro-optic sensors for electric field measurements. II. Choice of the crystals and complete optimization of their orientation," *J. Opt. Soc. Am. B*, Vol. 19, 2704–2715, 2002.

Incorporation of Optical Fiber-loop and FBG as Displacement and Temperature Sensors for Structure Monitoring

M. Kamil Abd-Rahman and N. Jannah Muhd-Satar
Faculty of Applied Science, Universiti Teknologi MARA, Shah Alam 40450, Malaysia

Abstract— This paper presents a distributed optical fiber sensor system consisting of single-mode fiber-loop sensor incorporating fiber Bragg grating (FBG) for displacement and temperature detections. The fiber-loop sensor was geometrically designed using SMF-28 to exhibit optical attenuation due to the micro-bending effect in the fiber. The bending effect would develop higher optical loss when the loop diameter is reduced due to the force action of displacement. FBG incorporated in the system not only functions as discrete localized point-to-point detection of minor structural-displacement, it also served as temperature sensor. Temperature-compensating fiber would distinct the temperature sensing effect from the effect of structural displacement. The system is capable to detect faults at several different locations by providing distributed sensing points along more than 25-km-length of detection. Optical time-domain reflectometer (OTDR) was used to sense optical attenuation along the length of fiber which acts as the sensing arm of the fiber-loop sensor-heads distributed precisely along the detection-length. The fiber-loop sensing-head has a sensitivity of 0.0361 dB/mm displacement. The incorporated FBG sensor has a slightly lower sensitivity of 0.0621 dB/mm. The optical fiber sensor system was used to model the displacement of a hill-slope structure.

1. INTRODUCTION

Monitoring of engineering structures has becoming increasingly important in the past decades in giving out alarms and early warnings due to structure failure, which would lead to catastrophic damages. Many techniques and sensors had been discovered to continuously access the performance of the structures [1] especially for safety reasons. With an improve process in the optical fiber sensor (OFS) technology, the procedures of monitoring the performances of specific properties over time will provide an accurate information and data during the operation, the manufacturing process and throughout the lifetime of the structure. In addition, optical networks sensing system were meant to expand and improved the physical infrastructures.

Advances in the development of sensing systems for structural health monitoring makes optical fiber become highly demanded [2]. Optical fiber sensors (OFSs) have gained much attention in recent years due to their ability to sense variety of physical and chemical measurement such as strain, stress, displacement, position, vibration, humidity, pressure, temperature, viscosity and several other parameters. FOSs is a perfect option in sensing area for remote data telemetry over kilometers of length without corruption from electric and electromagnetic interference. The issues of reliability of optical fiber sensors are very important because of their role in critical application where a failure of a sensor will have consequences on cost and safety [3]. Basically, the OFSs work by detecting decreasing in transmission light due to bending of the fiber because of the microbending effect. Microbending is a mechanical perturbation of a fiber waveguide causes a redistribution of light power among the many modes in the fiber [4]. One of the extremely featured of OFSs is it can be multiplexed and distributed along a single fiber. With certain design, distributed sensing can be archived along the length of a fiber [5]. The distributed OFSs have been proved to be a very suitable and useful technique for monitoring and early warning of fault during structural monitoring process [6].

There are many different types of OFSs available in the market such as FBG sensor. FBG consist of a periodic modulation of the index of refraction along the fiber core [7] and act as a wavelength-encoded sensor and will be able to provide an absolute measurement of physical perturbation [8] during monitoring process. The Bragg wavelength varies with the change in ambient temperature as denoted by the shift in its wavelength.

$$\lambda_B = 2n_{eff}\Lambda\left[\alpha + \frac{1}{n_{eff}}\frac{dn_{eff}}{dT}\right]\Delta T \tag{1}$$

where ΔT is the temperature variation, α is the thermal expansion coefficient, Λ is pitch length of the grating and dn_{eff}/dT indicate the thermo-optic coefficient of the optical fiber.

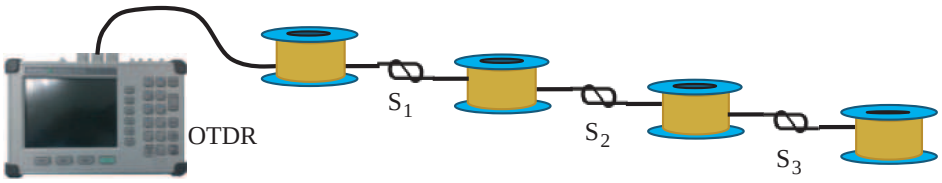

Figure 1: Distributed displacement measurement setup using OTDR.

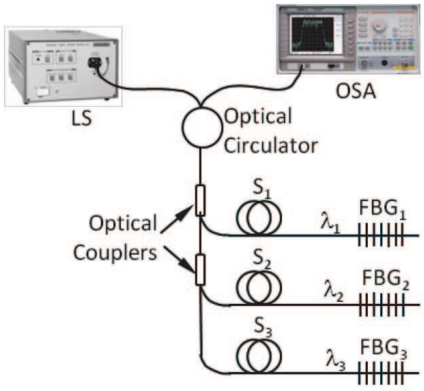

Figure 2: Incorporated SMF-sensors and FBGs.

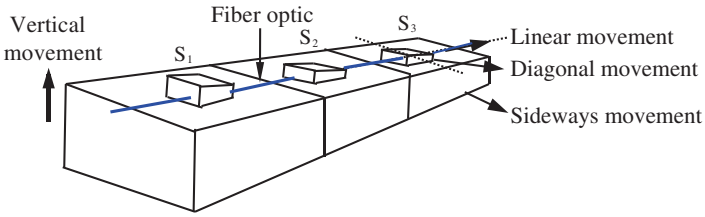

Figure 3: Hill-slope simulator model.

2. EXPERIMENTAL DETAILS

SMF-28 optical fiber was geometrically designed into a sensing-head loop where the decreased in the loop diameter will introduces attenuation into the sensor system. The attenuation recorded is due to the induced microbending effect in the optical fiber. The schematic of an optical time domain reflectometer (OTDR) sensing method is illustrated in Figure 1 where three SMF-sensor heads (S_1, S_2 and S_3) were located at different position along 500-m length of the fiber. Introducing displacement in sensing head can be detected by OTDR with accurate fault locations and magnitude of the displacement. The SMF-sensor then was incorporated with FBG for displacement and temperature detection. Three FBGs labeled as λ_1, λ_2 and λ_3 with 10 mm gauge length operated at wavelength 1544.3 nm, 1547.4 nm and 1550.4 nm respectively was shown in Figure 2. An optical spectrum analyzer (OSA) was used to analyze the change in temperature and optical loss in the SMF sensor head. A broadband source with wavelength 1550 nm was used as a light source (LS). The OFS system was installed on the slope simulator model as in Figure 3 to simulate the displacement of hill-slope structure. The hill-slope simulator model was divided into three portions. S_1, S_2 and S_3 were located at different position on the slope simulator. The simulated ground movement can be detected by OTDR within the adjacent sensor probe.

3. RESULT AND DISCUSSION

Figure 4 presents two traces of transmitted optical signal in the optical fiber. Step drop in return loss of transmitted optical signal shows that microbending incurred at particular location. OTDR locates the fault at 374.2-m by single sensor head (S_3) indicate by trace A while trace B shows three fault detected by S_1, S_2 and S_3. Figure 5(a) shows an optical transmittance displayed and analyzed by OSA when SMF-sensor head detected a displacement based on the experimental setup in Figure 2. Operated reflected wavelength of FBG become an indication to determine which SMF-sensor head responded to the displacement. In addition, the location of displacement occurred can also be known. FBGs detect temperature variation as illustrated by the shift in the operated wavelength represent by Figure 5(b). Increase in the displacement applied to the optical fiber resulted in exponential increased in the return loss of the sensor as in Figure 6(a). Both measurement method of OTDR and OSA shows an exponential attenuation behaviour. The fiber-loop sensing-head has a sensitivity of 0.0361 dB/mm displacement while the incorporated FBG sensor has a slightly lower sensitivity of 0.0621 dB/mm as plotted in Figure 6(b). A model to detect ground movement on a hill-slope was simulated. The optical attenuation due to linear-, vertical-, sideway-, and diagonal movement is shown in Figure 7(a). The OTDR start to detect a fault of displacement

when the ground was displaced about 5 ± 1-mm from the original position. The sensitivities of the linear-, vertical-, sideway-, and diagonal movement were recorded as 0.179 dB/cm, 0.122 dB/cm, 0.095 dB/cm, and 0.193 dB/cm respectively as shown in Figure 7(b). Due to the higher sensitivity recorded in this simulation, OTDR response faster to the diagonal-movement for initial fault detection on the ground.

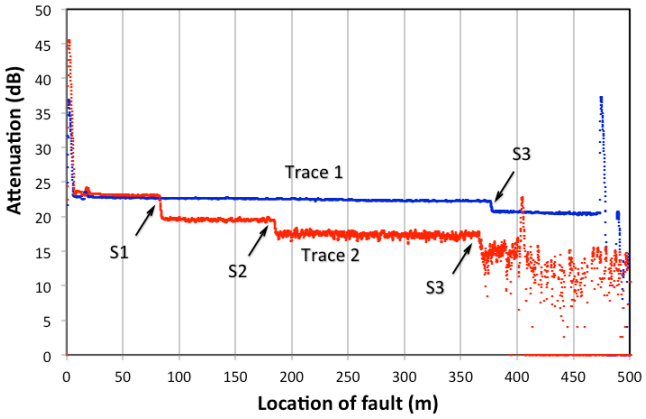

Figure 4: Faults detected by S_1, S_2 and S_3.

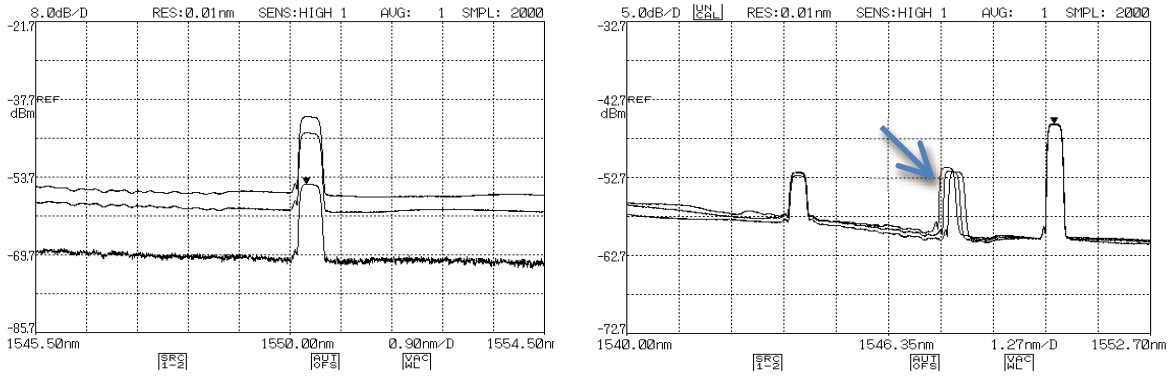

(a) (b)

Figure 5: (a) Decreased in optical signal when displacement occurred. (b) Wavelength shift with temperature change indicated by λ_2.

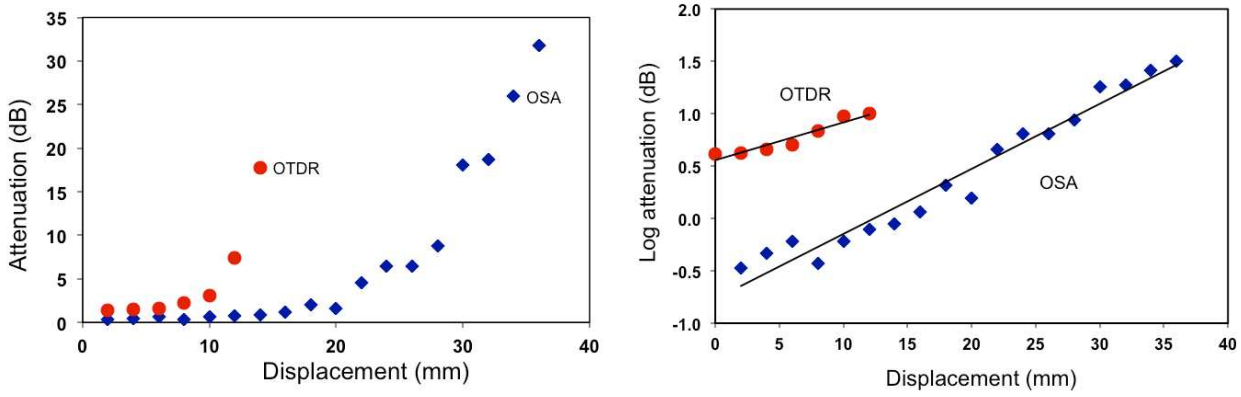

(a) (b)

Figure 6: (a) Exponential attenuation behavior with the increase in the displacement. (b) Slightly higher sensitivity of measured using OTDR.

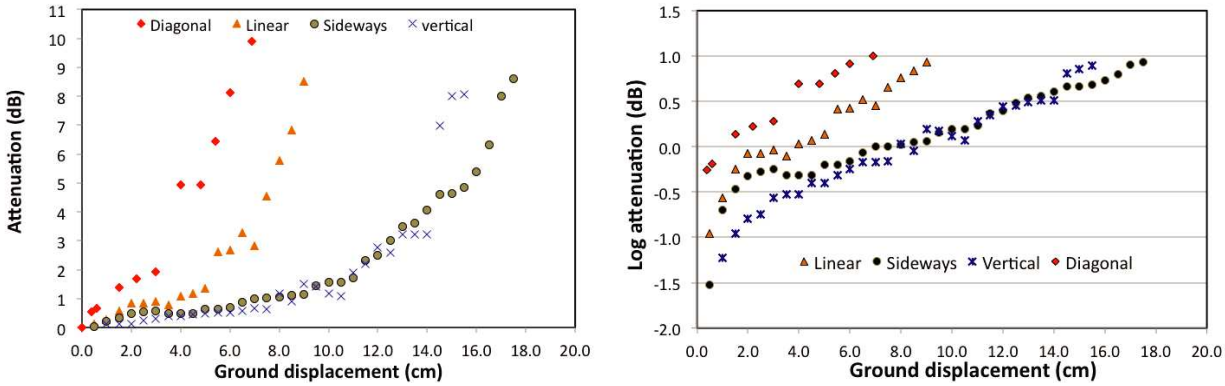

Figure 7: (a) Attenuation incurred in OFS for various ground movements direction. (b) Higher sensitivity of OFS to diagonal direction of ground movement.

4. CONCLUSIONS

We have demonstrated a distributed displacement OFS system using fiber-loop sensor-head and FBG that can be used to detect and monitor engineering structures. The sensor heads can be positioned and distributed along more than 25-km line-of-detection and detected using OTDR. Incorporating fiber-sensor-head and FBG allow measurement of both displacement and temperature variation. The OTDR provides higher sensitivity to the fiber-loop sensor-head system. The OFS system was used to model ground movement on hill-slope and it is feasible to be used to simulate ground movement at geo-technical sites. The OFS was found to be more sensitive to diagonal-direction movement of the ground and OFS is capable to detect 5-mm of ground movement.

ACKNOWLEDGMENT

We acknowledge the Faculty of Applied Science, Universiti Teknologi MARA, Shah Alam for the facilities and to RMI (UiTM) and MOHE for the financial support through FRGS grant (FRGS/1/10/ST/UITM/02/02).

REFERENCES

1. Grattan, S. K. T., S. E. Taylor, P. A. M. Basheer, T. Sun, and K. T. V. Grattan, "Structural health monitoring — better solutions using fiber optic sensor?" *IEEE Sensors*, 811–814, 2009.
2. Grattan, K. T. V. and T. Sun, "Fiber optic sensor technology: An overview," *Journal of Sensors and Actuators A*, Vol. 82, 40–61, 2000.
3. Severin, I., R. E. Abdi, and M. Poulain, "Mechanical and chemical characteristics of hermetically coated silica fibre," *Journal of Surface and Coatings Technology*, Vol. 202, 2494–2499, 2007.
4. Berthold, J. W., "Historical review of microbend fiber optic sensors," *Journal of Lightwave Technology*, Vol. 7, 1193–1199, 1995.
5. Pinto, N. M. P., O. Frazao, J. M. Baptista, and J. L. Santos, "Quasi-distributed displacement sensor for structural monitoring using a commercial OTDR," *Journ. of Optics and Lasers in Eng.*, Vol. 44, 771–778, 2006.
6. Wang, B. J., K. Li, B. Shi, and G. Q. Wei, "Test on application of distributed fiber optic sensing technique into soil slope monitoring," *Journal of Landslides*, Vol. 6, 61–68, 2009.
7. Abd-Rahman, M. K., M. N. Taib, and A. Ibrahim, "Application of optical fiber Bragg grating sensor for structure monitoring," *Materials Science Forum*, Vol. 517, 202–206, 2006.
8. De-Oliveira, R., et al., "Experimental investigation of the effect mould thermal expansion on the development of internal stresses during carbon fibre composite processing," *Journal of Composites A*, Vol. 39, 1083–1090, 2008.

Multi-long-period Gratings for the Optimization of Pump Absorption in Microstructured Optical Fiber Lasers

T. Palmisano[1], **M. Surico**[1], **A. D'Orazio**[2], **M. De Sario**[2], **L. Mescia**[2], **V. Petruzzelli**[2], **and F. Prudenzano**[1]

[1]DIASS Dipartimento di Ingegneria dell'Ambiente e per lo Sviluppo Sostenibile
Politecnico di Bari, Via E. Orabona, Bari 4-70125, Italy
[2]DEE Dipartimento di Elettrotecnica ed Elettronica
Politecnico di Bari, Via E. Orabona, Bari 4-70125, Italy

Abstract— In this paper, a double-stage optical coupler is designed with the aim to enhance the characteristics of a laser constituted by an ytterbium doped, double cladding microstructured optical fiber (MOF). The optical coupler consists of a cascade of multiple long-period gratings (MLPG) inscribed in the fiber core region. More precisely, it is made up of two different stages, the former is designed outside of the laser cavity, before the input mirror, while the latter is designed in the active fiber region, i.e., inside the cavity. Each stage includes a cascade of different gratings. The whole double-stage multiple long-period grating (DS-MLPG), including both the outside and inside parts, increases the pump power transfer from the inner cladding modes towards the fundamental core mode. A homemade numerical code has been developed for the investigation of the DS-MLPG. It models the coupler by taking into account the coupled-mode equations and the rate equations. The dependence of the fiber laser characteristic on the DS-MLPG parameters, such as the grating period and the length, have been investigated. The simulations highlight that an improvement of the pump power absorption and an increasing at least 10% of the output signal power can be obtained by employing a suitable DS-MLPG. In fact, a large amount the total input pump power can be more efficiently transferred from the inner cladding modes towards the fundamental mode guided into the core. As a consequence, a reduction of the total length of the fiber laser and a minimization of the length-dependent nonlinear effects can be obtained.

1. INTRODUCTION

The feasibility of high power optical fiber lasers has been largely demonstrated during the last years. Novel fiber designs, aimed at enhancing nonlinearity and damage thresholds such as the fabrication of high-brightness pump sources have allowed to reach the output power of single mode fiber lasers close to the kilowatt level. A power scaling potential towards 10 kW with state-of-the-art fiber technology seems nowadays feasible [1]. Recently, the research interest has been further focused on the development of innovative components and techniques to obtain ever increasing power levels and beam quality.

Double cladding fibers (DCFs) are largely employed in this area. In fact, they allow the exploitation of the cladding pumping technique, which enables the usage of low-cost and multimode pump sources and the reduction of the thermal load density. Nevertheless, the conventional, i.e., not microstructured, DCFs do not permit an easy handling of the heat capacity, inner cladding numerical aperture, and single-mode core size. The development of lasers based on microstructured optical fibers (MOFs) permits to follow a valid alternative to overcome the aforesaid drawbacks, occurring in the conventional optical fibers, and limiting their potential application.

Long period gratings (LPGs) have been exploited in many applications as filters, gain flatteners for erbium-doped fiber amplifiers, dispersion compensators, sensors, etc. [2–7].

In this paper, a DS-MLPG is designed to enhance the coupling of the pump power into the ytterbium doped core of a MOF. The proposed DS-MLPG is an interesting example of laser component to be integrated to enhance the emission efficiency. The design of similar couplers, to be applied to different fibers and/or rare-earth ion doping, can be performed by following an analogous approach.

The MLPG design/investigation exhibits a practical interest because different techniques allowing grating inscription into MOF core and/or cladding have been demonstrated by experimental works [2–9]. The first demonstration of optical fiber gratings written in photonic crystal fibers was reported in [2]. The fiber consisted of a germanium-doped photosensitive core surrounded by a hexagonal periodic airhole lattice in a silica matrix [2]. It was demonstrated that the gratings facilitated coupling to higher-order leaky modes. Moreover, long-period fiber gratings were fabricated

in all-solid photonic bandgap fibers (PBGFs) by UV illumination in [8]. The fabricated grating allowed the resonant couplings from fundamental mode to guided and radiative supermodes (rod modes), and bandgap-like modes. The LPG inscription into the optical fiber was considered as a method to investigate the modal and dispersive properties of the fiber [8]. Moreover, the first fabrication of femtosecond-laser-drilled structural LPGs in a large-mode-area PCF was reported in [9]; a focused femtosecond infrared laser was used for fabricating an LPG with only 9 periods and a grating length $< 4\,\mathrm{mm}$, which exhibited resonance strength of over 20 dB.

2. THEORY

The model describes an ytterbium doped MOF laser cavity. The simulation of the laser characteristics is performed by taking into account the presence of the DS-MLPG, which enables interaction among the two-fold degenerate fundamental mode guided in the fiber core (HE_{11}) and the inner cladding modes, at the pump wavelength. The optical coupler consists of a cascade of LPGs inscribed in the fiber core region. Two different coupler stages are designed, the former is designed outside of the laser cavity, before the input mirror, while the latter is designed in the active fiber region, i.e., inside the cavity. Each coupler stage includes a different cascade of gratings. The whole DS-MLPG increases the pump power transfer from the inner cladding modes towards the fundamental core mode.

A homemade computer code has been ad hoc developed. The two main coupler design items are: a) the MOF electromagnetic investigation and b) the solution of a nonlinear system of differential equation including the coupled mode equations and the rate equations. The modal electromagnetic field profile and the propagation constant of the guided modes are computed via an efficient full-vectorial finite element method. The Sellmeier equation expressing the wavelength dispersion of silica is reported in [10].

More precisely, the power exchanged among the fundamental core mode and the cladding pump modes in the double stage coupler has been modeled by using the coupled mode theory CMT derived in slowly varying envelope approximation SVEA [3]. The grating is obtained by means of a refractive index perturbation, $\Delta n(z)$, uniform in the fiber transverse plane and expressed as in [3]. The fabrication technology to obtain an LPG in the core of a MOF is reported in literature [2]. A quasi-two level scheme is employed to describe the ytterbium activated glass-system. The pump and the signal wavelengths being $\lambda_p = 980\,\mathrm{m}$ and $\lambda_s = 1060\,\mathrm{nm}$, respectively.

The coupled mode equations are derived from the multimode CMT by taking into account the light-matter interaction phenomena occurring in the active medium. The equation system describes amplitude variation of the transverse field profile of the forward propagation modes at the pump wavelength, of both the forward and backward propagating signals at the laser wavelength, via the evolution of the transverse coupling coefficients between the interacting modes [3, 11, 12]. The variation of the amplitudes of the forward and backward propagating signals at the laser wavelength is calculated by considering a suitable gain coefficient [11, 12]. The longitudinal coupling coefficients are neglected because they are generally $2 \div 4$ orders of magnitude smaller than the transverse coupling coefficients [3], and a small index perturbation has been considered [3].

The modified coupled mode equations describing the quasi-two level scheme for an ytterbium activated glass-system are:

$$\frac{dA_{\mu}^{pump}}{dz} = i\sum_{v=1}^{N}\{A_{v}^{pump}K_{v\mu}\exp\left[i(\beta_v-\beta_\mu)z\right]\} + \frac{1}{2}\alpha(z,\lambda_p)A_{\mu}^{pump} \quad \mu = 1,2,\ldots,N \tag{1}$$

$$\frac{dA_{siginal}^{\pm}}{dz} = \pm\frac{\alpha(z,\lambda_s)}{2}A_{siginal}^{\pm} \tag{2}$$

where N is the number of the considered pump modes, A_{μ}^{pump} (A_{v}^{pump}) is the amplitude of the transverse field profile of the forward propagation μth (vth) mode at the pump wavelength λ_p, β_v and β_μ are the propagation constants of the modes v and μ, $K_{v\mu}$ is the transverse coupling coefficient between the modes v and μ. $A_{siginal}^{+}$ and $A_{siginal}^{-}$ are the amplitudes of the forward and backward propagating signals at the laser wavelength λ_s, respectively.

3. NUMERICAL RESULTS

MLPGs design and behavior, is illustrated via an example pertaining to an ytterbium doped MOF laser, having a transversal section reported in [13].

The MLPG design has been performed as reported in [4, 5, 12]. The homemade computer code described in [4, 5] has been extended in order to simulate: i) multiple long period grating MLPG in passive fiber (grating cascade to be inscribed before the laser cavity), ii) MLPG in active fiber (to be inscribed within the laser cavity), iii) DS-MPLG i.e., both passive grating cascade (before the laser cavity) and active grating cascade (within the laser cavity). A first validation of the code was performed in the case of the passive conventional fiber with grating reported in [3–5]. The validation of the code for modeling the active behavior without grating was tested in previous work [14]. As further model validation, the code was applied in the case of an Yb-doped cladding-pumped fiber laser with LPG pump coupling [6], the fiber was not microstructured. In all cases a good agreement with literature was obtained.

After the code validation, a lot of simulations have been performed in order to evaluate the transmission spectrum of different gratings and to identify the better grating cascade geometry. The pump wavelength is $\lambda_p = 976\,\text{nm}$, and the signal wavelength $\lambda_s = 1060\,\text{nm}$, the emission and absorption cross sections at signal and pump wavelength are reported in [14], the ytterbium concentration is $N_{Yb} = 5\times10^{25}\,\text{ions/m}^3$ (uniformly distributed in the core of the fiber), input mirror reflectivity $R_1 = 99\%$, output mirror reflectivity $R_2 = 6\%$. Table 1 reports the parameters of the grating cascade before the input laser cavity (first stage of DS-MLPG) and Table 2 reports those of the cascade within the laser cavity (second stage of DS-MLPG). Table 3 reports the parameters of a single stage grating cascade MLPG optimized to be inscribed only within the laser cavity. Fig. 1 illustrates the comparison among the laser characteristics, in the case of laser optimized without grating (point curve), laser optimized with a MLPG inscribed entirely within the cavity (dash curve), laser optimized with the DS-MLPG (full curve); the laser length is $L = 0.83\,\text{m}$. The slope efficiencies are $S = 0.71$, 0.84 and 0.87, respectively. The DS-MLPG, including both the outside and inside parts, increases the pump power transfer from the inner cladding modes towards the fundamental core mode and allows an increasing of the laser performance. For a laser length $L = 3\,\text{m}$ and an input pump power of 1 W, the output power is increased of 7.89% via DS-MLPG with respect the case without grating. For a laser length reduced to 1 m the increasing of output power is of 17.4%. As a consequence, a reduction of the total length of the laser can be obtained to parity of output power. The DS-MPLG allows an increasing of the output power almost equal to that which can be obtained by employing a passive optimized MPLG before the laser cavity as

Table 1: Parameters of first stage of DS-MLPG.

Grating length [cm]	Grating periods Λg [mm]
5.895	0.4994
4.03	0.21649
14.005	0.25051

Table 2: Parameters of second stage of DS-MLPG.

Grating length [cm]	Grating periods Λ [mm]
1.85	0.1709
4.555	0.55185
5.855	0.44255
1.65	0.187075
5.98	0.37655
10.02	0.359375
12.51	0.45145

Table 3: Parameters of internal MLPG.

Grating length [cm]	Grating periods Λ [mm]
3.100	0.1705
2.195	0.1872
2.251	0.2285
3.095	0.4238
8.050	0.4229
9.100	0.3765
19.69	0.3594
20.97	0.5539

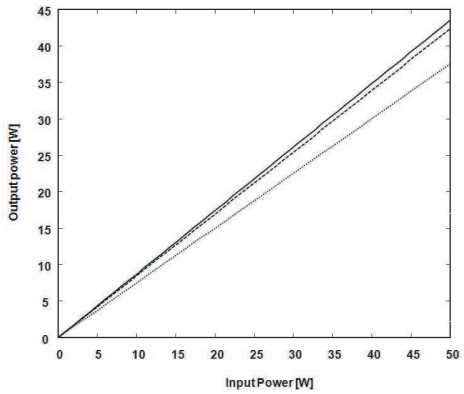

Figure 1: Laser characteristic: without grating (point curve), with a MLPG inscribed entirely within the cavity (dash curve), with DS-MLPG (full curve), the laser length is $L = 0.83\,\mathrm{m}$.

reported in [4, 5]. The main advantage of the DS-MPLG is the simultaneous enhancement of pump absorption by rare earth and the coupling of the cladding modes with the fundamental one at the pump wavelength. These interactions occurring simultaneously in the second stage of the coupler permit to avoid the deleterious steep of the pump power into the core which could induce nonlinear phenomena. The coupler could be particularly useful for the minimization of the length-dependent nonlinear effects.

4. CONCLUSIONS

A double-stage multiple long-period grating has been designed. It allows a significant improvement of the laser performance or a reduction of laser fiber length to parity of output power. As a consequence, a reduction of the total length of the laser and a minimization of the length-dependent nonlinear effects can be obtained. The model/software can be employed for the design of other laser sources, having more complex MOF transversal sections and different dopants and/or codoping ions.

ACKNOWLEDGMENT

The work has been partially developed within the COST ACTION MP0702.

REFERENCES

1. Limpert, J., F. Roser, S. Klingebiel, T. Schreiber, C. Wirth, T. Peschel, R. Eberhardt, and A. Tunnermann, "The rising power of fiber lasers and amplifiers," *IEEE Journal of Selected Topics in Quantum Electronics*, Vol. 13, No. 3, 537–545, 2007.
2. Eggleton, B. J., P. S. Westbrook, R. S. Windeler, S. Spalter, and T. A. Strasser, "Grating resonances in air-silica microstructured optical fibers," *Opt. Lett.*, Vol. 24, 1460–1462, 1999.
3. Erdogan, T., "Cladding-mode resonances in short-and long-period fiber grating filters," *J. Opt. Soc. Am. A*, Vol. 14, 1760–1773, 1997.
4. Mescia, L., "Design of long-period gratings in cladding-pumped microstructured optical fiber," *J. Opt. Soc. Am. B*, 1883–1839, 2008.
5. Calò G., A. D'orazio, M. De Sario, L. Mescia, V. Petruzzelli, L. Allegretti, T. Palmisano, and F. Prudenzano, "Improvement of the pump power coupling in double cladding photonic crystal fiber," *IEEE/LEOS Winter Topical Meeting Series*, 146–147, 2008.
6. Baek, S., S. Roh, Y. Jeong, and B. Lee, "Experimental demonstration of enhancing pump absorption rate in cladding-pumped ytterbium-doped fiber laser using pump-coupling long-period gratings," *IEEE Photon. Technol. Lett.*, Vol. 18, 700–702, 2006.
7. Allsop, T., K. Kalli, K. Zhou, G. Smith, Y. Laia, G. Smith, M. Dubov, D. Webb, and I. Bennion, "Long period gratings written into a photonic crystal fibre by a femtosecond laser as directional bend sensors," *Opt. Commun.*, Vol. 281, No. 20, 5092–5096, 2008.
8. Long, J., W. Zhi, L. Yange, K. Guiyun, and D. Xiaoyi, "Ultraviolet-inscribed long period gratings in all-solid photonic bandgap fibers," *Opt. Express*, Vol. 16, No. 25, 21119–21131, 2008.

9. Shujing, L., J. Long, J. Wei, W. Dongning, L. Changrui, and W. Ying, "Structural long period gratings made by drilling micro-holes in photonic crystal fibers with a femtosecond infrared laser," *Opt. Express*, Vol. 18, No. 6, 5496–5503, 2010.
10. Fleming, J. W., "Dispersion in GeO_2-SiO_2 glasses," *Appl. Opt.*, Vol. 23, 4486-4493, 1984.
11. Paschotta, R., J. Nilsson, A. Tropper, and D. Hanna, "Ytterbium-doped fiber amplifiers," *IEEE J. Quantum Electron.*, Vol. 33, 1049–1056, 1997.
12. Mescia, L., T. Palmisano, M. Surico, and F. Prudenzano, "Long-period gratings for the optimization of cladding-pumped microstructured optical fiber laser," *Optical Materials*, Vol. 33, 236–240, 2010.
13. Carlone, G., A. D'orazio, M. De Sario, L. Mescia, V. Petruzzelli, and F. Prudenzano, "Design of double-clad erbium doped holey fibre amplifier," *J. of Non-Crystalline Solids*, Vol. 351, No. 21–22, 1840–1845, 2005.
14. D'Orazio, A., M. De Sario, L. Mescia, V. Petruzzelli, and F. Prudenzano, "Design of double-clad ytterbium doped microstructured fibre laser," *Applied Surfaces Sciences*, Vol. 248, No. 1–4, 499–502, 2005.

Two-components Electric-field Sensor for Ultra Wide Band Polarimetric Measurements

Y. Gaeremynck[1,2], P. Jarrige[1,2], L. Duvillaret[1], G. Gaborit[1,2] and F. Lecoche[1]

[1]Kapteos SAS, rue Lac de la Thuile, F-73376 Le Bourget-du-Lac Cedex, France
[2]IMEP-LAHC, CNRS, University of Savoie, F-73376 Le Bourget-du-Lac Cedex, France

Abstract— Measurement of each component of an electric (E) field remains a key problem when no invasiveness and ultra wide bandwidths are required. We present here a novel pigtailed electro-optic (EO) probe, based on isotropic EO crystals, that allows to simultaneously measure, rigorously at the same location, two orthogonal components of the E field. Such EO probe will permit to make accurate polarimetric measurements like polarization-state real-time characterization of any electromagnetic wave, either in time- or frequency-domain. First measurements, performed at the frequency of 388 kHz in between rotating electrodes, validate the principle.

1. INTRODUCTION

When dealing with ultra wide band electromagnetic characterization, the choice of instruments is dramatically reduced as we find only antennae and EO probes. Compared to EO probes, antennae present the advantage of a huge sensitivity but their bandwidth is limited to only $\sim$ 4–5 decades [1] whereas EO probes cover without any problem 8 decades. Another key advantage of EO probes concerns their very low invasiveness due to their fully dielectric composition. A few realization of two- or three-components EO probes have been carried out these last ten years [2]. However, all these realisations were done using either multiple sensors or a single sensor probed by multiple laser beams. We present here a novel EO probe constituted of a single sensor probed by a single laser beam which polarization state is used to carry the information about two E field components.

In the first part, we deal with the use of isotropic EO crystals for E-field probing. Then, we follow by the theory and the experimental setup. The two last sections are devoted to the experimental validation.

2. USE OF AN ISOTROPIC ELECTRO-OPTIC CRYSTAL FOR E-FIELD PROBING

EO sensors use the Pockel's effect which induces a linear variation of EO crystal refractive indices with the applied E field. When a laser probe beam propagates through an EO crystal its polarization state could be modified by the applied E field. Depending on the incoming polarization state of the laser probe beam and on the polarization treatement done after the crossing of the EO crystal, one or two components of the applied E field can be retrieved. It has been shown [3] that only isotropic EO crystals potentially permit to get simultaneously access to two orthogonal components of the E field. Isotropic EO crystals belong to the crystallographic groups $\bar{4}3\,\mathrm{m}$ and 23. These crystals exhibit a unique independant EO coefficient $r_{41} = r_{52} = r_{63}$ and their refractive index variation Δn, induced by the E-field $\vec{E}$, can be expressed as [3]:

$$\Delta n = \sqrt{\left(\overrightarrow{\Delta K_a} \cdot \vec{E}\right)^2 + \left(\overrightarrow{\Delta K_b} \cdot \vec{E}\right)^2} \tag{1}$$

where $\overrightarrow{\Delta K_a}$ and $\overrightarrow{\Delta K_b}$ ($\perp \overrightarrow{\Delta K_a}$) are the sensitivity vectors of the EO crystal.

As seen on (1), a refractive index variation of the EO crystal occurs if the applied E field is not perpendicular to the plane defined by $\overrightarrow{\Delta K_a}$ and $\overrightarrow{\Delta K_b}$. Consequently, an isotropic EO crystal potentially permits to simultaneously measure two components of the applied E field with the balancing coefficients $\Delta K_a = ||\overrightarrow{\Delta K_a}||$ and $\Delta K_b = ||\overrightarrow{\Delta K_b}||$. Both moduli and orientations of $\overrightarrow{\Delta K_a}$ and $\overrightarrow{\Delta K_b}$ depend on the orientation of the laser probe beam wave vector $\vec{k}$ in the crystallographic referential. As isotropic EO crystals are characterized by only two parameters (EO coefficient r_{41} and refractive index n), the sensitivity vectors present always the same behavior (see Fig. 1). On this figure are represented the moduli ΔK_a and ΔK_b as the distance to the origin for any direction of $\vec{k}$ belonging to a eighth of sphere delimited by the crystallographic axes $\langle 100 \rangle \equiv x$, $\langle 010 \rangle \equiv y$ and $\langle 001 \rangle \equiv z$. Indeed, both $x = 0$, $y = 0$ and $z = 0$ planes correspond to symmetry planes

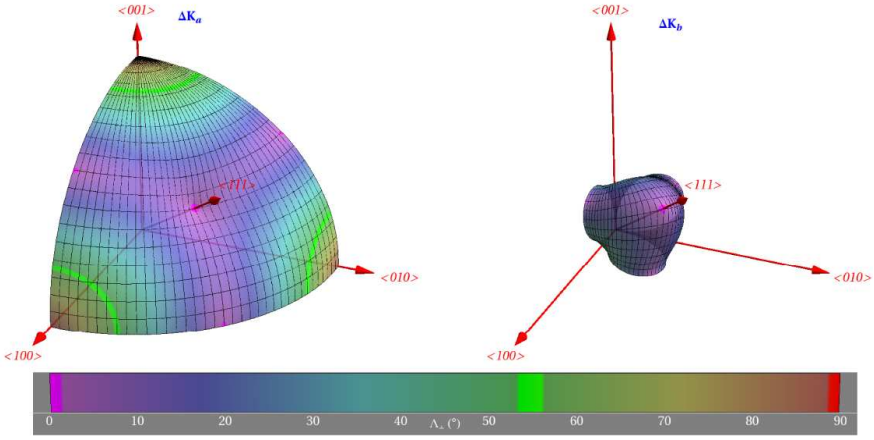

Figure 1: Representation of moduli ΔK_a and ΔK_b for isotropic EO crystals.

for $\overrightarrow{\Delta K_a}$ and $\overrightarrow{\Delta K_b}$. Another important parameter is the angle $\Lambda_\perp$ between $\vec{k}$ and the direction perpendicular to the plane defined by $\overrightarrow{\Delta K_a}$ and $\overrightarrow{\Delta K_b}$. Indeed, a null value of $\Lambda_\perp$ indicates that the EO crystal allows only transverse E-fields measurements. The condition $\Lambda_\perp = 90°$ occurs only for a wave vector $\vec{k}$ colinear either to x, y or z. In that case, $\Delta K_b = 0$ and the EO crystal allows only longitudinal E-field measurements.

For the specific direction $\langle 111 \rangle$, $\overrightarrow{\Delta K_a}$ and $\overrightarrow{\Delta K_b}$ present exactly the same modulus which corresponds to ΔK_b maximum. Moreover, as $\Lambda_\perp = 0$, this means that we get a transverse EO probe presenting a constant sensivitity whatever the direction of $\vec{E}$ in the plane perpendicular to $\vec{k}$. A first practical demonstration of such two-component E-field sensor has been carried out in 2007 [4] in free space. Let us notice that this configuration is perfectly suited for polarimetric measurements. However, without a pigtailed probe, practical applications are drastically limited. This strong limitation has pushed the development of a pigtailed version of such polarimetric probe.

3. THEORY AND EXPERIMENTAL SETUP

Figure 2 presents the experimental setup where a "break-up" pigtailed EO probe has been used in order to get access to several experimental parameters. First, a linearly polarized laser probe beam is sent through a polarizing maintaining fiber (PMF) up to a ZnTe crystal in front of which a quarter wave plate L1 is placed. The orientation of the neutral axes of L1 about the eigen dielectric axes of the input PMF (PMF_{in} on Fig. 2) is $\pi/4 - \delta$. For $\delta = 0$, the laser probe beam polarization is converted into a circular polarization at the entrance of the ZnTe crytal. After passing forth and back through the EO crystal, the laser probe beam is sent, via the output PMF (PMF_{out} on Fig. 2), to a polarization analyzer. This polarization analyzer is composed of several optical elements with two $\lambda/4$ and $\lambda/2$ wave plates (L2 and L3 on Fig. 2) whose neutral axes are rotated of 45° and 22°5 about the laboratory referential, respectively. These wave plates permit to convert the incoming polarization state of the laser probe beam so that the optical powers received by photodiodes PD_1 to PD_4 give relevant information about the E-field components E_x and E_y.

Using Jones' formalism [5], it is obvious to show that optical powers P_1 to P_4, received by photodiodes PD_1 to PD_4, can be expressed as:

$$P_1 = \frac{1}{2}(1 + \sin 4\delta \cos\theta) + \frac{\Delta\phi}{2}(\cos 4\delta \sin 2\alpha \cos\theta + \cos 2\delta \cos 2\alpha \sin\theta) \quad (2)$$

$$P_2 = \frac{1}{2}(1 - \sin 4\delta \cos\theta) - \frac{\Delta\phi}{2}(\cos 4\delta \sin 2\alpha \cos\theta + \cos 2\delta \cos 2\alpha \sin\theta) \quad (3)$$

$$P_3 = \frac{1}{2}(1 - \sin 4\delta \sin\theta) + \frac{\Delta\phi}{2}(\cos 2\delta \cos 2\alpha \cos\theta - \cos 4\delta \sin 2\alpha \sin\theta) \quad (4)$$

$$P_4 = \frac{1}{2}(1 + \sin 4\delta \sin\theta) - \frac{\Delta\phi}{2}(\cos 2\delta \cos 2\alpha \cos\theta - \cos 4\delta \sin 2\alpha \sin\theta) \quad (5)$$

$\Delta\phi$ is the E-field induced phase difference between the two eigen polarization states of the laser probe beam during its propagation through the EO crystal. Having $\Delta\phi \ll 1$, a first order development into series has been used. α is the orientation of the crystal dielectric axes in the laboratory

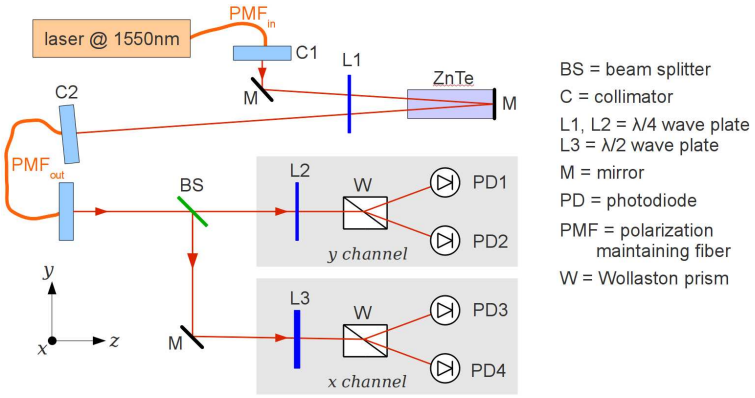

Figure 2: Schematic representation of the experimental setup.

referential. It is possible to show that any rotation γ of the applied E field in the x-y plane induces a $\gamma/2$ rotation of α. θ is the dephasing between the two eigen polarizations of the laser probe beam during its propagation through the output PMF. θ depends on the pressure applied to the fiber, on its temprature T and on the wavelength λ of the laser probe beam. To avoid any drift induced by the output PMF on optical powers P_1 to P_4, θ must be kept constant independently of PMF temperature variations. For that purpose, stress or temperature induced variations of θ should be compensated by laser wavelength tuning. Neglecting $\Delta\phi$ terms, a null value of θ is obtained as soon as the equality $P_3 = P_4$ is satisfied (see (4) and (5)). Defining by S_{error} the imbalance between P_3 and P_4, we get:

$$S_{error}(\Delta\phi \ll 1) = P_4 - P_3 \cong \sin 4\delta \sin\theta \tag{6}$$

In fact, as soon as the frequency of the applied E field is high enough ($>\sim 50\,\mathrm{Hz}$) a simple low pass filter can be used to reject the EO modulation representated by $\Delta\phi$ terms. However, δ must be different of zero for using the condition $S_{error} = 0$ to cancel θ. From now on, let us consider this latter condition fullfiled. Assuming $\delta \ll 1$ we get:

$$P_1 - P_2 \cong \Delta\phi \sin(2\alpha) = E_y \tag{7}$$

$$P_3 - P_4 \cong \Delta\phi \cos(2\alpha) = E_x \tag{8}$$

As seen on (7) and (8) the difference $P_1 - P_2$ and $P_3 - P_4$ give direct access to the E-field components E_x and E_y. However an *a priori* tricky compromise has to be found as the obtention of precise values of E_x and E_y requires very low values of δ whereas a precise cancellation of θ requires high values of δ. This is the reason why we have built a "break-up" pigtailed EO probe in order to be able to tune δ around 0.

4. EXPERIMENTAL VALIDATION

We have used a $\langle 111 \rangle$ 4.5-mm long ZnTe crystal to get two balanced sensitivity vectors $\overrightarrow{\Delta K_a}$ and $\overrightarrow{\Delta K_b}$. First of all, we have characterized the evolution of S_{error} with a change of temperature of the output PMF. The value of δ was lower than 1°. For that purpose, the fiber was heated during a few seconds and then we acquired the signal during the decreasing of the temperature.

Measurements on Fig. 3(a) have been fitted using (6) considering a mono-exponential temporal decrease of PMF temperature, this latter temporal decrease leading, in turn, to a mono-exponential temporal evolution of θ. From this adjustment, the thermalization time constant of PMF in air is obtained: $\tau = 127.8 \pm 0.3\,\mathrm{s}$. The same experiment has been repeated for different values of δ. For each of them, we have fitted the data with the above-mentioned model in order to extract the evolution of S_{error} with δ (see Fig. 4).

Measurements are in very good agreement with the theoretical fit derived from (6):

$$S_{error} \propto \sin(4\delta) \tag{9}$$

With increasing values of δ, the error signal S_{error} increases as well, leading to a more precise cancellation of θ. But, inversely, the useful EO signal decreases. However, from (2)–(5), it is obvious to show that the EO signal loss, induced by non-zero values of δ, remain lower than 0.5 dB for $\delta < 5°$. Thus, a compromise exists and validates the possibility of making a two-component pigtailed E-field sensor based on Pockels' effect.

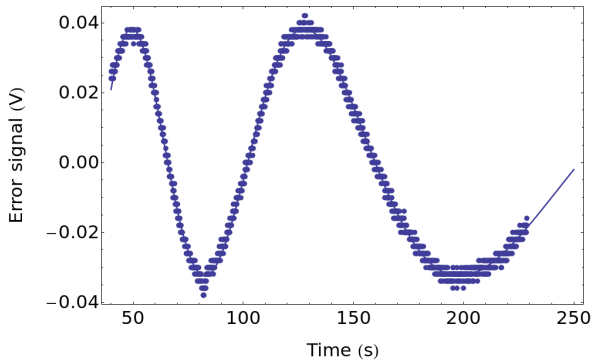

Figure 3: Measurements (dots) and fit (solid line) of S_{error} during temperature change of the output PMF.

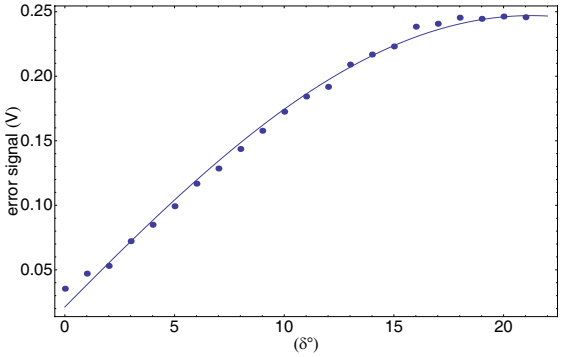

Figure 4: Amplitude of temperature-induced variations of S_{error} (dots) and theoretical fit (solid line).

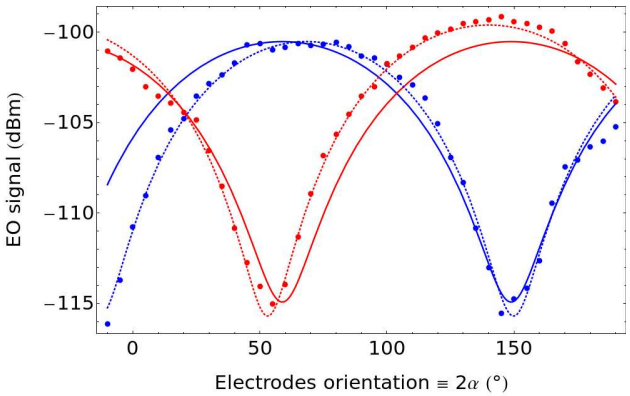

Figure 5: EO measurement (dots) of both E_x (in blue) and E_y (in red) components. Theoretical fits assuming a constant (solid line) or slowly varying (dotted line) PMF temperature.

5. FIRST TWO-COMPONENT E-FIELD MEASUREMENT

For this experimental validation, the ZnTe crystal has been inserted in between two parallel electrodes mounted on a rotation stage. A CW signal at 388 kHz has been applied to the electrodes and the EO signal has been measured using a spectrum analyzer with a 10-Hz analysis bandwidth. The laser wavelength has been tuned twice to cancel S_{error} at beginning and in middle of the experiment. Indeed, due to access of a single spectrum analyzer, the measurement has been done in two steps; by recording first the EO signal related to E_x and then the signal related to E_y.

Figure 5 shows this first measurement. The solid-line theoretical fit is derived from (7) and (8). As seen, a progressive shift occurs with electrodes orientation increase for E_y component and with electrodes orientation decrease for E_x component. These shifts express a slight temperature evolution of the PMF during the measurement. In order to take such evolution into account, a slight linear temporal drift of θ has been added to Equations (7) and (8). We have also considered a tiny imbalance of the sensitivity vectors in order to take the imperfect orientation of the EO crystal into account. This time, a very good agreement is observed between measurements and theory, bringing out the importance of maintaining θ at a very low value in real-time.

6. CONCLUSION

We have presented a novel non invasive E-field probe able to simultaneously measure exactly at the same location and at the same time two orthogonal components of the E field. Moreover, this EO probe intrinsically presents a flat response from quasi DC up to a few tens of GHz, thus opening a wide field of applications like precise polarimetric measurements.

ACKNOWLEDGMENT

This work was supported by the French "Health and Radiofrequency" Foundation, under Biocapteo project and by the DGA (French Military Programs Management and Procurement Agency).

ACKNOWLEDGMENT

The authors acknowledge the DGA (French Military Programs Management and Procurement Agency) for its support.

REFERENCES

1. Kanda, M. and L. D. Driver, "An isotropic electric-field probe with tapered resistive dipoles for broad-band use, 100 kHz to 18 GHz," *IEEE Trans. Microwave Theory Tech.*, Vol. 35, 124–130, 1987.
2. Kuo, W. K., Y.-T. Huang, and S.-L. Huang, "Three-dimensional electric-field vector measurement with an electro-optic sensing technique," *Opt. Lett.*, Vol. 24, 1546–1548, 1999.
3. Duvillaret, L., S. Rialland, and J.-L. Coutaz, "Electro-optic sensors for electric field measurements. II. Choice of the crystals and complete optimization of their orientation," *J. Opt. Soc. Am. B*, Vol. 19, 2704–2715, 2002.
4. Gaborit, G., J.-L. Coutaz, and L. Duvillaret, "Vectorial electric field measurement using isotropic electro-optic crystals," *Appl. Phys. Lett.*, Vol. 90, 241118-1–3, 2007.
5. Yariv, A., *Optical Electronics*, Saunders College Publishing, 1991.

A Novel Idea of Quantum Cryptography Coupled with Handover Satellite Constellation for World Cover Communications

Aris Skander[1], **Messai Abderraouf**[1], **Merabtine Nadjim**[2], **Mosleh M. Al-Harthi**[2], **and Benslama Malek**[1]

[1]LET Laboratory, Faculty of Engineering, Mentouri University, Constantine 25000, Algeria
[2]Electrical Engineering Departments, Faculty of Engineering, Taif University, Saudi Arabia

Abstract— Quantum cryptography is a new branch of physics and cryptography which exploit quantum mechanical phenomena to guarantee the secrecy of cryptographic keys. BB84 proposed the well known protocol that quantum key distribution could also be implemented using polarization photon between quantum systems. In this paper new model of implement BB84 protocol with Handover satellite constellation for possible to couple with quantum communications for more security and free space transmissions. So, the essential work carried in our research paper concerns a new idea development in satellites transmission whit implement of Quantum Key Distribution (QKD) algorithm based on photon encrypted code, including reducing the telecommunication interruption risks and this will provide indeed of a better free space communication quality.

1. INTRODUCTION

Quantum communications offers many advantages for secure data transmission, e.g., confidentiality, integrity, eavesdropper's detectability. Information is encoded in quantum bits (qubits), intrinsic physical properties, such as polarization of a photon. Quantum physics allows encoding information using the correlation between two or more particles (photons, atoms). Quantum Key Distribution (QKD) is one of the innovative methods of information processing that emerged from the properties of "superposition of states" and "entanglement".

QKD allows two (or more) parties to know when a communication channel is completely secure to exchange an encrypted key.

QKD is used before classical information is transmitted over conventional non-secure communication channels like telephone lines, RF links and optical fibre networks. Since quantum physics laws state that a single particle like a photon cannot be split or cloned, it certifies the absolute security of communication.

Quantum communication channels however are limited on Earth. Optical fiber link losses and current photon-detector technology limit the maximum span length without using regeneration (amplification) to 100 km; while for free space transmission the limit is the visible horizon [1]. Such problems are in principle nearly absent in space, and are less severe in ground to space links. In fact, quantum links in free space combined with fiber counterparts could extend secure communication between points on earth to a global level.

2. QUANTUM CRYPTOGRAPHY

Quantum cryptography can be classified into two major categories: QC based on single photons and QC based on photon pairs. The well known concept for quantum key distribution based on single photon is the BB84 scheme. The BB84 scheme uses single photons transmitted from Alice to Bob, who are prepared at random in four partly orthogonal polarization states 0°, 45°, 90°, and 135° [2]. If Eve tries to extract information about the polarization of the photons she will inevitably introduce errors, which Alice and Bob can detect by comparing a random subset of the generated keys. Other protocols based on non orthogonal quantum states uses single photons transmitted from Alice to Bob [3]. The security of these protocols relies on the impossibility of measuring the wave function of a quantum system without imposing a back action on the state. This back action will usually result in an increase in errors across the communication channel.

In 1991, Ekert proposed the well known protocol that quantum key distribution could also be implemented using entanglement between quantum systems [4].

3. QUANTUM CRYPTOGRAPHIC ALGORITHM

In the quantum situation, most algorithms are based on communications pre sharing quantum states, such as the EPR pair, which is impossible with the existing technology since quantum memory remains an open technology challenge. Including by these, we present a novel quantum cryptographic algorithm, is implemented by quantum computation, which can be realized by current technology. Because each process is under the control of the key and the final ciphertext, the eavesdropper cannot acquire fixed ciphertext without the key. In our point of view, the quantum computing algorithms can be used to affirm our free-space communication in the following four ways [5]:

1. Open-air communication: usually "horizontal" telecommunication that happens below 100 km height. For channel, the air is used instead of optical cable.
2. Earth-satellite communications: it happens through greater heights than the Open air communication, usually between 300 and 800 km altitude. Signal encoding and decoding is used to produce quantum error correction that allows operation in noisy environment.
3. Satellite broadcast: Quantum algorithms can improve the effective bandwidth, thus the brand is better utilized as in traditional cases.
4. Inter-satellite communication: the communication between satellites where the channel is the free-space. Any kind of coding and encoding can be used, to increase stability.

4. PROBLEMATIC IN FREE SPACE COMMUNICATIONS

The main goal of this paper is to develop a prototype approach of optical laser satellite communication terminal applications on micro-satellites in LEO and space-to-ground constellations. The outputs of the sources are coupled together using an optical combiner. The photons are sent through space from the satellite to each Optical Ground Support Equipment (OGSE), where they are analyzed. In the case of simultaneous key transmission, one station reveals publicly to the other some random elements of the received key. If the elements match its proper key, then the key is secure.

In the case of consecutive key transmission, one station sends a logical combination (XOR) of both keys to the other station. From this, one unconditionally secure key is computed.

Micro-satellite constellations in LEO orbits can inter-communicate and communicate with the ground station using laser beams as the carrier (Figure 1). Space environment add constraints like temperatures range, vibrations, radiations. Thus components have to be selected and tested for space qualification, especially for sensitive components like laser diodes and nonlinear crystals.

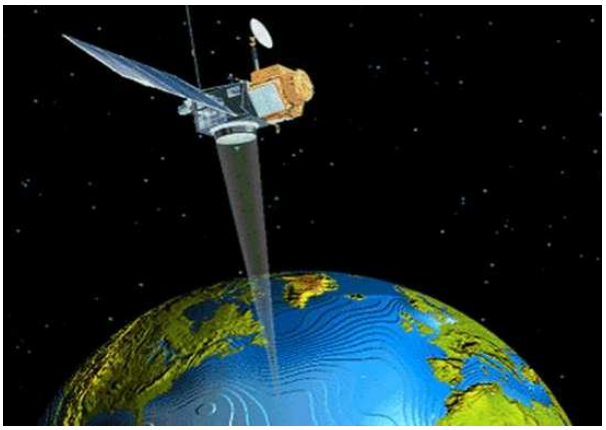

Figure 1: The communication scenario between a LEO satellite and ground station.

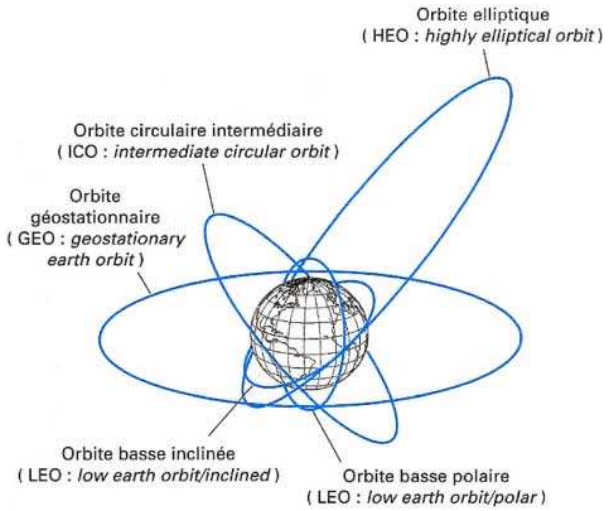

Figure 2: The various satellites constellations.

5. IMPORTANT CONCEPTS ON SATELLITE

5.1. The Satellite Constellation

To enable global coverage through terminals and with the same transmission quality of terrestrial cellular networks becomes essential to use several satellites (constellation), preferably at low or medium altitude (LEO, MEO and HEO), that reduce the propagation delay of typical geostationary (GEO) and also liaising with little power. A constellation of satellites is characterized by the altitude of the satellite, the number of satellites, the number of planes, and the number of satellites per plane [6].

5.2. The Handover Notion

The use of satellites in low and medium altitudes, moving with a speed different from the land speed, calls for the constant presence of handover from one satellite to another, because each mobile terminal is located under the cover of a given satellite for a limited time while in terrestrial cellular networks, the transfers were due to mobility of the subscriber moving within the coverage area.

It is therefore necessary to ensure that each time a link between a ground station and a satellite becomes bad, a link switching to another satellite in the constellation is possible (problem of the handover) [6].

The main situations of Handover in satellite systems are:

- Intra-satellite handover:
  - Handover occurs from one beam to another.
  - The mobile station is still in the footprint of the satellite but in another cell.
- Inter-Satellite Handover [7]:
  - Handover is done from one satellite to another.
  - The mobile station leaves the footprint of a satellite to that of another.
- Handover between bases stations (handover gateway).
  - Handover of a base station to another.
  - The mobile station is still in the footprint of the satellite base station but the fate of the footprint.
- Inter-System Handover
  - Handover of a satellite network to a terrestrial cellular network.
  - The mobile station can reach a terrestrial network which as lower latency and less expensive.

6. PRACTICAL CONSIDERATIONS

In principal, the distribution of the key information over wide geographical coverage may require that larger distances be subdivided into shorter segments. The problem with this concept is that the required quantum transmitters are still beyond the scope of present day technology. Perhaps, a suitable technique to bridging the large distances is free space satellite-based optical communication systems. By exploiting this technique, free space optical communication systems could enable the realization of secure key exchange between two widely separated locations on the globe.

Much as satellite communication systems is viewed as an alternative solution to the realization of relatively long-distance secure key exchange, obtainment of global scale key exchange is still challenging. This is owed to the fact that long-distance propagation of the optical beam is affected by several atmospheric and geographical problems.

In this regard, some of the most outstanding problems include [8]:

a) Atmospheric turbulence which leads to wave front distortion.
b) Environmental vibration effects which lead to pointing errors.
c) The absorption, scattering and reflection of radiation in the lower layers.

7. RESEARCH OBJECTIVES

In today's quantum communication systems, two major issues which are being investigated are the need to extend transmission distance let alone increasing the secure communication key rate [9]. As it was suggested above, the desire to extend the transmission distance is to focus efforts on satellite-based free space communications systems. Thus, the focus of this work is to obtain long-distance satellite-based free space quantum communication with better secure communication bit rate by pursuing the following specific objectives:

- To develop a mathematical model to analyses the performance of BB84 protocol over satellite-based quantum communication links between a ground station and a satellite in the low earth orbit (LEO), taking into account the various atmospheric effects.
- To develop a suitable theoretical model in order to investigate the physical layer limitation of satellite vibration in satellite-based quantum optical communication systems.
- To compare the performance of single photon pulsed polarization based BB84 signal for the satellite-based free space quantum optical communication links between a ground station and a satellite in a LEO, against individual eavesdropping attacks [10].

8. QUANTUM SATELLITES NETWORKS SOLUTION

The use of satellites to distribute quantum photon transmission (and single photons) provides a unique solution for long-distance quantum communication networks. This overcomes the principle limitations of Earth-bound technology, i.e., the range of the order of 100 km afforded by both optical fiber and by terrestrial free-space links.

The scenarios involving an Earth-based transmitter terminal allow sharing quantum transmission either between ground and satellite, or between two ground stations, or between two satellites and thus to communicate between such terminals employing quantum communication protocols. In the simplest case, a straight uplink to one satellite-based receiver [see Fig. 3] can be used to perform secure quantum key distribution (QKD) between the transmitter station and the receiver. Here, one of the photons is being detected right at the transmitter site and thus the entangled photon source is used as a triggered source for single photons.

If the satellite acts as a relay station [see Fig. 4], the same protocol can be established between two distant Earth-based communication parties.

Shared entanglement between two parties can be achieved by pointing each of the photons of an entangled pair either toward an Earth-based station and a satellite or toward two separate satellites [see Fig. 5]. Another set of satellite-based relays can be used to further distribute the entangled photons to two ground stations.

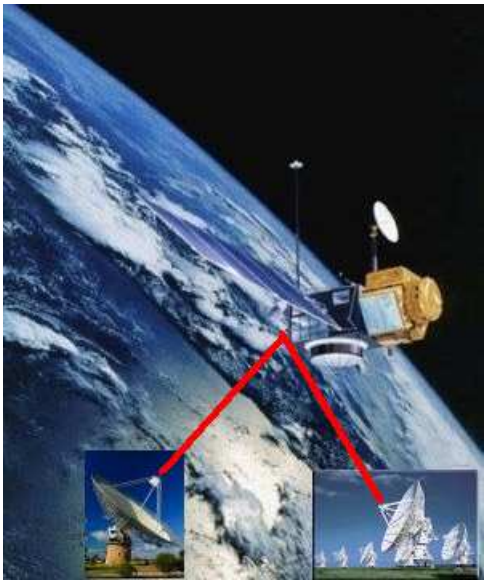

Figure 3: The communication between satellite and transmitter station.

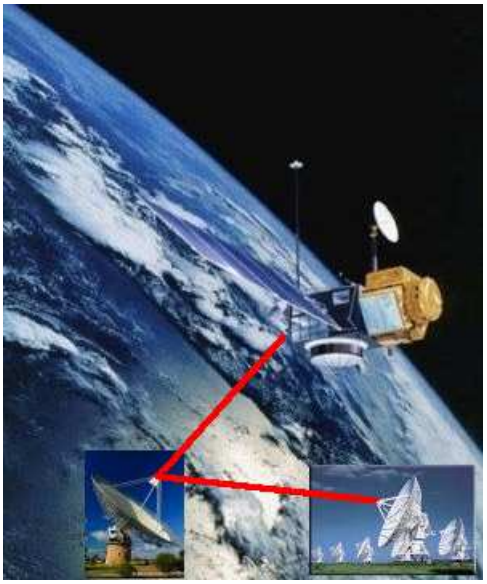

Figure 4: The communication between satellite and different transmitter stations.

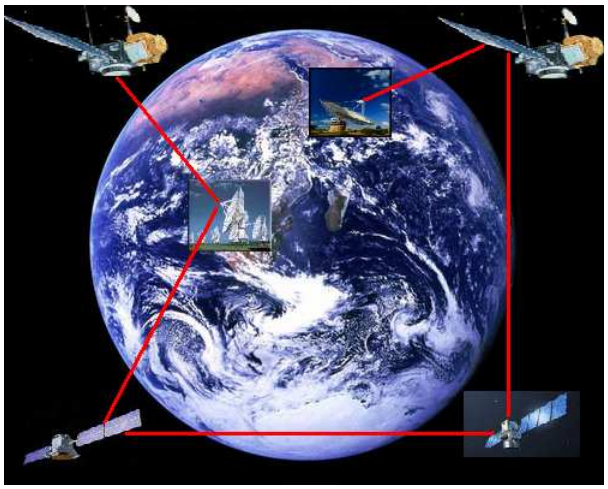

Figure 5: The communication between satellite and different relays transmitter stations.

In the present paper, we propose various scenarios for entanglement-assisted global and space-based quantum communication. While this in itself is already an interesting and outstanding experimental challenge, there are various specific novel opportunities which such a technology would offer. First and from a technological perspective foremost is the possibility to establish a secure and efficient communication using the methods of entanglement based quantum cryptography. As we explained above, that way one could not only establish a secure communication link between two arbitrary locations on Earth. It would also be possible to establish secure communication from Earth to satellites or between satellites. This would certainly increase the security of satellite remote control, which at present is a highly sensitive area and, thus far, an unsolved technical problem.

Using three scenarios of secure key exchange in the free space, it is not difficult to exchange the key between two points. The problem suggested here is the cover of a huge space. So we need networks of satellite coverage, shown in Fig. 5.

9. CONCLUSION

We have made a modest contribution for securing quantum information using satellites constellation approach in quantum transmission data. Several experiments have demonstrated the viability of the conduction of free space quantum cryptography at the surface of the Earth, we propose in this survey different new idea and analysis about quantum transmission between Handover satellites and ground station in order not to lose the information, and to secure the information during the communications between the users. Our future aim is to elaborate an algorithm capable of detecting and correcting errors in quantum satellites cryptography.

REFERENCES

1. Bennet, C. H. and G. Barassad, "Quantum cryptography: Public key distribution and coin tossing," *Proceedings of IEEE International Conference on Computers, Systems, and Signal Processing*, 175–179, Bangalore, India, 1984.
2. Bennet, C. H., "Quantum cryptography using any two non orthogonal states," *Phys. Rev. Lett.*, Vol. 68, 3121–3124, 1992.
3. Gisin, N. and S. Wolf, "Quantum cryptography on noisy channels: Quantum versus classical key-agrement protocols," *Phys. Rev. Lett.*, Vol. 83, No. 20, 4200–4203, November 1999.
4. Ekert, A. K., "Quantum cryptography based on Bell's theorem," *Phys. Rev. Lett.*, Vol. 67, No. 6, 661–663, 1991.
5. Bacsardi, L., "Using quantum computing algorithms in future satellite communication," *Acta Astronautica*, Vol. 57. No. 2–8, 224–229, 2005.
6. Takesue, H., E. Diamanti, T. Hhonjo, C. langrock, M. Fejer, K. Iinoue, and Y. yamamoto. "Differential phase shift quantum key distribution experiment over 105 km fibre," *New Journal of Physics*, Vol. 7, 232, 2005.

7. Cho, S., I. F. Akyildiz, M. D. Bender, and H. Uzunalioglu, "A new connection admission control for spotbeam handover in LEO satellite networks," *Wireless Networks*, Vol. 8, No. 4, 403–415, July 2002.
8. Merabtine, N., S. Aris, and M. Benslama, "A hand check study by orbital modelling for world cover communications," *4th International Conference: Sciences of Electronic, Technologies of Information and Telecommunication — SETIT'2007*, Hammamet, Tunisia, March 25–29, 2007.
9. Weier, H., T. Schmitt-Manderbach, et al., "Free space quantum key distribution: Towards a real life application," *Fortschr. Phys.*, Vol. 54, No. 8–10, 840–845, 2006.
10. Aris, S., M. Benslama, and M. Planat, "The quantum cryptography-solution to the problem due to the principle of uncertainty of Heisenberg," *WSEAS Transactions on Communications*, Vol. 5, No. 5, 948–953, May 2006.
11. Merabtine, N., S. Aris, and M. Benslama, "A contribution to a communication quality improvement by a hand check survey," *Journal of Mobile Communication*, Vol. 1, No. 1–4, 21–25, 2006.

Statistical Modelling of the Polarization Mode Dispersion in the Single Mode Optical Fiber Links

L. Cherbi
Laboratory of Instrumentation
University of Sciences and Technology Houari Boumediene, USTHB, Algeria

Abstract— In this work, we propose a second method of modelling of the PMD in a single mode optical fiber links with strong coupling, based on the formalism of Jones and the model of Dal Farno. We compared the results gotten to those of the first method that we already proposed in our previous works while comparing them with measured ones. A very good agreement between theory and experience is reported, confirming the validity of the proposed method.

1. INTRODUCTION

The PMD is a property of the optical fiber in which the energy of the signal for a given wavelength decomposes to two orthogonal polarization modes possessing two different propagation speeds. The difference between the times of propagation of the two polarization modes is called differential Group delay (DGD). The PMD leads to widening of the pulses propagated in the fiber as well as a limitation of the transmission performances. The main reason of the PMD in the optical fiber is the birefringence. The description of the PMD in a fiber is complicated because the two modes of polarization can exchange the energy between them; this phenomenon is linked to the uncertain modes coupling. The PMD in a fiber varies uncertainly with the wavelength and also with its environmental conditions. There is not exact mathematical model which permits to calculate its value, what leads us to look for the statistical models permitting to value this phenomenon. In this work, we propose a second method of modelling of the PMD in a single mode optical fiber links with strong coupling, based on the formalism of Jones and the model of Dal Farno, while dividing the link in a set of birefringent elements of different lengths, for which their birefringence is calculated with a given method according to used material in the fiber, and which are oriented in an random direction in relation to the other. We compared the results gotten to those of the first method that we already proposed in our previous works [1] while comparing them with measured ones when using the Jones Matrix Eigen values Method (JME) [2]. A very good agreement between theory and experience is reported, confirming the validity of the proposed method.

2. THE MODEL OF SIMULATION FOR THE CALCULATION OF THE PMD OF A FIBER

All optical wave of arbitrary polarization can be represented as the linear superposition of two orthogonal vectors of the HE_{11} modes in the monomode optical fiber [3, 4].

In the ideal case where the waveguide has the cylindrical symmetry, these two modes are degenerate in terms of their properties of propagations. The loss of degeneration of the polarization modes can be called as birefringence where one can express it as a difference of effective indices of the two modes. In order to calculate the PMD of a fiber, we started by implementation of an algorithm to calculate its birefringence.

2.1. The Calculation of the Birefringence

In the monomode optical fiber, there is only one mode witch propagates LP_{01} or HE_{11} in the core, this mode composed of two components of orthogonal electrical fields for which the amplitude and the frequency vary, one of its components is in direction of the axis x ($\cos\theta$) and the other is in direction of the axis y ($\sin\theta$). The rays (ax, ay) and refraction index (nx, ny) of the core according respectively to the axes x, y are slightly different, this difference is due to the birefringence that is given by the relation:

$$\Delta B = Bx - By \tag{1}$$

We calculated $\Delta\beta$ while determining the two propagation constants Bx and By, solutions of the propagation equations of the modes LP_{01x} and LP_{01y} by the method of Dichotomy.

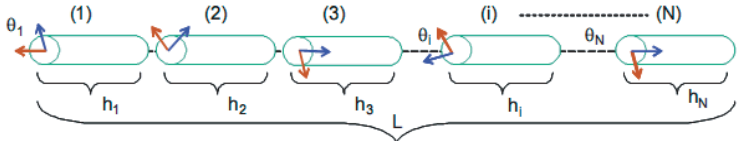

Figure 1: Blade of the birefringence model.

2.2. Calculation of the PMD in the Short Regime

The model that we used in our simulation is called "blade of birefringence" [5], it permits the modelling of a fiber of L length by a concatenation of N small different length sections oriented in an random manner. Each section possesses a set of birefringence's axes. This model is schematized by the Figure 1.

Jones' matrix that describes a concatenation of sections of different lengths of a birefringent fiber can be given by [5]:

$$T(V,e) = \prod_{i=1}^{N} R(-\theta_i) M_i(V,e) R(\theta_i) \tag{2}$$

$$T(V,e) = \prod_{i=1}^{N} \begin{pmatrix} \cos\theta_i & -\sin\theta_i \\ \sin\theta_i & \cos\theta_i \end{pmatrix} \begin{pmatrix} \exp\left(i\dfrac{Bh_i}{2}\right) & 0 \\ 0 & \exp\left(-i\frac{Bh_i}{2}\right) \end{pmatrix} \begin{pmatrix} \cos\theta_i & \sin\theta_i \\ -\sin\theta_i & \cos\theta_i \end{pmatrix} \tag{3}$$

where N is the number of sections of the fiber, B represents the value of "i" birefringent segment that we determined with the method given in the Section 2.1. θ_i represents the angle of polarization of "i" segment witch is a random quantity distributed in [0, π]. "h_i" is the length of "i" segment that one generated by a gauss distribution around a mean length $L_{\text{moy}} = L/N$, with a standard deviation of 25% of L_{moy}.

The DGD can be calculated from the eigen values $\rho 1$ and $\rho 2$ of the matrix product $T(V1 + dV)$. $T^{-1}(V1)$, $T(V1 + dV)$ and $T^{-1}(V1)$ are Jones' matrixes for two values closes to the normalized frequency $V1$ and $V1 + dV$, the DGD for a wavelength is determined while using the following relation:

$$\Delta\tau(V1) = \left|\frac{\arg(\rho 1/\rho 2)}{d\varpi}\right| \tag{4}$$

$d\varpi$is the variation of the angular frequency and it is given by:

$$d\varpi = \frac{C \cdot dV}{a \cdot \sqrt{n1^2 - n2^2}} \tag{5}$$

where 'a' is the ray of core, C is the speed of light. The PMD is calculated from the average of the DGD according to the following relation

$$PMD = \frac{\langle\Delta\tau\rangle_\lambda}{L} \tag{6}$$

where $\langle\Delta\tau\rangle\lambda$ is the average of the DGD calculated according to wavelength.

2.3. Calculation of PMD in the Long Regime

Dal Forno [6] describes a numerical simulation model founded on Jones' formalism without neglecting the effect of coupling that is very important in the case of the long regime what gives a strong variation of the DGD according to wavelength. We applied this model by considering a monomode fiber like a concatenation of unequal lengths of segments and random angles of orientation of the axes on which decompose every time the modes of polarization, we calculated the birefringence like described in Section 2.1. The mathematical description of this model is given by the matrix $T(w)$ witch describes a concatenation of unequal sections of the fiber, and witch is expressed by

the following formalism:

$$T(\omega) = \prod_{n=1}^{N} B_n(\omega) R(\alpha_n) \tag{7}$$

$$= \prod_{n=1}^{N} \begin{bmatrix} e^{j\left(\sqrt{\frac{3\prod}{8}} b\omega \frac{\sqrt{h_n}}{2+\Phi_n}\right)} & 0 \\ 0 & e^{-j\left(\sqrt{\frac{3\prod}{8}} b\omega \frac{\sqrt{h_n}}{2+\Phi_n}\right)} \end{bmatrix} \begin{bmatrix} \cos\alpha_n & \sin\alpha_n \\ -\sin\alpha_n & \cos\alpha_n \end{bmatrix} \tag{8}$$

where N is the number of segments, B_n is the matrix of the birefringence of segment i that we already calculated by the method given in the Section 2.1. $R(\alpha n)$ is the randomly variation of the coupling angle between the axes of the segment and witch is an uniformly distributed random quantity in $[0\ \pi]$. h_n is the length of segment i generated by a Gauss distribution around a mean length $L_{\text{moy}} = L/N$, with standard deviation Δh of 25% of L_{moy}.

3. RESULTS AND INTERPRETATION

The values of the DGD calculated for only one step of wavelength (DGD (λ)), can be displayed in histogram as it is shown on (Figure 3). The comparison of this DGD distribution (λ), to the one of Maxwell indicates if the fiber presents a strong coupling and also the conformity of the method used for the calculation of these DGD. If the function of Maxwell constitutes a good smoothing for the calculated or measured DGD values distribution, the fiber is characterized then appropriately and the average (or the square mean root RMS) is calculated with precision. In order to test the validity of the modelling methods that one used, one compared the obtained results with those measured in [1], done on the same type of fiber.

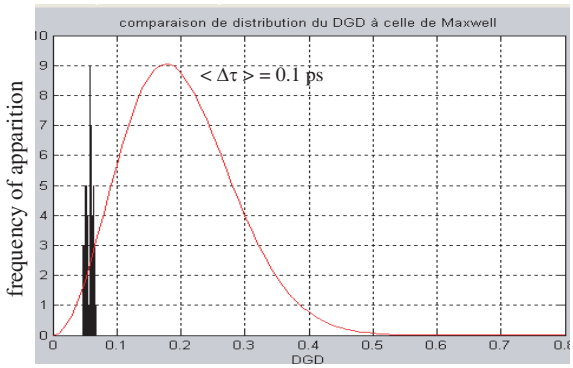

Figure 2: The histogram giving the variation of the calculated DGD by the method [1] in a single mode fiber of length 2716 m.

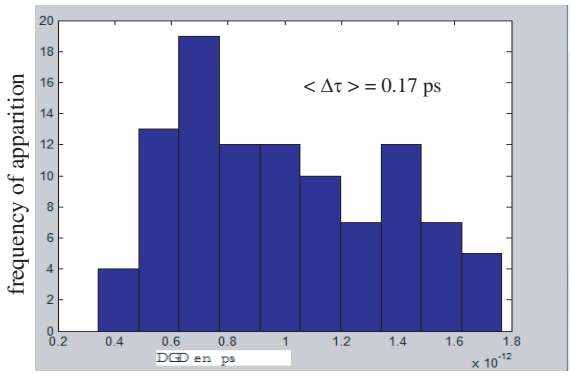

Figure 3: The histogram giving the variation of the calculated DGD by the method of blade of birefringence for a fiber of 2716 m length.

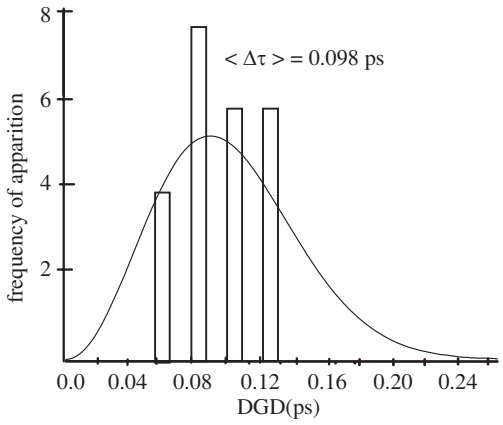

Figure 4: The histogram giving the variation of the measured DGD for a fiber's length of 2716 m.

We used the model of "blade of birefringence" for the calculation of PMD of the two fibers of lengths of 2716 m and 4231 m with the same characteristics taken in the measures (a step's wave length of 10 nm, rays of the core: $ax = 4.14$ nm, $ay = 4.13$ nm and refractive index $nx = 1.4503$, $ny = 1.4502$).

From the Figure 3, one sees that the average of the calculated DGD is $\langle \Delta\tau \rangle = 0.17$ ps, a value that is not very close to the values found in the measures done with the method of JME in [1] where $\langle \Delta\tau \rangle = 0.098$ ps (Figure 4) and to those of the first proposed method in [1] (Figure 2). The Figure 2 shows the variation of the DGD for a fiber of 2716 m length that we determined by another method described in [1]. One notices that there is not a big variation of the DGD according to wavelength in the three cases of calculated and measured results but the shape of smoothing in the method of "blade of birefringence" is more close to a Maxwell distribution (Figure 3) that in the case of the DGD deducted by the method of [1] and those measured. What confirms that the fiber doesn't present a strong coupling for this length.

According to the Figure 6, one notices that the DGD don't vary meaningfully with the wavelength what means that the coupling is weak for this length ($L = 10$ km); for $L = 80$ km one notices

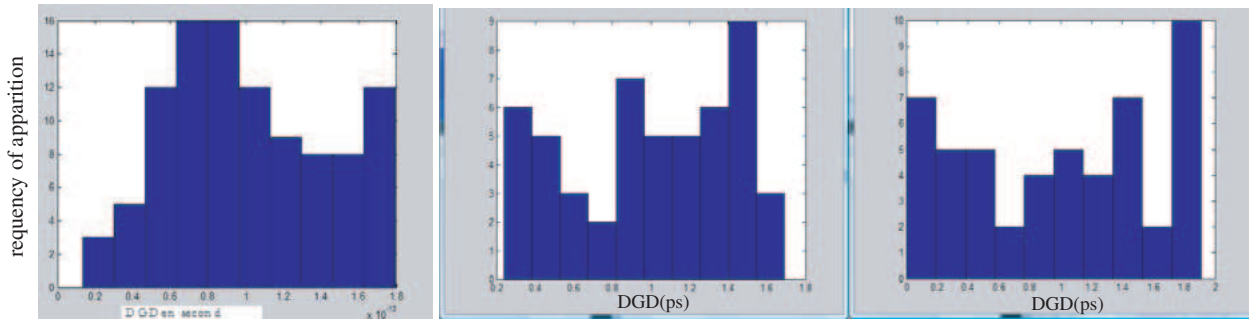

(a) (b) (c)

Figure 5: The histogram of the variation of the calculated DGD by blade of birefringence model for (a) $L = 4231$ m, (b) $L = 10$ km, (c) $L = 80$ km.

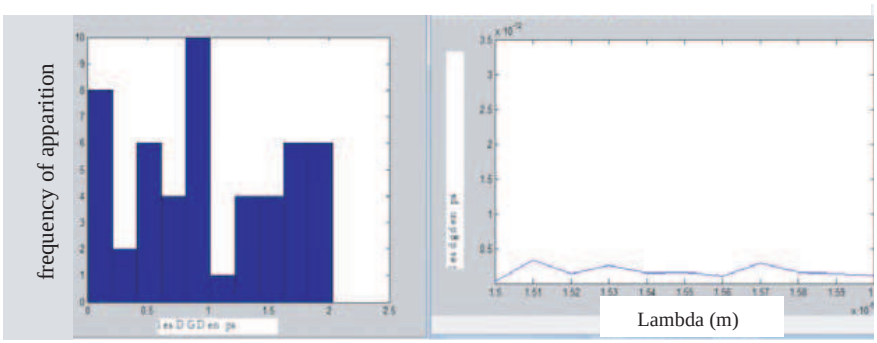

(a) (b)

Figure 6: (a) The histogram of the calculated DGD with the method of Dal Forno. (b) Variation of the measured DGD according to wavelength for $L = 10$ km.

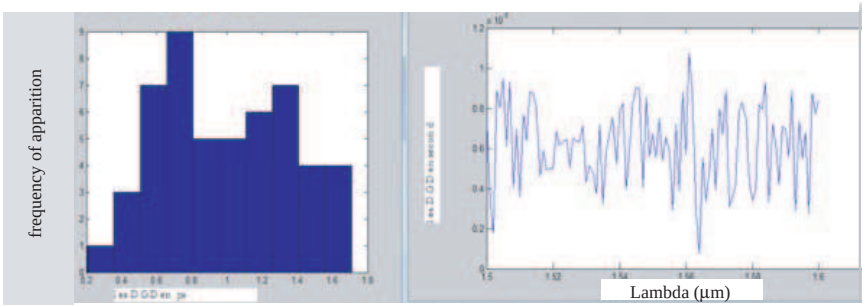

(a) (b)

Figure 7: (a) The histogram of the calculated DGD with the method Dal Forno. (b) Variation of the measured DGD according to wavelength for $L = 80$ km.

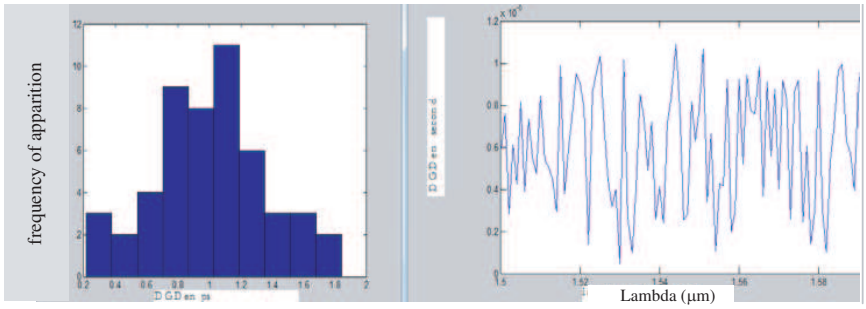

(a) (b)

Figure 8: (a) The histogram of the calculated DGD with the method of Dal Forno. (b) Variation of the measured DGD according to wavelength for $L = 200\,\text{km}$.

the random variation of the DGD according to wavelength as well as the shape of their distribution that comes closer of the one of the Maxwell function (Figure 7). We applied the model of "blade of birefringence for different lengths of fibers and one noted according to the presented histograms in Figure 5 that their smoothing by the Maxwell function is bad what means that this method is not really reliable for distances superior to 10 km. What lead us to use another method for these lengths that is the Dal Forno Method.

For a fiber length of 200 km, the model of 'Dal forno' confirms the real results that show a strong coupling from 200 km where one clearly see the random variation of the DGD and the smoothing of their distribution that has the perfect shape of a Maxwell (Figure 8).

4. CONCLUSION

We notice that the two methods (blade of birefringence and Dal forno) give the good results closer to the real ones and the DGD vary according to the nature of the modes coupling present in the length of used fiber. This coupling is not important until the length ($L = 10\,\text{km}$) where one notices that beyond this length, it becomes more important.

For the long regime (more than 10 km), we took the same features of fiber, but of different length ($L = 10\,\text{km}$, $L = 80\,\text{km}$, $L = 200\,\text{km}$) where we applied the two models, and one noticed that the method of blade of birefringence doesn't give good results for the long distances.

For the method of Dal Forno, we noted that the DGD vary meaningfully according to the wavelength and the smoothing of its distribution function is smoothed better with the Maxwell function. We compared our results with those of [1], we arrived to the same conclusion for the same lengths of fibers, what confirms that this method agrees better for the long distances where the coupling of the modes is strong.

REFERENCES

1. Cherbi, L. and M. Mehenni, "Modelling of the polarization mode dispersion in the single mode optical fiber links," *Conference on Modelling Aspects in Optical Metrology, Proc. of SPIE*, Vol. 7390, 739018, SPIE, Munich, Allemagne, June 2009.
2. Cherbi, L., M. Mehenni, and M. Wegmeller, "Mesure de la dispersion des modes de la polarisation dans les fibres optiques spun par la méthode d'analyse des valeurs propres de la matrice de Jones," $25^{iéme}$ *Journées Nationales d'Optique Guidées JNOG*, 176–178, Metz, France, Novembre 2006.
3. Biondini, G. and W. L. Kath, "Importance sampling for polarization-mode dispersion: Techniques and applications," *Journal of Lightwave Technology*, Vol. 22, No. 4, April 2004.
4. Cherbi, L., A. Azrar, M. Mehenni, and R. Aksas, "Characterization of the polarization in the spun fibers," *Microwave And Optical Technology Letters*, Vol. 51, No. 2, 341–347, Wiley Intersciences, February 2009, ISSN: 0895-2477, DOI: 10.1002/mop. 24045.
5. Boudrioua, N., "Etude et optimisation d'une chaîne de transmission numérique sur fibre optique: Vers une compensation électronique de la PMD," l'Université Paul Verlaine, Metz, 2007.
6. Dal Forno, A. O., A. Paradisi, R. Passy, and J. P. Von Der Weid, "Experimental and theoretical modeling of polarization-mode dispersion in single-mode fibers," *IEEE Photonics Technology Letters,* Vol. 12, No. 3, 269–298, March 2000.

Electromagnetic Compatibility of Portable RF Emitters in Uniquos Health Environment: Regulatory Issues

F. Censi, **G. Calcagnini**, **E. Mattei**, **M. Triventi**, **and P. Bartolini**
Italian National Institute of Health (ISS), Italy

Abstract— Wireless technology has reached a significant success and diffusion in healthcare: several wireless technology applications have been developed to improve patient care (medical device and patient traceability, immediate access and exchange of diagnostic and therapeutic information, etc ...). Given the potential diffusion of RFID technology, care must be paid on the potential risks deriving from the use of RFID device in healthcare, among which one of the most important is the electromagnetic interference with medical devices. Particularly important is the analysis of the regulatory issues concerning the electromagnetic compatibility of medical devices, to analyze if and how the application of the current standards allow an effective control of the possible risks associated to the electromagnetic interference with medical devices.

1. INTRODUCTION

RFID (radio frequency identification) is a technology which uses electromagnetic coupling in the radio frequency (RF) portion of the electromagnetic spectrum to uniquely identify an object, animal, or person. An RFID system consists of a reader (an antenna which acts as the transceiver) and a transponder (the tag). The antenna uses RF waves to transmit a signal that activates the transponder. When activated, the tag transmits data back to the antenna. The data is used to notify a programmable logic controller that an action should occur. The action could be as simple as raising an access gate or as complicated as interfacing with a database. RFID readers can be either fixed (e.g., a doorway) or portable hand-held devices. RFID tags can be passive or active, i.e., without or with intrinsic power source, respectively. RFID is a technology which permeates into many application fields, and has notably increased its diffusion and rate of adoption in the last decades. One of the area where RFID could potentially introduce many benefits is the healthcare: numerous applications using RFID technology have been developed to improve patient care (by tracking medical devices, drugs, patients etc ...). Although several advantages come from the introduction of such a technology in healthcare, there is one important potential risk: the electromagnetic interference with medical devices [1], since RFID systems emit electromagnetic waves. In this manuscript we analyze the regulatory framework concerning this issue. We present both standards regarding electromagnetic immunity of medical devices and standards for electromagnetic compatibility (EMC) of RFID systems and we analyze whether and how the application of these standards addresses all potential risks associated to electromagnetic interference to medical devices.

2. RFID REGULATIONS

RFID operates in unlicensed spectrum space, sometimes referred to as ISM (Industrial, Scientific and Medical) but the exact frequencies that constitute ISM may vary depending on the regulations in different countries. Typical RFID operating frequency bands are reported in Table 1, together with the corresponding maximum transmission power. Indeed, from a regulatory point of view, since RFID systems are intentional radiators of radio wave, they are controlled under local radio laws and regulations. In Europe, the radio and telecommunication equipments are regulated by the European Radio and Telecommunications Terminal Equipment Directive. The main objective of the Directive is to establish a regulatory framework for the placing on the market, free movement and putting into service of radio equipment and telecommunications terminal equipment in the territory of the European Union. The applications, frequency bands and power-levels relating to the use of short range devices, like RFID systems, are defined in the recommendation CEPT REC 70-03 of the European Conference of Postal and Telecommunications Administrations. The European Telecommunications Standards Institute (ETSI) has developed harmonised standards for many short range devices. Electromagnetic compatibility of RFID is regulated by three ETSI standards, which cover the frequency range from 9 kHz to 40 GHz [2–4]. In USA RFID systems, as devices that transmit RF energy, are subject to Federal Communications Commission (FCC) regulation. FCC rules are located in Title 47 of the Code of Federal Regulations. Part 15 of Title 47 concerns radio

Table 1: Frequency ranges and associated maximum allowed field strengths/transmission powers for RFID technology.

RFID systems	
Frequency ranges	Maximum field strengths/transmission powers
125 e 134.5 kHz	$\sim 64\,\mathrm{dB\mu A/m}$ at 10 m
13.56 MHz	42–60 $\mathrm{dB\mu A/m}$ at 10 m
865–956 MHz	2 W
2.45 GHz	2 W, 4 W (USA, Canada)
5.8 GHz	2 W, 4 W (USA,Canada)

frequency devices and covers the regulations under which an intentional, unintentional, or incidental radiator can be operated, as well as the technical specifications, administrative requirements and other conditions relating to the marketing of these devices. The pertinent FCC rules for RFID concern RF emissions limits, power restrictions and uses of certain frequencies. Table 1 shows the maximum allowed field strengths/transmission powers for the RFID systems. The limits are referred to the regulations operating in USA and Europe. For some frequency ranges, power limits are similar in both regions; when limits differ, it is clearly indicated in the table.

3. MEDICAL DEVICES REGULATIONS

In the European Union, medical devices are regulated by the EC directives, which define the "essential requirements", e.g., protection of health and safety that goods must meet when they are placed on the market. Electromagnetic immunity is an essential requirements for medical devices, and the harmonised standard EN 60601-1-2: Medical electrical equipment — Part 1: General requirements for safety. 2. Collateral Standard: Electromagnetic compatibility — Requirements and tests — covers this topic.

In USA, the Food and Drug Administration (FDA) regulates medical equipments differently from European union. As far as electromagnetic compatibility is concerned, the FDA is becoming increasingly concerned about the EMC aspects of medical devices, and FDA inspectors are requiring assurance from manufacturers that they have addressed EMC concerns during the design process, and that the device will operate properly in its intended electromagnetic environment. FDA refers to reviewers guideline to assure that medical devices are properly designed to be immune to EMI. The document "Guide to Inspections of Electromagnetic Compatibility Aspects of Medical Devices Quality Systems," encourages manufacturers to use IEC 60601-1-2 Medical Equipment, Electromagnetic Compatibility Requirements and Tests as the EMC standard. As a result, in most cases, IEC 60601-1-2 has effectively become the unofficial, de facto, EMC standard that has to be met for medical equipment. Since the harmonized standard EN 60601-1-2 does not substantially differ from IEC 60601-1-2, in the following we will refer to IEC/EN 60601-1-2 as the standard concerning the electromagnetic compatibility of medical devices. The most important issues established by the up-to-date revision of the IEC/EN 60601-1-2:2007 are the following:

1) the manufacturers must specify the levels of immunity of medical devices in the accompanying documents (e.g., user manual), providing sufficient technical justification if the declared immunity levels are different from those specified by the standards (indicated in Table 2);

Table 2: Minimum immunity levels according to the IEC/EN 60601-1-2.

	Immunity level	
Frequency range	Life-supporting device	Not life-supporting device
Conducted RF (150 kHz–80 MHz)	10 V (rms)	3 V (rms)
Radiated RF (80 MHz–2.5 GHz)	10 V/m	3 V/m

2) the manufacturer must provide in the accompanying documents a declaration about the

P = Rated maximum output power of the transmitter (W)	Recommended separation distance between portable and mobile RF communications equipment and the life-support medical device		
	150kHz-80MHz $D = 12\sqrt{P}/V$	80MHz-800 MHz $D = 12\sqrt{P}/E$	800MHz-2.5 GHz $D = 23\sqrt{P}/E$
0,01			
0,1			
1			
10			
100			

V= medical device immunity level in V (rms) for the frequency range 150kHz-80 MHz
E= medical device immunity level in V/m for the frequency range 80 MHz-2.5 GHz
D= distance, in meters

P=Rated maximum output power of the transmitter (W)	Recommended separation distance between portable and mobile RF communications equipment and the not life-support medical device		
	150kHz-80MHz $D = 3.5\sqrt{P}/V$	80MHz-800 MHz $D = 3.5\sqrt{P}/E$	800MHz-2.5 GHz $D = 7\sqrt{P}/E$
0,01			
0,1			
1			
10			
100			

V= medical device immunity level in V (rms) for the frequency range 150kHz-80 MHz
E= medical device immunity level in V/m for the frequency range 80 MHz-2.5 GHz
D= distance, in meters

Figure 1: Guidance tables reported in the IEC/EN 60601-1-2 for the computation of the recommended separation distance between portable and mobile RF communications equipment and the medical device, according to the immunity level of the device, and to the power and operating frequency of the portable RF equipment. These tables must be filled according to the indicated formulas, considering the immunity level of the medical device (V or E) and the maximum output power of the portable RF transmitter. Note that for the lowest acceptable immunity level of medical devices (10 V and 10 V/m for life support, 3 V and 3 V/m for the not life support) the tables give the same safety distances.

electromagnetic immunity of the medical device, including information about the electromagnetic environment where the medical device works as intended (e.g., recommended separation distances between the medical device and portable/mobile RF communication equipments, see Figure 1);

3) manufacturers, responsible organizations and operators have a shared responsibility to ensure that medical devices are used in a compatible electromagnetic environment where the medical devices performs as intended.

4. RFID AND MEDICAL DEVICES

When mobile RFID readers are brought to operate in hospital setting, they must be considered as portable RF communication equipments. Thus, in order to provide the electromagnetic environment where the performance of the medical device would be expected to be normal, a separation distance between the RFID system and the medical devices must be assured. In other words, electromagnetic interference caused by RFID to medical devices can be avoided if the RFID reader is far enough from medical devices. How far depends on the level of electromagnetic immunity of the medical device, and on the emitted power and operating frequency of the RFID reader, according to the formulas included in the IEC/EN 60601-1-2:2007 (Figure 1). Considering the minimum level of immunity of a life-support medical device (10 V rms from 150 kHz and 80 MHz and 10 V/m from 80 MHz to 2.5 GHz), the minimum separation distance (in cm) from RFID reader and medical devices is reported in Table 3, for the typical RFID operating frequencies and emitted powers (see Table 1). In Table 3 the columns associated to the frequencies 125 kHz/134.5 kHz, 13.56 MHz and 5.8 GHz are empty. As far as the frequencies 125 kHz/134.5 kHz and 5.8 GH are concerned, the standard does not take into account potable RF equipment operating at frequencies below 150 kHz and above 2.5 GHz, although RFID systems (as well as other wireless systems) operating in these frequency bands are or will be soon used in healthcare facilities. At 13.56 MHz there is a misalignment between the standard IEC/EN 60601-1-2 and the RFID regulations concerning the expression of the transmission power of the portable RF equipment: in RFID regulations, the power limit is expressed in terms of the maximum magnetic field generated by the antenna at a distance of 10 m

(in Ampere/meter), while in the standard IEC/EN 60601-1-2 the power limit is expressed in terms of antenna's effective radiated power (in Watt). Since the relationship between the magnetic field generated by the antenna and the effective radiated power depends, at these frequencies, from the physical characteristics of the antenna and requires electromagnetic expertise, the computation of the recommended separation distance from a RFID systems operating at 13.56 MHz is neither immediate nor general.

Table 3: Minimum recommended separation distances between portable RFID equipment and a life-support medical device, having the minimum level of immunity according to the IEC/EN 60601-1-2. Frequency ranges 125 kHz, 134.5 kHz, and 5.8 GHz are not contemplated in the standard. At 13.56 MHz there is a misalignment between the standard IEC/EN 60601-1-2 and the standard on RFID respect to the modality in which portable equipment transmission power is expressed.

Rated maximum output power of transmitter (W)	Recommended separation distances between portable and mobile RF communications equipment and the medical device (cm)				
	Sistemi RFID				
	125 kHz 134.5 kHz	13.56 MHz	865–956 MHz	2.45 GHz	5.8 GHz
0.01			23	23	
0.1			73	73	
0.2			103	103	
0.5			163	163	
1			230	230	
2			325	325	
4 (USA, CANADA)			-	460 (USA, CANADA)	

5. CONCLUSIONS

According to the standard IEC 60601-1-2, to assure an electromagnetic environment where the medical device performs as intended, portable RFID transmitters cannot be used in close proximity to the medical device (but those emitting less than few mW). The recommended separation distances shall be provided by the medical device's manufacturer, at least for RFID operating at 800 MHz and 2.4 GHz. The responsible healthcare organization must assure that these separation distances are respected, i.e., that there is an adequate electromagnetic environment. The responsible organization can obtain additional information on the potential risk of electromagnetic interference by performing ad hoc tests [12].

REFERENCES

1. Ashar, B. S. and A. Ferriter, "Radiofrequency identification technology in health care: Benefits and potential risks," *JAMA*, Vol. 298, No. 19, 2305–2307, Nov. 21, 2007.
2. ETSI EN 300 330-2, "Electromagnetic compatibility and radio spectrum matters (ERM); short range devices (SRD); radio equipment in the frequency range 9 kHz to 25 MHz and inductive loop systems in the frequency range 9 kHz to 30 MHz; Part 2: Harmonized EN under article 3.2 of the R&TTE directive," 2001.
3. ETSI EN 300 220-1, "Electromagnetic compatibility and radio spectrum matters (ERM); short range devices (SRD); radio equipment to be used in the 25 MHz to 1000 MHz frequency range with power levels ranging up to 500 mW; Part 1: Technical characteristics and test methods," 2006.
4. ETSI EN 300 440-1 V1.5.1, "European standard (telecommunications series) electromagnetic compatibility and radio spectrum matters (ERM); short range devices; radio equipment to be used in the 1 GHz to 40 GHz frequency range; Part 1: Technical characteristics and test methods, March 2009.

5. "COUNCIL DIRECTIVE of 14 June 1993 concerning medical devices," 93/42/EEC, Medical Device Directive MDD, Bruxelles, 1993.
6. "COUNCIL DIRECTIVE of 20 June 1990 on the approximation of the laws of the Member States relating to active implantable medical devices," 90/385/EEC, Active Implantable Medical Device Directive AIMD, Bruxelles, 1990.
7. "COUNCIL DIRECTIVE of 27 October 1998 on in vitro diagnostic medical devices," 98/79/EC, Bruxelles, 1998.
8. IEC/EN 60601-1-2, "Medical electrical equipment — Part 1: General requirements for safety 2. Collateral standard: Electromagnetic compatibility — Requirements and tests, 2007.
9. Houliston, B., D. Parry, C. S. Webster, and A. F. Merry, "Interference with the operation of medical devices resulting from the use of radio frequency identification technology," *N. Z. Med. J.*, Vol. 122, No. 1297, 9–16, Jun. 19, 2009.
10. Christe, B., E. Cooney, G. Maggioli, et al., "Testing potential interference with RFID usage in the patient care environment," *Biomed. Instrum. Technol.*, Vol. 42, No. 6, 479–484, Nov.–Dec. 2008.
11. Van Der Togt, R., E. J. van Lieshout, R. Hensbroek, et al., "Electromagnetic interference from radio frequency identification inducing potentially hazardous incidents in critical care medical equipment," *JAMA*, Vol. 299, No. 24, 2884–2890, June 25, 2008.
12. ANSI C63.18, "Recommended practice for an on-site, ad hoc test method for estimating radiated electromagnetic immunity of medical devices to specific radiofrequency transmitters," *IEEE*, 1997.

Three Dimensional Safety Distance Analysis around a Cellular Base Station

F. Üstüner
TÜBİTAK BİLGEM UEKAE, Turkey

Abstract— The safety distance concept is widely used in the installation of cellular base stations to define a radiation hazard zone around the periphery of the base station. In this paper, three dimensional safety distance analysis around a specific cellular base station is carried out using ray optic techniques with the diffraction theory included. The calculated electric field equivalent to health limit is plotted in a contour line form to illustrate the safety distance around the base station. The resulting plots illustrate the radiation hazard areas.

1. INTRODUCTION

The safety distance concept is widely used in the installation of cellular base stations to define a radiation hazard zone around the periphery of the base station. The safety distance around base stations is usually determined using basic antenna gain and RF output power level parameters with the application of free space electromagnetic wave attenuation formulas. A widely used formula giving a first order engineering approximation is:

$$E = \frac{\sqrt{30 \cdot P_t \cdot G_t}}{d} \tag{1}$$

where E is the electric field in free space at far-field in V/m, P_t is the RF transmitter power output in Watts, G_t is the numerical gain of the RF transmitter antenna and d is the distance between the observation point and RF transmitter antenna in meters. However such an approach gives usually worst case results and sometimes alarms the people in the surrounding area unnecessarily.

In order to solve a lawsuit between a local resident and a cellular phone operator, a national court requested the expert view on the safety distance around the base station based on ICNIRP Guidelines [1]. To give the correct answer for this appeal, it is decided to carry out a more realistic calculation of the safety distance around the base station. In this paper, three dimensional safety distance analysis around a specific cellular base station is carried out using ray optic techniques with the diffraction theory included. To carry out this analysis, NEC Basic Scattering Code (NEC BSC) [2] from Ohio State University is chosen as the ray optic calculation tool.

The base station antennas are modeled with array antennas giving the same radiation patterns of the real antennas in both elevation and azimuth planes. All details of the antennas such as their $+45°/-45°$ polarization, tilt angles, directions are included in the electromagnetic model. The residential house on which the base station antennas are mounted is modeled with the same geometry and material properties. The RF parameters of the base station's radio equipment are taken into account in the calculations. The calculated electric field equivalent to health limit is plotted in a contour line form to illustrate the safety distance around the base station.

2. PROBLEM DEFINITION

The base station under consideration is located in a rural area. The residential house on which the base station is located is a two-storey house having a roof terrace instead of a classical roof with tiles. The base station communication shelter and the antennas are located in the terrace. The antennas are mounted on a small mast. The building has a concrete frame and the walls are constructed from bricks covered by thin layers of concrete in both sides. The base station under consideration is operated as part of a GSM 1800 Mobile Phone Operator Network. The base station antenna system comprises three antennas oriented towards different sectors. Antennas are of array type antennas. They are X-polarized to have polarization diversity. X-polarized antennas use radiators which are arranged in $+45°$ and $-45°$ to the vertical axis of the antenna. X-polarized antennas are used to provide polarization diversity, a technique which uses 2 orthogonally polarized antennas and compares the resulting signals. The gain of each antenna in the base station is 17.7 dBi. The elevation plane half power beam width is 7.1°, and the azimuth plane half power beam width is 68°. The first antenna is oriented towards 95° with respect to True North. Second antenna and third

antenna are looking to 195°, and 330° respectively. Antennas are adjustable down-tilt antennas. First antenna is tilted down by 2°, second antenna by 4° and the third antenna by 2°. The height of the antenna from the ground is 12 m. The radiation patterns of the antenna are given in Figure 1.

The antennas have two inputs for two polarizations; +45° and −45°. Each antenna input is supplied from a combiner/divider unit having 28 W (44.5 dBm) power output. In the computations, it is assumed that the each polarization is fed in-phase by 14 W RF power output (28 W for each antenna).

3. MODELING AND COMPUTATIONS

For simulations, each antenna is modeled as an antenna array in order to have the similar gain and radiation patterns. 28 radiating elements are arranged as an array of 14×2, 14 elements being in the elevation plane. All radiating elements are fed with equal amplitude and in-phase inputs. A spacing of 10 cm is left between array elements in vertical direction and 9 cm in horizontal direction. This array structure is replicated for the other polarization. A reflector metal plate having a dimension of 140×20 cm is placed at 4.1 cm in the back side of the array elements (See Figure 2(a)). The modeled antenna azimuth and elevation patterns are shown in Figure 2(b) and Figure 2(c) respectively. As seen the model antenna approximates the response of the base station antenna closely, especially in the main lobes.

Afterwards, the building on which the antennas are mounted is modeled. The building is modeled by using plates as dictated by the NEC BSC code. In order to include the effects of the building material's (the concrete) electrical parameters, the following parameters are used for modeling (relative dielectric permittivity $\varepsilon_r = 3$, conductivity $\sigma = 4.8e - 2$ S/m and relative magnetic permeability $\mu_r = 1$). The base station communication shelter located in the terrace of

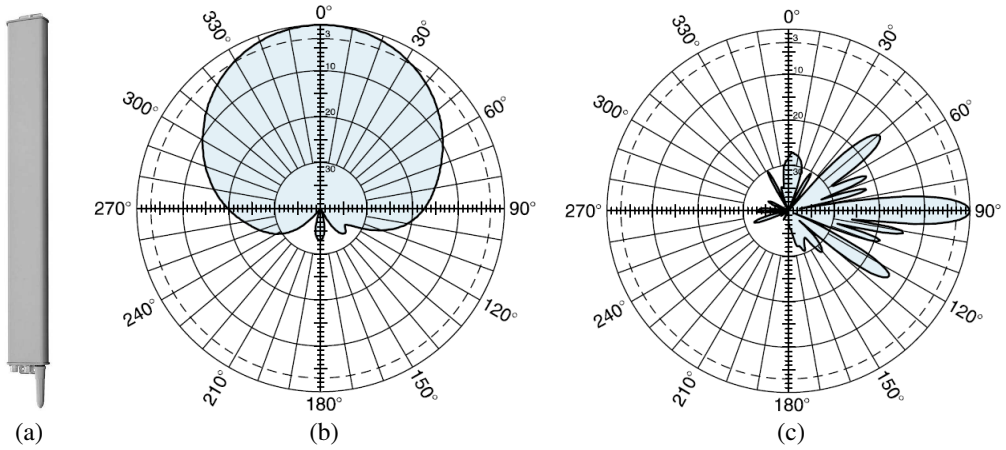

Figure 1: (a) Antenna, and (b) its azimuth plane and (c) elevation plane radiation patterns.

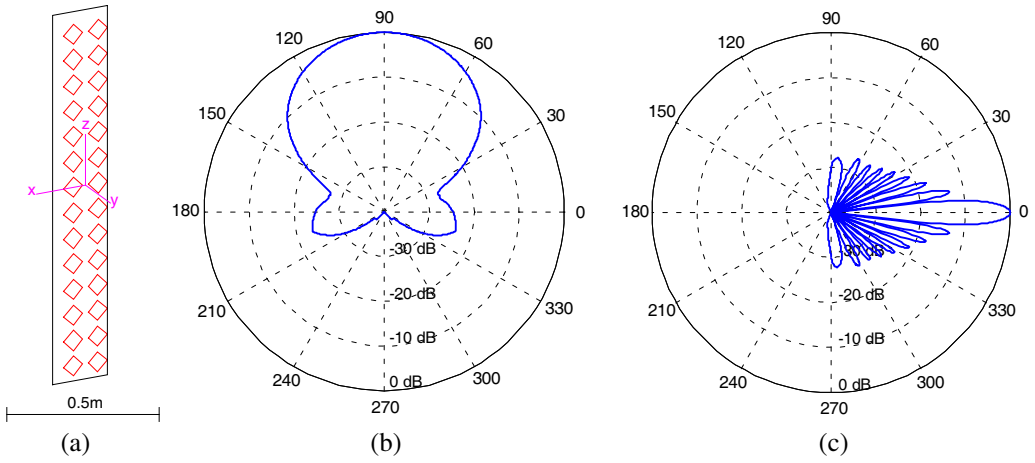

Figure 2: (a) Antenna model, and (b) its azimuth plane and (c) elevation plane radiation patterns.

the building is modeled using perfect conductor plates. The ground level of the building is modeled via an infinitely large ground plane having the rocky soil earth parameters (relative dielectric permittivity $\varepsilon_r = 5$, conductivity $\sigma = 2e-3\,\mathrm{S/m}$ and relative magnetic permeability $\mu_r = 1$). The geometry of the house with the antennas is given in Figure 3.

The electric field is calculated at X-Y grid points around the periphery of the house at 1 meter spacing in both directions forming a $50 \times 50\,\mathrm{m}$. calculation area with the antennas being in the

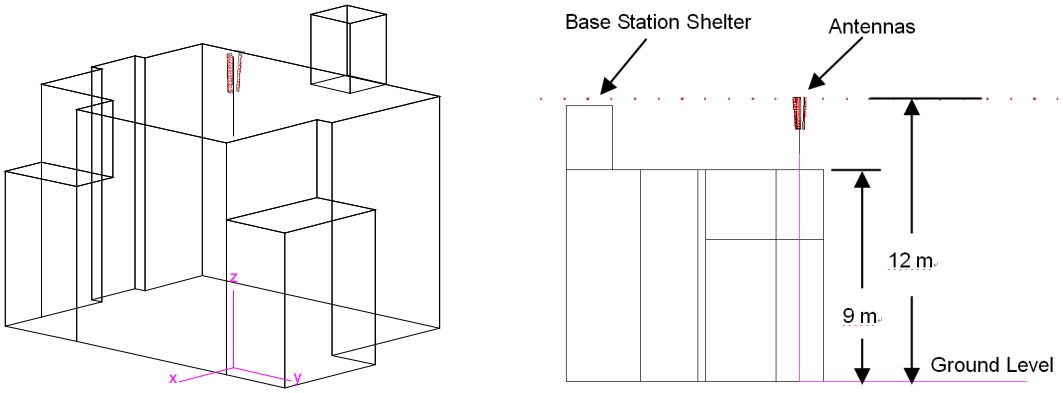

Figure 3: Base station building model (a) isometric view, (b) side view.

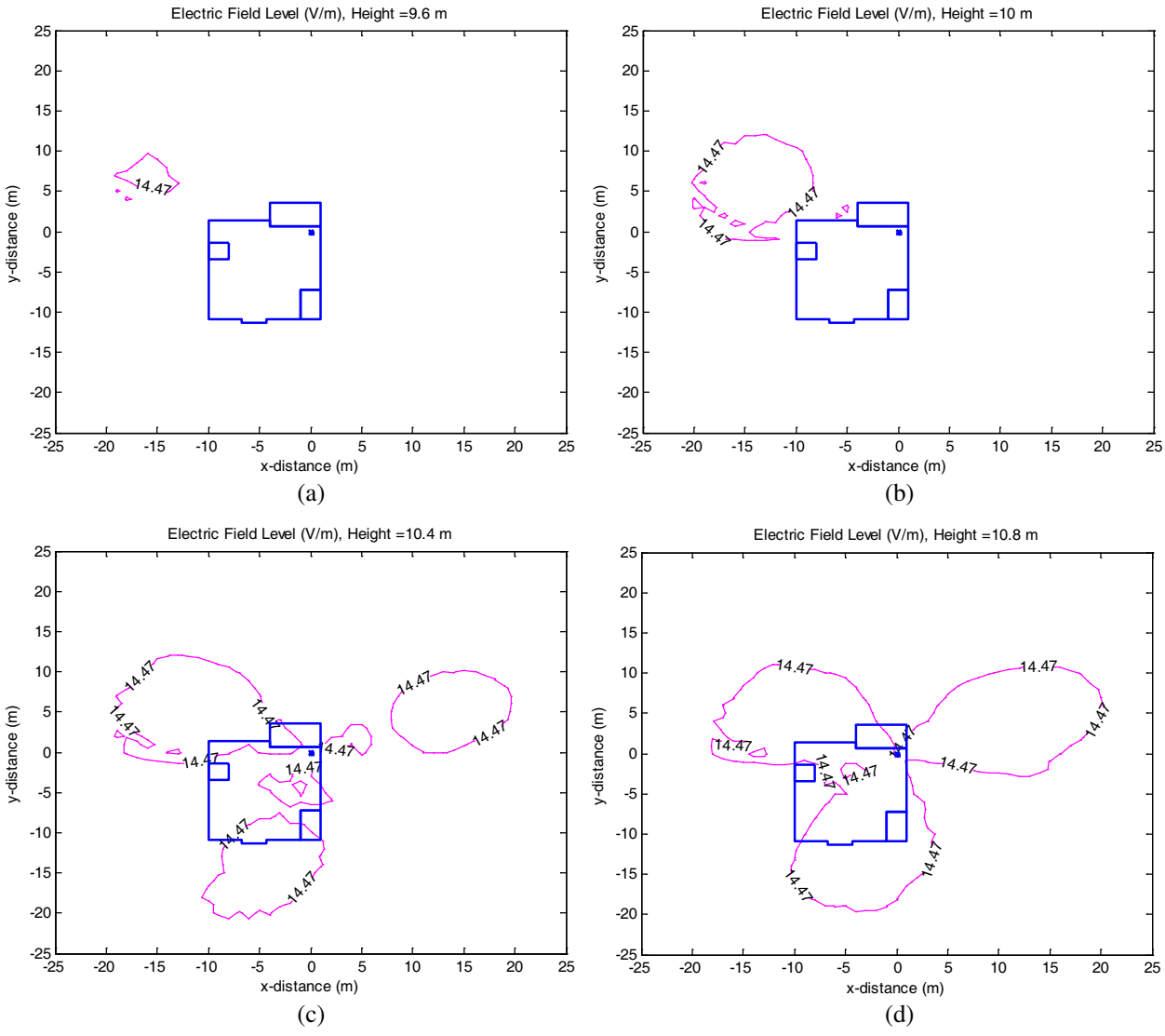

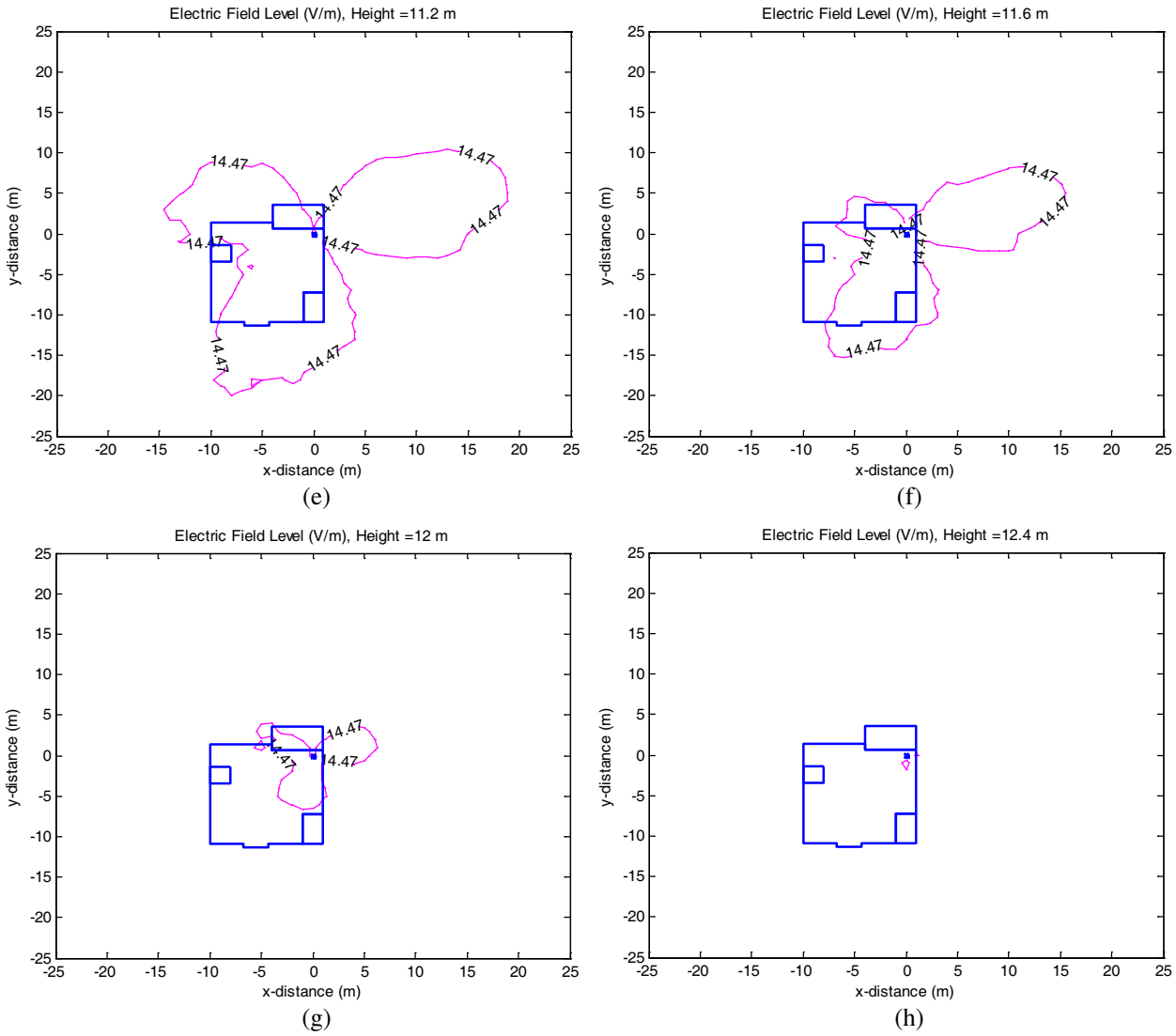

Figure 4: Analysis Results for Different Heights. (a) 9.6 m, (b) 10.0 m, (c) 10.4 m, (d) 10.8 m, (e) 11.2 m, (f) 11.6 m, (g) 12.0 and (h) 12.4 m.

center. This calculation is repeated for every 0.2 m height from 7.0 m to 12.6 m. All antennas with their double polarizations are kept active during the simulation and the calculated electric field is the complex result of the radiation coming from all antennas.

4. ANALYSIS RESULTS

The resulting electric field at every height is plotted in a contour line whose limit level is determined by the "Information and Communication Technologies Authority (BTK)", a body governing all communication issues in Turkey. Although the ICNIRP Guidelines' maximum permissible exposure limit for general public safety for 1800 MHz is 58.34 V/m ($1.375 \cdot f^{1/2}$), the Turkish Authority lowers this to 14.47 V/m by adopting a lower factor ($0.341 \cdot f^{1/2}$) [3]. The contour line plots for 14.47 V/m are given for all heights from 9.6 to 12.4 m at every 0.4 m height in Figure 4. The contour line actually demonstrates the safety distance around the base station. Below 9.6 m and above 12.4 m, no safety distance contour line is given because the electric field is under the limit level at all locations at these heights. As seen from the figures, the safety distance increases at the heights at which the main lobes of the antennas illuminate the surroundings.

5. CONCLUSIONS

Although the health limit levels are well established and the cellular base station RF infrastructures are well known, there is still continuing debate about the radiation hazard level of the base sta-

tions. In this work, the problem is taken from the analysis point of view and the change in safety distance around a specific base station is analyzed by using ray optic techniques. The analysis result emphasizes the effect of the antenna pattern in the resulting safety distances.

REFERENCES

1. ICNIRP — International Commission on Non-Ionizing Radiation Protection, "Guidelines for limiting exposure to time varying electric, magnetic and electromagnetic fields (up to 300 GHz)," *Health Physics*, Vol. 74, No. 4, 494–522, 1998.
2. Marhefka, R. J., *NEC — Basic Scattering Code (BSC) Version 4.2*, ElectroScience Laboratory, Ohio State University, Ohio, 2000.
3. Information and Communication Technologies Authority, "Regulation on determination, measurement methods and supervision of the limit values of the electromagnetic field force from the fixed telecommunication devices operating within the frequency range of 10 kHz–60 GHz," No. 24460, Turkey's Official Gazette, December 7, 2001.

Application of the Green's Function to Calculating the Impedance of a Uniform Current Density between Two Multilayered Media

J. Acero[1], **C. Carretero**[1], **R. Alonso**[2], **Ó. Lucía**[1], **and J. M. Burdío**[1]

[1]Dep. Ingeniería Electrónica y Comunicaciones, Universidad de Zaragoza, Spain
[2]Dep. Física Aplicada, Universidad de Zaragoza, Spain

Abstract— The equivalent impedance of a system consisting of a uniform current density placed between two multilayered planar media is derived by using the Green's function. The impedance is posed in terms of a semi-analytical expression in which the different physical and geometric parameters of the system are taken into account. Both media consist of several layers of homogeneous materials which are characterized by means of their physical properties. This system is the basis of many practical applications, such as non-destructive sensing devices, induction heating or electromagnetic field shielding. Considering these applications, the magnetoquasistatic (MQS) regime is adopted in this analysis. The analysis also shows that the impedance comprises two contributions: the first one is dependent of the sources of the fields; the second one is defined by the effect of the media. According to this analysis, a Green's function solution is obtained for each contribution and the total impedance is obtained by adding the two solutions. The convolution of the Green's function solutions with the current density is required to obtain the equivalent impedance of the system; in this case such convolution is reduced to a product in a transformed version of the problem. Taking advantage of the axial symmetry of the problem, a spectral transform like the Hankel Transform is used. Some experimental results are provided in order to verify the developed impedance expression. These results show the dependence of the complex impedance with respect to the frequency, which is measured by means of conventional impedance analyzers.

1. INTRODUCTION

The case study is represented in Fig. 1. The uniform current density is represented by a coil carrying a constant current density of amplitude $\mathbf{J}_e$ at angular frequency ω. The multilayered upper and lower media consists of N and M layers of homogeneous material, respectively. The kth layer is characterized by its electrical conductivity σ_k and relative magnetic permeability $\mu_{r\,k}$. The thickness of each layer is d_k and other relevant geometrical dimensions of both the coil and the media are also presented in the Fig. 1. The system exhibits axial symmetry.

This model results of practical interest in different areas, such as magnetic devices for power electronics, non-destructive sensing, induction heating, wireless power transference and electromagnetic field shielding. This interest has fostered the appearing of several studies dealing with the considered system. However, such studies have often been tackled by means of a model of the coil consisting of adding the effect of several circular filamentary currents [1–3]. Other approaches include the effect of some materials surrounding the coil [4, 5]; moreover some models carried out by Finite Element Analysis (FEA) tools have also been proposed [6, 7].

The use of filamentary currents to model the system shown in Fig. 1 gives rise to some convergence problems in calculating the self inductance of the coil, due to the filamentary current models a singularity. In order to avoid these problems, in this paper the equivalent impedance is obtained by using the Green's function. The obtained model is verified by means of impedance measurements.

2. GREENŚ FUNCTION OF THE INTEREST SYSTEM

In the mentioned areas of interest the quasi-static approximation could be assumed considering the small dimensions of the typical systems with respect to the involved wavelengths. Thus, a vector potential $\mathbf{A}$ such that the magnetic flux density is $\mathbf{B} = \nabla \times \mathbf{A}$ and $\nabla \cdot \mathbf{A} = 0$, satisfies Poisson's equation

$$\nabla^2 \mathbf{A} - j\omega\sigma\mu\mathbf{A} = -\mu\mathbf{J}_e. \tag{1}$$

where $\mathbf{J}_e$ is the current in the coil, and current with harmonic-time dependence has also been considered.

The solution of the last equation can be derived by means of the Green's function $g(\mathbf{r}, \mathbf{r}')$, where the vector positions $\mathbf{r}$ and $\mathbf{r}'$ refers to the coordinate of the source and the coordinate of the

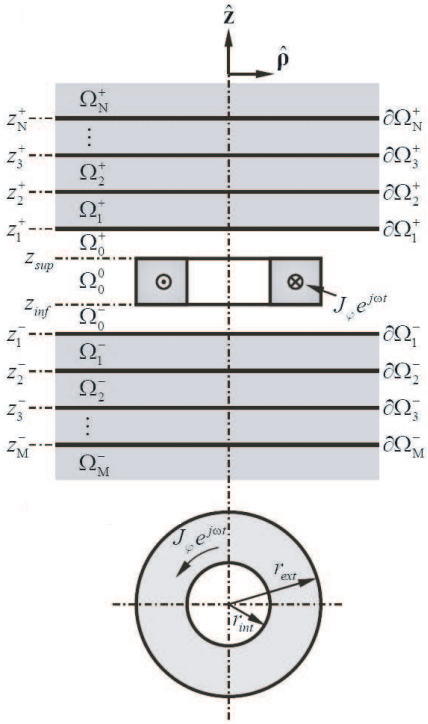

Figure 1: Representation of a system consisting of constant current density between two half spaces.

interest point, respectively. The function $g(\mathbf{r}, \mathbf{r}')$ is the solution of a diffusion equation which is similar to (1). This equation is the following

$$\nabla^2 g(\mathbf{r}, \mathbf{r}') - j\omega\mu\sigma g(\mathbf{r}, \mathbf{r}') = -\delta(\mathbf{r} - \mathbf{r}'). \tag{2}$$

Therefore, the vector potential generated by a current density $\mathbf{J}_e$ occupying the $\mathbf{r}'$ coordinates is

$$\mathbf{A}(\mathbf{r}) = \int \mu \mathbf{J}_e(\mathbf{r}')\, g(\mathbf{r}, \mathbf{r}') d\mathbf{r}'. \tag{3}$$

Considering that the system of Fig. 1 is invariant under translational displacements according to parallel directions with respect to the boundaries, and also considering the axial symmetry of the system, it could take advantage of a spectral transformation, like the Fourier-Bessel Transform. This couple of considerations allows reducing (3) to the following one:

$$\mathbf{A}(\beta, z) = \int \mu \mathbf{J}_e(\beta, z')\, g(\beta, z, z') dz', \tag{4}$$

where $\mathbf{J}_e(\beta, z')$ and $g(\beta, z, z')$ represents the Fourier-Bessel Transform of $\mathbf{J}_e(\mathbf{r}')$ and $g(\mathbf{r}, \mathbf{r}')$, respectively, and β is the integral kernel of the Fourier-Bessel Transform.

The function $g(\beta, z, z')$, belonging to the transformed domain, has to be a solution of (2), when the corresponding inverse transform is applied. Performing this operation and also defining the following parameter $\eta = \sqrt{\beta^2 + j\omega\mu\sigma}$, it results

$$\partial_z^2 g(\beta, z, z') - \eta^2 g(\beta, z, z') = -\delta(z - z'). \tag{5}$$

The solution of the homogeneous equation corresponding to he last one is the following

$$g(\beta, z, z') = A(\beta)\, e^{\eta(z - z')} + B(\beta)\, e^{-\eta(z - z')}. \tag{6}$$

Assuming linearity of the media, the Green's function for a punctual excitation current between the two multilayered media can be calculated adding the Green's function of the excitation in the

air and the Green's function that considers the multilayered structure. These functions are named $g_{air}(\beta, z, z')$ and $g_{u\_l}(\beta, z, z')$, respectively. Thus, the whole Green's function is given by

$$g(\beta, z, z') = g_{air}(\beta, z, z') + g_{u\_l}(\beta, z, z'), \tag{7}$$

where the notation u_l refers to the upper and lower media. The function $g_{air}(\beta, z, z')$ is obtained through the general solution (6) and considering the properties of the air. In that case, the transformed Green's function in the air reduces to the following expression

$$g_{air}(\beta, z, z') = \frac{e^{-\beta|z-z'|}}{2\beta}. \tag{8}$$

The function $g_{u\_l}(\beta, z, z')$ can be calculated by means of the general solution (6) applied to each layer of the structure because current densities $\mathbf{J}_e$ do not take place at these positions. Moreover a couple of additional considerations must be taken into account. First, the Green's function must be finite, thus coefficients B_{M^-} and A_{N^+} must be equal to zero. Second, the coefficients for the kth layer can be obtained applying the boundary conditions between contiguous layers. These conditions, expressed in terms of transformed Green's functions, are the following

$$g_{k-1}(\beta, z_k, z') = g_k(\beta, z_k, z'), \tag{9}$$

$$\frac{1}{\mu_{k-1}}\partial_z g_{k-1}(\beta, z_k, z') = \frac{1}{\mu_k}\partial_z g_k(\beta, z_k, z'). \tag{10}$$

The coefficients A_k and B_k for the different layers, i.e., $k \in [M^- \ldots N^+]$, can be calculated by applying (10) and (10) in each layer recursively. Thus, the Green's function representing the contribution of the media is

$$g_{u\_l}(\beta, z, z') = \frac{1}{2\beta}\frac{\left(e^{-\beta d'_u} + \phi_l e^{-\beta(d'_u+2d'_l)}\right)\phi_u e^{-\beta d_u} + \left(e^{-\beta d'_l} + \phi_u e^{-\beta(d'_u+2d'_l)}\right)\phi_l e^{-\beta d_l}}{1 - \phi_u\phi_l e^{-2\beta(d'_u+d'_l)}}. \tag{11}$$

where distances d'_u, d'_l, d_u and d_l corresponds to $z_1^+ - z'$, $z' - z_1^-$, $z_1^+ - z$ and $z - z_1^-$ respectively, and coefficients ϕ_u and ϕ_l can be found in some references [8].

3. IMPEDANCE OF THE COIL

In order to apply (4), the Fourier transform [9], of the excitation current, $\mathbf{J}_e(\beta, z')$, is required. It can be demonstrated that such transform is given by the following expression

$$\mathbf{J}_e(\beta, z) = jJ_\varphi \Pi(\beta, r_{int}, r_{ext})\,\varphi, \tag{12}$$

where

$$\begin{aligned}\Pi(\beta, r_{int}, r_{ext}) &= \frac{\pi}{2\beta} r_{ext}\left[J_1(\beta r_{ext}) H_0(\beta r_{ext}) - J_0(\beta r_{ext}) H_1(\beta r_{ext})\right] \\ &\quad - r_{int}\left[J_1(\beta r_{int}) H_0(\beta r_{int}) - J_0(\beta r_{int}) H_1(\beta r_{int})\right],\end{aligned} \tag{13}$$

being H_0 and H_1 Struve functions [9]. Considering (3), (4), (8), (12) and (13), the vector potential at the positions of the coil ($z_{inf} \le z \le z_{sup}$) due to the excitation current is

$$\mathbf{A}_{air}(\rho,z) = \frac{\mu_0}{2}\frac{n}{h^2\left(r_{ext}^2 - r_{int}^2\right)} I \cdot \int_0^\infty \frac{\Pi(\beta, r_{int}, r_{ext})}{\beta}\left(2 - e^{-\beta(z-z_{\inf})} - e^{-\beta(z_{sup}-z)}\right) J_1(\beta\rho)\, d\beta\hat{\varphi}, \tag{14}$$

similarly, the vector potential at ($z_{inf} \le z \le z_{sup}$) due to the contribution of the media results

$$\begin{aligned}\mathbf{A}_{u\_l}(\rho, z) &= \frac{\mu}{2}\frac{n}{h^2\left(r_{ext}^2 - r_{int}^2\right)} I \int_0^\infty \frac{\Pi(\beta, r_{int}, r_{ext})}{\beta}\frac{\left(1 - e^{-\beta h}\right)}{1 - \phi_u\phi_l e^{-2\beta(d_{uc}+h+d_{lc})}} \\ &\quad \cdot \Big(\phi_u e^{-2\beta d_{uc}} e^{\beta(z-z_{sup})} + \phi_u\phi_l e^{-2\beta(d_{uc}+h+d_{lc})}\left(e^{\beta(z-z_{inf})} + e^{-\beta(z-z_{sup})}\right) \\ &\quad + \phi_l e^{-2\beta d_{ul}} e^{-\beta(z-z_{inf})}\Big) J_1(\beta\rho)\, d\beta\hat{\varphi},\end{aligned} \tag{15}$$

where n is the number of turns of the coil, I is the total current of the coil, and d_{uc}, d_{lc} are defined as $z_1^+ - z_{sup}$, $z - inf - z_1^-$, i.e., d_{uc}, d_{lc} corresponds to the distance between the coil and the upper and lower multilayer, respectively.

Considering that the electric field is related with the vector potential trough $\mathbf{E} = -j\omega\mathbf{A}$, an electromotive force (emf) can be obtained integrating this field along the path of the coil. Given the relationship between the emf and the impedance, and also considering (14) and (15), the impedances for the coil in the air and the contribution of the media results

$$Z_{air} = 2j\omega\pi\mu_0 \frac{n^2}{h^2\left(r_{ext}^2 - r_{int}^2\right)} \int_0^\infty \frac{\Pi^2\left(\beta, r_{int}, r_{ext}\right)}{\beta^2} \left(\beta h + e^{-\beta h} - 1\right) d\beta, \tag{16}$$

$$Z_{u\_l} = \frac{j\omega\pi\mu_0 n^2}{h^2\left(r_{ext}^2 - r_{int}^2\right)} \int_0^\infty \frac{\Pi^2\left(\beta, r_{int}, r_{ext}\right)}{\beta^2\left(1 - \phi_u\phi_l e^{-2\beta(d_{uc}+h+d_{lc})}\right)} \left(1 - e^{-\beta h}\right)^2 \cdot \left(\phi_u e^{-2\beta d_{uc}} + \phi_l e^{-2\beta d_{ul}} + 2\phi_u\phi_l e^{-2\beta(d_{uc}+d_{lc})} e^{-2\beta h}\right) d\beta. \tag{17}$$

It should be noted that Z_{air} is purely imaginary and, therefore, it corresponds to an inductance independent of the frequency, which is in accordance with the adopted constant current model.

4. EXPERIMENTAL RESULTS

An experimental setup according the system shown in the Fig. 1 has been built to verify the impedance model. Frequency dependent impedances have been measured by means of a precision LCR meter (Agilent E4980A). The tested coils consist of 24 turns of multistranded wire (Litz wire). Litz wires having fine strands spread effectively the current over the cross section of the cables, thus, the assumption of constant currents density is almost fulfilled. The used Litz wire consists of 35 strands with diameter 150 µm. The height of the coil is $h = 4$ mm. The lower medium was made with ferrite bars of finite thickness of 3.5 mm. A relative permeability of 2000 was and a null electrical conductivity was assumed for the ferrite. On the other hand, the upper medium consists of a copper disk with 10 mm of thickness. The explored frequency range was comprised between 1 kHz to 1 MHz. In these experiments the distance from the coil to upper medium varies from 4 mm to 8 mm, whereas the distance from the coil to the lower medium was fixed at 1.5 mm. Figs. 2(a) and 2(b) show the comparison between calculated and measured results, both resistance and inductance. As it can be seen, when the distance between the upper medium and the coil is increased, the resistance is reduced and the inductance is increased. The reason is that the conductive media used in the upper medium effectively shields the magnetic field generated by the coil. At the considered frequency range (from 1 kHz to 1 Mhz) the agreement between the model and the measurements is enough to consider acceptable the model.

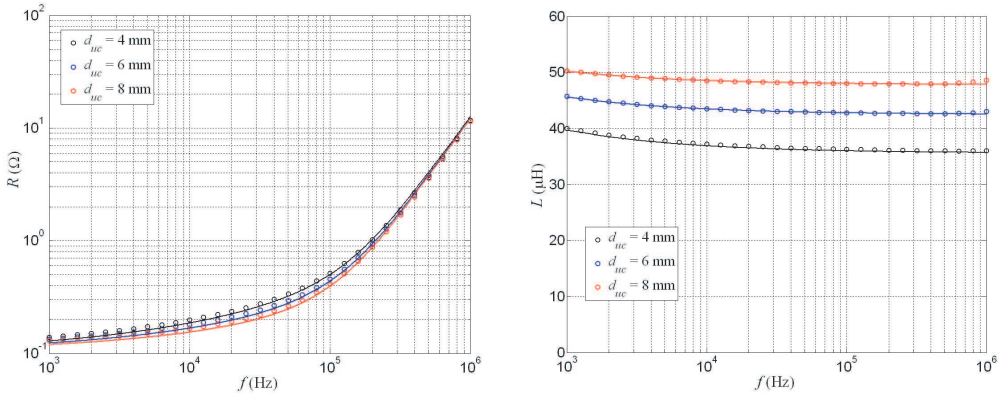

(a) (b)

Figure 2: Comparison between calculated and measured impedance of the coil between the media. (a) Resistances. (b) Inductances.

5. CONCLUSIONS

Integral expressions for calculating the equivalent impedance of a coil between two multilayered media have been developed. This system has several practical applications. The impedance model

was derived by means of the Green's function, which implies a more general frame than others whose developments are based on filamentary currents Moreover, the convergence of the model is improved with respect to the mentioned methods and also the computation time is reduced. The model has been experimentally validated through impedance measurements of a coil with the additional media. The results points that analytical studies based on Green's functions permit to model with remarkably accuracy systems involving constant current densities and several media.

ACKNOWLEDGMENT

This work was partly supported by the Spanish MICINN under Project CSD2009-00046 and Project TEC2010-19207, by DGA under Project PI065/09, and by Bosch and Siemens Home Appliances Group.

REFERENCES

1. Adler, M. S., "A field-theoretical approach to magnetic induction heating of thin circular plates," *IEEE Trans. Magn.*, Vol. 10, No. 12, 1118–1125, 1974.
2. Burais, N., et al., "Electromagnetic field formulation for eddy current calculations in non-destructive testing systems," *IEEE Trans. Magn.*, Vol. 18, No. 6, 1058–1060, 1982.
3. Ditchburn, R. J., S. K. Burke, and M. Posada, "Eddy-current nondestructive inspection with thin spiral coils: Long cracks in steel," *J. Nondestruct. Eval.*, Vol. 22, No. 2, 63–77, 2003.
4. Acero, J., et al., "Electromagnetic induction of planar windings with cylindrical symmetry between two half-spaces," *J. Appl. Phys.*, Vol. 103, 104905(8), 2008.
5. Roshen, W. A., "Effect of finite thickness of magnetic substrate on planar inductors," *IEEE Trans. Magn.*, Vol. 26, No. 1, 270–275, 1990.
6. Miyoshi, T., M. Sumiya, and H. Omori, "Analysis of an induction heating system by the finite element method combined with a boundary integral equation," *IEEE Trans. Magn.*, Vol. 23, No. 3, 1827–1832, 1987.
7. Br, O., et al., "A finite element formulation for eddy current carrying ferromagnetic thin sheets," *IEEE Trans. Magn.*, Vol. 33, No. 3, 1173–1178, 1997.
8. Acero, J., et al., "Modeling of planar spiral inductors between two multilayer media for induction heating applications," *IEEE Trans. Magn.*, Vol. 42, No. 11, 3719–3729, 2006.
9. Abramowitz, M. and I. A. Stegun, *Handbook of Mathematical Functions*, Dover Publications, New York, 1970.

Heavy Ions Acceleration of Solar Wind in Electromagnetic and Gravitational Fields

Ying Weng[1] and Zi-Hua Weng[2]

[1]College of Chemistry and Chemical Engineering, Xiamen University, Xiamen 361005, China
[2]School of Physics and Mechanical and Electrical Engineering, Xiamen University, Xiamen 361005, China

Abstract— The paper studies the acceleration mechanism of heavy ions of the solar wind in the interplanetary magnetic field. By means of the octonions, we can draw out the forces in the electromagnetic and gravitational fields, and rephrase the Lorentz force, gravity, and inertial force etc. The study claims that there are some new force terms besides the known force terms, and one new force term can cause the electrons trammel the ions. The contrary motion between the ion and the electron offers the resistance against the movement of ions. Consequently the heavy ions keep going forward, while the light ions hobble and alter the directions frequently. Associating with the ion velocity, the resistance limits the maximum velocity of ions, especially in the space far from the sun, although the ions are accelerated in the magnetic field.

1. INTRODUCTION

The solar wind [1] mostly consists of the electrons and protons, and about 10% helium ions, and about 0.1% ions of other elements including the carbon, nitrogen, and oxygen etc. The observational facts state that the velocities of helium ions are higher than that of the protons [2]. Similarly the oxygen ions move more rapidly than the helium ions. It activates to suppose there may be one mechanism to accelerate heavy ions preferentially. By means of the octonion field theory the paper attempts to explain why the heavy ions displace faster in the solar wind.

In 1861 J. C. Maxwell [3] first represented the electromagnetic theory with the quaternion, which was invented by W. R. Hamilton in 1843 [4]. Nowadays the gravitational field can be described by the quaternion as well, although the quaternion space for gravitational field is quite different to that for electromagnetic field. Simultaneously the electromagnetic field and gravitational field can be depicted in the octonion space, which comprises the electromagnetic quaternion space and the gravitational quaternion space [5].

In the octonion space we can define the field strength, field source, linear momentum, angular momentum, torque, and force of electromagnetic and gravitational fields. The force involves the known force terms such as Coulomb electric force, Lorentz force, Newtonian gravity [6], and inertial force etc. And this force definition encompasses some new force terms. One new force term will cause the charged particles move along the lines of magnetic force.

Due to the existence of magnetic strength, the higher charge ions move quicker, as well as the heavier ions displace more steadily. Contrastively the electrons transfer slowly to the contrary direction for their negative charges. The electrons form the resistance medium to slow down positive ions, so that the ions with various charges have different maximum velocity in the solar wind. For the same one ion the acceleration effect may be different in solar surfaces for different magnetic strengths, especially in the solar open field regions.

2. GRAVITATIONAL AND ELECTROMAGNETIC FIELDS

The gravitational field and electromagnetic field both can be illustrated by the quaternion, and their quaternion spaces will be combined together to become the octonion space [7]. In other words, the characteristics of gravitational field and electromagnetic field can be described with the octonion space simultaneously.

2.1. Octonion space

In the quaternion space for gravitational field, the basis vector $\mathbb{E}_g = (1, \mathbf{i}_1, \mathbf{i}_2, \mathbf{i}_3)$, and the radius vector $\mathbb{R}_g = (r_0, r_1, r_2, r_3)$, with the velocity $\mathbb{V}_g = (v_0, v_1, v_2, v_3)$. In the quaternion space for electromagnetic field, the basis vector $\mathbb{E}_e = (\mathbf{I}_0, \mathbf{I}_1, \mathbf{I}_2, \mathbf{I}_3)$, the radius vector $\mathbb{R}_e = (R_0, R_1, R_2, R_3)$, and the velocity $\mathbb{V}_e = (V_0, V_1, V_2, V_3)$, with $\mathbb{E}_e = \mathbb{E}_g \circ \mathbf{I}_0$.

The $\mathbb{E}_e$ is independent of the $\mathbb{E}_g$. Both of them can be combined together to become the basis vector $\mathbb{E}$ of the octonion space, that is, $\mathbb{E} = (1, \mathbf{i}_1, \mathbf{i}_2, \mathbf{i}_3, \mathbf{I}_0, \mathbf{I}_1, \mathbf{I}_2, \mathbf{I}_3)$. The octonion radius vector is $\mathbb{R} = \Sigma(\mathbf{i}_i r_i + k_{eg}\mathbf{I}_i R_i)$, and the velocity is $\mathbb{V} = \Sigma(\mathbf{i}_i v_i + k_{eg}\mathbf{I}_i V_i)$. Herein $r_0 = v_0 t$, t is the time, v_0 is

the speed of gravitational intermediate boson, and V_0 is the speed of electromagnetic intermediate boson; the symbol $\circ$ denotes the octonion multiplication; k_{eg} is the coefficient.

Sometimes the electric charge may be combined with the mass to become the electron or the proton etc, we obtain the $k_{eg}R_i\mathbf{I}_i = r_i\mathbf{i}_i \circ \mathbf{I}_0$ and $k_{eg}V_i\mathbf{I}_i = v_i\mathbf{i}_i \circ \mathbf{I}_0$, with $\mathbf{i}_0 = 1$. In the same way, the gravitational intermediate boson and electromagnetic intermediate boson can be combined together to become the photon etc in some cases.

Table 1: The octonion multiplication table.

	1	$\mathbf{i}_1$	$\mathbf{i}_2$	$\mathbf{i}_3$	$\mathbf{I}_0$	$\mathbf{I}_1$	$\mathbf{I}_2$	$\mathbf{I}_3$
1	1	$\mathbf{i}_1$	$\mathbf{i}_2$	$\mathbf{i}_3$	$\mathbf{I}_0$	$\mathbf{I}_1$	$\mathbf{I}_2$	$\mathbf{I}_3$
$\mathbf{i}_1$	$\mathbf{i}_1$	-1	$\mathbf{i}_3$	$-\mathbf{i}_2$	$\mathbf{I}_1$	$-\mathbf{I}_0$	$-\mathbf{I}_3$	$\mathbf{I}_2$
$\mathbf{i}_2$	$\mathbf{i}_2$	$-\mathbf{i}_3$	-1	$\mathbf{i}_1$	$\mathbf{I}_2$	$\mathbf{I}_3$	$-\mathbf{I}_0$	$-\mathbf{I}_1$
$\mathbf{i}_3$	$\mathbf{i}_3$	$\mathbf{i}_2$	$-\mathbf{i}_1$	-1	$\mathbf{I}_3$	$-\mathbf{I}_2$	$\mathbf{I}_1$	$-\mathbf{I}_0$
$\mathbf{I}_0$	$\mathbf{I}_0$	$-\mathbf{I}_1$	$-\mathbf{I}_2$	$-\mathbf{I}_3$	-1	$\mathbf{i}_1$	$\mathbf{i}_2$	$\mathbf{i}_3$
$\mathbf{I}_1$	$\mathbf{I}_1$	$\mathbf{I}_0$	$-\mathbf{I}_3$	$\mathbf{I}_2$	$-\mathbf{i}_1$	-1	$-\mathbf{i}_3$	$\mathbf{i}_2$
$\mathbf{I}_2$	$\mathbf{I}_2$	$\mathbf{I}_3$	$\mathbf{I}_0$	$-\mathbf{I}_1$	$-\mathbf{i}_2$	$\mathbf{i}_3$	-1	$-\mathbf{i}_1$
$\mathbf{I}_3$	$\mathbf{I}_3$	$-\mathbf{I}_2$	$\mathbf{I}_1$	$\mathbf{I}_0$	$-\mathbf{i}_3$	$-\mathbf{i}_2$	$\mathbf{i}_1$	-1

2.2. Field Equations

In the octonion space, the gravitational potential is $\mathbb{A}_g = (a_0, a_1, a_2, a_3)$, while the electromagnetic potential is $\mathbb{A}_e = (A_0, A_1, A_2, A_3)$, with $\mathbb{A}_e = \mathbb{A}_q \circ \mathbf{I}_0$. They can be combined together to become the octonion field potential $\mathbb{A} = \mathbb{A}_g + k_{eg}\mathbb{A}_e$.

The octonion field strength $\mathbb{B} = \Sigma(\mathbf{i}_i b_i + k_{eg}\mathbf{I}_i B_i)$ is defined as $\mathbb{B} = \Diamond \circ \mathbb{A} = \mathbb{B}_g + k_{eg}\mathbb{B}_e$, and consists of gravitational strength $\mathbb{B}_g$ and electromagnetic strength $\mathbb{B}_e$, with the gauge equations $b_0 = 0$ and $B_0 = 0$. Herein $\Diamond = \partial_0 + \Sigma(\mathbf{i}_j\partial_j)$; $\partial_i = \partial/\partial r_i$; $\nabla = \Sigma(\mathbf{i}_j\partial_j)$.

The gravitational strength $\mathbb{B}_g$ includes two components, $\mathbf{g} = (g_{01}, g_{02}, g_{03})$ and $\mathbf{b} = (g_{23}, g_{31}, g_{12})$,

$$\mathbf{g}/v_0 = \mathbf{i}_1(\partial_0 a_1 + \partial_1 a_0) + \mathbf{i}_2(\partial_0 a_2 + \partial_2 a_0) + \mathbf{i}_3(\partial_0 a_3 + \partial_3 a_0), \quad (1)$$

$$\mathbf{b} = \mathbf{i}_1(\partial_2 a_3 - \partial_3 a_2) + \mathbf{i}_2(\partial_3 a_1 - \partial_1 a_3) + \mathbf{i}_3(\partial_1 a_2 - \partial_2 a_1), \quad (2)$$

while the electromagnetic strength $\mathbb{B}_e$ consists of $\mathbf{E} = (B_{01}, B_{02}, B_{03})$ and $\mathbf{B} = (B_{23}, B_{31}, B_{12})$,

$$\mathbf{E}/v_0 = \mathbf{I}_1(\partial_0 A_1 + \partial_1 A_0) + \mathbf{I}_2(\partial_0 A_2 + \partial_2 A_0) + \mathbf{I}_3(\partial_0 A_3 + \partial_3 A_0), \quad (3)$$

$$\mathbf{B} = \mathbf{I}_1(\partial_3 A_2 - \partial_2 A_3) + \mathbf{I}_2(\partial_1 A_3 - \partial_3 A_1) + \mathbf{I}_3(\partial_2 A_1 - \partial_1 A_2). \quad (4)$$

In the octonion space, the electric current density $\mathbb{S}_e = q\mathbb{V}_g \circ \mathbf{I}_0$ is the source for electromagnetic field, and the linear momentum density $\mathbb{S}_g = m\mathbb{V}_g$ for gravitational field. The octonion field source $\mathbb{S}$ satisfies

$$\mu\mathbb{S} = -(\mathbb{B}/v_0 + \Diamond)^* \circ \mathbb{B} = \mu_g\mathbb{S}_g + k_{eg}\mu_e\mathbb{S}_e - \mathbb{B}^* \circ \mathbb{B}/v_0, \quad (5)$$

where q is the electric charge density; m is the mass density; μ is one coefficient, and μ_g is the gravitational constant, and μ_e is the electromagnetic constant; $k_{eg}^2 = \mu_g/\mu_e$; $*$ denotes the conjugate of octonion.

The octonion field energy density is $\mathbb{B}^* \circ \mathbb{B}/\mu_g = \mathbb{B}_g^* \circ \mathbb{B}_g/\mu_g + \mathbb{B}_e^* \circ \mathbb{B}_e/\mu_e$. And $\mathbb{B}_g^* \circ \mathbb{B}_g/(2\mu_g)$ is the energy density of gravitational field, while $\mathbb{B}_e^* \circ \mathbb{B}_e/(2\mu_e)$ is that of electromagnetic field.

3. GRAVITATIONAL AND ELECTROMAGNETIC FORCES

The electromagnetic and gravitational forces can be defined from the octonion energy. The force terms include the inertial force, gravitational force, electric force, magnetic force, gradient of energy, and interacting force between the magnetic strength with magnetic moment, etc.

In the case for coexistence of electromagnetic field and gravitational field, the octonionic angular momentum density $\mathbb{L} = l_0 + \Sigma(l_j\mathbf{i}_j) + L_0\mathbf{I}_0 + \Sigma(L_j\mathbf{I}_j)$ is defined from the octonion linear momentum density $\mathbb{P} = \mu\mathbb{S}/\mu_g$ and octonion radius vector $\mathbb{R}$.

$$\mathbb{L} = (\mathbb{R} + k_{rx}\mathbb{X}) \circ \mathbb{P}, \quad (6)$$

where $\mathbb{P} = \Sigma(p_i\mathbf{i}_i + P_i\mathbf{I}_i)$; $\mathbb{X} = \Sigma(x_i\mathbf{i}_i) + k_{eg}\Sigma(X_i\mathbf{I}_i)$, with $k_{rx}\mathbb{X} \ll \mathbb{R}$ and $k_{rx} = 1$. The derivation of octonion physics quantity $\mathbb{X}$ is similar to the Hertz vector, and will yield the gravitational potential as well as the electromagnetic potential. The angular momentum density $\mathbb{L}$ includes the scalar part l_0, orbital angular momentum density $\Sigma(l_j\mathbf{i}_j)$, and some other omissible terms etc.

Table 2: The multiplication of the physical quantity in the octonion space.

definition	meaning
$\nabla \cdot \mathbf{w}$	$-(\partial_1 w_1 + \partial_2 w_2 + \partial_3 w_3)$
$\nabla \times \mathbf{w}$	$\mathbf{i}_1(\partial_2 w_3 - \partial_3 w_2) + \mathbf{i}_2(\partial_3 w_1 - \partial_1 w_3) + \mathbf{i}_3(\partial_1 w_2 - \partial_2 w_1)$
∇w_0	$\mathbf{i}_1\partial_1 w_0 + \mathbf{i}_2\partial_2 w_0 + \mathbf{i}_3\partial_3 w_0$
$\partial_0\mathbf{w}$	$\mathbf{i}_1\partial_0 w_1 + \mathbf{i}_2\partial_0 w_2 + \mathbf{i}_3\partial_0 w_3$
$\nabla \cdot \mathbf{W}$	$-(\partial_1 W_1 + \partial_2 W_2 + \partial_3 W_3)\mathbf{I}_0$
$\nabla \times \mathbf{W}$	$-\mathbf{I}_1(\partial_2 W_3 - \partial_3 W_2) - \mathbf{I}_2(\partial_3 W_1 - \partial_1 W_3) - \mathbf{I}_3(\partial_1 W_2 - \partial_2 W_1)$
$\nabla \circ \mathbf{W}_0$	$\mathbf{I}_1\partial_1 W_0 + \mathbf{I}_2\partial_2 W_0 + \mathbf{I}_3\partial_3 W_0$
$\partial_0\mathbf{W}$	$\mathbf{I}_1\partial_0 W_1 + \mathbf{I}_2\partial_0 W_2 + \mathbf{I}_3\partial_0 W_3$

3.1. Energy and Torque

In the case for coexistence of electromagnetic field and gravitational field, the octonion energy density $\mathbb{W} = w_0 + \Sigma(w_j\mathbf{i}_j) + \Sigma(W_i\mathbf{I}_i)$ is defined from the octonion angular momentum density $\mathbb{L}$ and octonion field strength $\mathbb{B}$,

$$\mathbb{W} = v_0(\mathbb{B}/v_0 + \Diamond) \circ \mathbb{L}, \tag{7}$$

where the $-w_0/2$ is the energy density, which includes the kinetic energy, potential energy, field energy, and work etc; the $\mathbf{w}/2 = \Sigma(w_j\mathbf{i}_j)/2$ is the torque density.

In the electromagnetic field and gravitational field, the energy density and torque density can be detected in the space $\mathbb{E}_g$, while the other vectorial parts $\mathbf{W}_0 = W_0\mathbf{I}_0$ and $\mathbf{W} = \Sigma(W_j\mathbf{I}_j)$ can not be currently, although the latter two have an effect on the power and force also.

3.2. Power and Force

In the presence of electromagnetic and gravitational fields, the octonion power density $\mathbb{N} = n_0 + \Sigma(n_j\mathbf{i}_j) + \Sigma(N_i\mathbf{I}_i)$ is defined from the octonion energy density $\mathbb{W}$ and field strength $\mathbb{B}$,

$$\mathbb{N} = v_0(\mathbb{B}/v_0 + \Diamond)^* \circ \mathbb{W}, \tag{8}$$

where $-n_0/(2v_0)$ is the power density, and the $\mathbf{n} = \Sigma(n_j\mathbf{i}_j)$ is the function of forces. But the other vectorial parts $\mathbf{N}_0 = N_0\mathbf{I}_0$ and $\mathbf{N} = \Sigma(N_j\mathbf{I}_j)$ may not be detected in the space $\mathbb{E}_g$ at present.

The octonion force $\mathbf{f}$ of gravitational and electromagnetic fields is defined as $\mathbf{f} = -\mathbf{n}/(2v_0)$,

$$\begin{aligned} -2v_0\mathbf{f} \;=\; & v_0\nabla^* w_0 + v_0\partial_0\mathbf{w} + v_0\nabla^* \times \mathbf{w} + (\mathbf{g}/v_0 + \mathbf{b})^* \times \mathbf{w} + w_0(\mathbf{g}/v_0 + \mathbf{b})^* \\ & + k_{eg}(\mathbf{E}/v_0 + \mathbf{B})^* \times \mathbf{W} + k_{eg}(\mathbf{E}/v_0 + \mathbf{B})^* \circ \mathbf{W}_0, \end{aligned} \tag{9}$$

where the force $\mathbf{f}$ includes the inertial force, gravity, Lorentz force, gradient of energy, and interacting force between dipole moment with magnetic strength etc.

In the gravitational and electromagnetic fields, the above means that the force definition is much more complicated than before, and encompasses some new force terms. One of them can be used to explain the acceleration phenomena of heavy ions in the solar wind.

4. ACCELERATION OF HEAVY IONS

Study of the solar wind revealed the velocities of helium ions are higher than that of the protons, as well as the oxygen ions move more rapidly than the helium ions. The researchers speculate that there exist one mechanism to accelerate heavy ions preferentially. By means of the octonion force the paper narrates why the heavy ions shift faster than the light ions in the solar wind.

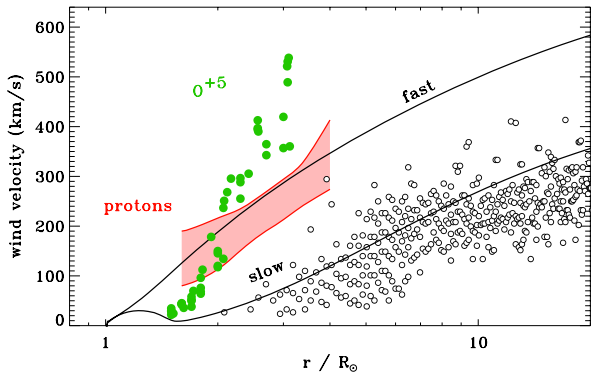

Figure 1: The outflow speeds of protons (red) and O^{+5} ions (green) in the solar wind detecting by UVCS are compared with the speeds of blobs from LASCO (open circles). (Cranmer, 2009).

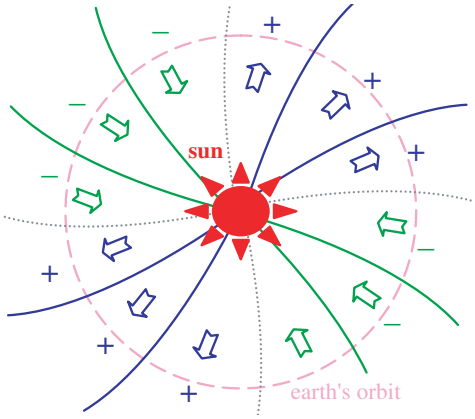

Figure 2: As one part of the Sun's magnetic field, the interplanetary magnetic field travels outward in a spiral pattern of a gigantic pinwheel due to the Sun's rotation from IMP-1.

4.1. Interplanetary Magnetic Field

The interplanetary magnetic field is one part of the Sun's magnetic field that is stretched into the interplanetary space. Because of the Sun's rotation, the interplanetary magnetic field travels outward in a spiral pattern of a gigantic pinwheel. The interplanetary magnetic field originates in the open regions of solar magnetic field. And the field lines emerging from one region do not return to a conjugate region. The direction of magnetic field in the Sun's northern hemisphere is opposite to that in the southern hemisphere.

Along the plane of the Sun's magnetic equator, the oppositely directed open field lines run parallel to each other and are separated by the heliospheric current sheet. The current sheet is tilted and warped, and it has a wavy structure as it extends into interplanetary space. Because the Earth is located sometimes above and sometimes below the rotating current sheet, it experiences regular and periodic changes in the polarity of the interplanetary magnetic field. These periods of alternating positive or negative polarity are known as magnetic sectors. In each magnetic sector, the solar magnetic fields possess same one polarity.

4.2. Ions' Movements

In the magnetic sector, the ions of solar wind will be affected by the new force term $qv_0\Sigma(B_j\mathbf{i}_j)$, besides the inertial force, Lorentz force, gravity, and gradient of energy etc.

Because of the term $qv_0\Sigma(B_j\mathbf{i}_j)$, the ions will move along the lines of magnetic force in the interplanetary magnetic field, while the electrons along the opposite direction. Therefore the latter forms the resistance medium to counterwork the ions locomotion by means of a small quantity of collisions between the ion and electron. The case is quite similar to the air to impose the atmospheric drag to cumber the movement of the stone and of the paper in the earth's aerosphere.

When the ion is much heavier than the electron in the solar wind, the heavy ion loses only a tiny kinetic energy in the course of collision, and will keep the same movement direction almost. If the mass of ion is small, the case will be quite other, the light ion may lose a lot of kinetic energy sometimes and change the movement direction after some collisions. In the result, the heavy ions keep going forward, while the light ions hobble and alter the directions frequently, in the case of the same average frequency of the ion-electron collisions.

The contrary motion between the ion and the electron will offer the resistance against the ions of the solar wind shift in the interplanetary magnetic field. And the resistance may be associated with the ion velocity, and then will limit the maximum velocity of the ion, especially in the interplanetary space far from the sun. For each kind of ion there is its own magnitude of maximum velocity in the solar wind.

As an inference, the ion and the electron will be accelerated continuingly on anywhere of the interplanetary magnetic field when the $B_j \neq 0$, even in the place quite far from the sun.

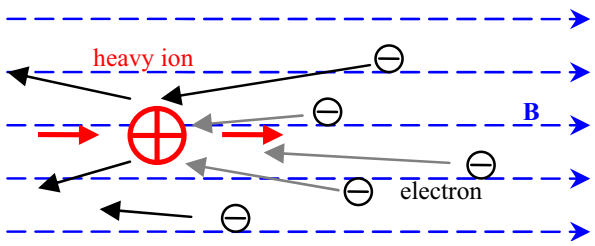

Figure 3: The heavy ions move along the lines of magnetic force, while the electrons along the opposite direction. The heavy ion only loses a tiny kinetic energy in the course of collision, and keeps the same movement direction almost.

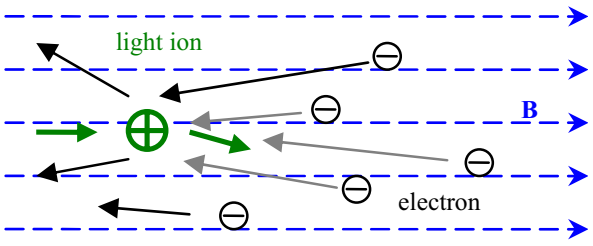

Figure 4: The interacting scheme of a light ion with the electrons in the interplanetary magnetic field. The light ions lose part of kinetic energy after some collisions, and then slow down and alter the directions frequently.

5. CONCLUSIONS

In the electromagnetic and gravitational fields, the field equations and the force can be rephrased with the algebra of octonions. The related conclusions include the field equation and the force, and their applications on the mechanism of heavy ion acceleration in the solar wind.

Making use of the algebra of octonions, we can deduce the field equation and the force definition, and find that one new electromagnetic force term can impose the charge particles to move along the lines of magnetic force. Consequently the ions in the solar wind will be accelerated along the lines of magnetic force, while the electrons move along the opposite direction. The electrons will be combined together to become the resistance medium to cumber the ions movements. The drag coming from the ion-electron collisions has an impact on the movements of the light ions obviously. Because of associating with the velocity, the drag force will limit the maximum velocity of ions of the solar wind in the interplanetary magnetic field.

It should be noted that the study for the acceleration mechanism of heavy ions in the electromagnetic and gravitational fields examined only one simple case in the octonion space. Despite its preliminary characteristics, this study can clearly indicate that the acceleration mechanism of heavy ions in the interplanetary magnetic field can be deduced from the force definition with the algebra of octonions, and obtain some inferences such as the continuingly acceleration of ions in the interplanetary space far away from the sun. For the future studies, the research will concentrate on only the different acceleration features of various kinds of heavy ions in the solar wind.

ACKNOWLEDGMENT

This project was supported partially by the National Natural Science Foundation of China under grant number 60677039.

REFERENCES

1. Tu, C., C. Zhou, E. Marsch, L. Xia, L. Zhao, J. Wang, and K. Wilhelm, "Solar wind origin in coronal funnels," *Science*, Vol. 308, No. 5721, 519–523, 2005.
2. Cranmer, S. R., "Coronal holes," *Living Reviews in Solar Physics*, Vol. 6, 3–65, 2009.
3. Maxwell, J. C., *A Treatise on Electricity and Magnetism*, Dover Publications Inc., New York, 1954.
4. Hamilton, W. R., *Elements of Quaternions*, Longmans, Green & Co., London, 1866.
5. Weng, Z.-H., "Wave equations in electromagnetic and gravitational fields," *PIERS Proceedings*, 971–975, Cambridge, USA, July 5–8, 2010.
6. Newton, I., *The Mathematical Principles of Natural Philosophy*, Dawsons of Pall Mall, London, 1968.
7. Cayley, A., *The Collected Mathematical Papers of Arthur Cayley*, The Cambridge University Press, Cambridge, 1889.

Magneto-optic and Electro-optic Effects in Electromagnetic Fields

Zi-Hua Weng
School of Physics and Mechanical & Electrical Engineering, Xiamen University, Xiamen 361005, China

Abstract— The magneto-optic effects and electro-optic effects are the essential optic effects, although their theoretical explanations are not unified in the classical electromagnetic theory. Describing with the algebra of octonions, the electromagnetic theory can derive the magneto-optic effects and the electro-optic effects from the same one force definition in the paper. The magneto-optic effect is deduced from the known force term, while the electro-optic effect is from the new force term in the octonion space. This description method is different to that in the quantum theory as well as the index ellipsoid approach. The study claims that the magneto-optic and electro-optic effects will be impacted by not only the refractive index and field energy but also the field strength and other physical quantities.

1. INTRODUCTION

The magneto-optic and electro-optic effects can be used to explain the birefringent phenomenons and the rotation of polarized plane in the optical medium. The magneto-optic effect includes the Larmor precession, Zeeman effect, and Faraday effect in the magnetic field. The Faraday effect is an interaction between the light and magnetic field in a medium. The electro-optic effect involves the Stark effect, Pockels effect [1], and Kerr effect in the electric field. The Pockels effect produces birefringence in an optical medium, and the birefringence is proportional to the electric field, whereas in the Kerr effect it is quadratic in the field.

At present two theoretical methods have been proposed to explain the above optic effects. The theoretical basis of the magneto-optic effects was developed by J. MacCullagh [2], G. B. Airy, J. C. Maxwell, and H. A. Rowlland [3] etc.. While the refringent index ellipsoid approach [4] was presented to describe the electro-optic effects. In the magnetic field, the Faraday effect corroborates that the light and electromagnetism are related. In the electric field, the Pockels effect can explain some birefringent phenomenons in the crystals and noncentrosymmetric media, including the lithium niobate, gallium arsenide, electric-field poled polymers, and glasses etc..

In the electromagnetic field and gravitational field described with the algebra of octonion [5], the magneto-optic effects, the electro-optic effects, and some new optic effects can be deduced from the same one force definition. Especially the electro-optic effects can be derived from the new force terms, including the Stark effect, Pockels effect, and Kerr effect etc..

2. FORCE IN ELECTROMAGNETIC AND GRAVITATIONAL FIELDS

The algebra of quaternions was first used by J. C. Maxwell [6] to describe the electromagnetic theory. At present the gravitational theory can be depicted with the quaternion also. But the quaternion space for gravitational field is independent to that for electromagnetic field [7], and these two quaternion spaces are perpendicular to each other. Two quaternion spaces can be combined together to become one octonion space, consequently the properties of gravitational field and electromagnetic field can be described with the algebra of octonions simultaneously.

The force terms of electromagnetic field and gravitational field can be defined from the torque and energy in the octonion space. This force definition covers all known force terms in the classical theories, including the inertial force, Newtonian gravitational force, Coulomb electric force, Lorentz magnetic force, gradient of energy, and the interacting force between the magnetic strength with magnetic moment, etc..

2.1. Linear Momentum

In the octonion space, we can define the linear momentum from the field source. In the quaternion space for the gravitational field, the basis vector is $\mathbb{E}_g = (1, \mathbf{i}_1, \mathbf{i}_2, \mathbf{i}_3)$, the radius vector is $\mathbb{R}_g = \Sigma(r_i\mathbf{i}_i)$, and the velocity is $\mathbb{V}_g = \Sigma(v_i\mathbf{i}_i)$. In that for the electromagnetic field, the basis vector is $\mathbb{E}_e = (\mathbf{I}_0, \mathbf{I}_1, \mathbf{I}_2, \mathbf{I}_3)$, the radius vector is $\mathbb{R}_e = \Sigma(R_i\mathbf{I}_i)$, and the velocity is $\mathbb{V}_e = \Sigma(V_i\mathbf{I}_i)$, with the relation $\mathbb{E}_e = \mathbb{E}_g \circ \mathbf{I}_0$. The $\mathbb{E}_e$ is independent of the $\mathbb{E}_g$, and that they can combine together to become the basis vector $\mathbb{E}$ of octonion space, that is $\mathbb{E} = (1, \mathbf{i}_1, \mathbf{i}_2, \mathbf{i}_3, \mathbf{I}_0, \mathbf{I}_1, \mathbf{I}_2, \mathbf{I}_3)$. $i = 0, 1, 2, 3$.

The octonion radius vector is $\mathbb{R} = \Sigma(r_i\mathbf{i}_i + k_{eg}R_i\mathbf{I}_i)$, and the velocity is $\mathbb{V} = \Sigma(v_i\mathbf{i}_i + k_{eg}V_i\mathbf{I}_i)$. Herein $r_0 = v_0 t$, t is the time; v_0 is the speed of gravitational intermediate boson, V_0 is the speed of electromagnetic intermediate boson; the $\circ$ denotes the octonion multiplication.

The gravitational potential $\mathbb{A}_g = \Sigma(a_i\mathbf{i}_i)$ combines with electromagnetic potential $\mathbb{A}_e = \Sigma(A_i\mathbf{I}_i)$ to become the octonion field potential $\mathbb{A} = \mathbb{A}_g + k_{eg}\mathbb{A}_e$. The field strength $\mathbb{B} = \Diamond \circ \mathbb{A} = \mathbb{B}_g + k_{eg}\mathbb{B}_e$ consists of the gravitational strength $\mathbb{B}_g = \Sigma(b_i\mathbf{i}_i)$ and electromagnetic strength $\mathbb{B}_e = \Sigma(B_i\mathbf{I}_i)$. The gravitational strength $\mathbb{B}_g$ includes two parts, $\mathbf{g}/v_0 = \partial_0\mathbf{a} + \nabla a_0$, and $\mathbf{b} = \nabla \times \mathbf{a}$. Meanwhile the electromagnetic strength $\mathbb{B}_e$ involves two components, $\mathbf{E}/v_0 = \partial_0\mathbf{A} + \nabla \circ \mathbf{A}_0$, and $\mathbf{B} = \nabla \times \mathbf{A}$. The gauge equations are $b_0 = 0$ and $B_0 = 0$. Herein k_{eg} is one coefficient for the dimensional homogeneity. The operator $\partial_i = \partial/\partial r_i$, $\nabla = \Sigma(\mathbf{i}_j\partial_j)$, and $\Diamond = \Sigma(\mathbf{i}_i\partial_i)$, with $j = 1, 2, 3$.

In the octonion space, the electric current density $\mathbb{S}_e = q\mathbb{V}_e$ is the source for the electromagnetic field, and the linear momentum density $\mathbb{S}_g = m\mathbb{V}_g$ for the gravitational field.

The octonion field source $\mathbb{S}$ satisfies

$$\mu\mathbb{S} = -(\mathbb{B}/v_0 + \Diamond)^* \circ \mathbb{B} = \mu_g\mathbb{S}_g + k_{eg}\mu_e\mathbb{S}_e - \mathbb{B}^* \circ \mathbb{B}/v_0, \tag{1}$$

where $\mathbb{B}^* \circ \mathbb{B}/\mu_g = \mathbb{B}_g^* \circ \mathbb{B}_g/\mu_g + \mathbb{B}_e^* \circ \mathbb{B}_e/\mu_e$; $k_{eg}^2 = \mu_g/\mu_e$; μ_g and μ_e are the gravitational constant and electromagnetic constant respectively; q is the electric charge density; m is the mass density; $*$ denotes the conjugate of octonion.

From the linear momentum density $\mathbb{P} = \mu\mathbb{S}/\mu_g = \Sigma(p_i\mathbf{i}_i) + \Sigma(P_i\mathbf{I}_i)$, we can define the octonion angular momentum density $\mathbb{L} = (\mathbb{R} + k_{rx}\mathbb{X}) \circ \mathbb{P} = \Sigma(l_i\mathbf{i}_i + L_i\mathbf{I}_i)$ in the electromagnetic field and gravitational field. Herein k_{rx} is a coefficient for the dimensional homogeneity; $\mathbf{l} = \Sigma(l_j\mathbf{i}_j)$, $\mathbf{L}_0 = L_0\mathbf{I}_0$, $\mathbf{L} = \Sigma(L_j\mathbf{I}_j)$; $\mathbb{X} = \Sigma(x_i\mathbf{i}_i) + k_{eg}\Sigma(X_i\mathbf{I}_i)$. The derivation of physics quantity $\mathbb{X}$ yields the gravitational potential and the electromagnetic potential simultaneously.

Table 1: The octonion multiplication table.

	1	$\mathbf{i}_1$	$\mathbf{i}_2$	$\mathbf{i}_3$	$\mathbf{I}_0$	$\mathbf{I}_1$	$\mathbf{I}_2$	$\mathbf{I}_3$
1	1	$\mathbf{i}_1$	$\mathbf{i}_2$	$\mathbf{i}_3$	$\mathbf{I}_0$	$\mathbf{I}_1$	$\mathbf{I}_2$	$\mathbf{I}_3$
$\mathbf{i}_1$	$\mathbf{i}_1$	-1	$\mathbf{i}_3$	$-\mathbf{i}_2$	$\mathbf{I}_1$	$-\mathbf{I}_0$	$-\mathbf{I}_3$	$\mathbf{I}_2$
$\mathbf{i}_2$	$\mathbf{i}_2$	$-\mathbf{i}_3$	-1	$\mathbf{i}_1$	$\mathbf{I}_2$	$\mathbf{I}_3$	$-\mathbf{I}_0$	$-\mathbf{I}_1$
$\mathbf{i}_3$	$\mathbf{i}_3$	$\mathbf{i}_2$	$-\mathbf{i}_1$	-1	$\mathbf{I}_3$	$-\mathbf{I}_2$	$\mathbf{I}_1$	$-\mathbf{I}_0$
$\mathbf{I}_0$	$\mathbf{I}_0$	$-\mathbf{I}_1$	$-\mathbf{I}_2$	$-\mathbf{I}_3$	-1	$\mathbf{i}_1$	$\mathbf{i}_2$	$\mathbf{i}_3$
$\mathbf{I}_1$	$\mathbf{I}_1$	$\mathbf{I}_0$	$-\mathbf{I}_3$	$\mathbf{I}_2$	$-\mathbf{i}_1$	-1	$-\mathbf{i}_3$	$\mathbf{i}_2$
$\mathbf{I}_2$	$\mathbf{I}_2$	$\mathbf{I}_3$	$\mathbf{I}_0$	$-\mathbf{I}_1$	$-\mathbf{i}_2$	$\mathbf{i}_3$	-1	$-\mathbf{i}_1$
$\mathbf{I}_3$	$\mathbf{I}_3$	$-\mathbf{I}_2$	$\mathbf{I}_1$	$\mathbf{I}_0$	$-\mathbf{i}_3$	$-\mathbf{i}_2$	$\mathbf{i}_1$	-1

2.2. Forces

In the case for coexistence of electromagnetic field and gravitational field, the octonion energy density $\mathbb{W} = v_0(\mathbb{B}/v_0 + \Diamond) \circ \mathbb{L}$ is defined from the octonion angular momentum density $\mathbb{L}$ and octonion field strength $\mathbb{B}$. Herein $\mathbb{W} = \Sigma(w_i\mathbf{i}_i) + \Sigma(W_i\mathbf{I}_i)$; the $-w_0/2$ is the energy density, the $\mathbf{w}/2 = \Sigma(w_j\mathbf{i}_j)/2$ is the torque density.

In the octonion space, the octonion power density $\mathbb{N}$ is defined as follows,

$$\mathbb{N} = v_0(\mathbb{B}/v_0 + \Diamond)^* \circ \mathbb{W}, \tag{2}$$

where $\mathbb{N} = \Sigma(n_i\mathbf{i}_i) + \Sigma(N_i\mathbf{I}_i)$. The $f_0 = -n_0/(2v_0)$ is the power density, and the $\mathbf{f} = -\mathbf{n}/(2v_0)$ is the force density, with the vectorial part $\mathbf{n} = \Sigma(n_j\mathbf{i}_j)$ in the $\mathbb{E}_g$. The other two vectorial parts $\mathbf{N}_0 = N_0\mathbf{I}_0$ and $\mathbf{N} = \Sigma(N_j\mathbf{I}_j)$ both are in the $\mathbb{E}_e$, and may not be detected at present.

The force density $\mathbf{f}$ in the gravitational and electromagnetic fields is,

$$\begin{aligned} -2\mathbf{f} = {} & \nabla^* w_0 + \partial_0\mathbf{w} + (\mathbf{g}/v_0 + \mathbf{b})^* \times \mathbf{w}/v_0 + \nabla^* \times \mathbf{w} + w_0(\mathbf{g}/v_0 + \mathbf{b})^*/v_0 \\ & + k_{eg}(\mathbf{E}/v_0 + \mathbf{B})^* \times \mathbf{W}/v_0 + k_{eg}(\mathbf{E}/v_0 + \mathbf{B})^* \circ \mathbf{W}_0/v_0, \end{aligned} \tag{3}$$

where the force density $\mathbf{f}$ includes that of the inertial force, gravity, Lorentz force, gradient of energy, and interacting force between dipole moment with magnetic strength etc.. This force definition is much more complicated than that in the classical field theories, and encompasses some new force terms about the gradient of energy etc..

Table 2: The multiplication of the physical quantity in the octonion space.

definitions	*meanings*
$\nabla \cdot \mathbf{p}$	$-(\partial_1 p_1 + \partial_2 p_2 + \partial_3 p_3)$
$\nabla \times \mathbf{p}$	$\mathbf{i}_1(\partial_2 p_3 - \partial_3 p_2) + \mathbf{i}_2(\partial_3 p_1 - \partial_1 p_3) + \mathbf{i}_3(\partial_1 p_2 - \partial_2 p_1)$
∇p_0	$\mathbf{i}_1 \partial_1 p_0 + \mathbf{i}_2 \partial_2 p_0 + \mathbf{i}_3 \partial_3 p_0$
$\partial_0 \mathbf{p}$	$\mathbf{i}_1 \partial_0 p_1 + \mathbf{i}_2 \partial_0 p_2 + \mathbf{i}_3 \partial_0 p_3$
$\nabla \cdot \mathbf{P}$	$-(\partial_1 P_1 + \partial_2 P_2 + \partial_3 P_3)\mathbf{I}_0$
$\nabla \times \mathbf{P}$	$-\mathbf{I}_1(\partial_2 P_3 - \partial_3 P_2) - \mathbf{I}_2(\partial_3 P_1 - \partial_1 P_3) - \mathbf{I}_3(\partial_1 P_2 - \partial_2 P_1)$
$\nabla \circ \mathbf{P}_0$	$\mathbf{I}_1 \partial_1 P_0 + \mathbf{I}_2 \partial_2 P_0 + \mathbf{I}_3 \partial_3 P_0$
$\partial_0 \mathbf{P}$	$\mathbf{I}_1 \partial_0 P_1 + \mathbf{I}_2 \partial_0 P_2 + \mathbf{I}_3 \partial_0 P_3$

3. FARADAY MAGNETO-OPTIC EFFECT

In the gravitational field and electromagnetic field, the definition of the force density can draw out Rowlland's equation for the magneto-optic effect. Further the Rowlland's equation can be used to explain the Faraday effect in the glass, crystal, and liquid etc..

In case the physical system is on the torque steady state, the torque density of the charged particle, $\mathbf{w}$, will be a constant vector in the magnetic field, that is, $(\partial_0 \mathbf{w} + \nabla^* \times \mathbf{w}) = 0$. When $(\mathbf{g}/v_0 + \mathbf{b}) = 0$ and $x_0 = 0$, Eq. (3) will be reduced to

$$-2\mathbf{f} \approx \nabla^* w_0 \approx k_{eg}(\nabla^* \circ \mathbf{A}_0) \circ \mathbf{P}_0 + k_{eg}\, \mathbf{P} \times (\nabla^* \times \mathbf{A}). \tag{4}$$

When $\mathbf{f} = 0$, the above can be reduced further as follows,

$$\partial_t \mathbf{E} \circ \mathbf{I}_0 = \partial_t^2 \mathbf{A} \circ \mathbf{I}_0 + \sigma \partial_t (\partial_t \mathbf{D} \times \mathbf{H}^*), \tag{5}$$

where $\mathbf{H} = \mathbf{B}/\mu_e$, $\mathbf{D} = \varepsilon \mathbf{E}$, $\partial_t = \partial/\partial t$, $\sigma = (qV_0)^{-1}$. For a tiny volume-distribution region of the optical medium, $\mathbf{H}$, $\mathbf{D}$, and σ are all mean values.

Considering the following relation obtained from Maxwell equation,

$$\partial_t \mathbf{E} = v_0^2 \nabla \times \mathbf{B} = -v_0^2 \nabla^2 \mathbf{A},$$

Eq. (5) can be rewritten as

$$v_0^2 \nabla^2 \mathbf{A} \circ \mathbf{I}_0 = \partial_t^2 \mathbf{A} \circ \mathbf{I}_0 + \varepsilon\sigma\partial_t \left\{(-v_0^2 \nabla^2 \mathbf{A}) \times \mathbf{H}^*\right\}. \tag{6}$$

Setting the linearly polarized light transmits along the z-axis in the coordinate system (r_0, r_1, r_2, r_3), the above can be reduced to Rowlland's equation for magneto-optic effect,

$$v_0^2 \partial_3^2 A_1 - \partial_t^2 A_1 + M H_3 \partial_t (\partial_3^2 A_2) = 0, \quad v_0^2 \partial_3^2 A_2 - \partial_t^2 A_2 - M H_3 \partial_t (\partial_3^2 A_1) = 0,$$

where H_3 is the z-axis component of $\mathbf{H}$, and $M = -v_0^2 \varepsilon \sigma$.

According to the form of above equations, we can suppose that one solution is

$$A_1 = A\cos(\alpha t - \beta r_3)\cos(\gamma t), \quad A_2 = A\cos(\alpha t - \beta r_3)\sin(\gamma t), \tag{7}$$

and making the substitution we find

$$v^2 = (\alpha/\beta)^2 = v_0^2 + M H_3 (1 - M\lambda^2 H_3 / 8\pi n^2), \tag{8}$$

where v and v_0 are the speed of light in the medium and the vacuum respectively. α is the angular frequency of the transmitted light. γ is the rotation angular velocity of linearly polarized light transmitted along the optical axis. β is the reciprocal of the speed of light.

The total angle of rotation of the linearly polarized light will evidently be, $\theta = \gamma D/v$. Combining with the dispersion formula, $d\beta/d\alpha = (n/v)\{n - \lambda(dn/d\lambda)\}$, the rotation angle is,

$$\theta = M'(n/\lambda_0)^2 \left\{n - \lambda(dn/d\lambda)\right\} H_3 D, \tag{9}$$

where M' is a constant coefficient. n is the refractive index, λ is the wavelength, and D is the length of substance. $\beta\lambda_0 = 2\pi n$, $\alpha\lambda_0 = 2\pi v$, $\lambda = \lambda_0/n$, and $v = v_0/n$. λ_0 is the wavelength in the vacuum.

The inference is accordant to the existing results from M. E. Verdet, M. Faraday, J. B. Biot, J. MacCullagh, G. B. Airy, H. A. Rowland, and J. C. Maxwell etc.. When the **A** and **H** in Eq. (6) are both 3-dimensional quantities, the obtained rotation angle of linearly polarized light will be more complex than the above. In the magnetic field, the first-order Faraday effect is linear in the applied magnetic field, while the second-order Faraday effect is quadratic in the magnetic field. Taking account of the contribution from the force term $(\partial_0\mathbf{w} + \nabla^* \times \mathbf{w})$ in the force definition Eq. (3), we can deal with the second-order Faraday effect.

Table 3: The optic effects and related equations of electromagnetic field.

optic effects	*equations*
Faraday effect	$0 = \nabla^* w_0$
magneto-optic Kerr effect	$0 = \nabla^* w_0$
Voigt and Cotton-Mouton effects	$0 = \nabla^* w_0 + k_{eg}\mathbf{B}^* \times \mathbf{W}/v_0$
self-focusing in the magnetic field	$0 = \nabla^* w_0$
Stark effect	$0 = \partial_0\mathbf{w} + \nabla^* \times \mathbf{w} + k_{eg}(\mathbf{E}/v_0)^* \times \mathbf{W}/v_0$
Pockels effect	$0 = \nabla^* w_0 + \partial_0\mathbf{w} + \nabla^* \times \mathbf{w}$
Kerr effect	$0 = \nabla^* w_0 + \partial_0\mathbf{w} + \nabla^* \times \mathbf{w} + k_{eg}(\mathbf{E}/v_0)^* \times \mathbf{W}/v_0$
self-focusing in the electric field	$0 = \nabla^* w_0 + \partial_0\mathbf{w} + \nabla^* \times \mathbf{w}$

4. POCKELS ELECTRO-OPTIC EFFECT

In the gravitational field and electromagnetic field, the definition of force density can conclude some equations, which can be used to explain the Pockels electro-optic effect in the glass, crystal, and liquid etc.. The Pockels electro-optic effect was discovered in 1893 to cause the refractive index to vary approximately in proportion to the electric strength.

In case the physical system is on one general case, and has to be considered the effect of the **w** besides of the w_0. When $(\mathbf{g}/v_0 + \mathbf{b}) = 0$ and $x_0 = 0$, Eq. (3) will be reduced to

$$-2\mathbf{f} \approx \nabla^* w_0 + \partial_0\mathbf{w} + \nabla^* \times \mathbf{w} \approx k_{eg}(\nabla^* \circ \mathbf{X}_0) \circ \mathbf{Z}_0 + k_{eg}(\partial_0\mathbf{X}_0 + \nabla \circ \mathbf{X}_0) \times \mathbf{Z}, \tag{10}$$

where $\mathbf{Z}_0 = \partial_0\mathbf{P}_0 + \nabla \cdot \mathbf{P}$, and $\mathbf{Z} = \partial_0\mathbf{P} + \nabla \circ \mathbf{P}_0 + \nabla \times \mathbf{P}$.

When $\mathbf{f} = 0$, the above can be reduced further as follows,

$$\partial_t\mathbf{A}_E \circ \mathbf{I}_0 = \partial_t^2\mathbf{X} \circ \mathbf{I}_0 + \sigma\partial_t(\mathbf{A}_E \times \mathbf{Z}), \tag{11}$$

where $\partial_t = \partial/\partial t$, $\sigma = v_0/Z_0$, $\mathbf{A}_E = \partial_0\mathbf{X} + \nabla \circ \mathbf{X}_0$, $\mathbf{A}_B = \nabla \times \mathbf{X}$, $\mathbf{Z}_0 = Z_0\mathbf{I}_0$. For a tiny volume-distribution of the optical medium, **P**, $\mathbf{A}_E$, $\mathbf{A}_B$, and σ are all mean values.

Considering the $\mathbb{A} = \Diamond \circ \mathbb{X}$ and $\mathbb{X} = \Diamond^* \circ \mathbb{Y}$, with $\mathbb{Y}$ being an octonion, we get

$$\partial_t\mathbf{A}_E = v_0^2\nabla \times \mathbf{A}_B = -v_0^2\nabla^2\mathbf{X},$$

Eq. (11) can be rewritten as

$$v_0^2\nabla^2\mathbf{X} \circ \mathbf{I}_0 = \partial_t^2\mathbf{X} \circ \mathbf{I}_0 + \sigma\partial_t\left\{(-v_0^2\nabla^2\mathbf{X}) \times \mathbf{Z}\right\}. \tag{12}$$

In the coordinate system (r_0, r_1, r_2, r_3), setting the linearly polarized light transmit along the z-axis, which is the optical axis in the longitudinal Pockels effect, the above can be reduced to,

$$v_0^2\partial_3^2 X_1 - \partial_t^2 X_1 + MZ_3\partial_t(\partial_3^2 X_2) = 0, \quad v_0^2\partial_3^2 X_2 - \partial_t^2 X_2 - MZ_3\partial_t(\partial_3^2 X_1) = 0,$$

where Z_3 is the z-axis component of **Z**, $M = -v_0^2\sigma$.

According to the form of above equations, we can suppose that one solution is

$$X_1 = X\cos(\alpha t - \beta r_3)\cos(\gamma t), \quad X_2 = X\cos(\alpha t - \beta r_3)\sin(\gamma t), \tag{13}$$

and making the substitution we find

$$v^2 = (\alpha/\beta)^2 = v_0^2 + MZ_3\left(1 - M\lambda^2 Z_3/8\pi n^2\right), \tag{14}$$

where v is the speed of light in the medium. $\beta\lambda = 2\pi n$, and $\alpha\lambda = 2\pi v$.

Therefore, the total rotation angle of the linearly polarized light will evidently be, $\theta = \gamma D/v$. Combining with the dispersion formula, $d\beta/d\alpha = (n/v)\{n - \lambda(dn/d\lambda)\}$, the rotation angle will be reduced to, $\theta = M'(n/\lambda_0)^2\{n - \lambda(dn/d\lambda)\}Z_3 D$. Further considering the Ohm's law $\mathbf{J} = \sigma'\mathbf{E}$ and the condition formula $\mathbf{Z} = k'\mathbf{J}$, we obtain the result $Z_3 \approx k'(\partial_t \sigma')E_3$ when $\partial_t E_3 \approx 0$. And the angle θ can be written as follows

$$\theta = M''(n/\lambda_0)^2 \{n - \lambda(dn/d\lambda)\} E_3 D,$$

where M'', k', and σ' are coefficients. E_3 is the z-axis component of $\mathbf{E}$. $\mathbf{J}$ is the current density. M' is a constant coefficient. n is the refractive index, λ is the wavelength, and D is the length of substance. $\beta\lambda_0 = 2\pi n$, $\alpha\lambda_0 = 2\pi v$, $\lambda = \lambda_0/n$, and $v = v_0/n$. λ_0 and v_0 are the wavelength and the speed of light in the vacuum respectively.

This inference is accordant to the existing results from F. C. A. Pockels etc.. The above can be considered as one kind of theoretical explanations, besides the index ellipsoid theory as well as the quantum theory. And that the angle θ can be affected by some force terms in the electric field. When $\mathbf{X}$ and $\mathbf{Z}$ in Eq. (12) are both 3-dimensional quantities, the obtained rotation angle of linearly polarized light will be more complex than the above. In the electric field, the Pockels effect is linear in the applied electric field, while the Kerr electro-optic effect is quadratic in the electric field. Taking account of the contribution of force terms regarding $k_{eg}(\mathbf{E}/v_0)^* \times \mathbf{W}$ in Eq. (3), we may deal with the Kerr electro-optic effect.

5. CONCLUSIONS

In the electromagnetic field and gravitational field described with the algebra of octonions, the magneto-optic effect and electro-optic effect are derived from the same one force definition formula. In the octonion space, the Faraday effect is from the term $\nabla^* w_0$, while the Pockels effect from the terms $(\nabla^* w_0 + \partial_0 \mathbf{w} + \nabla^* \times \mathbf{w})$. And that the rotation angle is affected by other force terms.

The theoretical explanation in this paper is different to the classical index ellipsoid approach as well as the quantum theory. This work indicates that the optic effects will be impacted by not only the refractive index and field energy but also the field strength and other factors.

It should be noted that the study for the optic effects impacted by the force terms examined only some simple cases under the octonion force definition deducing from the torque and energy. Despite its preliminary character, this study can clearly indicate that the magneto-optic effect and electro-optic effect both can be derived from the same one force definition in the electromagnetic field and gravitational field. For the future studies, the research will focus on the theoretical explanations about the birefringent phenomenon in the optical medium as well as the experimental validations of the self-focusing in the electromagnetic fields.

ACKNOWLEDGMENT

This project was supported partially by the National Natural Science Foundation of China under grant number 60677039.

REFERENCES

1. Rao, K. V. and T. S. Narasimhamurty, "Pockels' effect in α-quartz," *Journal of Modern Optics*, Vol. 19, No. 4, 319–325, 1972.
2. MacCullagh, J. H., *The Collected Works of James MacCullagh*, J. H. Jellett and S. Haughton, ed., Longmans, Green & Co., London, 1880.
3. Rowlland, H. A., "On the new theory of magnetic attractions, and the magnetic rotation of polarized light," *Philosophical Magazine*, Series 5, Vol. 11, No. 68, 254–261, 1881.
4. Barrett, T. W., "Changes in the refractive index ellipsoid isotropies, symmetric anisotropies, and depolarization ratios of potassium hyaluronate solutions as a function of pH," *Biopolymers*, Vol. 18, No. 2, 351–358, 1979.
5. Cayley, A., *The Collected Mathematical Papers of Arthur Cayley*, The Cambridge University Press, Cambridge, 1889.
6. Maxwell, J. C., *A Treatise on Electricity and Magnetism*, Dover Publications Inc., New York, 1954.
7. Weng, Z.-H., "Electromagnetic forces on charged particles," *PIERS Proceedings*, 361–363, Moscow, Russia, August 18–21, 2009.

Test Method for Evaluating Asphalt-covered Concrete Bridge Decks Using Ground Penetrating Radar

J. Rhazi
Department of Civil Engineering, Université de Sherbrooke
Sherbrooke (Québec), J1K 2R1, Canada

Abstract— This paper presents the synthesis of an experimental investigation concerning concrete corrosivity and delamination effects on electromagnetic wave propagation in reinforced concrete. It demonstrates that the data analysis procedure, proposed in the ASTM D6087 "Standard Test Method for Evaluating Asphalt-Covered Concrete Bridge Decks Using Ground Penetrating Radar (GPR)", is not always valid. A novel methodology of GPR data processing that allows the detection of areas of high probability of rebar corrosion in concrete is presented.

1. INTRODUCTION

In North America, corrosion of steel rebar is the greatest factor in limiting the life expectancy of reinforced concrete bridge decks [1]. The corrosion products (rust) cause the creation of cracks (delamination) at or just above the level of the reinforcement and this affects the structural capacity of theses structures.

The use of ground-penetrating radar (GPR) technique as a non-destructive testing tool for assessing the condition of reinforced concrete bridge decks has become a topic of great interest since the 1970's [2–5]. In 1997, the Amercian Society for Testing and Material (ASTM) published the first standard on this topic: ASTM-D6087 "Standard Test Method for Evaluating Asphalt-Covered Concrete Bridge Decks Using Ground Penetrating Radar (GPR)".

There are two different GPR data processing methodologies described in the latest version of the ASTM-D6087 (08). Both methods employ reflection amplitudes. The fist one is relative to the detection of delamination (concrete deterioration), and the second one relates to the assessment of rebar corrosion (rebar deterioration).

In 1999, a research project was undertaken by the research group on NDT and instrumentation (Université de Sherbrooke, Canada) concerning the evaluation of reinforced concrete bridge decks by the GPR technique. Up to now, GPR surveys have been carried out on approximately 30 bridge decks [6]. The results of these surveys were compared with the result of the half-cell potential (HCP) tests and core data. The main results of this project are discussed in the following sections.

2. DETECTION OF DELAMINATION

The first data processing method in the ASTM D6097, the attenuation technique, predicts the presence of delamination at or above the level of the top layer of reinforcing bar on the basis of the following condition: $Vb < 0.385\,Vbs$, where Vb is reflection amplitudes from the bridge deck bottom, each scan, Vbs is maximum reflection amplitudes from the bridge deck bottom (all scans), and 0.385 is a constant derived from research data.

Figure 1 shows a GPR profile collected on a reinforced concrete bridge deck. The horizontal axis represents the distance along the deck (m), and the vertical axis is depth (cm). This profile indicates that the reflection amplitude from the bridge deck bottom is almost zero between 1–4 m, around 5 m and around 7 m. According to ASTM D6097, the concrete is delaminated in these areas. The core from the position 5, 6 m (Figure 1) shows effectively a delamination in concrete.

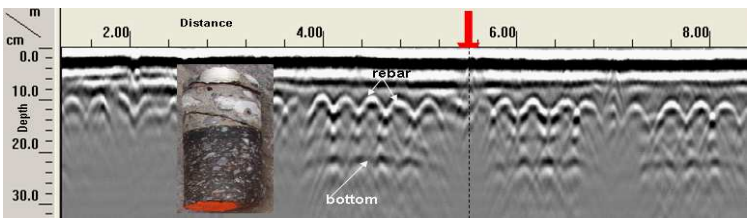

Figure 1: GPR profile showing delamination in concrete.

Figure 2 is another GPR profile which shows that the reflection amplitude from the bottom between 7 and 9 m is similar to that observed elsewhere in this profile. However, hammer sounding of the deck according to the ASTM D4580 "Standard Practice for Measuring Delaminations in Concrete Bridge Decks by Sounding" showed that the concrete is delaminated in this area. This indicates that the ASTM criterion for delamination detection is not always valid.

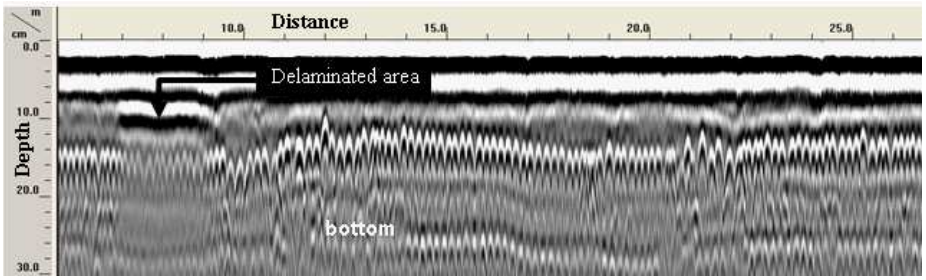

Figure 2: GPR profile showing that delamination has little effect on the reflection amplitude from the bottom.

3. DETECTION OF CORROSION ACTIVITY

The second data processing method described in the ASTM D6087 standard, the top reinforcing reflection technique, was added to the standard in 2005. It utilizes the relative reflection amplitudes from the top layer of reinforcing to assess rebar corrosion. In this method, rebar corrosion is active if: $A < A_{\max} - B\,\mathrm{dB}$, where A is reflection amplitudes from the top layer of reinforcing, each scan (in dB), $A_{\max}$ is maximum reflection amplitudes from the top layer of reinforcing (in dB) and B is a factor between 6 to 8 dB derived from other deterioration assessment techniques such as bridge deck bottom inspection and core data.

Figure 3 illustrates the limitation of this approach. It shows a GPR profile and the half-cell potential (HCP) data collected at the same location on a bridge deck. According to the ASTM C876 "Standard Test Method for Half-Cell Potentials of Uncoated Reinforcing Steel in Concrete", the corrosion probability of rebar is greater than 90% if the HCP value is lower than -350 mV and the corrosion probability is lower than 10% if the HCP value is greater than -200 mV.

Figure 3 shows that the HCP values are, in general, lower that -350 mV, except in areas around 10 m and 24 m. Between 12 m and 22 m, the probability of corrosion is high and the reflection amplitude at the top rebar is effectively low. However, between 4 and 9 m, the probability of rebar corrosion is also high but the reflection amplitude at the top rebar is similar to that observed at about 10 m where the corrosion probability is low (potential = -116 mV). This result show that the ASTM approach concerning the evaluation of rebars corrosion is also not always valid.

4. THE PROPOSED APPROACH

Our experimental work shows that the attenuation of radar waves in reinforced concrete is low in areas where the HPC value is high (> -200 mV), and that this attenuation is high in areas where the HPC value is low (< -350 mV). Figure 3 shows this correlation which was observed on most of the bridge decks investigated. It was found that the reflection amplitudes from the bridge deck bottom give more reliable information on the corrosion activity than the reflection amplitudes from the top layer of reinforcing.

The explanation of the correlation between the HCP data and radar wave attenuation can be based on the electrical resistivity of the concrete.

Figure 4 gives the variation of the HCP data with electrical resistivity of concrete. This correlation was obtained upon more than 400 measurements on structures in service. Electrical resistivity measurements were done at the same locations as the HCP measurements with a Wenner probe [7]. The dispersion of the data is notable because electrical resistivity of concrete varies in a large manner in concrete. However, globally, electrical resistivity values increase when the HCP values increase, which is in agreement with previously published results on this subject [7]. The approximation of the correlation by an exponential curve is also presented in Figure 4. It can be shown that the HPC value of -350 mV corresponds approximately to the resistivity value of 100 Ω·m.

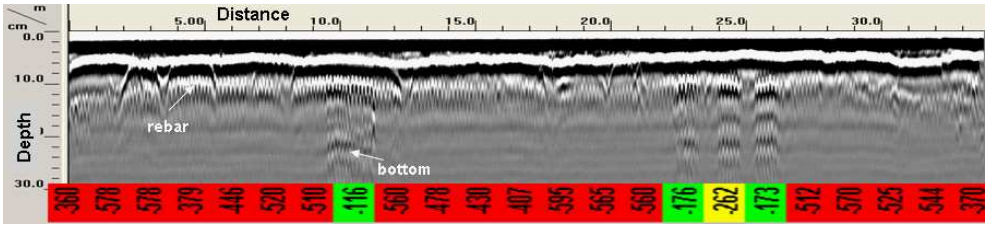

Figure 3: Variation of rebar reflection amplitude as a function of corrosion activity.

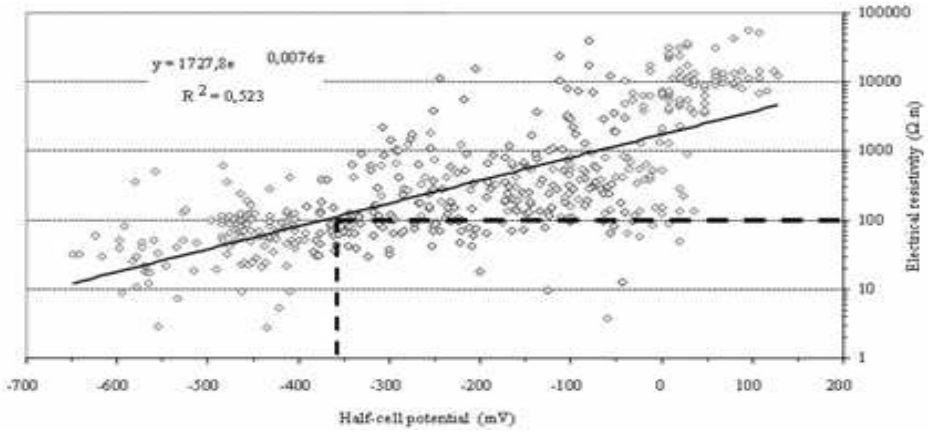

Figure 4: Experimental correlation between the HCP and electrical resistivity of concrete.

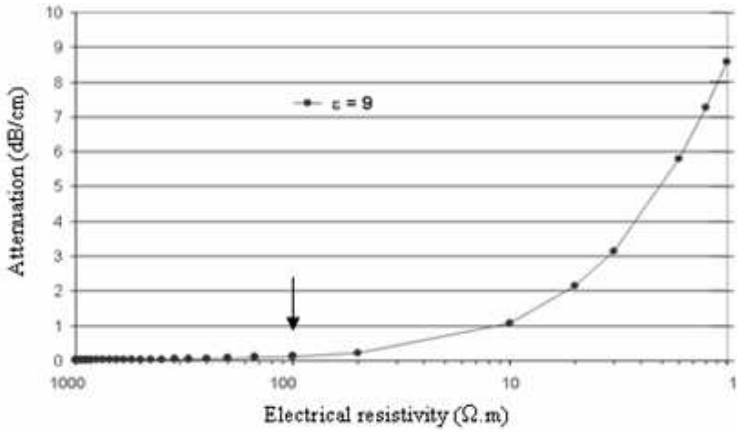

Figure 5: Radar wave attenuation vs electrical resistivity of concrete.

Hence, areas of reinforced concrete bridge decks with high corrosion probability of rebar (HCP $< -350\,\mathrm{mV}$) have electrical resistivity lower that $100\,\Omega{\cdot}\mathrm{m}$.

Figure 5 gives the correlation between the attenuation of radar waves in concrete and the electrical resistivity of concrete. This correlation is obtained from the equation of electromagnetic wave propagation in concrete with a relative permittivity (ε'_r) of 9 and for a wave frequency of 1 GHz. As shown in this figure, the attenuation is negligible for high electrical resistivity and its effect on wave propagation becomes, at a resistivity value, lower than $100\,\Omega{\cdot}\mathrm{m}$.

5. CONCLUSION

In the light of the results presented in this paper, it appears possible to characterise the corrosion activity in reinforced concrete bridge decks by means of electromagnetic waves attenuation in the whole thickness of concrete deck. This approach appears more reliable than that relating to rebar reflection amplitude.

ACKNOWLEDGMENT

This research was supported by the Ministry of Transportation of Québec and the Natural Sciences and Engineering Research Council of Canada.

REFERENCES

1. Berke, N. S. and M. C. Hicks, "Electrochemical methods of determining the corrosivity of steel in concrete," *25th Anniversary Symposium Committee G1, ASTM*, ASTM STP 1000, 425–440, Philadelphia, 1990.
2. Alongi, A. V., "Radar examination of condition of two interstate highway bridge decks," *Niagara Falls*, Penetradar Corporation, New York, 1973.
3. Cantor, T. and C. Kneeter, "Radar as applied to evaluation of bride decks," *Transportation Research Record*, No. 853, Transportation Research Board, Washington, D.C., 1982.
4. Chung, T., C. R. Carter, D. G. Manning, and F. B. Holt, "Signature analysis of radar waveform taken on asphalt-covered bridge decks," ME-84-01, Ontario Ministry of Transp. and Communications, Res. and Dev. Branch, Ontario, Canada, 1984.
5. Manning, D. G. and F. B. Holt, "Detecting delamination in concrete bridge decks," *Concrete International*, Vol. 2, No. 11, 34–41, 1980.
6. Rhazi, J., "Comparative study of NDT techniques applied to concrete bridge decks," Report No. GR-99-01-01, Department of Civil Engineering, Université de Sherbrooke, 1999 (in French).
7. Gowers, K. R. ans S. G. Millard, "Measurement of concrete resistivity for assessment of corrosion severity of steel using wenner technique," *ACI Materials Journal*, Vol. 96, No. 5, 536–541, 1999.

Characterization of the GPR Surface Waves for Civil Engineering Applications

B. Filali[1], **J. Rhazi**[2], **F. Boone**[3], **and G. Ballivy**[2]

[1]Civil Engineering and Electrical Engineering Departments, Sherbrooke University, Qc, Canada
[2]Civil Engineering Department, Sherbrooke University, Qc, Canada
[3]Electrical Engineering Department, Sherbrooke University, Qc, Canada

Abstract— The electromagnetic (EM) surface wave is defined as a part of the volume wave propagating along the interface between to different mediums. This kind of EM waves may be used to assess geological or construction mediums. They are especially needed when no echoes are detected from nearly bottom interfaces. In this purpose, we proceed to the characterization of the surface wave by modeling electromagnetic waves centred at 400 MHz frequency. It is visualised in the time domain as a trace on a radargramme, so its travel time and attenuation are obtained from the isolated wave impulse. From different travel times in different mediums, the depth of the propagation layer is deduced approximately and shown to be sufficient for non destructive testing in civil engineering. In addition, we observed that this layer depth increases with distance from the source. This propagation layer depth values are found same as that calculated by attenuation, where we obtained close values for the entire frequency spectrum. The frequency variation of the propagation depth is also observed and explained.

1. INTRODUCTION

The ground penetrating radar (GPR) is a commonly used technic for non destructive testing (NDT) in civil engineering [1]. Many applications exist to assess materials by GPR technics in geophysics [2] and civil engineering [3]. Radar waves are widely affected by concrete properties, giving us many information about this material state [4]. As a GPR assessment technic, the use of the radar surface wave (RSW) is shown to be useful for the surface layer concrete [3]. Nevertheless, the surface propagation layer of this wave kind is not determined, so the depth of the probed layer is unknown. We cite an important research work evaluating this depth at 20 cm minimum for frequencies between 100 MHz and 450 MHz [5]. Accurate values and behavior of this propagation layer depth are found in this purpose by calculus based on an explained approach. The calculation is done on simulation data of models with the finite elements method (FEM) using the COMSOL software.

2. GPR SURFACE WAVE DEFINITION

The radar surface wave (RSW) are always generated at the interface between to mediums with different refractive indexes n. This wave is defined as a surface propagating part of the volume wave in the medium with higher n. It can be detected at contact with the surface or closely over it. Physical studies of this wave kind is made in several works since late fifties [2, 6–8]. In these studies, we can find the propagation expression of the RSW including its amplitude variation during propagation and its travel speed. A wavefronts model is illustrated to explain this wave propagation.

3. CHARACTERIZATION OF THE RSW IN THE TIME DOMAIN BY FEM MODELING

In this section, antenna radiation is simulated in a bi-dimensional model in order to calculate the depth of the RSW propagation layer. In this model, an interface is required between two mediums simulating air and concrete, so the RSW propagates on the concrete surface. RSW propagation speed is related to the global refraction index n of the overall layer under the surface. So imposing an in-depth gradient on the concrete refraction index makes possible the calculation of the RSW propagation depth.

The in-depth gradient of n is defined as a linear variation from $n = \sqrt{6}$ at the surface to $n = 3$ at 10 cm depth (from a dried state of concrete to its common state [4]). The propagation depth of RSW can be deduced from the calculation of the overall propagation index probed by the wave speed. In fact, the propagation speed gives a refraction index value higher than that purely on the surface.

The depth probed by the RSW propagation is considered equivalent to that of a TDR probe [5]. In this work, to deduce the overall layer depth, the RSW propagation is modeled as a set of travels. These travels are equivalents to reflections on an infinitely thin multiple layers, at different depthes y under the surface. Superposition of theses reflections to the pure surface wave affects the overall travel time by making it longer due to the higher n at deeper thin pseudo layers. This superposition gives one single travel equivalent to reflection on a layer situated at P_n depth. We have an overall wave travel along a total distance $D = \sqrt{P_n^2 + x^2}$, where x is the surface travel distance. The depth P_n is considered equals about half that of the total propagation layer P_{RSW}.

So to get the propagation depth, a mean formula based on the CRIM model (mixing relationship [9]) can be used. The geometrical consideration of a pseudo reflection model lead to the following expression.

$$T = \frac{n_{RSW} D}{c} = \int_0^{P_n} \frac{Dn(y)}{cP_n} dy \tag{1}$$

where T is the taken time to travel along D. P_n is the equivalent overall reflection depth, n_{RSW} is the mean refraction index probed during the propagation, $n(y) = \sqrt{6} + 10(3 - \sqrt{6})y$ is the real refraction index as expressed in vertical positions y, and c is the speed of light.

The function $n(y)$ being linear, we have an easy to solve integral in (1). We can obtain the following formula expressing the propagation depth:

$$P_n = 0.2 \frac{n_{RSW} - \sqrt{6}}{3 - \sqrt{6}} \tag{2}$$

The RSW speed is calculated from its trace curve tangent (curve of distance versus its arrival time). From the model, we can extract the radiation signal on the surface at 10 cm distance from the antenna up to 1 m in steps of 1 cm. The RSW picks are easily identified on each radar signal. In the following figure the RSW trace is represented for two comparative cases: concrete with constant refraction index, and an other with refraction index as function $n(y)$.

In the Figure 1(a), we show the RSW trace for the two mediums: the homogenous one, and the n-gradient one. For each trace curve, the tangent at any point equals the punctual wave speed. As a comparison, we can see that the wave speed (tangent) of the n-gradient medium is less than that of the homogenous medium. However, this tangent becomes slightly close to that of the homogenous medium at the higher distance from the antenna (the two curves become nearly parallel). This means that the probed refraction index increases with the distance, and doesn't equal the surface n value everywhere.

This curve characteristic leads to the conclusion that the propagation layer is deeper when increasing the distance. Moreover, the pseudo reflection depth P_n is calculated and shown in the Figure 1(b). Its value equals about 10 cm at 20 cm distance distance from antenna , increasing to nearly 20 cm at 80 cm distance. The depth value uncertainty is due to that of the travel time value equals 4.4 ps. From the relationship (2), we found $\Delta P_n = 1$ cm.

The RSW gives an interesting characterization depth for construction materials in civil engineering assessment applications. It can be varied from 20 ± 2 cm up to nearly 40 ± 2 cm by changing

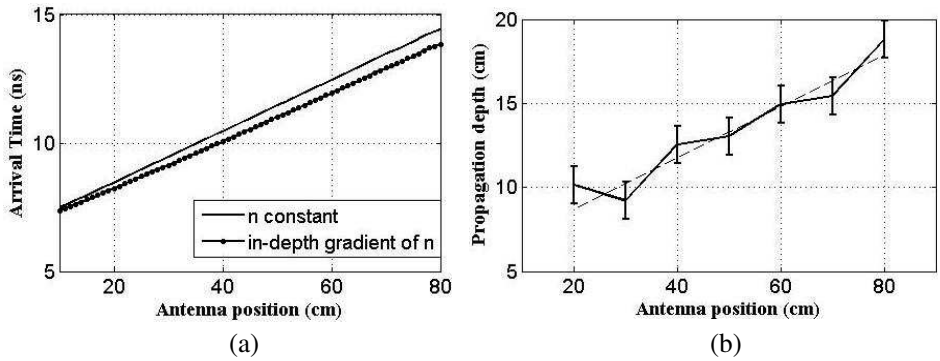

Figure 1: The RSW analysis in time domain. (a) The RSW trace of extrated wave signals for the two medium cases. (b) The propagation depth versus distance.

the distance from the antenna between 20 cm and 80 cm. This distance effect may be explained theoretically by the geometry of the Fresnel zones implied in the RSW ray [10].

4. FREQUENCY DOMAIN CHARACTERIZATION OF THE RSW BY THE FEM MODELING

In the frequency domain, the RSW is characterized by its amplitude spectrum at frequencies between 200 MHz and 600 MHz. The medium's main property affecting the amplitude is its attenuation factor. So, a complex refraction index $n^* = n' - jn''$ should be introduced in a medium to distinguish the RSW behavior in frequency domain. As we used the real n gradient at the time domain characterization section, in the frequency domain, an in-depth gradient of n'' will be introduced in the propagation medium in order to calculate the RSW probed depth.

The RSW propagation is simulated successively in three medium cases: the first is without attenuation, the second having homogeneous attenuation ($n'' = 0.5$ constant), and the third having an in-depth constant gradient such as n'' varies from 0 at the surface to 0.5 at 10 cm depth. In all the three cases, the complex refractive index is $n^* = 3 - jn''$.

The RSW propagation depth calculation is based on the same model as the previous section. So we consider the same layer at depth P_n of the overall pseudo reflection. The mixing relationship leads to the following attenuation expression:

$$\log A_n = \frac{2\pi f D}{c} n''_{RSW} = \frac{2\pi f}{c} \int_0^{P_n} \frac{D}{P_n} n''(y) dy \tag{3}$$

where A_n is the total attenuation, P_n is the propagation depth, n''_{RSW} is the overall n'' probed during propagation, $n''(y)$ is the imaginary refraction index as expressed in vertical positions y, and c is the speed of light.

As we used the property $n''(y) = -0.05y$, the TDR model and geometrical considerations lead to the following propagation depth relationship:

$$P_n = 40 n''_{RSW} \tag{4}$$

The attenuation is calculated from the amplitudes of the extracted RSW signal on the surface at positions between 10 cm and 1 m from the antenna in steps of 1 cm. These amplitudes are first normalized to that extracted from the non attenuating medium in order to remove geometrical and undulatory attenuation effects. So only the absorption attenuation is considered.

In order to calculate a local n''_{RSW} at positions X, we consider the relative amplitude A_r which is the ratio $\frac{A_n(X+10)}{A_n(X-10)}$. This is the attenuation along segments 20 cm length giving us the mean n''_{RSW} value at positions 20 cm, 40 cm, 60 cm and 80 cm for each frequency. This is shown in the Figures 2(a) and 2(b) for the homogenous medium and the gradient medium. We can see in the homogenous medium case that the relative attenuation remains same for all positions, while it increases with distance in the gradient medium case. Such behavior shows that the gradient makes the distinction between the different RSW propagation zones for different wave travel distances. We have higher attenuation, therefore higher probed depth for farther reception positions.

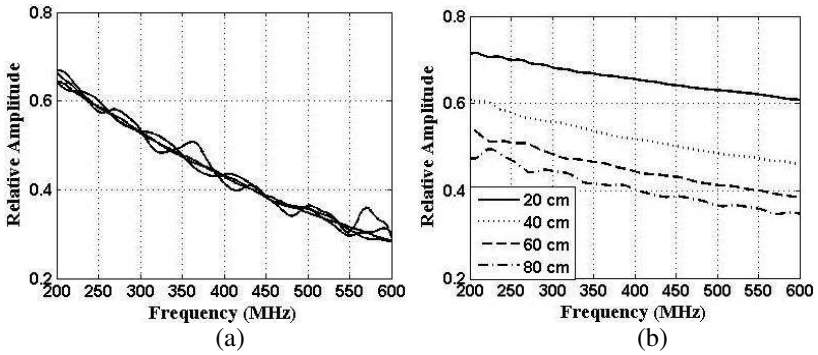

Figure 2: Relative attenuation in the two mediums at different positions. (a) Homogenous medium. (b) Gradient medium.

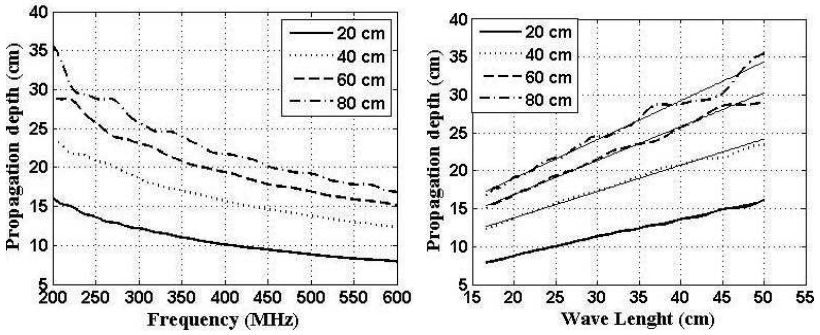

(a) (b)

Figure 3: Calculated propagation depth in the two mediums at different frequencies. (a) Homogenous medium. (b) Gradient medium

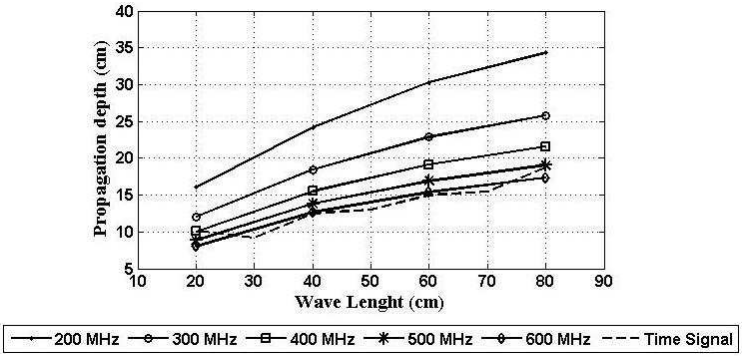

Figure 4: Propagation depth presentation versus positions.

Using the relationship (4), the propagation depth is deduced at the four positions for all the frequency and wavelength band (Figure 3(a)). We observe clearly the depth's increase at lower frequencies, in addition to that at farther positions. This important frequency effect makes possible the distinction of deeper propagation zones by increasing the signal wavelength. The depth variation in wavelengthes is practically linear as shown in the Figure 3(b). We can therefore make accurate interpolation and extrapolation.

Finally, the depth representation versus positions is shown in Figure 4 for five different frequencies. The depth calculated by the travel time method is very close to that of the attenuation method at higher frequencies, confirming the accuracy of our calculation approach.

This analysis method gives useful values of the propagation depth. However, the more accurate depth value will be higher, when we consider that the deeper propagation layers' contribution on the RSW amplitude is less then that of the higher layers.

5. CONCLUSION

In this research work, data given from FEM simulation are used to characterize the RSW propagation zone and its probed depth. By the time domain method, we found depth values from 20 cm to 40 cm, when the distance from the antenna is increased from 20 cm to 80 cm. According to an independent different method based on the attenuation property, the same values of the depth are found with more accuracy. In addition, more values are given for different frequencies which show an increase of depth up to nearly 70 cm with higher wavelengths near 50 cm. We can therefore control the depth extend whether by changing wavelength or increasing distance from the antenna. This leads to an interesting technic of assessment in civil engineering and geophysics domains. Some explanations are made about the depth behavior, but more theoretical treatise is recommended to predict general formulation instead of an empirical tendency. Laboratory tests on real soil surface is strongly recommended in order to confirm the simulated characteristics of the RSW propagation and define technical limits.

ACKNOWLEDGMENT

This research task was undertaken within the industrial Chair framework of the Natural Sciences and Engineering Research Council of Canada (NSERC) for the concrete structures inspection (Sherbrooke University). The authors thank the NSERC and the Chair industrial partners for the financial support to the research group GRAI at civil engineering department of Sherbrooke University.

REFERENCES

1. Daniels, D. J., *Ground Penetrating Radar*, 2nd Edition, IEE Radar, Sonar, Navigation, and Avionics Series, London, 2004.
2. Annan, A. P., "Radio interferometry depth sounding: Part 1 — Theoretical discussion," *Geophysics*, Vol. 38, No. 3, 557–580, 1973.
3. Klysz, G., J. P. Balayssac, and S. Laurens, "Spectral analysis of radar surface waves for on-destructive evaluation of cover concrete," *NDT & E Int.*, Vol. 37, No. 3, 221–227, 2004.
4. Soustos, M. N., H. J. Bungey, S. G. Millard, M. R. Shaw, and A. Patterson, "Dielectric properties of concrete and their influence on radar testing," *NDT & E Int.*, Vol. 34, 419–425, 2001.
5. Galagedara, L. W., G. W. Parkin, and J. D. Redman, "An analysis of the ground-penetrating radar direct ground wave method for soil water content measurement," *Hydrol. Processes*, Vol. 17, 3617–3628, 2003.
6. Sommerfeld, A. J. W., *Partial Differential Equations in Physics*, 1957th Edition, Pure and Applied Mathematis, v.1., New York, 1957.
7. Brekhovskikh, L. M., *Waves in Layered Media*, Applied Mathematics and Mechaics, New York, 1960.
8. Wait, J. R., *Electromagnetic Waves in Stratified Media*, IEEE/OUP Series on Electromagnetic Wave Theory, New York, 1995.
9. Jol, H. M. and M. J. Harry, *Ground Penetrating Radar Theory and Applications*, Amsterdam, 2009.
10. Van Overmeeren, R. A., S. V. Sariowan, and J. C. Gehrels, "Ground penetrating radar for determining volumetric soil water content; Results of comparative measurements at two test sites," *J. Hydrol*, Vol. 197, No. 1–4, 1997.

Simulation and Detection Limit of EM Waves in Masonry Structures with Application of an Algorithm for Image Processing

R. Hamrouche[1, 2], G. Klysz[1], J. P. Balayssac[1], J. Rhazi[2], and G. Ballivy[2]

[1]LMDC (Laboratoire Matériaux et Durabilité des Constructions), UPS, INSA, Université de Toulouse
135 avenue de Rangueil, 31 077 Toulouse Cedex 04, France
[2]Department of Civil Engineering, University of Sherbrooke, Sherbrooke, Québec J1K 2R1, Canada

Abstract— The objective of this work is to use Ground Penetrating Radar for the inspection of brick masonry structures and, in particular, to look for deep unfilled joint defects by developing a specific signals processing algorithm that facilitate interpretation of GPR profils and improve its accuracy. This will help the manager to quantify the volume of mortar to be re-injected in case of reinforcing work.

As a first approach, to better understanding propagation of EM waves in a complex medium as brick masonry structures, a numerical modeling of a GPR antenna with a central frequency of 1.5 GHz is used to simulate the propagation of EM waves in brick masonry structure including different size of deep unfilled joint defects. The simulations are carried out in a separated bistatic configuration. For each transmitter position, several signal acquisitions are implemented using a regularly spaced crescent pattern for the receivers.

The developed signal processing algorithm is based on inverse methods applied in the time domain, it analyzes the travel times of the reflected signals by making the assumption that each point of the modeled space is a reflector. The calculation of the travel time, which helps to identify the signal corresponding to each point of space, is made by using an estimated speed of the direct wave between transmitter and receivers in the material, which is then regarded as representative of the whole of the simulated environment.

Finally, the developed signal processing algorithm is applied on different simulated signals; the goal is to define its detection limits in terms of size, spacing and depth of the unfilled joint defects. Therefore highlight the improvements that could make the algorithm for the interpretation and the accuracy of GPR signals from brick masonry structures.

1. INTRODUCTION

In the framework of a project supported by the Midi Pyrenees Region for the conservation of built heritage we focused our study on brick masonry structures. In such structures, the degradation of mortar jointing creates a weakening which can lead to considerable mechanical damage. The mortar acts as a binder and ensures continuity between the bricks, so the deterioration of this continuity is a risk for the integrity of the masonry structure [1]. Several Non Destructive Testing Methods are currently used on masonry structures, their purpose being to determine the geometry and the internal structure [2]. Some of these techniques are commonly used for masonry investigation and are the subject of RILEM recommendations [3]. These techniques are: Radar, Microseismic, Impact-echo (reflection and transmission), Sonic (direct and indirect), Ultrasonic (impulse-echo and tomography) and Conductivity measurements [1, 2].

The principle of the GPR technique is the emission of an electromagnetic wave by a transmitting antenna on the surface of a structure. Changes in the propagation medium, such the presence of reinforcement or unfilled joints (air voids) send back part of these waves towards the surface, where they are recorded by a receiving antenna. The applications of GPR to civil engineering structures relate mainly to void, steel rebar or pipe detection and location, and also to the estimation of the thickness of slabs [4, 5]. Other studies also show the ability of the technique to estimate the water content of concrete [6, 7]. The main difficulty remains the interpretation of the recorded radar echoes. Some experience is required to exploit all the information, as is the case for masonry structures [8], where studies show that it is difficult to obtain quantitative data with the use of GRP for the control of grouting of unfilled joints [9]. For this reason, many methods of inversion and data migration have been developed to refocus the scattered signals in the image space at their real position [10]. Many of the imaging algorithms used for GPR were developed with seismic applications provided by the geophysical community [11, 12], and a RILEM recommendation has been edited for NDT of masonry structures [13].

The present study focuses on the limits of GPR for the detection of air voids in term of dimension and horizontal resolution. This by applying specific GPR measurement procedures and processing on simulated signals.

2. DETAILS OF THE RESEARCH

In this study, using a numerical model of a 1.5 GHz GPR antenna (Model 5100) from GSSI® developed and validated by Klysz et al. [14, 15]. First we simulate the propagation of electromagnetic waves in an environment that represents the heterogeneous structure of a masonry structure. Different positions and sizes of air voids are integrated in the structure. Secondly, a specific algorithm for image processing is applied on the simulated signals to enhance the detection of air voids.

3. DESCRIPTION OF THE ALGORITHM

The algorithm proposed to image the internal condition of the material assumes that, on the studied area, (a) all points that make up the area are potentially reflecting, and (b) the propagation velocity is constant and the travel paths are linear (Figure 1).

The algorithm does not need the velocity or geometric models that are generally used in the migration and inversion of data respectively [16]. It is based on two essential points: The determination of time zero and the estimation of wave velocity by using the direct wave. The WARR technique (Wide Angle Reflection Refraction) [17, 18] is used to obtain the direct wave velocity. The propagation velocity and the correction of time zero are deduced from the slope of the linear regression computed on these experimental points (Time zero = −offset/velocity). Then it is assumed that all the points of the investigated area are reflectors. Using the calculated time zero and velocity, it is possible to accurately estimate the time required for the EM wave to go from the transmitter to each supposed reflecting point then return to the receivers. These times allow the potential echo corresponding to each point of the investigated space to be located in the whole signal recorded for each receiver position. Then a time window is applied to the signal to extract this potential echo. The time window is defined to be the same as the duration of the emitted signal. The n windowing signals corresponding to n receiver positions are summed. The result is placed in a matrix according to the spatial coordinates of the assumed reflector. Once all the points have been processed, the matrix is displayed as an image.

4. NUMERICAL SIMULATIONS

2D simulations of the propagation of electromagnetic waves in heterogeneous walls (327 cm long and 58 cm thick) were carried out. In the heterogeneous walls (masonry structures), the size of the bricks was $48 \times 28 \times 5$ cm and the thickness of the lime mortar joint was 2 cm, the electromagnetic properties of bricks and joints were estimated at $\varepsilon'_r = 3$ and $\sigma = 0.02$ S/m for brick and $\varepsilon'_r = 6$ and $\sigma = 0.065$ S/m for the joints in lime mortar [19]. During the measurements, the position of the transmitter was fixed in the middle of a brick, and the receiver took 10 positions separated by one centimeter, the first one being at 13.9 cm from the transmitter. The voids were introduced in the wall parallel to the measurement surface (Figure 2).

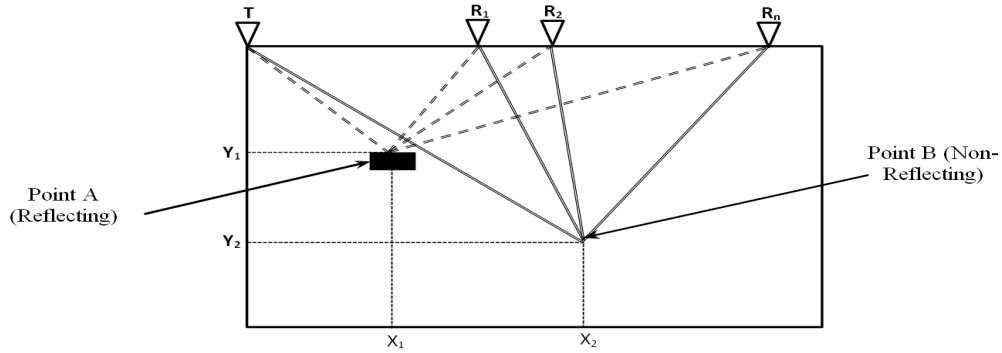

Figure 1: The assumed constant velocity propagation and linear travel.

To estimate the limit of detection in heterogeneous medium, two air voids with dimensions of 0.5×0.5 cm and 2×2 cm were separately simulated at a depth of 28 cm below the measurement surface.

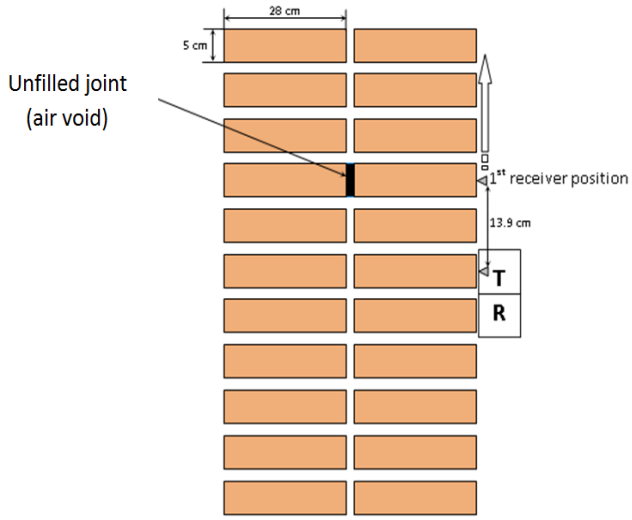

Figure 2: Air void parallel to the measurement surface.

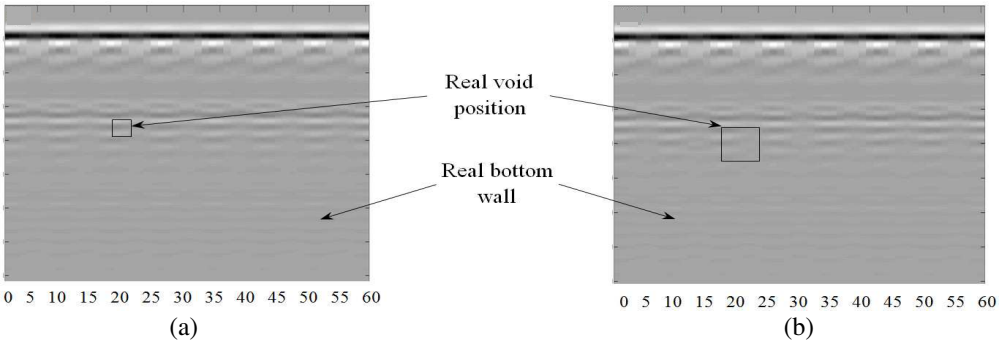

Figure 3: (a) B-scan with air void (0.5×0.5 cm). (b) B-scan with air void (2×2 cm).

The case of the heterogeneous wall is very complex because of the multitude of interfaces between brick and mortar, which makes the signal difficult to interpret. On the simulated B-scans obtained on the heterogeneous wall (Figure 3), a multitude of reflections can be seen.

The image reconstructed by means of the processing algorithm is presented in Figure 4. Several remarks can be made:

- The interface between the bricks and the mortar is clearly visible at about 30 cm depth on the image.
- The rear face of the wall can be detected even if it is not as clear as the interface.
- The defect 0.5×0.5 cm in Figure 4(a) is undetectable.
- Finally, the defect 2×2 cm Figure 4(b) along the mortar joint is represented by a clearly visible localized color contrast.

We can distinguish the defect and its position is close to the real position in the structure (beginning at 28 cm below the measurement surface, 24 cm in the horizontal direction from the first transmitter position of the first acquisition).

To estimate the limit of horizontal resolution in heterogeneous medium, a pair of two air voids with same dimensions of 5×2 cm were simulated simultaneously at a depth of 28 cm below the measurement surface and spaced by 5 then 10 cm for the heterogeneous medium.

The corresponding B-scans obtained on the heterogeneous walls are shown in Figure 5.

In the results from the algorithm (Figure 6), the two voids spaced by 5 cm are seen on Figure 6(a) as one defect; the 5 cm of mortar between the two voids are undetectable. In Figure 6(b) we can distinguish the two voids spaced by 10 cm of mortar and represented with dimensions close to the real dimensions of the voids, as well as its real position beginning at 28 cm deep and 24 cm in the horizontal direction from the first transmitter position.

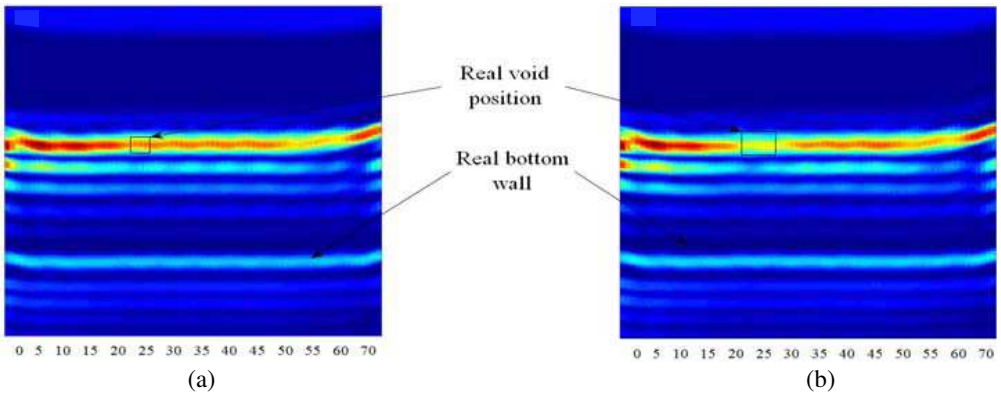

Figure 4: (a) Result given by the algorithm (0.5×0.5 cm). (b) Result given by the algorithm (2×2 cm).

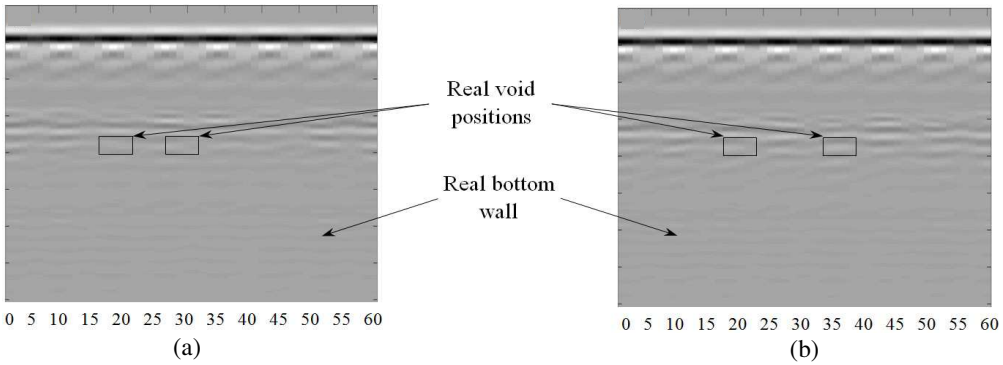

Figure 5: (a) B-scan with two air voids spaced by 5 cm. (b) B-scan with two air voids spaced by 10 cm.

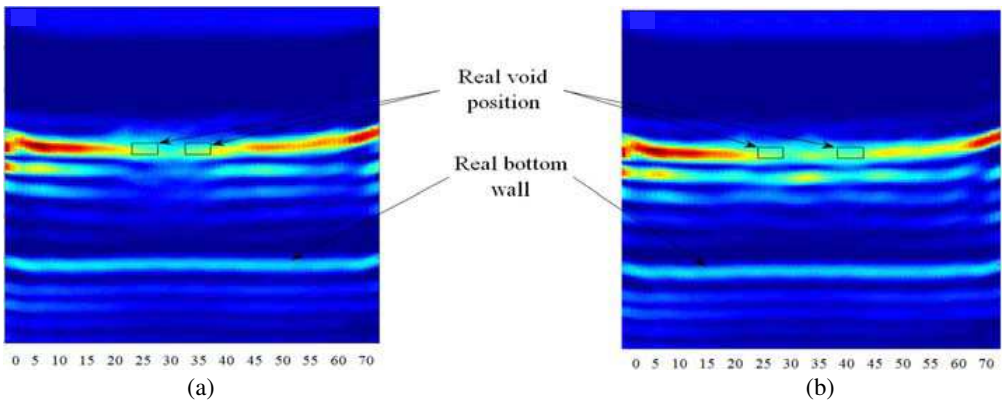

Figure 6: (a) Result given by the algorithm (5 cm spacing). (b) Result given by the algorithm (10 cm spacing).

Concerning computer time, one construction image takes less than 1 minute on a very basic computer.

5. CONCLUSIONS

The purpose of this study was to enhance the use of GPR for the detection of unfilled joints in masonry structures and, more specifically, to optimization and develop better signal processing methods. A signal processing algorithm based on velocity and time zero estimation was developed and its application to simulated signals provided encouraging results as it permitted good location of unfilled joints. The validation of this process on a full-scale wall provided very promising results with satisfactory precision and a very low cost in calculation time, results will be published soon.

Still the estimation of wave velocity requires the development of procedures to correct the estimation error especially for heterogeneous medium and so to increase the accuracy of results.

An improvement of the algorithm is needed to characterize the size of the defect because, currently, the result gives only the location of the upper part of the defect.

REFERENCES

1. Binda, L. and C. Maierhofer, "Strategies for the assessment of historic masonry structures," RILEM Paper, 103–124, 2005, https://www.rilem.net/boutique/fiche.php?page=0&cat=conference&field=produits.titreProduit&mot=strategies+for+the+assessment+of+historic+masonry+structures&valider=ok&reference=comp013-004.
2. McCann, D. M. and M. C. Forde, "Review of NDT methods in the assessment of concrete and masonry structures," *NDT & E International*, Vol. 34, 71–84, 2001.
3. "RILEM TC 127-MS recommendations of RILEM TC 127-MS: Tests for masonry materials and structures, - MS.D3: Radar investigation of masonry; - MS.D4: Measurement of local dynamic behaviour for masonry; - MS.D8: Electrical conductivity investigation of masonry," *Mater. Struct.*, Vol. 34, 131–143, 2001.
4. Barrile, V. and R. Pucinotti, "Application of radar technology to reinforced concrete structures: A case study," *NDT & E International*, Vol. 38, 596–604, 2005.
5. Hugenschmidt, J., "Concrete bridge inspection with a mobile GPR system," *Construction and Building Materials*, Vol. 16, 147–154, 2002.
6. Sbartaï, Z., S. Laurens, J. Balayssac, G. Arliguie, and G. Ballivy, "Ability of the direct wave of radar ground-coupled antenna for NDT of concrete structures," *NDT & E International*, Vol. 39, 400–407, 2006.
7. Klysz, G. and J. Balayssac, "Determination of volumetric water content of concrete using ground-penetrating radar," *Cement and Concrete Research*, Vol. 37, 1164–1171, 2007.
8. Colla, C., P. C. Das, D. McCann, and M. C. Forde, "Sonic, electromagnetic and impulse radar investigation of stone masonry bridges," *NDT & E International*, Vol. 30, 249–254, 1997.
9. Maierhofer, C. and S. Leipold, "Radar investigation of masonry structures," *NDT & E International*, Vol. 34, 139–147, 2001.
10. Leuschen, C. and R. Plumb, "A matched-filter-based reverse-time migration algorithm for ground-penetrating radar data," *IEEE Trans. Geosci. Remote Sensing*, Vol. 39, 929–936, 2001.
11. Neyrat, M., Contribution à l'étude de G.P.R. (Ground Penetrating Radar) multicapteurs. Méthodes directes et inverses en temporel, 2009, http://www.unilim.fr-/theses/2009/sciences/2009limo4003/notice.htm.
12. Leparoux, D., D. Gibert, and P. Cote, "Adaptation of prestack migration to multi-offset ground-penetrating radar (GPR) data," *Geophys. Prospect.*, Vol. 49, 374–386, 2001.
13. "RILEM TC 177-MDT recommendations of RILEM TC177-MDT: Masonry durability and on-site testing MD.E.1 determination of moisture distribution and level using radar in masonry built with regular units," *Mater. Struct.*, Vol. 38, 283–288, 2005.
14. Klysz, G., X. Ferrieres, J. Balayssac, and S. Laurens, "Simulation of direct wave propagation by numerical FDTD for a GPR coupled antenna," *NDT & E International*, Vol. 39, 338–347, 2006.
15. Ferrieres, X., G. Klysz, P. Mazet, and J. Balayssac, "Evaluation of the concrete electromagnetics properties by using radar measurements in a context of building sustainability," *Computer Physics Communications*, Vol. 180, 1277–1281, 2009.
16. Daniels, D. J., *Ground Penetrating Radar*, 2nd Edition, Institution of Engineering and Technology, 2004.
17. Viriyametanont, K., S. Laurens, G. Klysz, J. Balayssac, and G. Arliguie, "Radar survey of concrete elements: Effect of concrete properties on propagation velocity and time zero," *NDT & E International*, Vol. 41, 198–207, 2008.
18. Klysz, G., J. Balayssac, and X. Ferrières, "Evaluation of dielectric properties of concrete by a numerical FDTD model of a GPR coupled antenna — Parametric study," *NDT & E International*, Vol. 41, 621–631, 2008.
19. Hamrouche, R., et al., "Numerical modeling of ground-penetrating radar (GPR) for the investigation of jointing defects in brick masonry structures," *Non-Destructive Testing in Civil Engineering, NDTCE*, 2009.

GPR Limits for Thin Layers in Concrete Detection: Numerical and Experimental Evaluation

A. Van der Wielen, L. Courard, and F. Nguyen
University of Liege, Belgium

Abstract— The Ground Penetrating Radar (GPR) is a nondestructive technique increasingly used in civil structures inspection. In those structures, thin layers, presenting a relatively small thickness compared to their area, are common and induce a complex multiple reflection scheme of the GPR waves on the two interfaces limiting the layer. The theoretical relationships predicting the reflected amplitude are based on multiple simplifying assumptions that are not matched by most commercial GPR impulse machines. In the first part of this study, we confronted the theoretical curves with numerical finite difference simulations performed with GprMax2D, with both a continuous sine wave and a realistic pulse derived from measurements. In the second part, we performed experiments on two concrete slabs, separated with an air space of variable thickness. The measured amplitude appeared to be different from the predictions, probably due to surface noise.

1. INTRODUCTION

1.1. The Ground Penetrating Radar

The Ground Penetrating Radar is an impulse device, often functioning with two bowtie antennas. It is increasingly used in the civil engineering structures inspection, due to the apparition of new commercial antennas with frequencies rising up to 3 GHz.

1.2. Thin Layers Detection

The exact equation for reflection from a single embedded layer and considering simple harmonic waves was reported by Rayleigh [1]. The extension of this theory to seismic wavelets was then proposed by Widess [2], who set the limit of thin layers to $\lambda/8$ and observed a linearity between the layer thickness and the reflection amplitude.

More recently, different authors [3–5] proposed to perform CMPs and use the amplitude (and phase) versus offset (A(P)VO) curves to extract more information from the thin layer measurements with GPR, for geological applications.

2. THEORETICAL BACKGROUND FOR THIN LAYERS DETECTION WITH GPR

The reflection of radar waves on an interface is described by the reflection coefficient R, equal to the quotient of the amplitude of the incident wave I, and the amplitude of the reflected wave (Figure 1(a)). In transverse electric mode (the most commonly used in GPR), the reflection coefficient is governed by Eq. (1), in which ε_{r1} and ε_{r2} are the dielectric permittivities of the layers and θ_1 is the incident angle:

$$R = \frac{\cos\theta_1 - \sqrt{\frac{\varepsilon_{r2}}{\varepsilon_{r1}} - \sin^2\theta_1}}{\cos\theta_1 + \sqrt{\frac{\varepsilon_{r2}}{\varepsilon_{r1}} - \sin^2\theta_1}} \tag{1}$$

Figure 1(b) shows the resulting reflection coefficient for various dielectric permittivity contrasts as a function of the incident angle. We observe that when the deepest layer is faster (i.e., when the ratio is lower than 1), the reflection coefficient grows smoothly to reach the value of one whereas when it is slower (ratio greater than 1), the reflection coefficient reaches the value of one as soon as it reaches the critical angle (from which there is theoretically no more transmission).

When a signal meets a thin layer, it undergoes multiple reflections between the two interfaces limiting this layer (Figure 2(a)). The amplitude of the resulting wave is dependent on the interferences between the reflected waves, which can be constructive or destructive in function of the transfer time into the layer, itself dependant on the thickness and filling material of the layer.

If both geometric and intrinsic attenuations can be neglected, and if the signal is a continuous plane sinusoid, the resulting reflection coefficient swings between 0 for purely destructive interferences to, for constructive interferences:

$$R_{121} = \frac{2R_{12}}{1 + R_{12}^2} \tag{2}$$

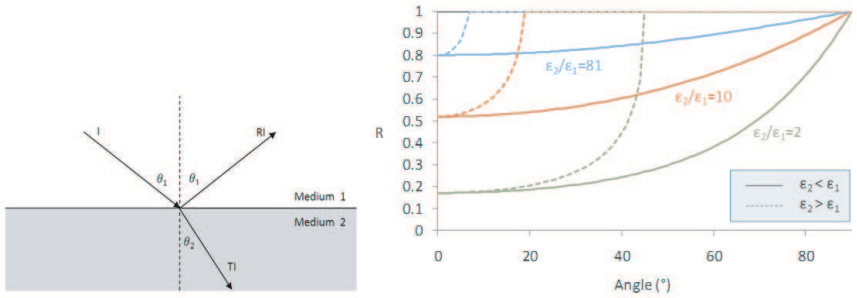

(a) (b)

Figure 1: (a) Reflection of a wave on an interface. (b) Evolution of the reflection coefficient in function of the permittivity contrast and incidence angle.

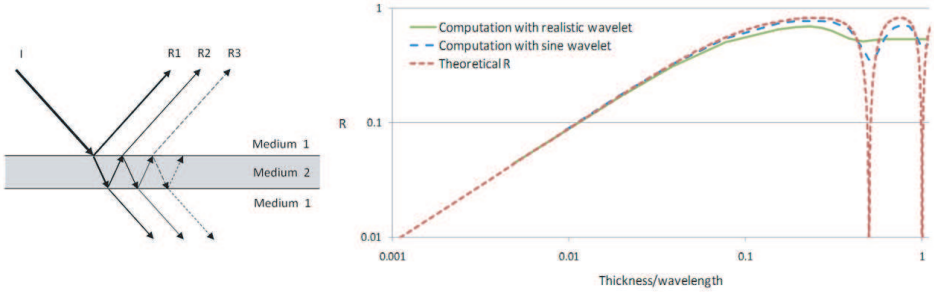

(a) (b)

Figure 2: (a) Multiple reflexion scheme on a thin layer. (b) Evolution of the reflection coefficient in function of the permittivity contrast and incidence angle.

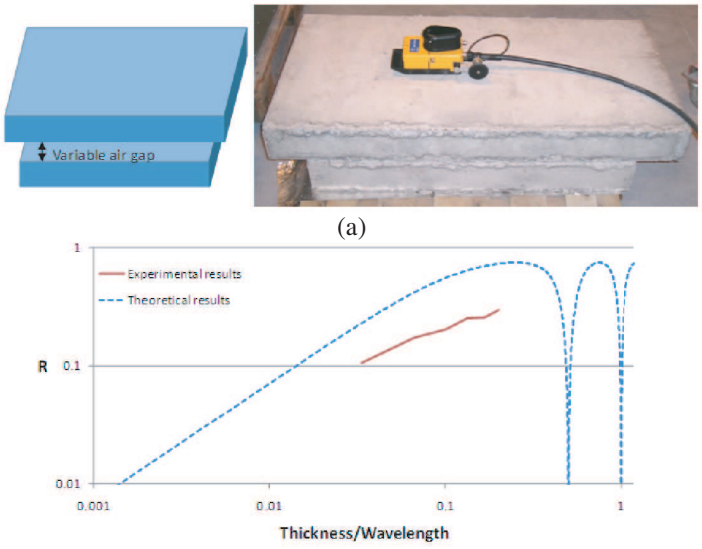

(a)

(b)

Figure 3: (a) Experimental setup. (b) Reflection coefficient in function of the thickness/wavelength ratio.

In Eq. (2), R_{121} is the reflection coefficient for a thin layer, while R_{12} is the coefficient corresponding to the reflection on a simple interface between the two media (Eq. (1)). The reflection occurring on the thin layer has then a greater amplitude than a reflection that would occur on a simple interface. The evolution of R_{121} with the ratio of the layer thickness on the wavelength in the thin layer is drawn in Figure 3(b).

When the thickness of the layer can be considered as low compared to the wavelength (ratio up

to 0.09), the reflection coefficient becomes directly proportional to the layer thickness [2, 6]. The parameters influencing theoretically the visibility of the layer are then the frequency of the antenna (influencing the wavelength), the layer thickness and its filling (which influences the wave speed and thus the wavelength). In a lesser extent, the attenuation in the medium, the depth of the layer, the roughness of the interfaces or the measurement noise can also have an influence.

3. NUMERICAL EVALUATION OF THIN LAYERS DETECTION LIMIT

In the first simulations, performed with the finite differences program GprMax2D [7], a continuous sinusoidal wave (2.3 GHz) was introduced to match the theoretical results. All the simulations were performed for an air layer placed at a depth of 10 cm into concrete ($\frac{\varepsilon_{r2}}{\varepsilon_{r1}} = 10$) and a 4 cm antenna separation. The reflection coefficient was obtained by comparing the maximum peak-to-peak amplitude (after suppression of the direct wave) to the amplitude of a wave reflected on a metallic plane. Doing this way, the contributions of the geometric and intrinsic attenuations are suppressed, as well as the radiation pattern effects. Those parameters decrease globally the measured amplitude, but are independent of the reflection coefficient.

Two parameters that werent corrected are the geometric attenuation into the thin layer (which is different for each ray, depending on the number of reflections) and the fact that the simulated wave is not plane but cylindrical due to the proximity and frequency of the source. The numerical results, displayed in Figure 2(b), appeared to be in a relatively good concordance with the analytical predictions. The best concordance between numerical and analytical predictions was obtained for vertically incident analytical rays while the angle for the numerical rays is 11.5°.

In a second set of simulations, a realistic pulse derived from measurements performed with our radar (a Mala 2.3 GHz antenna) was introduced into GprMax2D instead of a continuous sine. The reflection coefficient of the realistic pulse is rapidly attenuated, because the two wavelets get separated from each other. Nevertheless, we can observe that for layers thinner than $\lambda/11$, the reflection coefficient depends linearly on the thickness/wavelength ratio, with a linearity coefficient equal to [1]:

$$4\pi \frac{R_{12}}{(1 - R_{12}^2)} \tag{3}$$

4. COMPARISON WITH EXPERIMENTAL RESULTS

In reality, a key point that should be considered is the signal noise. Indeed, no wavelet will be detected if its amplitude is inferior to the global noise. The amplitude ratio of the direct wave in the air to the permanent noise of the signal is evaluated to 1.5 10^{-3}. This is theoretical lowest reflection coefficient detected by radar, will never be detected in reality, as geometric and intrinsic attenuation decrease the amplitude with the propagation distance, respectively proportionally and with a negative exponential factor. Another parameter that can modify the amplitude is the presence of the interface air-concrete just below the radar. Surprisingly, in numerical simulation, this tends to increase the amplitude of the measured wavelet. This increase hasn't be observed yet in laboratory.

The first experimental study was performed on two 10 cm thick concrete slabs. They were cast vertically in order to present very smooth and parallel surfaces. Between the slabs, a variable air gap was introduced (Figure 3(a)). As for the computations, the direct wave was subtracted from the resulting signal, and the amplitude was compared to the amplitude obtained with a metallic sheet instead of the air gap. Results are shown in Figure 4b, in which they are compared to a theoretical curve calculated for a reflection coefficient air-concrete of 0.45. This coefficient was derived from experimental wave speed evaluation and confirmed by comparing the measured amplitudes of air-concrete and air-metal reflections.

The results show a quasi-linear behavior, but shifted towards lower reflection coefficients, compared to the theoretical curve. This could be explained by the difficulty to remove the direct wave from the measurements, which could be explained by two phenomena. The first one is the presence of numerous air bubbles appearing beneath the entire concrete surface, which create very different traces influencing the mean trace measured on the slabs. Moreover, both the direct wave and the signal mean amplitude revealed to be affected by a time drift during the radar first minutes of operation. A global error may then have occurred into the direct wave subtraction or into the total reflection comparison.

5. CONCLUSION

When the excitation signal is sinusoidal, FDTD simulation results are close to theory. This is also the case for realistic pulses if the thickness remains inferior to $\lambda/11$ (for a 10% error). For those thicknesses, we have a linear dependence, which was confirmed by the experimental tests. However, probably due to the presence of surface imperfections, the measured reflection coefficients didn't match the theoretical ones very well. In the future, the same tests will be performed on very smooth and homogeneous slabs to avoid this difficulty.

ACKNOWLEDGMENT

This research was financed by the FNRS (Belgian national fund for scientific research).

REFERENCES

1. Rayleigh, J. W. S., *The Theory of Sound*, 2nd Edition, Vol. 2, Dover Publications, New York, 1945.
2. Widess, M. B., "How thin is a thin bed?," *Geophysics*, Vol. 38, 1176–1180, 1973.
3. Bradford, J. H. and J. C. Deeds, "Ground-penetrating radar theory and application of thin-bed offset-dependent reflectivity," *Geophysics*, Vol. 71, K47–K57, 2006.
4. Gregoire, C. and F. Hollender, "Discontinuity characterization of the spectral content of ground penetrating radar (GPR) reflections — Application of the Jonscher model," *Geophysics*, Vol. 69, 1414–1424, 2004.
5. Deparis, J. and S. Garambois, "On the use of dispersive APVO GPR curves for thin-bed properties estimation: Theory and application to fracture characterization," *Geophysics*, Vol. 74, No. 1, J1–J12, 2009.
6. Annan, A. P., *Near-surface Geophysics Part 1: Concepts and Fundamentals*, 357–438, Society of Exploration Geophysicists, New York, 2005.
7. Giannopoulos, A., "Modelling ground penetrating radar by GprMax," *Constr. Build. Mater.*, Vol. 19, No. 10, 775–762, 2005.

Insulated Concrete form Void Detection Using Ground Penetrating Radar

Roger Roberts, **Ken Corcoran**, **Michael Arvanitis**, **and Alan Schutz**
Geophysical Survey Systems Inc., Salem, NH, USA

Abstract— Insulated concrete form (ICF) construction consists of interlocking polystyrene forms and poured-in-place concrete. The forms are left in place after the concrete is poured to form an efficient insulation barrier. Consequently, it is difficult to ascertain the presence of flaws in the concrete, such as voids at the boundary between the form and the concrete, using traditional inspection methods without removing, and thus damaging the polystyrene forms. In a research investigation, it was found that ground penetrating radar (GPR) utilizing a 1.6 GHz center-frequency antenna is useful for locating voids at the concrete-form boundary and voids buried in the concrete The highest quality data were obtained from vertical profile lines. The detection of the voids was possible by performing a background-removal process to the data that stripped the direct-coupling between the transmit and receive antennas, which effectively isolated the concrete surface reflection. Mapping the change in arrival time and amplitude of the concrete surface reflection was useful in characterizing, to some extent, the dimensions and depths of the voids. The detection of voids buried 2.5 to 10.8 cm (1.0 to 4.3 in.) in the concrete was also achieved after 3 days of curing. Additional data processing was required to enhance the detectability of the buried voids. The generation of a 3-D dataset and subsequently viewing thin depth slices of data was useful in distinguishing the void reflections from the reinforcing reflections.

1. INTRODUCTION

Ground penetrating radar (GPR) is a non-destructive testing methodology that employs the transmission and reception of radio waves to detect inhomogeneities in many different media. The method has been used for over 40 years for a wide range of imaging purposes. In the past 10 years the method has been used extensively for concrete imaging applications. Examples abound in published literature of its use for the detection of reinforcing in concrete and concrete deterioration. [1] presents a thorough review of research performed in this area.

There does not appear to be much work done in the area of using GPR for assessment of insulated concrete form (ICF) construction. Insulated concrete form construction consists of interlocking polystyrene forms and poured-in-place concrete. The forms are left in place after the concrete is poured to form an efficient insulation and sound barrier. The construction method first appeared in the late 1960s (see web address reference at end of paper) and has steadily grown in popularity. It is difficult to ascertain the presence of flaws in the concrete, such as voids at the boundary between the form and the concrete using traditional inspection methods without removing, and thus damaging the polystyrene forms. It has been observed in a study conducted by the Portland Concrete Association (PCA) that proper procedures must be followed when pouring concrete in ICFs or voids readily develop [3]. Ground Penetrating Radar (GPR) was implemented in the PCA study and did successfully locate a number of voids.

It is already known that GPR can be used to detect voids in ICF forms. However, there are a number of things that are not apparent such as: (1) how difficult it is to detect these voids (i.e., does it require an expert user); (2) what are the range of void sizes that can be detected; (3) can voids buried in the concrete be detected — and if so, how soon after the concrete is poured? The investigation presented in this paper was conducted to answer these questions. The following sections of this paper detail the construction of 2 ICF sections with voids and the application of GPR to detect and characterize the voids.

2. ICF FORMS WITH VOIDS

Two flat panel ICF forms with dimensions 1.2×1.2 m (4×4 ft) were procured for the investigation. The forms consist of 5.4 cm (2.125 in.) thick polystyrene walls separated by 18.1 cm (7.125 in.). The walls are connected using 0.6 cm (0.25 in.) diameter steel ties as shown in Fig. 1(a).

In typical construction, horizontal and vertical reinforcing bars are tied to the steel ties. In this investigation 13 mm (0.5 in.) diameter reinforcing bars were used. Vertical reinforcing bars were placed at a 30 cm (12 in.) interval. Horizontal reinforcing was also spaced at 30 cm (12 in.) intervals.

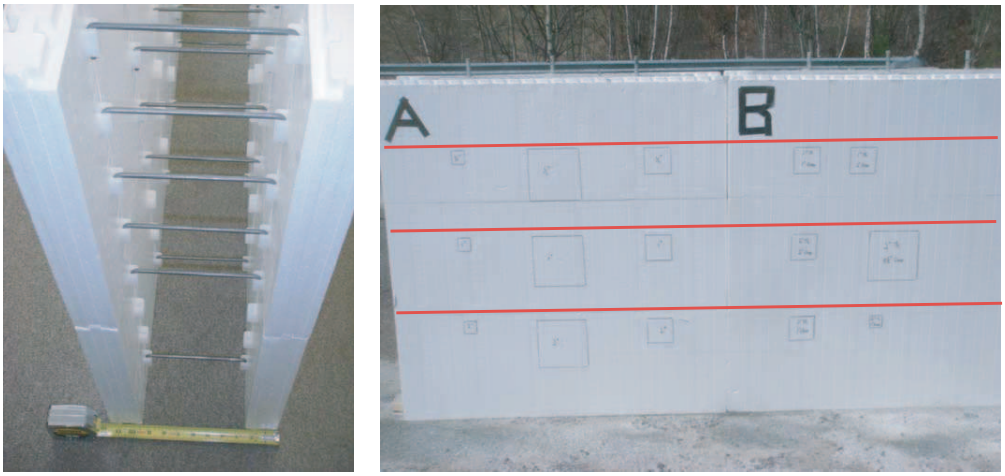

(a) (b)

Figure 1: (a) Insulated concrete form. This picture shows the steel ties connecting the two 5.4 cm (2.1 in.) thick polystyrene forms. (b) Two 1.2×1.2 m (4×4 ft) ICF forms with outline of voids drawn on surface. All the voids in Block A are flush to the backside of the form and all the voids in Block B are buried. The red lines denote the location of horizontal reinforcing bars.

The numerous photos in the ICF paper [3] reveal voids forming beneath the horizontal reinforcing. Consequently, the voids emplaced in the ICF forms for this investigation were all located below the horizontal reinforcing. The voids were created using closed-cell styrofoam sealed in thin plastic and taped to either the side of a form for flush mounting, or to one or more reinforcing bars and steel ties for cases where the void was buried in the concrete. Fig. 1(b) shows the location and (x, y) dimensions of the voids on the two 1.2×1.2 m (4×4 ft) ICF sections. The red lines in Fig. 1(b) denote the position of the horizontal reinforcing. All the voids in ICF Section A are flush to the polystyrene form. Three different void (x, y) sizes were used: (1) 4.5×4.5 cm (1.8×1.8 in.); (2) 9.0×9.0 cm (3.6×3.6 in); and (3) 18.1×18.1 cm (7.1×7.1 in.). The top row of voids in Section A were all 1.3 cm (0.5 in.) in thickness and the middle and bottom rows were 2.7 and 5.4 cm (1.0 and 2.1 in.) in thickness, respectively. The width of the largest void was chosen to match the spacing between the clips in the forms for steel tie attachment. The fractional areas of the mid-size and smallest voids relative to the largest void were 1/4 and 1/16, respectively.

All the voids in Section B, except for the largest void in Section B, were buried between 2.5 and 5.1 cm (1.0 and 2.0 in.) in depth. The largest void was buried 10.8 cm (4.3 in.) in the concrete. The thicknesses of the buried voids were between 2.7 and 5.4 cm (1.0 and 2.1 in.).

A 3000 PSI pea gravel concrete was poured in two lifts. Each lift was vibrated using a 1.5 HP electric concrete vibrator with a 5.1 cm (2 in.) head. The vibrator was inserted into the sections of concrete that were clear of voids or sections that contained thin voids (so as to avoid the possibility of the vibrator knocking the voids off their taped locations) and lifted at a rate of about 2.5 cm (1.0 in.) per second.

3. DATA COLLECTION

A GSSI StructureScan Mini handheld GPR unit was used for data collection. The unit, shown in Fig. 2, has 1.6 GHz center-frequency transmit and receive antennas separated by 6 cm (2.4 in.).

Data were collected on the concrete over a number of days starting one day following pouring. As expected, the voids flush to the form were immediately apparent in the data that was only minimally processed using vertical FIR filters and automatic gain. Fig. 3 shows the minimally processed data obtained from vertical lines centered over the different size targets. The vertical axis in the images is depth relative to the surface of the polystyrene, using the radar wave velocity in free space in the depth calculation. The top of the voids therefore correspond to the back side of the polystyrene at 5.4 cm (2.1 in.) depth in the figures. The backside arrival time and the direct-coupling arrival time interfere to create the thick white-black-white band in the data.

The arrival times from the voids in the minimally processed data presented in Fig. 3 are not sufficiently isolated from the direct coupling to allow void size estimation.

Data were also obtained over horizontal lines. The voids were also detected in data obtained

Figure 2: GSSI StructureScan Mini handheld GPR unit used for data collection.

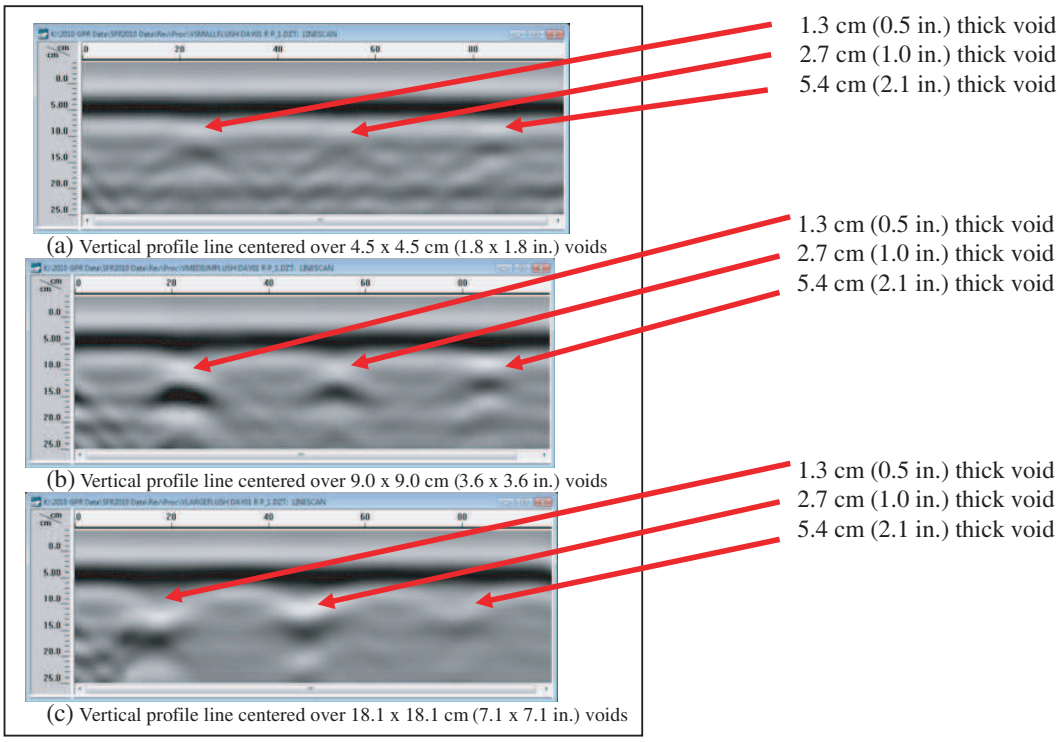

Figure 3: Minimally processed data obtained from vertical profile lines centered over 1.3, 2.7, and 5.4 cm (0.5, 1.0, and 2.1 in.) thick voids flush to the backside of one of the ICF forms.

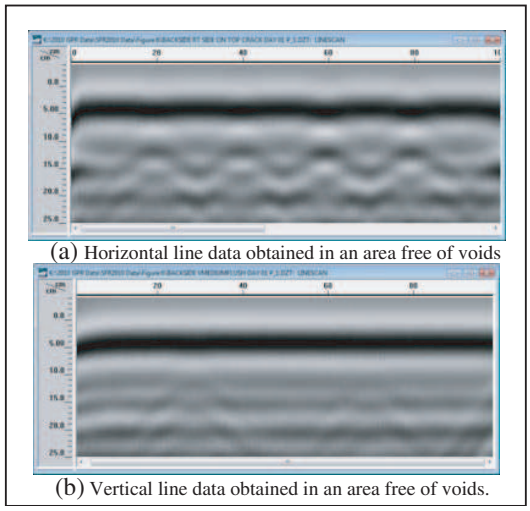

Figure 4: Comparison of (a) horizontal profile line data and (b) vertical profile line data in areas free of voids.

along horizontal lines. However, the horizontal line data were negatively impacted by reflections from the plastic backing behind the sockets in which the metal ties fit. These reflections, although weak, interfere with the reflections from the voids. The interference was even more significant when attempting to detect the buried voids. In Fig. 4, data obtained by vertical and horizontal profile lines away from known void locations are compared. All subsequent figures and discussion focus on data obtained from vertical profile lines.

Subsequent to the profile line data obtained over the centers of the voids in day 1, additional data were obtained in Day 8 along vertical profiles spaced approximately 5.1 cm (2 in.) apart. The 3D images generated from the data were useful in the detection of the buried voids.

4. FLUSH VOID DATA ANALYSIS

Detecting voids flush to the backside of the ICF form using the appropriate GPR equipment is a straight-forward task that does not require any significant data processing or extensive training. The gathering of quantitative information, such as the void surface area and thickness requires further data processing. The fact that the polystyrene form has very similar electromagnetic properties to air means that a scan of data obtained with the antenna in air can be subtracted from the scans of data obtained on the form to remove the direct-coupling and therefore isolate the reflection from the backside of the form. Deviations in the backside arrival time would then be associated with voids and the magnitude of the time deviation would be assumed to be associated with void thickness. This methodology was performed on a sequence of vertical profile lines obtained at a 5.1 cm (2.0 in.) spacing over the voids 8 days following pouring. Fig. 5 shows a vertical profile line over the 9.0×9.0 cm (3.6×3.6 in.) voids. The yellow line in Fig. 5 tracks the peak of the concrete surface reflection. The corresponding calculated thickness of the polystyrene is plotted in the bottom half of Fig. 5. The void surface extents are indicated by the red lines.

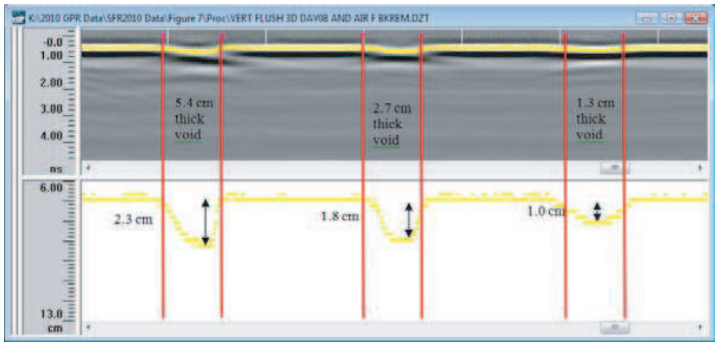

Figure 5: Data from vertical profile over centers of 9.0×9.0 cm (3.6×3.6 in.) voids flush to backside of the form. The Yellow line tracks the concrete surface reflection after performing an airwave subtraction. The backside arrival times converted into polystyrene thickness are plotting on the bottom half of the figure.

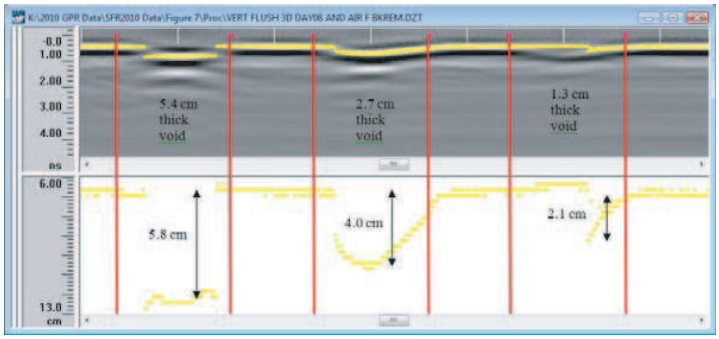

Figure 6: Data from vertical profile over centers of 18.1×18.1 cm (7.1×7.1 in.) voids flush to backside of the form. The Yellow line tracks the concrete surface reflection after performing an airwave subtraction. The backside arrival times converted into polystyrene thickness are plotted on the bottom half of the figure.

There is a measureable increase in the arrival time from the concrete surface reflection that generally correlates with the thickness of the 1.3 cm (0.5 in.) void and underestimates the thickness

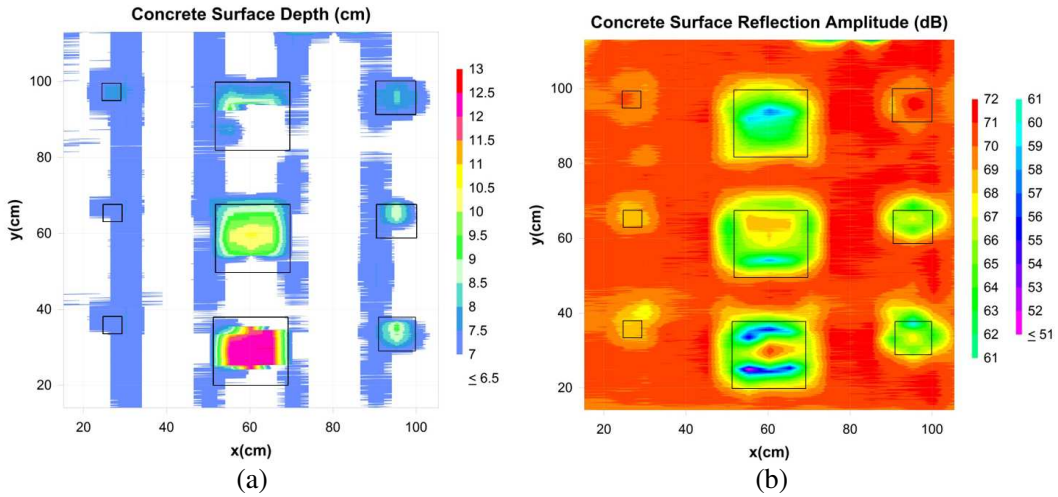

Figure 7: (a) Calculated polystyrene thickness (which is also the concrete surface depth) obtained from plotting the concrete surface reflection arrival times from a series of vertical profile lines. Black outlines correspond to the surface extents of voids flush to the backside of the form. (b) Concrete surface reflection amplitudes from a series of vertical profile lines. Black outlines correspond to the surface extents of voids flush to the backside of the form.

of the 2.7 cm (1.0 in.) and 5.4 cm (2.1 in.) voids. The arrival times from the bottom of the largest surface area voids, shown in Fig. 7, overestimate the true thickness of the voids.

Diffractions from the top edges of the voids and the reflections from the nearby horizontal reinforcing constructively and/or destructively interfere with the reflections from the bottom of the voids, which result the variations in calculated void thickness obtained by tracking the positive peak of the reflection waveform. The impact of the nearby reinforcing is particularly evident in the surface reflection arrival from the right side of the 1.3 cm (0.5 in.) thick void in Fig. 6. Close examination of Fig. 6 also reveals that the increase in time doesn't necessarily relate to the lateral extents of the voids. A clearer picture of the relationship between increasing concrete surface reflection arrival times and the size and thickness of voids emerges when the surface reflection is tracked for vertical profile line data obtained at 5.1 cm (2 in.) increments over the form. The calculated polystyrene thickness from the surface reflection associated with a sequence of profile lines is presented in Fig. 7(a). The black outlines correlated to the surface extents of the voids.

All of the voids are detectable in Fig. 7(a). The maximum calculated void thickness for voids with extents 9.0 × 9.0 cm (3.6 × 3.6 in.) or greater with thicknesses of up to 2.5 cm (1 in.) are generally related to the actual void thickness. The surface extents of the voids are more difficult to accurately assess. The vertical bands in Fig. 7(a) are associated with the plastic anchor that is embedded in the polystyrene at approximately 20 cm (8 in.) intervals. One out of every 4 vertical profile lines crossed directly over the anchor.

The amplitude of the delayed surface reflection was also plotted and is shown in Fig. 7(b). Interestingly, there is very good correlation between the surface extents of the 18.1 × 18.1 cm (7.1 × 7.1 in.) voids, and somewhat less correlation with the 9.0 × 9.0 cm (3.6 × 3.6 in.) voids. The 4.5 × 4.5 cm (1.8 × 1.8 in.) voids also create a 1–3 dB amplitude anomaly.

5. BURIED VOIDS DATA ANALYSIS

The vertical profile line data were found to be the most useful for buried target detection because they contained less clutter from the vertical plastic supports and metal ties. The clutter that was present in the data from these objects appeared as horizontal bands.

Additional data processing was performed on the buried void data to remove all the continuous horizontal reflections and clutter bands. An average scan was obtained for each profile and subtracted from the data. The data were then bandpass filtered and a 2-point 10–48 dB gain was applied to the data to accommodate for propagation loss.

The processed data from a vertical profile line over three 9.0 × 9.0 cm (3.6 × 3.6 in.) voids buried 2.5 to 5.1 cm (1.0 to 2.0 in.) deep are shown in Fig. 8. The three images in the figure were obtained after 3, 8, and 14 days of curing. To the trained eye, the targets buried 2.5 cm (1 in.) were detectable and distinguishable from the reinforcing reflections after 3 days of curing. The center

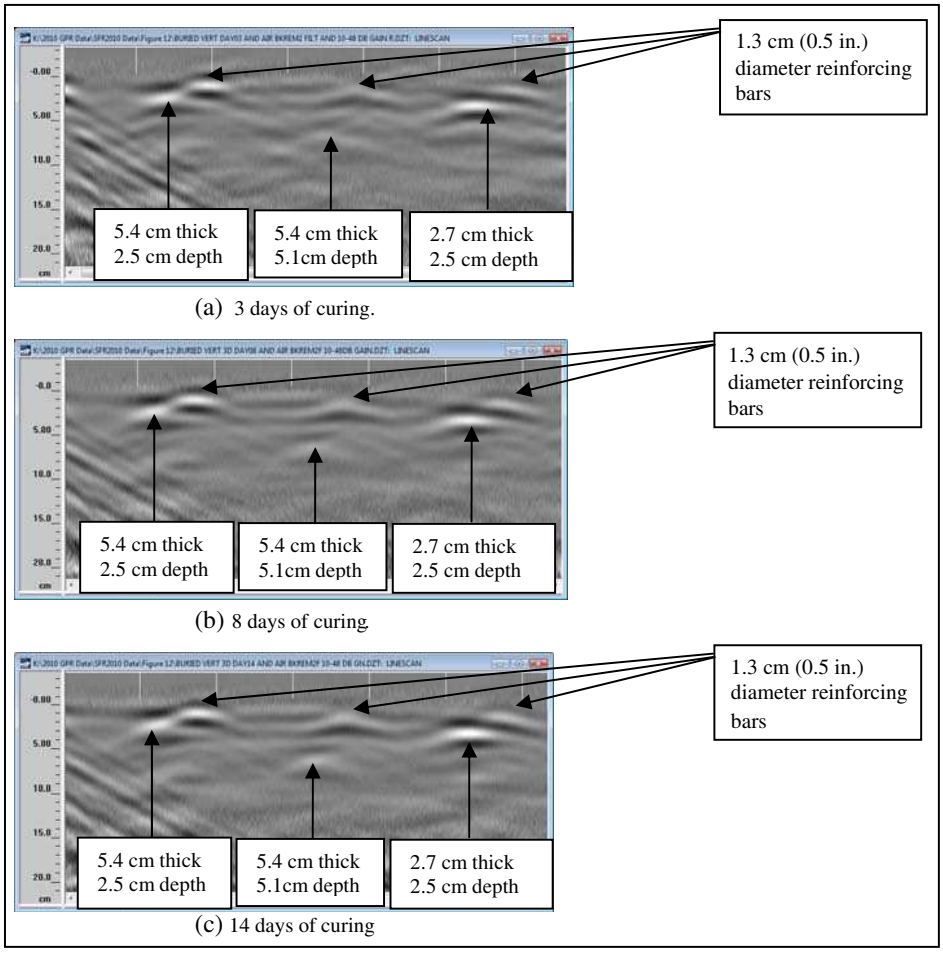

Figure 8: Comparison of data obtained from vertical profile over 9.0×9.0 cm (3.6×3.6 in.) voids buried 2.5 and 5.1 cm (1 and 2 in.) depths in the concrete following 3, 8, and 14 days of curing.

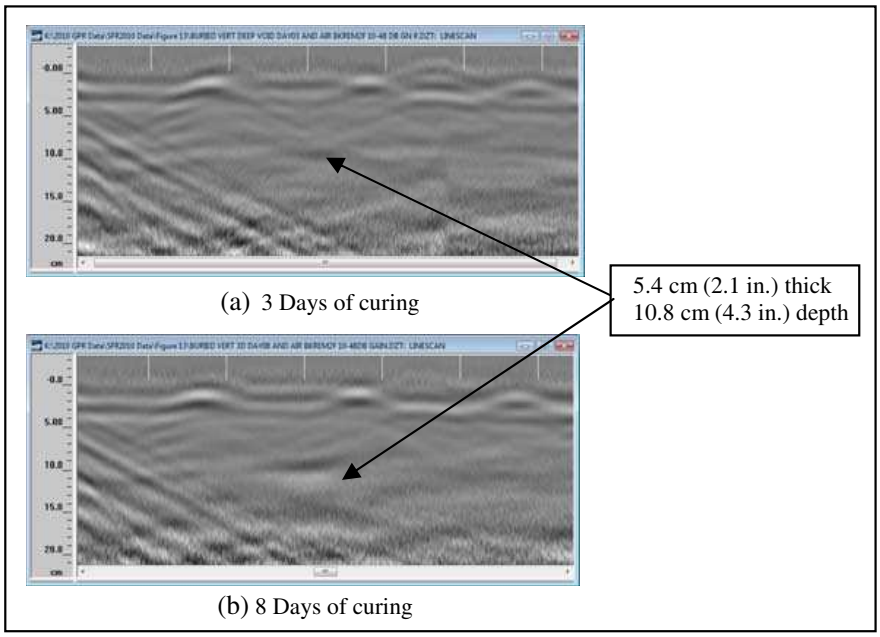

Figure 9: Comparison of data obtained from vertical profile over 9.0×9.0 cm (3.6×3.6 in.) voids buried 2.5 and 5.1 cm (1 and 2 in.) depths in the concrete following 3, 8, and 14 days of curing..

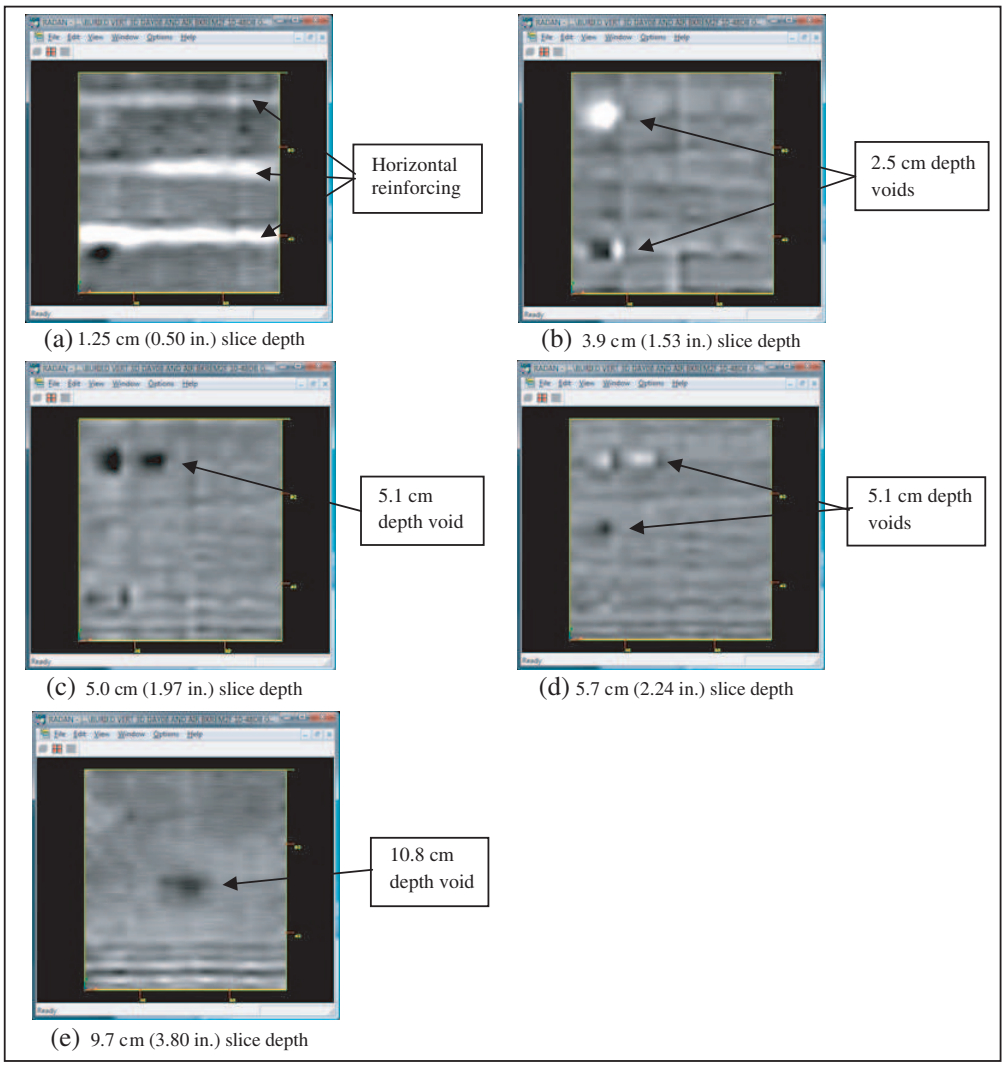

Figure 10: Thin, 0.1 cm (0.04 in.), depth slices from vertical line data after 8 days of curing over buried voids.

target, buried at a 5.1 cm (2.0 in.) depth is not easily isolated from the surrounding clutter. After 8 days of curing, this reflection is noticeable.

Figure 9 shows that the 18.1 × 18.1 cm (7.1 × 7.1 in.) target buried 10.9 cm (4.3 in.) in the concrete is detectable in both the 3 and 8 day data obtained from vertical profile lines over the center of the void. Again, to the trained eye, the presence of this void is evident, but to the unpracticed observer, it is far from clear that this is a void. It may be necessary in some cases to obtain a better understanding of the locations of the reinforcing and enhance the detectability of the buried voids by collecting a series of vertical profiles and creating a 3-D data cube.

Then horizontal slices of the data can be viewed in a 3-D rendering graphics program to image the voids. Fig. 10 shows 0.1 cm (0.04 in.) thick depth slices from vertical profiles obtained over the buried targets after 8 days of curing.

The thin slices capture the portion of the reflection waveform at the particular arrival time, which is converted to depth in Fig. 10. Therefore, the voids appear as light or dark anomalies, depending on the portion of the reflection waveform the slice intersects. The locations of the horizontal reinforcing are depicted in Fig. 10 at a slice depth of 1.25 cm (0.50 in.) The 2.5 cm (1 in.) deep voids are observed in a 3.9 cm (1.53 in.) depth slice. Both 5.1 cm (2 in.) deep voids are shown in the 5.7 cm (2.24 in.) depth slice. The void buried 10.9 cm (4.3 in.) is the dominant feature in the 9.7 cm (3.8 in.) depth slice.

6. DISCUSSION

It is a straight-forward task to detect, and to some degree characterize, voids flush to the backside of the ICF forms using appropriate GPR equipment, data collection, and data processing techniques.

The detection of these voids could conceivably be performed during pouring to locate sections of concrete that require additional vibration.

Alternatively, after the concrete is consolidated, GPR can be used as a quality control tool to assess the extent of voids flush to the back side of the form. The data collection methodology could consist of either a random set of vertical profile lines of data in which the percentage of voids detected per linear meter of data could be extrapolated to estimate the percentage of voids in the entire concrete structure. A second, more detailed, approach is to obtain data at a regular spacing and map the void extents in 3D coordinates so as to reconstruct the void surface area and provide an estimate of void depth as shown in Figs. 8(a) and 9.

The detection and characterization of voids buried in the concrete is limited by the clutter in the data caused by steel reinforcing, steel ties, plastic anchors embedded in the polystyrene forms, and the attenuation rate of the radar waves. Obtaining data from vertical profile lines minimizes the clutter from the regularly-spaced construction materials. The additional data processing steps yielded data that contained mostly reflections from the horizontal reinforcing and the voids. The main challenge after a minimum amount of curing, which will vary depending on the concrete mix, is to distinguish the reflections from the reinforcing from reflections from voids. The fact that the horizontal reinforcing are truly horizontal and must be placed at regular intervals because they are tied to the steel ties is significant in terms of distinguishing reinforcing reflections from void reflections. An experienced GPR operator could collect a number of vertical profiles, taking care to start the profile at the same vertical location, and mark out the reinforcing locations on the ICF surface. Then, any anomalies that appear in the data between the reinforcing reflections would necessarily be associated with voids. The alternative is to obtain data along a series of vertical parallel profile lines and construct 3-D depth slices, which were very useful in detecting all the buried voids $9.0 \times 9.0\,\text{cm}$ ($3.6 \times 3.6\,\text{in.}$) in dimensions after 8 days of curing in this study.

7. CONCLUSIONS

This investigation of the detectability of surface and buried voids in ICF concrete construction using GPR reveals that GPR, when appropriate equipment, data collection, and data processing techniques are employed, is very useful for detecting and characterizing surface voids. In terms of data collection, vertical profile line data contained less clutter from the metal ties and plastic anchors than horizontal profile line data. It was also found that buried voids can be detected after as little as 3 days of curing, depending on the concrete. The detectability of the buried voids increases as the concrete cures. Care must be exercised in interpreting data to locate buried voids as there can be confusion between void reflections and similar appearing reinforcing reflections. In some cases it may be beneficial to construct a 3-D data volume from a series of parallel lines of data and view depth slices to isolate the void reflections from the reinforcing reflections, which appear as continuous horizontal bands in the depth-slice data.

ACKNOWLEDGMENT

Special thanks to KeyTec, Japan and Ikarashi Construction for providing the ICF forms and technical assistance.

REFERENCES

1. He, X.-Q., Z.-Q. Zhu, Q.-Y. Liu, and G.-Yi. Lu, "Review of GPR rebar detection," *PIERS Proceedings*, 804–813, Beijing, China, March 23–27, 2009.
2. www.ecomii.com/building/insulated-concrete-forms.
3. Gajda, J. and A. M. Dowell, *Concrete Consolidation and the Potential for Voids in ICF Walls*, 20 pages, RD134, Portland Cement Association, Skokie, Illinois, 2003,

Prospective Applications of EM fields in Medicine

J. Vrba, **L. Oppl**, **D. Vrba**, **J. Vorlíček**, **B. Vrbová**, **and D. Havelka**
Department of EM Field, Czech Technical University, Technická 2, Prague 16627, Czech Rep.

Abstract— Medical applications of microwaves (i.e., a possibility to use microwave energy and/or microwave technique and technology for therapeutical purposes) are a quite new and a very rapidly developing field. Microwave thermotherapy is being used in medicine for the cancer treatment and treatment of some other diseases since early eighties. In this contribution we would like to offer general overview of present activities in the Czech Republic, i.e., clinical applications and results, technical aspects of thermo therapeutic equipment and last but not least, prospective diagnostics based on microwave principals ant technology and instrumentation.

1. INTRODUCTION

In this paper we would like to outline scope and new trends in medical applications of microwaves (i.e., microwave energy, microwave technique and technology), see Refs. [1–4]. We can divide these results and new trends into two major groups:

- clinical results and trends,
- technical results and trends.

2. CLINICAL RESULTS AND TRENDS

Applications of microwaves in medicine is a quite a new field of a high interest in the world (since early 80's). It is necessary to mention one of the most important trends in the research of medical applications of microwaves, i.e., the thermal effects of EM field (since early 80's a microwave thermotherapy is used for cancer treatment, for urology in BPH treatment and for some other areas of medicine; it can be used also in combination with other complementary treatment methods, eventually).

To give a basic overview, we can divide medical applications of microwaves in following three basic groups according to purpose, how are microwaves used:

- Microwave energy and/or technique used for the **treatment of patients** (with the use of either thermal or non-thermal effects — sometimes both of these types of effects can play its role).
- Microwave energy and/or technique used for **diagnostics of diseases** (e.g., by aid of permittivity measurements, attenuation measurements and very prospective in the near future can be a microwave tomography).
- Microwave energy and/or technique used as a **part of a treatment or diagnostic system** (e.g., linear accelerator).

As is given above, until now medical applications of microwaves are above all represented by the treatment methods based on thermal effect — i.e., we can speak about the Microwave thermotherapy, which can be further divided into three different modalities distinguished according to the goal temperature level or interval:

- diathermia: heating up to 41°C (applications in physiotherapy)
- hyperthermia: heating into the interval of 41–45°C (applications in oncology)
- thermodestruction/thermoablation: over 45°C (applications in urology)

First three of the following list of thermotherapeutical applications are just largely used in many countries around the world, last three instead are in this moment in the phase of very promissing projects:

- Oncology — cancer treatment.
- Physiotherapy — treatment of rheumatic diseases.
- Urology — BPH tratment.
- Cardiology — heart stimulations.

- Surgery — growing implants.
- Opthalmology — retina corrections.

e.g., in cancer treatment is thermotherapy usually used in the combination with some of other modalities used in the clinical oncology (e.g., radiotherapy, chemotherapy, immunotherapy or chirurgical treatment). It is used in USA, Japan and in many countries in Europe, including Czech Republic, from early 80s. Up to now local microwave hyperthermia for cancer treatment and thermotherapy of BPH are the most significant medical application of microwaves here In Czech Republic we have treated more than 500 patients. Results of the treatment of one of our patients group is given the following table:

Table 1: Clinical results of cancer treatment by radiotherapy.

Complete response of the tumor	**52.4 %**
Partial response of the tumor	**31.7 %**
Without response	**15.9 %**

Successful treatment thus has been indicated in the case of 84% of patients. This corresponds very well to the results published in EU and USA. Actual informations about microwave thermotherapy and its new developments is possible to get from "International Journal of Hyperthermia" issued by European Society for Hyperthermia Oncology (ESHO) together with North American Hyperthermia Society (NAHS) and Asian Society of Hyperthermia Oncology (ASHO). On the following photography, one of our patient represents typical results of the treatment.

before the treatment *at the end of the treatment*

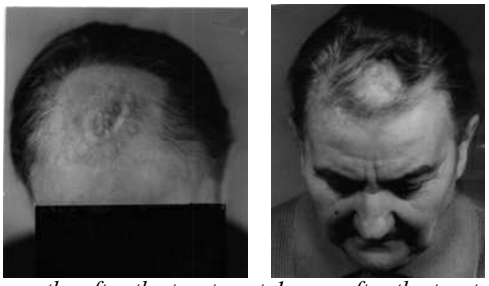

2 months after the treatment *1 year after the treatment*

Photo 1: Patient treated at the Institute of Radiation Oncology in Prague (combination of hyperthermia and radiotherapy).

Very interesting results for the future can give the research of microwave medical applications based on non-thermal effects. In the literature it is possible just now to identify research projects on:

- pain "reduction" (analogicaly to analgetics),
- possibility to increase of reaction capabilities of a human being,
- to examine the teaching capabilities, etc.

3. TECHNICAL RESULTS AND TRENDS

Our work is since 1981 focused on the design, optimization and tests of the microwave applicators for medical applications, above all for hyperthermia cancer and/or prostate treatment. This means to design a microwave structure capable:

- to transfer electromagnetic energy into the biological tissue,
- to get the best approximation of the area to be treated by the 3D distribution of SAR.

During last years we were interested in the local external applicators working at 434 MHz and 2450 MHz. These applicators were used for the treatment of more then 500 patients with superficial or subcutaneous tumors (up to the depth approx. 4–6 cm). Now, following new trends in this field, we continue our research in the important directions of deep local and regional applicators.

Most important technical fields of microwave thermotherapy development (covered also in our activities) can be specified as:

- Applicators: development and optimization of new applicators for more effective local, intracavitary and regional treatment.
- Treatment planning: mathematical and experimental modeling of the effective treatment.
- Noninvasive temperature measurement: research of the possibilities of new techniques (like NMR and US) for exact noninvasive measurements.
- Microwave medical diagnostics (e.g., Microwave Tomography).

4. DEEP LOCAL APPLICATORS

For the deep local thermotherapy treatment are very suitable waveguide type applicators based on the principle of either dielectric filled waveguide or on the principle of evanescent modes (i.e., waveguides excited below its cut-off frequency) — which is our specific solution and original contribution to the theory of microwave hyperthermia applicatorsTechnology of evanescent mode applicators enable us to design applicators with as small aperture as necessary also for relatively low frequencies, e.g., from 10 to 100 MHz, needed for deep penetration into the biological tissue (i.e., up to 10 centimetres under the body surface).

5. APPLICATORS COMPATIBLE WITH NON-INVASIVE TEMPERATURE MEASUREMENTS

As compatibility with non-invasive temperature measurements (ultrasound or NMR) is asked, it is important to minimize the metallic mass of the applicator. Therefore the applicator itself can be created by two inductive loops tuned to resonance by capacitive elements. Dimensions of the inductive elements are to be designed by our software, developed for this purpose. Optimum coupling between resonating loops is adjusted by microwave network analyzer. The position of the loops is fixed by perplex holder. As the heated tissue has high dielectric losses, both loops are very well separated and no resonance in heated area can occur. From this follows, that either the position of the loops with respect to heated area or the distance between the loops is not critical.

As an excellent compatibility of the applicator with non-invasive temperature measurement system (ultrasound or MR) is a fundamental condition for our project, we should have to use non-magnetic metallic sheets of minimized dimensions to create the conductive elements of the applicator. Therefore the applicator itself (see Fig. 1) is created by two inductive loops tuned to resonance by capacitive elements. Dimensions of these resonant loops were designed by our software, developed for this purpose. Coupling between coaxial feeder and resonant loops (not shown in Fig. 1) as well as a mutual coupling between resonating loops could be adjusted to optimum by microwave network analyzer.

The position of the loops is fixed by Perspex holder. There is a special cylindrical space for experimental animal in lower part of this holder. As the heated tissue has high dielectric losses, both loops are very well separated and so no significant resonance in heated area can occur. From this follows, that either the position of the loops with respect to heated area or the distance between the loops is not very critical. Evaluation of the discussed applicator:

First measurements to evaluate the basic properties of the discussed applicator were done on agar phantom of muscle tissue:

- evaluation of basic microwave properties (transfer of EM energy to the tissue, reflections),
- evaluation of compatibility with US and MR,
- calculation and measurement of SAR and temperature distribution and its homogeneity.

Exact tuning of the resonant loops to frequency 915 MHz has been easy and we could optimize the coupling between the coaxial feeder and resonant loops as well, reflection coefficient less than

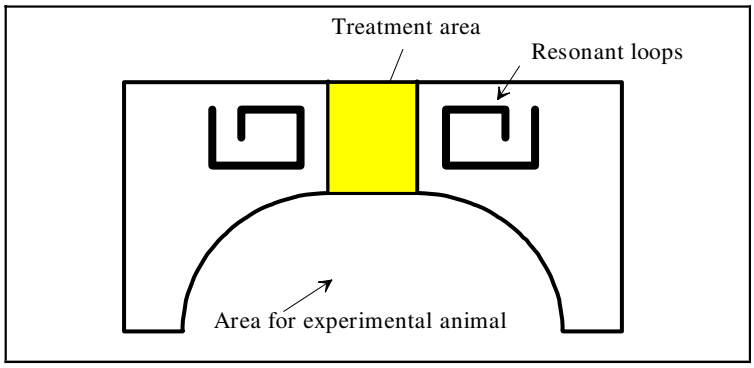

Figure 1: Arrangement of discussed microwave hyperthermia applicator.

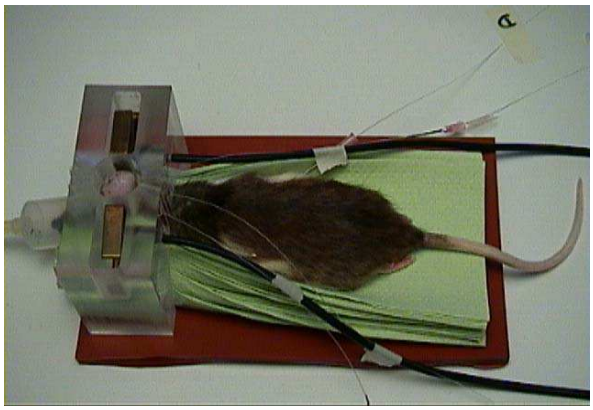

Figure 2: Photograph of the discussed applicator.

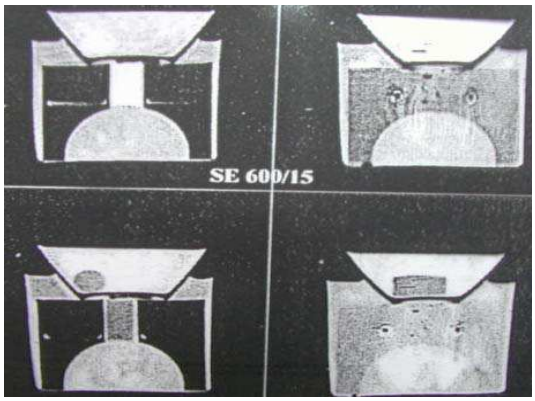

Figure 3: MR images of the discussed applicator for different levels of excited power.

0.1. We have tested the power to be delivered to the applicator to obtain sufficient temperature increase (approximately 4°C in less than 5 minutes is required). With power 10 W delivered to each loop for period of 2 minutes we succeeded to obtain the temperature increase of approximately 7°C. To keep the increased temperature for a long time, 2 W in each loops were sufficient. Similar values were obtained during first experiments on rats also. Even with higher level of delivered microwave power we did not observe the change of resonant frequency (caused by increased temperature of the loops).

We have tested the influence of the applicators on US diagnostics and MR imaging and the result of this evaluation shows very good compatibility. Only a negligible deterioration of the US images has been observed when the incident power was kept under 100 W.

Details about influence of microwave power on MR imaging are given in Fig. 3. We can see here a sequence of images of the discussed applicator made by MR unit for four different cases. First case (upper left) is image for the case without power excitation of the applicator. Second case (left down) a power of 10 W has been delivered to each loop. We can see quite clear configuration of the applicator set-up. Third case (upper right) gives situation when 20 W has been delivered to each loop. Slight noise but still quite a clear configuration of the applicator set-up can be observed. Fourth case (right down) gives situation when 40 W has been delivered to each loop. In this case noise disturbed the possibility to observe the configuration of the applicator.

6. CALCULATION AND MEASUREMENT OF THE TEMPERATURE DISTRIBUTION

In theoretical and experimental evaluation, the grade of homogeneity of the temperature distribution in the target area has been tested, see the Fig. 4. Our mathematical approach is based on idea of waveguide TM_{01} mode excited in the agar phantom under the given conditions (see the dashed lines). Measurement of SAR (full lines) has been done on agar phantom of the muscle tissue. Very good agreement has been obtained when verifying these results numerically (Fig. 5).

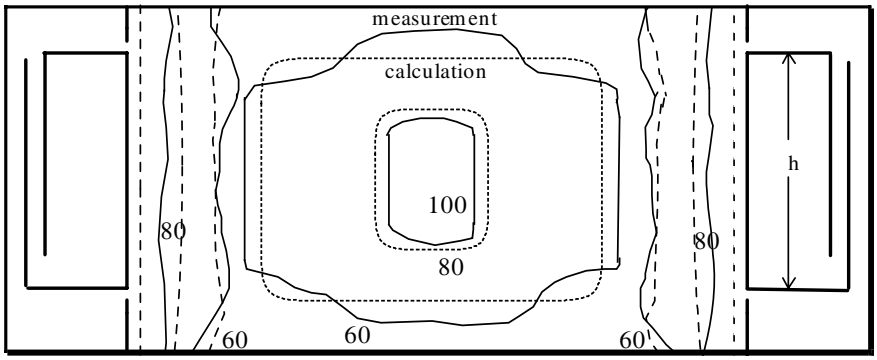

Figure 4: Normalized SAR distribution (both calculated and measured) in the heated agar phantom.

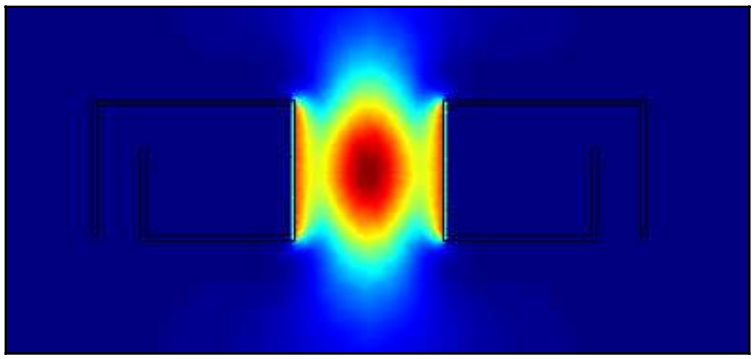

Figure 5: Numerical SAR analysis made by software product FEMLAB.

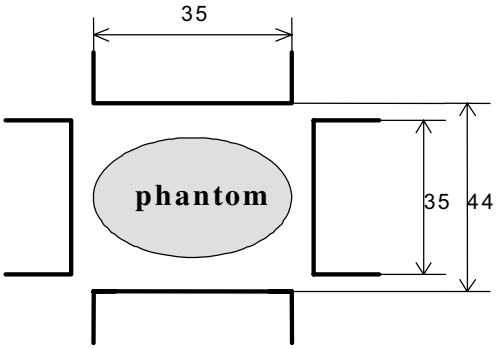

Figure 6: Set up of proposed regional applicator (4 evanescent mode waveguides applicators).

7. NEW PRINCIPLES FOR THE REGIONAL APPLICATORS

Goal of this work is the development of the new applicators with higher treatment effects. Methodological approach for the solution of the problem will be theoretical and experimental study of the new types of regional applicators. Our aim is to improve the present theoretical model to optimize the temperature distribution in the treated area.

We can design the regional applicators on the basis of the analytical description of the excited electromagnetic field for the case of simplified homogeneous model of the treated biological tissue. For a more realistic case of the non-homogeneous dielectric composition of the biological tissue the analytical calculation does not guarantee enough exact results. Therefore we would need to build the equipment for experimental tests of the applicators and we will study the possibilities of its numerical mathematical modeling.

8. CONCLUSIONS

Goal of this paper was to present basic overview of present state in the field of medical applications of microwaves plus to mention the basic trends for the near future. That has been done both

from clinical and technical points of view. Further new type of microwave applicator for cancer treatment has been described.

ACKNOWLEDGMENT

This research has been supported by the research program of the Ministry of Education and Youth of the Czech Republic: Transdisciplinary research in the area of BME.

REFERENCES

1. Field, S. B. and C. Franconi, Editors, "Physics and technology of hyperthermia," *NATO Seminar Proceedings*, Urbino, Italy, 1986.
2. Hand, J. and J. R. James, Editors, *Physical Techniques in Clinical Hyperthermia*, Wiley, New York, 1986.
3. Franconi, C., J. Vrba, and F. Montecchia, "27 MHz hybrid evanescent-mode applicators with flexible heating field for deep and safe subcutaneous hyperthermia," *International Journal of Hyperthermia*, Vol. 9, No. 5, 655–674, 1993.
4. Vrba, J., C. Franconi, and F. Montecchia, "Evanescent-mode applicators for subcutaneous hyperthermia," *IEEE Trans. on Biomedical Engineering*, Vol. 40, No. 5, 397–407, May 1993.

Applicators for Research of Biological Effects of EM Field

Jan Vrba[1], **Lukas Visek**[1], **Ladislav Oppl**[1], **and Luca Vannucci**[2]

[1]Department of EM Field, Czech Technical University in Prague, Prague, Czech Republic
[2]Institute of Microbiology, Czech Academy of Sciences, Prague, Czech Republic

Abstract— Research of interactions between EM field and biological systems is of growing interests elsewhere. Also here in czech republic there are several groups working in this field, often in international co-operations. We will describe here mainly basic technical equipment developed for 5 different research projects in the discussed area of interactions of EM field and biological systems.

1. INTRODUCTION

In present time, four research institutions here in the Czech Republic run research projects focused on studies of interactions between EM field and biological systems. These institutions are technically supported by Dept. of EM Field of the Czech Technical University in Prague. In this contribution, we would like to give more details about that projects and obtained technical results (i.e., description of developed exposition systems).

Three of discussed projects (1 in Germany and 2 here in Czech Republic) are basic research for simulation of the microwave hyperthermia treatment. Other two projects (both in Czech Republic are focused on simulation of the case of exposition by mobile phone.

In the modern view, cancer is intended as a complex illness, involving the cells that undergo to transformation, their environment, and the general responses at biochemical and biological levels induced in the host. Consequently, the anti-cancer btreatment protocols need to be multi-modal to reach curative effects. Especially after the technical improvements achieved in the last 15 years by bio-medical engineering, microscopy devices, and molecular biology methods, the combinations of therapeutic procedures are growing in interest in basic and clinical research.

The combination of applied biological research together to the physical sciences can offer important perspectives in anticancer therapy (e.g., different methodologies and technical devices for application of energies to pathological tissues).

The modern bioengineering knowledge applied to traditional tools, as the microscopy, has largely renewed and expanded the fields of their applications (e.g., *in vivo* imaging), pushing the interest for direct morpho-functional investigations of the biomedical problems.

2. WAVEGUIDE APPLICATOR

Very good results of EM field expositions in biological experiments can be obtained by simple but efficient waveguide applicators, see example in Fig. 1.

Waveguide offer a very big advantage — in approximately of fifty percents of its aperture the irradiated electromagnetic field is very near to a plane wave, which is basic assumption for good homogeneity of the heating and optimal treatment penetration.

Here described system is being used (shared) for research projects by two two institutions (Institure of Radiation Oncology in Prague and Institute of Microbiology of the Czech Academy of Sciences).

Figure 1: Waveguide applicator for biological experiments.

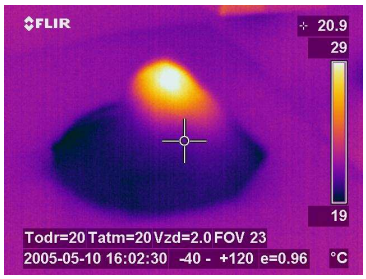

Figure 2: Waveguide applicator for biological experiments.

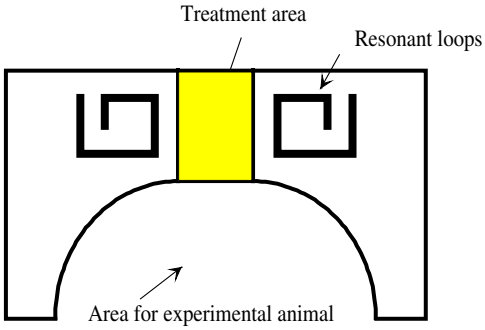

Figure 3: Arrangement of discussed microwave hyperthermia applicator.

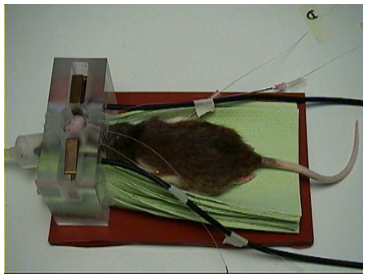

Figure 4: Photograph of the discussed applicator.

Aperture of this waveguide is 4.8×2.4 cm and it is excited at frequency 2.45 GHz. Effective heating is in the middle of the real aperture — its size is approximately 2.4×2.4 cm. Waveguide is filled by teflon to reduce its cut-off frequency. Power from generator is possible to control from 10 to 180 W, in these experiments we work between 10 and 20 W mostly.

3. EVALUATION OF WAVEGUIDE APPLICATOR

To evaluate this applicator from technical point of view we made a series of experiments, see, e.g., Fig. 2, where you can see example of measurement of temperature distribution by IR camera.

Here, you can see temperature distribution obtained on surface of a model of mouse made from agar — with a simulated tumour on mouse back. Experiment has been done by heating phantom during 2 minutes delivering a power of 10 W. Maximum of temperature increase has been found approximately 10°C. Similar results with different increase in temperature we have got also in other technical experiments on phantom or live mouse when power or heating time was changed.

4. ARRAY APPLICATOR

The main goal of the planned biological experiment is a hyperthermia treatment of the experimentally induced pedicle tumours of the rat to verify the feasibility of ultrasound diagnostics and magnetic resonance imaging respectively to map the temperature distribution in the target area of the treatment. That means to heat effective volume of approximately cylindrical shape (diameter approx. 2 cm, height approx. 3 cm). Temperature to be reached is 41°C or more (i.e., temperature increase of at least 4°C from starting point 37°C), time period of heating is 45 minutes.

Considering the necessary effective heating depth for the planned experiments, we have found 915 MHz to be suitable frequency. As an excellent compatibility of the applicator with non-invasive temperature measurement system (ultrasound or NMR) is a fundamental condition for our project, we should have to use non-magnetic metallic sheets of minimised dimensions to create the conductive elements of the applicator. Therefore the applicator itself (see Figs. 3 and 4) is created by two inductive loops tuned to resonance by capacitive elements [4, 5]. Dimensions of these resonant loops were designed by our software, developed for this purpose. Coupling between coaxial feeder and resonant loops (not shown in Fig. 3) as well as a mutual coupling between resonating loops could be adjusted to optimum by microwave network analyser.

This applicator has been developed for German Cancer Research Institute in Heidelberg. And it is being used there for a series of animal experiments to study effect of hyperthermia on tumours and possibility to combine hyperthermia with chemotherapy etc.

Compatibility of this applicator with a Magnetic resonance unit (MR) has been studied and it has been demonstrated.

ACKNOWLEDGMENT

This work was supported by the Czech Academy of Sciences, Institutional Research Concepts No. AV0Z50200510: "Hyperthermia and anticancer immunomodulation, morpho-functional study of micro-environmental interactions in melanoma model".

REFERENCES

1. Vrba, J., *Medical Applications of Microwaves*, CTU Press, Prague, 2003 (In Czech).

2. Hand, J. and J. R. James, *Physical Techniques in Clinical Hyperthermia*, Wiley, New York, 1986.
3. Franconi, C., J. Vrba, et al., "27 MHz hybrid evanescent-mode applicators," *Int. Journal of Hyperthermia*, Vol. 9, No. 5, 655–674, 1993.
4. Vrba, J., C. Franconi, et al., "Evanescent-mode applicators for hyperthermia," *IEEE Trans. on Biomedical Engineering*, Vol. 40, No. 5, 397–407, May 1993.

Microwave Applicators for Industrial Purposes

Jan Vrba[1], **Milan Stejskal**[2], **Jan Vrba (Jr.)**[3], **Tomas Vydra**[1], **and Marika Pourova**[1]

[1]Department of Electromagnetic Field, Czech Technical University in Prague
Technická 2, 166 27 Prague 6, Czech Republic
[2]Research Institute of Textile Machines, U jezu 4, Liberec, Czech Republic
[3]Institute of Theoretical Electrotechnic, RWTH Aachen, Aachen, Germany

Abstract— In this paper, we describe our new results dealing with microwave industrial applicators used for drying of textile materials. We have designed and evaluated two different types of these applicators: open-resonator-type and waveguide-type one. We describe here basic models of the discussed applicators, results of numerical modelling and experimental evaluation as well. Prototype of microwave drying machine working at frequency 2.45 GHz is reported.

1. INTRODUCTION

We work in the field of medical and industrial applications of microwave technique and technology more than thirty years. In this contribution, we will describe our new microwave industrial applicators used for drying of textile materials, which means a very thin layers with not very well defined position in the applicator. Moreover complex permittivity of dried textile is not constant during the procedure — it is changing through the time with respect to decrease content of moisture.

We have designed and evaluated two different types of these applicators: open-resonator-type and waveguide-type one. We would like to present theoretical models of the discussed applicators, results of EM field and SAR numerical modeling and experimental evaluation as well. Prototype of microwave drying machine working at frequency 2.45 GHz will be reported.

2. OPEN RESONATOR TYPE APPLICATOR

Further reported microwave drying machine consists of many drying cells (17 in our prototype machine) — each of them is based on the idea of open resonator (i.e., Fabry-Perrot resonator), see Fig. 1(a). Each of these cells has its own magnetron placed in waveguide holder. Dried textile material is in the middle plane between parallel conductive plates, distance between these plates is equal to $(3/2)\lambda$. In the Fig. 1(b), there is a calculated 2D distribution of electric field strength. Plane of the textile material is in this 2D model given by an abscissa in the middle of the resonator — in the same plane there is an expected maximum of electric field strength.

Optimization of the cells in longitudinal direction of drying machine is given by criteria to create maximum of electric field strength in the plane of dried textile (E field vector parallel to the textile plane), see diagrams in Figs. 2 and 3. We can describe each of the discussed cells by a simple schematic sketch (Fig. 2 upper part) and from it we can create oriented graph of this structure (Fig. 2-down).

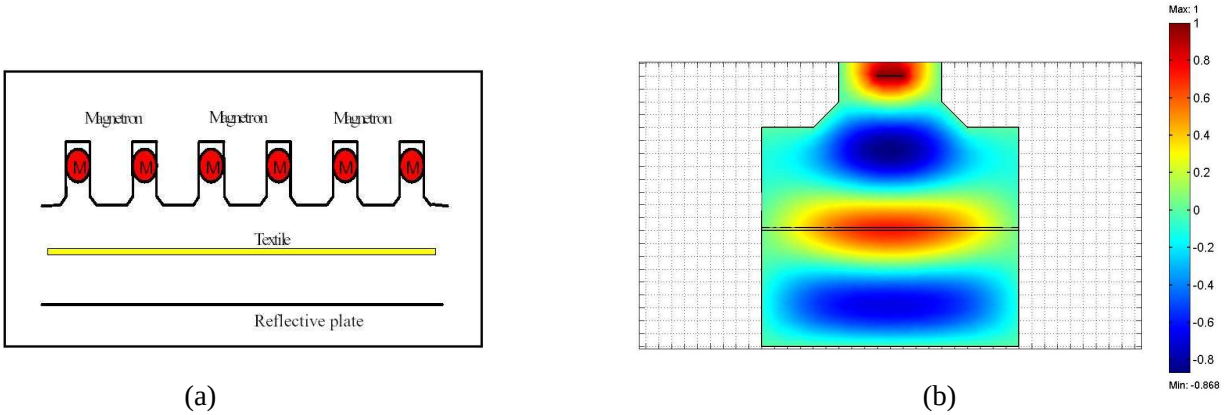

(a) (b)

Figure 1: (a) Schematics of 6 cells of open resonator type applicator for drying of textile materials. (b) E field strength 2D distribution in each one of that cells.

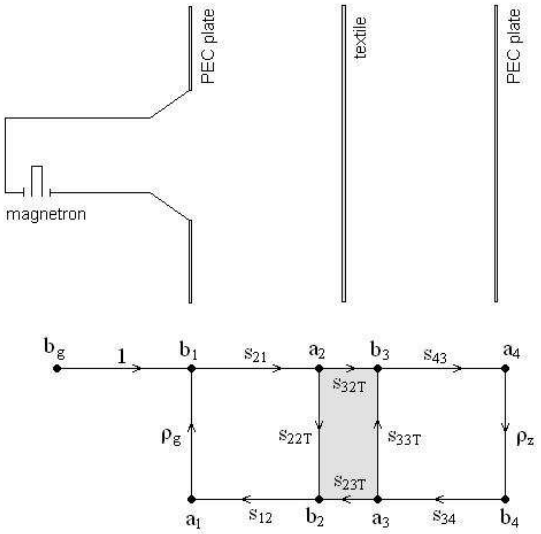

Figure 2: Tools for optimization of microwave dryer in longitudinal direction: oriented graph.

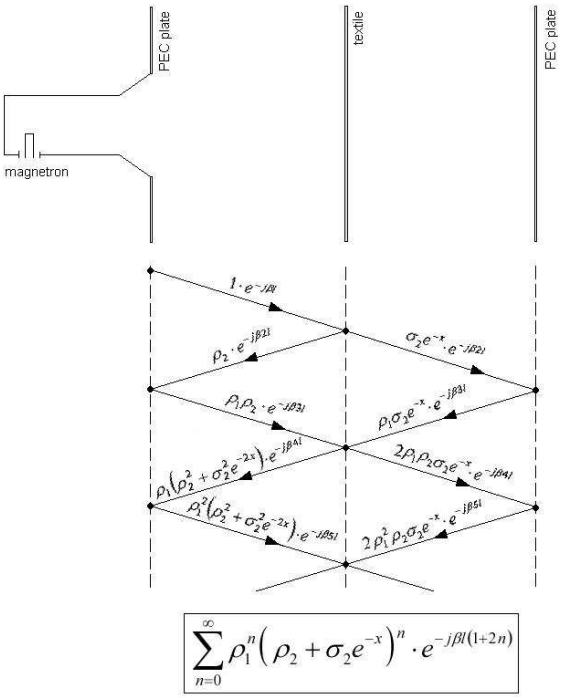

Figure 3: Tools for optimization of microwave dryer in longitudinal direction: graph of waves inside discussed applicator and resulting E field strength in textile plane.

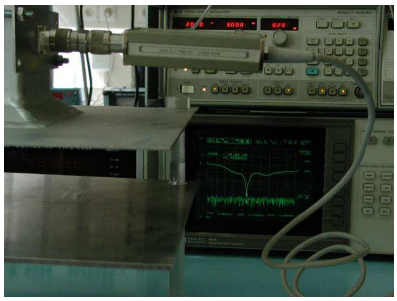

Figure 4: Measurement of S_{11} parameter.

Figure 5: Measurement of S_{21} parameter.

Alternatively, we can create diagram of EM waves inside this structure (Fig. 3-middle) and we will arrive to the resulting expression (Fig. 3-down) to be used for calculation of either E field strength or SAR distribution in the discussed applicator.

Figure 4 gives an example of measured S_{11} scattering parameter with respect to frequency. Resonance at 2.45 GHz has been easily obtained by tuning of the applicator by changing its length.

Figure 5 gives an example of possibility to map H or E field strength inside discussed applicator by aid of electric or magnetic dipole (elementary dipole or a small loop) via measurements of S_{21} scattering parameter with respect to frequency. Resonance at 2.45 GHz has been approved.

For our experiments we have built a prototype of discussed apparatus with 17 heating cells: a matrix of 6 cells in first raw, next 5 cells in the second raw and again 6 cells in the third raw - see apertures in the upper conductive plate in Fig. 6.

Optimization of overall microwave dryer means to approach to the best possible homogeneity of absorbed microwave energy (SAR) respectively homogeneity of the temperature in the textile material.

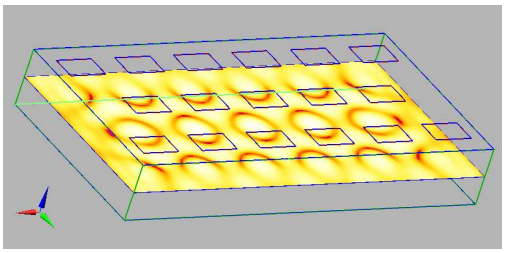

Figure 6: Microwave drying machine 3D schematics and SAR distribution in the plane of the wet textile material (6 cells in first raw, next 5 cells in the second raw and again 6 cells in third raw — calculated by SEMCAD).

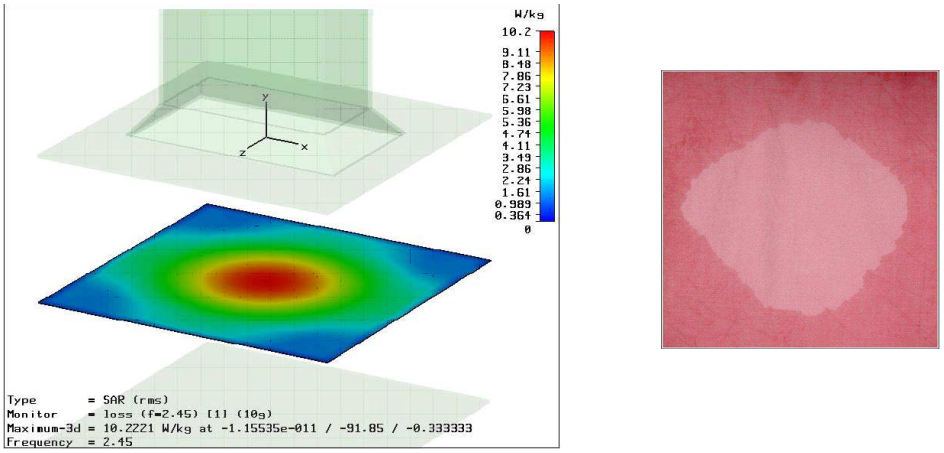

Figure 7: SAR calculated for one cell of drying machine and lower part gives an example of drying experiment.

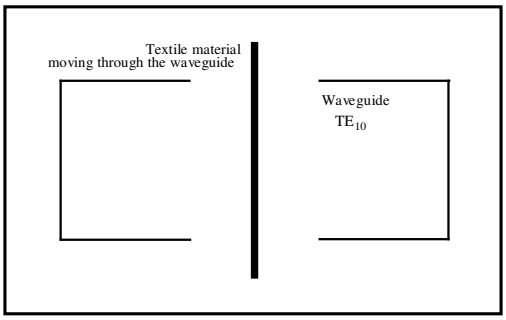

Figure 8: Waveguide-type applicator (example of one cell) for drying of textile materials.

Quite a good homogeneity of SAR can be observed and further improvement of its homogeneity is obtained thanks to the movement of textile material through microwave drying machine.

In upper part of Fig. 7, we can see SAR characteristics calculated for one cell of drying machine and lower part gives an example of drying experiment. Both process are not identical from physical point of view, even though there can be seen a very good agreement in its results.

3. WAVEGUIDE TYPE APPLICATOR

Waveguide applicator is waveguide with a longitudinal slot in wider side of waveguide. This slot is situated in the middle of this side, because maximum of electric field strength is here. Waveguide proportions choose so as to dominant mode TE_{10} could spread only inside to waveguide on working frequency. Waveguide applicator is displayed on next Fig. 8. Working frequency of waveguide is 2.45 GHz, so we can chose between two waveguides type R22 and R26. Our choice was waveguide R22, because working frequency is in upper bandwith section of dominant mode, and therefore waveguide R22 should have lower attenuation constant in comparison with the waveguide R26.

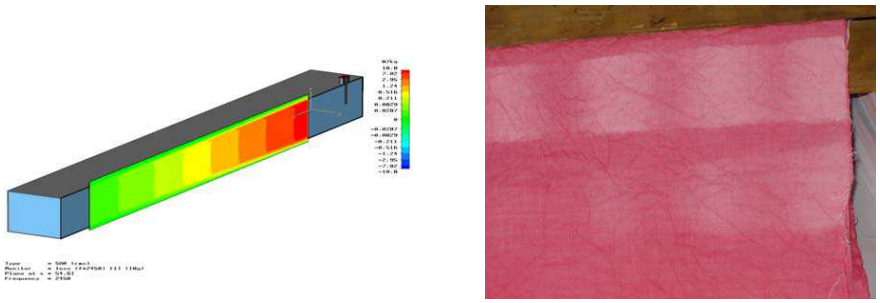

(a) (b)

Figure 9: SAR calculated (a) and measured (b) for the waveguide type applicator.

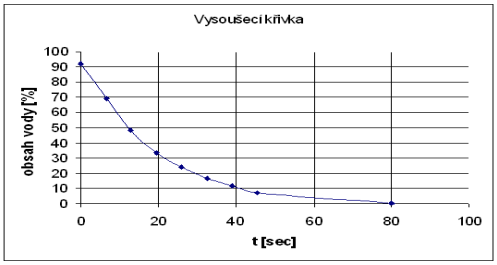

Figure 10: Typical drying characteristics of here described microwave drying systems (moisture in percents on vertical axis).

Figure 11: A prototype of microwave drying machine built in Cooperation of Czech Technical University in Prague and Research Institute of Textile Machines in Liberec.

Figure 12: Microwave part of the microwave drying machine.

Next figure gives an idea about SAR distribution, both simulated (A) and measured (B — lower strip is result of 6.5 s drying, the upper one belongs to 13 s.). In both cases, we can see a maximum of absorbed power from the side microwave input. But with decreasing moisture also SAR/temperature goes down and so we can create SAR maximum traveling along dried material.

4. RESULTS OF TEXTILE DRYING

Next figure shows results of measurements of the moisture content in the dried textile material with respect to time. We can observe, that microwave drying is very effective for moisture level above approximately 30%. Efficiency of microwave drying during our experiments was between 50 and 80% (it goes down when level of moisture inside dried textile material is decreased during drying process).

5. PROTOTYPE OF MICROWAVE MACHINE FOR TEXTILE DRYING

Based on theoretical considerations a prototype of microwave drying machine has been built by Research Institute of Textile Machines and Technical University in Liberec, see Fig. 11. Following Fig. 12 gives a look inside microwave part of the system. Waveguide horn apertures of several cells can be seen here (together with holes used to withdraw of the moisture).

6. CONCLUSION

As novel results of our work we would like to mention description and basic evaluation of two different microwave industrial applicators to be used for drying of textile materials: open-resonator-type and waveguide-type one. Principle of prototype of microwave drying machine working at frequency 2.45 GHz has been reported in details.

REFERENCES

1. Vrba, J., *Applications of Microwave Techniques*, CTU Press, 2001.
2. Stejskal, M., J. Vrba, R. Klepl, and L. Oppl, "Microwave drier for fabrics," European Patent number EP1319914 A2 18-06-2003.
3. Vrba, J., "Microwave drying of textile materials," Series of Research Reports, 2001–2004.
4. Pourová, M., "Microwave drying of textile materials," Diploma Thesis, CTU, 2003.
5. Žák, O., "Waveguide applicator for drying of textile materials," Diploma Thesis, CTU, 2004.

Closed-form Green's Functions for Stratified Uniaxial Anisotropic Medium

P. P. Ding[1, 2], S. Zouhdi[1], L. W. Li[2], and S. P. Yeo[2]

[1]Laboratoire de Genie Electrique de Paris, Supelec, France
[2]Department of Electrical and Computer Engineering, National University of Singapore, Singapore

Abstract— The spatial-domain Green's functions for electric and magnetic fields are cast into closed forms with two-level approximation of the spectral-domain Green's functions in the stratified uniaxial anisotropic medium. The spectral-domain Green's functions for general source and observation points are derived by the wave iterative algorithm. The explicit formulations reduced to the isotropic case agrees well with the existing results corresponding to the isotropic medium. By using the discrete complex image method, the closed-form Green's functions are obtained in the spatial domain. Numerical examples show that the closed-form Green's functions in the stratified uniaxial anisotropic medium have good accuracy and efficiency.

1. INTRODUCTION

The dyadic Green's function in the stratified uniaxial anisotropic medium has attracted much attention because of its wide range of practical applications, ranging from geophysics to microwave integrated circuits [1–4]. For the last decades, several methods have been employed for the derivation of the spectral-domain Green's functions in the stratified uniaxial anisotropic medium, including wave iterative technique [5] and cylindrical vector eigenfunction expansion method [6]. The wave iterative technique uses the kDB system of coordinates and the Fourier transform to derive the unbounded Green's function formulation and then the dyadic Green's function in any arbitrary layer is obtained in terms of the global upward and downward reflection and transmission matrices. The cylindrical vector eigenfunction expansion technique uses the Ohm-Rayleigh method and a set of solenoidal vector wave functions to derive the unbounded Green's function and then the general scattering dyadic Green's function in any arbitrary layer is obtained by using the scattering superposition. Due to the sufficiently complicated formulations in terms of the defined dyadic or matrix, the closed-form Green's functions in the spatial domain are quite difficult to obtain by the two methods.

It is the purpose of this paper to present a complete set of formulations for the dyadic Green's function in the stratified uniaxial anisotropic medium and to calculate the closed-form Green's functions in the spatial domain. The electromagnetic fields are obtained in terms of dyadic Green's functions of electric or magnetic type represented in the spatial domain. Section 2 deals with the formulations of the dyadic Green's functions for arbitrary locations of the source and observation point. By using the discrete complex image method (DCIM), the closed-form Green's function can be successfully obtained [7]. In Section 3, in order to verify the accuracy of the present formulations, they are compared with existing results corresponding to isotropic medium which have been well-documented [8, 9]. Then, several numerical results are presented to show the efficiency and accuracy of the closed-form Green's function, compared with the exact Green's function obtained by the numerical integration.

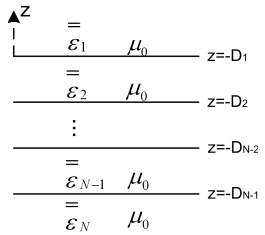

Figure 1: Geometry of the stratied uniaxial anisotropic medium.

2. FORMULATION

For the sake of illustration, we consider a stratified uniaxial anisotropic medium with optic axis in the $\hat{z}$ direction, as shown in Fig. 1. The wave iterative method presented in [5] is employed to construct the dyadic Green's functions in the spectral domain. In the presence of an arbitrary oriented electric current point source, the Green's functions can be represented as (1), (8), (13), corresponding to the relatively different locations between the source point and the observation point. The source and observation point is located at the layer m and n, respectively. The formulations related with the magnetic field Green's functions and the magnetic sources have the similar forms, which are not detailed here. The fields are assumed to vary harmonically as $e^{-i\omega t}$ in this work.

When $m = n$,

$$\begin{aligned}
\overline{\overline{G}}_{nn}(\mathbf{r},\mathbf{r}') = {} & \frac{1}{i\omega\hat{z}\cdot\overline{\overline{\varepsilon}}_n\cdot\hat{z}}\hat{z}\hat{z}\delta(\mathbf{r}-\mathbf{r}') - \frac{\omega\mu_n}{4\pi}\int_0^\infty dk_\rho\, k_\rho\cdot J_0(k_\rho\rho)\cdot\Big[e^{i\gamma_{\mathrm{I}\alpha}^{(n)}(z_n-z_n')}\mathbf{e}_{\mathrm{I}\alpha}^{(n)}\mathbf{u}_{\mathrm{I}\alpha}^{(n)} \\
& + e^{i\gamma_{\mathrm{II}\alpha}^{(n)}(z_n-z_n')}\mathbf{e}_{\mathrm{II}\alpha}^{(n)}\mathbf{u}_{\mathrm{II}\alpha}^{(n)} + e^{i\gamma_{\mathrm{I}u}^{(n)}(z_n-z_n')}A_1^{(1,1)}\mathbf{e}_{\mathrm{I}u}^{(n)}\mathbf{u}_{\mathrm{I}u}^{(n)} + e^{i\gamma_{\mathrm{I}u}^{(n)}z_n-i\gamma_{\mathrm{II}u}^{(n)}z_n'}A_1^{(1,2)}\mathbf{e}_{\mathrm{I}u}^{(n)}\mathbf{u}_{\mathrm{II}u}^{(n)} \\
& + e^{i\gamma_{\mathrm{II}u}^{(n)}z_n-i\gamma_{\mathrm{I}u}^{(n)}z_n'}A_1^{(2,1)}\mathbf{e}_{\mathrm{II}u}^{(n)}\mathbf{u}_{\mathrm{I}u}^{(n)} + e^{i\gamma_{\mathrm{II}u}^{(n)}(z_n-z_n')}A_1^{(2,2)}\mathbf{e}_{\mathrm{II}u}^{(n)}\mathbf{u}_{\mathrm{II}u}^{(n)} + e^{i\gamma_{\mathrm{I}u}^{(n)}z_n-i\gamma_{\mathrm{I}d}^{(n)}z_n'}A_2^{(1,1)}\mathbf{e}_{\mathrm{I}u}^{(n)}\mathbf{u}_{\mathrm{I}d}^{(n)} \\
& + e^{i\gamma_{\mathrm{I}u}^{(n)}z_n-i\gamma_{\mathrm{II}d}^{(n)}z_n'}A_2^{(1,2)}\mathbf{e}_{\mathrm{I}u}^{(n)}\mathbf{u}_{\mathrm{II}d}^{(n)} + e^{i\gamma_{\mathrm{II}u}^{(n)}z_n-i\gamma_{\mathrm{I}d}^{(n)}z_n'}A_2^{(2,1)}\mathbf{e}_{\mathrm{II}u}^{(n)}\mathbf{u}_{\mathrm{I}d}^{(n)} + e^{i\gamma_{\mathrm{II}u}^{(n)}z_n-i\gamma_{\mathrm{II}d}^{(n)}z_n'}A_2^{(2,2)}\mathbf{e}_{\mathrm{II}u}^{(n)}\mathbf{u}_{\mathrm{II}d}^{(n)} \\
& + e^{i\gamma_{\mathrm{I}d}^{(n)}z_n-i\gamma_{\mathrm{I}u}^{(n)}z_n'}A_3^{(1,1)}\mathbf{e}_{\mathrm{I}d}^{(n)}\mathbf{u}_{\mathrm{I}u}^{(n)} + e^{i\gamma_{\mathrm{I}d}^{(n)}z_n-i\gamma_{\mathrm{II}u}^{(n)}z_n'}A_3^{(1,2)}\mathbf{e}_{\mathrm{I}d}^{(n)}\mathbf{u}_{\mathrm{II}u}^{(n)} + e^{i\gamma_{\mathrm{II}d}^{(n)}z_n-i\gamma_{\mathrm{I}u}^{(n)}z_n'}A_3^{(2,1)}\mathbf{e}_{\mathrm{II}d}^{(n)}\mathbf{u}_{\mathrm{I}u}^{(n)} \\
& + e^{i\gamma_{\mathrm{II}d}^{(n)}z_n-i\gamma_{\mathrm{II}u}^{(n)}z_n'}A_3^{(2,2)}\mathbf{e}_{\mathrm{II}d}^{(n)}\mathbf{u}_{\mathrm{II}u}^{(n)} + e^{i\gamma_{\mathrm{I}d}^{(n)}(z_n-z_n')}A_4^{(1,1)}\mathbf{e}_{\mathrm{I}d}^{(n)}\mathbf{u}_{\mathrm{I}d}^{(n)} + e^{i\gamma_{\mathrm{I}d}^{(n)}z_n-i\gamma_{\mathrm{II}d}^{(n)}z_n'}A_4^{(1,2)}\mathbf{e}_{\mathrm{I}d}^{(n)}\mathbf{u}_{\mathrm{II}d}^{(n)} \\
& + e^{i\gamma_{\mathrm{II}d}^{(n)}z_n-i\gamma_{\mathrm{I}d}^{(n)}z_n'}A_4^{(2,1)}\mathbf{e}_{\mathrm{II}d}^{(n)}\mathbf{u}_{\mathrm{I}d}^{(n)} + e^{i\gamma_{\mathrm{II}d}^{(n)}(z_n-z_n')}A_4^{(2,2)}\mathbf{e}_{\mathrm{II}d}^{(n)}\mathbf{u}_{\mathrm{II}d}^{(n)}\Big] \qquad (1)
\end{aligned}$$

where

$$\mathbf{A}_2 = \Big[\mathbf{G}_u^{(n)}(z_n=-D_n)\Big]^{-1}\cdot\mathbf{R}_{Dn,n+1}\cdot\mathbf{N}_n\cdot\Big[\mathbf{G}_d^{(n)}(z_n=-D_n)\Big] \qquad (2)$$

$$\mathbf{A}_1 = \mathbf{A}_2\cdot\mathbf{G}_d^{(n)}(z_n=D_{n-1})\cdot\mathbf{R}_{Un,n-1}\cdot\mathbf{G}_u^{(n)}(z_n=-D_{n-1}) \qquad (3)$$

$$\mathbf{A}_3 = \Big[\mathbf{G}_d^{(n)}(z_n=-D_{n-1})\Big]^{-1}\cdot\mathbf{R}_{Un,n-1}\cdot\mathbf{M}_n\cdot\Big[\mathbf{G}_u^{(n)}(z_n=-D_{n-1})\Big] \qquad (4)$$

$$\mathbf{A}_4 = \mathbf{A}_3\cdot\mathbf{G}_u^{(n)}(z_n=D_n)\cdot\mathbf{R}_{Dn,n+1}\cdot\mathbf{G}_d^{(n)}(z_n=-D_n) \qquad (5)$$

$$\mathbf{M}_n = \Big[\mathbf{I}-\mathbf{G}_u^{(n)}(z_n=-D_{n-1}+D_n)\cdot\mathbf{R}_{Dn,n+1}\cdot\mathbf{G}_d^{(n)}(z_n=-D_n+D_{n-1})\cdot\mathbf{R}_{Un,n-1}\Big]^{-1} \qquad (6)$$

$$\mathbf{N}_n = \Big[\mathbf{I}-\mathbf{G}_d^{(n)}(z_n=-D_n+D_{n-1})\cdot\mathbf{R}_{Un,n-1}\cdot\mathbf{G}_u^{(n)}(z_n=-D_{n-1}+D_n)\cdot\mathbf{R}_{Dn,n+1}\Big]^{-1} \qquad (7)$$

When the source point z' is located above the observation point z, α is equal to d. Otherwise, α is equal to u.

When $m > n$,

$$\begin{aligned}
\overline{\overline{G}}_{nm}(\mathbf{r},\mathbf{r}') = {} & -\frac{\omega\mu_m}{4\pi}\int_0^\infty dk_\rho\, k_\rho\cdot J_0(k_\rho\rho)\cdot\Big[e^{i\gamma_{\mathrm{I}u}^{(n)}(z_n+D_n)+i\gamma_{\mathrm{I}u}^{(m)}(-z_m'-D_{m-1})}B_1^{(1,1)}\mathbf{e}_{\mathrm{I}u}^{(n)}\mathbf{u}_{\mathrm{I}u}^{(m)} \\
& + e^{i\gamma_{\mathrm{I}u}^{(n)}(z_n+D_n)+i\gamma_{\mathrm{II}u}^{(m)}(-z_m'-D_{m-1})}B_1^{(1,2)}\mathbf{e}_{\mathrm{I}u}^{(n)}\mathbf{u}_{\mathrm{II}u}^{(m)} + e^{i\gamma_{\mathrm{II}u}^{(n)}(z_n+D_n)+i\gamma_{\mathrm{I}u}^{(m)}(-z_m'-D_{m-1})}B_1^{(2,1)}\mathbf{e}_{\mathrm{II}u}^{(n)}\mathbf{u}_{\mathrm{I}u}^{(m)} \\
& + e^{i\gamma_{\mathrm{II}u}^{(n)}(z_n+D_n)+i\gamma_{\mathrm{II}u}^{(m)}(-z_m'-D_{m-1})}B_1^{(2,2)}\mathbf{e}_{\mathrm{II}u}^{(n)}\mathbf{u}_{\mathrm{II}u}^{(m)} + e^{i\gamma_{\mathrm{I}u}^{(n)}(z_n+D_n)+i\gamma_{\mathrm{I}d}^{(m)}(-z_m'-D_m)}B_2^{(1,1)}\mathbf{e}_{\mathrm{I}u}^{(n)}\mathbf{u}_{\mathrm{I}d}^{(m)} \\
& + e^{i\gamma_{\mathrm{I}u}^{(n)}(z_n+D_n)+i\gamma_{\mathrm{II}d}^{(m)}(-z_m'-D_m)}B_2^{(1,2)}\mathbf{e}_{\mathrm{I}u}^{(n)}\mathbf{u}_{\mathrm{II}d}^{(m)} + e^{i\gamma_{\mathrm{II}u}^{(n)}(z_n+D_n)+i\gamma_{\mathrm{I}d}^{(m)}(-z_m'-D_m)}B_2^{(2,1)}\mathbf{e}_{\mathrm{II}u}^{(n)}\mathbf{u}_{\mathrm{I}d}^{(m)} \\
& + e^{i\gamma_{\mathrm{II}u}^{(n)}(z_n+D_n)+i\gamma_{\mathrm{II}d}^{(m)}(-z_m'-D_m)}B_2^{(2,2)}\mathbf{e}_{\mathrm{II}u}^{(n)}\mathbf{u}_{\mathrm{II}d}^{(m)} + e^{i\gamma_{\mathrm{I}d}^{(n)}(z_n+D_{n+1})+i\gamma_{\mathrm{I}u}^{(m)}(-z_m'-D_{m-1})}B_3^{(1,1)}\mathbf{e}_{\mathrm{I}d}^{(n)}\mathbf{u}_{\mathrm{I}u}^{(m)} \\
& + e^{i\gamma_{\mathrm{I}d}^{(n)}(z_n+D_{n+1})+i\gamma_{\mathrm{II}u}^{(m)}(-z_m'-D_{m-1})}B_3^{(1,2)}\mathbf{e}_{\mathrm{I}d}^{(n)}\mathbf{u}_{\mathrm{II}u}^{(m)} + e^{i\gamma_{\mathrm{II}d}^{(n)}(z_n+D_{n+1})+i\gamma_{\mathrm{I}u}^{(m)}(-z_m'-D_{m-1})}B_3^{(2,1)}\mathbf{e}_{\mathrm{II}d}^{(n)}\mathbf{u}_{\mathrm{I}u}^{(m)} \\
& + e^{i\gamma_{\mathrm{II}d}^{(n)}(z_n+D_{n+1})+i\gamma_{\mathrm{II}u}^{(m)}(-z_m'-D_{m-1})}B_3^{(2,2)}\mathbf{e}_{\mathrm{II}d}^{(n)}\mathbf{u}_{\mathrm{II}u}^{(m)} + e^{i\gamma_{\mathrm{I}d}^{(n)}(z_n+D_{n+1})+i\gamma_{\mathrm{I}d}^{(m)}(-z_m'-D_m)}B_4^{(1,1)}\mathbf{e}_{\mathrm{I}d}^{(n)}\mathbf{u}_{\mathrm{I}d}^{(m)} \\
& + e^{i\gamma_{\mathrm{I}d}^{(n)}(z_n+D_{n+1})+i\gamma_{\mathrm{II}d}^{(m)}(-z_m'-D_m)}B_4^{(1,2)}\mathbf{e}_{\mathrm{I}d}^{(n)}\mathbf{u}_{\mathrm{II}d}^{(m)} + e^{i\gamma_{\mathrm{II}d}^{(n)}(z_n+D_{n+1})+i\gamma_{\mathrm{I}d}^{(m)}(-z_m'-D_m)}B_4^{(2,1)}\mathbf{e}_{\mathrm{II}d}^{(n)}\mathbf{u}_{\mathrm{I}d}^{(m)} \\
& + e^{i\gamma_{\mathrm{II}d}^{(n)}(z_n+D_{n+1})+i\gamma_{\mathrm{II}d}^{(m)}(-z_m'-D_m)}B_4^{(2,2)}\mathbf{e}_{\mathrm{II}d}^{(n)}\mathbf{u}_{\mathrm{II}d}^{(m)}\Big] \qquad (8)
\end{aligned}$$

where

$$\mathbf{B}_1 = \mathbf{Y}_{mn}^{(u)} \cdot \mathbf{M}_m \tag{9}$$

$$\mathbf{B}_2 = \mathbf{B}_1 \cdot \mathbf{G}_u^{(m)}(z_m = -D_{m-1} + D_m) \cdot \mathbf{R}_{Dm,m+1} \tag{10}$$

$$\mathbf{B}_3 = \mathbf{R}_{Un,n-1} \cdot \mathbf{G}_u^{(n)}(z_n = -D_{n-1} + D_n) \cdot \mathbf{B}_1 \tag{11}$$

$$\mathbf{B}_4 = \mathbf{B}_3 \cdot \mathbf{G}_u^{(m)}(z_m = -D_{m-1} + D_m) \cdot \mathbf{R}_{Dm,m+1} \tag{12}$$

When $m < n$,

$$\begin{aligned}
\overline{\overline{G}}_{nm}(\mathbf{r},\mathbf{r}') = -\frac{\omega\mu_m}{4\pi}\int_0^\infty dk_\rho\, k_\rho \cdot J_0(k_\rho\rho) \cdot \Big[& e^{i\gamma_{\mathrm{I}u}^{(n)}(z_n+D_n)+i\gamma_{\mathrm{I}u}^{(m)}(-z'_m-D_{m-1})} C_1^{(1,1)} \mathbf{e}_{\mathrm{I}u}^{(n)} \mathbf{u}_{\mathrm{I}u}^{(m)} \\
& + e^{i\gamma_{\mathrm{I}u}^{(n)}(z_n+D_n)+i\gamma_{\mathrm{II}u}^{(m)}(-z'_m-D_{m-1})} C_1^{(1,2)} \mathbf{e}_{\mathrm{I}u}^{(n)} \mathbf{u}_{\mathrm{II}u}^{(m)} + e^{i\gamma_{\mathrm{II}u}^{(n)}(z_n+D_n)+i\gamma_{\mathrm{I}u}^{(m)}(-z'_m-D_{m-1})} C_1^{(2,1)} \mathbf{e}_{\mathrm{II}u}^{(n)} \mathbf{u}_{\mathrm{I}u}^{(m)} \\
& + e^{i\gamma_{\mathrm{II}u}^{(n)}(z_n+D_n)+i\gamma_{\mathrm{II}u}^{(m)}(-z'_m-D_{m-1})} C_1^{(2,2)} \mathbf{e}_{\mathrm{II}u}^{(n)} \mathbf{u}_{\mathrm{II}u}^{(m)} + e^{i\gamma_{\mathrm{I}u}^{(n)}(z_n+D_n)+i\gamma_{\mathrm{I}d}^{(m)}(-z'_m-D_m)} C_2^{(1,1)} \mathbf{e}_{\mathrm{I}u}^{(n)} \mathbf{u}_{\mathrm{I}d}^{(m)} \\
& + e^{i\gamma_{\mathrm{I}u}^{(n)}(z_n+D_n)+i\gamma_{\mathrm{II}d}^{(m)}(-z'_m-D_m)} C_2^{(1,2)} \mathbf{e}_{\mathrm{I}u}^{(n)} \mathbf{u}_{\mathrm{II}d}^{(m)} + e^{i\gamma_{\mathrm{II}u}^{(n)}(z_n+D_n)+i\gamma_{\mathrm{I}d}^{(m)}(-z'_m-D_m)} C_2^{(2,1)} \mathbf{e}_{\mathrm{II}u}^{(n)} \mathbf{u}_{\mathrm{I}d}^{(m)} \\
& + e^{i\gamma_{\mathrm{II}u}^{(n)}(z_n+D_n)+i\gamma_{\mathrm{II}d}^{(m)}(-z'_m-D_m)} C_2^{(2,2)} \mathbf{e}_{\mathrm{II}u}^{(n)} \mathbf{u}_{\mathrm{II}d}^{(m)} + e^{i\gamma_{\mathrm{I}d}^{(n)}(z_n+D_{n-1})+i\gamma_{\mathrm{I}u}^{(m)}(-z'_m-D_{m-1})} C_3^{(1,1)} \mathbf{e}_{\mathrm{I}d}^{(n)} \mathbf{u}_{\mathrm{I}u}^{(m)} \\
& + e^{i\gamma_{\mathrm{I}d}^{(n)}(z_n+D_{n-1})+i\gamma_{\mathrm{II}u}^{(m)}(-z'_m-D_{m-1})} C_3^{(1,2)} \mathbf{e}_{\mathrm{I}d}^{(n)} \mathbf{u}_{\mathrm{II}u}^{(m)} + e^{i\gamma_{\mathrm{II}d}^{(n)}(z_n+D_{n-1})+i\gamma_{\mathrm{I}u}^{(m)}(-z'_m-D_{m-1})} C_3^{(2,1)} \mathbf{e}_{\mathrm{II}d}^{(n)} \mathbf{u}_{\mathrm{I}u}^{(m)} \\
& + e^{i\gamma_{\mathrm{II}d}^{(n)}(z_n+D_{n-1})+i\gamma_{\mathrm{II}u}^{(m)}(-z'_m-D_{m-1})} C_3^{(2,2)} \mathbf{e}_{\mathrm{II}d}^{(n)} \mathbf{u}_{\mathrm{II}u}^{(m)} + e^{i\gamma_{\mathrm{I}d}^{(n)}(z_n+D_{n-1})+i\gamma_{\mathrm{I}d}^{(m)}(-z'_m-D_m)} C_4^{(1,1)} \mathbf{e}_{\mathrm{I}d}^{(n)} \mathbf{u}_{\mathrm{I}d}^{(m)} \\
& + e^{i\gamma_{\mathrm{I}d}^{(n)}(z_n+D_{n-1})+i\gamma_{\mathrm{II}d}^{(m)}(-z'_m-D_m)} C_4^{(1,2)} \mathbf{e}_{\mathrm{I}d}^{(n)} \mathbf{u}_{\mathrm{II}d}^{(m)} + e^{i\gamma_{\mathrm{II}d}^{(n)}(z_n+D_{n-1})+i\gamma_{\mathrm{I}d}^{(m)}(-z'_m-D_m)} C_4^{(2,1)} \mathbf{e}_{\mathrm{II}d}^{(n)} \mathbf{u}_{\mathrm{I}d}^{(m)} \\
& + e^{i\gamma_{\mathrm{II}d}^{(n)}(z_n+D_{n-1})+i\gamma_{\mathrm{II}d}^{(m)}(-z'_m-D_m)} C_4^{(2,2)} \mathbf{e}_{\mathrm{II}d}^{(n)} \mathbf{u}_{\mathrm{II}d}^{(m)} \Big]
\end{aligned} \tag{13}$$

where

$$\mathbf{C}_4 = \mathbf{Y}_{mn}^{(d)} \cdot \mathbf{N}_m \tag{14}$$

$$\mathbf{C}_3 = \mathbf{C}_4 \cdot \mathbf{G}_d^{(m)}(z_m = -D_m + D_{m-1}) \cdot \mathbf{R}_{Dm,m-1} \tag{15}$$

$$\mathbf{C}_2 = \mathbf{R}_{Dn,n+1} \cdot \mathbf{G}_d^{(n)}(z_n = -D_n + D_{n-1}) \cdot \mathbf{C}_4 \tag{16}$$

$$\mathbf{C}_1 = \mathbf{C}_2 \cdot \mathbf{G}_d^{(m)}(z_m = -D_m + D_{m-1}) \cdot \mathbf{R}_{Um,m-1} \tag{17}$$

It is illustrated that the dyadic Green's functions in the spatial domain are expressed in terms of Sommerfeld integrals in the spectral domain. Among those acceleration techniques for the calculation of the spatial-domain Green's functions, DCIM has been proven to have excellent accuracy and efficiency [10, 11]. In this work, the two-level DCIM is employed to calculate the closed-form Green's functions.

3. NUMERICAL EXAMPLES

This section is to investigate the accuracy and efficiency of the proposed algorithm. Firstly, one element of the field Green's function in the spectral domain is compared with the corresponding portion from the potential Green's function which has been well-documented [9], in the case of the isotropic medium. The relationship between the Green's function in the electric field integral equation (EFIE) and that in the mixed-potential integral equation (MPIE) is as follows,

$$\overline{\overline{G}}^{EJ} = i\omega\mu_0 \overline{\overline{G}}^{AJ} + \frac{1}{i\omega\varepsilon_0} \nabla\nabla' G^{VJ} \tag{18}$$

where, $\overline{\overline{G}}^{AJ}$ represents the dyadic Green's functions for magnetic vector potential and G^{VJ} represents the Green's function for electric scalar potential. Fig. 2 shows that the magnitude of $\widetilde{G}_{zz}^{EJ}$ obtained by the present algorithm agrees very well with that from the MPIE.

Secondly, the algorithm is applied to the approximation of the closed-form Green's functions for a four-layer planar uniaxial anisotropic medium. The reference solution, used for the assessment of the accuracy of the closed-form approximation, is obtained through the numerical integration of the spectrum on deformed paths parallel to the real axis [8]. The number of samples is $N = 1024$ for the

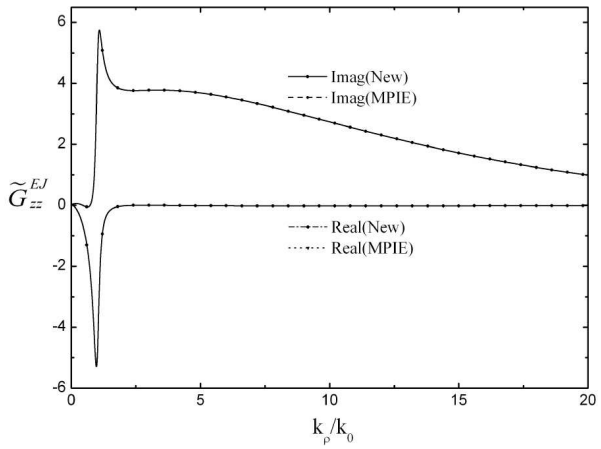

Figure 2: Magnitude of $\widetilde{G}_{zz}^{EJ}$ versus k_ρ for a four-layer isotropic medium. The solid lines correspond to results obtained by the present algorithm while the dots correspond to results from MPIE.

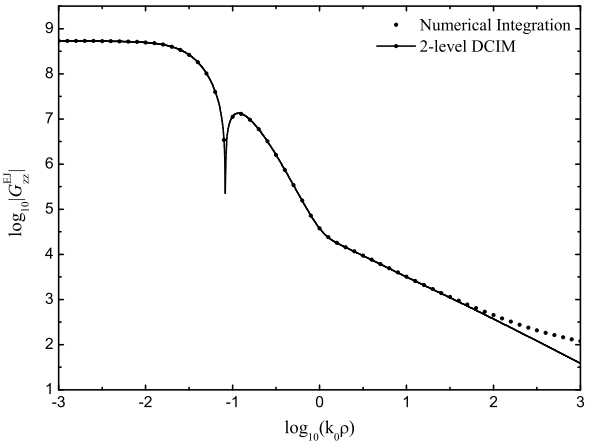

Figure 3: Values of G_{zz}^{EJ} versus ρ for $m = n$. The solid lines correspond to results obtained by the DCIM method while the dots correspond to results obtained by the numerical integration.

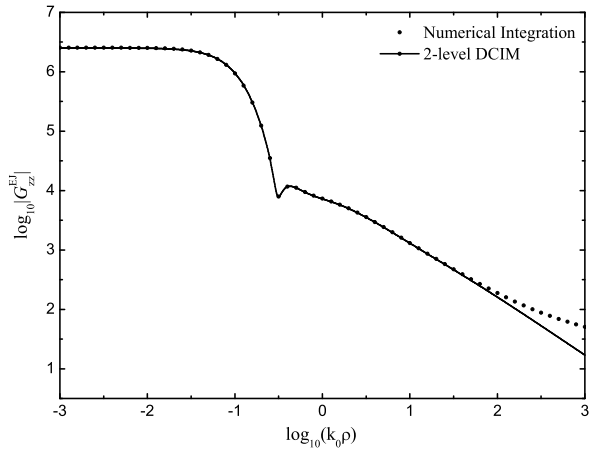

Figure 4: Values of G_{zz}^{EJ} versus ρ for $m < n$. The solid lines correspond to results obtained by the DCIM method while the dots correspond to results obtained by the numerical integration.

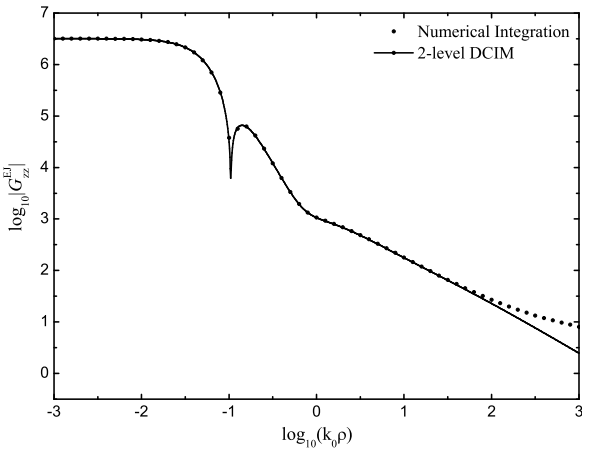

Figure 5: Values of G_{zz}^{EJ} versus ρ for $m > n$. The solid lines correspond to results obtained by the DCIM method while the dots correspond to results obtained by the numerical integration.

path of each level and the operating frequency is 3 GHz. Fig. 3 shows the magnitude of the spatial-domain Green's fucntion G_{zz}^{EJ} evaluated in the case of the source point and the observation point in the same layer (where $m = n = 2$, $z' = -1.2$ mm and $z = -0.2$ mm). The permittivity tensors for the four layers are $\overline{\overline{\varepsilon}}_1 = \varepsilon_0\overline{\overline{\mathrm{I}}}$, $\overline{\overline{\varepsilon}}_2 = \{2.1, 0, 0; 0, 2.1, 0; 0, 0, 2.121\}\cdot\varepsilon_0$, $\overline{\overline{\varepsilon}}_3 = \{9.8, 0, 0; 0, 9.8, 0; 0, 0, 9.898\}\cdot\varepsilon_0$ and $\overline{\overline{\varepsilon}}_4 = \varepsilon_0\overline{\overline{\mathrm{I}}}$. Fig. 4, shows the magnitude of G_{zz}^{EJ} in the case of $m = 1$, $n = 3$, $z' = 0$ mm and $z = -1.5$ mm. The permittivity tensors are $\overline{\overline{\varepsilon}}_1 = \varepsilon_0\overline{\overline{\mathrm{I}}}$, $\overline{\overline{\varepsilon}}_2 = \{2.1, 0, 0; 0, 2.1, 0; 0, 0, 2.31\}\cdot\varepsilon_0$, $\overline{\overline{\varepsilon}}_3 = \{9.8, 0, 0; 0, 9.8, 0; 0, 0, 10.78\}\cdot\varepsilon_0$ and $\overline{\overline{\varepsilon}}_4 = \varepsilon_0\overline{\overline{\mathrm{I}}}$. For the magnitude of G_{zz}^{EJ} in Fig. 5, the permittivity tensors are $\overline{\overline{\varepsilon}}_1 = \varepsilon_0\overline{\overline{\mathrm{I}}}$, $\overline{\overline{\varepsilon}}_2 = \{2.1, 0, 0; 0, 2.1, 0; 0, 0, 4.2\}\cdot\varepsilon_0$, $\overline{\overline{\varepsilon}}_3 = \{9.8, 0, 0; 0, 9.8, 0; 0, 0, 19.6\}\cdot\varepsilon_0$ and $\overline{\overline{\varepsilon}}_4 = \varepsilon_0\overline{\overline{\mathrm{I}}}$. The source point, $z' = -2.5$ mm, is in the layer $m = 3$ and the observation point $z = -0.2$ mm is in the layer $n = 2$. It is demonstrated that the DCIM-based results have an excellent agreement with the numerical integration results in the three cases for $\rho < 15.9\lambda_0$. Here, ρ represents the horizontal distance between the source point and observation point and λ_0 represents the wavelength in the free space. The accuracy could be improved with the extraction of singularity's contribution when $\rho \geq 15.9\lambda_0$. The computational time used for DCIM is less than 60 s for each case, while the computational time for numerical integration method is 137 s per point. It can be inferred from the numerical results that the closed-form Green's function for the stratified uniaxial anisotropic medium can be calculated accurately and efficiently by the present algorithm, compared with the numerical integration results.

4. CONCLUSION

In this paper, a complete set of closed-form Green's functions are provided for the stratified uniaxial anisotropic medium with an arbitrary distribution of electric current sources. The spectral-domain Green's functions in the electric field form are derived by using the wave iterative algorithm. The magnitude of the spectral-domain Green's function based on this algorithm is compared with that obtained from the potential Green's function in isotropic medium and a good agreement is observed. The closed-form Green's functions are calculated by using the 2-level DCIM. Finally, numerical results demonstrate the accuracy and efficiency of the algorithm.

REFERENCES

1. Michalski, K. A. and D. Zheng, "Electromagnetic scattering and radiation by surfaces of arbitrary shape in layered media: Part II: Implementation and results for contiguous half-spaces," *IEEE Trans. Antennas Propagat.*, Vol. 38, No. 3, 345–352, 1990.
2. Geng, N. and L. Carin, "Wide-band electromagnetic scattering from a dielectric BOR buried in a layered lossy dispersive medium," *IEEE Trans. Antennas Propagat.*, Vol. 47, No. 4, 610–619, 1999.
3. Mosig, J. R., "Arbitrarily shaped microstrip structures and their analysis with a mixed potential integral equation," *IEEE Trans. Microw. Theory Tech.*, Vol. 36, No. 2, 314–323, 1988.
4. Park, I., R. Mittra, and M. I. Aksun, "Numerical efficient analysis of planar microstrip configurations using closed-form Green's functions," *IEEE Trans. Microw. Theory Tech.*, Vol. 43, No. 2, 390–400, 1995.
5. Habashy, T. M., S. M. Ali, and J. A. Kong, "Dyadic Green's functions in a planar stratified, arbitrarily magnetized linear plasma," *Radio Science*, Vol. 26, No. 3, 701–715, 1991.
6. Li, L. W., J. H. Koh, T. S. Yeo, M. S. Leong, and P. S. Kooi, "Cylindrical vector eigenfunciton expansion of green dyadics for multilayered anisotropic media and its application to four-layered forest," *IEEE Trans. Antennas Propagat.*, Vol. 52, No. 2, 466–477, 2004.
7. Aksun, M. I., "A robust approach for the derivation of closed-form Green's functions," *IEEE Trans. Microwave Theory Tech.*, Vol. 44, No. 5, 651–658, 1996.
8. Chew, W. C., *Waves and Fields in Inhomogeneous Media*, Van Nostrand Reinhold, New York, 1990.
9. Zhang, M., L. W. Li, and Y. F. Tian, "An efficient approach for extracting poles of Green's functions in general multilayered media," *IEEE Trans. Antennas Propagat.*, Vol. 56, No. 1, 269–273, 2008.

Sidelobe Reduction in Offset Dish Parabolic Antennas Using Metallic Scatters

Ali Harmouch[1], **Walid Kamali**[2], **and Chadi El Moucary**[3]

[1]Computer and Communication Department, American University of Science and Technology, Lebanon
[2]Faculty of Engineering & IT, AL Manar University of Tripoli, Lebanon
[3]Electrical, Computer and Communication Engineering Department, Notre Dame University, Lebanon

Abstract— Offset feed antennas are most commonly used for satellite applications, where very high gain is needed. The benefit of the offset configuration is that it positions the feed horn away from the dish itself so that it does not cast a shadow on the dish. However, this yields to bigger sidelobes which results in a significant interference problem especially between adjacent antennas. Adding metallic scatters (strips) to the antenna at specific positions and with specific dimensions and shapes would significantly minimize the sidelobe level and consequently enhance its directional characteristics. A detailed analysis of the suggested design was performed based on a huge series of electromagnetic simulations and testing experiments, which have clearly demonstrated a sidelobe reduction of about 10 dB.

1. INTRODUCTION

Offset parabolic reflectors are in widespread use, because of their low aperture blockage and simplicity. Despite this fact, offset parabolic reflectors suffer from high level of sidelobes (SLL) compared to center-fed parabolic reflector antennas which makes them vulnerable to interference and which also reduces their directivity and gain [1]. It is well known that conventional offset reflector antennas have asymmetrical sidelobes with respect to the main lobe, therefore, for many applications, it is highly advantageous to minimize their sidelobes, thereby increasing their directivity and gain.

The demand for wireless communication systems of increasing sophistication and ubiquity has led to the need for more efficient systems design [2]. In order to improve the wireless systems; one of the major tasks to start with is to improve the antenna; which is a major key element in today's and future wireless communication system. Now to improve an antenna one important challenge to achieve is reducing side lobe level. This reduction should not of course, affect the main or the back lobe. Reducing side lobe level is desirable because for antennas used as receivers, sidelobes make the antenna much more exposed to noise from any other signal coming from any other source. For transmitting antennas sidelobes represent security weakness, as an unintended receiver may pick up the classified communication. One major difficulty is that the higher the sidelobe level, the more likely an antenna is to interfere with or be interfered with by a receiver in the direction of the largest sidelobe. In addition, the increase of sidelobes means that the power is being lost and spread in undesired directions as waste.

Several studies have been proposed and conducted for minimizing SLL and enhancing directional characteristics of offset parabolic reflectors and results have shown a significant decrease in the level of sidelobes but the proposed approaches required a great change in the configuration and geometry of the antenna [7–10] which makes these methods not competitive compared to the proposed technique.

The proposed technique of reducing sidelobe level in offset parabolic reflectors have been applied before to center-fed parabolic reflectors and results have shown a decrease of SLL by almost 20 dB by simply adding conducting strips to the main reflector [11].

The purpose of this paper is to apply the "strip positioning" method to offset reflectors which has been proven to be **simple, efficient** and **low cost**. Any parabolic antenna can be constructed or even modified using the "strip positioning" method (Fig. 1), to have less sidelobes and consequently less interference. However the conducting strips should be located specifically to achieve the desired reduction in sidelobes level.

This paper is organized as follows. In Section 2, we formulate the sidelobe reduction problem. The method used and various considerations are given in Section 3. In Section 4, simulation results and optimization process are presented. Concluding remarks are given in Section 5.

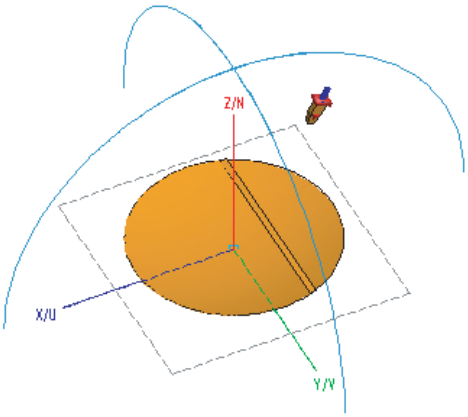

Figure 1: Metallic strips added on an offset dish parabolic antenna.

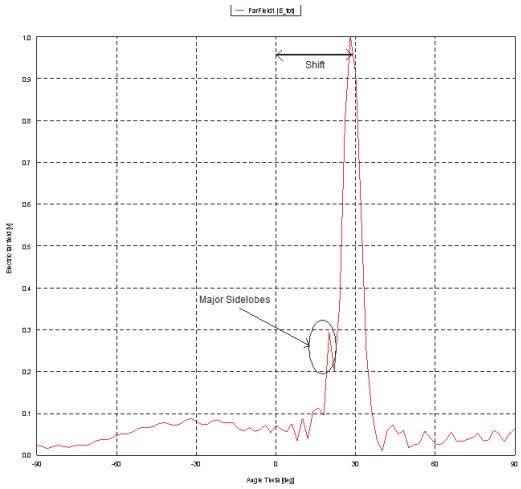

Figure 2: Radiation pattern of an offset antenna without strips.

2. DESCRIPTION OF THE PROBLEM

For a specific offset parabolic antenna, it is known that the far field is nothing but the Fourier transform of the aperture distribution [1]. Taking into the consideration that the aperture field is uniform, the plot of Fourier transform of this aperture field gives an idea about the antenna pattern. The radiation pattern of the offset reflector antenna would have the maximum of the main lobe shifted from the direction normal to the axis of the antenna by an angle which depends on the primary source shift. This shift is intentionally introduced in order to scan the pattern along a specific direction without a physical rotation of the main reflector itself. This would enhance the mechanical properties of the antenna but unfortunately is accompanied by a significant increase of the first sidelobes in the direction of the primary source's shift as shown in Fig. 2.

It is obvious from the above picture that the level of the first sidelobe is significant and may cause interference problems especially in the receiving mode, and negatively affect the directional characteristics of the antenna in the transmission mode. So to minimize the SLL several techniques have been used for such a purpose and have successfully decreased the sidelobe level by tens of decibels, however these techniques required a great change in the geometry and configuration of the antenna which makes the proposed methods being incompetent from the practical point of view. Therefore, and for this reason a new technique of reducing sidelobes has been proposed and considered in this paper to eliminate the major drawbacks of the already used approaches.

3. STRIP POSITIONING METHOD

The new technique suggests using metallic strips or scatters which are to be added and attached to the main reflector at a certain specific location and with a specific dimension and shape. In the next figure (Fig. 3), it is shown that adding a metallic strip to the antenna would constructively scatter the incoming wave radiated by the primary source in the direction of the main reflector and consequently reduces the SLL significantly [11]. The position of the strip on the main reflector is so critical, so the purpose of this article is to find out the optimum position of the strips with respect to the focal direction as well as to determine the best shape of strips and also the effect of the numbers of scatters on the directional characteristics of such antennas. Remember that Fig. 3 shows only figurative patterns of the effect of the strips.

For this reason, when using the "strip positioning" method the following should be considered: first the strips should be made out of a perfect conductor in order to desirably scatter or diffract the incident wave from the primary source, then the strips position should be well determined. It is very decisive to find the positions of the strips in order to have the desired reduction of side lobe level.

Based on results shown in Fig. 2, it is clear that the region of great sidelobes are within the range of angles between 15 and 30 degrees, therefore the strips are to be placed somewhere within that range to be considered as a knife-edge diffractor which causes a constructive diffraction loss that minimizes the sidelobe radiation.

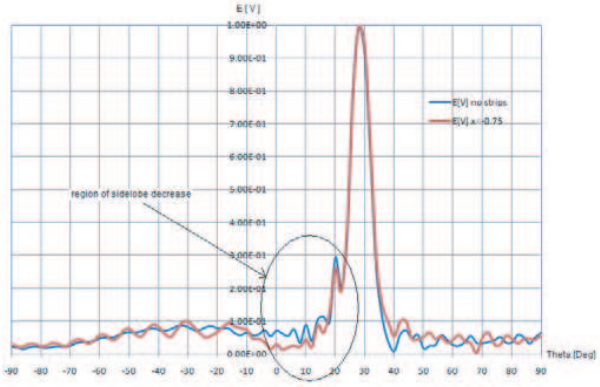

Figure 3: Effects of strips on the offset antenna's radiation pattern.

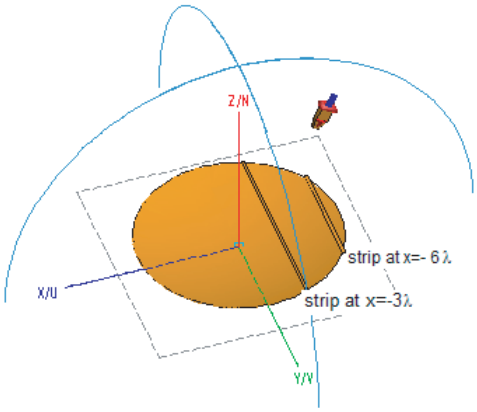

Figure 4: Offset antenna with 2 strips at -3λ and -6λ.

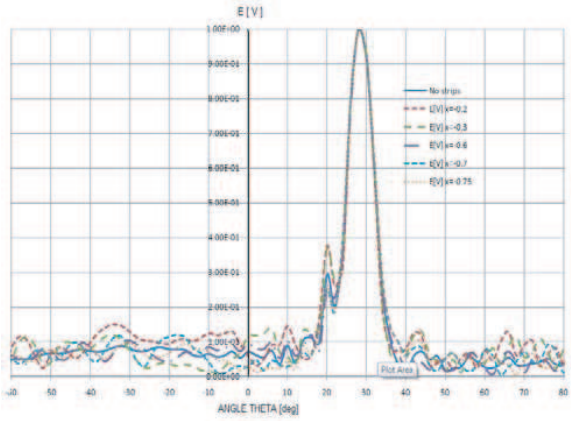

Figure 5: Effects of strip's position on the offset antenna pattern.

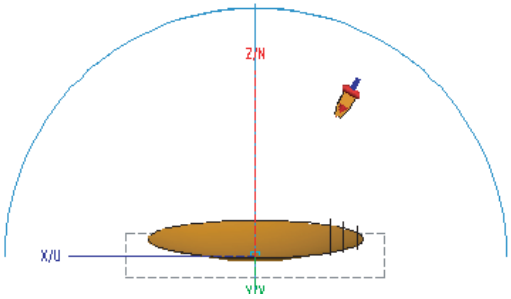

Figure 6: Offset antenna with 3 sharp strips at -4.4λ, -5.2λ and -6λ.

Figure 3 shows that metallic strips surely reduce the sidelobe level in the region adjacent to the main lobe and which is in the area of primary source's shift. However this reduction is not significant and needs for an optimization approach in order to achieve better results. So, the next step is to find out the best strip position and then study the effects of adding more strips to the main reflector of the offset antenna.

4. SIMULATION RSULTS OF THE OPTIMIZATION PROCESS

In Fig. 3 one can notice that the region where to place the scatters is ranging from -3λ to -6λ as shown below in Fig. 4.

Several simulations have been conducted using Method of Moments on rectangular strips of width $w = 0.4\lambda$ to provide a detailed prediction of the optimum strip position (Fig. 5).

Results in Fig. 5 show that as the metallic strip approaches the periphery of the main reflector on which the strips are placed, the reduction in the sidelobe level is more significant. The position at which a maximum reduction was achieved is around -5.5λ, where this reduction has reached almost 15% or around 4 dB in the direction of the first sidelobe peak. The obtained results are of a great importance, however, for more enhancements of the antenna's directional characteristics several simulations were also conducted by simply changing the orientation of the rectangular conducting strips with respect to the incident wave radiated from the primary source. Several strips are now placed on the main reflector and which are seen as knife edge diffractors from the primary source location and which are expected to better diffract the incoming rays and scatter them in a way that provides better reduction in the major sidelobes which are adjacent to the main lobe. At this stage the best position of the knife edge diffractors is selected according to the optimized results shown

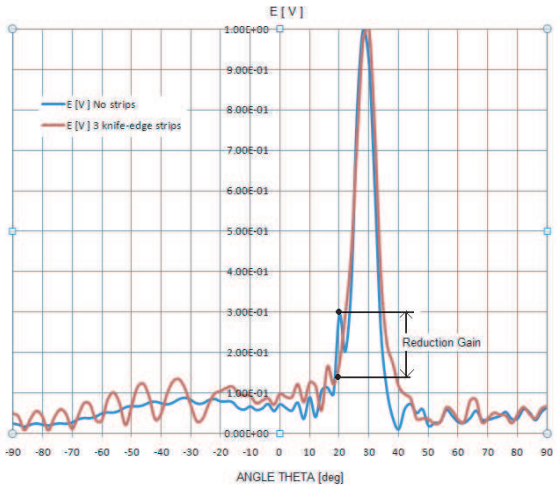

Figure 7.

in Fig. 5 and which is around -5λ. Simulations were conducted on an offset parabolic reflector antenna with three, four and five knife edge strips located around the above mentioned optimum position, however, the best results were achieved when three sharp edges were placed on the main reflector exactly at $x = -4.4\lambda$, -5.2λ and -6λ as shown in Fig. 6.

Results have shown a very significant decrease of the first sidelobe, which is considered as the most dangerous one, by almost 40 to 45% which is equivalent to a reduction of six to seven decibels in the direction of the first sidelobe peak as shown in Fig. 7.

5. CONCLUSION

The proposed strip positioning method, in comparison with other methods, provides significant sidelobe reduction in addition to its simplicity and low cost. Furthermore, this technique does not require a great change in the already existing antennas, but only requires a strip attachment at a specific location over the parabolic reflector, which makes this technique very practical in real life applications. For future work, it would be desirable to use different strip configurations such as cylindrical, blade and others.

REFERENCES

1. Balanis, C., *Antenna Theory*, 3rd Edition, Wiley, 2005
2. "IEEE standard test procedures for antennas," *IEEE Std.*, 149, 1965.
3. http://www.thefreedictionary.com/lobe.
4. Searle, A. D. and A. T. Humphrey, "Low sidelobe reflector antenna design," *Tenth International Conference on Antennas and Propagation, (Conf. Publ.)*, Vol. 1, No. 436, 17–20, April 14–17, 1997. Retrieved on January 26, 2008 from IEEE databases.
5. Schrank, H., "Low sidelobe reflector antennas," *Antennas and Propagation Society Newsletter,* Vol. 27, No. 2, 5–16, April 1985. Retrieved on January 26, 2008 from IEEE databases.
6. Satoh, T., E. Shizuo, N. Matsunaka, S. Betsudan, T. Katagi, and T. Ebisui, "Sidelobe level reduction by improvement of strut shape," *IEEE Transactions on Antennas and Propagation, [legacy, pre-1988]*, Vol. 32, No. 7, 698–705, July 1984. Retrieved on January 26, 2008 from IEEE databases.
7. Jenn, D. C. and W. V. T. Rusch, "Low sidelobe reflector design using resistive surfaces," *IEEE Antennas Propagat., Soc./URSI Int. Symp. Dig.*, Vol. 1, 152, May 1990. Retrieved on January 26, 2008 from IEEE databases.
8. Jenn, D. C. and W. V. T. Rusch, "Low sidelobe reflector synthesis and design using resistive surfaces," *IEEE Trans. Antennas Propagat.*, Vol. 39, 1372, September 1991. Retrieved on January 26, 2008 from IEEE databases.
9. MONK, A. D. and P. J. B. Clarricoats, "Adaptive null formation with a reconfigurable reflector antenna," *IEEE Proc. H*, 1995, 142, Vol. 3, 220–224, . Retrieved on January 26, 2008 from IEEE databases.

10. Lam, P., S.-W. Lee, K. Lang, and D. Chang, "Sidelobe reduction of a parabolic reflector with auxiliary reflectors," *IEEE Transactions on Antennas and Propagation, [legacy, pre-1988]*, Vol. 5, No. 12, 1367–1374, December 1987. Retrieved on January 26, 2008 from IEEE databases.
11. Harmouch, A., E. Nassar, D. Akiki, W. Beaineh, and N. Chamy, "FDTD Simulation of Reflector Antenna with Metallic Strips for Side Lobe Reduction," *IEEE Conference ACTEA 2009*, Notre Dame University, Lebanon, 2009.

Computational Electromagnetic Tools for EMC in Aerospace

Jesus Alvarez[1], **Salvador G. Garcia**[2], **L. Diaz Angulo**[2], **and A. Rubio Bretones**[2]

[1]Cassidian Air Systems, EADS-CASA, Spain
[2]University of Granada, Spain

Abstract— The classical Yee FDTD method has become a powerful tool in computational electromagnetics. Its application to EMC certification of aircrafts, under High Intensity Radiated Field (HIRF) conditions, is a current topic of interest in aerospace industry in order to reduce costs at the design stage.

In this work, we present the details of a high performance FDTD-based tool capable of HIRF simulation of large air vehicles, developed under the EU FP7 HIRF-SE project. The objective of this project, which joins 44 industrial and academic partners, is the creation of a synthetic environment where all kind of computational tools (FDTD, MoM, FEM, TDIE, Power Balance, TLM, ...) share a common interfacing language based in AMELET HDF, to be able to simulate totally/partially the behavior of aircrafts and rotorcrafts in a given electromagnetic scenario.

Although the FDTD method is well documented in literature, not all the published ideas are adequate enough for real life problems. The right choice of robust enhancements to deal with the specifical situations found in EMC in aeronautics, is critical to yield stable, fast and accurate simulators. Efficient techniques for the modeling of cables, composites, carbon fibber laminates, arbitrary dispersive materials, slots, etc., will be described in this work.

Parallel computing techniques for distributed memory architectures, will also be described, in the context of the development of a high performance computer FDTD simulator.

Finally, an emerging technique, the Discontinuous Galerkin Time Domain method (DGTD), will be described as a promising alternative to FDTD. The ability of DGTD to use finite element meshes, combined with its explicit time-domain nature, is proven to provide a superior accuracy, at a fraction of the CPU and memory time required by FDTD to achieve the same results.

1. INTRODUCTION

The Finite Difference Time Domain (FDTD) method is well-known in the electromagnetic community [1], where it has become the most popular and powerful general-purpose numerical method employed in computer simulation. No other method has been successfully employed in such a broad scope, for almost any type of problem from low frequencies up to optical ones involving almost any kind of material.

The classical FDTD method employs a second order finite centered approximation to the space and time derivatives to solve Maxwell's curl equations in time-domain. It defines an orthogonal cubic spatial grid based on the Yee unit-cell [2]: each field component of the electromagnetic field is sampled and evaluated at different space positions and the magnetic and electric fields are obtained at time instants delayed by half time step. The materials are modeled by specifying their characteristic constants at every grid point, usually in homogeneous regions, at whose interfaces proper continuity conditions are needed [3]. The simulation of open problems is carried out by placing truncation conditions, like Perfectly Matched Layers (PML), in the terminating planes of the grid.

The time advancing algorithm is conditionally stable and explicit, that is, the fields at each time instant are obtained as a function of previous values. The Courant stability criterion imposes an upper limit to the time increment bounded by the minimum space increment employed in the discretization $\Delta t \leq \Delta_{\min}/(c\sqrt{3})$.

2. LIMITATIONS OF FDTD

The FDTD method presents two main sources of inaccuracy: the staircased approximation of curved geometries, and the phase errors, which are anisotropic and can become especially important for electrically large problems:

- The staircasing errors can be addressed by employing fine space discretizations to handle the fine geometrical details where needed, while keeping coarser meshes elsewhere. Several techniques are available: uneven meshing, subgridding, conformal, etc. UGRFDTD implements

the uneven mesh spacing technique for its robustness, stability and ease of mesh generation. This technique employs a geometrically graded mesh to make the transitions from coarsely to finely meshed regions.

- The dispersion error requires the reduction of the space step everywhere in the problem. A common rule of the thumb for the upper bound in the mesh size for a FDTD simulation is $\Delta_{\max} \leq \lambda/15$, with λ being the free-space wavelength and $\Delta_{\max}$ the maximum space-step of the meshing. However, when electrically large problems are present, this bound can become stricter. The phase error in FDTD actually depends on the space step and increases with the traveling distance. For instance, a single trip of a plane-wave along a typical distance in a small aircraft (16 m), can accumulate a phase error as big as 20 degrees at 1 GHz, for cells of 1.5 cm.

In summary, both limitations can be treated by using more space cells and more computer memory. An hence, more CPU, not only because of the increase of the space cells, but also because of the reduction of the time step needed for stability.

3. FDTD FOR EMC: UGRFDTD

UGRFDTD is a full-wave 3D parallel solver based in the classical FDTD method developed at the University of Granada (Spain), in collaboration with the private company EADS-CASA, with enhancements from the University of La Sapienza (Italy) and the University of York (UK). It has been designed to handle the specific necessities of EMC assessment in the aeronautical industry, as part of the HIRF-SE project [4] within the Aeronautics and Air Transport call of 7th Framework Program.

UGRFDTD allows the user to find the time-domain EM response of a whole air-vehicle geometry, including dispersive, composite, and anisotropic materials, loaded thin-wires and their junctions, everything treated with state-of-the-art formulations.

UGRFDTD uses the AMELET HDF [5] specification developed by AxesSim as a standard to specify any electromagnetic problem, regardless of the numerical engine used for its simulation. The main advantage AMELET HDF resides in the fact that a single file contains the whole input data needed by any simulator: geometry, mesh (structured/unstructured), simulation data, etc. The output results are also plugged into the same input file, so that any postprocessing tool can perform the requested calculations (power, impedance, etc.) on them. Furthermore multiple simulators share a common way to communicate among them. For instance, the output fields calculated along the cable paths can be used by cable modeling tools to accurately simulate their behavior. Preprocessing modeling tools, like GiD from CIMNE [6], are used to accomplish the task of AMELET HDF file generation, from the physical models.

4. FDTD IDEAS WHICH WORK FOR EMC

FDTD has been for 20 years a very active field of research with thousands of papers devoted to its full development. Different approaches to deal with a given extension (e.g., dispersive materials, ABCs, etc.) can be usually found in the literature, making it often difficult to choose the best one (in terms of efficiency and accuracy) among them.

In this section, we detail some of the extensions used in UGRFDTD to simulate EMC problems. We do not intend to be either systematic or categoric by only focusing on these techniques, we assume that better approaches may exist, however the ones shown below have been thoroughly tested, and provide reliable, robust and stable algorithms for real EMC problems.

4.1. Thin-wire Modeling

A main need in EMC is the ability to handle multiconductor cables and their junctions. We have chosen to employ Holland-based algorithms [7–9] to deal with them. In this approach, the wires and FDTD equations are decoupled, and communicate only at the wire points: a 1D transmission-line model is used to find the currents and voltages along the wires, and 3D Maxwell curl equations for the rest of the problem. This technique permits to deal with: junctions of single wires of different radii, distributed resistance and inductance/capacitance per unit length, open air or material termination through lumped resistances, and multiwire cable modeling.

4.2. Material Dispersion Handling

Usually, material parameters are provided by manufacturers as experimental data measured over a frequency range. The technique based on [10, 11] can be successfully used to model dispersive

dielectric/magnetic materials, since the complex permittivity/permeability data (in frequency domain) can be expanded in terms of complex-conjugate pole-residue fractions, either analytically, or by vector fitting techniques from the experimental curves [12]. An auxiliary differential equation formulation is used to couple the polarization currents related with each pole-residue fraction, to Maxwell curl equations. Lorentz, Drude or Debye dispersions are just particular cases that can also be handled with this technique.

4.3. Composite Material Modeling

Panels of composite materials have become common in aircraft manufacturing, because of their low weight and good mechanical properties. Isotropic and anisotropic composite modeling has been implemented following the Surface Impedance Boundary Condition (SIBC) technique given in [13, 14]. The behavior of the planar composite is modeled by an impedance matrix, coupling the electric fields at each side of the panel to the magnetic fields at either side, both in an isotropic manner (plain composites) or anisotropically (carbon fiber reinforced composites). The impedances are expressed as the sum of complex-conjugate pole-residue fractions, found by vector fitting techniques either from experimental curves, or from theoretical analysis. A time-domain convolutional form is chosen to yield the time-domain expressions from the frequency-domain ones.

4.4. Anisotropic Materials

The treatment of anisotropic materials is handled by using both finite differences and averages to approximate the field components defined at non-existent positions of Yee's grid [15].

4.5. Absorbing Boundary Conditions

Several *flavors* of PML technique have appeared in the literature since Berenger's key publication [16]. Among them, the complex frequency shifted formulation of PML (CFS-PML) proposed in [17, 18] to improve the absorption capabilities of PML has been implemented into UGRFDTD. A main advantage of CFS-PML resides in the fact that it keeps the usual FDTD equations in the main domain, only requiring the addition of convolutional terms in the PML regions, thus permitting the truncation of multilayered problems, even involving dispersive materials.

4.6. Parallelization

The technique described in [19] has been employed for the MPI parallelization of UGRFDTD. For this purpose, we divide the problem in one direction in slices, which are handled by each cluster node. At the end of each time step, the information of the magnetic fields at the interfaces between adjacent slices (which is the only one needed for self-consistency) is shared via MPI messages. OMP directives are used to parallelize the code within each node. At this moment, without cache-specific optimizations, UGRFDTD is able to reach 200 Mcells/second in dual Xeon X5680 machine.

5. EXAMPLE: AIRCRAFT SIMULATION

A numerical model provided by Evektor of an aircraft 14 m long, 16 m wingspan (Figure 1) has been used for cross-validation of UGRFDTD with the commercial software EMA3D [20]. A set of wires, not shown in the figure, run in its interior. It has been modeled with a uniform mesh of $\Delta = 1.5$ cm and illuminated with a pulsed Gaussian plane wave with -20 dB decay at 869.79 MHz. This problem has 340 Mcells and requires 31.3 h and 10.2 GB to simulate 1.5 µs in a dual Xeon X5680 machine.

Figure 2 shows the magnetic field computed for a point beneath the cockpit, which is weakly coupled to rest of the structure. Excellent agreement with the commercial tool is found. As expected, the solution converges to 0 very slowly, due to the resonant behavior of this kind of structures.

6. DGTD: AN ALTERNATIVE TO FDTD

As mentioned above, FDTD has drawbacks related to the staircased approximation that it employs for curved boundaries. A recent alternative to FDTD is given by he Discontinuous Galerkin Time Domain (DGTD) method which is experimenting an increasing development in computational electromagnetics [21].

DGTD employs a discontinuous Galerkin weighting procedure to handle the spatial part of time-domain Maxwell's curl equations. Like in the finite elements (FETD) method, the space is divided into M non-overlapping elements (e.g., curvilinear tetrahedra), in each of which the solution is expanded in a set of nodal or vector [22] basis functions of arbitrary order. The temporal part

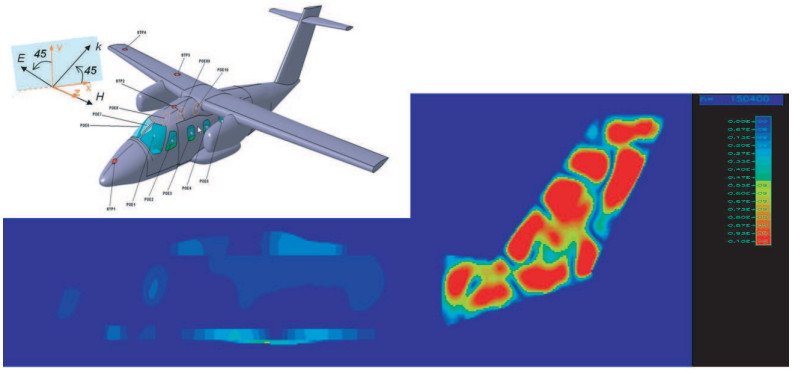

Figure 1: EVEKTOR'S Aircraft model and a snapshot of its simulation with UGRFDTD.

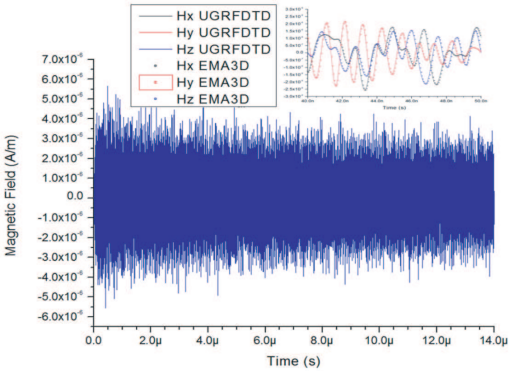

Figure 2: Time-domain results for the magnetic field in a point beneath the aircraft cockpit.

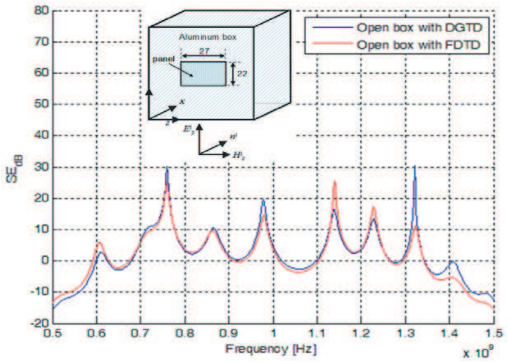

Figure 3: Time-domain results for the magnetic field.

of Maxwell curl equations can be handled by finite differences or by any other finite integration technique.

In DGTD the solution is allowed to be discontinuous at the boundaries between adjacent elements (unlike in FETD), and continuous numerical fluxes are employed at the interface to connect the solution between them. The resulting algorithm is quasi-explicit in space, only requiring the inversion of M square matrices of $Q \times Q$ elements (with Q the number of basis functions) during the initialization phase. DGTD is as general as FDTD, and easily parallelized.

The UGR has developed a parallel DGTD tool taking profit of the framework of HIRF-SE, which may become an actual alternative to FDTD. Just a simple figure of merit: to achieve the accuracy of DGTD we may require FDTD resolutions over 90 cells/λ (for typical problems) [22], which, in terms of CPU, means that DGTD can be 5 times faster to achieve a given physical time, requiring 5 times less memory. For illustration, Figure 3 shows results for the shielding effectiveness of an open aluminum box illumined normally with a plane wave, found both by DGTD and UGRFDTD.

7. CONCLUSIONS

In this paper, we have shown in a nutshell a successful approach to build a parallel FDTD simulator for EMC assessment. The different extensions incorporated into the UGRFDTD simulator have proven to be stable and robust enough for this kind of problems.

The DGTD method has been briefly described as a promising alternative to FDTD for its accuracy and computer requirements.

ACKNOWLEDGMENT

The work described in this paper and the research leading to these results has received funding from the European Community's Seventh Framework Programme FP7/2007-2013, under grant agreement No. 205294 (HIRF-SE project), and from the Spanish National Projects TEC2010-20841-C04-04, CSD2008-00068, and the Junta de Andalucia Project P09-TIC-5327.

REFERENCES

1. Taflove, A. and S. Hagness, *Computational Electrodynamics: The Finite-difference Time-domain Method*, 3 Edition, Artech House, Boston, MA, 2005.
2. Yee, K. S., "Numerical solution of initial boundary value problems involving Maxwell's equations in isotropic media," *IEEE Transactions on Antennas and Propagation*, Vol. 14, No. 3, 302–307, Mar. 1966.
3. Garcia, S. G. and A. R. Bretones, B. G. Olmedo, and R. Gómez Martín, "Finite difference time domain methods," *Time Domain Techniques in Computational Electromagnetics*, D. Poljak, Ed., 91–132, WIT Press, 2003.
4. http://www.hirf-se.eu/.
5. http://code.google.com/p/amelet-hdf/.
6. http://gid.cimne.upc.es/.
7. Holland, R. and L. Simpson, "Finite-difference analysis of EMP coupling to thin struts and wires," *IEEE Transactions on Electromagnetic Compatibility*, Vol. 23, No. 2, 88–97, May 1981.
8. Bérenger, J.-P., "A multiwire formalism for the FDTD method," *IEEE Transactions on Electromagnetic Compatibility*, Vol. 42, No. 3, 257–264, Aug. 2000.
9. Edelvik, F., "A new technique for accurate and stable modeling of arbitrarily oriented thin wires in the FDTD method," *IEEE Transactions on Electromagnetic Compatibility*, Vol. 45, No. 2, 416–423, May 2003.
10. Okoniewski, M., M. Mrozowski, and M. A. Stuchly, "Computationally efficient algorithms for multi–term dielectric dispersion in FDTD," *IEEE Antennas and Propagat. Soc. Int. Symp.*, Vol. 1, 364–367, Montréal, Canada, Jul. 1997.
11. Han, M., R. Dutton, and S. Fan, "Model dispersive media in finite-difference time-domain method with complex-conjugate pole-residue pairs," *IEEE Microwave and Wireless Components Letters*, Vol. 16, No. 3, 119–121, Mar. 2006.
12. Gustavsen, B. and A. Semlyen, "Rational approximation of frequency domain responses by vector fitting," *IEEE Transactions on Power Delivery,* Vol. 14, No. 3, 1052–1061, Jul. 1999.
13. Sarto, M. S., "A new model for the FDTD analysis of the shielding performance of thin composite structures," *IEEE Transactions on Electromagnetic Compatibility*, Vol. 41, No. 4, 298–306, Nov. 1999.
14. Holloway, C., M. Sarto, and M. Johansson, "Analyzing carbon-fiber composite materials with equivalent-layer models," *IEEE Transactions on Electromagnetic Compatibility*, Vol. 47, No. 4, 833–844, Nov. 2005.
15. Garcia, S. G., T. M. Hung-Bao, R. G. Martín, and B. G. Olmedo, "On the application of finite methods in time domain to anisotropic dielectric waveguides," *IEEE Transactions on Microwave Theory and Techniques*, Vol. 44, No. 12, 2195–2206, Dec. 1996.
16. Berenger, J.-P., "A perfectly matched layer for the absorption of electromagnetic waves," *Journal of Computational Physics*, Vol. 114, No. 1, 185–200, 1994.
17. Kuzuoglu, M. and R. Mittra, "Frequency dependence of the constitutive parameters of causal perfectly matched anisotropic absorbers," *IEEE Microwave Guided Wave Letters*, Vol. 6, No. 12, 447–449, Dec. 1996.
18. Roden, J. A. and S. D. Gedney, "Convolution PML (CPML): An efficient FDTD implementation of the CFS-PML for arbitrary media," *Microwave and Optical Technology Letters*, Vol. 27, No. 5, 334–339, Dec. 2000.
19. Wenhua, Y., R. Mittra, T. Su, Y. Liu, and X. Yang, *Parallel Finite-difference Time-domain Method*, Artech House, Boston, MA, 2006.
20. http://www.electromagneticapplications.com/.
21. Hesthaven, J. S. and T. Warburton, "Nodal high-order methods on unstructured grids-i. Time-domain solution of Maxwell's equations," *Journal of Computational Physics*, Vol. 181, 186–211, 2002.
22. Alvarez, J., L. D. Angulo, M. F. Pantoja, A. R. Bretones, and S. G. Garcia, "Source and boundary implementation in vector and scalar DGTD," *IEEE Transactions on Antennas and Propagation*, Vol. 58, No. 6, 1997–2003, 2010.

An Efficient Computational Method Based on Current Measurements for Fields Radiated by a Thin Antenna or a PLC Line

M. Chaaban[1], **K. El khamlichi Drissi**[1], **C. Pasquier**[1], **and A. Ismail**[2]

[1]Blaise Pascal University LASMEA, 24 Avenue des Landais, Aubière 63177, France
[2]Lebanese University, IUT Saida, BP813, Saida, Lebanon

Abstract— Although the PLC system is being continuously improved, there are still concerns about issues such as emissions, immunity and standardization. Such issues are important since PLC operates in an environment already populated by other services operating at the same frequencies, so that fair co-existence is needed. Simulating the complete PLC network or any significant part of it using full wave methods or numerical techniques such as the method of moments proves to be of limited practical use due to the fact that PLC networks extend over many wavelengths. In this paper we propose an efficient method to compute the near and far radiated fields of a PLC line. Our study focuses on the radiation phenomenon, which is described by the electromagnetic field. The radiation can be easily determined if the current distributions on the lines are known. We note that the determination of currents on the elements will be our main concern. Thus, the distribution of the current is represented in the form of exponentially damped sinusoids. Their current values are introduced into a software code that is developed using the Frequency Domain (FD), on antenna model. This may be very useful for radiated field computation in the far and near zones, as it is less computationally demanding.

1. INTRODUCTION

In practice, it is hard to measure the radiated field. Moreover, it is hard to install sensors and to predict the variation of the field in time and space. We may measure the value of the field in a measurement point. To this end, the principle of the proposed method is based on current measurement which is much easier than field measurement. From the measured values, the geometry of the PLC line antenna and the position of observation point, we may evaluate the radiated field at any point. Later, the known current distribution is extrapolated with Matrix Pencil (MP) algorithm and introduced into a software code developed here that allows the representation of EM field radiation at any observation point in free space.

2. FIELD RADIATED EQUATIONS

An integral model based on antenna theory is presented to study the mechanisms of radiation for a wire system. Knowing the distribution of the current $I(s, z)$, the fields are obtained from integral Equations (2)–(4) derived from Maxwell's equations [1].

The integral formulation derived from antenna theory related to a software code developed in [2] allows the representation of EM field radiation at any observation point in free space. The main innovation we propose in this model is the integral formulation able to compute the field in the near zone. A survey of the literature shows that it is almost impossible to find analytical formula to calculate the field at close range area. Therefore, whatever the mode of propagation in the line, we consider that the current in the line is known obtained by measurement and extrapolated with MP algorithm.

For a given current distribution, the proposed model calculates the radiated field by using the vector potential given by

$$\vec{A_z}(p) = \frac{\mu_0}{4\pi} \int_0^L I(p, z) \frac{e^{-\gamma_0 R(z)}}{R(z)} dz\vec{z}. \tag{1}$$

where $I(s, z)$ is the current distribution along the conductor, $p = j\omega$ is the Laplace variable, $R(z) = \sqrt{\rho^2 + (Z - z)}$ is the distance between the elementary dipole and the observation point M, $\gamma_0 = j\beta_0 = \frac{p}{c}$ is the propagation constant in free space and L is the length of the line.

Later the electromagnetic fields are expressed by:

$$H_\varphi = -\frac{1}{\mu_0}\frac{\partial A_z}{\partial \rho} \tag{2}$$

$$E_\rho = -\frac{j\omega}{\beta_0^2}\frac{\partial^2 A_z}{\partial \rho \partial z} \tag{3}$$

$$E_Z = -\frac{j\omega}{\beta_0^2}\left(\frac{\partial^2 A_z}{\partial z^2} + \beta_0^2 A_z\right) \tag{4}$$

3. THE PRINCIPLE OF THE CURRENT-ESTIMATION METHOD

This section details the basis theoretical results of the Matrix Pencil algorithm. Generally, we found in several articles such as those in [3] and [4], the shape modeling of a signal $s(z)$ from a physical measurement, observed in space (or time) and containing a noise, as follows:

$$s(z) = y(z) + n(z) \quad 0 \le z \le L \tag{5}$$

where,

$$s(z) = \text{measured signal} \quad y(z) = \text{clean signal} \quad n(z) = \text{noise}$$

$$y(k) = \sum_{i=1}^{M} \mathcal{R}_i q_i^k \qquad k = 0,\ \ldots,\ N-1 \tag{6}$$

where

$$q_i^k = e^{p_i Z_e k} = e^{(\alpha_i + \imath\omega_i) Z_e k} \tag{7}$$

$\mathcal{R}_i$ = residue or complex amplitude Z_e = represents the sampling period
p_i = complex pole α_i = attenuation factors of negative values (8)
ω_i = angular frequencies

We use the following discretization in space

$$y(k) = y(kZ_e) \tag{9}$$

finally the complete form of the equation becomes:

$$s(kZ_e) = y(kZ_e) + n(kZ_e) \approx \sum_{i=1}^{M} \mathcal{R}_i q_i^k + n(kZ_e) \tag{10}$$

In formula (9), the M complex poles q_i and complex residues $\mathcal{R}_i$ are the unknowns to be determined. This parameter M is very important for the separation of the proper signal from noise. The proper choice of M will be detailed in [5].

Indeed, Figure 2 proves that the signal reconstruction is possible using MPM. The signal provided by the software Feko for a given current (original signal) traversing a line of length L/λ can be successfully reconstructed (reconstructed signal) with a low number of poles.and residues (in this case, $M = 2$).

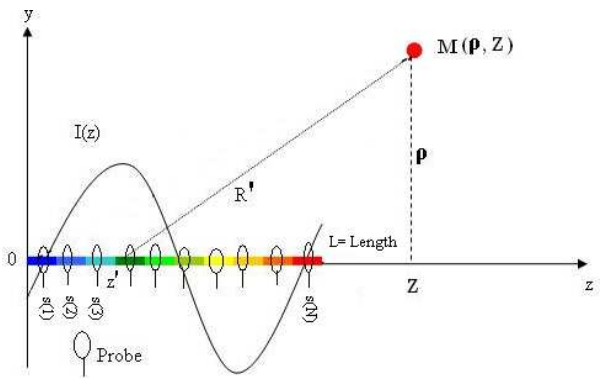

Figure 1: A cross-section of an electric line.

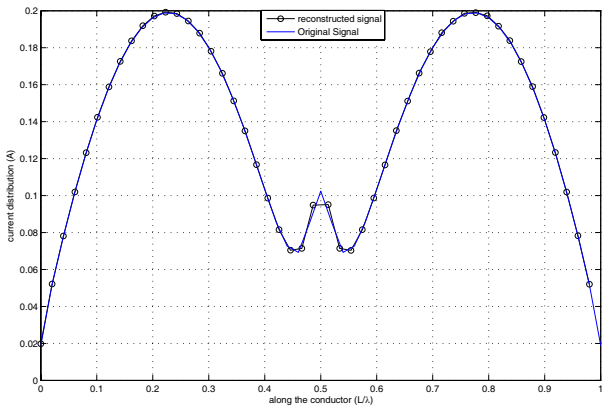

Figure 2: Original signal with the reconstructed one.

4. CONVENTIONAL MPM

Starting from an undamped exponential data sequence of length N obtained from the model given in Equation (9) upon setting the value of n to 1, MPM chooses a free parameter, L, known as the pencil parameter such as $M \leq L \leq N$. The proper choice of L results in significant robustness against noise. The next step is to construct a Hankel data matrix:

$$\mathbf{S} = \begin{bmatrix} s(1) & \cdots & s(L+1) \\ s(2) & & s(L+2) \\ \vdots & \ddots & \vdots \\ s(N-L) & \cdots & s(N) \end{bmatrix}. \tag{11}$$

Using the above matrix, two matrices are derived which in MATLAB notation are given as follows:

$$\mathbf{S}_0 = \mathbf{S}(:, 1:L) \tag{12}$$

$$\mathbf{S}_1 = \mathbf{S}(:, 2:L+1). \tag{13}$$

The matrix pencil for the two matrices $\mathbf{S}_0$ and $\mathbf{S}_1$ is defined as their linear combination $\mathbf{S}_1 - \lambda\mathbf{S}_0$, with λ a scalar parameter. In the absence of noise and by virtue of the assumed signal model, it is easily verified that $\mathbf{S}_0$ and $\mathbf{S}_1$ admit the following Vandermonde decomposition:

$$\mathbf{S}_0 = \mathbf{Q}_1\mathbf{C}\mathbf{Q}_2 \tag{14}$$

$$\mathbf{S}_1 = \mathbf{Q}_1\mathbf{C}\mathbf{Q}_0\mathbf{Q}_2 \tag{15}$$

where

$$\mathbf{Q}_1 = \begin{bmatrix} q_1 & \cdots & q_d \\ q_1^2 & & q_d^2 \\ \vdots & & \vdots \\ q_1^{(N-L)} & \cdots & q_d^{(N-L)} \end{bmatrix} \tag{16}$$

$$\mathbf{Q}_2 = \begin{bmatrix} 1 & q_1 & q_1^{L-1} \\ 1 & q_2 & q_2^{L-1} \\ \vdots & & \\ 1 & q_d & q_d^{L-1} \end{bmatrix} \tag{17}$$

$$\mathbf{Q}_0 = \operatorname{diag}\{q_1, q_2, \cdots, q_d\} \tag{18}$$

$$\mathbf{C} = \operatorname{diag}\{c_1, c_2, \cdots, c_d\} \tag{19}$$

revealing the fundamental shift-invariant property in the column and row spaces. The matrix pencil can then be written as:

$$\mathbf{S}_1 - \lambda\mathbf{S}_0 = \mathbf{Q}_1\mathbf{C}\left[\mathbf{Q}_0 - \lambda\mathbf{I}\right]\mathbf{Q}_2. \tag{20}$$

Consequently, each value of $\lambda = q_m$ is a rank reducing number of the pencil. The estimates of q_m are therefore the generalized eigenvalues of the matrix pair: $[\mathbf{S}_1, \mathbf{S}_0]$.

For noisy data, Total Least Squares Matrix Pencil (TLSMP) is usually preferred in which the singular value decomposition is used to prefilter the complex signals, and then conventional procedures follow. For more details, the reader can refer to [5].

5. ELECTROMAGNETIC FIELDS

The known current distribution is extrapolated with Matrix Pencil (MP) algorithm and replaced by a set of poles and residues.

$$I_z(p) = \sum_{i=1}^{M} \mathcal{R}_i q_i^k \quad k = 0, \ \ldots, \ N-1 \tag{21}$$

$$\vec{A_z(p)} = \sum_{i=1}^{M} \vec{A_z^i(p)} \tag{22}$$

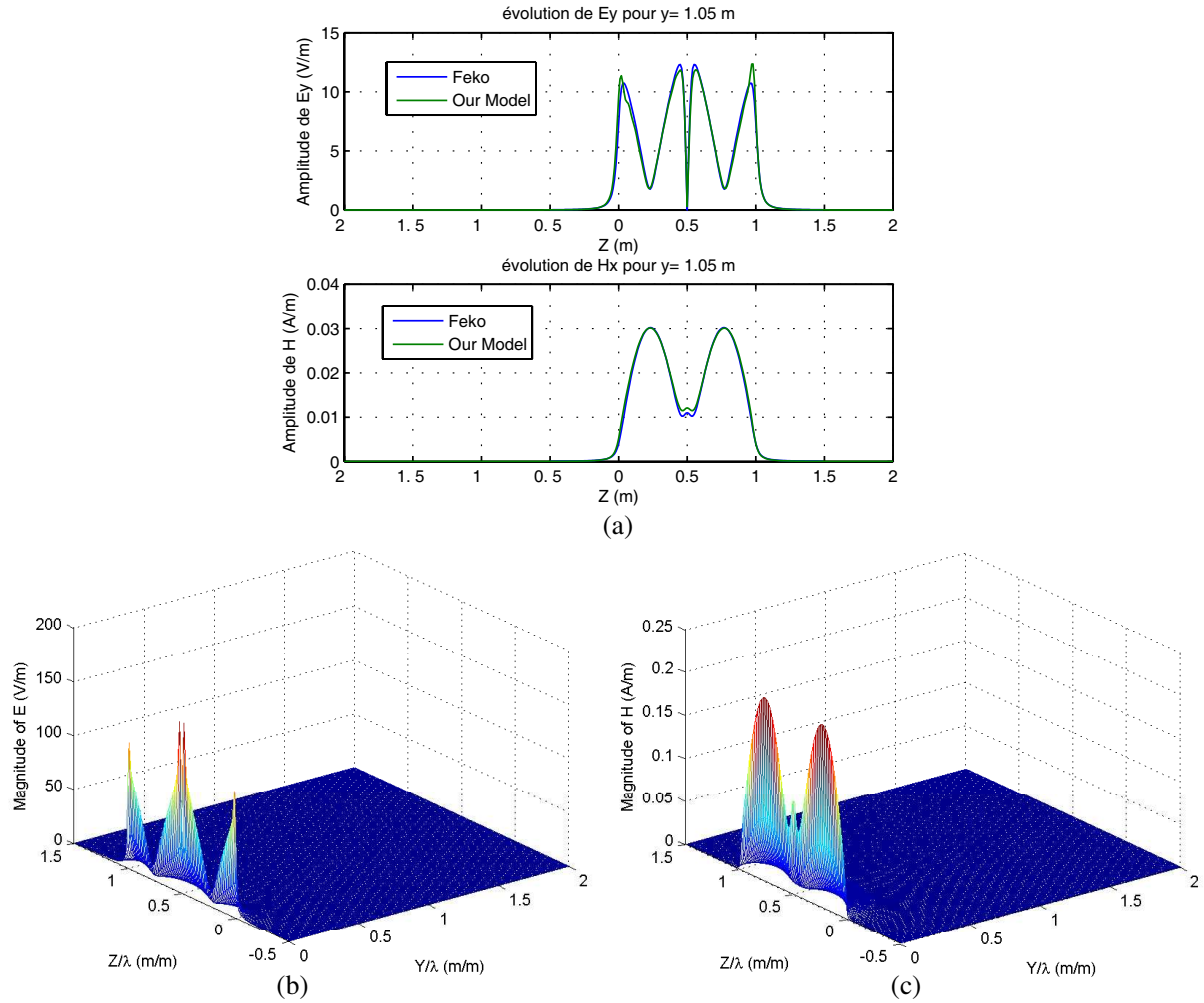

Figure 3: (a) Comparison between Feko and our model. (b) Magnitude of electric radiated field. (c) Magnitude of magnetic radiated field.

with

$$A_z^i(\vec{p}) = \frac{\mu_0}{4\pi}\mathcal{R}_i \int_0^L \frac{e^{p_i z - \gamma R(z)}}{R(z)} dz\vec{z}. \tag{23}$$

In this section, we present a simple example of a line traversed by the current depicted in Figure 2. To verify the validity of the proposed model we compare the radiated field obtained from Equation (20) with the radiated field provided by Feko. As shown in Figure 3(a), there is good agreement between both fields.

6. CONCLUSION

In this paper, we presented a practical model to estimate the radiated field by any electric line. Our model can analytically express the radiated field by using an analytical current expression derived from MPM algorithm currents. This model is very useful to derive the electromagnetic field with less computations. The current distribution is derived from MPM algorithm estimates. Consequently, direct measurements of currents become sufficient to estimate the radiated field in near and far zones. In our study, we use a current distribution model. By using antenna theory, the derived current can be expressed as a sum of complex exponentials [3] and will be the base of new general formulas.

ACKNOWLEDGMENT

The work presented in this article is sponsored by CEDRE project referenced 07SciF22/L11; it corresponds to a bilateral collaboration between the University of Blaise Pascal and the Lebanese

University. The first author would like to thank the Lebanese CNRS for the financial support of his Ph.D. work.

REFERENCES

1. King, R. W. P., G. J. Fikioris, and R. B. Mack, *Cylindrical Antennas and Arrays*, 2002, www.cambridge.org/9780521431071.
2. Chaaban, M., K. El Khamlichi Drissi, et al., "Rayonnement en zone proche d'un CPL en espace libre," *5th International Conference: Sciences of Electronic, Technologies of Information and Telecommunications, SETIT*, Tunisia, March 22–26, 2009.
3. Sarkar, T. K., F. Hu, Y. Hua, and M. Wicks, "A real time signal processing technique for approximating a function by a sum of complex exponentials utilizing the matrix-pencil approach-signal processing," *A Review Journal*, (Invited Paper), Vol. 4, No. 2, 127–140, April 1994.
4. Arnautovski-Toseva, V., K. El Khamlichi Drissi, et al., "Application de la mthode de pencil pour lanalyse des rponses impulsionnelles des conducteurs filaires," CEM, 14me Colloque International de Compatibilit Lectromagntique, CD ROM, B1, mai 20–23, Paris, France, 2008.
5. Hua, Y. and T. K. Sarkar, "Matrix pencil method for estimating parameters of exponentially damped/undamped sinusoids in noise," *IEEE Transactions on Acoustics, Speech and Signal Processing*, Vol. 38, 1990.

Multi-GPU Accelerated Finite-difference Time-domain Solver in Open Computing Language

T. P. Stefanski[1,2], **N. Chavannes**[3], **and N. Kuster**[2]

[1]ETH Zurich, Integrated Systems Laboratory, Gloriastrasse 35, Zurich 8092, Switzerland
[2]IT'IS Foundation, Zeughausstrasse 43, Zurich 8004, Switzerland
[3]SPEAG Software R&D, Zeughausstrasse 43, Zurich 8004, Switzerland

Abstract— This paper presents results of an evaluation of a novel multi-GPU OpenCL FDTD solver. Multi-GPU implementations are necessary, not only to speed up computations but also to aggregate relatively small GPU memories. The advantage of this solver is its portability between hardware manufactured by different vendors and also between highly specialized and parallel computing architectures available on the market, i.e., GPUs and multi-core CPUs. In our implementation, the computational domain is decomposed along the slowest direction, and electromagnetic field boundary data is shared between neighboring subdomains allocated on different GPUs. The communication overhead between GPUs is proportional to the area of the boundary and represents the rate-limiting step of the method. Portability and efficiency of the developed code were tested on a double CPU machine supported by four GPUs. For the utilized hardware devices, the communication overhead can be hidden by computations for sufficiently large simulation domains, giving scaling efficiency higher than 90%. Porting the OpenCL code dedicated to GPUs directly to multi-core CPUs gives unsatisfactory performance due to the application of architecture specific features in the GPU code. OpenCL kernels of the related FDTD code were therefore optimized to improve performance on multi-core CPUs. Despite this, OpenCL FDTD implementation on CPUs was up to 1.5 times slower than on a commercially available FDTD solver developed in the OpenMP standard. Subsequently, this paper presents an application of the developed multi-GPU OpenCL FDTD code in solving a real-life problem of computational electromagnetics in order to demonstrate its performance and applicability.

1. INTRODUCTION

Parallelism recently substituted clock frequency as the performance driver for processors. For years, processing speed has resulted from the clock rate and instruction-level parallelism. Hence, single-thread (single-process) codes executed faster on newer processors without any modification. Evolution of processors into multi-core chips has forced multi-threaded (multi-process) software coding to fully utilize the hardware. Further difficulties in software development have now resulted from a tremendous number of highly specialized processor architectures being on the market, i.e., multi-core central processing units (CPUs), graphics processing units (GPUs) and also devices that merge both technologies in a single-die chip. Therefore, development of computational electromagnetics codes that are scalable and portable between available and future hardware architectures has become a real challenge. These facts motivate us to continue investigations focused on parallel implementations of the numerical methods of electromagnetics in computing hardware.

Application of Open Computing Language (OpenCL) [1] in computational electromagnetics might be a solution to the aforementioned problems as it maintains portability between hardware architectures and efficiency of the low-level programming interface. OpenCL is a framework for parallel programming of heterogeneous platforms consisting of multi-core CPUs, GPUs, and other modern processors. This standard opens the way to building heterogeneous computing systems that may simultaneously deploy the computational power of multi-core CPUs and GPUs for the tasks best suited to them. OpenCL unifies the process of code development for heterogeneous computing systems using one programming environment (compiler) to target substantially different processing elements.

We recently reported the results of an OpenCL implementation of the finite-difference time-domain (FDTD) [2] method on a single computing device [3]. In this contribution we report an extension of that method, allowing execution on either multi-GPU or multi-core multi-CPU based computing architectures. Multi-GPU implementations are necessary, not only to speed up computations but also to aggregate relatively small GPU memories. In Section 2, multi-GPU implementation of the FDTD method in OpenCL is introduced. Evaluation of the developed code performance is presented in Section 3.

2. MULTI-GPU FDTD SOLVER

Our research group is focused on bio-electromagnetics and electromagnetic compatibility problems. FDTD is therefore our method of choice due to straightforward implementation of arbitrarily shaped structures (consisting of dispersive and non-linear materials) within the computational domain, the possibility of a wideband frequency response calculation with a single simulation run, and easy parallelization. Time evolution of the electromagnetic field is calculated in this method using central-difference approximations of the partial derivatives in Maxwell's curl equations [2]. Each step of the electromagnetic field update consists of (i) H-field components update within the domain, (ii) application of boundary conditions to the H-field, (iii) E-field components update within the domain, and (iv) application of boundary conditions to the E-field. The FDTD update equations [2] are omitted here for the sake of brevity.

Let N_x, N_y, N_z denote respectively the number of cells along the x, y, z directions in the computational domain before decomposition. Let us assume orientation of data in the memory, i.e., electromagnetic field and material data, with z and x being respectively the fastest and slowest-varying dimension. In our implementation, decomposition is performed along the slowest-varying direction, refer to Fig. 1. The size of the subdomain on the kth GPU (GPU_k) is equal to $N_x^k + 1$ where:

$$N_x = \sum_k N_x^k \tag{1}$$

An additional zy-slice of data (N_x^k+1) represents the boundary condition in the local, associated to a particular GPU, subdomain. This slice is added at the beginning of the transverse H-field data arrays (H_y, H_z-transverse components at the boundary between subdomains on different GPUs) and at the end of the transverse E-field components (E_y, E_z) data arrays. The exchange of transverse H- and E-field components between subdomains is performed respectively during applications of the boundary conditions to the H- and E-fields [steps (ii) and (iv) in the time marching scheme]. When the E-field update is completed on GPU_k, the boundary data is sent to GPU_{k-1} for the purpose of being used there as a boundary condition in the H-field update. Analogously, when the H-field update is completed on GPU_k, the boundary data is sent to GPU_{k+1} for the purpose of being used there as a boundary condition in the E-field update. These communication schemes are described schematically in Fig. 2, including the special case of the periodic boundary condition in the x-direction.

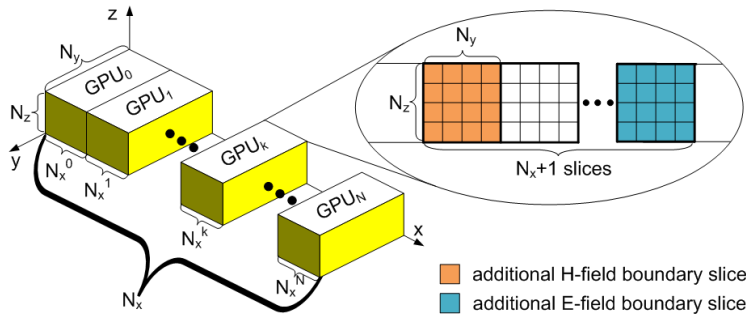

Figure 1: Domain decomposition scheme for the multi-GPU OpenCL FDTD solver. Size of the subdomain on the GPU is increased by one slice to implement the boundary condition for field updates.

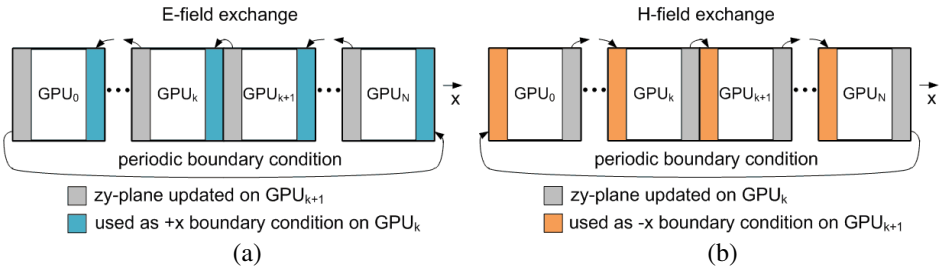

Figure 2: Communication between GPUs. (a) E-field exchange, (b) H-field exchange.

For each memory copying between GPUs, data is copied first from the sending GPU to the CPU host memory space. Then from the CPU to the receiving GPU. Unfortunately, the OpenCL driver did not allow data to be transferred directly between GPUs at the time of this paper preparation. The communication overhead between GPUs is proportional to the area of the boundary and represents the rate-limiting step of the method.

Each GPU then executes FDTD updates as presented in the case of single-GPU OpenCL code [3]. Updates are performed in the loop along the slowest direction. Rectangular zy-tiles of the field values, being the same size as blocks of threads, are transferred to the low-latency local (shared) memory using coalesced memory access. A single thread in a rectangular block of threads updates a single cell per one loop step, using two zy-tiles of data recently downloaded into the local memory.

Although the host machine supports many CPUs placed in different sockets on a motherboard, they are visible by the OpenCL driver as a single computing device with an aggregated number of cores (computing units). Decomposition of the domain is therefore not necessary in the case of code execution on a multi-CPU machine. The developed GPU code is executable on a multi-CPU machine without any changes, but the obtained simulation throughput is very low. CPU update kernels were therefore modified to avoid usage of the local memory which is not supported in hardware by CPU (its function is realized by a cache memory). In this improved implementation, every thread in the cuboidal group of threads updates a single cell directly using data stored in the global memory.

3. NUMERICAL RESULTS

Performance of the single-device OpenCL FDTD solver is presented in Fig. 3 for the sake of comparison. Simulation results were obtained for the vacuum bounded by Mur ABCs and excited by a dipole antenna located in its center (multi-material simulation). OpenCL simulations were executed on Tesla C1060 (4 GB RAM) and Radeon HD5870 (1 GB RAM) GPUs and on an Intel i7 920 (4 cores) CPU. CPU simulations performed up to 35% worse in comparison to a highly-optimized commercial OpenMP FDTD solver for the recently released OpenCL driver. OpenCL code performed on the Tesla device on average 10% worse than CUDA implementation. Porting OpenCL FDTD code optimized for Tesla architecture to the Radeon GPU (recently released driver) gave a similar or slightly lower performance (by up to 10%).

In the next test, domain size along the x-direction was varied while the communication overhead (number of either E- or H-field data to be sent between two GPUs) was fixed at about 1 MB (zy-plane: 361×361 cells, two transverse components) and 0.25 MB (zy-plane: 181×181 cells, two transverse components). The vacuum bounded by Mur ABCs and excited by a dipole antenna located in its centre (multi-material domain) was simulated on up to four HD5870 GPUs. Characteristics of the simulation speed vs. domain size are presented in Fig. 4.

The average speed of the single GPU simulations is equal to (a) 426 Mcells/sec, and (b) 406 Mcells/sec. For peak speed, equal to 1498 Mcells/sec in case (b), the scaling efficiency is better than 90%. This shows that the communication overhead can be hidden by computations for sufficiently large simulation domains. Both cases show that simulation speed grows with increasing domain size and decreasing communication overhead. Saturation of the characteristics is visible when communication time becomes a small part of the computations.

Figure 5 shows runtimes of a realistic simulation of an electromagnetic field interaction with the

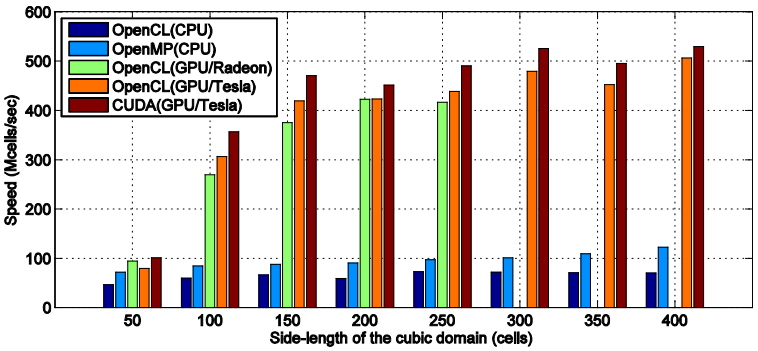

Figure 3: Speed of the OpenCL FDTD solver executed on a single GPU/CPU as a function of the side-length of the cubic domain.

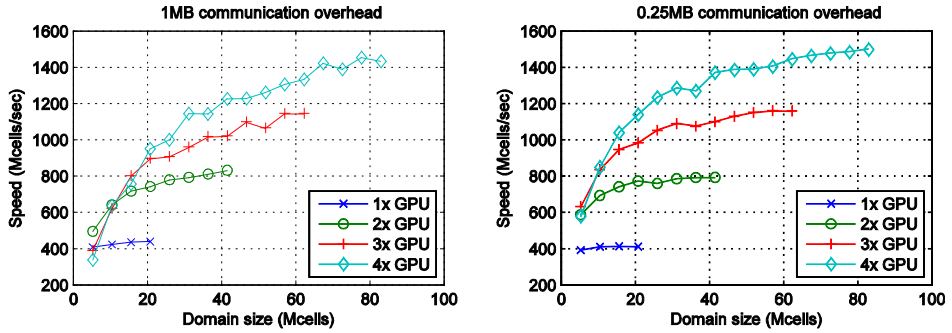

Figure 4: Speed of the multi-GPU (HD5870) OpenCL FDTD solver as a function of the domain size for fixed values of the communication overhead: (a) 1 MB, (b) 0.25 MB of either E- or H-field data.

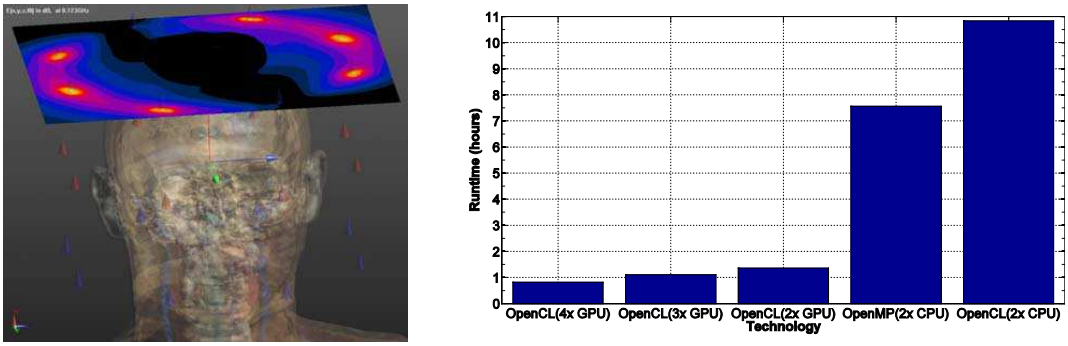

Figure 5: Runtimes for simulations of the electromagnetic field interaction with the human body (GPUs: HD5870-1 GB RAM, CPUs: 2×Xeon E5620-total 8 cores).

human body (mesh size: $314\times326\times326 = 33.4$ Mcells, 88114 iterations). Due to the large number of material parameters required for human body modeling, material data was not stored in the cached constant memory on the GPUs, which resulted in a slowdown of GPU simulations. Furthermore, observation data was very often transferred between the GPUs and the CPU for further processing and recording, which resulted in additional simulation slowdown. OpenCL code executed on ATI Radeon HD5870 GPUs was 6 (2×GPU) to 9 (4×GPU) times faster than a commercial OpenMP solver executed on two CPUs (2×Intel Xeon E5620). In this test OpenCL code executed on two CPUs required a 40% longer runtime than a highly optimized commercial solver parallelized using OpenMP standard.

4. CONCLUSIONS

We conclude that although OpenCL FDTD simulations perform at a slightly lower speed than either CUDA or OpenMP implementations, it allows the development of multi-GPU code that is portable between devices manufactured by different vendors and executable on modern multi-core CPUs. Therefore, it is anticipated that the OpenCL framework will increase in popularity in coming years, and might become the standard with respect to parallel programming.

REFERENCES

1. The OpenCL Specification, ver. 1.0, Khronos OpenCL Working Group, electronic file available at: http://www.khronos.org/registry/cl/specs/opencl-1.0.48.pdf, 2009.
2. Taflove A. and S. C. Hagness, *Computational Electrodynamics: The Finite-Difference Time-Domain Method*, 3rd Edition, Artech House, Boston, 2005.
3. Stefanski, T. P., N. Chavannes, and N. Kuster, "Parallel implementation of the finite-difference time-domain method in open computing language," *Proceedings of International Conference on Electromagnetics in Advanced Applications*, Sydney, Australia, September 2010.

Artificial Neural Network Modeling of Synchronous Reluctance Motor

Primoz Bajec[1], **Bogomir Zidaric**[1], **and Damijan Miljavec**[2]

[1]Hidria Institute for Materials and Technologies d.o.o., Slovenia
[2]Faculty of Electrical Engineering, University of Ljubljana, Slovenia

Abstract— The work handles with the application of artificial neural networks (ANN) in modeling of the synchronous reluctance motor. Motor geometry, used materials and excitation level dictate the motor performance. Mutual relations between these parameters were investigated due to some simplifications of model multidimensionality. To overcome the model complexity a proper ANN topology and data presentation to ANN were established. Final form of the non-linear model was achieved by joining all trained ANN. Model output results define the magnetic flux density distribution along the air-gap for both d- and q-mode excitations and specific motor geometry. The comparison between ANN model results and finite element calculations confirms the feasibility of use of established non-linear model for further investigation of SRM performance.

1. INTRODUCTION

Traditional motor design is in general composed of an iterative process where the engineer creates a basic design by applying engineering experience and skills into particular technical solutions of the motor. At each stage of the design, the device can be recalculated and the results are fed back to modify the previous motor design. The process using 2D or 3D finite element analyzes (FEA) has many advantages over conventional "calculate-built-test-recalculate" design. On the other hand the FEA process takes a lot of computational time for specific simulation. Owing to disadvantages of FEA the request to improve the design process was initiated and theresults are presented in the continuation of the paper.

In general, the SRM rotor is cross-laminated, with flux barriers placed around the air gap (Fig. 1(a)). They are mostly made of aluminum and are used to both diminish the q-axis flux flowing between poles and to permit the d-axis flux to flow largely unimpeded directly through the poles. This makes SRM to be, in its essence, an unexcited synchronous machine with its stator and stator windings like any other induction machine.As the flux barriers together with their two end rings form some kind of a squirrel cage, during the on-line start SRM shows its asynchronous character.

Most of the authors [1] study SRM with its rotor rotating synchronized with the resultant stator magnetic field. In such case, the effect of the rotor cage can be neglected. The same applies also for the case with the flux barriers are made of an electrically nonconductive material. In practice, the rotor cage is made of an electrically conductive material, such as aluminum, making phenomena in the rotor cage very intensive. For example, it permits SRM to start on-line and in the synchronous regime, it serves as a rotor dumping winding.

The paper focuses on the application of ANN in modeling of the synchronous reluctance motor in order to easethe design and performance evaluation of SRM.

2. CIRCUIT EQUATIONS GOVERNING SYNCHRONOUS RELUCTANCE MOTOR

The d-q voltage circuit equations in the rotor reference frame describing SRM with a squirrel cage by d- and q-axis rotor winding are [2]:

$$\begin{aligned} u_{sd} &= R_s i_{sd} + \frac{d\Psi_{sd}}{dt} - \omega_e \Psi_{sq} \qquad u_{sq} = R_s i_{sq} + \frac{\mathrm{d}\Psi_{sq}}{\mathrm{d}t} - \omega_e \Psi_{sd} \\ 0 &= R_{rd} i_{rd} + \frac{\mathrm{d}\Psi_{rd}}{\mathrm{d}t} \qquad\qquad 0 = R_{rq} i_{rq} + \frac{\mathrm{d}\Psi_{rq}}{\mathrm{d}t} \end{aligned} \tag{1}$$

In the above equations indices s and r refer to the stator and rotor magnitudes, respectively, and d and q for the d- and q-axis values, respectively. Magnetic flux linkages Ψ shown in (1) are defined by:

$$\Psi_{sd} = L_{sd} i_{sd} + M_d i_{rd} \quad \Psi_{sq} = L_{sq} i_{sq} + M_q i_{rq} \quad \Psi_{rd} = L_{rd} i_{rd} + M_d i_{sd} \quad \Psi_{rq} = L_{rq} i_{rq} + M_q i_{sq} \tag{2}$$

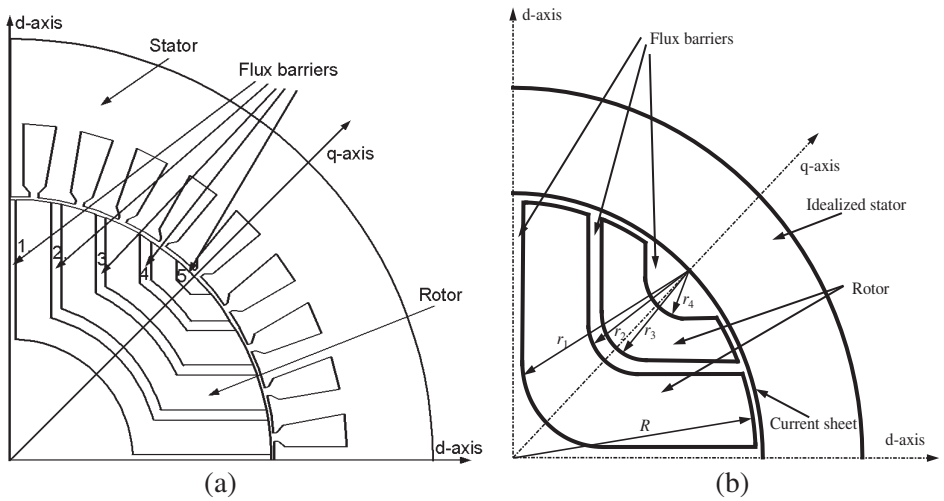

Figure 1: (a) SRM cross-section with a segmented rotor. (b) Idealized model of SRM.

where M_d represents the mutual inductance between the stator and rotor direct inductances and M_q is the mutual inductance between the stator and rotor q-axis inductances. Based on the definitions above, the expression for the electromagnetic torque is (m is the number of phases and P is the number of poles):

$$T_{em} = \frac{m}{2}\frac{P}{2}\left(\Psi_{sd} i_{sq} - \Psi_{sq} i_{sd}\right) \tag{3}$$

3. NON-LINEAR MODEL OF SRM WITH NEURAL NETWORKS

All electric and magnetic performances of synchronous reluctance motor depend on its geometric construction, used materials and on excitation level. It is almost impossible to express exact mathematical equations which would take into account all these influential parameters. The main idea is to develop such a model that will incorporate the influence of key parameters for specific desired SRM design. Or in other words, for desired input parameters (motor geometry, material and excitation level) the model should give the results usable to calculate motor output performance.

The model of SRM used in this analysis was idealized for the purposes of studying of artificial neural network application in such a problem (Fig. 1(b)). The main idealization was in slot-less stator geometry and in motor excitation. The current sheet placed on the stator side of the air gap represents the ideal excitation. These two changes in respect to real motor were also used to investigate the effect of different rotor geometry on magnetic flux density distribution in the air gap.

The m-phase stator winding may be in a form of d- and q-winding, each being identical to the original m-phase winding, except that their axes lie respectively along the d and q axis. The values of current sheets on the stator inner surface at any space angle θ from d-axis in d and q modes are:

$$A_d = \frac{\pi}{\tau_p}\frac{4}{\pi}\frac{m}{2}\frac{k_w}{p}\sqrt{2} I_d N \sin\left(\frac{P}{2}\theta\right) = A_{dm}\sin\left(\frac{P}{2}\theta\right), \tag{4}$$

$$A_q = \frac{\pi}{\tau_p}\frac{4}{\pi}\frac{m}{2}\frac{k_w}{p}\sqrt{2} I_q N \cos\left(\frac{P}{2}\theta\right) = A_{qm}\cos\left(\frac{P}{2}\theta\right). \tag{5}$$

where τ_p is the pole pitch and k_w is the winding factor. This is a fairly accurate approximation, ignoring space harmonics in the MMF wave caused by stator currents being located at discrete points instead of being sinusoidally distributed around the stator.

To set-up a non-linear model of SRM with neural networks it was necessary to investigate the dependence between magnetic flux density, excitation level, rotor inner geometry and rotor radius (at the same time idealized stator outer diameter). Magnetic flux density distribution was calculated using FLUX 2D [3]. The model was excited with different constant values of both current sheets (4, 5). The geometry changes were achieved by variation of rotor inner radii r_1, r_2, r_3, r_4 (Fig. 1(b)) and by variation of rotor radius R (or pole pitch). At any geometry change and for specific excitation level A_{dm} and A_{qm} the magnetic flux density distributions B_d and B_q along the

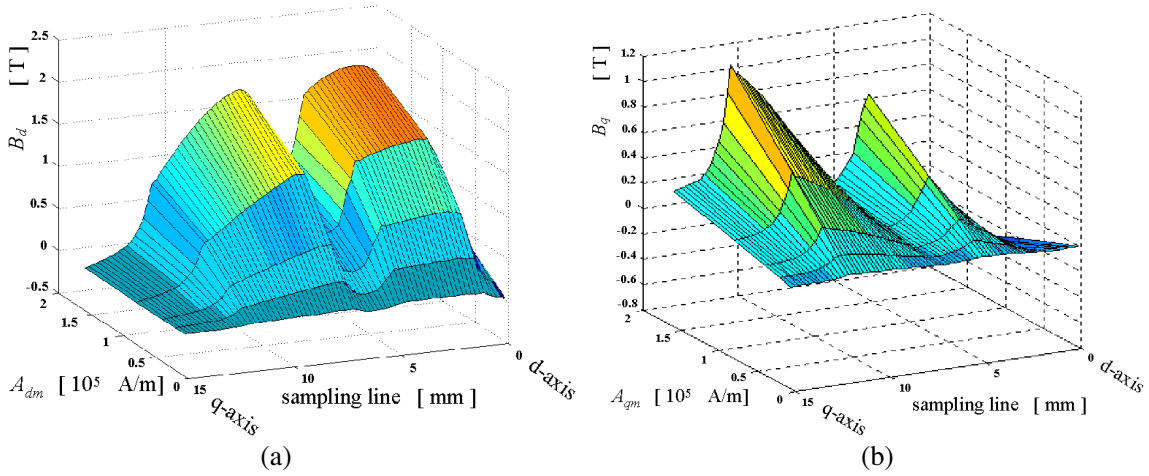

Figure 2: (a) B_d at different excitation levels A_{dm}. (b) B_q at different excitation levels A_{qm}.

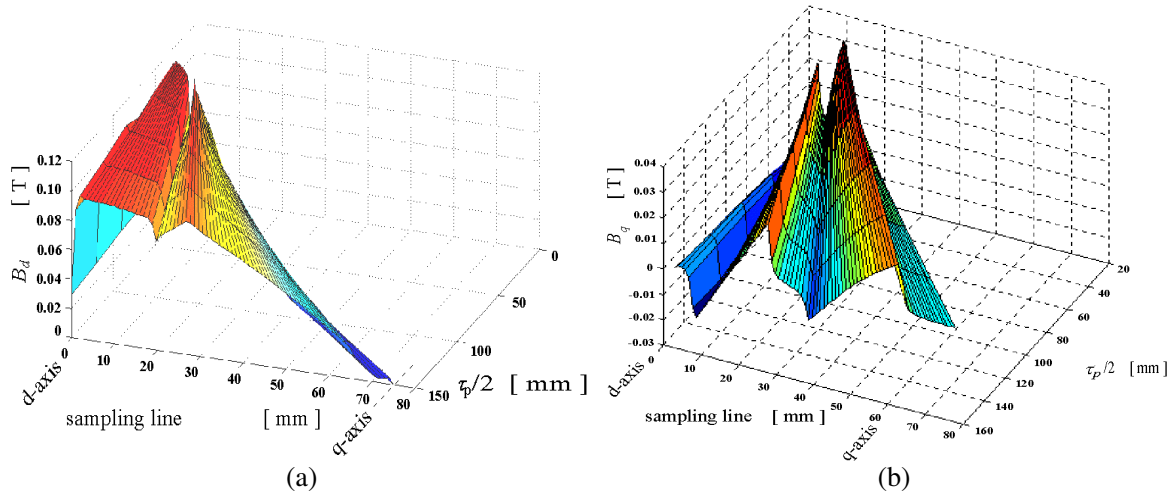

Figure 3: (a) B_d distribution for different rotor radii R (pole pitches). (b) B_q distribution for different rotor radii R.

air gap were calculated. Meanwhile, the effective width of the air gap including the effect of stator slotting (Carter's coefficient) remains constant all the time. The distance between sampled points along the air gap was at every one third of air gap width. This value was chosen due to necessity of a good approximation of the flux density distribution between sampled points. The distribution of B_d along the air gap for certain rotor geometry in function of different excitation levels A_d is shown in Fig. 2(a). The distribution of B_q was calculated for the same motor geometry with excitation levels $A_{qm} = A_{dm}$ and it is presented in Fig. 2(b). The distributions of B_d and B_q in function of rotor radius R at certain excitation level A_{dm} and A_{qm} are shown in Fig. 3(a) and Fig. 3(b).

Knowing the dependence of these magnetic field distributions (Figs. 2 and 3) the neural network training data set can be reduced. For example, the shape of surface from Fig. 2(a) can be described with five magnetic flux density distributions calculated at different excitation levels A_{dm} and then interpolated with each other. All other surfaces (Figs. 2(b), 3(a), 3(b)) can be described by calculating field distributions at both extremities and then interpolated with each other due to their linear dependence. In this way the training data set for specific rotor geometry was reduced from twenty to nine calculated field distributions. In other words, required training data set to describe all training geometries at different excitations was reduced for more than 50%.

4. APPLICATION OF ARTIFICIAL NEURAL NETWORKS

The suitability of applying ANN to find the magnetic flux density distribution for desired design of SRM was explored. Conventional types of feed-forward ANN were used. They are commonly

known as multilayer back-propagation ANN. The MATLAB with Neural Network toolbox [4] was used to program the ANN. The basic ANN system is composed of input data $\{x\}$, corresponding target data $\{y\}$ and artificial neural network. Using given data pairs $(\{x\}, \{y\})$ the ANN learns the mapping $\{x\} \rightarrow \{y\}$. In the process of training, the ANN merely computes the mapping function. The ANN has input layer, hidden layers with number of neurons and output layer. Each neuron has weight (w) and bias (b). The mapping from one layer to next one is done with transfer function σ. The capability of approximation mainly depends on ANN topology, number of used neurons in hidden layer and on proper presentation of learning data set to the ANN. During the learning process the ANN is trying to reduce sum-square-error (SSE) between presented target data and calculated output ANN results.

Input data and corresponding target data form a training data set and they are used to train network until it can associate input data with specific target data. The trained back-propagation network tends to give reasonable answer when presented with inputs that it has never seen (testing data set). This means that ANN doesn't need to be trained on all possible combination of input/target data combinations to give correct output on given input data set. This advantage of ANN generalization can also be used to diminish the number of training data calculated with finite element method.

A pair of data set for each mode (d and q) of model excitation was prepared. Each pair consists of training and testing data. First data set used to train the ANN include the magnetic flux density distribution along the air gap from d to q axis for d mode excitation as target data matrix. Input data r_1, r_2, r_3, r_4, R (τ_p), A_d and A_q were in vector form. During this study, the number of different training geometries at specific excitation levels was 200.

During training process different ANN topology, number of used neurons, transfer functions and presentations of training data set to the neural network were investigated. Magnetic field distributions as output results of trained ANN for the training geometry were very satisfactory. Meanwhile, the results carried out from the same trained ANN for rotor geometry from testing data set were completely unusable. We tried to overcome this problem by applying more hidden neurons, using different transfer functions such as "logsig" and "radbas" [4], changing ANN topology to two hidden layers, reducing SSE and increasing the number of training epoch. The results were all the time quite the same, unusable. It was found out that the main problem is in the presentation of training data set to ANN.

New and different preparation of training and testing data set was inevitable. The form of each input vector changed to matrix form. The number of these new matrices became the same as the number of training geometries. Each matrix is so composed of five rows in which first four elements present rotor geometry and fifth one is an index of sampled point. So, the number of columns is equal to number of sampled points. Target data matrix has rows equal to number of sampled points and columns equal to number of input data matrix.

First column of first input matrix is presented to ANN atthe same time as first element of first target matrix column. Then, second column of first input matrix and second element of first target matrix column. This is repeated until all input and target matrices are submitted to ANN in training process.

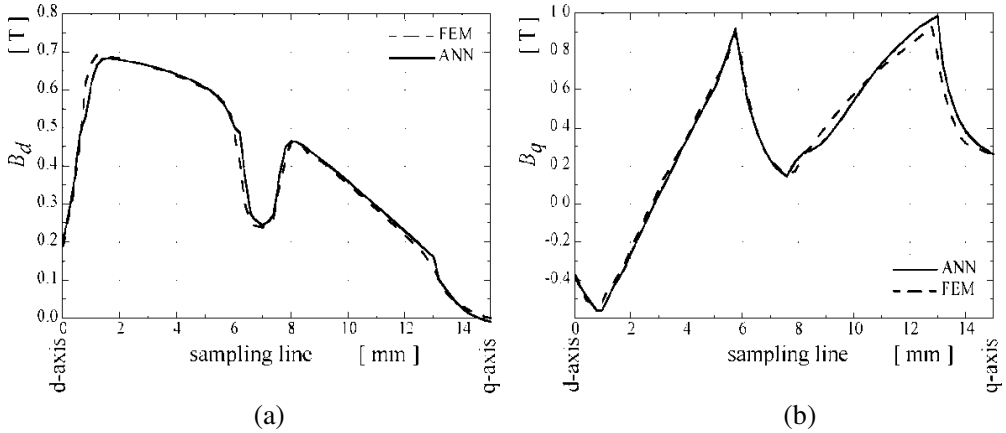

Figure 4: (a) B_d distribution comparison between FEM and ANN. (b) B_q distribution comparison.

To take into account the magnetic non-linearity of B_d (Fig. 2(a)) for all two hundred training geometries, five ANN were trained each one for each excitation level. Another two ANN for q-mode excitation extremities (Fig. 2(b)), two ANN for B_d in function of $R\ (\tau_p)$, and two for B_q in function of $R\ (\tau_p)$. The non-linear model of SRM is then established by joining of all eleven trained ANN.

During the training process the number of hidden neurons changed. The best results were achieved using twelve hidden neurons with "tansig" transfer function and an output neuron with linear transfer function (6),

$$\sigma_1(z) = \frac{e^z - e^{-z}}{e^z + e^{-z}} \quad \sigma_2(z) = z, \tag{6}$$

where z is formed as the sum of weighted inputs and bias value of neuron. The results for testing data set for one d-mode excitation level are shown in Fig. 4(a) and for q-mode in Fig. 4(b), compared with the FEM results.

5. CONCLUSIONS

Non-linear model of SRM with ANN was established. The model input parameters are: rotor geometry defined with inner radii (Fig. 1b), rotor semi-diameter and excitation levels. Output model results are: direct B_d and quadrature B_q magnetic flux density distribution along the air-gap. During the study it was necessary to reduce the model complexity, develop proper ANN topology and data presentation to ANN. Results from the non-linear model were compared with finite element modeling results. The similarity between them confirms the use of artificial neural networks in these kinds of problems. Proposed method can be also applied in a field of special electric machines and in condition monitoring of electric machines.

REFERENCES

1. Ueyato, K., T. Senjyu, and Y. Tomori, "Modeling and vector control of synchronous reluctance motors including stator iron loss," *IEEE Trans. Ind. App.*, Vol. 30, No. 4, 971–976, 1994.
2. Lubin, T., H. Razik, and A. Rezzoug, "On-line efficiency optimization of a synchronous reluctance motor," *Electric Power System Research*, Vol. 77, 484–493, 2007.
3. FLUX2D, software for electromagnetic design, User manual, CEDRAT, 2008.
4. Beale, M. H., M. T. Hagan, and H. B. Demuth, *Neural Network Toolbox 7 User's Guide*, The MathWorks, Inc., Natic, USA, 2010.

Effect of Ga-doping on the Magnetic and Magnetocaloric Properties of (LaCaSr)(MnGa)O_3 Compound

A. Omri[1], **M. Bejar**[1], **M. Sajieddine**[2], **E. Dhahri**[1], **E. K. Hlil**[3], **and M. A. Valente**[4]

[1]Laboratoire de Physique Appliquée, Faculté des Sciences de Sfax
Université de Sfax, B. P. 1171, Sfax 3000, Tunisia
[2]Laboratoire de Physique et Mécanique des Matériaux, Faculté des Sciences et Techniques
Université Sultan Moulay Sliman, B. P. 523, Béni-Mellal 23000, Morocco
[3]Institut Néel, CNRS, Université J. Fourier, B. P. 166, Grenoble 38042, France
[4]Physics Department (UA), Campus Universitario, Aveiro 3810-193, Portugal

Abstract— Magnetoclaoric proprieties of $AMn_{1-x}Ga_xO_3$ (A = $La_{0.75}Ca_{0.08}Sr_{0.17}$ and $x = 0.175$) compound have been investigated. Isothermal measurements of magnetization allow us, through thermodynamic Maxwell relations, to determine the magnetic entropy change. We have discovered a large magnetic entropy change ($-\Delta S_M$) at Curie temperature. The ΔS_M increases from 0.45 to 2.91 J/kg·K when the applied magnetic increasing from 0.5 to 5 T respectively. The discrepancy between theoretical and experimental values of ($-\Delta S_M$) was explained by the fact that Landau model does not take the exchange interactions and Jahn-Teller effect on the magnetic properties. This result shows that this compound can be considered as potential candidate for magnetic refrigerants.

1. INTRODUCTION

Numerous studies have been devoted to the manganites such as the magnetoelectric (ME), the magnetocaloric effect (MCE).... The ME effect belongs to an entirely new class called as ferroelectromagnetics. These materials are also used in high speed power and signal distribution, microwave field and current measurements. The magnetocaloric effect (MCE) has been a subject of intense research owing to its possible application in magnetic refrigeration. This application is becoming a promising technology to replace the conventional gas-compression refrigeration due to its high efficiency, low noise, softer vibration and longer using time [1, 2].

Recently, an increase interest has been observed in this field due to efforts in developing novel materials with large magnetic entropy. The recent researches one carried out with the aim of optimizing the physical properties of the manganites for the magnetic refrigeration application [3]. Perovskite based manganese oxide with the general formula $R_{1-x}A_xMnO_3$ (R = trivalent rare earth, A = divalent ion) [4] display a variety of physical proprieties such as the paramagnetic to ferromagnetic transition. The mixed state valence of manganese ions plays a paramount role of double exchange (DE) and super exchange (SE) mechanisms [4, 5], which is at the base of the metal behavior and the ferromagnetic properties. The basic processes of the DE mechanism, proposed by Zener in 1951 [5], was the hopping of e_g electron from Mn^{3+} ($t_{2g}^3\ e_g^1$) to Mn^{4+} ($t_{2g}^3\ e_g^0$) ions via O^{2-} one. In manganites is possible to substitute both at A and Mn site. A-site doping is known to control the Mn^{3+}/Mn^{4+} ratio. Compared to A-site doping, Mn-site doping is more important because it not only modifies the Mn^{3+}-O^{2-}-Mn^{4+} network but also brings about many new exchange interactions between the Mn ions and the doped transition metal ions.

The aim of this work is to provide a through understanding of Ga substitution influence at Mn site on the magnetic and magnetocaloric properties in $AMn_{0.825}Ga_{0.175}O_3$ compound.

2. EXPERIMENTAL

The $AMn_{0.825}Ga_{0.175}O_3$ compound was prepared by a standard solid ceramic method at high temperatures. Stoichiometric amounts of La_2O_3, $SrCO_3$, MnO_2, $CaCO_3$ and Ga_2O_3 precursors were mixed and then heated at 673 K for 12 hours to achieve decarbonation. Finally, the compound was sintered at 1273 K for 2 days in air. The magnetic properties were explored with a vibrating sample BS2 magnetometer developed in Louis Neel Laboratory of Grenoble. Isothermal magnetization (M) versus applied magnetic field ($\mu_0 H$) curves were collected by temperature step every 5 K under an applied magnetic field varying from 0 to 5 T.

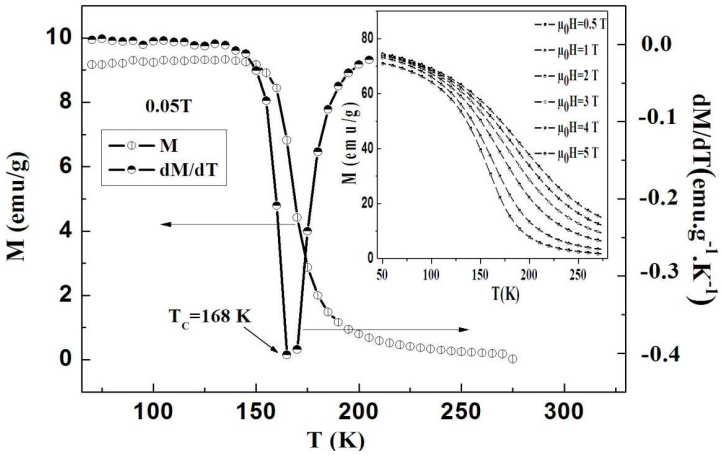

Figure 1: Magnetization and its derivative deduced from (dM/dT) for $AMn_{0.825}Ga_{0.175}O_3$ sample. The inset shows the temperature dependence of magnetization for $AMn_{0.825}Ga_{0.175}O_3$ sample measured at different applied magnetic field.

3. RESULTS AND DISCUSSIONS

To investigate the doping effect of the Mn magnetic ion by non magnetic d^{10} Ga^{3+} one [6] on the magnetic properties of $AMn_{0.825}Ga_{0.175}O_3$ compound, the temperature dependence of magnetization was measured at applied magnetic field 0.05 T. The $M(T)$ curve reveals that sample exhibits a single transition from a ferromagnetic to a paramagnetic phase at the Curie temperature of 168 K defined by the peak of dM/dT (T) curve (Figure 1(a)).

Figure 1(b) shows the temperature dependence of magnetization for $AMn_{0.825}Ga_{0.175}O_3$ sample measured at different applied magnetic field $(\mu_0 H)$. Indeed, the $M(T, \mu_0 H)$ curves reveal the presence of ferromagnetic-paramagnetic transition qualified from the second order, where magnetization varies continuously in range transition temperature. Also, we can conclude that there is broad magnetic entropy associated with a ferromagnetic-paramagnetic transition at Curie temperature.

The magnetocaloric effect (MCE) was estimated, in terms of isothermal magnetic entropy change $(-\Delta S_M)$, using the $M(T, \mu_0 H)$ data and employing the thermodynamic Maxwell equation [7–11]:

$$\left(\frac{\partial S}{\partial (\mu_0 H)}\right)_T = \left(\frac{\partial M}{\partial T}\right)_{\mu_0 H} \tag{1}$$

From Eq. (1), the isothermal entropy change can be calculated by means of magnetic measurements:

$$\Delta S_M \left(T, \mu_0^H\right) = S_M \left(T, \mu_0^H\right) - S_M \left(T, 0\right) = \int_0^{\mu_0^H} \left(\frac{\partial M \left(T, \mu_0^H\right)}{\partial T}\right) d\left(\mu_0^H\right) \tag{2}$$

Numerical evaluation of $(-\Delta S_M)$ by the variation of external applied field was carried out by approximating the above equation to the following relation:

$$\Delta S_M \left(\frac{T_1^+ T_2}{2}\right) = \frac{1}{T_2 - T_1} \left[\int_0^{\mu_0 H} M \left(T_2, \mu_0 H\right) d\left(\mu_0 H\right) - \int_0^{\mu_0 H} M \left(T_1, \mu_0 H\right) d\left(\mu_0 H\right)\right] \tag{3}$$

By using a program carried out in our laboratory by Pr. N. Fourati and E. Dhahri based on Eq. (3), we have determined $(-\Delta S_M)$ variation. We have plotted the variation of the magnetic entropy changes $(-\Delta S_M)$ as a function of temperature at several applied magnetic fields (a-inset of Figure 2). It is noted that this variation is very significant with the vicinity of the Curie temperature, which is towards 165 K. The application of a magnetic field varying from 0.5 to 5 T induces a variation of $(-\Delta S_M)$ from 0.45 to 2.91 J/kg·K, respectively.

The large magnetic entropy change in manganites is caused by the spin-lattice coupling in the magnetic ordering process. The strong spin-lattice coupling arising from a reasonable variation in

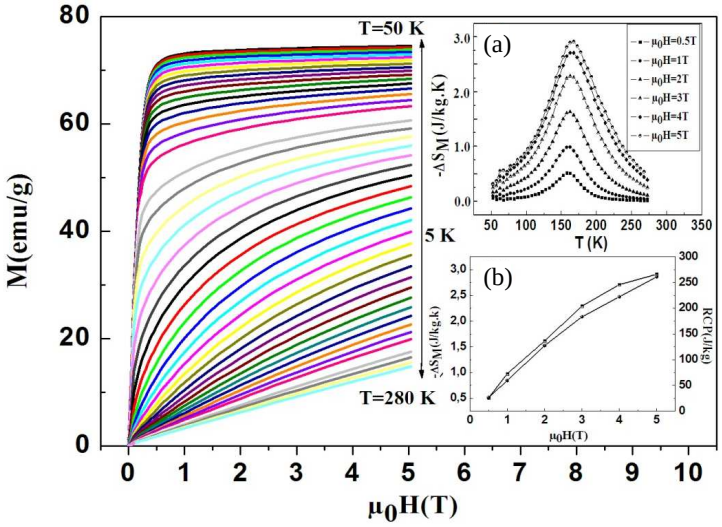

Figure 2: Isothermal magnetization for $AMn_{0.825}Ga_{0.175}O_3$ sample measured vs. magnetic field around T_C. The inset (a) Temperature dependence of the magnetic entropy change under different magnetic fields, (b) represents the maximum entropy change and RCP values vs. applied magnetic field.

d(Mn/Ga)-O bond length and (Mn/Ga)-O-(Mn/Ga) bond angle at T_C may also contribute to the enhancement of the observed magnetic entropy change.

Figure 2 shows isothermal magnetization (M) curves for $AMn_{0.825}Ga_{0.175}O_3$ sample measured in the magnetic field range of 0–5 T at various temperatures. From these curves, we can conclude that the magnetization increases sharply with applied magnetic field.

The maximum of magnetic entropy changes ($-\Delta S_M^{\max}$) upon the magnetic applied field changes of 0.5 and 5 T are about 0.45 and 2.91 J/kg·K, respectively. This maximum was found to exhibit a linear rise with increasing field (b-inset of Figure 2). The magnetic cooling efficiency of a magnetocaloric material can be evaluated by considering the magnitude of ($-\Delta S_M$) and its Full-Width at Half Maximum (δT_{FWHM}) [12, 13].

The Relative Cooling Power (RCP) factor was calculated, using the following equation:

$$\mathrm{RCP} = |\Delta S_M^{\max}| \times \delta T_{FWHM} \tag{4}$$

The RCP factor represents a good way for comparing and selecting potential substances for the magnetic refrigerant application. The inset b of Figure 2 presents the RCP data plotted as a function of magnetic applied field. We can mention that RCP increases from 27 to 261 J/kg when $\mu_0 H$ increasing from 0.5 to 5 T, respectively. For comparison, the maximum of ($-\Delta S_M$) and the RCP values for other samples are summarized in Table 1. We can deduce that our compound presents comparable values and could be considered as a potential and a good candidate for magnetic refrigeration.

It is well known that the magnetic Gibbs free energy for the magnetic systems $G(T, M)$, in general, can be expressed as a Landau expansion in magnetization as [15, 16]:

$$G(T,M) = G_0 + \left(\frac{1}{2}\right) A(T) M^2 + \left(\frac{1}{4}\right) B(T) M^4 + \left(\frac{1}{6}\right) C(T) M^6 - M(\mu_0 H) \tag{5}$$

Using the equilibrium condition, ($\frac{\partial G}{\partial M} = 0$), we obtain the equation below, which describes the total magnetization in the vicinity of the Curie temperature:

$$\frac{\mu_0 H}{M} = A(T) + B(T) M^2 + C(T) M^4 \tag{6}$$

where A, B and C coefficients are temperature dependent parameters obtained from Eq. (2) [12–17].

The corresponding magnetic entropy can be obtained by a differentiation of the magnetic part of the Gibbs free energy with respect to temperature:

$$-\Delta S_M(T, \mu_0 H) = \left(\frac{1}{2}\right) A' M^2 + \left(\frac{1}{4}\right) B' M^4 + \left(\frac{1}{6}\right) C' M^6 \tag{7}$$

Table 1: $(-\Delta S_M)$ and RCP values at T_C under a magnetic field for several typical magnetic refrigeration materials.

Materials	$\mu_0 H$ (T)	T_C (K)	$-\Delta S_M$ (J/kg·K)	RCP (J/kg)	Reference
Gd	2	299	4.2		[16]
$La_{0.70}Ca_{0.15}Sr_{0.15}Mn_{0.975}Fe_{0.025}O_3$	2	336.4		115.75	[17]
$La_{2/3}(Ca_{0.50}Sr_{0.50})_{1/3}MnO_3$	1	337	1.7	38	[19]
$La_{0.75}Ca_{0\cdot125}Sr_{0.125}MnO_3$	1.5	282	1.5	108	[18]
$La_{0.75}Ca_{0.1}Sr_{0.15}MnO_3$	1.5	325	2.85	72	[18]
$La_{2/3}(Ca_{0.75}Sr_{0.25})_{1/3}MnO_3$	1	300	1.8	54	[19]
$La_{0.75}Ca_{0.08}Sr_{0.17}Mn_{0.825}Ga_{0.175}O_3$	2	168	1.71	127.5	Our work

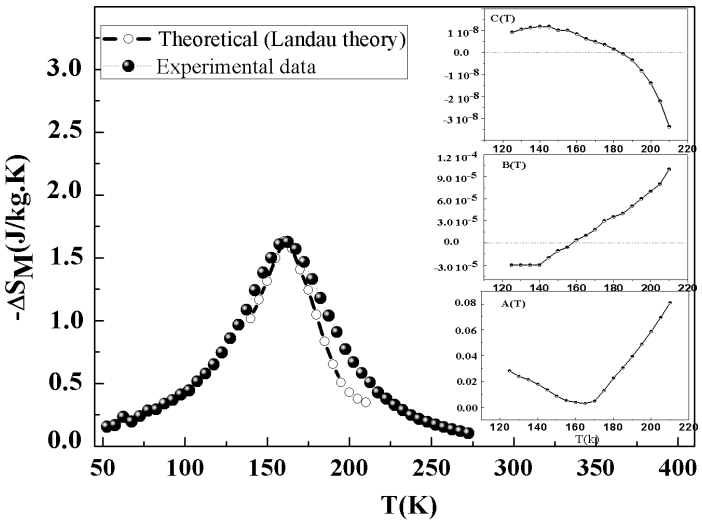

Figure 3: Theoretical and experimental magnetic entropy change for $AMn_{0.825}Ga_{0.175}O_3$ compound at magnetic field variation 0–2 T. Inset: temperature dependence of Landau coefficients. The units for $A(T)$, $B(T)$ and $C(T)$ are $T^2\,kg/J$; $T^4\,kg^3/J^3$ and $T^6\,kg^5/J^5$, respectively.

where A', B' and C' are the temperature derivatives of the Landau coefficients.

The temperature dependence of the parameters A and B is obtained from the linear region of the Arrott plot of $\frac{\mu_0 H}{M}$ versus M^2. The variations of $A(T)$, $B(T)$ and $C(T)$ values are shown in the inset of Figure 3. Using parameters A and B, determined from the experimental data, the magnetic entropy change is calculated from Eq. (7). Figure 3 shows the Landau theoretical and experimental magnetic entropy change $(-\Delta S_M)$ values. It is clear from the results that there is a discrepancy between the two $(-\Delta S_M)$ values, except above Curie temperature T_C. This discrepancy may be due to the fact that this Landau model does not take into account the influence of exchange interactions and the Jahn-Teller effect on the magnetic properties.

4. CONCLUSION

In this work, we have discussed the magnetic and magnetocaloric properties of $AMn_{0.825}Ga_{0.175}O_3$ compound. We have found that this sample displays a large maximum entropy change ($-\Delta S_M = 1.71\,J/kg{\cdot}K$) value at an applied magnetic field of 2 T with a relatively large RCP value (127.5 J/kg), which is well comparable with the commercial magnetic refrigerant materials. So, the $AMn_{0.825}Ga_{0.175}O_3$ compound could be considered as a potential and a good candidate for magnetic refrigeration.

ACKNOWLEDGMENT

This paper within the frame work of collaboration is supported by the Tunisian Ministry of Higher Education and Scientific Research, the Ministry of National Education, Higher Education, Executives training and Scientific Research of Morocco, and the Portuguese Ministry of Science, Technology and Higher Education.

REFERENCES

1. Tegus, O., E. Bruck, K. H. J. Buschow, and F. R. de Boer, "Transition-metal-based magnetic refrigerants for room-temperature applications," *Nature*, Vol. 415, 150–152, 2002.
2. Phan, M. H. and S.-C. Yu, "Review of the magnetocaloric effect in manganite materials," *J. Magn. Magn. Mater.*, Vol. 308, No. 2, 325–340, 2007.
3. Kitanovski, A. and P. W. Egolf, "Thermodynamics of magnetic refrigeration," *International Journal of Refrigeration*, Vol. 29, No. 1, 3–21, 2006.
4. Coey, J. M. D., M. Viret, and S. Von Molnar, "Mixed valence manganites," *Adv. Phys.*, Vol. 48, No. 2, 167, 1999.
5. Zener, N., *Phys. Rev.*, Vol. 82, 403, 1951.
6. Vertruyen, B., S. Hebert, A. Maignan, C. Martin, M. Hervieu, and B. Raveau, "Magnetic properties of Ga-doped lanthanum manganite with controlled oxygen stoichometry," *Crystal Engineering*, Vol. 5, No. 3–4, 299–306, 2002.
7. Kallel, N., S. Kallel, A. Hagaza, and M. Oumezzine, "Magnetocaloric properties in the Cr-doped $La_{0.7}Sr_{0.3}MnO_3$ manganites," *Physica B*, Vol. 404, 285–288, 2009.
8. Gutiérrez, J., J. R. Fernàndez, J. M. Barandiaràn, I. Orùe, and L. Righi, "Magnetocaloric effect in $(La_{0.55}Bi_{0.15})Ca_{0.3}MnO_3$ perovskites," *Sensors and Actuators A*, Vol. 142, 549–553, 2008.
9. Dhahri, J., A. Dhahri, M. Oumezzine, and E. Dhahri, "Effect of Sn-doping on the structural, magnetic and magnetocaloric properties of $La_{0.67}Ba_{0.33}Mn_{1_x}Sn_xO_3$compounds," *J. Magn. Magn. Mater.*, Vol. 320, 2613–2617, 2008.
10. Das, S. and T. K. Dey, "Magnetic entropy change in polycrystalline $La_{1-x}K_xMnO_3$ perovskites," *J. of Alloys and Compd.*, Vol. 440, 30–35, 2007.
11. Nisha, P., S. S. Pillai, A. Darbandi, A. Misra, K. G. Suresh, M. R. Varma, and H. Hahn, "Magnetism and magnetocaloric effect in nanocrystalline $La_{0.67}Ca_{0.33}Mn_{0.9}V_{0.1}O_3$ synthesized by nebulized spray pyrolysis," *J. Phys. D Appl. Phys.*, Vol. 43, 135001, 2010.
12. Kallel, S., N. Kallel, O. Peña, and M. Oumezzine, "Large magnetocaloric effect in Ti-modified $La_{0.70}Sr_{0.30}MnO_3$ perovskite," *Materials Letters*, Vol. 64, 1045–1048, 2010.
13. Tang, W., W. Lu, X. Luo, B. Wang. X. Zhu, W. Song, Z. Yang, and Y. Sun, "Particle size effects on $La_{0.7}Ca_{0.3}MnO_3$: Size-induced changes of magnetic phase transition order and magnetocaloric study," *J. Magn. Magn. Mater.*, Vol. 322, 2360–2368, 2010.
14. Dhahri, J., A. Dhahri, M. Oumezzine, E. Dhahri, M. Said, and H. Vincent, "Magnetocaloric properties of Cd-substituted perovskite-type manganese oxides," *J. of Alloys and Compd.*, Vol. 467, 44–47, 2009.
15. Mahato, R. N., K. Sethupathi, V. Sankaranarayanan, and R. Nirmala, "Co-existence of giant magnetoresistance and large magnetocaloric effect near room temperature in nanocrystalline $La_{0.7}Te_{0.3}MnO_3$," *J. Magn. Magn. Mater.*, Vol. 322, No. 17, 2537–2540, 2010.
16. Xu, Y., M. Meier, P. Das, M. R. Koblischka, and U. Hartmann, "Perovskite manganites: Potential materials for magnetic cooling at or near room temperature," *Crystal Engineering*, Vol. 5, No. 3–4, 383–389, 2002.
17. Tozri, A., E. Dhahri, and E. K. Hlil, "Magnetic transition and magnetic entropy changes of $La_{0.8}Pb_{0.1}MnO_3$ and $La_{0.8}Pb_{0.1}Na_{0.1}MnO_3$," *Materials Letters*, Vol. 64, 2138–2141, 2010.
18. Guo, Z. B., W. Yang, Y. T. Shen, and Y. W. Du, "Magnetic entropy change in $La_{0.75}Ca_{0.25-x}Sr_xMnO_3$ perovskites," *Solid State Commun.*, Vol. 105, No. 2, 89–92, 1998.
19. Mira, J., J. Rivas, L. E. Hueso, F. Rivadulla, and M. A. Lopez Quintela, "Drop of magnetocaloric effect related to the change from first- to second-order magnetic phase transition in $La_{2/3}(Ca_{1-x}Sr_x)_{1/3}MnO_3$," *J. Appl. Phys.*, Vol. 91, No. 10, 8903–8905, 2002.

The Design of a GPR Test Site for Underground Utilities

W. M. A. Wan Hussin and Mahmoud Bashir Alhasanat
School of Civil Engineering, University Science Malaysia (USM), Engineering Campus
14300 Nibong Tebal, Penang, Malaysia

Abstract— This paper proposes a design for GPR test site for underground utilities. A test site with the following parameters: 8 meters in width, 17 meters in length, and 4 meters in depth is the design proposed for construction in Malaysia. Differing samples of pipe sizes and materials are represented as buried objects for GPR survey. The site is designed to meet the changing needs of researchers so as to eliminate most of the commonly known GPR limitations.

1. INTRODUCTION

An Actual Field-based physical model or 'laboratory' is the best way to improve and best understand data interpretation. In ground penetrating radar (GPR), a closed laboratory is not suitable due to the high degree of clutter that occurs subsequent to wall and ceiling interference. A field model (test site) is therefore the most suitable strategy for actual GPR experiments. Although test sites are often costly and not easy to build, it provides significant advantages for purposes of GPR data interpretation through 1) the homogeneity of host materials; 2) clear interface contrast between buried objects and host materials; 3) the absence of moisture, and/or of any potential bodies that may reflect radar waves causing clutter; and 4) known sizes and materials of buried objects.

To determine the best approach for GPR image reconstruction in a real environment and compare different inversion techniques, simulations can be applied in a straightforwardly simple and distinct environment [1]. The underground is usually not homogenous so that GPR data is affected by varied factors such as: radio wave frequency; antenna beam width; velocity of propagation; dielectric properties of host material; contrast of the dielectric constant of host material and buried object; ratio of existing moisture; wave propagation depth or attenuation; congestion of buried objects; and varying clutter due to unwanted reflected signals. Some of these factors can be controlled by human effort while others cannot. Signal propagation loss due to imaginary components of dielectric ground permittivity depends on the characteristics of the materials which constitute the soil. Changes in the dielectric are constant with depth and any loss in material is because of the presence of moisture [2].

Images acquired from reflected signals are data, and do not constitute photographs of buried objects beneath the surface under investigation. In reality, any radar image represents amplitudes of reflected signals from the interfaces while exhibiting different dielectric properties [3]. While many problems face GPR, if a researcher attempts to solve problem, other extant GPR limitations often do not allow the achievement of good results. In view of this, a good test site can filter out most of these GPR limitations after which the research may focus on the problem to be solved. Furthermore, real time calibration for GPR is costly and is not available in most developed countries; therefore, test sites offer reliable calibrations for GPR using synthetically buried objects.

GPR data interpretation can be difficult because of uncertainty about buried objects. To reduce ambiguity in data interpretation, a better designed GPR test site is vital. The test site is actually not for simulation of the real world but rather for the solving of specific problems. Colla, et al. [4] claimed that: "It is expected that simulation will allow the interpretation of actual surveys to be more readily understood, which will in turn allow a better engineering assessment to be made of a structure under investigation."

There exist many GPR test sites and that differ with regards to purpose. For example, a test site at Laboratoire Central des Ponts et Chaussees (LCPC) in Nantes, France, was built in 1996 and comprises a pit of 26 meters by 20 meters with a depth of 4 meters. The test site is divided into five sections with different types of object buried in different host materials [5]. Another test site has been constructed in Azienda Agraria at La Tuscia University in Viterbo. It consists of a pit filled with sand and gravel with dimensions of 4 meters and 6 meters and a depth of 1.2 meters and is isolated with a PVC sheath [6]. Applied Research Associates, Inc. (ARA) has established a test site in South Royalton, Vermont [7]. A geophysical test site of IAG/USP located in São Paulo City in Brazil, has an area of 1500 square meters. Buried objects with different geometries and

Figure 1: Location of the test site.

types of targets are buried at depths varying from 0.5 to 2 m [8]. Two archaeological tests sites are also established in Illinois and Washington. The one in Illinois uses moist clay and silt to bury features ranging in depth from 30 to 60 cm below the ground surface, and the site in Washington uses dry wind-blown sand to bury objects of varied features ranging in depth from 50 to 150 cm [9]. Elena, et al. [1] constructed a GPR test site at the Canadian Forces Base in Borden where the water table at the site was 3 to 4 m. Empty pipes with different types and diameters were buried about 5 meters apart at a depth of 1.25 meters in which the host material used was the same excavated soil.

This paper proposes a design for a test site for the purpose of GPR calibration. This test site: 8 meters wide, 17 meters long and 4 meters deep is designed for construction at the Universiti Sains Malaysia Engineering Campus in Pulau Pinang, Malaysia. Different samples of underground utilities of variable sizes and materials are presented as buried objects.

2. DESIGN METHODOLOGY

The location of the test site is chosen precisely with the aid of GIS for optimum site selection (see Figure 1). Existing digital maps including technical information of the Engineering Campus were used and a buffer zone analysis depending on criteria set was decided.

2.1. Criteria for Test Site Location

1. The location should be inside the Engineering Campus.
2. The site should be positioned at least 25 meters away from buildings, metal constructions, electric poles, trees, car parks and water bodies to decrease noise as much as possible.
3. The site should be easily accessible through a paved road.
4. No buried utility should exist at the proposed site.
5. A Dimension of 8 by 17 meters is considered reasonable to save costs.
6. The bottom level of the site should be higher than the water table by at least one and half metes to avoid soil dent.

2.2. Criteria Considered for the Design

1. The depth is 4 meters.
2. Length of samples: 4 meters and closed at both ends.
3. Dry sand is used for the host material covered with PVC instead of asphalt or concrete.
4. It can be affixed by small hooks in existing concrete walls.
5. PVC sheath is used to host the sand and isolate it from water table and rain water.
6. Objects should be buried one meter apart to avoid intense hyperbolic overlapping.

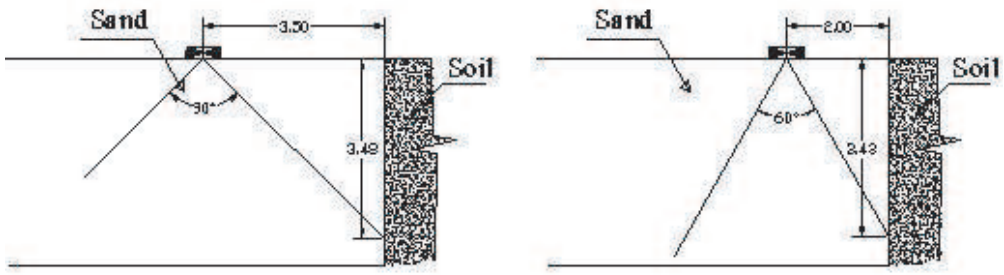

Figure 2: Interfaces detection distance results of antenna cone beam angle of 90 and 60 degrees.

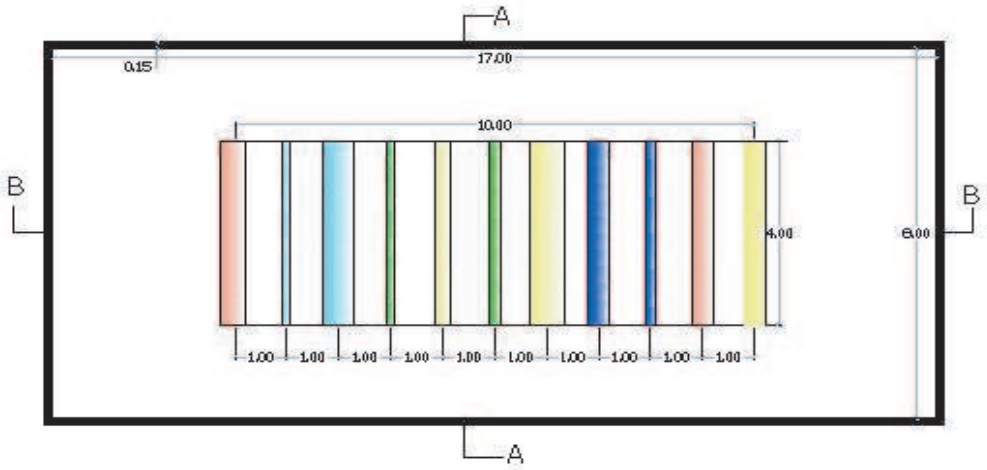

Figure 3: Design plan view.

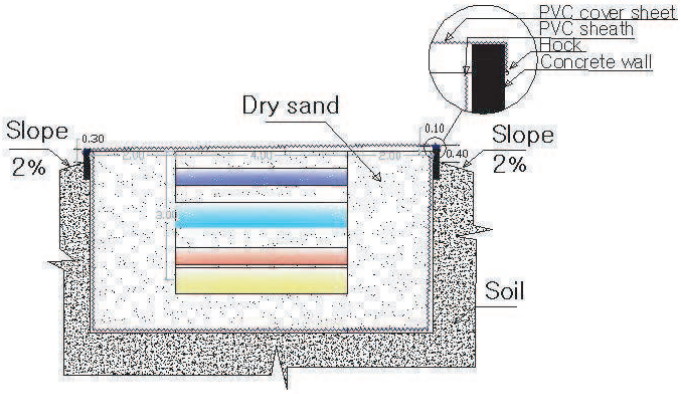

Figure 4: Section A-A.

7. The experimental site's borders were determined at 2 meters from either border width-wise and 3.5 meters from either border length-wise. Calculations depend on the angle of the beam from the antenna cone, and the design supposes maximum angles of 90 and 60 degrees respectively for perpendicular survey. Therefore, a distance of two meters from the interface wall was decided as the interface detection over a distance of 3.43 m (Figure 2), while targets are designed to be buried with a maximum depth of 3 m. Thus, any feature or noise shown in the radar image having a depth greater than 3 meters should be ignored.
8. The purpose of the design is for underground utility, specifically pipes (Figures 3–5).

3. ADVANTAGES OF THE PROPOSED SITE

1. There exists no such site in Malaysia. The test site at the Department of Survey and Mapping Malaysian Headquarters in Kuala Lumpur has many restrictions and was designed to simulate the real world which is full of noises and distracting clutter.

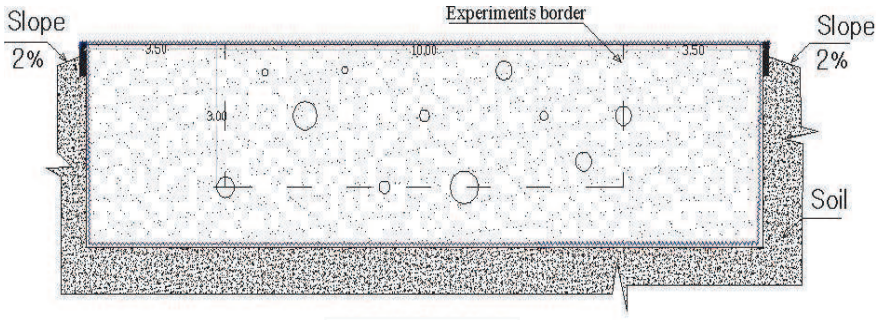

Figure 5: Section B-B.

2. It is always raining in Malaysia, so the land has a high ratio of moisture, thus using dry sand with PVC sheath and cover will prevent moisture and isolate it from the water table.
3. The site is designed to be able to replace targets because no hard upper layer (asphalt or concrete) was used thus making digging of sand easier and cost efficient.
4. No additional clutter is present due to the absence of a hard upper layer.
5. No intensive clutter emanates from the interface between sand and soil which sometimes create confusing interpretation as it appears as target in the radar image. By reducing the site size area, this problem is minimized.
6. It eliminates most of the common limitations encountered by the GPR process which have led researchers to focus on problems under investigation.

4. CONCLUSIONS

The proposed design is considered to address most of common problems facing radar image interpretation in order to have a better understanding of buried objects. The proposed design does not simulate the real world literally but allows researchers to obtain better outcomes comfortably.

REFERENCES

1. Pettinelli, E., A. Di Matteo, E. Mattei, L. Crocco, F. Soldovieri, J. Redman, and A. L. Annan, "GPR response from buried pipes: Measurement on field site and tomographic reconstructions," *IEEE Transactions on Geoscience and Remote Sensing,* Vol. 47, No. 8, 2639–2645, 2009.
2. Lester, J. and L. Bernold, "Innovative process to characterize buried utilities using ground penetrating radar," *Automation in Construction*, Vol. 16, No. 4, 546–555, 2007.
3. Loulizi, A., "Development of ground penetrating radar signal modeling and implementation for transportation infrastructure assessment," Virginia Polytechnic Institute and State University, Blacksburg, 2001.
4. Colla, C., C. Burnside, M. Clark, K. Broughton, and M. Forde, "Comparison of laboratory and simulated data for radar image interpretation," *NDT & E International*, Vol. 31, No. 6, 439–444, 1998.
5. Grandjean, G., J. Gourry, and A. Bitri, "Evaluation of GPR techniques for civil-engineering applications: Study on a test site," *Journal of Applied Geophysics,* Vol. 45, No. 3, 141–156, 2000.
6. Pasquo, B., E. Pettinelli, G. Vannaroni, A. di Matteo, E. Mattei, A. de Santis, P. Annan, and D. Redman, "Design and construction of a large test site to characterize the GPR response in the vadose zone," *2007 4th International Workshop on Advanced Ground Penetrating Radar*, 106–109, 2007.
7. Eppstein, M. and D. Dougherty, "Efficient three-dimensional data inversion: Soil characterization and moisture monitoring from cross-well ground-penetrating radar at a Vermont test site," *Water Resources Research*, Vol. 34, No. 8, 1889–1900, 1998.
8. Porsani, J., E. Slob, R. Lima, and D. Leite, "Comparing detection and location performance of perpendicular and parallel broadside GPR antenna orientations," *Journal of Applied Geophysics,* Vol. 70, No. 1, 1–8, 2010.
9. Conyers, L., "Moisture and soil differences as related to the spatial accuracy of GPR amplitude maps at two archaeological test sites," *Tenth International Conference on Ground Penetrating Radar*, Delft, The Netherlands, 2004.

A New Algorithm to Estimate the Size of an Underground Utility via Specific Antenna

M. B. Alhasanat and W. M. A. Wan Hussin
School of Civil Engineering, Universiti Sains Malaysia, Engineering Campus, Pulau Pinang, Malaysia

Abstract— This paper presents a new algorithm to extract the diameter of a buried utility from a GPR image depending on its hyperbolic shape. To know the exact size of a buried utility would be a great achievement as size sometimes indicates the type and purpose of a utility. The algorithm does not depend on wave velocity or electric properties as these factors are already calculated via GPR software. This algorithm can be used 'on-site' to determine the diameter of any buried object.

1. INTRODUCTION

Ground penetrating radar is currently one of the most efficient tools used for locating underground utilities [1]. Though its ability is to detect metal and non-metal buried objects, underground utility sizing is more difficult and there is very little evidence of this utilization in industrial practice. Images obtained from the reflected signals are not photographs of objects beneath the surface being investigated [2]. As GPR cannot determine the exact shape or utility material, consequently, the type and purpose of the utility remains unknown. To know the exact size of the buried utility would be a great achievement as size sometimes indicates the type and purpose of utility. This paper presents a new algorithm for the extraction of the diameter of buried utilities using GPR imaging depending on hyperbolic shapes.

Buried objects have a number of important characteristics for civil engineering applications such as size estimation, material recognition and shape estimation. Pasolli et al. [3] provides a good review about the measurement of buried sizes and he claims that most of research activities are focused on buried object detection, location and depth, but works on object sizing are few. A method to estimate cylindrical object sizes using hyperbolic signatures was developed and the result indicate that the method is fully capable of estimating the radius and depth of buried objects to within 10% [4]. Another study has reported that the introduction of a weighting factor in Hough's transformation has shown that there is a correlation between radius, depth and velocity for given experimental uncertainties [5]. Yet another study carried out to estimate an 18 cm radius concrete pipe at 1 m depth, used an antenna at 600 MHz based on the generalized Hough transformation resulted with an estimated radius of 17.4 cm $\pm$ 5.9 cm [6]. Estimating the depth, size and dielectric characteristics of buried cylindrical objects is also proposed based on neural networks [7]. Xian-Qi et al. [8] provided a good review regarding the measurement of buried size. Varied methods and algorithms utilizing artificial neural network techniques and Hough's transformation to estimate the diameter of underground utilities and/or reinforcement bar sizes in concrete have also been reported [9–13].

2. METHODOLOGY

GPR has both an antenna transmitter and receiver. The first transmits radio waves into the ground and the second receives the reflected radar waves from any buried object under the surface. For the purpose of this investigation, a shielded dipole antenna with a cone that has a 90 degree spouse opening is considered. The pulse transmitted from the antenna has an elliptical footprint area underneath, and the long axis of the elliptical footprint is oriented in the direction of the dragging antenna.

While the antenna's drag and elliptical footprint's edge touches the buried object, a hyperbola is automatically shaped on the radar image based on the travel time of the signal's return between the buried object and dynamic antenna. In other words, no hyperbola will appear if the radar wave does not touch an object. As the wave line creates a tangent with the buried object, a hyperbola is produced exactly beneath the antenna at a distance equals to the tangent line (Figure 1). When the antenna is at the top of the same object, half of the hyperbola is completed (Figure 2). From here, it is concluded that half of the hyperbola is shaped when a quarter of the object's perimeter is revealed by the GPR.

From Figures 1 and 2, ΔT is added to obtain a complete triangle (Figure 3). It is evident that:

$$X^2 + Y^2 = (\Delta T + T)^2 \tag{1}$$

It is well known that a triangle has an interior angle of 180 degrees; therefore the third angle of this triangle should be 45 degrees, and the two angles of the same measure indicate that the two sides should be equal in length. Thus, X should be equal Y.

Manipulating the Equation (1):

$$\Delta T = \sqrt{(2X^2)} - T \tag{2}$$

Manipulating the Equation (2):

$$\Delta T = 1.4142136 * X - T \tag{3}$$

The circle's radius is the distance from the circle's center and is perpendicular to the tangent or ΔT. Thus, the radius is drawn and a triangle is produced as shown in Figure 4. Therefore, $\Delta T = R$.

Manipulating the Equation (3):

$$D = 2.8284271 * X - 2T \tag{4}$$

Actually using two parameters X and T may not give good result during image accuracy, therefore the third factor y should be involved.

Manipulating above equations:

$$R = \sqrt{2}\,T - X - y \tag{5}$$

Manipulating the Equation (4):

$$D = 2.8284271 * T - 2X - 2y \tag{6}$$

where D is the diameter of the buried object; X is the horizontal distance between the beginning and the top of the hyperbola; T is the vertical distance to the beginning of the hyperbola, and y is the pipe depth.

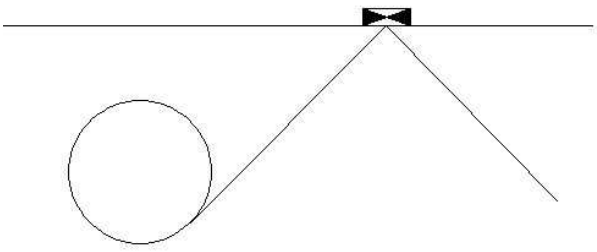

Figure 1: Radar wave is tangential to the buried object.

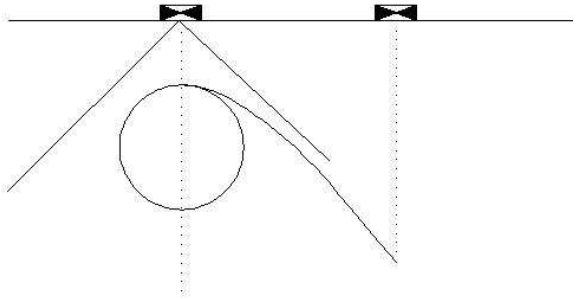

Figure 2: Half of hyperbola is completed.

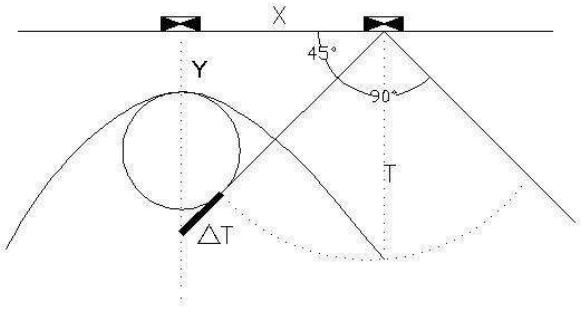

Figure 3: Relationship between ΔT and T.

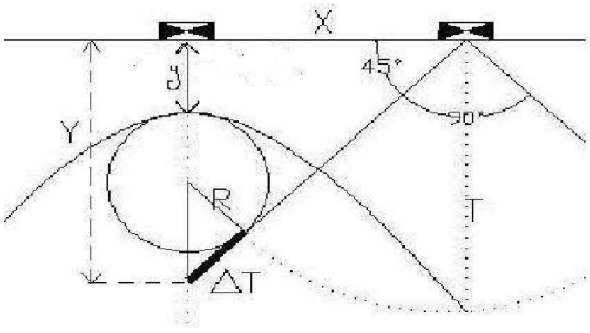

Figure 4: Relationship between radius R, ΔT, y and Y.

3. OTHER CONTRIBUTING FACTORS

There are however, several factors that can affect the hyperbolic shape in the process of estimating a buried object's size. Factors such as the dielectric proprieties of soil and pipes, frequency used, wave velocity, presence of moisture, and the speed of the dragging antenna are some of the major variables. However, these factors are already taken into consideration with the use of the software while the proposed algorithm is applied to the displayed GPR image that is processed. The calibration process carried out prior to detection work has, in fact, considered these factors as mentioned above. The proposed algorithm proves mathematically correct as well and as presented in the hyperbola above in Figures 3 and 4.

4. CONCLUSIONS

This algorithm does not depend on wave velocity or electric properties as these factors are already calculated via GPR software. This algorithm can be used 'on-site' to determine the diameter of any buried object. The values of D and T can be determined from the GPR software or through a simple program using Excel software, whereby interpreters then use the values of 'X' and 'T' as inputs to obtain the required information on the diameter of the buried object.

REFERENCES

1. Gurbuz, A. C., "Feature detection algorithms in computed images," Ph.D. Thesis, Georgia Institute of Technology, 2008.
2. Amara, L., "Development of ground penetrating radar signal modeling and implementation for transportation infrastructure assessment," Dissertation submitted to the Faculty of the Virginia Polytechnic Institute and State University, Blacksburg, Virginia, 2001.
3. Pasolli, E., F. Melgani, and M. Donelli, "Gaussian process approach to buried object size estimation in GPR images," *IEEE Geoscience and Remote Sensing Letters*, Vol. 7 No. 1, 141–145, 2010.
4. Shihab, S. and W. Al-Nuaimy, "Radius estimation for cylindrical objects detected by ground penetrating radar," *Subsurface Sensing Technologies and Applications*, Vol. 6, No. 2, 1–16, 2005.
5. Borgioli, G., L. Capineri, P. Falorni, S. Matucci, and C. G. Windsor, "The detection of buried pipes from time-of-flight radar data," *IEEE Trans. Geosci. Remote Sens.*, Vol. 46, No. 8, 2254–2266, Aug. 2008.
6. Windsor, C. G., L. Capineri, and P. Falorni, "The estimation of buried pipe diameters by generalized Hough transform of radar data," *PIERS Online*, Vol. 1, No. 3, 345–349, 2005.
7. Caorsi, S. and G. Cevini, "An electromagnetic approach based on neural networks for the GPR investigation of buried cylinders," *IEEE Geosci. Remote Sens. Lett.*, Vol. 2, No. 1, 3–7, 2005.
8. He, X.-Q., Z.-Q. Zhu, Q.-Y. Liu, and G.-Y. Lu, "Review of GPR rebar detection," *PIERS Proceedings*, 804–813, Beijing, China, March 23–27, 2009.
9. Shaw, M. R., T. C. K. Molyneaux, S. G. Millard, M. J. Taylor, and J. H. Bungey, "Assessing bar size of steel reinforcement in concrete using ground penetrating radar and neural networks," *Insight: Non-Destructive Testing and Condition Monitoring*, Vol. 45, No. 12, 813–816, 2003.
10. Utsi, V. and E. Utsi, "Measurement of reinforcement bar depths and diameters in concrete," *Tenth International Conference on Ground Penetrating Radar*, Delft, The Netherlands, June 21–24, 2004.
11. Yufryakov, B. A. and O. N. Linnikov, "Buried cylinders geometric parameters measurement by means of GPR," *PIERS Online*, Vol. 2, No. 2, 187–191, 2006.
12. Soldovieri, F., R. Persico, E. Utsi, and V. Utsi, "The application of inverse scattering techniques to the problem of rebar location in concrete," *Non Destructive Sensing and Evaluation*, Vol. 39, No. 7, 602–607, 2006.
13. Delbμo, S., P. Gamba, and D. Roccato, "A fuzzy shell clustering approach to recognize hyperbolic signatures in subsurface radar images," *IEEE Trans. Geosci. Remote Sens.*, Vol. 38, 1447–1451, 2000.

Combining Multi-frequency GPR Images and New Algorithm to Determine the Location of Non-linear Objects with Civil Engineering Applications

M. B. Alhasanat[1], **W. M. A. Wan Hussin**[1], **and A. B. A. Hassanat**[2]

[1]School of Civil Engineering, University Science Malaysia, P. Pinang, Malaysia
[2]IT Department, Mu'tah University, Mu'tah, Karak, Jordan

Abstract— This paper proposes a new method of combining multiple radar images from different frequencies to form a composite. The method uses *MatLab* software to automatically combine GPR images. The basic image combination depends on the depth of radar wave penetration and frequency resolution. This paper also proposes and establishes a new algorithm to determine the exact depth and location of small non-linier objects.

1. INTRODUCTION

Recently, there has been a huge interest in detecting and imaging shallow surface targets in a wide variety of areas. Many researchers have attempted to improve the quality of GPR images and portray better extractions for buried objects representing the real world. Ground penetrating radar is an efficient sub-surface imaging tool using a low-cost, nondestructive methodology that is capable of detecting metal and non-metal objects [1]. Radar imaging represents a cross section view of the underground and is not like other images which represent a topical view. The GPR image shows buried objects in a hyperbolic shape; the top of the hyperbola represents the exact location of buried object. It is a well known fact that GPR images are obtained by using a single radio-wave frequency. Presently, the GPR technique is not capable of producing images using more than one radio-wave frequency for the same image. GPR signals suffer from attenuation via the loss of energy over increasing travel distance of signals between transmitter and receiver [2]. This limits the GPR mechanism with regard to resolution and penetration [3]. Besides this factor, a good understanding antennas depth ranges is also required because penetrating radar waves depend on wave length; hence, the higher the antenna frequencies $\rightarrow$ the higher the attenuation. This means that lower frequencies have a higher probability for the GPR to differentiate the object utility from background noise (clutter) [2]. In other words, although higher radar-signal frequencies produce better resolution and quality GPR images, they also lead to lesser penetration of depth in the host medium. To the contrary, lower radar signal frequencies have higher penetration at greater depth but with lower resolution.

Therefore, GPR operators have to use different frequencies to ensure better results. As a result, interpreters often encounter multiple radar images of the same object, each from different frequencies that require separate interpretations. This large amount of data obtained from GPR techniques in a measurement campaign presents a great challenge from the perspective of GPR data interpreters [4], and the volume of raw data that need interpretation also causes more of a challenge [5]. This extensive amount of data is one of GPR's limitations and relates mainly to interpreting the results [6]. There are at present and for example, many methods and algorithms for routine interpretation that feature extracting certain portions of this data pool such as hyperbolic rogation, pattern recognition and others. However, in real time good interpreters do not depend completely on such automatic methods because such potentially dangerous interpretations can cost the loss of both lives and property. Locating gas pipes and electric cables before digging should be as precise as possible and the potential dangers of an incorrect mechanized interpretation imposes the restriction of manual interpretation and human judgment. On other hand, this manual interpretation of radar images of huge amount of data with data redundancy often leads to confusion, difficulties and/or perhaps wrong interpretation.

Such limitations may prevent GPR from being widely used. This paper proposes a new method of combining all radar images reaped from different frequencies on the same foci into one. Therefore, the interpreter does not encounter same object more than once. Thus, the problem of data redundancy is treated with this method. In addition, a 3D model is generated by using only one set of radar images from the same frequency. Hence, building 3D models utilizing high frequencies will definitely not show a deeply buried pipe or cable. Thus, this new method contributes

towards getting an optimum 3D model, by constructing a single set of radar images for objects under investigation from all frequencies.

2. METHODOLOGY OF COMBINATION

This study uses different frequencies with the intent of obtaining one good image of foci under investigating with maximum resolution at maximum depth. Three phases are used that combine multi-frequency GPR images, data collection, image processing and *mat-lab* software to automatically merge radar images for the final result (Figure 1).

2.1. Data Collection

Data is collected from an artificial site using four different frequency antennas ranging from 250 MHz to 900 MHz are used to measure the foci. This obtains four different images or bands whose resolutions and penetrating depth are dissimilar. The main data for this study is raw data and such raw data as extracted from these radar images represents a cross-sectional view of the underground with a unique feature of the radar image being the hyperbola. The horizontal coordinates on the radar image represent successive radar positions and the vertical coordinates represents depth.

2.2. Image Processing

This phase is completed with the aid of the GPR software. In order to get clear visualizing and explanation of the hyperbolic shapes, image processing is applied to the raw data such as moving to Start Time to correct the zero-point of the surface in order to determine the real depth; also Filtering is applied to delete noise and clutter, and the Gain is adjusted to maximally equalize the radar signals. After the radar image is ready for interpretation, the images are saved in JPEG format according to their respective frequencies; e.g., an image from 250 MHz is saved by using 250 and so on.

2.3. MATLAB Software

A small program was designed by mat-lab that works with any number of images and is designed to deal with JPEG formatted images. The program should be saved in a folder that contains

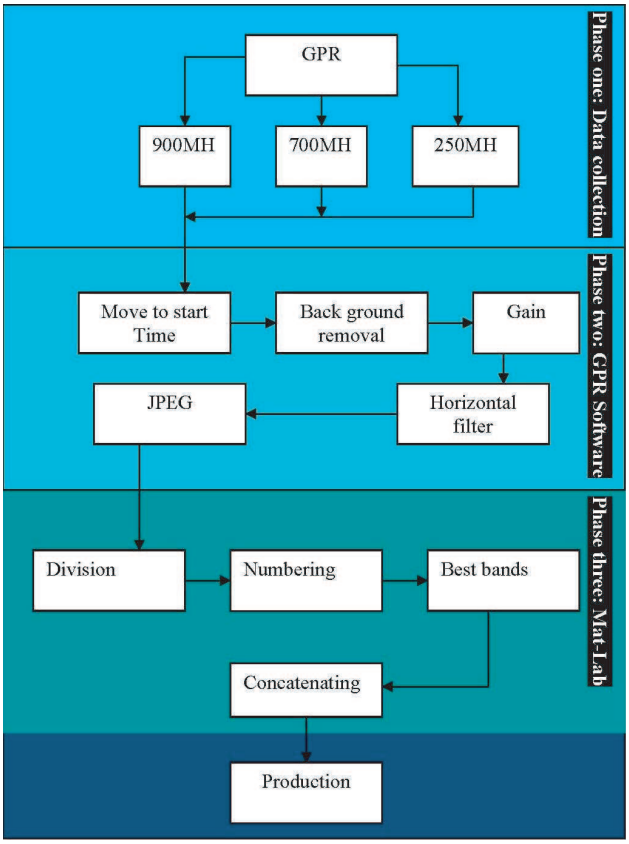

Figure 1: Methodology of combination chart.

all radar images and be ready for run. The 'Basic Image Combination' depends on radar-wave depth penetration and resolution. Therefore, each image will be subdivided and equalized to three horizontal slices with each slice at around 130 cm in depth all along the image's length no matter the slice's length. This is based on the fact that depth in radar imaging is represented from the top downwards. In this study, the division into three slices from three images is used, but if more images arise the division will also rise according to the number of images. A completed depth survey as shown by image is almost four meters, so that each slice represents about a 1.30 m component. Also, a decision to utilize three slices is because 900 MHz radio waves do not penetrate more than 1.30 m under normal conditions and 250 MHz radio waves penetrate to four meters. However, the best slices (bands) will finally be combined to obtain one image. The high frequency band widths are automatically apportioned to the top of the final image, and those from low frequencies automatically go to the bottom of the image. Remaining bands with medium frequencies lie in-between. The program is designed to take file names in descending order and after their division and will compile them in one file.

3. A NEW ALGORITHM TO DETERMINE THE LOCATION OF LINEAR OBJECTS

Regular radar image interpreters decide the exact location and depth of targets depending on a direct distance measurement from the top of the hyperbola in B-scan (Figure 2). However, in actuality that is not always the case due to a wide range of footprint from the antenna; especially those from the perpendicular axis of the survey's direction. Usually, a grid method is used to construct a 3D model, but for the two scans (Figure 3) conducted close enough to non-linear small buried objects, pipes or cables; a new algorithm is developed to help locate its exact location and depth.

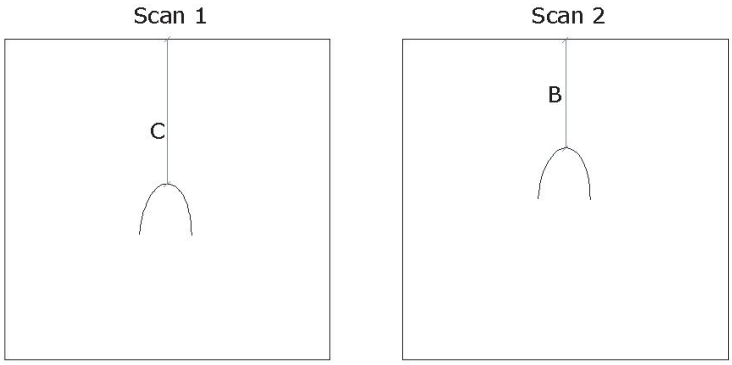

Figure 2: Direct distance measure to top of hyperbola in B-scans.

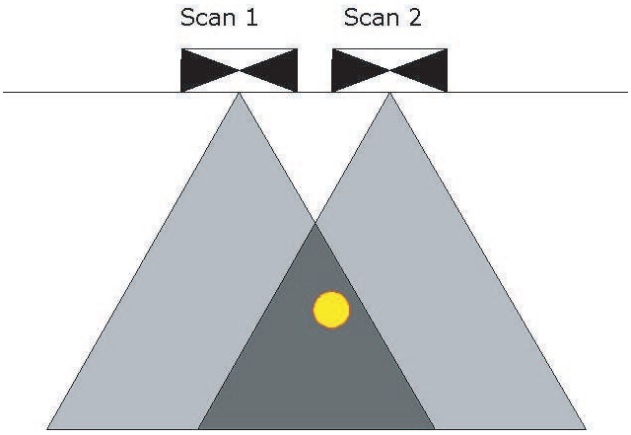

Figure 3: Two scans above non-linear target.

Comparing Figures 2 and 3, it is concluded that B-scans obviously don not represent the exact location and depth as shown in Figures 4(a) and (b).

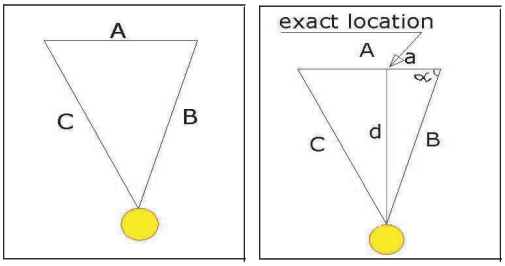

(a) (b)

Figure 4: Relationship between two scans and antenna positions.

To obtain the exact location and depth from (Figure 4(b)), the distance (d) represents exact depth, and (a) represents the distance from the antenna's position in scan 2, and that should be an exact location.

It is evident that:

$$\alpha = \arccos\left(\frac{B^2 + A^2 - C^2}{2AB}\right) \tag{1}$$

And

$$\sin\alpha = \frac{d}{B} \tag{2}$$

And

$$\cos\alpha = \frac{a}{B} \tag{3}$$

Therefore

$$a = \left(\frac{B^2 + A^2 - C^2}{2A}\right) \tag{4}$$

And

$$d = B\sin\arccos\left(\frac{B^2 + A^2 - C^2}{2AB}\right) \tag{5}$$

4. CONCLUSIONS

The new method will contribute towards obtaining an optimum 3D model through the use of only one set of radar images of objects under investigation utilizing all frequencies. In addition, data redundancy is treated in this paper. The new combination of a multi-frequency GPR image is not an alternate radar image, but represents an extremely useful pilot study for ongoing underground utilities and highway studies, and also allows for GPR to be a helpful tool in disaster management when needed. The proposed algorithm for exact location and depth is proven and it can be used on-site. The calculation is also very simple and it can be done either manually or via Excel software. The distance (A) between the two scans is decided already by the operator.

REFERENCES

1. Gurbuz, A. C., "Feature detection algorithms in computed images," Ph.D. Thesis, Georgia Institute of Technology, 2008.
2. Thomas, A., C. Rogers, D. Chapman, N. Metje, and J. Castle, "Stakeholder needs for ground penetrating radar utility location," *Journal of Applied Geophysics*, Vol. 67, No. 4, 345–351, 2009.
3. Lawrence, B. C., "Ground-penetrating radar processing and interpretation techniques for archaeology," *Fast Times*, Vol. 13, No. 3, 29–35, 2008.
4. Gamba, P. and S. Lossani, "Neural detection of pipe signatures in ground penetrating radar images," *IEEE Transactions on Geoscience and Remote Sensing*, Vol. 38, No. 2, 790–797, 2002.
5. He, X.-Q., Z.-Q. Zhu, Q.-Y. Liu, and G.-Y. Lu, "Review of GPR rebar detection," *PIERS Proceedings*, 804–813, Beijing, China, March 23–27, 2009.
6. Loulizi, A., "Development of ground penetrating radar signal modeling and implementation for transportation infrastructure assessment," Ph.D. Thesis, Blacksburg, Virginia Polytechnic Institute and State University, 2001.

Matching Technique Design for Multi-fed Full Wave Dipole Antenna

Yahya S. H. Khraisat[1, 2], **Khedher A. Hmood**[3], **and A. Anwar**[3]

[1]Electrical and Electronics Department, Al-Huson University College, Al-Balqa Applied University, Jordan
[2]Hijjawi Faculty for Engineering Technology, Telecommunications Engineering Department
Yarmouk University, P. O. Box 1375, Irbed 21110, Jordan
[3]School of Electrical and Electronic Engineering, Engineering Campus
Universiti Sains Malaysia, Seri Ampangan, Nibong Tebal 14300, Penang, Malaysia

Abstract— This paper is focused on the derivation of equations for a full-wave dipole antenna based on feeding techniques. The current distribution was measured, followed by the measurement of parameters of antenna like gain, radiation patterns and input impedance. Based on these observations four equations for current distribution were eventually formulated. These equations were then used to compute the values of the same parameters of the antenna. Finally, the values of parameters obtained practically and theoretically were compared to analyse the validity of the developed equations.

1. INTRODUCTION

In this paper, it was found that the full-wave antenna offers a high gain by devising the feeding and applying multi feeding instead of one. Novel design methodologies and implementation techniques for full wave antennas with dual and triple feeding are studied.

For a true harmonic operation, it is necessary that power is to be fed into the antenna is at an appropriate point. A full wave dipole antenna was to be fed by various methods. These methods can be classified into three categories; namely, symmetrical dual feeding, asymmetrical dual feeding and symmetrical trouble feeding. The analysis of the parameters of asymmetrical dual feeding full wave dipole antenna was discussed at Microwave Radar and Remote Sensing conference MRRS 2008 [1].

The current distributions were measured using a shielded loop [2] and [3] protruding through a slit in the antenna surface along its axis that gave exact and accurate measurement rather than sinusoidal distribution. The sinusoidal distributions of current and voltage are approximations rather than exact descriptions [4] and [5].

Next, the current distributions were modeled and formulated whose parameters were deduced from the measured current distribution by applying the current distribution data in models as derived by IEEE standard. According to [6], it is difficult to apply directly measured data in the forms derived by same authors.

2. DEVELOPMENT OF EQUATION FOR CURRENT DISTRIBUTION

This section presents results from an experimental investigation of current distribution test. This investigation serves to experimentally find the current distribution wave form, and to obtain formulas by using curve fitting and trial and error methods. The relative magnitude of the current distribution along the antennas was measured and normalized with respect to maximum amplitude. The measurements were conducted on half-wave dipole which is well known in its characteristics, on center-tap full-wave and on off-center full-wave dipole. Figure 1 shows the current distribution for Symmetrical dual feeding in-phase.

Curve fitting, trial and error were used to obtain formulated four equations that expressed in the following sections. Equations (1), (2), (3) and (4) represent the mathematical expression of the current distribution for Symmetrical dual feeding in-phase, Symmetrical dual feeding out-of-phase, asymmetrical dual feeding in-phase, and asymmetrical dual feeding out-of-phase respectively.

$$I(z) = \sin\beta\left(\frac{L}{2} - /z/\right) \tag{1}$$

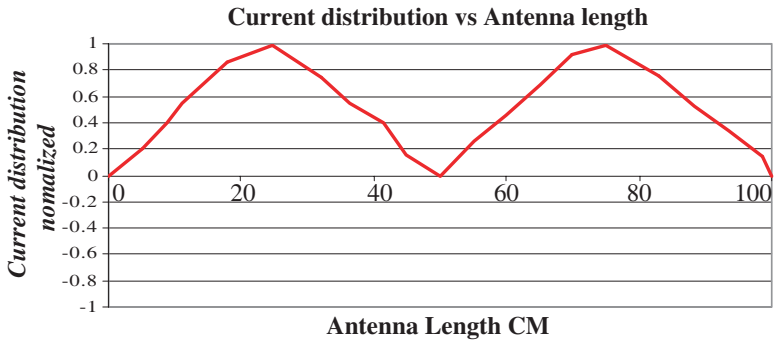

Figure 1: Measured current distribution for symmetrical dual feeding in-phase.

3. DERIVATION OF EQUATIONS FOR RADIATION PATTERN, GAIN, AND RADIATION RESISTANCE

According to the thin wire approximation and Maxwell Equations, the z-component of the radiated electric field for infinitesimal dipole is shown in Figure 2 and depicted in Equation (5) [7].

$$dE_\theta = \frac{j60\pi e^{j\omega(t-\frac{r}{c})} I(z)\sin\theta e^{jk(z\cos\theta)}}{\lambda r} dz \tag{2}$$

In the pervious section the current distribution model obtained is presented in Equation (1). This Equations is used to derive the radiation pattern of antenna.

Referring to pervious section, the predicated Equation for the current distribution is:

$$I(z) = I_{\max}\sin\beta\left(\frac{L}{2} - /z/\right)$$

where $\beta = 2^{\pi/\lambda}$. Expressions of the current distribution are as given below:

$$I = I_{\max}\sin\beta\left(\frac{L}{2} - z\right), \quad z \geq 0 \tag{3}$$

$$I = I_{\max}\sin\beta\left(\frac{L}{2} + z\right), \quad z \leq 0 \tag{4}$$

Substituting Equations (3) and (4) in Equation (2), yields

$$E_\theta = \int_{\frac{-l}{2}}^{0} \sin\left[k\left(\frac{l}{2}+z\right)\right] e^{jkz\cos\theta} dz + \int_{0}^{\frac{1}{2}} \sin\left[k\left(\frac{l}{2}-z\right)\right] e^{jkz\cos\theta} dz \tag{5}$$

Using Equation (6) to solve the Equation (5) gives Equation (7) [7]

$$\int e^{\alpha x}\sin(\beta x+\gamma)dx = \frac{e^{\alpha x}}{\alpha^2+\beta^2}\left[\alpha\sin(\beta x+\gamma) - \beta\cos(\beta x+\gamma)\right] \tag{6}$$

$$E_\theta = \frac{j\pi 60 I_0 e^{-j\omega(t-\frac{r}{c})}}{r}\left[\frac{\cos\left(\frac{\beta l}{2}\cos\theta\right) - \cos\left(\frac{\beta l}{2}\right)}{\sin\theta}\right] \tag{7}$$

In this study $L = \lambda = 1$. Substituting $\lambda = 1$ and simplifying Equation (7), yields

$$E_\theta = \frac{j60 I_0 e^{j\omega(t-\frac{r}{c})}}{r}\left[\frac{\cos(\pi\cos\theta)+1}{\sin\theta}\right] \tag{8}$$

$$H_\varphi = \frac{j60 I_0 e^{j\omega(t-\frac{r}{c})}}{2\pi r}\left[\frac{\cos(\pi\cos\theta)+1}{\sin\theta}\right] \tag{9}$$

Equations (8) and (9) represent the radiation pattern of E_θ and H_φ respectively for antenna A_1.

The total radiated power is:

$$\frac{1}{2}\mathrm{Re}\int_0^{2\pi}\int_0^{\pi} E_\theta H_\varphi^* r^2 \sin\theta d\theta d\varphi \tag{10}$$

$$H_\varphi = \frac{E_\theta}{\eta_o} \tag{11}$$

Substituting Equations (8) and (9) in Equation (10), yields

$$p = 60I_o^2 \int_0^{2\pi} \left[\frac{\cos(\pi\cos\vartheta)+1}{\sin\theta}\right]^2 \sin\theta d\theta \tag{12}$$

For numerical analysis and calculation, Matlab and MathCAD software were used to simplify Equation (12) and the derivation of the gain is

$$E_{\max} = \frac{120I_o}{r} \tag{13}$$

$$P = \int \frac{E^2}{120\pi} da \tag{14}$$

where $da = 2\pi r^2 \sin\theta d\theta$

$$p = \int_0^{2\pi} \frac{60^2 I_o^2}{120\pi r^2}\left[\frac{\cos(\pi\cos\theta)+1}{\sin\theta}\right]^2 2\pi\cdot r^2\sin\theta d\theta \tag{15}$$

$$p = 60I_o^2 \int_0^{2\pi} \left[\frac{\cos(\pi\cos\vartheta)+1}{\sin\theta}\right]^2 \sin\theta d\theta \tag{16}$$

Let $\cos\theta = u$, $\sin^2\theta = 1-u^2$, and $\sin\theta d\theta = du$

$$P = 60I_o^2 \int_{-1}^{1} \frac{(\cos(\pi u)+1)^2}{1-u^2} du \tag{17}$$

$$= 60I_o^2 \int_{-1}^{1} \left[\frac{\cos^2(\pi u)^2}{1-u^2} + \frac{2\cos(\pi u)}{1-u^2} + \frac{1}{1-u^2}\right] du \tag{18}$$

Let $1+u = \frac{v}{\pi}$, $du = dv/\pi$, $1-u = \frac{v'}{\pi}$, $du = dv'/\pi$

$$= 60I_o^2 \int_0^{2\pi} \left[\frac{\cos^2(v-\pi)}{v} + \frac{2\cos(v-\pi)}{v} + \frac{1}{v}\right] dv \tag{19}$$

$$= 60I_o^2 \int_0^{2\pi} \left[\frac{\frac{1}{2}(1+\cos 2v)}{v} - \frac{2\cos(v)}{v} + \frac{1}{v}\right] dv \tag{20}$$

$$P = 60I_o^2 \left[2\int_0^{2\pi}\left(\frac{(1-\cos v)}{v}\right)dv - \frac{1}{2}\int_0^{2\pi}\left(\frac{1-\cos(2v)}{v}\right)dv\right] \tag{21}$$

$$P = 60I_o^2 \left[2\int_0^{2\pi}\left(\frac{(1-\cos v)}{v}\right)dv - \frac{1}{2}\int_0^{2\pi}\left(\frac{1-\cos(2v)}{v}\right)dv\right] \tag{22}$$

$$P = 60I_o^2 \left[2\int_0^{2\pi}\left(\frac{(1-\cos v)}{v}\right)dv - \frac{1}{2}\int_0^{4\pi}\left(\frac{1-\cos(y)}{y}\right)dy\right] \tag{23}$$

$$P = 60I_o^2 \left[2(0.557+\ln(2\pi)-Ci(2\pi)) - \frac{1}{2}(0.577+\ln(4\pi)-Ci(4\pi))\right] \tag{24}$$

$$P = 60I_o^2\left[2(0.557+1.837-0.023)-\frac{1}{2}(0.577+2.531-0.006)\right] \quad (25)$$

$$P = 60I_o^2[3.319] = 199.1I_o^2 \quad (26)$$

$$P = 199.1I_o^2 = I_o^2R_{rad} \quad (27)$$

$$R_{rad} = 199.1\Omega \quad (28)$$

To determine $E_{\max}$, the function $[\frac{\cos(\pi\cos\theta)+1}{\sin\theta}]$ approaches its maximum as $\theta \to \pi/2$ and approaches zero as $\theta \to 0$ and π, thus

$$E_{\max} = \frac{j60I_oe^{-j\omega\left(t-\frac{r}{c}\right)}}{r}\left[\frac{\cos\left(\pi\cos\frac{\pi}{2}\right)+1}{\sin\frac{\pi}{2}}\right] \quad (29)$$

$$E_{\max} = \frac{j60I_oe^{-j\omega\left(t-\frac{r}{c}\right)}}{r}\left[\frac{1+1}{1}\right] \quad (30)$$

$$E_{\max} = \frac{120I_o}{r} \quad (31)$$

Equation (32) can be used to calculate the gain [8, 9].

$$G = \frac{E_{\max}^2r^2}{30P} \quad (32)$$

Substituting Equations (27) and (31) in Equation (32), yields

$$G = \frac{E^2r^2}{30P} = \frac{120I_o^2r^2}{30I_o^2199.1} = 2.41 \quad (33)$$

$$G = 10\log(2.41) = 3.82\,\text{dBi} \quad (34)$$

Half-power beam width is the angle between two solutions of Equation (8) [10].

$$\left[\frac{\cos(\pi\cos\theta)+1}{\sin\theta}\right] = \frac{1}{\sqrt{2}}; \quad 0 \le \theta \le \pi$$

Solving Equation (35) for θ and the numerical solution gives $\theta \approx 124^\circ$ and 66° and the half-power beam width of $124^\circ - 66^\circ = 48^\circ$.

4. CONCLUSIONS

Expressions for the current distribution, gain, and radiation patterns of full-wave dipole antennas were developed. The relation of the current distribution with the feeding modifications and the polarity of feeding were numerically and experimentally investigated. The expressions for current distribution were developed, and validated, and compared with the experimental results.

For symmetrical dual feeding in-phase, the equation of the current distribution is found to be similar to the conventional full-wave antenna Equation. For symmetrical dual feeding out-of-phase, the Equation follows the theoretical concept of the full-wave antenna (off-center fed). However, the Symmetrical feeding in-phase achieved 3.82 dBi gains.

REFERENCES

1. Yahya, S., H. Khraisat, K. A. Hmood, and A. Anwar, "Analysis of the parameters of asymmetrical dual feeding full wave dipole antenna," *Microwave and Remote Sensing Symposium (MRRS 2008)*, Kiev, Ukraine, September 22–24, 2008.
2. Edwards, H. N., "The measurement of current distribution in aerials at VHF," *Proc. I.R.E. Australia*, 351–355, 1963.
3. King, R. W. P. and G. S. Smith, *Antenna in Matter*, MIT Press, Cambridge, MA, 1981.
4. Hassan, S. I. S., "Matching in rhombic and pseudo rhombic antennae," Ph.D. Thesis, University of Exeter, 1987.
5. Idris, S. H., C. M. Hadzer, and M. Z. A. Ghgani, "A full-wave dipole antenna for mobile terminal application," *Technical Journal*, Vol. 8, EE-USM, 1999, ISNN 1594-6153.

6. Takamizawa, K., W. A. Davis, and W. L. Stutzman, "Novel techniques for analysis of array antenna," *UNSNC/URS. National Radio Science Meeting*, 176, CDROM, Boston, MA, 2001.
7. Balanis, C. A., *Antenna Theory-Analysis and Design*, 2nd Edition, John Willy & Sons Inc., 1997.
8. Irdis, S. S. H., "Antena dan perambatan," Pust Pengajian Kejuruteraan Elektrik dan Elektronik, Universiti Sains Malaysia, 1997.
9. Miller, E. K. and F. J. Deadrick, *Some Computational Aspects of Thin-Wire Modeling*, R. Mittra, editor, Springer-Verlag, New York, 1975.
10. Idris, S. H. and C. M. Hadzer, "Analysis of the radiation resistance and gain of full-wave dipole," *IEEE Antenna and Propagation Magazine,* Vol. 36, No. 5, 1994.
11. Idris, S. H., C. M. Hadzer, and M. Z. A. Ghgani, "A full-wave dipole antenna for mobile terminal application," *Technical Journal*, Vol. 8, EE-USM, 1999, ISNN 1594-6153.

Accurate Approximation of Error Probability for Two Types of Adaptive Antenna-based Receivers over Fading Channels

R. Haddad and R. Bouallèguee
Laboratory Research in Telecommunication 6'Tel, High School of Communication of Tunis, Tunisia

Abstract— Multipath fading and Multiple Access Interference (MAI) are the major constraints on the performance of wireless communication systems. Antenna arrays have been considered to increase the system capacity through mitigation of such impairments. In this paper, we focused our research on the performance of two kinds of smart antenna receivers in order to gain from the enhancements of both: multiuser detection and adaptive antenna.

1. INTRODUCTION

The use of adaptive antennas dates back to the 50's with their applications to radar and anti-jam problems. The primary goal of adaptive antennas is the automatic generation of beams (beamforming) that track e desired signal and possibly reject (or "null") interfering sources through linear combining of the signals captured by the different antennas.

Besides beamforming, another application of antenna arrays in Direction-of-arrival (DOA) estimation for source or target localization purposes. The leading DOA estimation methods are the MUSIC and ESPRIT algorithms [1].

In our paper, we propose a novel approach to evaluate the average probability of error (BER) formula in the context of asynchronous transmission for two types of receivers: the BPSK smart antenna receiver and the OQPSK smart antenna receiver. The proposed model is shown to provide the performance of the complex smart antenna receivers in Rayleigh as well as Ricean fading channels under different conditions [2–4].

Simulation results presented for the two types of receivers, under varying a variety of user, antenna and channel scenarios, confirm the validity and accuracy of the analytical results.

Our analysis is based on modeling the angular gain of the spatial filter that approximates the pass-band (or in-beam) and the stop-band (or out-beam) with an equivalent attenuation. The proposed model confirms the benefits of adaptive antennas in reducing the overall interference level (intercell/intracell) and to find an accurate approximation of the error probability.

In the two kinds of receivers, we assessed the impact of smart antenna systems and we considered the case of conventional single antenna receiver model as reference (single user/single antenna).

The outline of the paper is as follows: In Section 2, we introduce the system model followed by the channel models for the two types of receivers in Section 3. The average probability analysis and computation results are provided in Section 4, we conclude in Section 5.

2. SYSTEM MODEL

2.1. Signal Model with BPSK Modulation

The base band equivalent model is considered for asynchronous modulation waveforms $S_1(t)$, $S_2(t)$, ..., $S_K(t)$. The transmitted signal of the Kth user is:

$$x_k(t) = \sum\nolimits_i b_k^i S_k(t - iT) \tag{1}$$

$b_k^i \in \{-1, +1\}$ is the ith transmitted BPSK symbol and T is the symbol interval. The user's signal $x_k(t)$ propagates through a multipath channel, θ_k is the DoA of the kth user. The impulse response can be written as:

$$h_k(t) = \sum\nolimits_{m=1}^{L} \alpha_{k,m}\delta(t - \tau_{k,m}) \tag{2}$$

wherein $\alpha_{k,m}$ and $\tau_{k,m}$ are the complex gain and delay of the mth path. We assume that all the users have the same number of paths L, the delay $\tau_{k,m} \in [0, T]$ have increasing values: $0 \leq \tau_{k,1} \leq \tau_{k,2} \leq \ldots \leq \tau_{k,L} < T$, for $\forall k$.

Wherein $a(\theta_k)$ is the $M \times 1$ vector that describes the array response to the DoAθ_k, and the nth element for a linear of half-wavelength spaced antennas is:

$$[a(\theta_k)]_n = \exp(-j(n-1)\pi \sin\theta_k) \tag{3}$$

At the receivers, the $M \times 1$ vector of that received signal for the kth user.

$$r_k(t) = a(\theta_k) h_k(t) * x_k(t) \tag{4}$$

$$r_k(t) = a(\theta_k) \sum\nolimits_i b_k^i \sum\nolimits_{m=1}^{L} \alpha_{k,m} S_k(t - iT - \tau_{k,m}) \tag{5}$$

The received signal of the K users' signal can be written as:

$$r(t) = \sum\nolimits_{k=1}^{K} r_k(t) + \sigma n(t) \tag{6}$$

The noise $n(t)$ is assumed to be a zero-mean temporally and spatially uncorrelated Gaussian process, with $E[n \cdot n^*] = I \cdot \delta(\tau)$, σ^2 is the power of the AWGN. We assume that the spatial correlation of noise arising from intercell interference is not considered.

2.2. Signal Model with OQPSK Modulation

We assume that the MS transmitter of each user employs Offset Quadrature Phase Shift Keying (OQPSK) M-ary orthogonal modulation. The OQPSK modulation can be viewed as two independent BPSK signals.

The resultant signal goes into the in-phase (I) and quadrature (Q) channels simultaneously.

The transmitted signal s_k of the kth user can be written as [5]:

$$s_k(t) = W_k^{(q)}(t) a_k^{(I)}(t) \cos(\omega_c t) + W_k^{(q)}(t - T_0) a_k^{(Q)}(t - T_0) \sin(\omega_c t) \tag{7}$$

where $q = 1, 2, \ldots, Q$, $W_k^{(q)}(t)$ is a Hadamard-Walsh function of dimension Q which represents the qth orthogonal signal of the kth user's long code sequence, $ak(t)$ is the kth user's long code sequence, $a_k^{(I)}(t)$ and $a_k^{(Q)}(t)$ are the in-phase and quadrature phase pseudo-noise (PN) sequences, $T_0 = T/2$ is the delay for OQPSK signals. The power of each user is assumed unity (perfect power control). To simplify our study the PN codes are presented as follows:

$$a_k^{(I)}(t) = \sum_r a_{k,r}^{(I)}(t) p(t - T_C) \tag{8}$$

$$a_k^{(Q)}(t) = \sum_r a_{k,r}^{(Q)}(t) p(t - T_C) \tag{9}$$

where $a_{k,r}^{(I)}$ and $a_{k,r}^{(Q)}$ are i.i.d variables taking the values ± 1 with equal probability and $p(t)$ is the chip pulse shape which is assumed to be rectangular. The Equation (7) can be written as follows:

$$\begin{aligned} s_k(t) &= \mathcal{R}\left\{ \left[W_k^{(q)}(t) a_k^{(I)}(t) + j W_k^{(q)}(t - T_0) a_k^{(Q)}(t - T_0) \right] e^{-j\omega_c t} \right\} \\ s_k(t) &= \mathcal{R}\left\{ \widetilde{s_k}(t) e^{-j\omega_c t} \right\} \end{aligned} \tag{10}$$

where $\widetilde{s_k}(t) = S_k^{(I)}(t) + j S_k^{(Q)}(t)$ is the complex low pass equivalent of the transmitted signal.

The kth user propagates through a multipath channel with (AoA) θ_k. The complex equivalent representation of the channel impulse response between the lth multipath of the kth user and the nth element of array antenna is presented as follows:

$$\begin{aligned} \tilde{h}_{k,l,n}(t) &= \beta_{k,l} e^{-j(\Phi_{k,l} + 2\pi \frac{d}{\lambda}(n-1)\sin\theta_k)} \delta(t - \bar{\tau}_{k,l}) \\ \tilde{h}_{k,l,n}(t) &= \beta_{k,l} e^{-j\varphi_{k,l,n}} \delta(t - \bar{\tau}_{k,l}) \end{aligned} \tag{11}$$

where $\beta_{k,l}$, $\Phi_{k,l}$ and $\bar{\tau}_{k,l}$ are the path gain, phase and delay respectively, $\varphi_{k,l,n}$ is the overall phase which includes the path phase and the difference in propagation delays between the antennas. In this case of transmitter we assume that path gains follow the Rayleigh and Ricean distributions respectively.

To simplify our work, we assume that multipath channel parameters $\beta_{k,l}(t)$ and $\varphi_{k,l,n}(t)$ remain constant in the duration of Walsh symbol [6], so $\beta_{k,l}(t) = \beta_{k,l}$ and $\varphi_{k,l,n}(t) = \varphi_{k,l,n}$ for $t \in [0, T_W]$, where T_W is the Walsh symbol period.

3. ACCURATE ERROR PROBABILITY ANALYSIS

3.1. Error Probability for BPSK Receiver Model

In CDMA system with adaptive antenna array of antennas, the effect of spatial filter is to enhance the differences in the power of interfering users. The average error probability of a generic adaptive antenna receiver is given by [3]

$$P_e^{(2-D)}(E) = \sum_{K_I=0}^{K-1} \eta^{K_I} \chi(\eta, K, K_I) \begin{pmatrix} K-1 \\ K_I \end{pmatrix} P_e^{(1-D)}(E) \tag{12}$$

where K_I denotes the number of in-beam interferers, $(K - K_I - 1)$ is the number of out-beam interferers, $P_b^{(1-D)}$ is the probability of bit error for the scalar (single) antenna receiver, depends on the Beamforming criterion exploited and χ are defined as [3]

$$\eta = \frac{2\theta_{BW}}{\Delta\theta} \tag{13}$$

$$\chi = (1-\eta)^{K-K_I-1} \tag{14}$$

3.1.1. Error Probability in No-fading Channels

The average error probability for asynchronous CDMA systems has been widely investigated. A simple but accurate approximation was derived under the Gaussian approximation (for random spreading sequence of length N) with $M = 1$ is given by [3]:

$$P_e^{(1-D)}(E) = Q\left[\left(\frac{\sigma^2}{A^2} + \frac{K_I}{3N}\right)^{-1/2}\right] = \frac{1}{2}\left(1 - \frac{1}{\sqrt{1 + \frac{\sigma^2}{A^2} + \frac{K_I}{3N}}}\right) \tag{15}$$

The error probability for an adaptive array of M antennas can be obtained by substituting (15) in (12) gives an approximation for the error probability for an adaptive antenna array receiver.

$$P_e^{(2-D)}(E) = \sum_{K_I=0}^{K-1} \eta^{K_I} \chi(\eta, K, K_I) \begin{pmatrix} K-1 \\ K_I \end{pmatrix} Q\left[\left(\frac{\sigma^2}{MA^2} + \gamma(K_I)\right)^{-1/2}\right] \tag{16}$$

where $\gamma(K_I) = \frac{K_I}{4N} + \alpha_0 \frac{K-K_I-1}{3N}$ denotes the equivalent noise increasing due to the multi-access interference.

3.1.2. Error Probability in Rayleigh Fading Channels

In this section, we extend the concepts discussed above to the Rayleigh fading case.

The error probability of BPSK for propagation over Rayleigh faded channel ($K = 1$ and $M = 1$) is given by [7, 8]:

$$P_e^{(1-D)}(E) = \frac{1}{2}\left(1 - \frac{1}{\sqrt{1 + \frac{\sigma^2}{\sigma A^2}}}\right) \tag{17}$$

The overall impairment is the superposition of the AWGN and K_I interferers.

The error probability for asynchronous CDMA with K_I interferers is equivalent to the error probability for two fictitious interferers per actual interferer [9], thus doubling the overall number of interferers. The power of the interference (for random spreading sequence of length N) is ${\sigma_I}^2 = 2{\sigma_A}^2 K_I/3N$. The error probability of the asynchronous CDMA system for Rayleigh fading channel and with one antenna becomes:

$$P_e^{(1-D)}(E) = \frac{1}{2}\left(1 - \frac{1}{\sqrt{1 + \frac{\sigma^2}{\sigma_A^2} + \frac{2K_I}{3N}}}\right) \tag{18}$$

The error probability for an adaptive array of M antennas can be obtained by substituting (18) to (12) and increasing the overall noise to signal ratio accordingly:

$$P_e^{(2-D)}(E) = \sum_{K_I=0}^{K-1} \eta^{K_I} \chi(\eta, K, K_I) \begin{pmatrix} K-1 \\ K_I \end{pmatrix} Q\left[\left(\frac{\sigma^2}{M{\sigma_A}^2} + \gamma(K_I)\right)^{-1/2}\right] \tag{19}$$

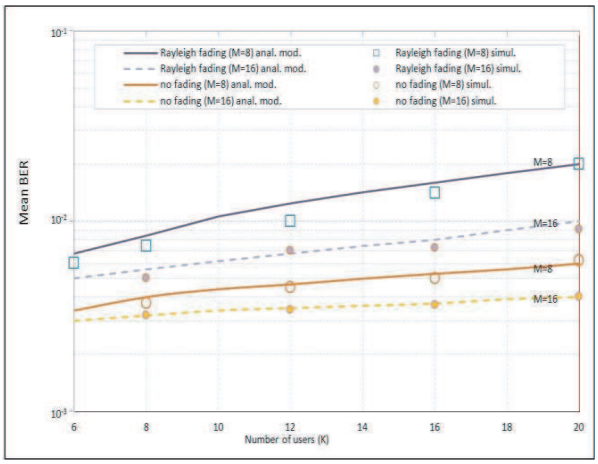

Figure 1: Average BER versus the number of users K for no-fading and Rayleigh fading channels for $L = 1$ path, $M = 8$, 16 antennas.

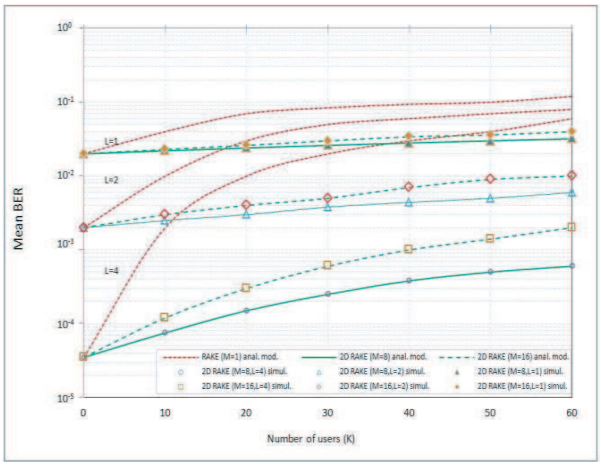

Figure 2: Average BER versus the number of users K in multipath $L = 1, 2, 4$ for Rayleigh fading channels $M = 8$ and 16 antennas

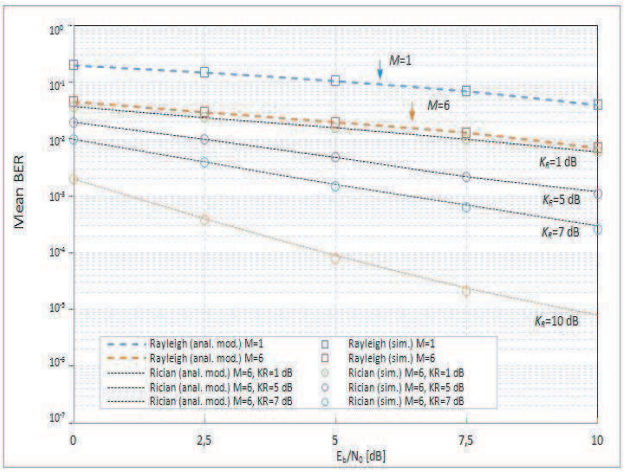

Figure 3: Average BER versus E_b/N_0 for $M = 6$ antennas, $K = 1$ with $L = 1$ path for Ricean and Rayleigh fading channels (for Ricean fading $K_R = 1, 5, 7, 10$ dB).

where $\gamma(K_I) = \frac{K_I}{2N} + 2\alpha_0 \frac{K-K_I-1}{3N}$.

4. COMPUTATION RESULTS AND DISCUSSION

4.1. Simulation Results for BPSK Receiver

Figure 1 illustrates the average BER versus the number of users K for no-fading and Rayleigh fading channels ($L = 1$ path), for $M = 8, 16$ antennas. It can be noticed that the same average BER can be obtained by doubling the number of antennas M and the number of users K either for no-fading or fading channels.

Figure 2 shows the average BER versus the number of users K for propagation over L paths frequency selective Rayleigh fading channel (for $L = 1, 2, 4$). The figures demonstrate either for varying SNR (previous section) or increasing number of users that multipath channels (large L) and angular diversity can significantly improve the performance when exploited jointly.

Figures 1 and 2, illustrate both the effect of varying the number of users and the number of antennas by doubling the number of antennas in each case ($M = 8$ and 16). Also, it can be noticed that the same average BER can be obtained by doubling the number of antennas M and the number of users K either for no-fading or Rayleigh fading channels (for $L = 1$). Therefore, as a rule of thumb, the average performance (or the level of the in-beam interference) remains the same as far as the ratio M/K remains constant.

4.2. Simulation Results for OQPSK Receiver in Ricean Fading Channels

Figure 3 shows the average BER versus E_b/N_0 for $M = 8$ antennas, $K = 1$ user with single path assuming Ricean fading with Rice factor $K_R = 1, 5, 7, 10\,\text{dB}$ respectively. We also show as reference the performance in Rayleigh fading (corresponding to $K_R = -\infty\,\text{dB}$) and conventional receiver ($M = 1$ with no Beamforming).

From Figure 3, it can be noticed that Beamforming improves the performance of the system. We realize that for low values of Rice factor, the performance is very close to the performance in Rayleigh fading. However for larger Rice factors, there is a tremendous improvement in the average BER. The simulation results show good agreements with analytical results for different Ricean factors.

5. CONCLUSIONS

This paper focused on the performance of smart antenna receiver with two types of modulation in the transmitted model (BPSK modulation and non-coherent M-ary orthogonal modulation) in Rayleigh and Ricean fading environments.

A simple analytical model has been proposed which evaluates merely the BER performance using a closed-form expression. The results obtained using this analytical model show good agreements with the simulation results.

An important parameter of the Adaptive antenna receiver with regards to quality and capacity of reducing interference is the number of users. That's why; we focused our work in varying the number of users and also to compare the BER performance. In the two cases, we assessed the impact of smart antenna systems, we considered the case of conventional single antenna receiver model as reference (single user/single antenna lower band for AWGN).

Also, we showed in simulations that we can influence in the number of antennas to evaluate BER. The BER is expected to fall well below the optimum when more number of antennas is used, but with a trade-off of increased cost and complexity. Besides, we noticed that the average performance (or the level of the in-beam interference) remains the same as far as the ratio M/K remains constant.

A continuation of the study, which we have already started, is to evaluate the average BER in forward link (base to mobiles) where each user experience the same temporal channel for all the received signals. In this case, the beamforming at the base station is decoupled from the receiver at the mobile terminals. In addition, the beamforming design could be synergic with the MUD receiver at mobiles.

REFERENCES

1. Balanis, C. A. and P. I. Ioannides, *Introduction to Smart Antennas*, Morgan and Claypool Publishers, 2007.
2. Haddad, R. and R. Bouallègue, "BER performance evaluation of two types of antenna array-based receivers in a multipath channel," *International Journal of Computer Networks & Communications (IJCNC)*, Vol. 2, No. 6, November 2010.
3. Haddad, R. and R. Bouallègue, *Exact BER Performance of Antenna Array-Based Receiver Using Multi-user Detection in a Multipath Channel*, Springer-Verlag, Berlin, Heidelberg, 2010.
4. Piazza, D., N. J. Kirsh, and A. Forenza, "Design and evaluation of a reconfigurable antenna array for MIMO systems," *IEEE Transactions on Antennas and Propagation*, Vol. 56, No. 3, 869–881, March 2008.
5. Bjerke, B. A., Z. Zvonar, and J. G. Proakis, "Antenna diversity combining aspects for WCDMA systems in fading multipath channels," *IEEE Transactions on Wireless Communications*, Vol. 3, No. 1, 97–106, 2004.
6. Monzigo, A. R. and T. Miller, *Introduction to Adaptive Arrays*, Sci. Tech. Publishing, 2004.
7. Spagnolini, U., "A simplified model for probability of error in DS/CDMA systems with adaptive antenna arrays," *Proc. IEEE International Conference on Communications (ICC)*, 2271–2275, June 2001.
8. Rappaport, T. S., *Wireless Communications: Principles and Practice*, 2nd Edition, Prentice Hall, 2002.
9. Stuber, G. L., *Principles of Mobile Communication*, 2nd Edition, Kluwer Academic Publishers, 2001.